



Shrikrishna Education Society's

SHRIKRISHNA MAHAVIDYALAYA, GUNJOTI

Tq. Omerga, Dist. Osmanabad




1.3.1 Institution integrates crosscutting issues relevant to Professional Ethics, Gender, Human Values, Environment and Sustainability into the Curriculum

1.3.1 Crosscutting related issues Part B

Plagiarism Check List

Index

Sr.No	Name of the Teacher	Page No
1.	Prof (Dr).K.S.Lohar	01-199
2.	Prof. (Dr). R.H.Kadam	200-481
3.	Prof. (Dr). S.M.Patange	482-595


Co-Ordinator
Internal Quality Assurance Cell
S.K.M. Gunjoti - 413 613
Dist. Osmanabad (M.S.)
IQAC Coordinator




PRINCIPAL
SHRIKRISHNA MAHAVIDYALAYA
GUNJOTI, TAL. OSMANABAD (M.S.)
Principal

Prof.(Dr.)K.S.LOHAR

Manuscript_for_plagarism corrected.docx

Synthesis, Structural and magnetic Properties of Ni²⁺ and In³⁺ doped Cobalt Ferrite

Abstract:

The substitution of In³⁺ ion in the Ni-Co ferrite were prepared having the chemical composition ($x = 0.0, 0.25, 0.5, 0.75, 1.0$; $y = 0.0, 0.03, 0.06, 0.08, 0.1$). The TGA/DSC pattern showed three major weight losses. At 600 °C the complete ferrite phase formation appears. The EDAX pattern of In³⁺ doped Ni-Co ferrite nano particles confirmed by stoichiometric composition of elements used in the ferrite synthesis. The XRD pattern shows some secondary phase with single phase cubic spinel. Lattice constants increase as increase in In³⁺ ions content. X-ray density increase whereas bulk density decreases. Infrared spectroscopy of synthesized samples shows absorption bands 'ν₂' around 400 cm⁻¹ and 'ν₁' at 600 cm⁻¹ are allocated to the intrinsic stretching vibrations of octahedral and tetrahedral complexes respectively. Scanning electron microscopy was applied to study the surface characteristics and uniform distribution of particle size and also prepared samples are porous in nature. Transmission electron microscopy carried out to obtain the particle size of synthesized ferrite samples and selected area electron diffraction pattern clearly shows that particles were well crystalline in nature. Magnetic measurements of ferrite nanoparticles were done by vibrating sample magnetometer (VSM). Preparation of bis-(indolyl) methane derivatives by utilizing Indole(1), aromatic aldehydes (2), using 40 mol % ($x = 1.0$; $y = 0.10$) nanoparticles as catalyst. The compound isolated with 88 % in 70 min.

1. Introduction

Spinel ferrites materials with a chemical formula AB_2O_4 has a commercial significant due to their outstanding electrical and magnetic characteristics [1]. These characteristics make spinel ferrite appropriate for various device applications viz; ¹² magneto-optic sensors, anode for batteries, sensors and catalysts, lasers, ²⁵ phosphorescent sources, microwave absorber, pigments etc. These properties of ferrites are highly subtle to the dopant composition and the processing conditions. Processing conditions are highly accountable for the structure crystallinity, crystal size and shape, phase purity etc. [2]. Various synthesis routes can be used to synthesize the spinel ferrite materials including; ceramic [3], co-precipitation [4], organometallic precursor [5], citrate precursor [5], ²⁴ sol-gel auto-combustion [6] etc. Herein, the ferrite samples was prepared by the sol-gel method since it is simple and cost-effective method.

¹⁹ The effect of In^{+3} ions on the structural, magnetic and catalytic characteristics of In^{+3} substituted Ni-Co ferrite with a chemical composition has been investigated in the present work.

2. Methods and materials

Nanocrystalline ferrite powders with compositions were synthesized by Sol-gel auto-combustion technique. The Analytical Reagent grade of Pure Nickel nitrate [$Ni(NO_3)_2 \cdot 6H_2O$], Cobalt nitrate [$Co(NO_3)_2 \cdot 6H_2O$], Indium Nitrate [$In(NO_3)_3 \cdot 9H_2O$], Ferric Nitrate [$Fe(NO_3)_3 \cdot 9H_2O$], and Citric acid [$C_6H_8O_7 \cdot H_2O$] were used as starting materials.

Reaction procedure was carried out in air atmosphere without protection of inert gases. The molar ratio of metal nitrates to citric acid was taken as 1:3. The metal nitrates were dissolved together in a minimum amount of double distilled water to get a clear solution. An aqueous solution of citric acid was mixed with metal nitrates solution, then ammonia solution was slowly added to adjust the $\text{pH} \cong 7$. The mixed solution was kept on to a hot plate with continuous stirring at $90\text{ }^\circ\text{C}$. During evaporation, the solution became viscous and finally formed a very viscous brown gel. When finally all water molecules were removed from the mixture, the viscous gel began frothing. After few minutes, the gel automatically ignited and burnt with glowing flints. The decomposition reaction would not stop before the whole citrate complex was consumed. The auto-combustion was completed within a minute, yielding the brown-colored ashes termed as a precursor. The as prepared powder then annealed at $600\text{ }^\circ\text{C}$ for 4 hrs.

The dried powder was characterized via Thermogravimetric analysis (TGA)/Differential scanning calorimetry (DSC) at heating rate of $10\text{ }^\circ\text{C}/\text{min}$ in nitrogen (N_2) atmosphere to determine the crystallization temperature by using Shimadzu SDT Q600 thermal analyzer. The energy dispersive analysis of X-ray (EDAX) was carried out to know the expected amount of element and stoichiometry present in the composition. The X-ray diffraction (XRD) patterns of samples were recorded at room temperature by using Cu-K_α radiation on Rikagu Miniflex X-ray diffractometer. X-ray diffraction data was recorded in the 2θ range of $20\text{--}70^\circ$ with a scanning rate of $2^\circ/\text{min}$. The lattice parameters, the oxygen position, and the cation distribution were determined. Infrared spectroscopy (IR) measurement was carried out in the range of $800\text{--}400\text{ cm}^{-1}$ on Perkin Elmer infrared Spectrophotometer. The morphological study carried out by Scanning Electron Micrograph (SEM) and was recorded using EDAX Oxford EDAX JEOL-JSM-5600N. Transmission Electron Microscope (TEM) Measurements were recorded

on Philips (Model CM 200). Magnetic measurements were obtained from a Vibrating Sample Magnetometer (VSM).

For catalytic activities, melting points were not corrected. $^1\text{H-NMR}$ spectra were recorded on Varian Gemini 300 MHz spectrometer. Chemical shifts are reported in δ units (ppm) relative to TMS as internal standard. Electron spray ionization mass spectra (ES-MS) were recorded on Water-Micromass Quattro-II spectrometer. All the reagents used were of AR grade and were used without further purification.

23

3. Results and discussion

22

The TGA of the $x = 0.50$ and $y = 0.06$ samples was decomposed in air medium in the temperature range $100\text{ }^\circ\text{C}$ to $1000\text{ }^\circ\text{C}$ is shown in Figure 1. In TGA pattern, undergoes a weight loss of 1.50% between $135\text{ }^\circ\text{C}$ and $285\text{ }^\circ\text{C}$ related to the decomposition of organic material. The weight loss in the range of $285 - 420\text{ }^\circ\text{C}$ of 4.380% is also observed. No weight loss is in the range of $400-700\text{ }^\circ\text{C}$ was observed, pointing towards the complete decomposition of the precursor $>600\text{ }^\circ\text{C}$ [7]. TGA is a dynamic characterization process and pointing towards the spinel phase formation below the temperature of $600\text{ }^\circ\text{C}$. However, the temperature noted by TGA for spinel crystal structure formation is predictable at much higher temperature. From the literature it was reported that complete elimination temperature for organics is $> 450\text{ }^\circ\text{C}$ for the sample prepared by acetate-citrate gelation and citrate-nitrate auto ignition technique. However, the estimation of particle size analysis is inappropriate below $< 450\text{ }^\circ\text{C}$ [8].

20

Elemental Analysis

16

Energy dispersive analysis of X-ray (EDAX) was carried to study the chemical composition in the prepared samples. As observed from Table 1 that the obtained results chemical composition obtained from the EDAX is in good agreement with the theoretical values. This is helpful to explain the alteration among the amount of the atomic ratio as obtained by the EDAX and the estimated amount [9].

15

5.3.3 X-Ray Diffraction Studies

The XRD patterns of nano ferrite particles of all the composition was characterized (Figure 3). (220), (311), (222), (400), (420) and (440) peaks were detected, confirming the formation of cubic spinel structure without any impurity. The lattice constant is consistent with the JCPDS file of NiFe₂O₄ phase (JCPDSno.48-0489) [10].

The broad peaks nature as observed from the XRD patterns pointed toward a small particle nature of the prepared samples. Shift in diffraction peaks position towards higher angle (2θ) is also an indication that the lattice parameter of Ni_xCo_{1-x}In_yFe_{2-y}O₄ is disturbed with In³⁺ substitutions [11].

The lattice parameter (a) was obtained through the relation:

18

As observed from Table 2 and Fig. 4 that ' a ' increased from 8.356 Å to 8.378 Å as In³⁺ ion concentration increases it is due to differs in ionic radii of In³⁺ ion (0.8 Å) larger ionic radii which replace Fe³⁺ ion (0.67 Å) smaller ionic radii [12].

The X-ray density (d_x) increased with In³⁺ substitution as listed in Table 2, since d_x is known to be proportional inversely to the ' a ' [13].

The bulk density ' d_B ' found to reduce with the In³⁺ ions substitution (Table 2) since In³⁺ ions triggers the sintering procedure in ferrites and leading to increment in bulk densities [14]. Figure 5 shows change of ' d_x ' and ' d_B ' with In³⁺ substitution.

The porosity (P) increased from 33.34–42.91 % with In^{+3} substitution (Table 2) due to increase in molecular weight and unit volume cell, however the degree of increment in molecular weight is higher compared to volume. Thus, variation in P leads to increase number of pores, scattering centers and vacancies. This in turn decrease the bulk densities with In^{+3} substitution. Such behavior in porosity and bulk density is correlated to decreased particle size [15].

The broad diffraction peaks exhibits the fine particle nature of ferrite powders. The average of crystalline diameter 'D_{XRD}' of the prepared samples was obtained from the peak (311) peak of XRD by using Scherer relation [16]:

The values of crystalline size is in the range of few nanometer and decreased from 45–35 nm with increase in In^{3+} substitution (Table 2). Such a decrease in crystallite size is responsible in decrease in bulk density decreased with In^{+3} substitution.

The ion hopping lengths for tetrahedral A-site (L_A) and octahedral B-site (L_B) were obtained, and the variation is shown in Fig. 6 and Table 2. The performance of hopping lengths with In^{3+} substitution is similar with 'a' and the difference in the ionic radii of the ions. Thus, such variation in hopping lengths made the magnetic ions larger with each other and resulted in increase in hopping lengths.

The allied parameters; tetrahedral and octahedral bond length (d_{AX} and d_{BX}) tetrahedral edge (d_{AXE} , d_{BXE} and d_{BXEU}) were calculated using the relation discussed elsewhere [17-18].

Allied parameters were increased with the In^{+3} ions substitution which is related to ionic radii of and the cation distribution of constituent ions in the presently investigated nano ferrite system. Figure 7 shows the variation of allied parameters and

the composition of In^{3+} ions content. The values of allied parameters are listed in Table 3.

Infrared Spectroscopy

The IR spectrum in the range $200\text{--}800\text{ cm}^{-1}$ were obtained for nano crystalline ferrite as shown in Figure 8. The observed bands ' ν_1 ' and ' ν_2 ' are the characteristic of stretching vibrations at the A-sites and the B-sites. The presence of Fe^{2+} ions in the ferrite system split the absorption band and thus Local deformations can take place because of Jahn–Teller effect [19] in Fe^{2+} ions that lead to a non–cubic constituent of the crystal field potential that resulted in to splitting of the observed bands.

The increase in 'V' and 'a' had impact on the position of absorption band, hence the absorption bands ' ν_1 ' shifts to higher value around $580\text{--}600\text{ cm}^{-1}$ with the In^{3+} ions substitution. The increase in the 'V' affect the stretching vibrations of $\text{Fe}^{3+}\text{--O}^{2-}$ bond which dose resulted in change in band position [20]. The change in the band locations is predictable due to the variances in the $\text{Fe}^{3+}\text{--O}^{2-}$ distances for the A- and B-sites. The absorption band ' ν_2 ' appears near about $350\text{--}400\text{ cm}^{-1}$ and absorption band ' ν_3 ' at near 250 cm^{-1} .

Scanning Electron Microscopy

The SEM images of typical samples; $x = 0.00$; $y = 0.00$ and $x = 0.50$; $y = 0.06$ are shown in Figure 9 (a) and (b) which had good spherical shape nature of the prepared material.

It is observed from SEM images particles are uniformly distributed. The grain growth is known to depend on grain boundary movement with the In^{3+} substitution. The detected variations in grain size propose that the substitution of In^{3+} in solid solution occurred through synthesis that allows a good homogeneousness in the powder and

thus, a more organized microstructure is attained. Further, amorphous and porous in nature of grains are observed through the SEM images [21].

Transmission Electron Microscopy

The typical TEM micrographs for $x = 0.00, y = 0.00$ and $x = 0.50, y = 0.06$ samples are given shown in Figure 10 (a) and (b) which are in spherical shape and showed uniform distribution of the particles. The particles are somewhat agglomerated because of the magneto statics interaction among the ferrite particles [22].

The average sizes of particles is found in the few nanometers and ranges from 30.5 nm to 45.5 nm and are shown in Table 2, which is agreement with the XRD investigations.

The SAED analysis of the prepared samples are displayed in Figure. 10 (a) and (b). Superimposed bright spot with Debye ring pattern specifies confirmed that In^{+3} substituted ferrite nanoparticles are well crystallized. Further, these pattern reveal that the particles are in nanometer size [23].

The particle size obtained from the TEM images are around 30–45 nm which is analogues with the estimation from XRD. Image J software was used to obtain the particle size from TEM images (Figure 10 (a) and (b)).

Magnetic studies

The hysteresis loops of Co^{2+} ion substituted of ferrite material was obtained at room temperature. The variation of magnetic properties with applied field is shown in Figure 11.

The saturation magnetization (M_s) observed to increase with In^{+3} substitutions. M_s of Ni–Co ferrite system is well-defined by the magnetic moments of each ions. In

the present work In^{+3} of $0 \mu_B$ magnetic moment were introduced in Ni–Co ferrite to replace Fe^{+3} ions of $5 \mu_B$ magnetic moment in the B-site [24]. Thus, substitution of In^{+3} ions at B-site resulted in the weakening of the magnetization at the B-site, that degrade the total M_s . The M_s is controlled by the super-exchange interactions among the A- and B-sites cations. Neel's molecular field model [25], the A–B super-exchange interaction dominate the intra-sub-lattice A–A and B–B interactions. Thus, the resultant magnetic moments are obtained by the totality of the magnetic moments of the A- and B- sublattices [26].

5.3.8 Catalytic Studies

A one-pot reaction, MCRs usually produce superior yields and are dissimilar from the two-component reactions in numerous features [27–28]. These reactions used for synthesis of complex molecules lead structure identification and optimization in chemical biology and drug discovery [29–30]. Moreover, the application of several conversions in a single operation is highly attuned with the objectives of sustainable and green chemistry [31]. Indole and its derivatives have paying attention a lot interest in recent decades due to their wide biological activities [32–33]. 3-substituted indole derivatives are general components of drugs and are commonly found to be of pharmaceutical attention in a diversity of therapeutic areas [34]. Among the 3-substituted indole derivatives, bis (indolyl) alkanes can be believed as an significant class of organic compounds due to their extensive occurrence in numerous natural products having biological activity [35]. Bis(indolyl)methanes are most active compounds for endorsing valuable estrogen metabolism [36–37]. Bis(indolyl)methanes have shown pharmaceutical activities such as anticancer [38–40], antiviral and

antimicrobial characteristics [42] and are recognized as a promoter of estrogen metabolism [42].

Thus, ²⁹the preparation of Bis(indolyl)methanes has acknowledged a lot interest since last few years. A modest process ¹¹for the preparation of bis(indolyl)methanes is the condensation of two equivalents of Indole with the carbonyl aldehydes. A variety of reagents such as Bronsted acids [43-44], Lewis acids [45-46], acetic acid [47], In(OTf) [48], InF₃ [49], silica bonded S-sulfonic acid [50], Zeolites [51], ionic liquids [52], have been used to for this transformation.

Most of these catalysts have one or more disadvantages such as longer reaction periods, low yields, severe reaction situations and use of expensive and/or toxic catalysts and solvents. Hence, there is an adequate necessity for a mild, clean and efficient route for the preparation of this worthy moiety.

The application of nanoparticles as catalysts in organic transformation had attract a substantial attention in this decade. Although application of a nano-catalyst might attain a considerable improvement of its catalytic activity, the significant task for green chemistry is the invention of novel technologies for catalyst separation and recycling to substitute conventional processes [53]. Therefore, ample consideration is given to apply the nanoparticles of magnetic metal oxides as a heterogeneous and easily recycled catalysts for numerous organic reactions [54]. Currently, nanoparticles of functionalized magnetite ferrite can be used as an effective catalyst in various chemical reactions such as CO oxidation [55], catalytic combustion of hydrocarbons [56] or selective oxidation and reduction of several organic molecules [57], synthesis of diazepine derivatives [58], ⁴ α -amino nitriles [59], 1,1-diacetates from aldehydes [60], 1,4-dihydropyridines [61], etc.

Considering the significance of multicomponent reaction [62-65], we used magnetic nanoparticles ($x = 1.0$; $y = 0.10$) as a recoverable and reusable catalyst for the preparation of *bis*-(indolyl)methanes.

Preparation of *bis*-(indolyl)methane derivatives using Indole (1), aromatic aldehydes (2), using 40 mol % ($x = 1.0$; $y = 0.10$) nanoparticles as catalyst. (Scheme 1) is reported herein.

A mixture of indole (10 mmol) (1) aromatic aldehydes (10 mmol) (2) and ($x = 1.0$; $y = 0.10$) (0.25 mmol) in 25 ml of ethanol was refluxed for the proper time (Table 28) (The completion of reaction was monitored by TLC, solvent system - 30% ethyl acetate in hexane). The extradiation of reaction mixture was done with ethyl acetate once the reaction completed where the ethyl acetate layer on evaporation provides the anticipated products.

A proper composition of ferrites were selected to synthesis of *bis*-(indolyl)methanes (3a) as model reaction to investigate the efficiency ferrite catalysis. The entire reaction was obtained by refluxing a mixture of indole (10 mmol) (1) aromatic aldehydes (10 mmol) (2) and ($x = 1.0$; $y = 0.10$) (0.25 mmol) in 25 ml of ethanol. The title compound 3a was isolated with 88% yield with the use of ($x = 1.0$ and $y = 0.1$) ferrites in shorter time (70 min) compared to other ferrite compositions (Table 5.4).

Once the ferrite composition was finalized, the quantity of spinel ferrites (catalyst load) was characterized for model reaction (3a). Numerous aldehydes were reacted with indole (1) with optimized conditions to attain substituted *bis*-(indolyl)methane (3a-3f) (Scheme 1, Table 5.5).

The re-usability and recovery of the catalyst was studied for ¹ model reaction (3a). The reaction was processed by refluxing a mixture of indole (10 mmol) (1) aromatic aldehydes (10 mmol) (2) and ($x = 1.0$; $y = 0.10$) (0.25 ¹ mmol) in 25 ml of ethanol.

Once the reaction is completed; catalyst re-cycling was obtained by fixing a strong magnetic at the bottom of flask, and the liquid solution removed from the flask. As obtained ⁴ solid catalyst washed with acetone and a fresh substrate was placed into the flask thereafter to allow reaction to continue for next run.

The reaction procedure was ¹ clean and after magnetically removal of catalyst mandatory to obtain the reaction mixture with ethyl acetate. The ethyl acetate layer on evaporation offer the anticipated products.

17%

SIMILARITY INDEX

PRIMARY SOURCES

- 1** K.A. Ganure, M.M. Langade, L.A. Dhale, K.S. Lohar. "Chromium substituted nickel ferrites ($\text{NiFe}_{2-x}\text{Cr}_x\text{O}_4$, $x=0.0, 0.1, 0.2, 0.3$, and 0.4) magnetically recoverable reusable heterogeneous nano catalysts", *Materials Today: Proceedings, 2020*
Crossref 117 words — 4%
- 2** www.socialresearchfoundation.com
Internet 55 words — 2%
- 3** Hashim, Mohd., Alimuddin, Sagar E. Shirsath, S.S. Meena, R.K. Kotnala, Shalendra Kumar, Pramod Bhatt, R.B. Jotania, and Ravi Kumar. "Study of structural and magnetic properties of (Co–Cu)Fe₂O₄/PANI composites", *Materials Chemistry and Physics, 2013*.
Crossref 52 words — 2%
- 4** U.M. Mandle, A.M. Pachpinde, D.R. Kulkarni, B.L. Shinde. "An efficient one pot multicomponent synthesis of pyrano pyrazoles using Cu²⁺ doped Ni-Zn nano ferrite catalyst", *Materials Today: Proceedings, 2020*
Crossref 32 words — 1%
- 5** S. M. Patange, Sagar E. Shirsath, G. S. Jangam, K. S. Lohar, Santosh S. Jadhav, K. M. Jadhav. " Rietveld structure refinement, cation distribution and magnetic properties of Al substituted NiFe O nanoparticles ", *Journal of Applied Physics, 2011*
Crossref 17 words — 1%
- 6** Pathak, T.K.. "Structural and magnetic phase evolution study on needle-shaped nanoparticles of magnesium ferrite", *Ceramics International, 201001* 16 words — 1%

-
- 7 Haralkar, S.J., R.H. Kadam, S.S. More, Sagar E. Shirsath, M.L. Mane, Swati Patil, and D.R. Mane. "Intrinsic magnetic, structural and resistivity properties of ferromagnetic $Mn_{0.5}Zn_{0.5}Al_xFe_{2-x}O_4$ nanoparticles", Materials Research Bulletin, 2012. 14 words — < 1%
Crossref
-
- 8 R. H. Kadam, A. R. Biradar, M. L. Mane, Sagar E. Shirsath. " Sol-gel auto-combustion synthesis of Li MnFe O and their characterizations ", Journal of Applied Physics, 2012. 14 words — < 1%
Crossref
-
- 9 Gurav, S.K., Sagar E. Shirsath, R.H. Kadam, and D.R. Mane. "Low temperature synthesis of $Li_{0.5}Zr_xCo_xFe_{2.5-2x}O_4$ powder and their characterizations", Powder Technology, 2013. 13 words — < 1%
Crossref
-
- 10 Arvind Singh, Gurpreet Kaur, Bubun Banerjee. "Recent Developments on the Synthesis of Biologically Significant bis/tris(indolyl)methanes under Various Reaction Conditions: A Review", Current Organic Chemistry, 2020. 12 words — < 1%
Crossref
-
- 11 Shou-Ri Sheng. "Synthesis of Bis(indolyl)methanes Using Recyclable PEG-Supported Sulfonic Acid as Catalyst", Catalysis Letters, 03/2009. 11 words — < 1%
Crossref
-
- 12 Aurelija GATELYTĖ. "Sol-Gel Synthesis and Characterization of Selected Transition Metal Nano-Ferrites", Materials Science, 09/16/2011. 11 words — < 1%
Crossref
-
- 13 R. L. Dhiman, S. P. Taneja, V. R. Reddy. "Preparation and Characterization of Manganese Ferrite Aluminates", Advances in Condensed Matter Physics, 2008. 10 words — < 1%
Crossref
-

Internet

10 words — < 1 %

15 dyuthi.cusat.ac.in
Internet

10 words — < 1 %

16 Ketan A. Ganure, Laxman A. Dhale, Sagar E. Shirsat, Kishan S. Lohar. "Morphological Study of Lanthanum-Doped Nano Spinel Ferrite via Normal Micelles Method", Journal of Inorganic and Organometallic Polymers and Materials, 2018
Crossref

10 words — < 1 %

17 acta.chem-soc.si
Internet

9 words — < 1 %

18 D. V. Phugate, Rameshwar B. Borade, S. B. Kadam, L. A. Dhale, R. H. Kadam, Sagar E. Shirsath, A. B. Kadam. "Effect of Ho³⁺ Ion Doping on Thermal, Structural, and Morphological Properties of Co–Ni Ferrite Synthesized by Sol-Gel Method", Journal of Superconductivity and Novel Magnetism, 2020
Crossref

9 words — < 1 %

19 www.researchsquare.com
Internet

9 words — < 1 %

20 B. G. Toksha, Sagar E. Shirsath, M. L. Mane, S. M. Patange, S. S. Jadhav, K. M. Jadhav. "Autocombustion High-Temperature Synthesis, Structural, and Magnetic Properties of CoCr Fe O (0 ≤ x ≤ 1.0)", The Journal of Physical Chemistry C, 2011
Crossref

8 words — < 1 %

21 M. Rahimi, M. Eshraghi, P. Kameli. "Structural and magnetic characterizations of Cd substituted nickel ferrite nanoparticles", Ceramics International, 2014
Crossref

8 words — < 1 %

22 www.iosrjournals.org
Internet

8 words — < 1 %

23 H. M. Widatallah, I. A. Al-Omari, A. M. Gismelseed, O. A. Yassin, A. D. Al-Rawas, M. E. Elzain, A. A. Yousif, O. A. Osman. "Mössbauer and magnetic study of Mn²⁺- and Cr³⁺-substituted spinel magnesioferrites of the composition Mg_{1-x}Mn_xFe_{2-2x}Cr_{2x}O₄", Hyperfine Interactions, 2006
8 words — < 1%
Crossref

24 res.mdpi.com
Internet
8 words — < 1%

25 Verma, V.. "Remarkable influence on the dielectric and magnetic properties of lithium ferrite by Ti and Zn substitution", Solid State Communications, 200910
8 words — < 1%
Crossref

26 Raghvendra Singh Yadav, Jaromir Havlica, Jiri Masilko, Lukas Kalina et al. "Impact of Nd³⁺ in CoFe₂O₄ spinel ferrite nanoparticles on cation distribution, structural and magnetic properties", Journal of Magnetism and Magnetic Materials, 2016
8 words — < 1%
Crossref

27 R.H. Kadam, A.P. Birajdar, Suresh T. Alone, Sagar E. Shirsath. "Fabrication of Co_{0.5}Ni_{0.5}CrxFe_{2-x}O₄ materials via sol-gel method and their characterizations", Journal of Magnetism and Magnetic Materials, 2013
7 words — < 1%
Crossref

28 Kokare, N.D.. "Oxalic acid as a catalyst for efficient synthesis of bis-(indolyl)methanes, and 14-aryl-14H-dibenzo[a,j]xanthenes in water", Chinese Chemical Letters, 200810
6 words — < 1%
Crossref

29 V. Jhansi Rani, K. Veena Vani, C. Venkata Rao. "PEG-SO₃H as a Catalyst for the Preparation of Bis-Indolyl and Tris-Indolyl Methanes in Aqueous Media", Synthetic Communications, 2012
6 words — < 1%
Crossref

30 R.H. Kadam, Suresh T. Alone, Maheshkumar L.
6 words — < 1%

Mane, A.R. Biradar, Sagar E. Shirsath. "Phase evaluation of Li+ substituted CoFe₂O₄ nanoparticles, their characterizations and magnetic properties", Journal of Magnetism and Magnetic Materials, 2014

Crossref

31 Lawrence Kumar, Manoranjan Kar. "Effect of La³⁺ substitution on the structural and magnetocrystalline anisotropy of nanocrystalline cobalt ferrite (CoFe_{2-x}La_xO₄)", Ceramics International, 2012

6 words — < 1%

Crossref

32 Dhanraj R. Mane. "Structural and magnetic characterizations of MnNiZn ferrite nanoparticles", physica status solidi (a), 07/15/2010

6 words — < 1%

Crossref

33 K.S. Lohar, A.M. Pachpinde, M.M. Langade, R.H. Kadam, Sagar E. Shirsath. "Self-propagating high temperature synthesis, structural morphology and magnetic interactions in rare earth Ho³⁺ doped CoFe₂O₄ nanoparticles", Journal of Alloys and Compounds, 2014

6 words — < 1%

Crossref

34 Birajdar, A.A.. "Role of Cr³⁺ ions on the microstructure development, and magnetic phase evolution of Ni⁰.₇Zn⁰.₃Fe₂O₄ ferrite nanoparticles", Journal of Alloys and Compounds, 20120125

6 words — < 1%

Crossref

EXCLUDE QUOTES

OFF

EXCLUDE MATCHES

OFF

EXCLUDE
BIBLIOGRAPHY

ON

Prof.(Dr.)K.S.LOHAR

BDM Ph.D Synopsis updated.doc

Ph.D. SYNOPSIS

METHOD DEVELOPMENT AND VALIDATION OF SIMULTANEOUS ESTIMATION AND IMPURITY PROFILING OF SOME DRUGS FROM THEIR PHARMACEUTICAL DOSAGE FORM USING MODERN ANALYTICAL TECHNIQUES

To be submitted

To

**DR. BABASAHEB AMBEDKAR MARATHWADA UNIVERSITY
AURANGABAD**



(NAAC Accredited at A Level)

**FOR THE AWARD OF THE DEGREE OF
DOCTOR OF PHILOSOPHY
IN PHARMACY**

By

Bhaskar Dagadu Musmade

Research Student

Under the Guidance of

Dr. Kishan S. Lohar

Professor

Department of Chemistry,

Dr. Babasaheb Ambedkar Marathwada University,

Aurangabad (M.S.) - 431 004,

INDIA

Chapter I : Introduction to pharmaceutical analysis

Nowadays the use of medicine has become an essential part of human being and animals. Current era of science and technology somehow simplified our work-load, at the same time give rise to mental stress, pollutions, competition. Hence the lifestyle has been entirely changed in respect of quality of food, climatic change etc. that resulting the increase number of diseases at various stages of life. A good quality medicine, though accurate, precise, sensitive and robust method of analysis required during the testing in pharmaceutical industries of medicine is essential to have a good and secure lifespan.

Pharmaceutical field is a lifesaving field and thus it is controlled worldwide by various regulatory authorities such as USFDA, MHRA, TGA, PIC/S, WHO etc. The pharmacopeias like USP/IP/Ph.Eur/BP/JP regularly informs the specific monograph for the drug products, and expients; thus these products are considered as certified products. The specific monographs includes the critical testing parameters like description. Identification, Assay, Uniformity of dosage unit, related substance, dissolution, microbial testing, preservative, water content/LOD and other specific test by dosage wise and nature of molecule. For quantitative and qualitative analysis now the modern analytical techniques are available like HPLC, UPLC, HPLC- MS, Gas chromatography, GC -MS, FTIR, and NMR. Now a day HPLC, UPLC, coupled with UV/PDA/DAD, RI, detectors is the commonly used separation techniques to check the purity of medicine.

Types of chromatography:

Based on the principle of separation, the chromatography is mainly classified in below two types.

- a) **Liquid chromatography:** The mobile phase is liquid and stationary phase is solid as well as liquid in this type. The liquid chromatography classified in adsorption chromatography, Thin layer chromatography, partition chromatography, column chromatography.
- b) **Gas Chromatography:** Here, the mobile phase is gaseous (nitrogen, helium) and stationery phase is solid as well as liquid.

Need of stability indicating Impurity, assay method:

The methods which has the capability to sense the changes with time in physical and chemical characteristics of molecule accurately is termed as stability indicating method. Stability indicating method implied in 21 CFR Part 211.165 and 211.166 (3): As per 21 CFR 211.164(e), reproducibility sensitivity, specificity, and accuracy of test methods engaged by

the firm should be recognized and documented and 211.166 (a) (3) requires that test methods be reliable, meaningful and specific.

Evaluation of drug and drug product at different stages, like raw material, intermediate, in process, finished products and during the stability study up to product expiry routine practice in pharmaceutical firm. The critical testing parameters like, assay, related substance, dissolution, uniformity of dosage unit, the stability indicating methods is necessary. In assay method, the principle analyte is accurately quantitate from 50 to 150% of working concentration without interference of any degradation products and in impurity method, each known and unknown impurities should be quantitate from its LOQ to 120% of specification limits.

Advantage of Simultaneous estimation method vs single content method:

For combination drug products estimation of individual analytes is time, resources, chemical and reagents consuming, and economically expensive. It is better to develop the method in such way that maximum constituents are to be separate accurately in single method. In analytical method development the first goal is to develop the cost effective, time saving, method, by considering this goal we developed the novel stability signifying technique for simultaneous estimation and impurity profiling methods of some drugs from their pharmaceutical dosage form.

Analytical method validation

The developed methods are checks its authentication in intended use by validating as per ICH /USP/guidelines. ICH issued harmonized guidelines for analytical method validation Q2 (R1) and several countries have their own validation guidelines like US-FDA, EMEA etc. Below validation parameters are employed for method validation and finding are reported.

- 1) Accuracy
- 2) Precision
- 3) Repeatability and intermediate precision.
- 4) Specificity
- 5) Limit of detection and limit of quantitation.
- 6) Linearity and range
- 7) Robustness

In addition some critical parameters like, filter validation, solution stability at room temperature has been completed for each method.

Chapter 2: Literature Review

Literature review on selected topics:

Literature review has been done on the selected drugs, drug products and its all types of formulation dosage forms. Literature review starts from physiochemical properties, pharmacopoeial status, and reported related methods. For organic impurities methods, collected the information of reported impurities in vendor's method of analysis of API, from reported research articles and different pharmacopoeias if official. After literature review the actual development was started by selection of appropriate analytical techniques.

2.1 Literature review on the progress and authentication of stability signifying RP HPLC technique for simultaneous approximation for Xylometazoline Hydrochloride and Ipratropium bromide from Nasal spray dosage form.

Intensive literature has been done on Xylometazoline and Ipratropium bromide in terms of their reported methods. It was observed that, various methods were reported for estimation of xylometazoline such as by Gas chromatography, HPTLC, HPLC, and by ultraviolet spectrophotometric techniques while individual determination of Xylometazoline HCL and Ipratropium bromide or combination with other drugs by using modern analytical techniques also reported. Few impurity profiling methods reported individually for both the drugs. At present none of the controlled technique has been reported for synchronized approximation of Xylometazoline HCL and Ipratropium bromide from nasal spray dosage forms. A developed method herein was validated s per ICH guideline and routinely used for analysis of commercial batches in quality control laboratories.

2.2 Literature review on impurity profiling method development and validation of Metformin hydrochloride and Teneligliptin Hydrobromide hydrate in their combination tablet dosage form by using RP-HPLC with UV/PDA detector.

While going through literature survey it was observed that few testified assay techniques are based on UV-visible spectroscopy method but such techniques have no stability indicating and thus not recognized by the Regulatory bodies. Few reported assay techniques are by using high performance thin layer chromatographic (HPTLC) methods. HPTLC technique has a limited sensitivity and therefore not acceptable for quantification purposes.

For this research work about 20 different reported research papers were evaluated and studied. Some methods for simultaneous determination of Metformin HCl and Teneligliptin were reported while related impurities methods for individual Metformin HCl and Teneligliptin were reported. At present no reported method are available for simultaneous quantification of known and unknown impurities of both the drugs in combination Tablet dosage form. Herein, an attempt was made to develop a novel approach stability indicating analytical HPLC method for the quantitation of organic impurities from MTF and TNG from the blend sample. The method developed herein is easy and robust which can be applied in the routine contamination testing studies in the quality control pharmaceutical company labs engaged in the drug combination, and also validated as per ICH Q1 (R2) standard.

2.3 Literature review on development and validation, of Fluocinolone Acetonide, Miconazole Nitrate, Chlorocresol, Methyl paraben and Propyl Paraben, form cream formulation dosage form, by using RPHPLC with UV/PDA detector

After intensive literature review it was observed that no reported method focused these molecules simultaneously in cream and ointment dosage form. The reported methods were available for estimation of Fluocinolone acetonide and Miconazole in combination dosage form but preservative contents not estimated from the same methods. There were some method for individual determination of Fluocinolone acetonide or combination with other drugs from cream, ointment and other dosage form, while some reported methods were available for Miconazole nitrate individually or with combination other drug substance in pharmaceutical dosage forms. Presently no reported method were observed for simultaneous estimation, of Fluocinolone acetonide, Miconazole nitrate, Chlorocresol, Methyl paraben and Propyl Paraben from the Pharmaceutical cream and ointment dosage form. Determination of such five content in single HPLC method is challenging work in terms of resolutions, column efficiency, and recovery, hence this developed work will helpful to researchers for saving the development cost and time, also save the routine analysis cost in pharmaceutical industries. Considering this advantage this method can be used in quality control laboratories for routine analysis. The developed method was successfully validated as per ICH guideline.

2.4 Literature review on method development, validation and estimation of relative response factor for the quantitation of known impurities of Mometasone Furoate in nasal spray dosage form by using RP HPLC with UV/PDA detector.

Most of the reported methods are either for the assay test of individual Mometasone Furoate or in combination with other drug substances and preservative content in various dosage forms, viz. Topical Cream, Ointment, Nasal spray and Inhaler. The forced degradation study is also reported in combination dosage form. The official monograph of Mometasone Furoate aqueous nasal spray in British pharmacopeia contains the related substance method by TLC method. The TLC method is comparatively less precise and accurate than HPLC method for the quantitation of such toxic impurities. The DMCF impurity (Impurity D as per Ph.Eur) has critical toxicity, skin and eye irritation, and also causes the reproductive toxicity. Now, at this juncture no technique is offer the detail impurity profiling by determining their relative response factors with respect to Mometasone Furoate from different pharmaceutical dosage form. Herein, we have developed the stability indicating, robust and accurate HPLC method for the determination of known and unknown substances along with the determination of the relative response factor for all the identified impurities with respect to Mometasone Furoate from Nasal spray product. The comprehensive authentication of developed technique was carried out as per ICH norms. The method reported herein can be effectively useful for the examination of marketed sample (Nasonex) and in-house nasal spray product.

2.5 Literature review on impurity profiling method development and validation of Metformin Hydrochloride and Vildagliptin from their combination Tablet dosage form.

Individual assay determination of Vildagliptin and combination with other drugs were reported by RP-HPLC, GC, electrophoresis, Spectrophotometry and spectrofluometric techniques. Ramzia L. El Bagry and et.al reported the Vildagliptin determination in presence of its synthetic mixture in presence of Metformin HCL and Pioglitazone .In this reported method, does not included the Vildagliptin known impurities as well as impurities of MTF like Melamine, Cyanoguanidine, MTF related compound B, MTF related compound C. Caroline Paola Uber and et.al developed the method by HPLC–MS for determination of Vildagliptin and Metformin HCL with its impurities, but no Vildagliptin impurities were reported and eluted by this method . E. Al-Qudah, and et.al, did the Forced degradation studies of Vildagliptin API in the presence of excipients, by using HPLC-UV, but known impurities not reported and eluted. To the best of our knowledge presently no methods are reported for the simultaneous determination and quantitation of known and unknown impurity profiling for Metformin HCL and Vildagliptin form their combination tablet dosage forms. Present study focused on simultaneous quantitation of known and

unknown degradants of MTF and VIL from their combination tablet dosage form. The developed method was validated as per ICH guideline and can be used in quality control laboratories for routine analysis of commercial batches.

Chapter 3: Objective of the study and drug profile

- 1) The objective of the present study is to development and validation of accurate, precise, method of analysis for selected drugs and drug products so as the patients will get the safe and better quality of medicine.
 - 2) To perform the force degradation study at various conditions such as, acid, base, thermal, photolytic, and oxidation for the drug and drug products under study.
 - 3) To authenticate the developed method by ICH /USP guideline to ensure the authentication of developed methods.
- 3.1 Development and authentication of stability indicating RP HPLC method for synchronized approximation for Xylometazoline Hydrochloride and Ipratropium bromide from Nasal spray dosage form.
 - 3.2 Impurity profiling technique development and authentication of Metformin hydrochloride and Teneligliptin hydrobromide hydrate in their combination tablet dosage form by using RP-HPLC with UV/PDA detector.
 - 3.3 Development and authentication of Fluocinolone Acetonide, Miconazole Nitrate, Chlorocresol, Methyl paraben and Propyl Paraben form cream formulation dosage form by using RPHPLC with UV/PDA detector.
 - 3.4 Method development, authentication and estimation of relative response factor for the quantitation of known impurities of Mometasone furoate in nasal spray dosage form by using RP HPLC with UV/PDA detector.
 - 3.5 Impurity profiling method development and authentication of metformin hydrochloride and Vildagliptin from their combination Tablet dosage form.

Drug Profile

This chapter describes the physicochemical, pharmacological aspects of selected drugs in the present research work. The profile of selected drugs has been included as below.

For First research work:

For first research work, xylometazoline HCl and Ipratropium bromide nasal spray was selected for simultaneous estimation by RP HPLC.

Drug profile of Xylometazoline Hydrochloride

Description	White or almost white, crystalline powder
Molecular formula	C ₁₆ H ₂₄ N ₂
IUPAC Name	2-(4-tert-Butyl-2,6-dimethylbenzyl)-2-imidazoline hydrochloride
Physicochemical Properties	
Molecular weight	244.37
Solubility	Freely Soluble in water, ethanol and methanol
Melting point	132.0°C
Dosage form	Nasal Spray, Nasal Drops
pKa	10.29
Storage	Store in cool, dry place in tightly closed container
Uses	Alpha- adrenoceptor agonist

Drug profile of Ipratropium Bromide

Description	White or almost white, crystalline powder
Molecular formula	C ₂₀ H ₃₀ BrNO ₃
IUPAC Name	(8-methyl-8-propan-2-yl-8-azoniabicyclo[3.2.1]octan-3-yl) 3-hydroxy-2-phenylpropanoate;bromide
Physicochemical Properties	
Molecular weight	332.46
Solubility	Soluble in water, freely soluble in methanol, slightly soluble in ethanol
Melting point	230°C
Dosage form	Nasal Spray, Nebulizer Solution, Pressurized Inhalation
pKa	15.15
Storage	Store in cool, dry place in tightly closed container

For second research work:

For second research work Metformin HCl and Tenepliptin Tablet selected for impurity profiling method. In this research work we have developed the method for quantitation of

known and unknown impurities of Metformin HCL and Teneiglipitin from their combination Tablet dosage form.

Drug profile of Metformin Hydrochloride

Table 3 Metformin HCl	
Description	White or almost white crystal
Molecular formula	C ₄ H ₁₂ ClN ₅
IUPAC Name	1,1-Dimethylbiguanide N,N-dimethylimidodicarbonimidic diamide
Physicochemical Properties	
Molecular weight	165.62
Solubility	Freely soluble in water, slightly soluble in ethanol, practically insoluble in acetone and methylene chloride
Melting point	221°C
Dosage form	Oral solution, Tablets, PR tablets
pKa	12.4
Storage	Store in cool, dry place in tightly closed container
Uses	Biguanide, treatment of diabetes mellitus

Drug profile of Teneiglipitin Hydrobromide hydrate

Table 4 Teneiglipitin Hydrobromide Hydrate	
Description	
Molecular formula	C ₄₄ H ₆₇ Br ₅ N ₁₂ O ₃ S ₂
IUPAC Name	[(2S,4S)-4-[4-(5-methyl-2-phenylpyrazol-3-yl)piperazin-1-yl]pyrrolidin-2-yl]-(1,3-thiazolidin-3-yl)methanone;hydrate;pentahydrobromide
Physicochemical Properties	
Molecular weight	1275.7

Solubility	Soluble in Ethanol, DMF, DMSO
Melting point	211°C
Dosage form	Tablet
pKa	
Storage	Store in cool, dry place in tightly closed container

Third research work:

In third research work we have selected the Fluocinolone acetonide, Miconazole nitrate, Chlorocresol, Methyl paraben and Propyl paraben ointment.

Drug profile of Fluocinolone Acetonide

Description	White or almost white, crystalline powder
Molecular formula	C ₂₄ H ₃₀ F ₂ O ₆
IUPAC Name	(1S,2S,4R,8S,9S,11S,12R,13S,19S)-12,19-difluoro-11-hydroxy-8-(2-hydroxyacetyl)-6,6,9,13-tetramethyl-5,7-dioxapentacyclo[10.8.0.0 ^{2,9} .0 ^{4,8} .0 ^{13,18}]icosa-14,17-dien-16-one
Physicochemical Properties	
Molecular weight	452.5
Solubility	Practically insoluble in water, Soluble in acetone, anhydrous ethanol, practically insoluble in heptane
Melting point	266°C -268°C
Dosage form	Ceram, Ointment, Topical solution.
pKa	13.9
Log P	2.48
Storage	Cream, Ointment
Uses	A glucocorticoid derivative used topically in the treatment of various skin disorders. It is usually employed as a cream, gel, lotion, or ointment. It has also been used topically in the treatment of inflammatory eye, ear, and nose disorders.

Drug profile of Miconazole Nitrate

Description	White or almost white powder
Molecular formula	C ₁₈ H ₁₄ Cl ₄ N ₂ O
IUPAC Name	1-[2-(2,4-dichlorophenyl)-2-[(2,4-dichlorophenyl)methoxy]ethyl]imidazole;nitric acid
Physicochemical Properties	
Molecular weight	479.1
Solubility	Very slightly soluble in water, sparingly soluble in methanol, slightly soluble in ethanol
Melting point	159°C-163°C
Dosage form	Powder, Cream, Ointment, Tablet, Spray, Gel
pKa	6.77
Log P	5.86
Storage	Store at 4°C
Uses	Miconazole is used to treat skin infections such as athlete's foot, jock itch, ringworm, and other fungal skin infections

Drug profile of Chlorocresol

Description	White or almost white, crystal or crystalline powder or pellets
Molecular formula	C ₇ H ₇ ClO
IUPAC Name	4-chloro-3-methylphenol
Physicochemical Properties	
Molecular weight	142.58
Solubility	Slightly soluble in water, very soluble in ethanol, freely soluble in fatty oils.
Melting point	64-66°C.
Dosage form	NA
pKa	9.55

Storage	Protected from light
Uses	Antiseptic, antimicrobial preservative

Drug profile of Methyl paraben

Table 8 Methyl paraben	
Description	Colorless crystals or white, crystalline powder
Molecular formula	C ₈ H ₈ O ₃
IUPAC Name	Methyl 4-hydroxybenzoate
Physicochemical Properties	
Molecular weight	152.2
Solubility	Slightly soluble in water; very soluble in ethanol, ether, acetone ; soluble in Trifluoroacetic acid
Melting point	131.0 °C
Dosage form	Used as preservative content
pKa	8.5
Storage	Store protected from light and moisture
Uses	Antimicrobial preservative

Drug profile of Propyl Paraben

Table 9 Propyl paraben	
Description	White crystalline powder
Molecular formula	C ₁₀ H ₁₂ O ₃
IUPAC Name	propyl 4-hydroxybenzoate
Physicochemical Properties	
Molecular weight	180.2
Solubility	soluble in ethanol, ethyl ether; slightly soluble in chloroform
Melting point	95-98°C
Dosage form	Used as preservative content

pKa	8.5
Storage	Store protected from moisture
Uses	antifungal agent, antimicrobial agent

Fourth research work:

In the fourth research work Mometasone nasal spray was selected for the development of impurity profiling method by RP HPLC.

Drug profile of Mometasone Furoate

Description	White or almost white powder
Molecular formula	C ₂₇ H ₃₀ Cl ₂ O ₆
IUPAC Name	[(8 <i>S</i> ,9 <i>R</i> ,10 <i>S</i> ,11 <i>S</i> ,13 <i>S</i> ,14 <i>S</i> ,16 <i>R</i> ,17 <i>R</i>)-9-chloro-17-(2-chloroacetyl)-11-hydroxy-10,13,16-trimethyl-3-oxo-6,7,8,11,12,14,15,16-octahydrocyclopenta[<i>a</i>]phenanthren-17-yl] furan-2-carboxylate
Physicochemical Properties	
Molecular weight	539.4
Solubility	Practically insoluble in water, soluble in acetone and in methylene chloride, slightly soluble in ethanol
Melting range	215°C-228°C
Dosage form	Nasal Spray, Cream, Ointment, scalp application
pka	13.84
Log P	2.1
Storage	Store in cool, dry place in tightly closed receptacles
Uses	Useful to treat skin treatment such as psoriasis, rash, allergies, eczema etc. Mometasone prevent swelling (inflammation), redness and itching. Mometasone is a medium-strength corticosteroid. It is available in several forms such as cream lotion (solution) and ointment.

Fifth research work:

Metformin HCl and Vildagliptin combination tablet was selected for impurity profiling

method in the fifth research work.

Drug profile of Vildagliptin

Table 11 Vildagliptin	
Description	White to off white crystalline powder.
Molecular formula	C ₁₇ H ₂₅ N ₃ O ₂
IUPAC Name	(2S)-1-[(2S)-2-[(3S)-3-hydroxy-1-adamantylamino]acetyl]pyrrolidine-2-carboxitrile
Physicochemical Properties	
Molecular weight	303.399 g/mole
Solubility	Soluble in Methanol and Dimethyl Sulfoxide, Practically insoluble in n-Hexane and very slightly soluble in Isopropyl Alcohol.
Melting range	149-155°C
Dosage form	Tablet
pKa	9.03
Log P	0.786
Storage	Store in a tightly closed container and protect from moisture.
Uses	Vildagliptin is a DPP-4 inhibitor approved for the treatment of type 2 diabetes.

Drug profile of Metformin Hydrochloride mentioned under second research work

Chapter 4: Development and authentication of stability indicating RP HPLC method for simultaneous estimation for Xylometazoline Hydrochloride and Ipratropium bromide from Nasal spray dosage form.

In present research we report the simultaneous estimation of the Xylometazoline Hydrochloride and Ipratropium bromide from Nasal spray dosage form. The developed method is employed for the analysis of finished as well as stability analysis of innovator /marketed formulation and in-house samples in ADL/QC.

Methods and materials:

Mobile phase preparation - 1.56 g of sodium di-hydrogen phosphate dihydrate and 0.5 g of 1-pentanesulphonic acid sodium salt was measured and transmitted into a flask comprising 1 L of HPLC grade water. The solution was sonicated for 15 min where the pH was maintained at 4.7 ± 0.1 using orthophosphoric acid. The solution was filtered by 0.45- μm syringe filter (MDI, India) and used as mobile phase A, while acetonitrile was used as the mobile phase B.

Diluent - Water was used as a diluent to synthesize the standard sample and placebo solutions.

Chromatographic conditions - The method parameters were optimized using Inertsil ODS 3V, 250×4.6 mm, 5 μm HPLC column to obtain a good column efficiency as per USP system suitability criteria. The column temperature was maintained at 45 °C. The mobile phase flow was attuned at 1.0 mL/min. Equivalent volume of (10 μl) sample, placebo, and standard samples were poured into the solution. The ipratropium bromide peak was eluted for 5 min and Xylometazoline HCL at about 12 min. The PDA detector was used during the method development for selection of wavelength and checking the peak purity of the samples subjected to force degradation. Both the compounds showed maximum absorbance at 210.0 nm.

Results and discussion:

Interfering peak was not noticed at the retention time of both the analytes in the placebo sample and the diluent indicating the peak purity of both the analyte peaks. The % RSD of six replicate injections was noticed as 0.59 and 0.42% for Xylometazoline HCl and ipratropium bromide, respectively, in the system precision study. The recovery of ipratropium bromide was around 99.4%, 101.1%, 101.6%, and for Xylometazoline HCl 98.3%, 101.3%, 101.5% at 50%, 100%, and 150%, respectively. The forced degradation examination indicates that 4.0% degradation in Xylometazoline and 13.8% degradation in Ipratropium bromide, whereas 18% base degradation detected in Ipratropium bromide. The method results showed linearity from 50% to 150% of working concentration where no substantial deviation noticed throughout robustness study.

Conclusions:

A simple, precise and robust RP-HPLC method with UV detector was developed for the simultaneous approximation of Xylometazoline hydrochloride and Ipratropium bromide for a

nasal spray dosage form. The method is authenticated as per the Q2 (R1) ICH guidelines. This method show high accuracy, preciseness, sensitivity, and time saving with low usage of organic solvents. Furthermore, it is appropriate for the routine examination in quality control laboratory.

Chapter 5: Impurity profiling method development and validation of Metformin hydrochloride and Teneiglipitin hydrobromide hydrate in their combination tablet dosage form by using RP-HPLC with UV/PDA detector

Herein, we report the development and authentication of a stability indicating HPLC method for the determination of related substance in Metformin hydrochloride and Teneiglipitin Hydrobromide hydrate combination Tablet dosage form. The known Melamine, cyanoguanidine impurities of Metformin HCL and Impurity A and Impurity B of Teneiglipitin were spiked in placebo along with individual API to monitor specificity and selectivity.

Methods and materials:

Mobile phase preparation -

2.72 g of potassium dihydrogen phosphate and 1 g of octane sulfonic acid sodium salt were transferred to 1000 mL water containing 1 mL triethylamine and 10 mL methanol in the glass mobile phase bottle. The bottle was sonicated to mix for 5 min and dissolve the reagents completely. The pH was adjusted to 3.0 using orthophosphoric acid. The mobile phase was then filtered through 0.45 μ m filter to remove the dissolved gases and contaminants and further used as mobile phase A. The HPLC grade methanol was used as mobile phase B.

Diluent - The mixture of water and acetonitrile (80:20) was used as the diluent.

Chromatographic conditions - Optimization of chromatographic conditions for optimum resolution, we tried Baker bond C18 (Make-Avantor), Symmetry C18 (Waters) and Inertsil ODS (GL, Lifesciences) columns. Maximum resolution between impurities and principle analyte peaks was achieved on BDS Hypersil C18, 250 \times 4.5 mm, 5 μ column at 35 $^{\circ}$ C with 1 mL/min flow rate in gradient elution mode.

Table 2 Gradient program

Time in min	% mobile phase A	% mobile phase B
0.1	75	25
10.0	70	30
45.0	40	60
55.0	40	60
55.01	75	25
65.0	75	25

Result and Discussion:

The method developed herein was accomplished to recover the substances precisely when spiked at 50% to 150% of the working concentration. The % similarity factor for standard 1 and 2 was noticed to be between 95 and 105% throughout the comprehensive authentication study. The % RSD of known impurities, single maximum and total impurities was found to be > 15% from six samples synthetization throughout the method and intermediate precision study. The LOD and LOQ values of MTF, CYN and melamine were found to be 0.37, 0.33, 0.30 $\mu\text{g/mL}$ and 1.11, 1.17, and 0.92 $\mu\text{g/mL}$, respectively. The LOD and LOQ values of TNG, TNG impurity A and TNG impurity B were found to be 0.14, 0.11, 0.11 $\mu\text{g/mL}$ and 0.42, 0.33, 0.34 $\mu\text{g/mL}$, respectively. During the specificity study no interference was detected at the retention time of known impurities, and principle analyte peaks from blank and placebo solution. In forced degradation study, we observed no significant degradation in acid (< 1%), alkali (3.5%), thermal (1.9%) and photolytic (< 1%) conditions. Significant degradation (11.6%) was observed during oxidative stress.

Conclusions:

The obtained result of authentication examination suggests that the developed method is accurate, precise, robust and linear. This developed method can be useful for stability study of the formulation products and demonstrate a very accurate results. We effectively discrete the impurities of both the drugs in single method, so patient will get safe and effective medication. Hence, the projected method is helpful to researchers searching to develop a cost and time effectiveness. None of the hazardous chemicals were used in the analysis, and also, the method require lesser quantity of organic solvents; thus, the method is benign and eco-friendly. The developed method can be successfully used for the routine testing of impurities in pharmaceutical products during the commercial manufacturing of batches.

2

Chapter 6: Development and validation, of Fluocinolone Acetonide, Miconazole Nitrate, Chlorocresol, Methyl paraben and Propyl Paraben, form cream formulation dosage form, by using RPHPLC with UV/PDA detector

Method and materials:

Preparation of mobile phase - Accurately pipetted 2 mL of Triethylamine was transferred in to a 1000 mL of water, the mixture was well mixed and the pH was adjusted to 7.2 with dilute Orthophosphoric acid. 10 ml of acetonitrile was added to the mixture and the mixed well, and the solution was sonicated and filtered through a 0.45 μ filter.

The pure acetonitrile was used as a mobile phase B.

Diluent - The mixture of mobile phase A and B in ratio of (15:85) % v/v was used as diluent.

Chromatographic condition - Hypersil BDS C18, 250 x 4.6 mm, 5 μ m, column was optimized at 45°C and chromatograms were monitored at 238nm based on the optimum response of all analytes. The mobile phase was pumped at 1.5 ml/minutes flow rate and 20 μ l injection volume was injected for all the solutions. The gradient was optimized for better separations of analytes and mentioned in below Table. The retention time of FL MI, CH, MP, PP, were obtained at about 10.8 min., 25.5 min., 9.8 min., 9.3 min., and 4.3 minutes respectively.

Time in minutes	% Mobile phase	
	A	B
0.1	65	35
30	5	95
33	5	95
33.1	65	35
38	65	35

Result and Discussion:

During the specificity study it was observed that, no any interfering peaks from the placebo and blank solution found at the retention time of each analytes the peak was pure. The recovery at 50,100 and 150% of FL was 99.4, 100.7, 100.4 % while for MI was found 98.5, 98.1, and 101.7% respectively. The recovery of MP was 101.1, 101,100.3 % and PP was

recovered 101,101.3, 101% at 50,100 and 150% of working concentration. The Chlorocresol recovered 100.5, 100.7 and 100.4% at 50,100, 150%. The correlation coefficient obtained for each molecule was more than 0.999 hence the method was found linear from 50 to 150% of sample preparation while during the robustness study, no significant variation observed in system suitability parameters.

Conclusion:

The precise and accurate method was developed for the simultaneous determination of Fluocinolone Acetonide, Miconazole Nitrate, Chlorocresol, Methyl paraben and Propyl Paraben, from cream formulation dosage form. The recovery of the method was found between 98 to 102% from 50 to 150%. In the linearity study, the correlation coefficient r^2 was found more than 0.999 as well as no any interference were observed during the specificity study. We tried to use minimum amount of organic solvents and chemicals in the method also no any hazardous chemicals used, hence the developed works is eco-friendly. This is the first developed method for such five contents in single method which is helpful for the researchers to save the development time and cost.

Chapter 7: Method development, validation and estimation of relative response factor for the quantitation of known impurities of Mometasone furoate in nasal spray dosage form by using RP HPLC with UV/PDA detector.

In the present research work we report the impurity profiling method for Mometasone Furoate from their Nasal spray dosage form. Simple isocratic elution of all the known and unknown degradants was achieved and related response factors were estimated for all known impurities.

Methods and material:

Mobile phase preparation - About 4.08g Potassium dihydrogen phosphate and 1 g of 1-Octane sulfonic acid sodium salt were transferred in 1000 ml of water, the mixture was sonicated to dissolve it completely and pH was adjusted to 3.0 ± 0.1 with dilute Orthophosphoric acid. The buffer was filtered through 0.45μ filter, degassed and used as a mobile phase A. Acetonitrile was used as a Mobile phase B.

Diluent - The mixture of Methanol, Water and Orthophosphoric acid in the ratio of 80:20:0.5%v/v/v was used as diluent.

Chromatographic condition - For better resolution between all the known impurities, unknown impurities and principle peak, the method was optimized by using Baker bond column operated at 50°C. The mobile phase A and B was separately pumped at 0.8 ml per min flow rate by keeping the composition 45:55%v/v respectively. All the solutions were injected with 50 μ l injection volume and the chromatogram was run for 60 minutes at 254 nm. Mometasone furoate along with the known impurities was injected as a system suitability solution.

Result and discussion:

The relative response factor of the all known impurities were estimated and reported. The RRF of 8DM impurity was 1.16, Impurity C was 2.02, DMC impurity was 1.34 and 0.88 for DMCF impurity. During the specificity study, no any interfering peak was observed from blank and placebo solution at the retention time of known impurities, unknown impurities and Mometasone furoate peak. The LOD values for Mometasone furoate, 8DM, Impurity G, DMC and DMCF impurity were found to be 0.005, 0.019, 0.002, 0.003, 0.004 μ g/mL and the LOQ values of 0.014, 0.058, 0.007, 0.009, 0.011 μ g/mL respectively. The recovery of each impurity and principle analytes were found between 89 to 108.6% which was well within the limits i.e. 85 to 115%. The correlation coefficients for all the impurities and Mometasone were more than 0.998 from LOQ to 150% , hence the method is linear and all the critical system suitability parameters like, RT, RRT, RRF , resolutions, Tailing factor, theoretical plates were within the limits during the robustness study.

Conclusions:

The simple isocratic stability indicating method was developed for the accurate quantification of known and unknown degradants of Mometasone furoate nasal spray. To avoid the consumptions of highly costly impurities, the relative response factor was calculated hence the developed method is cost effective. The developed method efficiently resolute all the peaks of known and unknown impurities from Mometasone furoate peak. Thus, this method can be useful in the quality control laboratory for the release and stability study of commercial batches of Mometasone furoate API and nasal spray product.

1
Chapter 8: Impurity profiling method development and validation of Metformin Hydrochloride and Vildagliptin from their combination Tablet dosage form.

In the present research work, we report related impurities separation, and quantitation from Metformin HCl and Vildagliptin from their combination Tablet dosage form. This is the regularly prescription drug products worldwide hence the impurity estimation and quantitation method has high demand in the market so that the patients will get the safe and pure medicine.

Methods and Material:

Mobile phase preparation - Accurately weighed 4.6 g Ammonium dihydrogen orthophosphate, and 1g Octane sulfonic acid sodium salt was transferred in 1 L HPLC grade water. The mixture was mixed well to dissolved, then sonicated and filtered through 0.45 μ filter. The pH was adjusted to 4 \pm 0.1 with dilute orthophosphoric acid and used as buffer. The well mixed and degassed mixture of buffer and Methanol in the ratio of 87:13 %v/v was used as mobile phase A. Degassed mixture of Methanol and buffer in the ratio of 95:5 was used as mobile phase B.

Chromatographic conditions - The mobile phase was pumped at 0.8 ml/minutes through BDS Hypersil C18, 250 x 4.6 mm, 5 μ columns which was operated at 35°C. The 10 μ l injection volume was load in to the column and the generated chromatograms were interpreted at 210 nm.

Gradient Program

Time in Min.	% M.P. A	% M.P B
0.1	100	0
15	100	0
50	80	20
60	80	20
60.1	100	0
75	100	0

Results and Discussion:

All the known impurities MTF and VIL along with principle analytes were well separate from each other's and no interference was observed from placebo and diluent at the retention time of each impurities and principle analytes. The force degradation study shows that the product is stable at thermal condition. In the basic condition 11.9% degradation was found

while 19.5 % degradation observed in peroxide condition and 12.8% in degradation observed in acidic condition. The method found linear to measure the accurate response of analytes over the range of LOQ to 150% of impurity limit. The correlation coefficient (r^2) for MTF and VIL is more than 0.996. Recovery of MTF and VIL in presence of placebo from LOQ to 150% was found between 85 to 115%. Hence the developed method has ability to recover all the impurities as well as analytes in selected diluent and volume and accurately quantitate from LOQ to 150%. The observed LOD and LOQ values of MTF is $0.33\mu\text{g/ml}$ and $1.03\mu\text{g/ml}$ where as for VIL is $0.19\mu\text{g/ml}$ and $0.57\mu\text{g/ml}$. During the robustness study, it was observed that no significant variation observed in system suitability parameters, like resolution, retention time and relative retention time hence the developed method is robust. In solution stability study at room temperature it was observed that all the solutions were stable up to 3 days at room temperature.

Conclusion:

The accurate, precise, linear related substance ²¹ method was developed for the Metformin HCl and Vildagliptin in Tablet dosage form. The method is found accurate and linear from LOQ to 150% of impurity specification limits. The method was employed for analysis for in-house developed as well as marketed samples. No any hazardous chemicals were used during development and validation study hence the method is ecofriendly. The method can be used in quality control department to analysis the commercial batches.

Chapter 9: Summary and Conclusions

This chapter covers the summary and conclusion of overall dissertation. This covers mainly the chapter wise summary and conclusion.

List of Publications/ Status

Published Articles:

1. Development and validation of stability indicating RP HPLC method for simultaneous estimation for Xylometazoline Hydrochloride and Ipratropium bromide from Nasal spray dosage form. Future Journal of Pharmaceutical Sciences (Published by Springer),(2021) 7:109.

Bhaskar Musmade, Prashant Sanatan, Surbhi Lokhande, Shrikant Kulkarni, Shrinivas Bhope, Sriram Padmanabhan, Amol Pachpinde and Kishan Lohar*

2. Impurity profiling method development and validation of metformin hydrochloride and Teneligliptin hydrobromide hydrate in their combination tablet dosage form by using RP-HPLC with UV/PDA detector , Future Journal of Pharmaceutical Sciences (Published by Springer),(2021) 7:218,

B. D. Musmade , M. L. Baraskar , V. N. Ghodke , S. G. Bhope , S. Padmanabhan and K. S. Lohar*

3. Method development, validation and estimation of relative response factor for the quantitation of known impurities of Mometasone furoate in nasal spray dosage form by using RP HPLC with UV/PDA detector, Pharmaceutical chemistry journal (published by Springer) (Accepted)

B.D. Musmade , A.V. Sawant, S.V. Kulkarni, S.D. Nage, Dr. S.G. Bhope, Dr. S. Padmanabhan, Dr. K.S. Lohar*

4. Development and validation, of Fluocinolone Acetonide, Miconazole Nitrate, Chlorocresol, Methyl paraben and Propyl Paraben, form cream formulation dosage form, by using RPHPLC with UV/PDA detector International journal of Science Engineering, and Management, Vol. 6, Issue 10, October 2021

Bhaskar Musmade, Durgesh Yadav, Shrinivas Bhope, Kishan Lohar*

5. Novel RP-HPLC Impurity Profiling method development and validation of Metformin HCL and Vildagliptin in their combination Tablet dosage form. Presented in International conference on pharmaceutical chemistry, Nanded, Maharashtra, 11&12th Jun 2022.

Bhaskar D. Musmade, Surbhi G. Lokhande, Shrinivas G. Bhope, Sriram Padmanabhan, Jaiprakash N. Sangshetti, Kishan S. Lohar*

References

1. Federal Register 65 (78), FDA, "International Conference on Harmonization: Draft Revised Guidance on Q1A(R) Stability Testing of New Drug Substances and Products 21446–21453" (21 April 2000) [ICHQ1A(R)]. This revised guideline reached Step 4 of the ICH process on 8 November 2000.
2. International Conference on Harmonisation (ICH), Harmonised Tripartite Guideline Q2(R1), 2005, *Validation of Analytical Procedures: Text and Methodology*, International Conference on Harmonization, Geneva, Switzerland.
3. International Conference on Harmonization (ICH), Harmonized Tripartite Guideline Q3A(R2), Impurities in New drug substances
4. International Conference on Harmonisation (ICH), Q14: Analytical Procedure Development and Revision of Q2 (R1) Analytical Validation, 14 November 2018.
5. Snyder, L. R., Kirkland, J. J. & Glajch, J. L. 2012. *Practical HPLC method development*, John Wiley & Sons.
6. Abdine HH, Belal F, Al-Badr AA (2003) Ipratropium bromide: physical properties. Profiles of drug Substances. Excipients and related methodology (30): 59-83.
7. Jyothi N, Gopal KV, Seshagiri Rao JVLN (2018) Development and validation of an HPLC method for the simultaneous estimation of the Salbutamol Sulphate and Ipratropium in inhalation dosage forms, International Journal of Pharma Sci 9(8).
8. Prajapati N, Dalal M (2016) Stability indicating liquid chromatographic method for estimation of Xylometazoline Hydrochloride in pharmaceutical dosage form. International Journal of Pharm Chem and Analysis. 3(3):124.
9. V. Kommineni, K. Chowdary, S.V. Prasad, Development of new stability indicating RP-HPLC method for simultaneous estimation of Metformin hydrochloride and Teneligliptin Hydrobromide and its validation as per ICH guideline, Indo Am.J. Sci. Vol. 4(05), PP 1109-1119.
10. US pharmacopeia, Fluocinolone acetonide cream, Currently Official on 13-May-2021 https://online.uspnf.com/uspnf/document/1_GUID-CF68AAAC-465B-4A27-AECA-BF302D4CF4D4_1_en-US
11. A.J. Patel, Development and Validation of Stability Indicating HPTLC Method for Simultaneous Estimation of Fluocinolone Acetonide and Miconazole Nitrate in Ointment, Austin chromatography, Volume 1, issued 5, 2014.
12. European Pharmacopoeia 6.0, Volume 2.0, page no 2441, (2008).
13. British pharmacopoeia, (3), 978 (2020).

ORIGINAL WORK

The work carried out under this research is novel, innovative and adds to the value in the field of development and validation of the Pharmaceuticals using Modern Analytical Techniques.

In the reported work, Modern Analytical Test Method has been developed and validated for employing in the pharmaceutical industry.

Same work has been already evaluated and validated for scale-up operations.

Dr. Kishan S. Lohar
Research Guide

Bhaskar D. Musmade
Research Student

BDM Ph.D Synopsis updated.doc

ORIGINALITY REPORT

15%

SIMILARITY INDEX

PRIMARY SOURCES

1	www.x-mol.com Internet	141 words — 2%
2	ijereee.com Internet	132 words — 2%
3	doaj.org Internet	98 words — 2%
4	crdd.osdd.net Internet	81 words — 1%
5	de.scribd.com Internet	53 words — 1%
6	www.gmpru.com Internet	52 words — 1%
7	repository-tnmgrmu.ac.in Internet	44 words — 1%
8	www.slideshare.net Internet	44 words — 1%
9	eprints.umm.ac.id Internet	42 words — 1%
10	www.drug2gene.com Internet	

39 words — 1%

11 1library.net
Internet

37 words — 1%

12 innovareacademics.in
Internet

25 words — < 1%

13 www.chemindustry.com
Internet

21 words — < 1%

14 reagents.alfa-chemistry.com
Internet

19 words — < 1%

15 archive.org
Internet

16 words — < 1%

16 bpac.org.nz
Internet

14 words — < 1%

17 irjponline.com
Internet

14 words — < 1%

18 doras.dcu.ie
Internet

13 words — < 1%

19 scholarworks.gsu.edu
Internet

13 words — < 1%

20 www.archive.org
Internet

13 words — < 1%

21 media.neliti.com
Internet

11 words — < 1%

22 www.asunchem.com

Internet

11 words — < 1%

23 www.chemspider.com
Internet

11 words — < 1%

24 ipindexing.com
Internet

10 words — < 1%

EXCLUDE QUOTES OFF

EXCLUDE SOURCES OFF

EXCLUDE BIBLIOGRAPHY ON

EXCLUDE MATCHES < 10 WORDS

Prof.(Dr.)K.S.LOHAR

Dr_KS_Lohar_manuscript_02.docx

By Prof. Lohar

Microstructure, Magnetic Properties of Ho³⁺ Substituted Ni-Cu-Zn Spinel Ferrites and Application for One Pot Synthesis of Dihydropyrimidinones

Abstract:

Nanoparticles of Ni-Cu-Zn spinel ferrites with Ho³⁺ substitution were synthesized through the sol-gel auto combustion route. It is illustrated from thermogravimetric analysis and differential thermal analysis curve that the decomposition of precursors takes place in the temperature range 315 - 425 °C. The Energy dispersive spectroscopy confirmed the mixing of the Fe, Ni, Cu, Zn, Ho elements in stoichiometry proportion with proper oxygen proportion in pure and substituted spinel ferrites with desired stoichiometry. X-ray diffraction pattern confirmed the formation of cubic spinel structure without any impurity phases. Lattice constant, X-ray density increases while average crystallite size decreases with increased Ho³⁺ substitution in Ni-Cu-Zn ferrites. The two strong IR absorption bands observed in the range 565–568 (ν_1) and 409 - 438 (ν_2) cm⁻¹. The obtained crystallite size lies between of 18 - 26 nm, confirmed from transmission electron microscopy. The microstructures of the calcinated spinel ferrites were evaluated by SEM and TEM. It is observed that the increase in concentration of Ho³⁺ ions saturation magnetization decreases. Prepared Ho³⁺ substituted Ni-Cu-Zn spinel ferrites were used as catalyst to synthesize the 3,4-dihydropyrimidin-2(1H)-ones.

1. Introduction

Nanoscience and Nanotechnology is the technology associated with materials in nanometer range and appliances based on them [1]. Ferrites are chemical composites with iron (III) oxide Fe_2O_3 as their major constituents [2]. The electrical conduction and magnetic interactions of the ferrites are significantly altered by substitution of trivalent or tetravalent cations and also affected by the site occupancy of cations between the tetrahedral A - and octahedral B-sites of spinel structure [3 - 6]. By tailoring the stoichiometry of the ferrite system structural, electrical and magnetic properties can be tuned [7]. The spinel ferrites have versatile applications such as magnetic drug delivery [8], information storage [9], super capacitor [10], magnetic refrigeration [11], gas sensors [12], and catalyst [13] etc.

NiCuZn ferrites have more attention of researchers due to their outstanding characteristics such as low magnetic losses, high permeability and high resistivity, which are suitable for microwave applications [14, 15]. The doping of trivalent rare-earth cations in ferrites are becoming the important components for sophisticated applications [16]. The substitution of little quantity of rare-earth cations improves structural, electrical and magnetic properties of ferrites [17, 18].

One-pot multicomponent reactions have more advantages over traditional reactions due to their rapidity, simplicity, atom-economy and shorter synthetic route [19] for the synthesis of bio-active molecules [20]. Now days, the use of heterogeneous catalysts has established significant interest in various disciplines, i.e. organic synthesis. Organic synthesis using heterogeneous catalysts have great advantage of catalyst recycle as compared to homogeneous catalyst. Iron oxide nanoparticles are used as heterogeneous catalyst as it is separated without filtration simply applying external magnet [21, 22]. The catalytic activity of spinel ferrites for these reactions arises due to the ease Fe can switch its oxidation state between 2+ and 3+ and hence spinel structure ferrites have stability under extremely reducing conditions. The Fe^{+3} reduced to Fe^{+2} without varying lattice arrangements, therefore original state is obtained on reoxidation [23].

Now days, magnetic spinel ferrites used as efficient catalyst in different chemical transformations such as synthesis of diazepine derivatives [24], α -amino nitriles [25], 1,1-diacetates from aldehydes [26], etc.

Dihydropyrimidinones have synthesized by Pietro Biginelli in 1893, by a one-pot three-component condensation of benzaldehyde, ethyl acetoacetate and urea under robustly acidic environment [27]. Also

Dihydropyrimidinones synthesized by microwave irradiation [28], ionic liquids [29], and using different types of catalysts such as lanthanide triflate [30], Sr(OTf)₂ [31], nanomagnetic-supported sulfonic acid [32], Fe(III) tosylate [33], FeCl₃-supported nanopore silica [34], etc.

The present report deals with the modification in the structural and magnetic properties of Ho³⁺ substituted Ni-Cu-Zn spinel ferrites with composition Ni_{0.2}Cu_{0.2}Zn_{0.6}Fe_{2-x}Ho_xO₄ (x = 0.00, 0.02, 0.04, 0.06, and 0.08). The targeted samples were synthesized by sol-gel auto-combustion method. The prepared samples at nano scale regime were used as a catalyst for one pot three component synthesis of Dihydropyrimidinones.

2. Methods and materials

Preparation of Ni_{0.2}Cu_{0.2}Zn_{0.6}Fe_{2-x}Ho_xO₄ ferrites: The nano-crystalline powders of Ni_{0.2}Cu_{0.2}Zn_{0.6}Fe_{2-x}Ho_xO₄ (x=0.00, 0.02, 0.04, 0.06, and 0.08) prepared using sol-gel auto-combustion method [35]. The stoichiometric quantities of analytical grade reagents of corresponding metal nitrates were dissolved in deionized water. The aqueous citric acid solution added in the metal nitrates to citric acid ratio of 1:3 and then NH₃ solution added to adjust pH ≈ 7 of solution. The resulting solution was heated on hot plate (90 °C) with continuous stirring. After some time the solution turns viscous and converted in to brown gel, with complete removal water molecule gel starts frothing and later on automatically get burnt. The process of auto-combustion accomplished in a minute, resulting in the formation of the brown ashes known as precursors. Calcination temperature is confirmed from TGA / DTA curve and all the precursors calcinated at 500 °C for four hours, gives final spinel ferrites.

Preparation of 3,4-dihydropyrimidin-2(1H)-ones: Aldehyde (1) (10 mmole), 1,3-dicarbonyl compound (2) (10 mmole), urea or thiourea (3) (15 mmole) were dissolved in ethanol to which catalyst Ni_{0.2}Cu_{0.2}Zn_{0.6}Fe_{2-x}Ho_xO₄ (20 mol %) spinel ferrite was mixed and then reaction mixture was heated at 80 °C with constant stirring for suitable time (monitored by TLC) as tabulated in Table 4. After completion of reaction, catalyst was separated by keeping the catalyst at the bottom of flask magnetically by using a strong permanent magnet, and the solution was removed. The entire mixture was then transferred into ice water, the precipitate of product obtained which is separated by filter paper, washed by water and dried. The product was purified by recrystallization using ethanol as a solvent. All the synthesized compounds were characterized by ¹H-NMR, Mass (ES-MS) and melting point.

Thermal analysis carried using simultaneous TGA and DTA of precursors at heating rate 10⁰ C / min in the range 25 °C to 800 °C on SDT Q600 V20.9 Build 20 in air. With EDAX, Inca Oxford, attached to the SEM the composition of calcinated samples determined. The structural parameters investigated by X-ray diffraction

Phillips-3710 X-ray diffractometer employed with Cu-K α radiation ($\lambda=1.5405\text{\AA}$) were used in the present study. Microstructure investigated by JEOL-JSM-5600-N Scanning Electron Microscope and on Philips-CM-200 Transmission Electron Microscope. Magnetic measurements carried at room temperature using PARC EG&G vibrating sample magnetometer.

21

3. Results and discussion

3.1. Thermogravimetric analysis (TGA) and differential thermal analysis (DTA)

Figure 1 represents typical TGA/DTA curve of $\text{Ni}_{0.2}\text{Cu}_{0.2}\text{Zn}_{0.6}\text{Fe}_{2-x}\text{Ho}_x\text{O}_4$ ($x=0.06$). The TGA curve shows two weight loss steps associated with endothermic and exothermic DTA peaks. The first weight loss step in the temperature 30-100 °C range is corresponding to endothermic peak around 80 °C, is due to evaporation of residual water from precursor. The second weight loss step in the 350-460 °C temperature region was corresponding to the exothermic peak around 400 °C, due to the decomposition of unreacted citric acid. No weight loss observed above 460 °C, representing the presence of only $\text{Ni}_{0.2}\text{Cu}_{0.2}\text{Zn}_{0.6}\text{Fe}_{2-x}\text{Ho}_x\text{O}_4$ in this temperature range. Therefore, the prepared precursors calcinated at 500 °C for four hour to get $\text{Ni}_{0.2}\text{Cu}_{0.2}\text{Zn}_{0.6}\text{Fe}_{2-x}\text{Ho}_x\text{O}_4$ spinel ferrites.

3.2. Elemental Analysis:

The chemical compositions of $\text{Ni}_{0.2}\text{Cu}_{0.2}\text{Zn}_{0.6}\text{Fe}_{2-x}\text{Ho}_x\text{O}_4$ ferrite nanoparticles are determined by EDAX. Fig.2 (a) and (b) shows the typical EDAX pattern for the $\text{Ni}_{0.2}\text{Cu}_{0.2}\text{Zn}_{0.6}\text{Fe}_{2-x}\text{Ho}_x\text{O}_4$, ferrite nanoparticles $x=0.00$ and $x=0.08$ respectively. The EDAX pattern confirmed the homogeneous mixing of the elements in desired composition. The values of observed and theoretical percentage of Fe, Ni, Cu, Zn, Ho and oxygen are in good agreement with theoretical % values of element (Table 1).

3.3. Structural Analysis

Figure 3 shows the XRD patterns of the calcinated $\text{Ni}_{0.2}\text{Cu}_{0.2}\text{Zn}_{0.6}\text{Fe}_{2-x}\text{Ho}_x\text{O}_4$ ferrites. XRD patterns illustrates single phase cubic spinel ferrite (JCPDS # 00-52-0277 and 00-74-0444) [36] was obtained for the pure NiCuZn ferrite and no other visible peak corresponding to the second phase was observed, which illustrated that Ho^{3+} could be entirely solid-soluted in cubic spinel structure or that the amount of the other phase was too small to be identified by XRD [37-38].

The lattice constant 'a' determined by equation discussed elsewhere [38] and given in Table 2. The calculated lattice constants are within range of 8.417 Å to 8.429 Å, increases with in Ho^{3+} ion concentration. The variation

in 'a' was mainly attributed to difference between the ionic radii of constituent ions. Here, smaller Fe³⁺ (0.67 Å) ions are substituted by larger Ho³⁺ (1.04 Å) ions [38].

X-ray density 'd_x' of Ho³⁺ substituted Ni-Cu-Zn ferrites samples were calculated using the following formula and tabulated in Table 2,

$$d_x = \frac{8M}{Na^3} \quad (1)$$

where 'a' is lattice constant, 'N' is the Avogadro's number and 'M' is molecular weight. The X-ray density in present spinel ferrites increased with Ho³⁺ ion concentration, due to the increased molecular weight of spinel ferrite.

Crystallite size (D_{XRD}) was obtained from the XRD pattern by employing Debye Scherrer method [39]. The calculated D_{XRD} lies within the range of 18 - 26 nm (Table 2). The crystallite size in present spinel ferrites was decreased with Ho³⁺ concentration, due to the increase in porosity.

The porosity 'P' in percentage was calculated by following equation discussed elsewhere [40]. The porosity 'P' in present spinel ferrites is increased with Ho³⁺ substitution. The increase the grain boundaries of the fine particles may resulted in enhancement in 'P', that illustrate the porous structure of the Ni_{0.2}Cu_{0.2}Zn_{0.6}Fe_{2-x}Ho_xO₄, ferrites.

The hopping lengths L_A and L_B were calculated using following equations [41],

$$L_A = \frac{a\sqrt{3}}{4} \quad (2)$$

$$L_B = \frac{a\sqrt{2}}{4} \quad (3)$$

It has been observed that both the hopping lengths are increased with the Ho³⁺ ion concentration (Table 2). Variations in hopping lengths are attributed to the variation in lattice constant and ionic radii of constituent ions.

Figure 4 illustrates the IR spectra of the Ni_{0.2}Cu_{0.2}Zn_{0.6}Fe_{2-x}Ho_xO₄, ferrites. The two major absorption bands observed in the range 565–568 (ν₁) and 409–438 (ν₂) cm⁻¹ (Table 3) are the characteristics of spinel ferrites. The ν₁ and ν₂ bands ascribed to the metal–oxygen vibrations at the A- and B-sites, respectively [42]. Values of two

bands ν_1 and ν_2 are different due to the difference in $\text{Fe}_B^{3+} - \text{O}_2^{2-}$ inter-ionic distance for the A- and B-sites. The vibrational frequency of bonds is dependent on the mass of cation, bond length and force constant of bond [43].

The force constants of A-site (K_A) and B-site (K_B) evaluated by the Waldron method [44] and values tabulated in Table 3. K_A and K_B in present spinel ferrites decreased from 2×10^5 to 1.78×10^5 dyne/cm and 1.19×10^5 to 0.82×10^5 dyne/cm, respectively, with increase in concentration of Ho^{3+} ions. The bond lengths at A and B sites (R_A and R_B) determined using the formula given by Gorter [45]. The R_A and R_B in present spinel ferrites are increased with the substitution of Ho^{3+} ions (Table 3).

The microstructure observation of the $\text{Ni}_{0.2}\text{Cu}_{0.2}\text{Zn}_{0.6}\text{Fe}_{2-x}\text{Ho}_x\text{O}_4$ spinel has been carried out by scanning electron microscopy (SEM). Typical SEM images were presented in Fig. 5 (a, $x = 0.02$ and b, $x=0.08$). The calcinated spinel ferrites were porous with a fine-particle microstructure. It is apparent that Ho^{3+} substituted NiCuZn ferrites revealed a little improved dense microstructure marked with little trapped porosity.

Typical TEM images of the $\text{Ni}_{0.2}\text{Cu}_{0.2}\text{Zn}_{0.6}\text{Fe}_{2-x}\text{Ho}_x\text{O}_4$ spinel ferrite are illustrated in Fig.6 (a, $x = 0.02$ and b, $x=0.08$). These TEM images indicate that sphere-like nanostructures obtained by presently employed sol-gel method. Particles are seems to uniform in particle size and microstructure and are agglomeration to some extent because of their magnetic interactions.

Selective area electron diffraction (SAED) pattern of typical composition of $\text{Ni}_{0.2}\text{Cu}_{0.2}\text{Zn}_{0.6}\text{Fe}_{2-x}\text{Ho}_x\text{O}_4$ spinel ferrite are shown in Fig. 7 (a, $x = 0.02$ and b, $x=0.08$). The SAED patterns indicate that spinel ferrites were well distributed. The bright spot in the SAED patterns were superimposed with Debye ring confirmed the polycrystalline nature of the prepared samples. These Debye rings are assigned to lattice planes and are in good analogy with those planes obtained by the XRD data.

Particle size distributions of the respective TEM images measured by ImageJ software and typical histograms shown in Fig. 8 (a, $x = 0.02$ and b, $x=0.08$). The particle size observed to decrease from 26.8 to 20.4 nm with increasing Ho^{3+} ion concentration. The observed particle size from TEM and XRD are consistent with each other (Table 2).

3.4 Magnetic Properties

Hysteresis loops of $\text{Ni}_{0.2}\text{Cu}_{0.2}\text{Zn}_{0.6}\text{Fe}_{2-x}\text{Ho}_x\text{O}_4$ spinel ferrite shown in Fig.9, which illustrates that prepared samples are soft magnetic material with very low coercivity. Saturation magnetization (M_s), coercivity (H_c), and magneton number (n_B) derived from hysteresis loops and are tabulated in table 4. Coercivity obtained from

the hysteresis loop was increased with the Ho³⁺ substitution. Ms for pure Ni_{0.2}Cu_{0.2}Zn_{0.6}Fe₂O₄ (x = 0.0) sample is 22.84 emu/g and it decreased to 16.05 emu/g for Ni_{0.2}Cu_{0.2}Zn_{0.6}Fe_{1.92}Ho_{0.08}O₄ (x = 0.08). The magneton number n_{B(Obs)} was determined from hysteresis loops [46]:

$$n_B(obs.) = \frac{Mw \times Ms}{5585} \quad (4)$$

Saturation magnetization decreases while observed magneton number increased with Ho³⁺ substitution. The increase in n_{B(Obs)} was attributed to the increased A-B magnetic interaction. The substitution of Fe³⁺ with Ho³⁺ the Ms and Mr may decrease as a result of decreased exchange interaction between Fe^{Td}-Fe^{Oh}, which is replaced by the weaker Fe^{Td}-Ho^{Oh} interaction [37, 38, 47].

Magneton number (observed) decreases with Ho³⁺ substitution. Coercivity obtained from the hysteresis loop is observed to increase Ho³⁺ concentration (Table 4)

The net magnetic moment (n_{B(Cal.)}) is determined using equation, n_{B(Cal.)} = M_B-M_A; where, M_A and M_B are the A and B sub-lattice magnetic moments, respectively, in μ_B [48]. Values of n_{B(Cal.)} for Ni_{0.2}Cu_{0.2}Zn_{0.6}Fe_{2-x}Ho_xO₄ were determined through cation distribution data and magnetic moment of Fe³⁺ (5μ_B), Ni²⁺ (2μ_B), Zn²⁺ (0μ_B), Cu³⁺ (1μ_B) and Ho³⁺ (10μ_B). The calculated Magneton number decreases with Ho³⁺ substitution. The magneton number (calculated) also decreases with Ho³⁺ substitution

3.4 Application for One Pot Synthesis of Dihydropyrimidinones

3,4-dihydropyrimidin-2(1H)-ones was prepared by one-pot three-component condensation of aromatic aldehydes (1), 1,3-dicarbonyl compounds (2) and urea/thiourea (3) using 10 mol % Ho³⁺ doped Ni_{0.2}Cu_{0.2}Zn_{0.6}Fe_{2-x}Ho_xO₄ spinel ferrites catalyst (Scheme 1).

Ethyl 6-methyl-4-(4-pyridyl)-2-oxo-1,2,3,4-tetrahydropyrimidine-5-carboxylate (4g): ¹H-NMR (DMSO-*d*₆, 300 MHz) δ 9.38 (s, 1H, NH), 8.50 (d, 2H), 7.85 (s, 1H, NH), 7.20 (d, 2H), 5.15 (d, 1H, J=3.3 Hz, H-4), 4.00 (q, 2H, OCH₂), 2.27 (s, 3H, CH₃), 1.09 (t, 3H, J= 7.2Hz, CH₃); Mass (ES/MS): m/z 260 (M-H, 100%).

Catalytic efficiency Ni_{0.2}Cu_{0.2}Zn_{0.6}Fe_{2-x}Ho_xO₄ spinel ferrites studied by screening five compositions x = 0.0, 0.02, 0.04, 0.06 and 0.08 to find out best ferrite composition (catalyst) for 3,4-dihydropyrimidin-2(1H)-one (4a) synthesis as a representative reaction. The 3,4-dihydropyrimidin-2(1H)-one compound 4a, was obtained with 95% yield with Ni_{0.2}Cu_{0.2}Zn_{0.6}Fe_{2-x}Ho_xO₄ (x = 0.06) spinel ferrites catalyst rapidly (100 min) compared to other spinel ferrites compositions (x = 0.0, 0.02, 0.04 and 0.08).

The quantity of ferrite composition (catalyst load) was optimized for model reaction (4a). The spinel ferrite as a catalyst was used in varying quantity of 0, 5, 10, 15 and 20 mol %. The decrease in ferrite catalyst quantity from 20 to 10 mol % does not affect the yield (Table 5). Therefore, 10 mol % of the catalyst $\text{Ni}_{0.2}\text{Cu}_{0.2}\text{Zn}_{0.6}\text{Fe}_{2-x}\text{Ho}_x\text{O}_4$ ($x = 0.6$) spinel ferrites was considered to obtain the maximum yield (95 %) in less reaction time (10 min).

The generality of this approach was assessed by reacting various aldehydes with 1,3-dicarbonyl compound (2) and urea or thiourea (3) under optimized conditions to obtain substituted 3,4-dihydropyrimidin-2(1H)-ones (4a-h) (Scheme 1).

In heterogeneous catalysis, reusability of the catalyst is an important aspect. The investigation of recovery and reusability of the catalyst was performed for model reaction (4a). Catalyst was recycled after the completion of reaction. For this a strong magnet was used to fix it at the bottom of the flask. The fixed solid catalyst washed twice with acetone. The next run of reaction was proceeded by introducing the fresh substrate into the flask. The catalyst was effectively reusable 5 times without losing its catalytic performance. (Cycle number and yield of 4a: 1, 95 %; 2, 95 %; 3, 95 %; 4, 94 %; 5, 93 %).

The work-up process was very simple and first catalyst was removed magnetically then the entire mixture transferred into ice water. The product precipitates out which is separated by filter paper, washed with water and dried. The as-obtained product was purified by recrystallization using ethanol as a solvent. The efficiency, easy handling and mild nature are advantageous aspect of the catalyst.

4. Conclusions:

Holmium substituted NiCuZn ferrites with composition $\text{Ni}_{0.2}\text{Cu}_{0.2}\text{Zn}_{0.6}\text{Fe}_{2-x}\text{Ho}_x\text{O}_4$ was successfully obtained by 'sol-gel auto combustion method'. Precursor powders calcinated at 500 °C. The observed elemental analysis from EDAX was in good agreement with the theoretical stoichiometry. The lattice constant, X-ray density and hopping lengths increased with increase in Ho^{3+} . The D_{XRD} was decreased from 26.2 to 19.9 nm with the substitution of Ho^{3+} confirmed by TEM. The two strong IR absorption bands observed in the range 565–568 (ν_1) and 409–439 (ν_2) cm^{-1} . SEM images confirmed the porous nature with a fine-grained microstructure. TEM images revealed sphere-like nanostructures and particles with agglomeration to some extent due to their magnetic interactions. Saturation magnetization decreased while observed magneton number increased with the increase in Ho^{3+} concentration. 3,4-dihydropyrimidin-2(1H)-ones synthesized using the one-pot three-component condensation of aromatic aldehydes, 1,3-dicarbonyl compounds and urea/thiourea using magnetic 10 mol % Ho^{3+} doped NiCuZn spinel ferrites catalyst.

15%

SIMILARITY INDEX

PRIMARY SOURCES

- 1 www.bioorganica.org.ua 71 words — 2%
Internet
- 2 K.A. Ganure, M.M. Langade, L.A. Dhale, K.S. Lohar. "Chromium substituted nickel ferrites (NiFe_{2-x}Cr_xO₄, x=0.0, 0.1, 0.2, 0.3, and 0.4) magnetically recoverable reusable heterogeneous nano catalysts", Materials Today: Proceedings, 2020 57 words — 2%
Crossref
- 3 Rohit Jasrotia, Pooja Puri, Ankit Verma, Virender Pratap Singh. "Magnetic and electrical traits of sol-gel synthesized Ni-Cu-Zn nanosized spinel ferrites for multi-layer chip inductors application", Journal of Solid State Chemistry, 2020 26 words — 1%
Crossref
- 4 Abdelmadjid Debache, Wassima Ghalem, Raouf Boulcina, Ali Belfaitah, Salah Rhouati, Bertrand Carboni. "Triethylamine Promoted Efficient Synthesis of 3,4-Dihydropyrimidin- 2(1H)-ones/thiones Using a Solvent-Free Biginelli Condensation", Letters in Organic Chemistry, 2010 21 words — 1%
Crossref
- 5 Hashem Sharghi, Mahboubeh Jokar. " Al O /MeSO H: A Novel and Recyclable Catalyst for One-Pot Synthesis of 3,4-Dihydropyrimidinones or Their Sulfur Derivatives in Biginelli Condensation ", Synthetic Communications, 2009 21 words — 1%
Crossref
- 6 D.R. Mane, Swati Patil, D.D. Birajdar, A.B. Kadam, Sagar E. Shirsath, R.H. Kadam. "Sol-gel synthesis of Cr³⁺ substituted Li_{0.5}Fe_{2.5}O₄: Cation distribution, structural and

-
- 7 Wen Pei, Qin Wang. " Synthesis of 3,4-Dihydropyrimidin-2(1H)-ones Using Ce(SO₄)₂-SiO₂ as a Heterogeneous and Recyclable Catalyst ", Synthetic Communications, 2010 18 words — 1%
- Crossref
-
- 8 S.M. Kabbur, U.R. Ghodake, D.Y. Nadargi, Rahul C. Kambale, S.S. Suryavanshi. "Effect of Dy³⁺ substitution on structural and magnetic properties of nanocrystalline Ni-Cu-Zn ferrites", Journal of Magnetism and Magnetic Materials, 2018 17 words — 1%
- Crossref
-
- 9 Bhattarai, S.R.. "N-Acylated chitosan stabilized iron oxide nanoparticles as a novel nano-matrix and ceramic modification", Carbohydrate Polymers, 20070625 16 words — 1%
- Crossref
-
- 10 K.S. Lohar, A.M. Pachpinde, M.M. Langade, R.H. Kadam, Sagar E. Shirsath. "Self-propagating high temperature synthesis, structural morphology and magnetic interactions in rare earth Ho³⁺ doped CoFe₂O₄ nanoparticles", Journal of Alloys and Compounds, 2014 15 words — < 1%
- Crossref
-
- 11 publications.waset.org 15 words — < 1%
- Internet
-
- 12 Wei-Yi Chen, Su-Dong Qin, Jian-Rong Jin. "Efficient Biginelli Reaction Catalyzed by Sulfamic Acid or Silica Sulfuric Acid under Solvent-Free Conditions", Synthetic Communications, 2007 14 words — < 1%
- Crossref
-
- 13 Xuesen Fan, Xinying Zhang, Yongmin Zhang. " Samarium chloride catalysed Biginelli reaction: one-pot synthesis of 3,4-dihydropyrimidin-2(1H)-ones ", Journal of Chemical Research, 2002 13 words — < 1%
- Crossref

14 Hojatollah Salehi, Qing-Xiang Guo. "A Facile and Efficient One-Pot Synthesis of Dihydropyrimidinones Catalyzed by Magnesium Bromide Under Solvent-Free Conditions", *Synthetic Communications*, 2004

Crossref

13 words — < 1%

15 scholarbank.nus.edu.sg

Internet

12 words — < 1%

16 Behzad Zeynizadeh, Karim Akbari Dilmaghani, Mahdi Yari. "NaHSO₄·H₂O as a Heterogeneous Acidic Reagent for Mild and Convenient Synthesis of 3,4-Dihydropyrimidin-2(1H)-ones and Their Sulfur Derivatives", *Phosphorus, Sulfur, and Silicon and the Related Elements*, 2009

Crossref

11 words — < 1%

17 Nagawade, R.R.. "Synthesis of new series of 1-Aryl-1,4-dihydro-4-oxo-6-methyl pyridazine-3-carboxylic acid as potential antibacterial agents", *European Journal of Medicinal Chemistry*, 200512

Crossref

11 words — < 1%

18 V.V. Awati, S.M. Rathod, Sagar E. Shirsath, Maheshkumar L. Mane. "Fabrication of Cu²⁺ substituted nanocrystalline Ni–Zn ferrite by solution combustion route: Investigations on structure, cation occupancy and magnetic behavior", *Journal of Alloys and Compounds*, 2013

Crossref

11 words — < 1%

19 Awati, V.V., S.M. Rathod, Sagar E. Shirsath, and Maheshkumar L. Mane. "Fabrication of Cu²⁺ substituted nanocrystalline Ni–Zn ferrite by solution combustion route: Investigations on structure, cation occupancy and magnetic behavior", *Journal of Alloys and Compounds*, 2013.

Crossref

9 words — < 1%

20 Mohd Hashim, Alimuddin, Sagar E. Shirsath, Shalendra Kumar, Ravi Kumar, Aashis S. Roy, Jyoti Shah, R.K. Kotnala. "Preparation and characterization chemistry of nano-crystalline Ni–Cu–Zn ferrite", *Journal of Alloys and Compounds*, 2013

9 words — < 1%

-
- 21 iopscience.iop.org 9 words — < 1%
Internet
-
- 22 Haixia Zhou, Miao He, Chunsheng Liu, Heng Jiang, Genxiang Luo. " One-Pot Synthesis of 3,4-Dihydropyrimidin-2(1)-ones using CuBr as Catalyst ", Preparative Biochemistry and Biotechnology, 2006 8 words — < 1%
Crossref
-
- 23 Surendra More, Ram Kadam, Ankush Kadam, Dhanraj Mane, Govind Bichile. "Structural properties and magnetic interactions in Al³⁺ and Cr³⁺ co-substituted CoFe₂O₄ ferrite", Open Chemistry, 2010 8 words — < 1%
Crossref
-
- 24 Verma, S., J. Chand, K.M. Batoo, and M. Singh. "Cation distribution and Mössbauer spectral studies of Mg_{0.2}Mn_{0.5}Ni_{0.3}In_xFe_{2-x}O₄ ferrites (x=0.0, 0.05 and 0.10)", Journal of Alloys and Compounds, 2013. 8 words — < 1%
Crossref
-
- 25 studentsrepo.um.edu.my 8 words — < 1%
Internet
-
- 26 Ashok Gadkari, Tukaram Shinde, Pramod Vasambekar. "Influence of rare-earth ions on structural and magnetic properties of CdFe₂O₄ ferrites", Rare Metals, 2010 8 words — < 1%
Crossref
-
- 27 Lohar, K.S., S.M. Patange, M.L. Mane, and Sagar E. Shirsath. "Cation distribution investigation and characterizations of Ni_{1-x}Cd_xFe₂O₄ nanoparticles synthesized by citrate gel process", Journal of Molecular Structure, 2013. 8 words — < 1%
Crossref
-
- 28 Gadkari, A.B.. "Structural analysis of Y³⁺-doped Mg-Cd ferrites prepared by oxalate co-precipitation method", Materials Chemistry and Physics, 20090415 7 words — < 1%
Crossref

EXCLUDE QUOTES OFF

EXCLUDE MATCHES OFF

EXCLUDE
BIBLIOGRAPHY ON

Prof.(Dr.)K.S.LOHAR

**Dr_KS_Lohar_manuscript_03 - plagiarism
removed.docx**

By Prof. Lohar

**Synthesis, Microstructure, Magnetic Properties and Catalytic
Applications of Co²⁺ and Cr³⁺ Doped Ni- Zn Spinel Ferrite**

Abstract

Cobalt and chromium doped nanocrystalline ferro spinels, with composition $\text{Ni}_{0.5}\text{Co}_x\text{Zn}_{0.5-x}\text{Fe}_{2-y}\text{Cr}_y\text{O}_4$ in step of ($x = y = 0.1$ to 0.5 in steps of 0.1) was synthesized by sol-gel auto-combustion route by using glycine as fuel, calcination temperature of samples confirmed from thermogravimetric analysis, differential scanning calorimetry analysis. The observed elemental stoichiometry from energy dispersive spectroscopy is in good agreement with the theoretical stoichiometry. The X-ray diffraction patterns illustrates all samples possess single- phase cubic spinel structure without the signature of any impurity or secondary phases. The lattice constant was decreased from $8.360 - 8.298 \text{ \AA}$ with the increase in concentrations of Co^{2+} and Cr^{3+} ions substitution to the Ni-Zn ferrite system. Zn^{2+} ions preferably occupying the tetrahedral site and Ni^{2+} , Co^{2+} , Cr^{3+} ions mainly penetrate octahedron site (B sub lattice). The Infrared spectra show two principle absorption bands (ν_1 and ν_2) around 600 cm^{-1} and 400 cm^{-1} . Scanning electron microscopy and Transmission electron microscopy images reveal well defined nanoparticles with slight agglomeration. Calculated and observed magneton number decreased with Co^{2+} and Cr^{3+} substitution. 1, 8-dioxodecahydroacridines synthesised using magnetically separable and reusable $\text{Ni}_{0.5}\text{Co}_x\text{Zn}_{0.5-x}\text{Fe}_{2-y}\text{Cr}_y\text{O}_4$ nanoparticles as a catalyst.

1. Introduction

Nowadays extensive attention paid towards magnetic ferrite nanoparticles due to its wide applications in, sensor [1-3], catalysis [4,5], biomedicine [6,7], MRI [8], drug delivery [9], magnetic recording [10], microwave devices [11] and magnetic ferro- fluids [12] etc. Nano ferro spinels have a general chemical composition $[\text{A}][\text{B}_2]\text{O}_4$, with two types of interstitial sites, the tetrahedral (A) site and the octahedral (B) site engaged by metal

4 cations [13, 14]. The electrical and magnetic properties of AB₂O₄-ferrites governed by A and B sub lattices in cubic spinel structure. By using the cations preference to a particular site, Co-Zn [15], Ni-Zn [16], Ni-Cu-Zn [17] and Ni-Co-Zn [18], etc. ferrites were developed. The electrical and magnetic properties of ferrites extensively altered by doping of trivalent ions like Al³⁺, Cr³⁺ etc. for Fe³⁺ ion [19-23].

Magnetite spinel ferrite used as efficient catalyst in different chemical transmissions such as pyrano pyrimidines [24], 1, 4-dihydropyridines [25], benzimidazoles [26], pyrroles [27], etc. The catalytic activity of spinel ferrite is because of migration of metal cations within A- and B-site without altering original spinel structure that makes them more effective catalyst for reactions [28]. Magnetite spinel ferrite catalyst easily separated with external magnetic field without filtration from reaction mixture [29]. The preparation methods were found to be of great importance for the different properties of ferrite; among them are sol- gel [30], co- precipitation [31], egg white route [32] and hydrothermal [33]. Acridine and its derivatives show various biological activities as anticancer [34], antitumor [35], anticonvulsant [36], analgesic [37], hypertensive and anti-inflammatory [38], antibacterial [39], antimalarial [40] etc. In literature number of methods adopted for synthesis of 1,8-dioxodecahydroacridines, which involves condensation of aromatic aldehydes, cyclic diketones and different nitrogen sources and various catalysts have been reported [41-46]. These methods have few drawbacks such as poor yields, requires more time, multistep synthesis, harsh reaction conditions, etc.

19 Herein we report synthesis, structural magnetic properties of the Ni_{0.5}Co_xZn_{0.5-x}Fe_{2-y}Cr_yO₄ (x = y = 0.1 to 0.5 in steps of 0.1) synthesised by sol gel method and its application as catalyst for of 1, 8-dioxodecahydroacridines synthesis (Scheme 1).

2. Methods and materials

Nanocrystalline spinel ferrites with composition $\text{Ni}_{0.5}\text{Co}_x\text{Zn}_{0.5-x}\text{Fe}_{2-y}\text{Cr}_y\text{O}_4$ ($x = y = 0.0$ to 0.5 in steps of 0.1) were synthesized by the sol-gel auto-combustion method [21], from corresponding metal nitrates of analytical grade reagent having purity 99% and glycine as a fuel, were used in the synthesis without any further treatment. All metal nitrates in desired stoichiometry were dissolved in deionised water to which glycine added in the metal nitrates to glycine 1:3 molar ratio. The $\text{pH} \approx 7$ of reaction mixture was maintained by gradually addition of the NH_3 solution. The solution was kept on a hot plate with constant stirring at 90°C . A viscous brown gel was formed as a result of evaporation of solution. After evaporation of all of the water molecules; the viscous gel obtained and it began to froth and get self ignited and burnt. The auto-combustion finished within a short time, giving brown ashes termed as the precursor.

The simultaneous TGA/DSC analysis carried on SDT Q 600 V20.9 Build 20 thermal analyser, with a heating rate 10°C per minutes in air atmosphere. The elemental composition investigated by Energy Dispersive X-Ray Analysis (EDAX, Inca Oxford, attached to the SEM). The crystallographic structures were identified by X-ray powder diffraction with $\text{Cu K}\alpha$ radiation ($\lambda = 1.5405\text{\AA}$) by Phillips-3710 X-ray diffractometer. Morphology and structure evaluated on JEOL-JSM-5600 N Scanning Electron Microscope and on Philips-CM-200 Transmission Electron Microscope. The IR spectra recorded in the range 200 to 800 cm^{-1} with Perkin Elmer infrared spectrophotometer. The magnetic measurements recorded at room temperature with PARC-EG&G-VSM-4500 vibrating sample magnetometer.

For catalytic reaction: the Melting points of synthesized compounds are recorded and are uncorrected. $^1\text{H-NMR}$ spectra of the compounds were recorded using Varian Gemini spectrometer (300 MHz). TMS is used as an internal standard for comparison of

¹⁴ Chemical shifts which were reported in δ units (ppm). Mass spectra were recorded using ¹² Electron spray ionization mass spectra (ES-MS) (¹² Water-Micro mass Quattro-II spectrometer). AR grade reagents were used without further purification.

Aromatic aldehyde ³ **1** (1 mmol), cyclic diketone **2** (2 mmol), ammonium acetate **3** (10 mmol) and $\text{Ni}_{0.5}\text{Co}_x\text{Zn}_{0.5-x}\text{Fe}_{2-y}\text{Cr}_y\text{O}_4$ ($x = y = 0.0$ to 0.5) (40 mol %) mixture was placed in 15 mL of ethanol under reflux for appropriate time. Reaction was continuously monitored by TLC. Under reflux the catalyst was removed using strong magnet placed at the bottom of flask. The hot reaction mixture was filtered. The solvent was then evaporated to get the crude product. The recrystallization of crude product was done using ethanol to get pure products.

⁵ 3. Results and Discussion

3.1. TGA/ DSC analysis

The decomposition pattern of Co^{2+} and Cr^{3+} substituted Ni-Zn ferrites ($x = y = 0.0$) precursor is shown in Fig.1., indicate four thermal effects, at onset temperature around 200 °C, the first endothermic peak is observed due to loss of co-ordinated water molecule 0.7479%. The second exothermic peak locate near temperature 350 °C shown more weight loss, 1.161% can be attributed to dehydration of crystalline water or chemisorbed water molecules and metals converted to metal oxides, they undergo solid state chemical reaction with formation of ferrites with liberation of oxygen molecules with mass loss 0.0821% is an slightly endothermic reaction. Small mass of 0.2552% increased for >400 °C due to the oxidation of Fe^{2+} to Fe^{3+} via endothermic reaction [47]. No significant mass loss > 575 °C was observed indicating the formation of ferro -spinel compounds. The other precursors of series shown similar type of decomposition patterns and convert

in to ferrites in the temperature range 550–600 °C. Similar type precursor's decomposition patterns were reported by many researchers [48-50]. Finally all precursors were calcinated at 600 °C for four hours to get desired nano ferro- spinels.

8 3.1. Elemental Analysis:

Energy Dispersive X-Ray Analysis (EDAX) was utilized to obtain the elemental stoichiometric composition of the samples. EDAX of a typical sample ($x = y = 0.3$) is represented by Fig. 2. The theoretical and observed elemental compositions are tabulated in Table 1. The observed elemental composition obtained by EDAX is consistent to the theoretical stoichiometry of elements.

3.3. Structural Analysis

The XRD patterns of $\text{Ni}_{0.5}\text{Co}_x\text{Zn}_{0.5-x}\text{Fe}_{2-y}\text{Cr}_y\text{O}_4$ shown in the Fig. 3. The XRD patterns illustrated the single phase formation of cubic spinel structure without any secondary phases for all samples. The lattice constant 'a' obtained through equation discussed elsewhere [51] and tabulated in Table 2. 'a' decreased from 8.360 to 8.298 Å with the increased Co^{2+} and Cr^{3+} ions substitution to the Ni-Zn ferrite system. It is related to ionic radii, in present spinel ferrite the smaller Co^{2+} (0.65 Å) ions replaced by the larger Zn^{2+} (0.74 Å) ions [52] and smaller Cr^{3+} (0.63 Å) by larger Fe^{3+} (0.67 Å) [21]. The X-ray density 'd_x' was calculated using equation discussed elsewhere [53]. The values of d_x are tabulated in Table 2 illustrates d_x decreased with increasing Co^{2+} and Cr^{3+} concentration.

The broad diffraction peaks exhibit the fine particle nature of ferrite powders. The average crystalline diameter 'D_{XRD}' of samples determined using Debye Scherer method [52]. D_{XRD} are listed in Table 2, illustrates that the crystalline size increases from 26.21 to 32.21 nm with Co and Cr substitution.

Bulk density d_B is determined by relation,

$$d_B = \frac{M}{V} \quad (1)$$

where V is volume ($v = \pi r^2 h$), M, r and h are the mass, radius and thickness of pellet, respectively. The values of d_B tabulated in Table 2, illustrate that d_B increased from 2.547 to 2.619 g/cm³. The percentage porosity 'P' determined using d_x and d_B :

$$P = 1 - \frac{d_B}{d_x} \times 100\% \quad (2)$$

As evidenced from Table 2, that the porosity increased from 51.290 ($x = 0.0$) to 52.877 ($x = y = 0.5$) with the Co²⁺ and Cr³⁺ substitution. Molecular weight (MW) and the unit cell volume (V) of Ni_{0.5}Co_xZn_{0.5-x}Fe_{2-y}Cr_yO₄ decreased with increasing Co²⁺ and Cr³⁺ concentration, though the rate of the decrease in MW is higher than that of V. Notably decrease in d_B increase the porosity (P). Apart from this, the increase in porosity is mainly attributed to the increase in D_{XRD} , which increased the grain boundaries of the particle [54].

The hopping lengths (L_A and L_B) determined from the relation discussed elsewhere [55]. It can be seen from Table 2 that L_A and L_B decreased with Co²⁺ and Cr³⁺ substitution. The decrease in both the hopping lengths with Co²⁺ and Cr³⁺ substitution is because of decreased lattice constant. The magnetic Co²⁺ and Cr³⁺ ions that occupy the B-sites will cause an increase in both A–A and A–B interactions and will decrease the B–B exchange interaction. This may be related to the transfer of Fe³⁺ ions from B-sites to A-sites due to the insertion of both Co²⁺ and Cr³⁺ ions to the B-sites. Moreover, the increase of Co²⁺ ions in the composition due to increase of x is associated with a decrease of Zn²⁺ ions [55].

3.4. Cation Distribution

The cation distribution was determined by the Bertaut method [56] between tetrahedral and octahedral sites, listed in Table 3. The Zn^{2+} ions preferably occupy the tetrahedral site (A sub lattice) and Ni^{2+} , Co^{2+} , Cr^{3+} ions mostly go into octahedral site (B sub lattice) [57]. However, Fe^{3+} ions occupy both the available A and B sub lattices. With rising Cr^{3+} concentration, the percentage of Fe^{3+} ions in B sites linearly decreased. The Cr^{3+} replaced Fe^{3+} from B-sites due of their favourable crystal field impact [57]. The ionic radii of the constituent ions $Zn^{2+}(0.81\text{\AA})$, $Cr^{3+}(0.63\text{\AA})$, $Co^{2+}(0.72\text{\AA})$ and $Fe^{3+}(0.67\text{\AA})$ could also be important in deciding cation occupancies [53].

Oxygen parameter (u), intensities of experimental and observed from XRD peaks and cation distribution are tabulated in Table 3. The mean ionic radius of the A and B-sites (r_A and r_B) was determined using the equations reported in literature [58]. r_A decreased and ' r_B ' increased with increasing Co^{2+} concentration. The increase of r_B is related to the increasingly high occupation of the B site by the smaller ionic radius of $Co^{2+}(0.72\text{\AA})$ ions that replacing $Zn^{2+}(0.74\text{\AA})$ ions [59].

3.5. Infrared spectroscopy

IR spectra for all compositions are given in Fig. 4. The spectrum shows two main principle absorption bands near 600 cm^{-1} (ν_1) and 400 cm^{-1} (ν_2) which is a common feature of spinel ferrites (Table 4). The appearance of these bands in these range confirm the spinel phase structure. The high frequency band (ν_1) is assigned to the vibration of the tetrahedral sites metal ions with oxygen ions whereas, the lower frequency one (ν_2) is assigned to the octahedral sites [60]. The values of A-site bond length (R_A) and B-site bond length (R_B) are tabulated in Table 4. R_A and R_B were decreased with increased Co^{2+} and Cr^{3+} content. The force constants K_t and K_o increases with increased Co^{2+} and Cr^{3+} content.

3.6. Scanning Electron Microscopy (SEM)

Typical SEM image of the prepared spinel ferrites ($x = y = 0.3$) given in Fig. 5. SEM images illustrate well defined nanoparticles with slight agglomeration of the sample with inhomogeneous broader grain size distribution. Agglomeration is due to the increased magneto crystalline anisotropy of different domains that varies in alignments of particles comes closer to each other [61].

3.7. Transmission Electron Microscopy (TEM)

Fig. 6 shows a typical TEM image and respective histogram (Fig. 7) of the sample ($x = y = 0.3$). Particle size 't' obtained from TEM analysis are around 24 - 36 nm and these are closer to the values are determined from XRD. The most of the nanoparticles are spherical; however, few elongated particles were also seen. The particles are slightly agglomerated as a result of the interaction between the magnetic nanoparticles. Selected area electron diffraction patterns of the sample ($x = y = 0.3$) is presented in Fig. 8. The superimposition Debye ring pattern to the bright spots illustrates the polycrystalline nature [52].

3.8. Magnetization

Magnetic hysteresis loops are given in Fig. 9. Magnetic properties of spinel oxides such as ferrites are mainly structure, composition and cation distribution dependent [62]. Neel's two sub-lattice models are used to study the magnetic behaviour, magnetic moment n_B is determined by equation discussed elsewhere [63]. Magnetization increased up to certain applied magnetic field above that it remains unchanged (Fig. 9). Saturation magnetization (M_s), coercivity (H_c), and magneton number (n_B) derived from hysteresis loops and are given in Table 5. M_s decreased from 36.546 to 3.397 emu/g, with increase in Co^{2+} and Cr^{3+} concentration. Remnant magnetization (M_r) decreased while coercivity

² increased with the increase in Co^{2+} and Cr^{3+} concentration. The increases in ⁷ coercivity could also be related to the higher magneto crystalline anisotropy of Co^{2+} ions as compared to the Fe^{3+} ions.

The net magnetic moment ($n_{\text{B}}\text{Cal.}$) is a ⁵ difference of the magnetic moments of A (M_{A}) and B (M_{B}) sub lattices, ($n_{\text{B}}\text{Cal.} = M_{\text{B}} - M_{\text{A}}$). The ⁶ $n_{\text{B}}\text{Cal.}$ values were determined using cation occupancy and magnetic moment of Fe^{3+} ($5\mu_{\text{B}}$), Ni^{2+} ($2\mu_{\text{B}}$), Zn^{2+} ($0\mu_{\text{B}}$), Co^{2+} ($3\mu_{\text{B}}$) and Cr^{3+} ($3\mu_{\text{B}}$) ions. Calculated and observed magneton numbers are given in Table 5. Calculated and observed magneton number decreased with Co^{2+} and Cr^{3+} substitution.

3.9. Catalytic Application

1, 8-dioxodecahydroacridines synthesised using magnetically separable and reusable $\text{Ni}_{0.5}\text{Co}_x\text{Zn}_{0.5-x}\text{Fe}_{2-y}\text{Cr}_y\text{O}_4$ nanoparticles as a catalyst (**Scheme 1**).

General Procedure

To study the catalytic efficiency of $\text{Ni}_{0.5}\text{Co}_x\text{Zn}_{0.5-x}\text{Fe}_{2-y}\text{Cr}_y\text{O}_4$ nanoferrites; the best ferrite composition was chosen for synthesis of 1, 8-Dioxodecahydroacridine (**5a**) from aromatic aldehyde ³ **1** (1 mmol), cyclic diketone **2** (2 mmol), ammonium acetate **3** (10 mmol), in ethanol as model reaction. The composition **4a** was extracted with 84% yield in the presence of (40 mol %) $\text{Ni}_{0.5}\text{Co}_x\text{Zn}_{0.5-x}\text{Fe}_{2-y}\text{Cr}_y\text{O}_4$ ($x = y = 0.2$) ferrite in shorter reaction time (80 min) compared to other compositions of ferrites.

The quantity of ferrite composition (catalyst load) was optimized for model reaction (**4a**). The spinel ferrite as a catalyst was used in varying quantity of 20, 30 and 40 mol %. The decrease in ferrite catalyst quantity from 40 to 20 mol % decreased the yield of reaction (Table 6).

The feasibility of current route was evaluated by using four aromatic aldehydes under optimized conditions to obtain substituted 1, 8-Dioxodecahydroacridine (**4a-d**) (Scheme 1). Results tabulated in Table 7.

In heterogeneous catalysis, reusability of the catalyst is an important aspect. The investigation of recovery and reusability of the catalyst was performed for model reaction (**4a**). The reaction was performed through aromatic aldehyde **1** (1 mmol), cyclic diketone **2** (2 mmol), ammonium acetate **3** (10 mmol), in ethanol in presence of (40 mol %) $\text{Ni}_{0.5}\text{Co}_x\text{Zn}_{0.5-x}\text{Fe}_{2-y}\text{Cr}_y\text{O}_4$ ($x = y = 0.2$) ferrite as catalyst. Catalyst was recycled after the completion of reaction. For this a strong magnet was used to fix it at the bottom of the flask. The fixed solid catalyst washed twice with acetone. The next run of reaction was proceeded by introducing the fresh substrate into the flask. The catalyst was effectively reusable 5 times without losing its catalytic performance. (Cycle number and yield of **4a**: 1- 84 %; 2- 84 %; 3- 83 %; 4- 82 %; 5- 81 %).

The work-up of these reactions was very easy, where we can remove catalyst by using strong magnet followed by filtration of hot reaction mixture. On drying the crude residue obtained was purified by recrystallization using ethanol. The efficiency, easy handling and mild nature are advantageous aspect of the catalyst.

4. Conclusion

Nanocrystalline ferrites, with composition of $\text{Ni}_{0.5}\text{Co}_x\text{Zn}_{0.5-x}\text{Fe}_{2-y}\text{Cr}_y\text{O}_4$ ($x = y = 0.1$ to 0.5 in steps of 0.1) were neatly prepared by the sol-gel auto-combustion route. The observed elemental analysis from EDAX is consistent to the theoretical stoichiometry of elements. The XRD patterns illustrate single- phase formation of cubic spinel structure. Lattice constant decreased from 8.360 to 8.298 Å, while the crystalline size increased from 26.21 to 32.21 nm with the increase in Co^{2+} and Cr^{3+} ions substitution to the Ni-Zn ferrite system. Zn^{2+} ions preferably occupying the tetrahedral site and Ni^{2+} , Co^{2+} , Cr^{3+}

ions mainly penetrate octahedron site (B sub lattice). The spectra showed two principle absorption bands (ν_1 and ν_2) near 600 cm^{-1} and 400 cm^{-1} . SEM and TEM images reveal well defined nanoparticles with slight agglomeration of the sample with inhomogeneous broader grain size distribution. Calculated and observed magneton number decreased with Co^{2+} and Cr^{3+} substitution. 1,8-dioxodecahydroacridines synthesised using magnetically separable and reusable $\text{Ni}_{0.5}\text{Co}_x\text{Zn}_{0.5-x}\text{Fe}_{2-y}\text{Cr}_y\text{O}_4$ nanoparticles as a catalyst.

12%

SIMILARITY INDEX

PRIMARY SOURCES

- 1** Mohd. Hashim, Alimuddin, Shalendra Kumar, Sagar E. Shirsath, R.K. Kotnala, Hanshik Chung, Ravi Kumar. "Structural properties and magnetic interactions in Ni_{0.5}Mg_{0.5}Fe_{2-x}Cr_xO₄ (0≤x≤1) ferrite nanoparticles", Powder Technology, 2012 42 words — 1%

Crossref
- 2** Gurav, S.K., Sagar E. Shirsath, R.H. Kadam, S.M. Patange, K.S. Lohar, and D.R. Mane. "Less magnetic and larger Zr⁴⁺-Zn²⁺ ions co-substituted structural and magnetic properties of ordered Li_{0.5}Fe_{2.5}O₄ nanoparticles", Materials Research Bulletin, 2013. 39 words — 1%

Crossref
- 3** Ali Amoozadeh, Sanaz Golian, Salman Rahmani. " TiO₂-coated magnetite nanoparticle-supported sulfonic acid as a new, efficient, magnetically separable and reusable heterogeneous solid acid catalyst for multicomponent reactions ", RSC Advances, 2015 32 words — 1%

Crossref
- 4** Huma Malik, Azhar Mahmood, Khalid Mahmood, Maria Yousaf Lodhi et al. "Influence of cobalt substitution on the magnetic properties of zinc nanocrystals synthesized via micro-emulsion route", Ceramics International, 2014 28 words — 1%

Crossref
- 5** Haralkar, S.J., R.H. Kadam, S.S More, Sagar E. Shirsath, M.L. Mane, Swati Patil, and D.R. Mane. "Substitutional effect of Cr³⁺ ions on the properties of Mg-Zn ferrite nanoparticles", Physica B Condensed Matter, 2012. 27 words — 1%

Crossref

6 Gurav, S.K., Sagar E. Shirsath, R.H. Kadam, and D.R. Mane. "Low temperature synthesis of $\text{Li}_{0.5}\text{Zr}_x\text{Co}_x\text{Fe}_{2.5-2x}\text{O}_4$ powder and their characterizations", Powder Technology, 2013. 26 words — 1%

Crossref

7 Pourya Motavallian, Behzad Abasht, Hassan Abdollah-Pour. "Zr doping dependence of structural and magnetic properties of cobalt ferrite synthesized by sol-gel based Pechini method", Journal of Magnetism and Magnetic Materials, 2018 17 words — 1%

Crossref

8 worldwidescience.org 17 words — 1%

Internet

9 Shirsath, Sagar E., Mahesh L. Mane, Yukiko Yasukawa, Xiaoxi Liu, and Akimitsu Morisako. "Self-ignited high temperature synthesis and enhanced super-exchange interactions of $\text{Ho}^{3+}\text{-Mn}^{2+}\text{-Fe}^{3+}\text{-O}^{2-}$ ferromagnetic nanoparticles", Physical Chemistry Chemical Physics, 2014. 14 words — < 1%

Crossref

10 S.J. Haralkar, R.H. Kadam, S.S More, Sagar E. Shirsath, M.L. Mane, Swati Patil, D.R. Mane. "Substitutional effect of Cr^{3+} ions on the properties of Mg-Zn ferrite nanoparticles", Physica B: Condensed Matter, 2012 14 words — < 1%

Crossref

11 Irshad Ali, Abdul Shakoor, M.U. Islam, Muhammad Saeed, Muhammad Naeem Ashiq, M.S. Awan. "Synthesis and characterization of hexagonal ferrite $\text{Co}_2\text{Sr}_2\text{Fe}_{12}\text{O}_{22}$ with doped polypyrrole composites", Current Applied Physics, 2013 13 words — < 1%

Crossref

12 S.A. Sadaphal, S.S. Sonar, M.N. Ware, M.S. Shingare. "Cellulose sulfuric acid: reusable catalyst for solvent-free synthesis of bis(indolyl)methanes at room temperature", Green Chemistry Letters and Reviews, 2008 13 words — < 1%

Crossref

13 S.T. Alone, Sagar E. Shirsath, R.H. Kadam, K.M. Jadhav. "Chemical synthesis, structural and magnetic properties of nano-structured Co–Zn–Fe–Cr ferrite", Journal of Alloys and Compounds, 2011
Crossref 12 words — < 1%

14 nopr.niscair.res.in
Internet 11 words — < 1%

15 R.H. Kadam, Suresh T. Alone, Maheshkumar L. Mane, A.R. Biradar, Sagar E. Shirsath. "Phase evaluation of Li⁺ substituted CoFe₂O₄ nanoparticles, their characterizations and magnetic properties", Journal of Magnetism and Magnetic Materials, 2014
Crossref 9 words — < 1%

16 C. Murugesan, Nagaiah Kambhala, S. Angappane, G. Chandrasekaran. "Influence of Zn concentration on the structural and magnetic properties of nanocrystalline Cu_{1-x}Zn_xFe₂O₄ mixed ferrites synthesized using novel combustion method", Journal of Magnetism and Magnetic Materials, 2017
Crossref 9 words — < 1%

17 Bhavya Bhushan. "Tailoring the Magnetic and Optical Characteristics of Nanocrystalline BiFeO₃ by Ce Doping", Journal of the American Ceramic Society, 03/2012
Crossref 8 words — < 1%

18 Haralkar, S.J., R.H. Kadam, S.S. More, Sagar E. Shirsath, M.L. Mane, Swati Patil, and D.R. Mane. "Intrinsic magnetic, structural and resistivity properties of ferromagnetic Mn_{0.5}Zn_{0.5}Al_xFe_{2-x}O₄ nanoparticles", Materials Research Bulletin, 2012.
Crossref 8 words — < 1%

19 Habjanič, Jelena, Marijana Jurić, Jasminka Popović, Krešimir Molčanov, and Damir Pajić. "A 3D Oxalate-Based Network as a Precursor for the CoMn₂O₄ Spinel: Synthesis and Structural and Magnetic Studies", Inorganic Chemistry
Crossref 8 words — < 1%

20 A. A. Birajdar, Sagar E. Shirsath, R. H. Kadam, M. L. Mane, D. R. Mane, A. R. Shitre. " Permeability and magnetic properties of Al substituted Ni Zn Fe O nanoparticles ", Journal of Applied Physics, 2012 7 words — < 1%
Crossref

21 Jani, K.H.. "Study of magnetic ordering in MnAl_xCr_xFe₂-₂O₄", Journal of Magnetism and Magnetic Materials, 200809 7 words — < 1%
Crossref

22 Allah Ditta, Muhammad Azhar Khan, Muhammad Junaid, R.M. Arif Khalil, Muhammad Farooq Warsi. "Structural, magnetic and spectral properties of Gd and Dy co-doped dielectrically modified Co-Ni (Ni_{0.4}Co_{0.6}Fe₂O₄) ferrites", Physica B: Condensed Matter, 2017 6 words — < 1%
Crossref

EXCLUDE QUOTES OFF
EXCLUDE BIBLIOGRAPHY ON

EXCLUDE MATCHES OFF

Prof.(Dr.)K.S.LOHAR

**Dr_KS_Lohar_manuscript_03 - plagiarism
removed.docx**

By Prof. Lohar

**Synthesis, Microstructure, Magnetic Properties and Catalytic
Applications of Co²⁺ and Cr³⁺ Doped Ni- Zn Spinel Ferrite**

Abstract

Cobalt and chromium doped nanocrystalline ferro spinels, with composition $\text{Ni}_{0.5}\text{Co}_x\text{Zn}_{0.5-x}\text{Fe}_{2-y}\text{Cr}_y\text{O}_4$ in step of ($x = y = 0.1$ to 0.5 in steps of 0.1) was synthesized by sol-gel auto-combustion route by using glycine as fuel, calcination temperature of samples confirmed from thermogravimetric analysis, differential scanning calorimetry analysis. The observed elemental stoichiometry from energy dispersive spectroscopy is in good agreement with the theoretical stoichiometry. The X-ray diffraction patterns illustrates all samples possess single- phase cubic spinel structure without the signature of any impurity or secondary phases. The lattice constant was decreased from $8.360 - 8.298 \text{ \AA}$ with the increase in concentrations of Co^{2+} and Cr^{3+} ions substitution to the Ni-Zn ferrite system. Zn^{2+} ions preferably occupying the tetrahedral site and Ni^{2+} , Co^{2+} , Cr^{3+} ions mainly penetrate octahedron site (B sub lattice). The Infrared spectra show two principle absorption bands (ν_1 and ν_2) around 600 cm^{-1} and 400 cm^{-1} . Scanning electron microscopy and Transmission electron microscopy images reveal well defined nanoparticles with slight agglomeration. Calculated and observed magneton number decreased with Co^{2+} and Cr^{3+} substitution. 1, 8-dioxodecahydroacridines synthesised using magnetically separable and reusable $\text{Ni}_{0.5}\text{Co}_x\text{Zn}_{0.5-x}\text{Fe}_{2-y}\text{Cr}_y\text{O}_4$ nanoparticles as a catalyst.

1. Introduction

Nowadays extensive attention paid towards magnetic ferrite nanoparticles due to its wide applications in, sensor [1-3], catalysis [4,5], biomedicine [6,7], MRI [8], drug delivery [9], magnetic recording [10], microwave devices [11] and magnetic ferro- fluids [12] etc. Nano ferro spinels have a general chemical composition $[\text{A}][\text{B}_2]\text{O}_4$, with two types of interstitial sites, the tetrahedral (A) site and the octahedral (B) site engaged by metal

4 cations [13, 14]. The electrical and magnetic properties of AB₂O₄-ferrites governed by A and B sub lattices in cubic spinel structure. By using the cations preference to a particular site, Co-Zn [15], Ni-Zn [16], Ni-Cu-Zn [17] and Ni-Co-Zn [18], etc. ferrites were developed. The electrical and magnetic properties of ferrites extensively altered by doping of trivalent ions like Al³⁺, Cr³⁺ etc. for Fe³⁺ ion [19-23].

Magnetite spinel ferrite used as efficient catalyst in different chemical transmissions such as pyrano pyrimidines [24], 1, 4-dihydropyridines [25], benzimidazoles [26], pyrroles [27], etc. The catalytic activity of spinel ferrite is because of migration of metal cations within A- and B-site without altering original spinel structure that makes them more effective catalyst for reactions [28]. Magnetite spinel ferrite catalyst easily separated with external magnetic field without filtration from reaction mixture [29]. The preparation methods were found to be of great importance for the different properties of ferrite; among them are sol- gel [30], co- precipitation [31], egg white route [32] and hydrothermal [33]. Acridine and its derivatives show various biological activities as anticancer [34], antitumor [35], anticonvulsant [36], analgesic [37], hypertensive and anti-inflammatory [38], antibacterial [39], antimalarial [40] etc. In literature number of methods adopted for synthesis of 1,8-dioxodecahydroacridines, which involves condensation of aromatic aldehydes, cyclic diketones and different nitrogen sources and various catalysts have been reported [41-46]. These methods have few drawbacks such as poor yields, requires more time, multistep synthesis, harsh reaction conditions, etc.

19 Herein we report synthesis, structural magnetic properties of the Ni_{0.5}Co_xZn_{0.5-x}Fe_{2-y}Cr_yO₄ (x = y = 0.1 to 0.5 in steps of 0.1) synthesised by sol gel method and its application as catalyst for of 1, 8-dioxodecahydroacridines synthesis (Scheme 1).

2. Methods and materials

Nanocrystalline spinel ferrites with composition $\text{Ni}_{0.5}\text{Co}_x\text{Zn}_{0.5-x}\text{Fe}_{2-y}\text{Cr}_y\text{O}_4$ ($x = y = 0.0$ to 0.5 in steps of 0.1) were synthesized by the sol-gel auto-combustion method [21], from corresponding metal nitrates of analytical grade reagent having purity 99% and glycine as a fuel, were used in the synthesis without any further treatment. All metal nitrates in desired stoichiometry were dissolved in deionised water to which glycine added in the metal nitrates to glycine 1:3 molar ratio. The $\text{pH} \approx 7$ of reaction mixture was maintained by gradually addition of the NH_3 solution. The solution was kept on a hot plate with constant stirring at 90°C . A viscous brown gel was formed as a result of evaporation of solution. After evaporation of all of the water molecules; the viscous gel obtained and it began to froth and get self ignited and burnt. The auto-combustion finished within a short time, giving brown ashes termed as the precursor.

The simultaneous TGA/DSC analysis carried on SDT Q 600 V20.9 Build 20 thermal analyser, with a heating rate 10°C per minutes in air atmosphere. The elemental composition investigated by Energy Dispersive X-Ray Analysis (EDAX, Inca Oxford, attached to the SEM). The crystallographic structures were identified by X-ray powder diffraction with $\text{Cu K}\alpha$ radiation ($\lambda = 1.5405\text{\AA}$) by Phillips-3710 X-ray diffractometer. Morphology and structure evaluated on JEOL-JSM-5600 N Scanning Electron Microscope and on Philips-CM-200 Transmission Electron Microscope. The IR spectra recorded in the range 200 to 800 cm^{-1} with Perkin Elmer infrared spectrophotometer. The magnetic measurements recorded at room temperature with PARC-EG&G-VSM-4500 vibrating sample magnetometer.

For catalytic reaction: the Melting points of synthesized compounds are recorded and are uncorrected. $^1\text{H-NMR}$ spectra of the compounds were recorded using Varian Gemini spectrometer (300 MHz). TMS is used as an internal standard for comparison of

¹⁴Chemical shifts which were reported in δ units (ppm). Mass spectra were recorded using ¹²Electron spray ionization mass spectra (ES-MS) (¹²Water-Micro mass Quattro-II spectrometer). AR grade reagents were used without further purification.

Aromatic aldehyde ³**1** (1 mmol), cyclic diketone **2** (2 mmol), ammonium acetate **3** (10 mmol) and $\text{Ni}_{0.5}\text{Co}_x\text{Zn}_{0.5-x}\text{Fe}_{2-y}\text{Cr}_y\text{O}_4$ ($x = y = 0.0$ to 0.5) (40 mol %) mixture was placed in 15 mL of ethanol under reflux for appropriate time. Reaction was continuously monitored by TLC. Under reflux the catalyst was removed using strong magnet placed at the bottom of flask. The hot reaction mixture was filtered. The solvent was then evaporated to get the crude product. The recrystallization of crude product was done using ethanol to get pure products.

⁵**3. Results and Discussion**

3.1. TGA/ DSC analysis

The decomposition pattern of Co^{2+} and Cr^{3+} substituted Ni-Zn ferrites ($x = y = 0.0$) precursor is shown in Fig.1., indicate four thermal effects, at onset temperature around 200 °C, the first endothermic peak is observed due to loss of co-ordinated water molecule 0.7479%. The second exothermic peak locate near temperature 350 °C shown more weight loss, 1.161% can be attributed to dehydration of crystalline water or chemisorbed water molecules and metals converted to metal oxides, they undergo solid state chemical reaction with formation of ferrites with liberation of oxygen molecules with mass loss 0.0821% is an slightly endothermic reaction. Small mass of 0.2552% increased for >400 °C due to the oxidation of Fe^{2+} to Fe^{3+} via endothermic reaction [47]. No significant mass loss > 575 °C was observed indicating the formation of ferro -spinel compounds. The other precursors of series shown similar type of decomposition patterns and convert

in to ferrites in the temperature range 550–600 °C. Similar type precursor's decomposition patterns were reported by many researchers [48-50]. Finally all precursors were calcinated at 600 °C for four hours to get desired nano ferro- spinels.

8 3.1. Elemental Analysis:

Energy Dispersive X-Ray Analysis (EDAX) was utilized to obtain the elemental stoichiometric composition of the samples. EDAX of a typical sample ($x = y = 0.3$) is represented by Fig. 2. The theoretical and observed elemental compositions are tabulated in Table 1. The observed elemental composition obtained by EDAX is consistent to the theoretical stoichiometry of elements.

3.3. Structural Analysis

The XRD patterns of $\text{Ni}_{0.5}\text{Co}_x\text{Zn}_{0.5-x}\text{Fe}_{2-y}\text{Cr}_y\text{O}_4$ shown in the Fig. 3. The XRD patterns illustrated the single phase formation of cubic spinel structure without any secondary phases for all samples. The lattice constant 'a' obtained through equation discussed elsewhere [51] and tabulated in Table 2. 'a' decreased from 8.360 to 8.298 Å with the increased Co^{2+} and Cr^{3+} ions substitution to the Ni-Zn ferrite system. It is related to ionic radii, in present spinel ferrite the smaller Co^{2+} (0.65 Å) ions replaced by the larger Zn^{2+} (0.74 Å) ions [52] and smaller Cr^{3+} (0.63 Å) by larger Fe^{3+} (0.67 Å) [21]. The X-ray density 'd_x' was calculated using equation discussed elsewhere [53]. The values of d_x are tabulated in Table 2 illustrates d_x decreased with increasing Co^{2+} and Cr^{3+} concentration.

The broad diffraction peaks exhibit the fine particle nature of ferrite powders. The average crystalline diameter 'D_{XRD}' of samples determined using Debye Scherer method [52]. D_{XRD} are listed in Table 2, illustrates that the crystalline size increases from 26.21 to 32.21 nm with Co and Cr substitution.

Bulk density d_B is determined by relation,

$$d_B = \frac{M}{V} \quad (1)$$

where V is volume ($v = \pi r^2 h$), M, r and h are the mass, radius and thickness of pellet, respectively. The values of d_B tabulated in Table 2, illustrate that d_B increased from 2.547 to 2.619 g/cm³. The percentage porosity 'P' determined using d_x and d_B :

$$P = 1 - \frac{d_B}{d_x} \times 100\% \quad (2)$$

As evidenced from Table 2, that the porosity increased from 51.290 ($x = 0.0$) to 52.877 ($x = y = 0.5$) with the Co²⁺ and Cr³⁺ substitution. Molecular weight (MW) and the unit cell volume (V) of Ni_{0.5}Co_xZn_{0.5-x}Fe_{2-y}Cr_yO₄ decreased with increasing Co²⁺ and Cr³⁺ concentration, though the rate of the decrease in MW is higher than that of V. Notably decrease in d_B increase the porosity (P). Apart from this, the increase in porosity is mainly attributed to the increase in D_{XRD} , which increased the grain boundaries of the particle [54].

The hopping lengths (L_A and L_B) determined from the relation discussed elsewhere [55]. It can be seen from Table 2 that L_A and L_B decreased with Co²⁺ and Cr³⁺ substitution. The decrease in both the hopping lengths with Co²⁺ and Cr³⁺ substitution is because of decreased lattice constant. The magnetic Co²⁺ and Cr³⁺ ions that occupy the B-sites will cause an increase in both A–A and A–B interactions and will decrease the B–B exchange interaction. This may be related to the transfer of Fe³⁺ ions from B-sites to A-sites due to the insertion of both Co²⁺ and Cr³⁺ ions to the B-sites. Moreover, the increase of Co²⁺ ions in the composition due to increase of x is associated with a decrease of Zn²⁺ ions [55].

3.4. Cation Distribution

The cation distribution was determined by the Bertaut method [56] between tetrahedral and octahedral sites, listed in Table 3. The Zn^{2+} ions preferably occupy the tetrahedral site (A sub lattice) and Ni^{2+} , Co^{2+} , Cr^{3+} ions mostly go into octahedral site (B sub lattice) [57]. However, Fe^{3+} ions occupy both the available A and B sub lattices. With rising Cr^{3+} concentration, the percentage of Fe^{3+} ions in B sites linearly decreased. The Cr^{3+} replaced Fe^{3+} from B-sites due of their favourable crystal field impact [57]. The ionic radii of the constituent ions Zn^{2+} (0.81Å), Cr^{3+} (0.63Å), Co^{2+} (0.72Å) and Fe^{3+} (0.67Å) could also be important in deciding cation occupancies [53].

Oxygen parameter (u), intensities of experimental and observed from XRD peaks and cation distribution are tabulated in Table 3. The mean ionic radius of the A and B-sites (r_A and r_B) was determined using the equations reported in literature [58]. r_A decreased and ' r_B ' increased with increasing Co^{2+} concentration. The increase of r_B is related to the increasingly high occupation of the B site by the smaller ionic radius of Co^{2+} (0.72 Å) ions that replacing Zn^{2+} (0.74 Å) ions [59].

3.5. Infrared spectroscopy

IR spectra for all compositions are given in Fig. 4. The spectrum shows two main principle absorption bands near 600 cm^{-1} (ν_1) and 400 cm^{-1} (ν_2) which is a common feature of spinel ferrites (Table 4). The appearance of these bands in these range confirm the spinel phase structure. The high frequency band (ν_1) is assigned to the vibration of the tetrahedral sites metal ions with oxygen ions whereas, the lower frequency one (ν_2) is assigned to the octahedral sites [60]. The values of A-site bond length (R_A) and B-site bond length (R_B) are tabulated in Table 4. R_A and R_B were decreased with increased Co^{2+} and Cr^{3+} content. The force constants K_t and K_o increases with increased Co^{2+} and Cr^{3+} content.

3.6. Scanning Electron Microscopy (SEM)

Typical SEM image of the prepared spinel ferrites ($x = y = 0.3$) given in Fig. 5. SEM images illustrate well defined nanoparticles with slight agglomeration of the sample with inhomogeneous broader grain size distribution. Agglomeration is due to the increased magneto crystalline anisotropy of different domains that varies in alignments of particles comes closer to each other [61].

3.7. Transmission Electron Microscopy (TEM)

Fig. 6 shows a typical TEM image and respective histogram (Fig. 7) of the sample ($x = y = 0.3$). Particle size 't' obtained from TEM analysis are around 24 - 36 nm and these are closer to the values are determined from XRD. The most of the nanoparticles are spherical; however, few elongated particles were also seen. The particles are slightly agglomerated as a result of the interaction between the magnetic nanoparticles. Selected area electron diffraction patterns of the sample ($x = y = 0.3$) is presented in Fig. 8. The superimposition Debye ring pattern to the bright spots illustrates the polycrystalline nature [52].

3.8. Magnetization

Magnetic hysteresis loops are given in Fig. 9. Magnetic properties of spinel oxides such as ferrites are mainly structure, composition and cation distribution dependent [62]. Neel's two sub-lattice models are used to study the magnetic behaviour, magnetic moment n_B is determined by equation discussed elsewhere [63]. Magnetization increased up to certain applied magnetic field above that it remains unchanged (Fig. 9). Saturation magnetization (M_s), coercivity (H_c), and magneton number (n_B) derived from hysteresis loops and are given in Table 5. M_s decreased from 36.546 to 3.397 emu/g, with increase in Co^{2+} and Cr^{3+} concentration. Remnant magnetization (M_r) decreased while coercivity

² increased with the increase in Co^{2+} and Cr^{3+} concentration. The increases in ⁷ coercivity could also be related to the higher magneto crystalline anisotropy of Co^{2+} ions as compared to the Fe^{3+} ions.

The net magnetic moment ($n_{\text{B}}\text{Cal.}$) is a ⁵ difference of the magnetic moments of A (M_{A}) and B (M_{B}) sub lattices, ($n_{\text{B}}\text{Cal.} = M_{\text{B}} - M_{\text{A}}$). The ⁶ $n_{\text{B}}\text{Cal.}$ values were determined using cation occupancy and magnetic moment of Fe^{3+} ($5\mu_{\text{B}}$), Ni^{2+} ($2\mu_{\text{B}}$), Zn^{2+} ($0\mu_{\text{B}}$), Co^{2+} ($3\mu_{\text{B}}$) and Cr^{3+} ($3\mu_{\text{B}}$) ions. Calculated and observed magneton numbers are given in Table 5. Calculated and observed magneton number decreased with Co^{2+} and Cr^{3+} substitution.

3.9. Catalytic Application

1, 8-dioxodecahydroacridines synthesised using magnetically separable and reusable $\text{Ni}_{0.5}\text{Co}_x\text{Zn}_{0.5-x}\text{Fe}_{2-y}\text{Cr}_y\text{O}_4$ nanoparticles as a catalyst (**Scheme 1**).

General Procedure

To study the catalytic efficiency of $\text{Ni}_{0.5}\text{Co}_x\text{Zn}_{0.5-x}\text{Fe}_{2-y}\text{Cr}_y\text{O}_4$ nanoferrites; the best ferrite composition was chosen for synthesis of 1, 8-Dioxodecahydroacridine (**5a**) from aromatic aldehyde ³ **1** (1 mmol), cyclic diketone **2** (2 mmol), ammonium acetate **3** (10 mmol), in ethanol as model reaction. The composition **4a** was extracted with 84% yield in the presence of (40 mol %) $\text{Ni}_{0.5}\text{Co}_x\text{Zn}_{0.5-x}\text{Fe}_{2-y}\text{Cr}_y\text{O}_4$ ($x = y = 0.2$) ferrite in shorter reaction time (80 min) compared to other compositions of ferrites.

The quantity of ferrite composition (catalyst load) was optimized for model reaction (**4a**). The spinel ferrite as a catalyst was used in varying quantity of 20, 30 and 40 mol %. The decrease in ferrite catalyst quantity from 40 to 20 mol % decreased the yield of reaction (Table 6).

The feasibility of current route was evaluated by using four aromatic aldehydes under optimized conditions to obtain substituted 1, 8-Dioxodecahydroacridine (**4a-d**) (Scheme 1). Results tabulated in Table 7.

In heterogeneous catalysis, reusability of the catalyst is an important aspect. The investigation of recovery and reusability of the catalyst was performed for model reaction (**4a**). The reaction was performed through aromatic aldehyde **1** (1 mmol), cyclic diketone **2** (2 mmol), ammonium acetate **3** (10 mmol), in ethanol in presence of (40 mol %) $\text{Ni}_{0.5}\text{Co}_x\text{Zn}_{0.5-x}\text{Fe}_{2-y}\text{Cr}_y\text{O}_4$ ($x = y = 0.2$) ferrite as catalyst. Catalyst was recycled after the completion of reaction. For this a strong magnet was used to fix it at the bottom of the flask. The fixed solid catalyst washed twice with acetone. The next run of reaction was proceeded by introducing the fresh substrate into the flask. The catalyst was effectively reusable 5 times without losing its catalytic performance. (Cycle number and yield of **4a**: 1- 84 %; 2- 84 %; 3- 83 %; 4- 82 %; 5- 81 %).

The work-up of these reactions was very easy, where we can remove catalyst by using strong magnet followed by filtration of hot reaction mixture. On drying the crude residue obtained was purified by recrystallization using ethanol. The efficiency, easy handling and mild nature are advantageous aspect of the catalyst.

4. Conclusion

Nanocrystalline ferrites, with composition of $\text{Ni}_{0.5}\text{Co}_x\text{Zn}_{0.5-x}\text{Fe}_{2-y}\text{Cr}_y\text{O}_4$ ($x = y = 0.1$ to 0.5 in steps of 0.1) were neatly prepared by the sol-gel auto-combustion route. The observed elemental analysis from EDAX is consistent to the theoretical stoichiometry of elements. The XRD patterns illustrate single- phase formation of cubic spinel structure. Lattice constant decreased from 8.360 to 8.298 Å, while the crystalline size increased from 26.21 to 32.21 nm with the increase in Co^{2+} and Cr^{3+} ions substitution to the Ni-Zn ferrite system. Zn^{2+} ions preferably occupying the tetrahedral site and Ni^{2+} , Co^{2+} , Cr^{3+}

ions mainly penetrate octahedron site (B sub lattice). The spectra showed two principle absorption bands (ν_1 and ν_2) near 600 cm^{-1} and 400 cm^{-1} . SEM and TEM images reveal well defined nanoparticles with slight agglomeration of the sample with inhomogeneous broader grain size distribution. Calculated and observed magneton number decreased with Co^{2+} and Cr^{3+} substitution. 1,8-dioxodecahydroacridines synthesised using magnetically separable and reusable $\text{Ni}_{0.5}\text{Co}_x\text{Zn}_{0.5-x}\text{Fe}_{2-y}\text{Cr}_y\text{O}_4$ nanoparticles as a catalyst.

12%

SIMILARITY INDEX

PRIMARY SOURCES

- 1 Mohd. Hashim, Alimuddin, Shalendra Kumar, Sagar E. Shirsath, R.K. Kotnala, Hanshik Chung, Ravi Kumar. "Structural properties and magnetic interactions in $\text{Ni}_{0.5}\text{Mg}_{0.5}\text{Fe}_{2-x}\text{Cr}_x\text{O}_4$ ($0 \leq x \leq 1$) ferrite nanoparticles", Powder Technology, 2012 42 words — 1%

Crossref
- 2 Gurav, S.K., Sagar E. Shirsath, R.H. Kadam, S.M. Patange, K.S. Lohar, and D.R. Mane. "Less magnetic and larger Zr^{4+} - Zn^{2+} ions co-substituted structural and magnetic properties of ordered $\text{Li}_{0.5}\text{Fe}_{2.5}\text{O}_4$ nanoparticles", Materials Research Bulletin, 2013. 39 words — 1%

Crossref
- 3 Ali Amoozadeh, Sanaz Golian, Salman Rahmani. " TiO_2 -coated magnetite nanoparticle-supported sulfonic acid as a new, efficient, magnetically separable and reusable heterogeneous solid acid catalyst for multicomponent reactions ", RSC Advances, 2015 32 words — 1%

Crossref
- 4 Huma Malik, Azhar Mahmood, Khalid Mahmood, Maria Yousaf Lodhi et al. "Influence of cobalt substitution on the magnetic properties of zinc nanocrystals synthesized via micro-emulsion route", Ceramics International, 2014 28 words — 1%

Crossref
- 5 Haralkar, S.J., R.H. Kadam, S.S More, Sagar E. Shirsath, M.L. Mane, Swati Patil, and D.R. Mane. "Substitutional effect of Cr^{3+} ions on the properties of Mg-Zn ferrite nanoparticles", Physica B Condensed Matter, 2012. 27 words — 1%

Crossref

6 Gurav, S.K., Sagar E. Shirsath, R.H. Kadam, and D.R. Mane. "Low temperature synthesis of $\text{Li}_{0.5}\text{Zr}_x\text{Co}_x\text{Fe}_{2.5-2x}\text{O}_4$ powder and their characterizations", Powder Technology, 2013. 26 words — 1%

Crossref

7 Pourya Motavallian, Behzad Abasht, Hassan Abdollah-Pour. "Zr doping dependence of structural and magnetic properties of cobalt ferrite synthesized by sol-gel based Pechini method", Journal of Magnetism and Magnetic Materials, 2018 17 words — 1%

Crossref

8 worldwidescience.org 17 words — 1%

Internet

9 Shirsath, Sagar E., Mahesh L. Mane, Yukiko Yasukawa, Xiaoxi Liu, and Akimitsu Morisako. "Self-ignited high temperature synthesis and enhanced super-exchange interactions of $\text{Ho}^{3+}\text{-Mn}^{2+}\text{-Fe}^{3+}\text{-O}_2\text{-}$ ferromagnetic nanoparticles", Physical Chemistry Chemical Physics, 2014. 14 words — < 1%

Crossref

10 S.J. Haralkar, R.H. Kadam, S.S More, Sagar E. Shirsath, M.L. Mane, Swati Patil, D.R. Mane. "Substitutional effect of Cr^{3+} ions on the properties of Mg-Zn ferrite nanoparticles", Physica B: Condensed Matter, 2012 14 words — < 1%

Crossref

11 Irshad Ali, Abdul Shakoor, M.U. Islam, Muhammad Saeed, Muhammad Naeem Ashiq, M.S. Awan. "Synthesis and characterization of hexagonal ferrite $\text{Co}_2\text{Sr}_2\text{Fe}_{12}\text{O}_{22}$ with doped polypyrrole composites", Current Applied Physics, 2013 13 words — < 1%

Crossref

12 S.A. Sadaphal, S.S. Sonar, M.N. Ware, M.S. Shingare. "Cellulose sulfuric acid: reusable catalyst for solvent-free synthesis of bis(indolyl)methanes at room temperature", Green Chemistry Letters and Reviews, 2008 13 words — < 1%

Crossref

13 S.T. Alone, Sagar E. Shirsath, R.H. Kadam, K.M. Jadhav. "Chemical synthesis, structural and magnetic properties of nano-structured Co–Zn–Fe–Cr ferrite", Journal of Alloys and Compounds, 2011
Crossref 12 words — < 1%

14 nopr.niscair.res.in
Internet 11 words — < 1%

15 R.H. Kadam, Suresh T. Alone, Maheshkumar L. Mane, A.R. Biradar, Sagar E. Shirsath. "Phase evaluation of Li⁺ substituted CoFe₂O₄ nanoparticles, their characterizations and magnetic properties", Journal of Magnetism and Magnetic Materials, 2014
Crossref 9 words — < 1%

16 C. Murugesan, Nagaiah Kambhala, S. Angappane, G. Chandrasekaran. "Influence of Zn concentration on the structural and magnetic properties of nanocrystalline Cu_{1-x}Zn_xFe₂O₄ mixed ferrites synthesized using novel combustion method", Journal of Magnetism and Magnetic Materials, 2017
Crossref 9 words — < 1%

17 Bhavya Bhushan. "Tailoring the Magnetic and Optical Characteristics of Nanocrystalline BiFeO₃ by Ce Doping", Journal of the American Ceramic Society, 03/2012
Crossref 8 words — < 1%

18 Haralkar, S.J., R.H. Kadam, S.S. More, Sagar E. Shirsath, M.L. Mane, Swati Patil, and D.R. Mane. "Intrinsic magnetic, structural and resistivity properties of ferromagnetic Mn_{0.5}Zn_{0.5}Al_xFe_{2-x}O₄ nanoparticles", Materials Research Bulletin, 2012.
Crossref 8 words — < 1%

19 Habjanič, Jelena, Marijana Jurić, Jasminka Popović, Krešimir Molčanov, and Damir Pajić. "A 3D Oxalate-Based Network as a Precursor for the CoMn₂O₄ Spinel: Synthesis and Structural and Magnetic Studies", Inorganic Chemistry
Crossref 8 words — < 1%

20 A. A. Birajdar, Sagar E. Shirsath, R. H. Kadam, M. L. Mane, D. R. Mane, A. R. Shitre. " Permeability and magnetic properties of Al substituted Ni Zn Fe O nanoparticles ", Journal of Applied Physics, 2012 7 words — < 1%
Crossref

21 Jani, K.H.. "Study of magnetic ordering in MnAl_xCr_xFe₂-₂O₄", Journal of Magnetism and Magnetic Materials, 200809 7 words — < 1%
Crossref

22 Allah Ditta, Muhammad Azhar Khan, Muhammad Junaid, R.M. Arif Khalil, Muhammad Farooq Warsi. "Structural, magnetic and spectral properties of Gd and Dy co-doped dielectrically modified Co-Ni (Ni_{0.4}Co_{0.6}Fe₂O₄) ferrites", Physica B: Condensed Matter, 2017 6 words — < 1%
Crossref

EXCLUDE QUOTES OFF
EXCLUDE ON
BIBLIOGRAPHY

EXCLUDE MATCHES OFF

Prof.(Dr.)K.S.LOHAR

Manuscript_1_3rd

by Ks Lohar

Submission date: 19-May-2020 12:37AM (UTC+1200)

Submission ID: 1326996866

File name: 3rd_Attempt_Dr_KS_Lohar_manuscript_01.docx (68.68K)

Word count: 2461

Character count: 13356

13
Synthesis and Characterization of Al³⁺ Substituted Ni-Cu-Zn Nano Ferrites

B. L. Shinde^a, U. M. Mandle^b, A. M. Pachpinde^c, K. S. Lohar^{d*}

Abstract

Ferro spinels with composition $\text{Ni}_{0.2}\text{Cu}_{0.2}\text{Zn}_{0.6}\text{Fe}_{2-x}\text{Al}_x\text{O}_4$ ($x = 0.0$ to 1.0 in steps of 0.2) were synthesized by co-precipitation method, in oxygen atmosphere, from corresponding analytical grade metal sulphates. TGA shows total mass loss around 30% up to 550°C temperature. X-ray diffraction studies confirm all composition with single phase spinel, cubic structure, with crystallite size 11 - 21 nm range. With increasing trivalent Al^{3+} content, lattice parameter 'a' decreases. Infrared spectra show two major absorption bands, the lower frequency band ν_2 observed in the range $433\text{-}463\text{ cm}^{-1}$, is assigned to octahedral site and higher frequency band ν_1 observed in the range $565\text{-}593\text{ cm}^{-1}$, assigned tetrahedral site. The microstructures of the calcinated samples investigated by SEM and TEM, indicates ferrite samples are porous and in nature. The magnetic properties such as saturation magnetization and magneton number decreases with increasing Al^{3+} concentration.

Keywords: Wet chemical method; Ni-Cu-Zn ferrites; TGA-DTA; XRD; IR; magnetisation.

1. Introduction

The ferro spinel compounds are mixed transition metal oxides with ferric oxide as a major constituent, having general formula MFe_2O_4 (where, $M = Mg, Ca, Ba, Mn, Co, Ni, Cu, Zn,$ etc). The spinel ferrites have a cubic close-packed face-centered structure formed by larger oxygen anions in which metal cations occupying the interstitial positions, ²⁴ the tetrahedral [A] sites and the octahedral [B] sites. The nano ferrite particles show tremendous change in physical properties over bulk ferrite [1]. ¹⁶ The structural, electrical, magnetic and catalytic activity of ferro-spinel compounds particularly depends upon the ¹⁷ cation distribution between the tetrahedral and octahedral site of spinel structure [2-3]. The nano ferro spinels are technologically significant materials due to their remarkable electrical and magnetic applications in field, such as high density information storage [4], semiconductor, gas sensors [5], pigments [6], catalysts [7], drug delivery and MR imaging [8], magnetic nanofluids [9], biomedicine [10], etc.

The Ni-Cu-Zn spinel ferrites were commonly used in electronic industry [11-13]. Ni-Cu-Zn ferrites are important material because of their characteristic features such as high resistivity, ²³ low value of coercivity, a high mechanical hardness and negligible eddy current loss [14-16]. ²⁶ The electrical and magnetic properties of spinel ferrites are expansively influenced by the doping of trivalent transition metal ions such as Al^{3+}, Cr^{3+} , or both as substituent(s) for Fe^{3+} ion [17-21]. The substitution of nonmagnetic ¹ Al^{3+} ions increases resistivity and hence decreases the dielectric losses and saturation magnetization, which are suitable for fabricating microwave devices [22-25]. Different methods used for ¹¹ synthesis of ferrites are sol gel auto-combustion, co precipitation, hydrothermal, micro emulsion, normal micelles etc [26 - 30]. Wet chemical ¹¹ co-precipitation method used to synthesize homogeneous and fine ferrite powder with high surface areas resulting improvised magnetic and catalytic properties [31, 32].

Herein, we report the study of thermal, structural and magnetic properties of Al³⁺ doped Ni-Cu-Zn spinel ferrites with nominal composition Ni_{0.2}Cu_{0.2}Zn_{0.6}Fe_{2-x}Al_xO₄ system (x = 0.0 to 1.0 in the steps of 0.2) synthesized by wet chemical co-precipitation method.

2. Experimental

Analytical grade corresponding metal sulphates are used in stoichiometric proportion to prepare Ni_{0.2}Cu_{0.2}Zn_{0.6}Fe_{2-x}Al_xO₄ (x = 0.0 to 1.0 in steps of 0.2) by co-precipitation method [33 - 35]. The stoichiometric amount of metal sulphates dissolved in deionized water to obtain clear solution; the initial pH of mixed solution was ≈ 3. A 2M sodium hydroxide solution used as precipitating agent, in oxygen atmosphere at 60 °C, dark brownish precipitate was obtained at pH ≈ 12 known as precursor. The precursor precipitate separated from mother liquor by simple filtration and the precipitate was washed with deionized water till free from Na₂SO₄ and dried in inert atmosphere.

3. Characterization

It seems that the systematic study of nature of solid state thermal influence reaction and phase evolution is important for determination of stoichiometry and phase purity. Simultaneous TGA-DTA analysis of precursor were carried on SDT Q600 V20.9 Build 20, analyser in air atmosphere at heating rate 10⁰ C / min within temperature range 25 °C to 1000°C. The precursors were finally calcinated at 550 °C, elemental stoichiometry confirmed from EDAX. The X-ray patterns recorded by X-ray Diffraction method at room temperature in the 2θ range, 20° to 70° using Cu-Kα radiation (λ=1.5404 Å). The IR spectra recorded in the range of 200-800 cm⁻¹ on a Perkin-Elmer infrared spectrometer. The scanning electron microscopy and transmission electron microscopy were used to study the microstructure of prepared samples, a room temperature magnetic measurement carried out by using PARC EG&G, VSM 4500 vibrating sample magnetometer.

4. Results and discussion

4.1. Thermogravimetric analysis

Typical TGA curve of precursor ($x = 0.0$) shown in Fig. 1, illustrates continuous mass loss occurs up to 550°C temperature. Total mass loss observed is around 30% up to 550°C temperature. No significant weight loss above 550°C temperature indicates the presence of only $\text{Ni}_{0.2}\text{Cu}_{0.2}\text{Zn}_{0.6}\text{Fe}_{2-x}\text{Al}_x\text{O}_4$ spinel ferrite above this temperature. Therefore all synthesized precursor's calcinated at 550 °C for 4 hours.

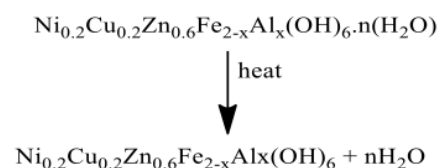
The solid precursor of metal hydroxides $\text{Ni}_{0.2}\text{Cu}_{0.2}\text{Zn}_{0.6}\text{Fe}_{2-x}\text{Al}_x(\text{OH})_6.n(\text{H}_2\text{O})$ prepared by co-precipitation method. The mass loss calculated from TGA analysis of each precursor metal hydroxide to fix $n\text{H}_2\text{O}$ [36]. Table 1, illustrates comparison between total mass loss % obtained by theoretical calculations and observed mass loss % of precursor metal hydroxide samples. The observed mass loss % is in good agreement with theoretical mass loss %. Thus the compositions of $n\text{H}_2\text{O}$ proposed in precursor metal hydroxides are confirmed. From the Fig.1, it is observed that the initial endothermic mass loss in TG curve corresponds to dehydration step (step I) in temperature range 80 - 160 °C, which shows loss of water of crystallization from precursor metal hydroxides to form an anhydrous metal hydroxides [35, 37]. While second exothermic part of TG curve (step II) in temperature range 450 - 550 °C corresponds to the oxidation of anhydrous metal hydroxides to corresponding ferro spinels [35, 38].

TGA curves Fig. 1 and 2 shows single step dehydration of precursor metal hydroxides with general formula, $\text{Ni}_{0.2}\text{Cu}_{0.2}\text{Zn}_{0.6}\text{Fe}_{2-x}\text{Al}_x(\text{OH})_6.n(\text{H}_2\text{O})$ where, $x = 0.0, 0.2, 0.4, 0.6, 0.8$ and 1.0 , to form anhydrous metal hydroxide having general formula $\text{Ni}_{0.2}\text{Cu}_{0.2}\text{Zn}_{0.6}\text{Fe}_{2-x}\text{Al}_x(\text{OH})_6$. The observed and theoretical mass loss % are tabulated in Table 1, indicate both theoretical and observed values are closely agree to each other, confirms molecular formulae of each precursor metal hydroxide compositions. Table 1, indicates stepwise mass loss % during

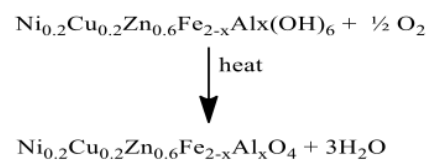
dehydration by TGA (observed) and are in good agreement with theoretical mass loss %. This supports the $n\text{H}_2\text{O}$ values given in general formula of precursor metal hydroxides. The second step shows oxidation of anhydrous metal hydroxides to form ferrites. Also values of mass loss % during second step (oxidation) by TGA (observed) and are in good agreement with mass loss % by theoretical calculations [34, 35]. TG % values for different temperature are given in Table 2.

The dehydration of precursor metal hydroxide to form anhydrous metal hydroxide (step I) and oxidation of metal hydroxide to form ferrite (step II) are given by general reactions as follows:

Step I:



Step II :



The thermo chemical behaviour of synthesized precursor illustrated in Fig. 1 by the TGA curve also could be revealed by DTA curves. It can be seen that the endothermic peak at around 80 – 175 °C corresponds to the removal of residual water from the samples [34, 35]. The weak DTA curve show endothermic peak around 350 °C due to dehydration. The exothermic peak in DTA around 550 °C is due to oxidation shows formation of ferrite sample [37]. Mass loss also occurs around 550 °C which confirms formation of nanoferrites [38].

4.2. Energy dispersive X-ray spectroscopy (EDAX)

The elemental stoichiometry of the spinel ferrites was determined by EDAX. Fig. 3 displays typical EDAX spectrum of the sample ($x = 0.4$).

The observed and theoretical elemental composition in synthesized spinel ferrites is illustrated in Fig. 4. The EDAX spectrum of the ferrite samples illustrates the presence of Ni, Cu, Zn, Fe, Al and oxygen as the major elements in the spinel ferrite samples. The observed % values of element are in good agreement with theoretical % values of element [39]. From Fig 4 it is observed that % of Fe decreases while % of Al increases.

4.3. X-ray diffraction analysis

The XRD patterns of the prepared $\text{Ni}_{0.2}\text{Cu}_{0.2}\text{Zn}_{0.6}\text{Fe}_{2-x}\text{Al}_x\text{O}_4$ (where, $x = 0.0$ to 1.0 in steps of 0.2) are shown in Fig. 5. The XRD patterns clearly indicates, all samples belongs to single-phase cubic spinel structures and there any extra impurity peaks not observed.

The lattice parameter 'a' was determined using the following relation [40].

$$a = d\sqrt{(h^2 + k^2 + l^2)} \quad (1)$$

Where, d is the inter-planer spacing and (hkl) is the index of the XRD reflection peak.

Calculated values of lattice constants tabulated in Table 3, indicate that lattice constant 'a' decreased from 8.4387 to 8.3307 Å with an increase in Al^{3+} content (x). The decrease in the lattice constant is due to replacement of Fe^{3+} ion having ionic radii 0.67 Å by relatively small Al^{3+} ions (0.50 Å) [41].

The X-ray densities (d_x) of all the samples are determined by the following equation discussed elsewhere,

$$d_x = \frac{8M}{Na^3} \quad (2)$$

Where '8' is the number of molecules per unit cell, 'M' is the molecular weight of sample, 'N' is the Avogadro's number and 'a' is lattice constant.

Calculated values of X-ray density given in Table 3, illustrates that, the X-ray density

decreases from 5.291 to 4.836 g/cm³ with increase in Al³⁺ content (x). This behaviour of X-ray density is related to the lattice constant and molecular weight of the sample. In current ferrite system, Fe³⁺ ions with atomic mass 55.847 amu are replaced by Al³⁺ ions having lower atomic mass 26.982 amu, may results in to decrease in X-ray density [21, 41].

The average crystallite diameter 'D_{XRD}' of sample calculated by using the Debye-Scherrer method [42],

$$D_{XRD} = \frac{C\lambda}{\beta_{1/2} \cos \theta} \quad (3)$$

Where, $\beta_{1/2}$ is the full width of half maximum in (2 θ), θ is the corresponding Bragg angle and $C = 0.9$. The variations in values of the crystallite size with Al³⁺ substitution are given in Table 3 indicate the crystallite size decreases from 20.15 nm to 11.59 nm with increasing Al³⁺ substitution, similar types results observed in literature [21, 41].

4.4. Infrared spectroscopy analysis

The infrared spectra show two major absorption bands ν_1 and ν_2 which are in the expected range illustrated in Fig. 6.

IR Band positions (ν_1 and ν_2) of Ni_{0.2}Cu_{0.2}Zn_{0.6}Fe_{2-x}Al_xO₄ are tabulated in Table 5. The low frequency band ν_2 in the range 433-463 cm⁻¹ is assigned octahedral site and high frequency band ν_1 in the range 565-593 cm⁻¹ assigned tetrahedral site. These bands are characteristics features of spinel structure; indicate that the normal feature of vibration of tetrahedral site is higher than that of octahedral site [43].

The force constants of tetrahedral and octahedral sites are determined by using the following relations discussed elsewhere [42]:

$$K_t = 7.62 \times M_1 \times \nu_1^2 \times 10^{-2} \quad (4)$$

$$K_o = 10.62 \times \frac{M_2}{2} \times \nu_2^2 \times 10^{-2} \quad (5)$$

Where, K_O is the force constant on octahedral site, K_T is the force constant on tetrahedral site, M_1 is molecular weight at tetrahedral site, M_2 is molecular weight at octahedral site, ν_1 is corresponding IR frequency on tetrahedral site, and ν_2 is corresponding IR frequency on octahedral site.

Force constant is the secondary derivative of potential energy, related to the site radius. The bond lengths R_A and R_B have been determined using Gorter equation [44]. The molecular weights of the tetrahedral M_1 and octahedral M_2 sites have been calculated using the cation distribution. The values of R_A , R_B and the force constants K_T and K_O are listed in Table 4.

4.5. Scanning electron microscopy (SEM)

Fig. 7 depicts scanning electron micrographs (SEM) of $Ni_{0.2}Cu_{0.2}Zn_{0.6}Fe_{2-x}Al_xO_4$ ($x = 0.0$ and $x = 0.4$), indicates ferrite sample having porous and amorphous nature. The ferrite particles are uniformly distributed with some agglomeration.

4.5. Transmission electron microscopy (TEM)

TEM image of the typical sample $x = 0.4$ is shown in Fig. 8, indicates particles were well distributed with slight agglomeration due high reactivity of samples by the heat treatment and magnetic interaction between particles. Selected area electron diffraction (SAED) patterns of the respective TEM images are also shown in Fig. 8. The Bragg' rings observed in these SAED patterns corresponding to specific 'd' values and that match perfectly with the 'd' values calculated from XRD. The polycrystalline nature of the sample was confirmed by superimposition of the bright spot with Debye ring pattern which is in accordance with XRD. As like XRD; SAED also confirmed that the sample does not possess any type of impurity or secondary phases.

Particles size distributions for $Ni_{0.2}Cu_{0.2}Zn_{0.6}Fe_{2-x}Al_xO_4$ ($x = 0.4$) shown in Fig. 9. Nanocrystalline particles were in the range of 5 - 45 nm, with size between 10 - 25 nm were most abundant (more than 75%).

4.6. Magnetization

The magnetization measured at room temperature, the parameters like saturation magnetization (M_s), coercivity (H_c), and magneton number (n_B) obtained from Hysteresis loop. The values of the magneton number and saturation magnetization are graphically represented by Figs. 10 and 11, respectively.

The magneton number observed (n_B Obs.) and calculated (n_B Cal.) magnetic moments were determined using the following equations [45, 46]:

$$n_B \text{ Obs.} = \frac{MW \times M_s}{5585} \quad (4)$$

$$n_B \text{ Cal.} = M_B - M_A \quad (5)$$

where, MW is the molecular weight of the composition and M_s is the saturation magnetization, M_B and M_A are the B and A sub-lattice magnetic moments in μ_B .

From Figs. 10 and 11, it is clear that the values saturation magnetization and magneton numbers are decreases with the increase in concentration of dopant Al^{3+} ion, is due to the decrease in A-B interaction. In the present ferrite system, magnetic Fe^{3+} ions having magnetic moment $5 \mu_B$ are replaced by non-magnetic Al^{3+} ions of $0 \mu_B$.

The Fig. 11 also illustrates that the coercivity increases from 308.24 Oe to 553.68 Oe with increase in Al^{3+} content x . While the saturation magnetization decreases from 16.446 emu/gm to 6.163 emu/gm with increase in Al^{3+} content x .

5. Conclusion

Ferro spinels with composition $Ni_{0.2}Cu_{0.2}Zn_{0.6}Fe_{2-x}Al_xO_4$ ($x = 0.0$ to 1.0 in steps of 0.2) were prepared by co-precipitation method. TGA shows total mass loss around 30% up to $550^\circ C$ temperature. The precursors were calcinated at $550^\circ C$ for 4 hours. The EDAX spectrum of the ferrite samples indicated the presence of Ni, Cu, Zn, Fe, Al and oxygen as the major elements in desired stoichiometry in the spinel ferrite samples. The XRD pattern clearly indicates that ferrites formed after sintering are belongs to single phase cubic spinel structure.

Crystallite size was observed in the range of 11 to 21 nm. The low frequency IR band ν_2 assigned to octahedral site and high frequency band ν_1 assigned to tetrahedral site. It can be illustrated from the SEM and TEM images that the prepared ferrite samples were amorphous and porous in nature and well distributed with slight agglomeration. With the increase in Al^{3+} content the saturation magnetization and magneton number decreases.

ORIGINALITY REPORT

34%

SIMILARITY INDEX

14%

INTERNET SOURCES

28%

PUBLICATIONS

22%

STUDENT PAPERS

PRIMARY SOURCES

- | | | |
|---|--|----|
| 1 | A. A. Birajdar, Sagar E. Shirsath, R. H. Kadam, M. L. Mane, D. R. Mane, A. R. Shitre. " Permeability and magnetic properties of Al substituted Ni Zn Fe O nanoparticles ", Journal of Applied Physics, 2012
Publication | 4% |
| 2 | ijsrr.org
Internet Source | 3% |
| 3 | S.K. Gurav, Sagar E. Shirsath, R.H. Kadam, D.R. Mane. "Low temperature synthesis of $\text{Li}_{0.5}\text{Zr}_x\text{Co}_x\text{Fe}_{2.5-2x}\text{O}_4$ powder and their characterizations", Powder Technology, 2013
Publication | 3% |
| 4 | K.A. Ganure, M.M. Langade, L.A. Dhale, K.S. Lohar. "Chromium substituted nickel ferrites ($\text{NiFe}_{2-x}\text{Cr}_x\text{O}_4$, $x=0.0, 0.1, 0.2, 0.3,$ and 0.4) magnetically recoverable reusable heterogeneous nano catalysts", Materials Today: Proceedings, 2020
Publication | 3% |
-

- | | | |
|----|--|----|
| 5 | aip.scitation.org
Internet Source | 2% |
| 6 | Vivek Chaudhari, Sagar E. Shirsath, M.L. Mane, R.H. Kadam, S.B. Shelke, D.R. Mane.
"Crystallographic, magnetic and electrical properties of Ni _{0.5} Cu _{0.25} Zn _{0.25} La _x Fe _{2-x} O ₄ nanoparticles fabricated by sol-gel method",
Journal of Alloys and Compounds, 2013
Publication | 2% |
| 7 | Submitted to Higher Education Commission
Pakistan
Student Paper | 2% |
| 8 | Submitted to Savitribai Phule Pune University
Student Paper | 2% |
| 9 | S.C Watawe, B.D Sutar, B.D Sarwade, B.K Chougule. "Infrared studies of some mixed Li-Co ferrites", International Journal of Inorganic Materials, 2001
Publication | 1% |
| 10 | Sagar E. Shirsath, R.H. Kadam, M.L. Mane, Ali Ghasemi, Yukiko Yasukawa, Xiaoxi Liu, Akimitsu Morisako. "Permeability and magnetic interactions in Co ²⁺ substituted Li _{0.5} Fe _{2.5} O ₄ alloys", Journal of Alloys and Compounds, 2013
Publication | 1% |
| 11 | Submitted to Universiti Teknologi Malaysia | |

12

K. B. Modi, M. K. Rangolia, M. C. Chhantbar, H. H. Joshi. "Study of infrared spectroscopy and elastic properties of fine and coarse grained nickel–cadmium ferrites", Journal of Materials Science, 2006

Publication

1%

13

B. B. Patil, A. D. Pawar, D. B. Bhosale, J. S. Ghodake, J. B. Thorat, T. J. Shinde. "Effect of La³⁺ substitution on structural and magnetic parameters of Ni–Cu–Zn nano-ferrites", Journal of Nanostructure in Chemistry, 2019

Publication

1%

14

M. A. Amer. "Mössbauer and Infrared Studies of the Ferrite System $\text{Co}_{0.6}\text{Zn}_{0.4}\text{Cu}_x\text{Fe}_{2-x}\text{O}_4$ ", physica status solidi (a), 09/16/1994

Publication

1%

15

B.L. Shinde, L.A. Dhale, K.S. Lohar. "Variation in Elastic Properties of Holmium Substituted Nickel Copper Zinc Ferrites", Asian Journal of Chemistry, 2017

Publication

1%

16

Kadhim A.M. Khalaf, A.D. Al Rawas, A.M. Gismelssed, Ahmed Al Jamel et al. "Influence of Cr substitution on Debye-Waller factor and related structural parameters of $\text{ZnFe}_{2-x}\text{Cr}_x\text{O}$

1%

4 spinels", Journal of Alloys and Compounds,
2017

Publication

17

Submitted to University of Pune

Student Paper

1%

18

Vinod N. Dhage, M.L. Mane, M.K. Babrekar, C.M. Kale, K.M. Jadhav. "Influence of chromium substitution on structural and magnetic properties of BaFe₁₂O₁₉ powder prepared by sol-gel auto combustion method", Journal of Alloys and Compounds, 2011

Publication

1%

19

Raghvendra Singh Yadav, Ivo Kuřitka, Jaromir Havlica, Miroslav Hnatko et al. "Structural, magnetic, elastic, dielectric and electrical properties of hot-press sintered Co_{1-x}Zn_xFe₂O₄ (x = 0.0, 0.5) spinel ferrite nanoparticles", Journal of Magnetism and Magnetic Materials, 2018

Publication

1%

20

A.M. Pachpinde, M.M. Langade, K.S. Lohar, S.M. Patange, Sagar E. Shirsath. "Impact of larger rare earth Pr³⁺ ions on the physical properties of chemically derived Pr_xCoFe_{2-x}O₄ nanoparticles", Chemical Physics, 2014

Publication

<1%

21

S.M. Patange, Sagar E. Shirsath, K.S. Lohar,

S.S. Jadhav, Nilesh Kulkarni, K.M. Jadhav.
"Electrical and switching properties of
NiAl_xFe_{2-x}O₄ ferrites synthesized by chemical
method", Physica B: Condensed Matter, 2011

Publication

<1%

22

Borhan, A.I., T. Slatineanu, A.R. Iordan, and
M.N. Palamaru. "Influence of chromium ion
substitution on the structure and properties of
zinc ferrite synthesized by the sol-gel auto-
combustion method", Polyhedron, 2013.

Publication

<1%

23

Bachhav, S.G.. "Microstructure and magnetic
studies of Mg-Ni-Zn-Cu ferrites", Materials
Chemistry and Physics, 20111003

Publication

<1%

24

V.K. Lakhani, T.K. Pathak, N.H. Vasoya, K.B.
Modi. "Structural parameters and X-ray Debye
temperature determination study on copper-
ferrite-aluminates", Solid State Sciences, 2011

Publication

<1%

25

waset.org

Internet Source

<1%

26

C Murugesan, B Sathyamoorthy, G
Chandrasekaran. "Structural, dielectric and
magnetic properties of Gd substituted
manganese ferrite nanoparticles", Physica
Scripta, 2015

<1%

27

S. M. Patange, Sagar E. Shirsath, G. S. Jangam, K. S. Lohar, Santosh S. Jadhav, K. M. Jadhav. " Rietveld structure refinement, cation distribution and magnetic properties of Al substituted NiFe O nanoparticles ", Journal of Applied Physics, 2011

Publication

<1%

28

Submitted to University of Sheffield

Student Paper

<1%

29

R.H. Kadam, A.P. Birajdar, Suresh T. Alone, Sagar E. Shirsath. "Fabrication of Co_{0.5}Ni_{0.5}Cr_xFe_{2-x}O₄ materials via sol-gel method and their characterizations", Journal of Magnetism and Magnetic Materials, 2013

Publication

<1%

30

Borhan, A.I., A.R. Iordan, and M.N. Palamaru. "Correlation between structural, magnetic and electrical properties of nanocrystalline Al³⁺ substituted zinc ferrite", Materials Research Bulletin, 2013.

Publication

<1%

31

Vinod N. Dhage, M.L. Mane, A.P. Keche, C.T. Birajdar, K.M. Jadhav. "Structural and magnetic behaviour of aluminium doped barium hexaferrite nanoparticles synthesized by solution combustion technique", Physica B:

<1%

Condensed Matter, 2011

Publication

Exclude quotes Off

Exclude matches Off

Exclude bibliography Off

Manuscript_2_2nd

by Ks Lohar

Prof.(Dr.)K.S.LOHAR

Submission date: 26-May-2020 01:53AM (UTC+1200)

Submission ID: 1331617785

File name: 2nd_Attempt_Dr_KS_Lohar_manuscript_02.docx (58.57K)

Word count: 2993

Character count: 17152

**Microstructure, Magnetic ¹Properties of Holmium Substituted Nickel Copper Zinc
Spinel Ferrites and Application for One Pot Synthesis of Dihydropyrimidinones**

Abstract:

Holmium Substituted Copper Nickel Zinc Spinel Ferrites synthesized by sol-gel auto combustion method. It is illustrated from TGA-DTA curve that the decomposition of precursors takes place in the temperature range 315 to 425 °C. The EDAX pattern confirmed the homogeneous mixing of the Fe, Ni, Cu, Zn, Ho and oxygen elements in pure and substituted spinel ferrites with desired stoichiometry. XRD pattern indicates formation of single phase cubic spinel. Lattice constant, X-ray density and porosity increases while particle size decreases with increase in Ho³⁺ substitution in Ni-Cu-Zn ferrite. The two strong IR absorption bands observed in the range 565–568 (ν₁) and 409 - 438 (ν₂) cm⁻¹. The obtained crystallite size lies between of 18 - 26 nm, confirmed from TEM. The microstructures of the calcinated ferrites were evaluated by SEM and TEM. It is observed that the increase in concentration of Ho³⁺ ions saturation magnetization decreases. Prepared Holmium Substituted Copper Nickel Zinc Spinel Ferrite used as catalyst for Synthesis of 3,4-dihydropyrimidin-2(1H)-ones via one-pot three-component condensation reaction.

Keywords: Sol-gel auto combustion, Ni-Cu-Zn ferrites, Saturation magnetization, Transmission Electron Microscopy, One pot synthesis.

1. Introduction

Nanoscience and Nanotechnology is the technology associated with materials in nanometer range and appliances based on them [1]. Ferrites are chemical composites with iron (III) oxide Fe_2O_3 as their major constituents [2]. The electronic and magnetic properties of the ferrites are significantly altered by substitution of trivalent or tetravalent cations and also influenced by cation distribution between the tetrahedral and octahedral site of spinel structure [3 - 6]. By tailoring the stoichiometry of the ferrite system structural, electrical, and magnetic properties are tuned [7]. The spinel ferrites have versatile applications in the field of magnetic drug delivery [8], information storage [9], super capacitor [10], magnetic refrigeration [11], gas sensors [12], and catalyst [13] etc.

NiCuZn ferrites have more attention of researchers due to their outstanding characteristics such as low magnetic losses, high permeability and high resistivity. NiCuZn ferrites widely studied for its microwave applications as they possess properties as a high Curie temperature and high permeability [14, 15]. The trivalent rare-earth ions doped ferrites are becoming the important components for sophisticated applications [16]. The substitution of little quantity of rare-earth ions improves electrical, structural magnetic properties of spinel ferrites [17, 18].

One-pot multicomponent reactions have more advantages over traditional reactions due to their rapidity, simplicity, atom-economy and shorter synthetic route [19] for the synthesis of bio-active molecules [20]. Now days, the use of heterogeneous catalysts has established significant interest in various disciplines, i.e. organic synthesis. Organic synthesis using heterogeneous catalysts have great advantage of catalyst recycle as compared to homogeneous catalyst. Iron oxide nanoparticles are used as heterogeneous catalyst as it is separated without filtration simply applying external magnet [21, 22]. The catalytic activity of spinel ferrites for these reactions arises due to the ease Fe can switch its oxidation state between 2+ and 3+. Due to the spinel structure ferrites have stability under extremely reducing conditions. The reduction of Fe^{+3} to Fe^{+2} occurs without varying lattice arrangements, so that original state is obtained on reoxidation [23].

Now days, magnetic spinel ferrites used as efficient catalyst in different chemical transformations such as synthesis of diazepine derivatives [24], α -amino nitriles [25], 1,1-diacetates from aldehydes [26], etc.

Dihydropyrimidinones have synthesized by Pietro Biginelli in 1893, which involves a three-component one-pot condensation of benzaldehyde, ethyl acetoacetate and urea under robustly acidic conditions [27]. Also Dihydropyrimidinones synthesized by microwave irradiation [28], ionic liquids [29], and using different types of catalysts such as lanthanide triflate [30], $\text{Sr}(\text{OTf})_2$ [31], nanomagnetic-supported sulfonic acid [32], Iron(III) tosylate [33], FeCl_3 -supported nanopore silica [34], etc.

The present work deals with the structural and magnetic properties of holmium substituted nickel copper zinc ferrite with composition $\text{Ni}_{0.2}\text{Cu}_{0.2}\text{Zn}_{0.6}\text{Fe}_{2-x}\text{Ho}_x\text{O}_4$ ($x=0.00, 0.02, 0.04, 0.06, \text{ and } 0.08$) synthesized by sol gel auto combustion method and application for one pot three component synthesis of Dihydropyrimidinones.

2. Experimental

2.1. Material and Synthesis

The nano-crystalline powders of $\text{Ni}_{0.2}\text{Cu}_{0.2}\text{Zn}_{0.6}\text{Fe}_{2-x}\text{Ho}_x\text{O}_4$ ($x = 0.0$ to 0.08 in steps of 0.2) prepared using sol-gel auto-combustion method [35]. The stoichiometric quantities of analytical grade reagents of corresponding metal nitrates were dissolved in deionized water. The aqueous citric acid solution added in the ratio of 1:3 (ratio metal nitrates to citric acid), then pH of solution adjusted to ≈ 7 , by addition of NH_3 solution. The resulting solution was heated on hot plate (90°C) with continuous stirring. After some time the solution turns viscous and converted in to brown gel, with complete removal water molecule gel starts frothing and later on automatically get burnt with glowing flints. The process of auto-combustion was accomplished in a minute, resulting in the formation of the brown-colored ashes known as a precursor. Calcination temperature is confirmed from TGA / DTA curve and all the precursor powders were calcinated at 500°C for four hours gives final spinel ferrites.

2.2. Characterization techniques

Thermal analysis carried using simultaneous TGA and DTA of precursors at heating rate $10^\circ\text{C} / \text{min}$ in the range 25°C to 800°C on SDT Q600 V20.9 Build 20 in air. With EDAX, Inca Oxford, attached to the SEM the composition of calcinated samples determined. The structural parameters investigated by X-ray diffraction Phillips X-ray diffractometer (Model 3710) employed with $\text{Cu-K}\alpha$ radiation ($\lambda=1.5405\text{\AA}$) were used in the present study. Microstructure of the samples studied on JEOL-JSM-5600-N Scanning Electron Microscope and on Philips-CM-200 Transmission Electron Microscope. Magnetic measurements carried at room temperature using PARC EG&G vibrating sample magnetometer VSM 4500.

3. Results and discussion

3.1. Thermal Analysis (TGA / DTA)

Fig.1 represents typical TGA/DTA curve of $\text{Ni}_{0.2}\text{Cu}_{0.2}\text{Zn}_{0.6}\text{Fe}_{2-x}\text{Ho}_x\text{O}_4$ ($x= 0.06$). The TGA curve shows two weight loss steps associated with endothermic and exothermic DTA peaks. The 1st weight loss step in the temperature $30\text{-}100^\circ\text{C}$ range is corresponding to endothermic peak around 80°C , is due to evaporation of residual water from precursor. The 2nd weight loss step in the temperature range of $350\text{-}460^\circ\text{C}$ is corresponding to the exothermic peak around 400°C , due to the decomposition of unreacted citric acid. No weight loss

observed above 460 °C, representing the presence of only $\text{Ni}_{0.2}\text{Cu}_{0.2}\text{Zn}_{0.6}\text{Fe}_{2-x}\text{Ho}_x\text{O}_4$ in this temperature range. Therefore, the prepared precursor samples sintered at 500 °C for four hour to get the $\text{Ni}_{0.2}\text{Cu}_{0.2}\text{Zn}_{0.6}\text{Fe}_{2-x}\text{Ho}_x\text{O}_4$ spinel ferrites.

3.2. Elemental Analysis:

The chemical compositions of $\text{Ni}_{0.2}\text{Cu}_{0.2}\text{Zn}_{0.6}\text{Fe}_{2-x}\text{Ho}_x\text{O}_4$ ferrite nanoparticles are determined by EDAX. Fig.2 (a) and (b) shows the typical EDAX pattern for the $\text{Ni}_{0.2}\text{Cu}_{0.2}\text{Zn}_{0.6}\text{Fe}_{2-x}\text{Ho}_x\text{O}_4$, ferrite nanoparticles $x=0.00$ and $x=0.08$ respectively. The EDAX pattern confirmed the homogeneous mixing of the elements in desired composition. The values of observed and theoretical percentage of Fe, Ni, Cu, Zn, Ho and oxygen are in good agreement with theoretical % values of element (Table 1).

3.3. Structural Analysis

Fig.3 shows the XRD patterns of the calcinated $\text{Ni}_{0.2}\text{Cu}_{0.2}\text{Zn}_{0.6}\text{Fe}_{2-x}\text{Ho}_x\text{O}_4$, ferrites. XRD patterns illustrates single phase cubic spinel ferrite (JCPDS # 00-52-0277 and 00-74-0444) [36] was obtained for the pure NiCuZn ferrite and no other visible peak corresponding to the second phase was observed, which illustrated that Ho^{3+} could be entirely solid-soluted in cubic spinel structure or that the amount of the other phase was too small to be identified by XRD [37-38].

The lattice constant 'a' calculated by equation discussed elsewhere [38] and given in Table 2. The calculated lattice constants are within range of 8.417 Å to 8.429 Å, increases with in Ho^{3+} ion concentration. The variation in lattice constant is mainly attributed to difference in ionic radii between the ions. In this ferrite system smaller Fe^{3+} (0.67 Å) ions are substituted by larger Ho^{3+} (1.04 Å) ions [38].

X-ray density 'd_x' of Ho^{3+} substituted NiCuZn ferrites samples were calculated using the following formula;

$$d_x = \frac{8M}{Na^3} \quad (1)$$

Where, 'a' is lattice constant, 'N' is the Avogadro's number and 'M' is molecular weight of sample. It is observed that the X-ray density increased with Ho^{3+} ion concentration (Table 2). This variation in X-ray density is related to the molecular weight of ferrite which increases with increase in Ho^{3+} ion concentration.

Crystallite size (D_{XRD}) of all the samples was obtained from the XRD pattern by employing Debye Scherrer method [39]. The obtained crystallite size lies in the range of 18 - 26 nm tabulated in Table 2. It is observed that, he crystallite size is decreased with Ho^{3+} substitution due to the increase in porosity.

The porosity 'P' in percentage was calculated by following equation [40];

$$P = 1 - \frac{d_B}{d_x} \quad (2)$$

Where d_B is bulk density and d_x is X-ray density. It is observed that, the porosity 'P' is increased with Ho^{3+} substitution. The increase the grain boundaries of the fine particles may results in enhancement in porosity. The increased values of porosity illustrate the porous structure of the $\text{Ni}_{0.2}\text{Cu}_{0.2}\text{Zn}_{0.6}\text{Fe}_{2-x}\text{Ho}_x\text{O}_4$, ferrites..

The hopping lengths L_A and L_B were determined using following relations [41],

$$L_A = \frac{a\sqrt{3}}{4} \quad (3)$$

$$L_B = \frac{a\sqrt{2}}{4} \quad (4)$$

It has been observed that both the hopping lengths are increased with the Ho^{3+} ion concentration (Table 2). Variations in hopping lengths are attributed to the variation in lattice constant and ionic radii of constituent ions.

Fig.4 illustrates the IR spectra of the $\text{Ni}_{0.2}\text{Cu}_{0.2}\text{Zn}_{0.6}\text{Fe}_{2-x}\text{Ho}_x\text{O}_4$, ferrites. The two major absorption bands observed in the range 565–568 (ν_1) and 409–438 (ν_2) cm^{-1} (Table 3) are the characteristics of spinel ferrites. The ν_1 and ν_2 bands assigned to the vibrations of the metal–oxygen bond in the tetrahedral-A and octahedral-B sites, respectively [42]. The values of two bands ν_1 and ν_2 are different due to the difference in $\text{Fe}_B^{3+} - \text{O}_2^{2-}$ inter-ionic distance for the octahedral and tetrahedral sites. The vibrational frequency of bonds is dependent on the mass of cation, cation to oxygen bond length and force constant of bond [43].

The force constant of tetrahedral site (K_t) and octahedral site (K_o) determined using the Waldron method [44] and values tabulated in Table 3. It is to be noted that values of force constants decreased from 2×10^5 to 1.78×10^5 dyne/cm and 1.19×10^5 to 0.82×10^5 dyne/cm tetrahedral site (K_t) and octahedral site (K_o) respectively with increase in concentration of Ho^{3+} ions. The bond lengths R_A and R_B were determined using the formula given by Gorter [45]. The values of the R_A and R_B are increased with the substitution of Ho^{3+} ions (Table 3).

The microstructure observation of the $\text{Ni}_{0.2}\text{Cu}_{0.2}\text{Zn}_{0.6}\text{Fe}_{2-x}\text{Ho}_x\text{O}_4$ spinel has been carried out by Scanning Electron Microscopy (SEM). Topical SEM images are presented in Fig.5 (a, $x = 0.02$ and b, $x=0.08$). The

calculated spinel ferrites were porous with a fine-particle microstructure. It is apparent that Ho^{3+} substituted NiCuZn ferrites revealed a little improved dense microstructure marked with little trapped porosity.

Typical TEM images of the $\text{Ni}_{0.2}\text{Cu}_{0.2}\text{Zn}_{0.6}\text{Fe}_{2-x}\text{Ho}_x\text{O}_4$ spinel ferrite are illustrated in Fig.6 (a, $x = 0.02$ and b, $x=0.08$). These TEM images indicate that sphere-like nanostructures obtained by presently employed sol-gel method. Particles are seems to uniform in particle size and microstructure and are agglomeration to some extent because of their magnetic interactions.

Typical selective area electron diffraction (SAED) pattern the $\text{Ni}_{0.2}\text{Cu}_{0.2}\text{Zn}_{0.6}\text{Fe}_{2-x}\text{Ho}_x\text{O}_4$ spinel ferrite are shown in Fig.7 (a, $x = 0.02$ and b, $x=0.08$). The SAED patterns indicate that spinel ferrites were well distributed crystalline in nature. The superimposition of the bright spot with Debye ring pattern illustrates polycrystalline nature. These Debye rings are assigned to lattice planes and are in good agreement with those planes obtained from XRD data.

Particle size distributions of the respective TEM images measured by ImageJ software and typical histograms shown in Fig.8 (a, $x = 0.02$ and b, $x=0.08$). The particle size decreases from 26.8 nm to 20.4 nm with increasing Ho^{3+} ion concentration, which is in good agreement with the average crystallite size determined from XRD (Table 2).

3.4 Magnetic Properties

Hysteresis loops of $\text{Ni}_{0.2}\text{Cu}_{0.2}\text{Zn}_{0.6}\text{Fe}_{2-x}\text{Ho}_x\text{O}_4$ spinel ferrite shown in Fig.9, which illustrates that prepared samples are soft magnetic material with very low coercivity. Saturation magnetization (M_s), coercivity (H_c), and magneton number (n_B) derived from hysteresis loops and are tabulated in table 4. Coercivity obtained from the hysteresis loop is observed to increase with the increase in Ho^{3+} substitution. Saturation magnetization for pure $\text{Ni}_{0.2}\text{Cu}_{0.2}\text{Zn}_{0.6}\text{Fe}_2\text{O}_4$ ($x = 0.0$) sample is 22.84 emu/g and it decreased to 16.05 emu/g for $\text{Ni}_{0.2}\text{Cu}_{0.2}\text{Zn}_{0.6}\text{Fe}_{1.92}\text{Ho}_{0.08}\text{O}_4$ ($x = 0.08$). The observed magneton number $n_{B(\text{Obs})}$ was determined from hysteresis loops. [46].

$$n_B(\text{obs.}) = \frac{M_w \times M_s}{5585} \quad (5)$$

Saturation magnetization decreases while observed magneton number increases with the increase in Ho^{3+} substitution. The observed increase in magneton number is attributed to decrease in A-B interaction. The substitution of Fe^{3+} with Ho^{3+} the M_s and M_r may decrease as a result of decreased exchange interaction between $\text{Fe}^{\text{Td}}\text{-Fe}^{\text{Oh}}$, which is replaced by the weaker $\text{Fe}^{\text{Td}}\text{-Ho}^{\text{Oh}}$ interaction [37, 38, 47].

Magneton number (observed) decreases with Ho^{3+} substitution. Coercivity obtained from the hysteresis loop is observed to increase with the increase in Ho^{3+} substitution (Table 4)

The net magnetic moment ($n_B \text{Cal.}$) is determined using relation, $n_B \text{Cal.} = M_B - M_A$; where, M_B and M_A are the B and A sub-lattice magnetic moments in μ_B [48]. The values of $n_B \text{Cal.}$ for $\text{Ni}_{0.2}\text{Cu}_{0.2}\text{Zn}_{0.6}\text{Fe}_{2-x}\text{Ho}_x\text{O}_4$ were determined using cation distribution and magnetic moment of Fe^{3+} ($5\mu_B$), Ni^{2+} ($2\mu_B$), Zn^{2+} ($0\mu_B$), Cu^{3+} ($1\mu_B$) and Ho^{3+} ($10\mu_B$). The calculated Magneton number decreases with Ho^{3+} substitution. The magneton number (calculated) also decreases with Ho^{3+} substitution

3.4 Application for One Pot Synthesis of Dihydropyrimidinones

3,4-dihydropyrimidin-2(1H)-ones synthesized by one-pot three-component condensation of aromatic aldehydes (1), 1,3-dicarbonyl compounds (2) and urea/thiourea using 10 mol % Ho^{3+} doped $\text{Ni}_{0.2}\text{Cu}_{0.2}\text{Zn}_{0.6}\text{Fe}_{2-x}\text{Ho}_x\text{O}_4$ spinel ferrites catalyst (Scheme 1).

Aldehyde (1) (10 mmole), 1,3-dicarbonyl compound (2) (10 mmole), urea or thiourea (3) (15 mmole) were dissolved in ethanol to which catalyst $\text{Ni}_{0.2}\text{Cu}_{0.2}\text{Zn}_{0.6}\text{Fe}_{2-x}\text{Ho}_x\text{O}_4$ (20 mol %) spinel ferrite added and resulting mixture heated at 80°C with constant stirring for suitable time (monitored by TLC) as tabulated in Table 4. After completion of reaction, catalyst was separated by fixing the catalyst at bottom of flask magnetically by using a strong magnet, and the solution was taken off. The reaction mixture then transferred into ice water, the solid product precipitates out which is separated by filtration, washed with water and dried. The product was purified by recrystallization using ethanol as a solvent. All the synthesized compounds were characterized by $^1\text{H-NMR}$, Mass (ES-MS) and melting point.

Ethyl 6-methyl-4-(4-pyridyl)-2-oxo-1,2,3,4-tetrahydropyrimidine-5-carboxylate (g): $^1\text{H-NMR}$ ($\text{DMSO-}d_6$, 300 MHz) δ 9.38 (s, 1H, NH), 8.50 (d, 2H), 7.85 (s, 1H, NH), 7.20 (d, 2H), 5.15 (d, 1H, $J=3.3$ Hz, H-4), 4.00 (q, 2H, OCH_2), 2.27 (s, 3H, CH_3), 1.09 (t, 3H, $J=7.2$ Hz, CH_3); Mass (ES/MS): m/z 260 (M-H, 100%).

Catalytic efficiency $\text{Ni}_{0.2}\text{Cu}_{0.2}\text{Zn}_{0.6}\text{Fe}_{2-x}\text{Ho}_x\text{O}_4$ spinel ferrites studied by screening five compositions $x = 0.0, 0.02, 0.04, 0.06$ and 0.08 to find out best ferrite composition (catalyst) for 3,4-dihydropyrimidin-2(1H)-one (a) synthesis as model reaction. The 3,4-dihydropyrimidin-2(1H)-one compound 5a, was obtained with 95% yield with $\text{Ni}_{0.2}\text{Cu}_{0.2}\text{Zn}_{0.6}\text{Fe}_{2-x}\text{Ho}_x\text{O}_4$ ($x = 0.06$) spinel ferrites catalyst in shorter time (100 min) than other spinel ferrites compositions ($x = 0.0, 0.02, 0.04$ and 0.08).

Then the amount of spinel ferrites (catalyst load) was optimized for model reaction (a). The spinel ferrite catalyst was added in amounts of 20, 15, 10, 5 and 0 mol %. It is observed that decrease in amount of catalyst

from 20 mol % to 10 mol % there is no effect on yield of reaction (Table 5). Therefore, 10 mol % of the catalyst $\text{Ni}_{0.2}\text{Cu}_{0.2}\text{Zn}_{0.6}\text{Fe}_{2-x}\text{Ho}_x\text{O}_4$ ($x = 0.6$) spinel ferrites was assumed to ensure the best yield (95 %) in short reaction time (10 min).

To assess the generality of this approach, various aldehydes were reacted with 1,3-dicarbonyl compound (2) and urea or thiourea (3) under optimized conditions to obtain substituted 3,4-dihydropyrimidin-2(1H)-ones (a-h) (Scheme 1).

Catalyst reusability is of most important factor in heterogeneous catalysis. The catalyst recovery and reusability was evaluated for the model reaction (a). After completion of reaction, catalyst was separated by fixing the catalyst at bottom of flask magnetically by using a strong magnet, and the solution was taken off. The catalyst washed 2 times with acetone and the fresh reaction mixture was added into the flask, for the next reaction run. The catalyst was repeatedly reused five times without any noticeable loss of its catalytic activity (Cycle number and yield of a: 1, 95 %; 2, 95 %; 3, 95 %; 4, 94 %; 5, 93 %).

The work-up process was very simple and first catalyst removed magnetically then the reaction mixture transferred into ice water, the solid product precipitates out which is separated by filtration, washed with water and dried. The product was purified by recrystallization using ethanol as a solvent. The efficiency, easy handling and mild nature are advantageous aspect of the catalyst.

The catalytic activity of spinel ferrites for these reactions arises due to the ease Fe can switch its oxidation state between 2+ and 3+. Due to the spinel structure ferrites have stability under extremely reducing conditions. The reduction of Fe^{+3} to Fe^{+2} occurs without varying lattice arrangements, so that original state is obtained on reoxidation [52].

4. Conclusion:

Holmium substituted NiCuZn ferrites with composition $\text{Ni}_{0.2}\text{Cu}_{0.2}\text{Zn}_{0.6}\text{Fe}_{2-x}\text{Ho}_x\text{O}_4$ ($x=0.00, 0.02, 0.04, 0.06$ and 0.08) were successfully prepared by sol gel auto combustion method. Precursor powders calcinated at 500 °C. The observed elemental analysis from EDAX was in good agreement with the theoretical stoichiometry. The lattice constant, X-ray density and hopping lengths increased with increase in Ho^{3+} . The crystallite size decreased from 26.2 nm to 19.9 nm with the substitution of Ho^{3+} confirmed by TEM. The two strong IR absorption bands observed in the range 565–568 (ν_1) and 409–439 (ν_2) cm^{-1} assigned to the vibrations of the metal ion–oxygen in the tetrahedral-A and octahedral-B sites, respectively. Force constant decreased while hopping R_A and R_B are

increased with the substitution of Ho^{3+} ions. SEM images confirmed the porous nature with a fine-grained microstructure. TEM images revealed sphere-like nanostructures and particles with agglomeration to some extent due to their magnetic interactions. Saturation magnetization decreased while observed magneton number increased with the increase in Ho^{3+} substitution. ¹¹ Synthesis of 3,4-dihydropyrimidin-2(1H)-ones via one-pot three-component condensation reaction of aromatic aldehydes, 1,3-dicarbonyl compounds and urea/thiourea using magnetic 10 mol % Ho^{3+} doped NiCuZn spinel ferrites catalyst.

ORIGINALITY REPORT

35%

SIMILARITY INDEX

16%

INTERNET SOURCES

28%

PUBLICATIONS

19%

STUDENT PAPERS

PRIMARY SOURCES

- | | | |
|---|---|----|
| 1 | B.L. Shinde, L.A. Dhale, K.S. Lohar. "Variation in Elastic Properties of Holmium Substituted Nickel Copper Zinc Ferrites", Asian Journal of Chemistry, 2017
Publication | 3% |
| 2 | www.bioorganica.org.ua
Internet Source | 2% |
| 3 | Submitted to Savitribai Phule Pune University
Student Paper | 2% |
| 4 | ijc.iaush.ac.ir
Internet Source | 2% |
| 5 | Zaheer, Zahid, Firoz A. Kalam Khan, Jaiprakash N. Sangshetti, Rajendra H. Patil, and K.S. Lohar. "Novel amalgamation of phthalazine–quinolines as biofilm inhibitors: One-pot synthesis, biological evaluation and in silico ADME prediction with favorable metabolic fate", Bioorganic & Medicinal Chemistry Letters, 2016.
Publication | 1% |
-

A. A. Birajdar, Sagar E. Shirsath, R. H. Kadam,

6

M. L. Mane, D. R. Mane, A. R. Shitre. " Permeability and magnetic properties of Al substituted Ni Zn Fe O nanoparticles ", Journal of Applied Physics, 2012

Publication

1%

7

M.V. Chaudhari, R.H. Kadam, S.B. Shelke, Sagar E. Shirsath, A.B. Kadam, D.R. Mane. "Combustion synthesis of Co²⁺ substituted Li_{0.5}Cr_{0.5}Fe₂O₄ nano-powder: Physical and magnetic interactions", Powder Technology, 2014

Publication

1%

8

K.A. Ganure, M.M. Langade, L.A. Dhale, K.S. Lohar. "Chromium substituted nickel ferrites (NiFe_{2-x}Cr_xO₄, x=0.0, 0.1, 0.2, 0.3, and 0.4) magnetically recoverable reusable heterogeneous nano catalysts", Materials Today: Proceedings, 2020

Publication

1%

9

worldwidescience.org

Internet Source

1%

10

www.science.gov

Internet Source

1%

11

etheses.saurashtrauniversity.edu

Internet Source

1%

12

K.S. Lohar, S.M. Patange, M.L. Mane, Sagar E.

1%

Shirsath. "Cation distribution investigation and characterizations of Ni_{1-x}Cd_xFe₂O₄ nanoparticles synthesized by citrate gel process", Journal of Molecular Structure, 2013

Publication

13

K.S. Lohar, A.M. Pachpinde, M.M. Langade, R.H. Kadam, Sagar E. Shirsath. "Self-propagating high temperature synthesis, structural morphology and magnetic interactions in rare earth Ho³⁺ doped CoFe₂O₄ nanoparticles", Journal of Alloys and Compounds, 2014

Publication

14

Haralkar, S.J., R.H. Kadam, S.S More, Sagar E. Shirsath, M.L. Mane, Swati Patil, and D.R. Mane. "Substitutional effect of Cr³⁺ ions on the properties of Mg-Zn ferrite nanoparticles", Physica B Condensed Matter, 2012.

Publication

15

baadalsg.inflibnet.ac.in

Internet Source

16

Submitted to Universiti Teknologi Malaysia

Student Paper

17

Behzad Mohammadi, Farahnaz K. Behbahani. "Recent developments in the synthesis and applications of dihydropyrimidin-2(1H)-ones and thiones", Molecular Diversity, 2018

18

Pawar, Ram A., Sunil M. Patange, Qudsiya Y. Tamboli, V. Ramanathan, and Sagar E. Shirsath. "Spectroscopic, elastic and dielectric properties of Ho³⁺ substituted Co-Zn ferrites synthesized by sol-gel method", *Ceramics International*, 2016.

Publication

19

Submitted to Higher Education Commission Pakistan

Student Paper

20

Submitted to West De Pere High School

Student Paper

21

www.mdpi.com

Internet Source

22

Chaudhari, M.V., Sagar E. Shirsath, A.B. Kadam, R.H. Kadam, S.B. Shelke, and D.R. Mane. "Site occupancies of Co–Mg–Cr–Fe ions and their impact on the properties of Co_{0.5}Mg_{0.5}Cr_xFe_{2-x}O₄", *Journal of Alloys and Compounds*, 2013.

Publication

23

Q. Wang, W. Pei. "Synthesis of 3,4-dihydropyrimidin-2(1H)-ones catalyzed by nafion-H under ultrasound irradiation and solvent-free conditions", *Journal of the Iranian*

1%

1%

1%

1%

1%

1%

24

dyuthi.cusat.ac.in

Internet Source

1%

25

O. A. Abd Allah. "Part 1: Synthesis of Polyfused Heterocyclic Systems Derived From 3-Phenyl-5,6,7,8-tetrahydro[1,2,4]triazolo[3,4- b] [1,3,4]thiadiazepine-6,8-dione", Phosphorus, Sulfur, and Silicon and the Related Elements, 2002

Publication

1%

26

A. T. RAGHAVENDER, K. M. JADHAV. " STRUCTURAL, MORPHOLOGICAL CHARACTERIZATION OF NANOPARTICLES SYNTHESIZED BY SOL-GEL METHOD ", International Journal of Modern Physics B, 2012

Publication

1%

27

www.irjet.net

Internet Source

1%

28

Hashim, Mohd, Alimuddin, Sagar E. Shirsath, Shalendra Kumar, Ravi Kumar, Aashis S. Roy, Jyoti Shah, and R.K. Kotnala. "Preparation and characterization chemistry of nano-crystalline Ni–Cu–Zn ferrite", Journal of Alloys and Compounds, 2013.

Publication

<1%

Rahul R. Nagawade, Sandeep A. Kotharkar,

29 Devanand B. Shinde. "Titanium(IV) chloride catalyzed one-pot synthesis of 3,4-dihydropyrimidin- 2(1H)-ones and thiones", Mendeleev Communications, 2005 $<1\%$
Publication

30 Raghavender, A.T.. "Effect of grain size on the Neel temperature of nanocrystalline nickel ferrite", Materials Letters, 20100531 $<1\%$
Publication

31 www.chalcogen.ro $<1\%$
Internet Source

32 scholarbank.nus.edu.sg $<1\%$
Internet Source

33 Nagawade, R.R.. "Synthesis of new series of 1-Aryl-1,4-dihydro-4-oxo-6-methyl pyridazine-3-carboxylic acid as potential antibacterial agents", European Journal of Medicinal Chemistry, 200512 $<1\%$
Publication

34 Belavi, P.B.. "Structural, electrical and magnetic properties of cadmium substituted nickel-copper ferrites", Materials Chemistry and Physics, 20120116 $<1\%$
Publication

35 Ahmad Shaabani, Ayoob Bazgir, Sakineh Arab-Ameri. " TETRABUTYLAMMONIUM $<1\%$

HYDROGEN SULFATE: AN EFFICIENT CATALYST FOR THE SYNTHESIS OF 3,4-DIHYDROPYRIMIDIN-2(1H)-ONES UNDER SOLVENT-FREE CONDITIONS ", Phosphorus, Sulfur, and Silicon and the Related Elements, 2004

Publication

36

Ghulam Mustafa, M.U. Islam, Wenli Zhang, Yasir Jamil, Abdul Waheed Anwar, Mudassar Hussain, Mukhtar Ahmad. "Investigation of structural and magnetic properties of Ce³⁺-substituted nanosized Co–Cr ferrites for a variety of applications", Journal of Alloys and Compounds, 2015

Publication

<1%

37

Submitted to Bilkent University

Student Paper

<1%

38

D. R. Mane, D. D. Birajdar, Swati Patil, Sagar E. Shirsath, R. H. Kadam. "Redistribution of cations and enhancement in magnetic properties of sol–gel synthesized Cu_{0.7-x} Co_x Zn_{0.3}Fe₂O₄ (0 ≤ x ≤ 0.5)", Journal of Sol-Gel Science and Technology, 2010

Publication

<1%

39

Labde, B.. "Structural and infra-red studies of Ni¹⁺+xPb^xFe²⁺-2xO⁴ system", Materials Letters, 200303

Publication

<1%

40

Lohar, K.S., S.M. Patange, M.L. Mane, and Sagar E. Shirsath. "Cation distribution investigation and characterizations of Ni_{1-x}Cd_xFe₂O₄ nanoparticles synthesized by citrate gel process", Journal of Molecular Structure, 2013.

Publication

<1%

41

Yonghong Zhang, Bin Wang, Xiaomei Zhang, Jianbin Huang, Chenjiang Liu. "An Efficient Synthesis of 3,4-Dihydropyrimidin-2(1H)-Ones and Thiones Catalyzed by a Novel Brønsted Acidic Ionic Liquid under Solvent-Free Conditions", Molecules, 2015

Publication

<1%

Exclude quotes Off

Exclude matches Off

Exclude bibliography Off

Prof.(Dr.)K.S.LOHAR

Manuscript_2_3rd

by Ks Lohar

Submission date: 27-May-2020 11:43PM (UTC+1200)

Submission ID: 1332749090

File name: 3rd_Attempt_Dr_KS_Lohar_manuscript_02.docx (58.53K)

Word count: 2828

Character count: 16375

**Microstructure, Magnetic Properties of Ho³⁺ Substituted Ni-Cu-Zn Spinel Ferrites and
Application for One Pot Synthesis of Dihydropyrimidinones**

Abstract:

²⁷ **Ho³⁺ Substituted Ni-Cu-Zn Spinel Ferrites** synthesized by sol-gel auto combustion method. It is illustrated from TGA-DTA curve that the decomposition of precursors takes place in the temperature range 315 to 425 °C. The EDAX ³⁸ pattern confirmed the homogeneous mixing of the Fe, Ni, Cu, Zn, Ho and oxygen elements in pure and substituted spinel ferrites with desired stoichiometry. XRD pattern indicates ¹ formation of single phase cubic spinel structure. Lattice constant, X-ray density increases while ⁷ average crystallite size decreases with increase in Ho³⁺ concentration. The two strong IR absorption bands observed in the range 565–568 (ν₁) and 409 - 438 (ν₂) cm⁻¹. The obtained crystallite size lies between of 18 - 26 nm, confirmed from TEM. The microstructures of the calcinated spinel ferrites were evaluated by SEM and TEM. It is observed that the increase in concentration of Ho³⁺ ions saturation magnetization decreases. Prepared Ho³⁺ substituted Ni-Cu-Zn spinel ferrites used as ¹ catalyst for synthesis of 3,4-dihydropyrimidin-2(1H)-ones.

Keywords: Sol-gel auto combustion, Ni-Cu-Zn spinel ferrites, Saturation magnetization, Transmission Electron Microscopy, One pot synthesis.

1. Introduction

Nanoscience and Nanotechnology is the technology associated with materials in nanometer range and appliances based on them [1]. Ferrites are chemical composites with iron (III) oxide Fe_2O_3 as their major constituents [2]. The electrical and magnetic properties of the ferrites are significantly altered by substitution of trivalent or tetravalent cations and also affected by distribution of cation between the tetrahedral and octahedral sites of spinel structure [3 - 6]. By tailoring the stoichiometry of the ferrite system structural, electrical, and magnetic properties are tuned [7]. The spinel ferrites have versatile applications such as magnetic drug delivery [8], information storage [9], super capacitor [10], magnetic refrigeration [11], gas sensors [12], and catalyst [13] etc.

NiCuZn ferrites have more attention of researchers due to their outstanding characteristics such as low magnetic losses, high permeability and high resistivity, which are suitable for microwave applications [14, 15]. The doping of trivalent rare-earth cations in ferrites are becoming the important components for sophisticated applications [16]. The substitution of little quantity of rare-earth cations improves structural, electrical and magnetic properties of ferrites [17, 18].

One-pot multicomponent reactions have more advantages over traditional reactions due to their rapidity, simplicity, atom-economy and shorter synthetic route [19] for the synthesis of bio-active molecules [20]. Now days, the use of heterogeneous catalysts has established significant interest in various disciplines, i.e. organic synthesis. Organic synthesis using heterogeneous catalysts have great advantage of catalyst recycle as compared to homogeneous catalyst. Iron oxide nanoparticles are used as heterogeneous catalyst as it is separated without filtration simply applying external magnet [21, 22]. The catalytic activity of spinel ferrites for these reactions arises due to the ease Fe can switch its oxidation state between 2+ and 3+ and hence spinel structure ferrites have stability under extremely reducing conditions. The Fe^{+3} reduced to Fe^{+2} without varying lattice arrangements, therefore original state is obtained on reoxidation [23].

Now days, magnetic spinel ferrites used as efficient catalyst in different chemical transformations such as synthesis of diazepine derivatives [24], α -amino nitriles [25], 1,1-diacetates from aldehydes [26], etc.

Dihydropyrimidinones have synthesized by Pietro Biginelli in 1893, by a one-pot three-component condensation of benzaldehyde, ethyl acetoacetate and urea under robustly acidic environment [27]. Also Dihydropyrimidinones synthesized by microwave irradiation [28], ionic liquids [29], and using different types of catalysts such as lanthanide triflate [30], $\text{Sr}(\text{OTf})_2$ [31], nanomagnetic-supported sulfonic acid [32], $\text{Fe}(\text{III})$ tosylate [33], FeCl_3 -supported nanopore silica [34], etc.

7
The present work deals with the structural and magnetic properties of **Ho³⁺ Substituted Ni-Cu-Zn Spinel Ferrites** with composition $\text{Ni}_{0.2}\text{Cu}_{0.2}\text{Zn}_{0.6}\text{Fe}_{2-x}\text{Ho}_x\text{O}_4$ ($x = 0.00, 0.02, 0.04, 0.06, \text{ and } 0.08$) synthesized by sol gel auto combustion method and application as catalyst for one pot three component synthesis of Dihydropyrimidinones.

2. Experimental

2.1. Material and Synthesis

The nano-crystalline powders of $\text{Ni}_{0.2}\text{Cu}_{0.2}\text{Zn}_{0.6}\text{Fe}_{2-x}\text{Ho}_x\text{O}_4$ ($x=0.00, 0.02, 0.04, 0.06, \text{ and } 0.08$) prepared using sol-gel auto-combustion method [35]. The stoichiometric quantities of analytical grade reagents of corresponding metal nitrates were dissolved in deionized water. The aqueous citric acid solution added in the metal nitrates to citric acid ratio of 1:3 and then NH_3 solution added to adjust $\text{pH} \approx 7$ of solution. The resulting solution was heated on hot plate (90°C) with continuous stirring. After some time the solution turns viscous and converted in to brown gel, with complete removal water molecule gel starts frothing and later on automatically get burnt. The process of auto-combustion accomplished in a minute, resulting in the formation of the brown ashes known as precursors. Calcination temperature is confirmed from TGA / DTA curve and all the precursors calcinated at 500°C for four hours, gives final spinel ferrites.

2.2. Characterization techniques

Thermal analysis carried using simultaneous TGA and DTA of precursors at heating rate $10^0\text{C} / \text{min}$ in the range 25°C to 800°C on SDT Q600 V20.9 Build 20 in air. With EDAX, Inca Oxford, attached to the SEM the composition of calcinated samples determined. The structural parameters investigated by X-ray diffraction Phillips-3710 X-ray diffractometer employed with $\text{Cu-K}\alpha$ radiation ($\lambda=1.5405\text{\AA}$) were used in the present study. Microstructure investigated by JEOL-JSM-5600-N Scanning Electron Microscope and on Philips-CM-200 Transmission Electron Microscope. Magnetic measurements carried at room temperature using PARC EG&G vibrating sample magnetometer.

3. Results and discussion

3.1. Thermal Analysis (TGA / DTA)

Fig.1 represents typical TGA/DTA curve of $\text{Ni}_{0.2}\text{Cu}_{0.2}\text{Zn}_{0.6}\text{Fe}_{2-x}\text{Ho}_x\text{O}_4$ ($x= 0.06$). The TGA curve shows two weight loss steps associated with endothermic and exothermic DTA peaks. The 1st weight loss step in the temperature $30\text{-}100^\circ\text{C}$ range is corresponding to endothermic peak around 80°C , is due to evaporation of residual water from precursor. The 2nd weight loss step in the temperature range of $350\text{-}460^\circ\text{C}$ is corresponding

to the exothermic peak around 400 °C, due to the decomposition of unreacted citric acid. No weight loss observed above 460 °C, representing the presence of only $Ni_{0.2}Cu_{0.2}Zn_{0.6}Fe_{2-x}Ho_xO_4$ in this temperature range. Therefore, the prepared precursors calcinated at 500 °C for four hour to get $Ni_{0.2}Cu_{0.2}Zn_{0.6}Fe_{2-x}Ho_xO_4$ spinel ferrites.

3.2. Elemental Analysis:

The chemical compositions of $Ni_{0.2}Cu_{0.2}Zn_{0.6}Fe_{2-x}Ho_xO_4$ ferrite nanoparticles are determined by EDAX. Fig.2 (a) and (b) shows the typical EDAX pattern for the $Ni_{0.2}Cu_{0.2}Zn_{0.6}Fe_{2-x}Ho_xO_4$, ferrite nanoparticles $x= 0.00$ and $x=0.08$ respectively. The EDAX pattern confirmed the homogeneous mixing of the elements in desired composition. The values of observed and theoretical percentage of Fe, Ni, Cu, Zn, Ho and oxygen are in good agreement with theoretical % values of element (Table 1).

3.3. Structural Analysis

Fig.3 shows the XRD patterns of the calcinated $Ni_{0.2}Cu_{0.2}Zn_{0.6}Fe_{2-x}Ho_xO_4$ ferrites. XRD patterns illustrates single phase cubic spinel ferrite (JCPDS # 00-52-0277 and 00-74-0444) [36] was obtained for the pure NiCuZn ferrite and no other visible peak corresponding to the second phase was observed, which illustrated that Ho^{3+} could be entirely solid-soluted in cubic spinel structure or that the amount of the other phase was too small to be identified by XRD [37-38].

The lattice constant 'a' determined by equation discussed elsewhere [38] and given in Table 2. The calculated lattice constants are within range of 8.417 Å to 8.429 Å, increases with in Ho^{3+} ion concentration. The variation in lattice constant is mainly attributed to difference in ionic radii between the ions. In this ferrite system smaller Fe^{3+} (0.67 Å) ions are substituted by larger Ho^{3+} (1.04 Å) ions [38].

X-ray density 'd_x' of Ho^{3+} substituted Ni-Cu-Zn ferrites samples were calculated using the following formula and tabulated in Table 2,

$$d_x = \frac{8M}{Na^3} \quad (1)$$

Where, 'a' is lattice constant, 'N' is the Avogadro's number and 'M' is molecular weight. The X-ray density in present spinel ferrites increased with Ho^{3+} ion concentration, due to the increased molecular weight of spinel ferrite.

Crystallite size (D_{XRD}) was obtained from the XRD pattern by employing Debye Scherrer method [39]. The obtained crystallite size lies in the range of 18 - 26 nm tabulated in Table 2. The crystallite size in present spinel ferrites is decreased with increase in Ho^{3+} concentration, due to the increase in porosity.

The porosity 'P' in percentage was calculated by following equation discussed elsewhere [40]. The porosity 'P' in present spinel ferrites is increased with Ho^{3+} substitution. The increase the grain boundaries of the fine particles may results in enhancement in porosity. The increased values of porosity illustrate the porous structure of the $Ni_{0.2}Cu_{0.2}Zn_{0.6}Fe_{2-x}Ho_xO_4$, ferrites..

The hopping lengths L_A and L_B were calculated using following equations [41],

$$L_A = \frac{a\sqrt{3}}{4} \quad (2)$$

$$L_B = \frac{a\sqrt{2}}{4} \quad (3)$$

It has been observed that both the hopping lengths are increased with the Ho^{3+} ion concentration (Table 2). Variations in hopping lengths are attributed to the variation in lattice constant and ionic radii of constituent ions.

Fig.4 illustrates the IR spectra of the $Ni_{0.2}Cu_{0.2}Zn_{0.6}Fe_{2-x}Ho_xO_4$, ferrites. The two major absorption bands observed in the range 565–568 (ν_1) and 409–438 (ν_2) cm^{-1} (Table 3) are the characteristics of spinel ferrites. The ν_1 and ν_2 bands assigned to the vibrations of the metal–oxygen bond in the tetrahedral-A and octahedral-B sites, respectively [42]. The values of two bands ν_1 and ν_2 are different due to the difference in $Fe_B^{3+} - O_2^{2-}$ inter-ionic distance for the octahedral and tetrahedral sites. The vibrational frequency of bonds is dependent on the mass of cation, bond length and force constant of bond [43].

The force constant of tetrahedral site (K_t) and octahedral site (K_o) calculated by Waldron method [44] and values tabulated in Table 3. The values of force constants in present spinel ferrites decreased from 2×10^5 to 1.78×10^5 dyne/cm and 1.19×10^5 to 0.82×10^5 dyne/cm tetrahedral site (K_t) and octahedral site (K_o) respectively with increase in concentration of Ho^{3+} ions. The bond lengths R_A and R_B determined using the formula given by Gorter [45]. The R_A and R_B in present spinel ferrites are increased with the substitution of Ho^{3+} ions (Table 3).

The microstructure observation of the $\text{Ni}_{0.2}\text{Cu}_{0.2}\text{Zn}_{0.6}\text{Fe}_{2-x}\text{Ho}_x\text{O}_4$ spinel has been carried out by Scanning Electron Microscopy (SEM). Typical SEM images are presented in Fig.5 (a, $x = 0.02$ and b, $x=0.08$). The calcinated spinel ferrites were porous with a fine-particle microstructure. It is apparent that Ho^{3+} substituted NiCuZn ferrites revealed a little improved dense microstructure marked with little trapped porosity.

Typical TEM images of the $\text{Ni}_{0.2}\text{Cu}_{0.2}\text{Zn}_{0.6}\text{Fe}_{2-x}\text{Ho}_x\text{O}_4$ spinel ferrite are illustrated in Fig.6 (a, $x = 0.02$ and b, $x=0.08$). These TEM images indicate that sphere-like nanostructures obtained by presently employed sol-gel method. Particles are seems to uniform in particle size and microstructure and are agglomeration to some extent because of their magnetic interactions.

Typical selective area electron diffraction (SAED) pattern the $\text{Ni}_{0.2}\text{Cu}_{0.2}\text{Zn}_{0.6}\text{Fe}_{2-x}\text{Ho}_x\text{O}_4$ spinel ferrite are shown in Fig.7 (a, $x = 0.02$ and b, $x=0.08$). The SAED patterns indicate that spinel ferrites were well distributed crystalline in nature. The superimposition of the bright spot with Debye ring pattern illustrates polycrystalline nature. These Debye rings are assigned to lattice planes and are in good agreement with those planes obtained from XRD data.

Particle size distributions of the respective TEM images measured by ImageJ software and typical histograms shown in Fig.8 (a, $x = 0.02$ and b, $x=0.08$). The particle size decreases from 26.8 nm to 20.4 nm with increasing Ho^{3+} ion concentration, which is in good agreement with the average crystallite size determined from XRD (Table 2).

3.4 Magnetic Properties

Hysteresis loops of $\text{Ni}_{0.2}\text{Cu}_{0.2}\text{Zn}_{0.6}\text{Fe}_{2-x}\text{Ho}_x\text{O}_4$ spinel ferrite shown in Fig.9, which illustrates that prepared samples are soft magnetic material with very low coercivity. Saturation magnetization (M_s), coercivity (H_c), and magneton number (n_B) derived from hysteresis loops and are tabulated in table 4. Coercivity obtained from the hysteresis loop is observed to increase with the increase in Ho^{3+} substitution. Saturation magnetization for pure $\text{Ni}_{0.2}\text{Cu}_{0.2}\text{Zn}_{0.6}\text{Fe}_2\text{O}_4$ ($x = 0.0$) sample is 22.84 emu/g and it decreased to 16.05 emu/g for $\text{Ni}_{0.2}\text{Cu}_{0.2}\text{Zn}_{0.6}\text{Fe}_{1.92}\text{Ho}_{0.08}\text{O}_4$ ($x = 0.08$). The observed magneton number $n_{B(\text{Obs})}$ was determined from hysteresis loops. [46].

$$n_B(\text{obs.}) = \frac{M_w \times M_s}{5585} \quad (4)$$

Saturation magnetization decreases while observed magneton number increases with the increase in Ho^{3+} substitution. The observed increase in magneton number is attributed to decrease in A-B interaction. The

substitution of Fe^{3+} with Ho^{3+} the M_s and M_r may decrease as a result of decreased exchange interaction between $\text{Fe}^{\text{Td}}\text{-Fe}^{\text{Oh}}$, which is replaced by the weaker $\text{Fe}^{\text{Td}}\text{-Ho}^{\text{Oh}}$ interaction [37, 38, 47].

Magneton number (observed) decreases with Ho^{3+} substitution. Coercivity obtained from the hysteresis loop is observed to increase with the increase in Ho^{3+} concentration (Table 4)

The net magnetic moment ($n_B \text{ Cal.}$) is determined using equation, $n_B \text{ Cal.} = M_B - M_A$; where, M_B and M_A are the B and A sub-lattice magnetic moments in μ_B [48]. The values of $n_B \text{ Cal.}$ for $\text{Ni}_{0.2}\text{Cu}_{0.2}\text{Zn}_{0.6}\text{Fe}_{2-x}\text{Ho}_x\text{O}_4$ were determined using cation distribution and magnetic moment of Fe^{3+} ($5\mu_B$), Ni^{2+} ($2\mu_B$), Zn^{2+} ($0\mu_B$), Cu^{3+} ($1\mu_B$) and Ho^{3+} ($10\mu_B$). The calculated Magneton number decreases with Ho^{3+} substitution. The magneton number (calculated) also decreases with Ho^{3+} substitution

3.4 Application for One Pot Synthesis of Dihydropyrimidinones

3,4-dihydropyrimidin-2(1H)-ones synthesized by one-pot three-component condensation of aromatic aldehydes (1), 1,3-dicarbonyl compounds (2) and urea/thiourea (3) using 10 mol % Ho^{3+} doped $\text{Ni}_{0.2}\text{Cu}_{0.2}\text{Zn}_{0.6}\text{Fe}_{2-x}\text{Ho}_x\text{O}_4$ spinel ferrites catalyst (Scheme 1).

Aldehyde (1) (10 mmole), 1,3-dicarbonyl compound (2) (10 mmole), urea or thiourea (3) (15 mmole) were dissolved in ethanol to which catalyst $\text{Ni}_{0.2}\text{Cu}_{0.2}\text{Zn}_{0.6}\text{Fe}_{2-x}\text{Ho}_x\text{O}_4$ (20 mol %) spinel ferrite added and then reaction mixture heated at 80°C with constant stirring for suitable time (monitored by TLC) as tabulated in Table 4. After completion of reaction, catalyst was separated by fixing the catalyst at bottom of flask magnetically by using a strong magnet, and the solution was taken off. The reaction mixture then transferred into ice water, the precipitate of product obtained which is separated by filtration, washed with water and dried. The product was purified by recrystallization using ethanol as a solvent. All the synthesized compounds were characterized by $^1\text{H-NMR}$, Mass (ES-MS) and melting point.

Ethyl 6-methyl-4-(4-pyridyl)-2-oxo-1,2,3,4-tetrahydropyrimidine-5-carboxylate (4g): $^1\text{H-NMR}$ ($\text{DMSO-}d_6$, 300 MHz) δ 9.38 (s, 1H, NH), 8.50 (d, 2H), 7.85 (s, 1H, NH), 7.20 (d, 2H), 5.15 (d, 1H, $J=3.3$ Hz, H-4), 4.00 (q, 2H, OCH_2), 2.27 (s, 3H, CH_3), 1.09 (t, 3H, $J=7.2$ Hz, CH_3); Mass (ES/MS) : m/z 260 (M-H, 100%).

Catalytic efficiency $\text{Ni}_{0.2}\text{Cu}_{0.2}\text{Zn}_{0.6}\text{Fe}_{2-x}\text{Ho}_x\text{O}_4$ spinel ferrites studied by screening five compositions $x = 0.0, 0.02, 0.04, 0.06$ and 0.08 to find out best ferrite composition (catalyst) for 3,4-dihydropyrimidin-2(1H)-one (4a) synthesis as model reaction. The 3,4-dihydropyrimidin-2(1H)-one compound 4a, was obtained with 95% yield

with $\text{Ni}_{0.2}\text{Cu}_{0.2}\text{Zn}_{0.6}\text{Fe}_{2-x}\text{Ho}_x\text{O}_4$ ($x = 0.06$) spinel ferrites catalyst in shorter time (100 min) than other spinel ferrites compositions ($x = 0.0, 0.02, 0.04$ and 0.08).

Then the amount of spinel ferrites (catalyst load) was optimized for model reaction (4a). The spinel ferrite catalyst was added in amounts of 20, 15, 10, 5 and 0 mol %. It is observed that decrease in amount of catalyst from 20 mol % to 10 mol % there is no effect on yield of reaction (Table 5). Therefore, 10 mol % of the catalyst $\text{Ni}_{0.2}\text{Cu}_{0.2}\text{Zn}_{0.6}\text{Fe}_{2-x}\text{Ho}_x\text{O}_4$ ($x = 0.6$) spinel ferrites was assumed to ensure the best yield (95 %) in short reaction time (10 min).

The generality of this approach was assessed by reacting various aldehydes with 1,3-dicarbonyl compound (2) and urea or thiourea (3) under optimized conditions to obtain substituted 3,4-dihydropyrimidin-2(1H)-ones (4a-h) (Scheme 1).

Catalyst reusability is of most important factor in heterogeneous catalysis. The catalyst recovery and reusability was evaluated for the model reaction (4a). After completion of reaction, catalyst was separated by fixing the catalyst at bottom of flask magnetically by using a strong magnet, and the solution was taken off. The catalyst washed 2 times with acetone and the fresh reaction mixture was added into the flask, for the next reaction run. The catalyst was repeatedly reused five times without any noticeable loss of its catalytic activity (Cycle number and yield of 4a: 1, 95 %; 2, 95 %; 3, 95 %; 4, 94 %; 5, 93 %).

The work-up process was very simple and first catalyst removed magnetically then the reaction mixture transferred into ice water, the solid product precipitates out which is separated by filtration, washed with water and dried. The product was purified by recrystallization using ethanol as a solvent. The efficiency, easy handling and mild nature are advantageous aspect of the catalyst.

4. Conclusion:

Holmium substituted NiCuZn ferrites with composition $\text{Ni}_{0.2}\text{Cu}_{0.2}\text{Zn}_{0.6}\text{Fe}_{2-x}\text{Ho}_x\text{O}_4$ ($x=0.00, 0.02, 0.04, 0.06,$ and 0.08) were successfully prepared by sol gel auto combustion method. Precursor powders calcinated at $500\text{ }^\circ\text{C}$.

The observed elemental analysis from EDAX was in good agreement with the theoretical stoichiometry. The lattice constant, X-ray density and hopping lengths increased with increase in Ho^{3+} . The crystallite size decreased from 26.2 nm to 19.9 nm with the substitution of Ho^{3+} confirmed by TEM. The two strong IR absorption bands observed in the range 565–568 (ν_1) and 409–439 (ν_2) cm^{-1} . SEM images confirmed the porous nature with a fine-grained microstructure. TEM images revealed sphere-like nanostructures and particles with agglomeration to some extent due to their magnetic interactions. Saturation magnetization decreased while observed magneton number increased with the increase in Ho^{3+} concentration. 3,4-dihydropyrimidin-2(1H)-ones synthesized via

15

one-pot three-component condensation of aromatic aldehydes, 1,3-dicarbonyl compounds and urea/thiourea

using magnetic 10 mol % Ho^{3+} doped NiCuZn spinel ferrites catalyst.

ORIGINALITY REPORT

27%

SIMILARITY INDEX

16%

INTERNET SOURCES

23%

PUBLICATIONS

16%

STUDENT PAPERS

PRIMARY SOURCES

- 1 worldwidescience.org 3%
Internet Source
- 2 www.bioorganica.org.ua 3%
Internet Source
- 3 jocpr.com 2%
Internet Source
- 4 Sangshetti, Jaiprakash N., Firoz A. Kalam Khan, Abhishek A. Kulkarni, Rajendra H. Patil, Amol M. Pachpinde, Kishan S. Lohar, and Devanand B. Shinde. "Antileishmanial activity of novel indolyl–coumarin hybrids: Design, synthesis, biological evaluation, molecular docking study and in silico ADME prediction", *Bioorganic & Medicinal Chemistry Letters*, 2016. 2%
Publication
- 5 A. A. Birajdar, Sagar E. Shirsath, R. H. Kadam, M. L. Mane, D. R. Mane, A. R. Shitre. " Permeability and magnetic properties of Al substituted Ni Zn Fe O nanoparticles ", *Journal of Applied Physics*, 2012 1%

6

K.A. Ganure, M.M. Langade, L.A. Dhale, K.S. Lohar. "Chromium substituted nickel ferrites ($\text{NiFe}_{2-x}\text{Cr}_x\text{O}_4$, $x=0.0, 0.1, 0.2, 0.3,$ and 0.4) magnetically recoverable reusable heterogeneous nano catalysts", Materials Today: Proceedings, 2020

Publication

1%

7

Submitted to Higher Education Commission Pakistan

Student Paper

1%

8

M.V. Chaudhari, R.H. Kadam, S.B. Shelke, Sagar E. Shirsath, A.B. Kadam, D.R. Mane. "Combustion synthesis of Co^{2+} substituted $\text{Li}_{0.5}\text{Cr}_{0.5}\text{Fe}_2\text{O}_4$ nano-powder: Physical and magnetic interactions", Powder Technology, 2014

Publication

1%

9

www.science.gov

Internet Source

1%

10

Mohd Hashim, Alimuddin, Sagar E. Shirsath, Shalendra Kumar, Ravi Kumar, Aashis S. Roy, Jyoti Shah, R.K. Kotnala. "Preparation and characterization chemistry of nano-crystalline Ni–Cu–Zn ferrite", Journal of Alloys and Compounds, 2013

Publication

1%

11

Haralkar, S.J., R.H. Kadam, S.S. More, Sagar E. Shirsath, M.L. Mane, Swati Patil, and D.R. Mane. "Intrinsic magnetic, structural and resistivity properties of ferromagnetic Mn_{0.5}Zn_{0.5}Al_xFe_{2-x}O₄ nanoparticles", Materials Research Bulletin, 2012.

Publication

1%

12

Submitted to Savitribai Phule Pune University

Student Paper

1%

13

Zhiguo Song, Xiaohu Sun, Xibao Yang. " One-pot Synthesis of 5-Unsubstituted 3,4-Dihydropyrimidin-2(1H)-ones from Aldehydes, Ketones, and Urea under Solvent-free Conditions ", Polycyclic Aromatic Compounds, 2015

Publication

1%

14

Lohar, K.S., S.M. Patange, M.L. Mane, and Sagar E. Shirsath. "Cation distribution investigation and characterizations of Ni_{1-x}Cd_xFe₂O₄ nanoparticles synthesized by citrate gel process", Journal of Molecular Structure, 2013.

Publication

<1%

15

Wei-Yi Chen, Su-Dong Qin, Jian-Rong Jin. "Efficient Biginelli Reaction Catalyzed by Sulfamic Acid or Silica Sulfuric Acid under Solvent-Free Conditions", Synthetic

<1%

Communications, 2007

Publication

16

Rahul R. Nagawade, Sandeep A. Kotharkar, Devanand B. Shinde. "Titanium(IV) chloride catalyzed one-pot synthesis of 3,4-dihydropyrimidin- 2(1H)-ones and thiones", Mendeleev Communications, 2005

Publication

<1%

17

Hashem Sharghi, Mahboubeh Jokar. " Al O /MeSO H: A Novel and Recyclable Catalyst for One-Pot Synthesis of 3,4-Dihydropyrimidinones or Their Sulfur Derivatives in Biginelli Condensation ", Synthetic Communications, 2009

Publication

<1%

18

Chaudhari, M.V., Sagar E. Shirsath, A.B. Kadam, R.H. Kadam, S.B. Shelke, and D.R. Mane. "Site occupancies of Co–Mg–Cr–Fe ions and their impact on the properties of $\text{Co}_{0.5}\text{Mg}_{0.5}\text{Cr}_x\text{Fe}_{2-x}\text{O}_4$ ", Journal of Alloys and Compounds, 2013.

Publication

<1%

19

Xuesen Fan, Xinying Zhang, Yongmin Zhang. " Samarium chloride catalysed Biginelli reaction: one-pot synthesis of 3,4-dihydropyrimidin-2(1)- ones ", Journal of Chemical Research, 2002

Publication

<1%

20 Labde, B.. "Structural and infra-red studies of $\text{Ni}^{1+}\text{xPb}\text{xFe}^{2+}\text{xO}^4$ system", Materials Letters, 200303 <1%
Publication

21 Patange, S.M.. "Rietveld refinement and switching properties of Cr^{3+} substituted $\text{NiFe}^{2+}\text{xO}^4$ ferrites", Materials Letters, 20100331 <1%
Publication

22 Hojatollah Salehi, Qing-Xiang Guo. "A Facile and Efficient One-Pot Synthesis of Dihydropyrimidinones Catalyzed by Magnesium Bromide Under Solvent-Free Conditions", Synthetic Communications, 2004 <1%
Publication

23 Kadam, R.H., Kirti Desai, Supriya R. Kadam, and Sagar E. Shirsath. "Variation in the structural and magnetic properties of heterovalent $\text{Mn}^{2+}\text{-Si}^{4+}$ substituted MnCrFeO nanoparticles", Solid State Sciences, 2013. <1%
Publication

24 scholarbank.nus.edu.sg <1%
Internet Source

25 Nagawade, R.R.. "Synthesis of new series of 1-Aryl-1,4-dihydro-4-oxo-6-methyl pyridazine-3-carboxylic acid as potential antibacterial agents", European Journal of Medicinal Chemistry, 200512 <1%

26

repository.um.edu.my

Internet Source

<1%

27

Kurtan, U., R. Topkaya, A. Baykal, and M.S. Toprak. "Temperature dependent magnetic properties of CoFe₂O₄/CTAB nanocomposite synthesized by sol–gel auto-combustion technique", *Ceramics International*, 2013.

Publication

<1%

28

Behzad Zeynizadeh, Karim Akbari Dilmaghani, Mahdi Yari. "NaHSO₄·H₂O as a Heterogeneous Acidic Reagent for Mild and Convenient Synthesis of 3,4-Dihydropyrimidin-2(1H)-ones and Their Sulfur Derivatives", *Phosphorus, Sulfur, and Silicon and the Related Elements*, 2009

Publication

<1%

29

O. A. Abd Allah. "Part 1: Synthesis of Polyfused Heterocyclic Systems Derived From 3-Phenyl-5,6,7,8-tetrahydro[1,2,4]triazolo[3,4- b] [1,3,4]thiadiazepine-6,8-dione", *Phosphorus, Sulfur, and Silicon and the Related Elements*, 2002

Publication

<1%

30

A. T. RAGHAVENDER, K. M. JADHAV. "STRUCTURAL, MORPHOLOGICAL CHARACTERIZATION OF NANOPARTICLES

<1%

SYNTHESIZED BY SOL-GEL METHOD ",
International Journal of Modern Physics B, 2012

Publication

31 www.irjet.net <1%
Internet Source

32 Submitted to Glenunga International High School <1%
Student Paper

33 ijc.iaush.ac.ir <1%
Internet Source

34 K.S. Lohar, A.M. Pachpinde, M.M. Langade, R.H. Kadam, Sagar E. Shirsath. "Self-propagating high temperature synthesis, structural morphology and magnetic interactions in rare earth Ho³⁺ doped CoFe₂O₄ nanoparticles", Journal of Alloys and Compounds, 2014 <1%
Publication

35 Anant C. Nawle, Ashok V. Humbe, M.K. Babrekar, S.S. Deshmukh, K.M. Jadhav. "Deposition, characterization, magnetic and optical properties of Zn doped CuFe₂O₄ thin films", Journal of Alloys and Compounds, 2017 <1%
Publication

36 Sujatha, Ch., K. Venugopal Reddy, K. Sowri Babu, A. RamaChandra Reddy, and K.H. Rao. "Effect of sintering temperature on <1%

electromagnetic properties of NiCuZn ferrite",
Ceramics International, 2012.

Publication

37

Chaudhari, Vivek, Sagar E. Shirsath, M.L. Mane, R.H. Kadam, S.B. Shelke, and D.R. Mane. "Crystallographic, magnetic and electrical properties of Ni_{0.5}Cu_{0.25}Zn_{0.25}LaxFe_{2-x}O₄ nanoparticles fabricated by sol-gel method", Journal of Alloys and Compounds, 2013.

<1%

Publication

38

Submitted to National Institute of Technology,
Rourkela

<1%

Student Paper

39

S.M. Kabbur, U.R. Ghodake, D.Y. Nadargi, Rahul C. Kambale, S.S. Suryavanshi. "Effect of Dy³⁺ substitution on structural and magnetic properties of nanocrystalline Ni-Cu-Zn ferrites", Journal of Magnetism and Magnetic Materials, 2018

<1%

Publication

40

Abdelmadjid Debache, Wassima Ghalem, Raouf Boulcina, Ali Belfaitah, Salah Rhouati, Bertrand Carboni. "Triethylamine Promoted Efficient Synthesis of 3,4-Dihydropyrimidin- 2(1H)-ones/thiones Using a Solvent-Free Biginelli Condensation", Letters in Organic Chemistry, 2010

<1%

Publication

41 Haralkar, S.J., R.H. Kadam, S.S More, Sagar E. Shirsath, M.L. Mane, Swati Patil, and D.R. Mane. "Substitutional effect of Cr³⁺ ions on the properties of Mg-Zn ferrite nanoparticles", *Physica B Condensed Matter*, 2012. <1%
Publication

42 B. P. Ladgaonkar. "Infrared absorption spectroscopic study of Nd³⁺ substituted Zn-Mg ferrites", *Bulletin of Materials Science*, 08/2002 <1%
Publication

43 Submitted to Jawaharlal Nehru Technological University <1%
Student Paper

44 Submitted to SASTRA University <1%
Student Paper

Exclude quotes Off

Exclude matches Off

Exclude bibliography Off

Prof.(Dr.)K.S.LOHAR

Manuscript_03 (2).docx

Evaluation of Microstructure, Magnetic Properties and Catalytic Application of Co²⁺ and Cr³⁺ Doped Ni- Zn Spinel Ferrite

Abstract

Cobalt and Chromium doped nanocrystalline ferro spinels, with composition Ni_{0.5}Co_xZn_{0.5-x}Fe_{2-y}Cr_yO₄ in steps of $x = y = 0.1, 0.2, 0.3, 0.4$ and 0.5 synthesized by sol-gel auto-combustion method with glycine as a fuel, calcination temperature of samples confirmed from TGA/DSC analysis. The observed elemental analysis from EDAX is in good agreement with the theoretical composition of elements. The XRD and Rietveld analysis of XRD patterns illustrate formation of single- phase cubic spinel structure. The lattice constant decreases while the crystalline size increases with the increase in concentrations of Co²⁺ and Cr³⁺ ions substitution. The I.R. spectra shown two principle absorption bands (ν_1 and ν_2) near 600 cm⁻¹ and 400 cm⁻¹, high frequency band (ν_1) is assigned to the intrinsic lattice vibration of the tetrahedral complexes Fe³⁺-O²⁻ whereas, the lower frequency one (ν_2) is attributed to the vibration of octahedral complexes. SEM and TEM images reveal well defined nanoparticles with slight agglomeration. Calculated and observed magneton number decreased with Co²⁺ and Cr³⁺ substitution. 1, 8-dioxodecahydroacridines synthesized using magnetically separable and reusable Ni_{0.5}Co_xZn_{0.5-x}Fe_{2-y}Cr_yO₄ nanoparticles as a catalyst. The catalyst is not only efficient but also mild and easy to handle.

Keywords: Ni-Zn ferrites; XRD; Rietveld refinement; Catalyst; 1, 8-dioxodecahydroacridines; Magnetization.

Introduction

40

There is a considerable increase in interest in ferrite nanoparticles because of their wide range applicability in, sensor (Deepty et al. 2020, Pathana et al. 2019 and Zhang et al. 2017), catalysis (Fardood et al. 2017 and Kazemi et al. 2018), biomedicine (Meidanchi et al. 2020 and Mehta 2017), MRI (Umut et al. 2019), drug delivery (Nigam et al. 2020), magnetic recording (Sharma et al 2017), microwave devices (Akhtar et al. 2017) and magnetic ferro-fluids (Liu et al. 2019), etc. Spinel ferrite has a general formula [A][B₂]O₄ where each spinel

unit cell comprised of 8 formula units. It has two types of crystallographic sites (sub-lattices) occupied by the metal cations, namely; the tetrahedral A- and the octahedral B-sites (Yadav et al. 2016 and Kaykan et al. 2020). These crystallographic sites govern the electric and magnetic properties of the spinel ferrite system. Mixed metal ion ferrite systems such as Co-Zn (Huang et al. 2016), Ni-Zn (Srinivas et al. 2020), Ni-Cu-Zn (Gholizadeh et al. 2017), Ni-Co-Zn (Stergiou et al. 2017) etc. ferrites were developed. It is reported that, the substitution of trivalent ions such as Al^{3+} and Cr^{3+} or their combination for Fe^{3+} ion considerably affect the properties of parent ferrite system (Jasrotia et al. 2020, Dipesh et al. 2016, Shinde et al. 2017, Penke et al. 2020 and Lin et al. 2018).

Now a days, magnetite spinel ferrites have been tested as a catalyst in various chemical reactions, such as synthesis of pyrano pyrimidines (Khazaei et al. 2015), 1, 4-dihydropyridines (Afridi et al. 2019), benzimidazoles (Shinde et al. 2019), pyrroles (Moghaddam et al. 2015), etc. The catalytic activity is associated to the exchange of metallic ions among the sub-lattices without altering the parent structure. At the same time these catalysts are highly effective for reactions (Vader 2017). Magnetite iron oxide nanoparticles catalyst can be easily separated using an external magnetic field, which achieves a simple separation of catalyst without filtration (Yoon et al. 2007). The preparation methods were found to be of great importance for the different properties of ferrite; among them are sol-gel (Toksha et al. 2008), co-precipitation (Han et al. 2012), egg white route (Gabal et al. 2013) and hydrothermal (Zahraei et al. 2015) methods.

Acridine and its derivatives show various biological activities as anticancer (Mosurkal et al. 2006), antitumor (Michon et al. 1995), anticonvulsant (Gensika-Kowalewska et al. 2017), analgesic (Sondhi et al. 2004), hypertensive and anti-inflammatory (Gutsulyak et al. 2005), antibacterial (Gündüz et al. 2019), antimalarial (Jones et al. 2009), etc. In literature number of methods adopted for synthesis of 1,8-dioxodecahydroacridines, which involves condensation of three components, aromatic aldehydes, cyclic diketones and different nitrogen sources and various catalysts have been reported (Rafiee et al. 2013, Dabiri et al. 2008, Rashedian et al. 2010, Davoodnia et al. 2012, Shen et al. 2009 and Fan et al. 2007). These methods have some limits including low yield, requires more reaction time, multi-step synthesis, harsh reaction conditions etc.

Herein we report synthesis, structural magnetic properties of the $Ni_{0.5}Co_xZn_{0.5-x}Fe_{2-y}Cr_yO_4$, in step of $x = y = 0.1, 0.2, 0.3, 0.4$ and 0.5 , synthesised by the sol gel method and its application as magnetically separable and reusable catalyst for synthesis of 1, 8-dioxodecahydroacridines (Scheme 1).

Methods and materials

Synthesis of Ni_{0.5}Co_xZn_{0.5-x}Fe_{2-y}Cr_yO₄: Nanocrystalline Co²⁺ and Cr³⁺ substituted Ni-Zn ferrites, composition of Ni_{0.5}Co_xZn_{0.5-x}Fe_{2-y}Cr_yO₄ were synthesized by the sol-gel auto-combustion method (Shinde et al. 2017) corresponding from analytical grade reagent having purity 99%, those were Nickel nitrate [Ni(NO₃)₂·6H₂O], Cobalt nitrate [Co(NO₃)₂·6H₂O], Zinc nitrate [Zn(NO₃)₂·6H₂O], Chromium Nitrate [Cr(NO₃)₃·6H₂O], Ferric nitrate [Fe(NO₃)₃·9H₂O] and 97% Glycine [NH₂-CH₂-COOH], were used in the synthesis without any further treatment. All nitrates were dissolved in distilled water to obtain a mixed solution in desired composition. The reaction procedure was carried out in an air atmosphere without the protection of inert gases. The molar ratio of metal nitrates to glycine was 1:3. The metal nitrates were dissolved together in the minimum amount of double-distilled water required to obtain a clear solution. An aqueous solution of glycine was mixed with the metal-nitrate solution and pH \cong 7 of reaction mixture was maintained by gradually addition of the ammonia solution. The mixed solution was kept on a hot plate with constant stirring at 90°C. A viscous brown gel was formed as a result of evaporation of solution. When all of the water molecules were evaporated; the viscous gel obtained and it began to froth, after few a minute, the gel self ignited and burnt with glowing flints. The auto-combustion completed within a short time, yielding brown coloured ashes referred as the precursor.

Catalytic application: Melting points are uncorrected. ¹H-NMR spectra were recorded on Varian Gemini 300 MHz spectrometer. Chemical shifts are reported in δ units (ppm) relative to TMS as internal standard. Electron spray ionization mass spectra (ES-MS) were recorded on Water-Micro mass Quattro-II spectrometer. All the reagents used were of AR grade and were used without further purification.

General Procedure: A mixture of aromatic aldehyde **1** (1 mmol), cyclic diketone **2** (2 mmol), ammonium acetate **3** (10 mmol) and Ni_{0.5}Co_xZn_{0.5-x}Fe_{2-y}Cr_yO₄ ($x = y = 0.0$ to 0.5) (40 mol %) in 15 mL of ethanol was refluxed for appropriate time. After completion of the reaction (monitored by TLC), the catalyst removed by fixing the catalyst magnetically at the bottom of the flask with a strong magnet, then the hot reaction mixture was filtered, dried to get the crude product as a residue. The resulting products were recrystallized using ethanol to get pure products.

Characterizations: The thermal analysis of synthesized precursors was performed using TGA/DSC, Thermal analyser SDT Q 600 V20.9 Build 20, by heating precursors from room temperature to 600 °C with a heating rate 10°C per minutes in air atmosphere. The crystallographic structures were identified by X-ray powder diffraction with Cu-K α radiation ($\lambda = 1.5405\text{\AA}$) by Phillips X-ray diffractometer (Model 3710). Morphology and structure of the samples were studied on JEOL-JSM-5600 N, Scanning Electron Microscope (SEM) and on Philips (model CM 200) Transmission Electron Microscope (TEM). The elemental composition determined by Energy Dispersive X-Ray Analysis (EDAX, Inca Oxford, attached to the SEM). EDAX measurements were carried out on the same point with electrons to give the chemical composition of essentially the core of the particle. The infrared spectra of all the samples were recorded at room temperature in the range 300 to 800 cm $^{-1}$ using Perkin Elmer infrared spectrophotometer. The magnetic measurements were performed at room temperature using a commercial PARC EG&G VSM 4500 vibrating sample magnetometer.

Result and Discussion

TGA/ DSC analysis

The decomposition pattern of Co $^{2+}$ and Cr $^{3+}$ substituted Ni-Zn ferrites ($x = y = 0.0$ to 0.5) precursors are shown in Fig.1 a-f., indicate four thermal steps, at onset temperature around 200 °C, the first endothermic peak is observed due to loss of co-ordinated water molecule $\approx 0.7479\%$. The second exothermic peak locate near temperature 350 °C shown more weight loss, $\approx 1.161\%$ can be attributed to dehydration of crystalline water or chemisorbed water molecules and metals converted to metal oxides, they undergo solid state chemical reaction with formation of ferrites with liberation of oxygen molecules with mass loss $\approx 0.0821\%$ is a slightly endothermic reaction. A slight increase in mass of $\approx 0.2552\%$ above 400 °C may be associated to the exchange of Fe $^{2+} \leftrightarrow$ Fe $^{3+}$ ions, which is a slightly endothermic reaction (Langbein et al. 1991), finally above 525 °C ferro-spinel complexes are exhibited. All the precursors of series showed similar type of decomposition patterns and finally converted in to ferrites, in the temperature around 550 °C. Similar type precursor's decomposition patterns were reported by many researchers (Chitra et al. 2016 and Srivastava et al. 2009). The total weight loss is very less (around 3%) where almost all organic materials decomposed during the auto-combustion process due to higher temperature during

combustion of glycine (-3.24 kcal/g) compare to other fuels. The reaction between ammonia (released from glycine) and NO_x from the decay of metal nitrates release the higher energy (Salunkhe et al. 2012). Finally all precursors were calcinated at 550 °C for four hours to get desired nano ferro- spinels.

Elemental Analysis

EDAX was carried out to investigate and compare the theoretical and experimental elemental stoichiometry of the synthesized Ni-Zn ferrite with Co^{2+} and Cr^{3+} substitutions. EDAX of $x=y=0.3$ sample is presented in Fig. 2. The observed atomic elemental compositions from EDAX and theoretical composition (Table 1) are analogues with each other.

Structural Analysis

XRD patterns shown in Fig. 3 display peaks related to the spinel ferrites structure without any other impurity/secondary phases. The lattice constant 'a' was obtained by equation (1) (Gawas et al. 2015),

'a' observed to decrease from 8.358 Å to 8.291 Å with the Co^{2+} and Cr^{3+} ions substitution to the Ni-Zn ferrite system, and is related the ionic radii of respective ions. Replacement of larger Fe^{3+} (0.67 Å) (Shinde et al. 2017) and Zn^{2+} (0.74 Å) ions (Slatineanu et al. 2013) by smaller Co^{2+} (0.65 Å) and Cr^{3+} (0.63 Å) ions, respectively, is responsible for the variation in 'a'.

Rietveld refined XRD patterns of the Co^{2+} and Cr^{3+} substituted Ni-Zn ferrites for $\text{Ni}_{0.5}\text{Co}_x\text{Zn}_{0.5-x}\text{Fe}_{2-y}\text{Cr}_y\text{O}_4$, ($x = y = 0.1, 0.2, 0.3, 0.4$ and 0.5) are illustrated in Figs. 4(a-e). No signature of any extra peak in Rietveld refined XRD patterns is detected revealing the formation of pure cubic spinel phase having space group of Fd-3m. Table 3 gives the Rietveld refined parameters such as goodness of fit (χ^2), profile R-factor (R_p), weighted profile R-factor (R_{wp}), expected R factor (R_{exp}), and 'a'. The χ^2 is in the range of 1.13 to 1.03 which are close to 1, confirming the goodness of refinement. 'a' is also calculated from the refined patterns showing decrease from 8.3515 to 8.3204 Å with the Co^{2+} and Cr^{3+} substitution in Ni-Zn ferrites and are analogous with the values calculated by the experimental patterns as well.

The X-ray density 'd_x' was obtained through the relation;

where M = Molecular weight (MW), n = number of molecules per formula unit volume (i.e 8 in case of cubic structure), N_A = Avogadro's number = 6.02214×10^{23} and V = Volume = a^3 .

' d_x ' found to decrease with increasing Co^{2+} and Cr^{3+} content (Table 2). The increase in ' d_x ' is related to the decrease in ' a '. Furthermore, ' d_x ' decreased for $x = y = 0.5$, and could be associated to the MW of the sample surpasses the ' V ' (Å^3) (Vegard 1921).

The broadness of XRD peaks confirming the nano nature of the prepared product. The average crystallite size ' D_{XRD} ' of powder samples was obtained from the most intense (311) peak of XRD and Scherer relation (Cullity 1956),

here k = Constant factor (0.94), D = crystallite Size, λ = wavelength of incident X-rays, θ_B = Bragg's angle and β = full width of half maxima.

The observed D_{XRD} are of the order in nm and listed in Table 2, illustrates that the crystalline size increases from 26.21 nm to 32.21 nm.

Bulk density ' d_B ' was obtained through equation;

Where, d_B = Bulk density, M = Mass of the pellet, V = volume of sample = $\pi r^2 h$, r and h are the radius and thickness of pellet, respectively.

The d_B increased from 2.547 to 2.619 (g/cm^3) (Table 2).

The porosity ' P ' of all the samples was obtained by using d_B and d_x values:

As evidenced from Table 2, that the porosity increases from 51.290 ($x = 0.0$) to 52.877 ($x = y = 0.5$) with the Co^{2+} and Cr^{3+} substitution. In the present series of $\text{Ni}_{0.5}\text{Co}_x\text{Zn}_{0.5-x}\text{Fe}_{2-y}\text{Cr}_y\text{O}_4$ both the ' MW ' and the ' V ' of the unit cell decreased with Co^{2+} and Cr^{3+} substitution. However, the degree of the decrease of ' MW ' is higher compared to ' V '. Thus, the ' d_B ' decreased with Co^{2+} and Cr^{3+} substitution, this resulted in increase in porosity. Apart from this, the increment in ' P ' is mainly attributed to the increase in D_{XRD} , which increase the number of grain boundaries (Gupta et al. 1968).

Hopping lengths (L_A and L_B) among the magnetic ions in the A- and B-sites were obtained through the equation discussed elsewhere (Mane et al. 2011).

It has been observed from Table 2 that the L_A and L_B decreased with Co^{2+} and Cr^{3+} substitution. The decrease in both the hopping lengths with Co^{2+} and Cr^{3+} substitution is due to the decrease in ' a '. The magnetic cobalt and chromium ions that occupy the B-sites will cause an increase in both A–A and A–B interactions and will decrease B–B interaction. This can be accredited to the migration of Fe ions from B- to A-sites due to the insertion of both Co^{2+} and Cr^{3+} ions to the B-sites. Moreover, the increase of Co^{2+} ions in the composition due to increase of x is associated with a decrease of Zn^{2+} ions. The Cr^{3+} substitution to the Fe^{3+}

ion difference between ionic radii of the ions bringing the ions closer to each other, thus resulted in decrease in L_A and L_B (Mane et al. 2011).

Cation Distribution

In general, the cation distribution in ferrite can be estimated from the XRD patterns. The Bertaut method (Weil et al. 1950) was used to obtain the site occupancy of the A- and B-sites (Table 4). The Zn^{2+} ions favor to inhabit the A-site whereas Ni^{2+} , Co^{2+} , Cr^{3+} ions inhabited at B-site (Han et al. 2004). However, Fe^{3+} ions occupy both A- and B-sites. Co^{2+} ions occupy the A-site due to the liking for large B-site energy. The percentage of Co^{2+} and Cr^{3+} ions in B-sites increased, and percentage of Fe^{3+} ions in B-sites decreased with the substitution of Co^{2+} and Cr^{3+} ions due to their favourable crystal field effects (Han et al. 2004). The ion radii of the Cr^{3+} (0.63 Å), Zn^{2+} (0.81 Å), Co^{2+} (0.72 Å) and Fe^{3+} (0.67 Å) could also an important factor for their site occupancy (Vegard 1921).

The experimental 'a', oxygen positional parameters 'u', the relative intensities of calculated and experimental XRD peaks are given in Table 4. The mean ionic radius of the A and B-sites (r_A and r_B) was obtained through the relations given somewhere else (Patange et al. 2009). 'r_A' decreases whereas 'r_B' increases with Co^{2+} increment (Table 4). The increase in r_B is related to the higher occupancy of the B site by the smaller Co^{2+} (0.72 Å) ions that replace Zn^{2+} (0.74 Å) ions (Shinde et al. 2013)

Infrared spectroscopy

IR spectra of all the compositions shows two major principle absorption bands (ν_1 and ν_2) near 600 and 400 cm^{-1} (Fig. 5 and Table 5) which confirm the spinel structure of the prepared samples. The ν_1 -band appeared at high frequency and ν_2 -band appeared at low frequency are assigned to the intrinsic lattice vibration of the A-site complexes $Fe^{3+}-O^{2-}$ and B-site complexes, respectively (Waldron 1955). Bond lengths for A-site (R_A) and B-site (R_B) tabulated in Table 5 shows decreasing trend with the Co^{2+} and Cr^{3+} content substitution. The A- and B-site force constants K_I and K_O increases with increase in the Co^{2+} and Cr^{3+} content.

Scanning Electron Microscopy (SEM)

Typical SEM micrograph of the prepared ferrites ($x = y = 0.3$) given in Fig. 6. SEM images revealed, well-defined grains with slight agglomeration of the prepared sample and irregular wider grain size distribution. Agglomeration resulted in an enhancement in magneto crystalline anisotropy due to number of different domains aligned together by coming nearer to each other (Raghasudha et al. 2016).

7 Transmission Electron Microscopy (TEM)

TEM examination were carried out to investigate the nano-morphology and crystal-phase of the prepared product. Fig. 7a depicts the typical TEM image and their corresponding histogram (Fig. 7b) for the sample ($x = y = 0.3$).

The obtained values of particle size from TEM analysis are around 24 - 36 nm and these numbers are consistent to the XRD analysis. Spherical shaped nanoparticles with tiny thickness observed mostly. Moreover, some particles with elongated shape also observed. These particles are partially accumulated together and also appeared to stacked on each other because of magnetic nature of prepared product. Fig. 7c shows typical selected area electron diffraction (SAED) pattern of the $x=y=0.3$ sample. Polycrystalline nature of the prepared sample is confirmed by the Debye-ring pattern which are composed of superimposition of the bright spots (Cullity 1956).

Magnetization

In general, magnetic assets of spinel ferrites are delicately govern by their chemical composition, crystal structure, defects, particle size, strain/stress, cation distribution etc. (Li et al. 2015). Neel's two sub-lattice models are useful to realize the magnetic performance of the ferrite, where Neel's magnetic moment ' n_B ' can be specified by the equation (Neel 1950). The super-exchange mechanism of ferrites are intensely govern by the cation distribution at A- and B-site. As per estimated cation distribution in the present work discussed above Co and Cr ions showed a solid liking towards the B-site (Khan et al. 2015).

The magnetization increase up to certain applied magnetic field above which magnetization remains almost saturated (Fig. 8). Saturation magnetization (M_s), coercivity (H_c) and magneton number (n_B) derived from hysteresis loops and are given in Table 6.

Saturation magnetization decreases from 36.546 to 3.397 emu/g, with increase in Co^{2+} and Cr^{3+} content. Remnant magnetization (M_r) obtained from the hysteresis loop is observed to reduce with the Co^{2+} and Cr^{3+} substitution. The increases in coercivity could also be related to the higher magneto crystalline anisotropy of Co^{2+} ions as compared to the Fe^{3+} ions.

The observed n_B (the saturation magnetization per formula unit in μ_B) was obtained by hysteresis loops. The net magnetic moment ($n_B \text{Cal.}$) can be obtained by the addition of the A and B sub lattices magnetic moments, i.e., $n_B \text{Cal.} = M_B - M_A$; where, M_B and M_A are the B and A site n_B in μ_B . The $n_B \text{Cal.}$ values were obtained by site occupancy data and magnetic moments of Fe^{3+} ($5\mu_B$), Ni^{2+} ($2\mu_B$), Zn^{2+} ($0\mu_B$), Co^{2+} ($3\mu_B$) and Cr^{3+} ($3\mu_B$). Calculated and observed magneton numbers are given in Table 6. Calculated and observed magneton number decreased with Co^{2+} and Cr^{3+} substitution.

Catalytic Application

1, 8-dioxodecahydroacridines synthesised using magnetically separable and reusable $\text{Ni}_{0.5}\text{Co}_x\text{Zn}_{0.5-x}\text{Fe}_{2-y}\text{Cr}_y\text{O}_4$ nanoparticles as a catalyst (Scheme 1).

First, the compositions of $\text{Ni}_{0.5}\text{Co}_x\text{Zn}_{0.5-x}\text{Fe}_{2-y}\text{Cr}_y\text{O}_4$ ($x = y = 0.0$ to 0.5 in steps of 0.1) nanoferrites was optimized to check their catalytic efficiency. To process the model reaction in ethanol; the best composition of $\text{Ni}_{0.5}\text{Co}_x\text{Zn}_{0.5-x}\text{Fe}_{2-y}\text{Cr}_y\text{O}_4$ was used to synthesize the 1, 8-Dioxodecahydroacridine (5a) from aromatic aldehyde **1** (1 mmol), cyclic diketone **2** (2 mmol), ammonium acetate **3** (10 mmol). The **4a** compound was isolated with 84% yield in the existence of $\text{Ni}_{0.5}\text{Co}_x\text{Zn}_{0.5-x}\text{Fe}_{2-y}\text{Cr}_y\text{O}_4$ ($x = y = 0.2$) ferrite (40 mol %) in quick reaction time (80 min) compared to other ferrite compositions. Thus, $\text{Ni}_{0.5}\text{Co}_x\text{Zn}_{0.5-x}\text{Fe}_{2-y}\text{Cr}_y\text{O}_4$ ($x = y = 0.2$) was chosen as the best catalysis for further reactions.

The 40, 30 and 20 mol % quantity of $\text{Ni}_{0.5}\text{Co}_x\text{Zn}_{0.5-x}\text{Fe}_{2-y}\text{Cr}_y\text{O}_4$ ($x = y = 0.2$) as a catalyst load was finalized for the reaction (**4a**). Decrease in yield of reaction was observed as the amount of catalyst reduced from 40 mol % to 20 mol % (Table 7).

To generalize our approach, 4 aromatic aldehydes were employed with elevated conditions to get substituted 1, 8-Dioxodecahydroacridine **4(a-d)** (Scheme 1). Results tabulated in Table 8. The possible mechanism is illustrated in Scheme 2.

The catalyst recovery and reusability was analysed for model reaction (4a). In the presence of $\text{Ni}_{0.5}\text{Co}_x\text{Zn}_{0.5-x}\text{Fe}_{2-y}\text{Cr}_y\text{O}_4$ ($x = y = 0.2$) ferrite (40 mol %) as catalyst; the reaction was processed by aromatic aldehyde **1** (1 mmol), cyclic diketone **2** (2 mmol), ammonium acetate **3** (10 mmol) in ethanol. Catalyst recycling was attained by forcing the catalyst magnetically at the bottom of the flask with a strong magnet once the reaction is completed (monitored by TLC). The reaction mixture was removed from the flask once the catalyst collected at the bottom of flask. The as-obtained catalyst was washed several times by acetone. Subsequently, the fresh substrate was placed into the flask for the reaction to continue for the coming cycle. The $\text{Ni}_{0.5}\text{Co}_x\text{Zn}_{0.5-x}\text{Fe}_{2-y}\text{Cr}_y\text{O}_4$ ($x = y = 0.2$) ferrite catalyst was reusable for five times without significantly losing its catalytic activity (Cycle number and yield of **4a**: 1- 84 %; 2- 84 %; 3- 83 %; 4- 82 %; 5- 81 %). These $\text{Ni}_{0.5}\text{Co}_x\text{Zn}_{0.5-x}\text{Fe}_{2-y}\text{Cr}_y\text{O}_4$ is magnetic and thus they are easily separable by with the introduction of hard-magnet which is a major benefit for a heterogeneous catalyst.

The process of such reactions can be precisely clean. The reaction mixture was filtered, dried to get the crude product as a residue. The resulting yields were recrystallized by ethanol to obtain clean product. The $\text{Ni}_{0.5}\text{Co}_x\text{Zn}_{0.5-x}\text{Fe}_{2-y}\text{Cr}_y\text{O}_4$ ($x = y = 0.2$) catalyst is efficient, mild and easy to processed.

Conclusion

Nanocrystalline ferrites, with composition of $\text{Ni}_{0.5}\text{Co}_x\text{Zn}_{0.5-x}\text{Fe}_{2-y}\text{Cr}_y\text{O}_4$ in step of $x = y = 0.1, 0.2, 0.3, 0.4$ and 0.5 were successfully made by the sol-gel technique. The observed elemental analysis from EDAX is in good agreement with the theoretical expectations. The XRD and Rietveld XRD patterns realize the spinel structure without the presence of any impurity. The 'a' decreased from 8.3558 Å to 8.291 Å, while the crystalline size increases from 26.21 nm to 32.21 nm with the Co^{2+} and Cr^{3+} ions substitution to the Ni-Zn ferrite system. Zn^{2+} ions occupy the A sub lattice and Ni^{2+} , Co^{2+} , Cr^{3+} ions enter B sub lattice. The spectra showed two major absorption bands (ν_1 and ν_2) near 600 cm^{-1} and 400 cm^{-1} corresponding to A and B-sites, respectively. SEM and TEM images reveal well defined nanoparticles with slight agglomeration of the product having irregular grain size distribution. Calculated and observed magneton number decreased with Co^{2+} and Cr^{3+} substitution. 1,8-dioxodecahydroacridines synthesized using magnetically separable and reusable

$\text{Ni}_{0.5}\text{Co}_x\text{Zn}_{0.5-x}\text{Fe}_{2-y}\text{Cr}_y\text{O}_4$ nanoparticles as a catalyst. The $\text{Ni}_{0.5}\text{Co}_x\text{Zn}_{0.5-x}\text{Fe}_{2-y}\text{Cr}_y\text{O}_4$ ($x = y = 0.2$) catalyst is efficient, mild and easy to processed.

17%

SIMILARITY INDEX

PRIMARY SOURCES

- 1** U.M. Mandle, A.M. Pachpinde, D.R. Kulkarni, B.L. Shinde. "An efficient one pot multicomponent synthesis of pyrano pyrazoles using Cu²⁺ doped Ni-Zn nano ferrite catalyst", *Materials Today: Proceedings*, 2020
124 words — 3%
Crossref
- 2** S.K. Gurav, Sagar E. Shirsath, R.H. Kadam, D.R. Mane. "Low temperature synthesis of Li_{0.5}Zr_xCo_xFe_{2.5-2x}O₄ powder and their characterizations", *Powder Technology*, 2013
40 words — 1%
Crossref
- 3** S.J. Haralkar, R.H. Kadam, S.S More, Sagar E. Shirsath, M.L. Mane, Swati Patil, D.R. Mane. "Substitutional effect of Cr³⁺ ions on the properties of Mg-Zn ferrite nanoparticles", *Physica B: Condensed Matter*, 2012
37 words — 1%
Crossref
- 4** pubs.rsc.org
Internet
32 words — 1%
- 5** R.H. Kadam, A.P. Birajdar, Suresh T. Alone, Sagar E. Shirsath. "Fabrication of Co_{0.5}Ni_{0.5}Cr_xFe_{2-x}O₄ materials via sol-gel method and their characterizations", *Journal of Magnetism and Magnetic Materials*, 2013
32 words — 1%
Crossref
- 6** Jaiprakash N. Sangshetti, Priyanka P. Dharmadhikari, Rashmi S. Chouthi, Bibi Fatema. "Water mediated oxalic acid catalyzed one pot synthesis of 1,8-dioxodecahydroacridines", *Arabian Journal of Chemistry*, 2017
29 words — 1%
Crossref

-
- 7 worldwidescience.org 24 words — 1%
Internet
-
- 8 linknovate.com 23 words — 1%
Internet
-
- 9 K.A. Ganure, B.L. Shinde, U.M. Mandle, L.A. Dhale, R.M. Tigote, K.S. Lohar. "Synthesis, structural and magnetic properties of Ni²⁺ and In³⁺ doped cobalt ferrite and application as catalyst for synthesis of Bis-(Indolyl) methane derivatives", Materials Today: Proceedings, 2021 18 words — < 1%
Crossref
-
- 10 K.S. Lohar, A.M. Pachpinde, M.M. Langade, R.H. Kadam, Sagar E. Shirsath. "Self-propagating high temperature synthesis, structural morphology and magnetic interactions in rare earth Ho³⁺ doped CoFe₂O₄ nanoparticles", Journal of Alloys and Compounds, 2014 16 words — < 1%
Crossref
-
- 11 D. R. Mane, D. D. Birajdar, Swati Patil, Sagar E. Shirsath, R. H. Kadam. "Redistribution of cations and enhancement in magnetic properties of sol-gel synthesized Cu_{0.7-x} Co_x Zn_{0.3}Fe₂O₄ (0 ≤ x ≤ 0.5)", Journal of Sol-Gel Science and Technology, 2010 16 words — < 1%
Crossref
-
- 12 A.A. Birajdar, Sagar E. Shirsath, R.H. Kadam, S.M. Patange, K.S. Lohar, D.R. Mane, A.R. Shitre. "Role of Cr³⁺ ions on the microstructure development, and magnetic phase evolution of Ni_{0.7}Zn_{0.3}Fe₂O₄ ferrite nanoparticles", Journal of Alloys and Compounds, 2012 15 words — < 1%
Crossref
-
- 13 S.M. Patange, Sagar E. Shirsath, K.S. Lohar, S.G. Algude, S.R. Kamble, Nilesh Kulkarni, D.R. Mane, K.M. Jadhav. "Infrared spectral and elastic moduli study of NiFe_{2-x}Cr_xO₄ nanocrystalline ferrites", Journal of Magnetism and Magnetic Materials, 2013 14 words — < 1%
Crossref
-

Andris Sutka, Gundars Mezinskis. "Sol-gel auto-combustion

- 14 synthesis of spinel-type ferrite nanomaterials", *Frontiers of Materials Science*, 2012 13 words — < 1%
Crossref
-
- 15 Ali Amoozadeh, Sanaz Golian, Salman Rahmani. "TiO₂-coated magnetite nanoparticle-supported sulfonic acid as a new, efficient, magnetically separable and reusable heterogeneous solid acid catalyst for multicomponent reactions", *RSC Advances*, 2015 12 words — < 1%
Crossref
-
- 16 Santosh Bhukal, Rimi Sharma, Suman Mor, Sonal Singhal. "Mg–Co–Zn magnetic nanoferrites: Characterization and their use for remediation of textile wastewater", *Superlattices and Microstructures*, 2015 12 words — < 1%
Crossref
-
- 17 Karim, A.. "Gamma irradiation induced damage creation on the cation distribution, structural and magnetic properties in Ni-Zn ferrite", *Nuclear Inst. and Methods in Physics Research, B*, 201009 12 words — < 1%
Crossref
-
- 18 Mohd. Hashim, Alimuddin, Shalendra Kumar, Sagar E. Shirsath, R.K. Kotnala, Hanshik Chung, Ravi Kumar. "Structural properties and magnetic interactions in Ni_{0.5}Mg_{0.5}Fe_{2-x}Cr_xO₄ (0 ≤ x ≤ 1) ferrite nanoparticles", *Powder Technology*, 2012 12 words — < 1%
Crossref
-
- 19 Nastaran Shamgani, Ahmad Gholizadeh. "Structural, magnetic and elastic properties of Mn_{0.3-x}Mg_xCu_{0.2}Zn_{0.5}Fe₃O₄ nanoparticles", *Ceramics International*, 2018 12 words — < 1%
Crossref
-
- 20 K. Venkatesan, Suresh S. Pujari, Kumar V. Srinivasan. "Proline-Catalyzed Simple and Efficient Synthesis of 1,8-Dioxo-decahydroacridines in Aqueous Ethanol Medium", *Synthetic Communications*, 2008 11 words — < 1%
Crossref
-
- 21 Gabal, M.A., W.A. Bayoumy, A. Saeed, and Y.M. Al Angari.

"Structural and electromagnetic characterization of Cr-substituted Ni–Zn ferrites synthesized via Egg-white route", Journal of Molecular Structure, 2015.

Crossref

11 words — < 1%

22

D.R. Mane, Swati Patil, D.D. Birajdar, A.B. Kadam, Sagar E. Shirsath, R.H. Kadam. "Sol–gel synthesis of Cr³⁺ substituted Li_{0.5}Fe_{2.5}O₄: Cation distribution, structural and magnetic properties", Materials Chemistry and Physics, 2011

Crossref

11 words — < 1%

23

Ayeleru, Olusola Olaitan. "Development of Value-Added Materials from Municipal Plastic Solid Waste", University of Johannesburg (South Africa), 2021

ProQuest

11 words — < 1%

24

Birajdar, A.A.. "Frequency and temperature dependent electrical properties of Ni⁰."7Zn⁰."3Cr^xFe²-"xO⁴ (0@?x@?0.5)", Ceramics International, 201205

Crossref

10 words — < 1%

25

aip.scitation.org

Internet

9 words — < 1%

26

www.socialresearchfoundation.com

Internet

9 words — < 1%

27

M.V. Chaudhari, R.H. Kadam, S.B. Shelke, Sagar E. Shirsath, A.B. Kadam, D.R. Mane. "Combustion synthesis of Co²⁺ substituted Li_{0.5}Cr_{0.5}Fe₂O₄ nano-powder: Physical and magnetic interactions", Powder Technology, 2014

Crossref

9 words — < 1%

28

Vishnu S. Shinde, Vitthal Vinayak, S. P. Jadhav, N. D. Shinde, Ashok V. Humbe, K. M. Jadhav. "Structure, Morphology, Cation Distribution and Magnetic Properties of Cr³⁺-Substituted CoFe₂O₄ Nanoparticles", Journal of Superconductivity and Novel Magnetism, 2018

Crossref

9 words — < 1%

29

Sagar E. Shirsath, M. L. Mane, Yukiko Yasukawa, Xiaoxi Liu, Akimitsu Morisako. "Chemical tuning of structure

formation and combustion process in
CoDy_{0.1}Fe_{1.9}O₄ nanoparticles: influence@pH",
Journal of Nanoparticle Research, 2013

Crossref

9 words — < 1%

30 Dhanraj R. Mane. "Structural and magnetic
characterizations of MnNiZn ferrite
nanoparticles", physica status solidi (a), 07/15/2010

Crossref

9 words — < 1%

31 Zolfigol, Mohammad Ali, Neda Bahrami-Nejad, and
Saeed Baghery. "A convenient method for the
synthesis of 1,8-dioxodecahydroacridine derivatives using 1-
methylimidazolium tricyanomethanide {[HMIM]C(CN)₃} as a
nanostructured molten salt catalyst", Journal of Molecular Liquids,
2016.

Crossref

9 words — < 1%

32 prod--journal.elifesciences.org

Internet

9 words — < 1%

33 www.esciencecentral.org

Internet

9 words — < 1%

34 Hankare, P.P.. "Synthesis and characterization of
CoCr_xFe_{2-x}O₄ nanoparticles", Journal of Alloys
and Compounds, 20091019

Crossref

8 words — < 1%

35 Sandip Sadaphal, Kiran Shelke, Swapnil Sonar,
Murlidhar Shingare. "Ionic liquid promoted synthesis
of bis(indolyl) methanes", Open Chemistry, 2008

Crossref

8 words — < 1%

36 Mohd Hashim, Alimuddin, Sagar E. Shirsath,
Shalendra Kumar, Ravi Kumar, Aashis S. Roy, Jyoti
Shah, R.K. Kotnala. "Preparation and characterization chemistry of
nano-crystalline Ni-Cu-Zn ferrite", Journal of Alloys and
Compounds, 2013

Crossref

8 words — < 1%

37 iopscience.iop.org

Internet

8 words — < 1%

38 Koseoglu, Y.. "Structural and magnetic properties of $\text{Co}_x\text{Zn}_{1-x}\text{Fe}_2\text{O}_4$ nanocrystals synthesized by microwave method", Polyhedron, 20090923 8 words — < 1%
Crossref

39 Javed Iqbal, M.. "Structural, electrical and magnetic properties of Zr-Mg cobalt ferrite", Journal of Magnetism and Magnetic Materials, 200803 8 words — < 1%
Crossref

40 A.M. Pachpinde, M.M. Langade, K.S. Lohar, S.M. Patange, Sagar E. Shirsath. "Impact of larger rare earth Pr^{3+} ions on the physical properties of chemically derived $\text{Pr}_x\text{CoFe}_{2-x}\text{O}_4$ nanoparticles", Chemical Physics, 2014 8 words — < 1%
Crossref

41 Chaudhari, M.V., Sagar E. Shirsath, A.B. Kadam, R.H. Kadam, S.B. Shelke, and D.R. Mane. "Site occupancies of Co–Mg–Cr–Fe ions and their impact on the properties of $\text{Co}_{0.5}\text{Mg}_{0.5}\text{Cr}_x\text{Fe}_{2-x}\text{O}_4$ ", Journal of Alloys and Compounds, 2013. 6 words — < 1%
Crossref

EXCLUDE QUOTES OFF
EXCLUDE BIBLIOGRAPHY ON

EXCLUDE MATCHES OFF

Prof.(Dr.)K.S.LOHAR

Paper 2 FLG - Revised.docx

ABSTRACT

An accurate, precise and robust technique was developed for the impurity profiling in the Metformin Hydrochloride and Teneligliptin Hydrobromide hydrate tablet. The gradient was optimized for better separation of impurities by using BDS Hypersil C18 250 x 4.6 mm, 5 μ column operated at 35°C. The Octane sulfonic acid and Phosphate buffer with Triethylamine at pH 3.0 used as mobile phase A and pure Acetonitrile used as mobile phase B, The mobile phase was pumped at 1.0 ml/minutes. The gradient was optimized for better resolution and chromatogram was monitored at 210 nm. The % recovery from LOQ to 50%, 100% and 150% for Teneligliptin was 90.8, 98.0, 99.4, 98.9% and for Metformin HCL was 98.2, 92.8, 92.1, 92.2%. The correlation coefficient r^2 was 0.999 for Metformin HCl, Teneligliptin, Melamine, Cyanocobalamin, Teneligliptin Impurity A, and 0.998 for Teneligliptin impurity B. Hence the method was found linear from LOQ to 150%. The method was found unaffected by change in method variance, in robustness evaluation. The stress study in acid, base, oxidation, and thermal degradation proved the stability indicating nature and specificity of the method. Hence the developed method is precise, accurate, robust, and linear, can be used as organic impurity analysis in quality control laboratories.

1. INTRODUCTION

Organic impurities in the pharmaceutical dosage forms are very critical parameters which indicate the purity, safety and efficacy of the products. Development of stability indicating methods for impurity profiling from the combination dosage forms are quite challenging work. Many critical parameters like detection wavelength of impurities of each drug, detection level, and label claim of each drug in the finished products play a vital role in the method development.

Metformin Hydrochloride

Metformin Hydrochloride is an orally administered biguanide derivative used to lower the blood glucose concentration in patients with noninsulin-dependent diabetes mellitus [1]. Chemically it is 1,1-Dimethylbiguanide hydrochloride having white to off-white crystals and easily soluble in water, marginally soluble in ethanol, almost insoluble in acetone and Methylene chloride. [2 ep].

Teneligliptin Hydrobromide Hydrate

IUPAC name of Teneligliptin is (2S,4S)-4-[4-(3-Methyl-1-phenyl-1H-pyrazol-5-yl)-1-piperazinyl]-2-pyrrolidinyl(1,3-thiazolidin-3-yl)methanone hydro bromide hydrate (2:5:1) and it is off white to cream colour powder [3ip]. Teneligliptin is strong, modest and long-performing DPP-1V inhibitor. [4]. It is a Dipeptidyl peptidase-4 (DPP-4) inhibitors are newly developed as an antidiabetic which demonstrate promising results in modifying glycemic control with a minimum risk of hypoglycemia and weight gain[5]

Literature review shows that the reported methods were for assay of Metformin HCl as well as Teneligliptin individually .Some methods were reported for the Simultaneous quantitation of Metformin HCl and Teneligliptin by HPLC []. Few methods were reported for Teneligliptin assay content and Metformin HCL in individually or combination with other drugs. Individual method of related substance in Metformin Hydrochloride was reported []. No reported method was found for the related substance analysis of Metformin Hydrochloride and Teneligliptin Hydrobromide hydrate in combination dosage form. In this report, we had developed the precise, accurate and stability indicating method for organic impurities determination from Metformin Hydrochloride and Teneligliptin Hydrobromide hydrate combination dosage form.

2. METHODS AND MATERIALS

The complete development and validation was performed by using liquid chromatographic system (Make-Shimadzu, Japan) LC-2010CHT, with VU/visible detector. Intermediate precision and selectivity study was performed on Waters e 2695 with PDA detector (Model- Waters 2998). The analytical balance (Make SANSUI, VIBRA, Model-HTR-220E) and microbalance (Make-Mettler Toledo, Model-Xp6 and XP26) used for weighing process. HPLC grade Methanol and acetonitrile (Make- Rankem) was used through the development and validation. The AR grade potassium dihydrogen phosphate (Make- Rankem), Octane sulfonic acid sodium salt (Make-FINAR) and Orthophosphoric acid (Make-RANKEM) used for buffer preparation. All AR grade chemicals and Class A type of glassware's were used throughout development and validation. The calibrated pH meter (Make- Mettler Toledo, Model- Seven compact) used for pH adjustment. The separation of all the impurities was obtained on BDS Hypersil C18, 250 x 4.6 mm, 5 μ column.

Mobile phase and diluent preparation: An accurately weighted 2.72 g potassium dihydrogen phosphate and 1g of octane sulfonic acid sodium salt was transferred in 1000 ml water containing 1 ml Triethylamine. The mixture was mixed well till dissolved completely. The pH was adjusted to 3.0 and resulting buffer was filtered through 0.45 μ filter and degassed well. To filtered and degassed buffer, 10 ml of methanol was added and mixed well and was used as mobile phase A. The pure methanol was used as mobile phase B. The mixture of water and Acetonitrile in the ratio of 80:20 was used as diluent.

Optimizations of chromatographic condition: For better separation and column efficiency, BDS Hypersil C18, 250 x 4.5 mm, 5 μ column was operated at 35°C temperature. The mobile phase A and B was separately pumped with 1 ml/minutes flow rate at gradient elution mode as shown in figure3. Based on optimum response of principle analytes and known impurities, 210 nm wavelengths were selected and sample cooler was set at 15°C. All the solutions were injected at 20 μ l injection.

System suitability solution preparation

Preparation of Solution A: Accurately weighed 4 mg of each Teneiglipitin Hydrobromide Hydrate working standard and Impurity A, and impurity B was transferred in 100 ml volumetric flask, about 70 ml of diluent was added and sonicated to dissolve completely. Precise volume was prepared with diluent and which later on mixed properly.

Preparation of Solution B: Accurately weighed 5 mg of each of Metformin Hydrochloride working standard, Melamine impurity, and Cynoguanidine impurity was transferred in 50 ml volumetric flask, added about 30 ml of diluent, sonicated to dissolved completely, volume was made up to the mark with diluent and mixed properly. Furthermore, 5 ml of solution A and solution B was transferred in 100 ml volumetric flask and diluted with diluent; the solution was mixed and used as system suitability solution.

Preparation of standard solution

Accurately weighed 4 mg of teneiglipitin hydrobromide hydrate working standard was transferred in separate 100 ml volumetric flask, 70 ml of diluent in each flask was added, sonicated to dissolved completely, volume was adjusted up to the mark with diluent and mixed

properly. About 5 mg of Metformin Hydrochloride working standard was transferred in 50 ml volumetric flask, dissolved and diluted to volume with diluent. Further 5 ml of each standard stock solution was transferred in a 100 ml volumetric flask; volume was adjusted up to the mark with diluent.

Sample preparation

Not fewer than ten tablets were taken to calculate average weight and ground in to a fine powder with the help of mortar pestle. Powder pellet of 500 mg of metformin HCl was transferred in a 100 ml volumetric flask, 70 ml diluent added, the flask was sonicated for 20 min. with intermittent shaking under controlled room temperature. The flask was removed, allowed to cool at room temperature; volume was adjusted up to the volume with diluent and mixed well. The solution was centrifuge at 5000 rpm for 10 min. The supernatant liquid was filtered through 0.45 μ nylon filter by discarding minimum 3 ml of filtrate and injected in to the HPLC system.

Placebo preparation

Placebo powder was weighed equal to sample weight only by subtracting the API weight. Further procedure was carried out as per sample preparation.

System suitability criteria

For robust and stability indicating method of related substance in combination drug products, the system suitability criteria like resolution, capacity factor, signal to noise ratio, theoretical plates are very important parameter. Due to long run time and solution stability issue, the two standard solution preparations were injected and monitor the similarity factor. The limit of similarity factor was set at 95% to 105%. The resolution between each impurity and principle peak was set minimum 2 as per USP system suitability criteria. The column efficiency for each impurity and principle analytes was kept minimum 2000 theoretical plates.

Impurity calculations

All the known impurities obtained in the sample chromatogram were calculated against the respective principle analytes in the standard solution. Apart from known impurities, we find out the unknown degradants by degrading the individual API and specified with relative retention

time with respective principle analytes. These degradants were calculated against the respective principle analytes peak in standard solution during the stability study. Rests of all unknown impurities were calculated against the Teneigliptin Hydrobromide hydrate peak in standard solution, as the low label claim in the formulation dosage form.

6

Method validation plan

The developed method was validated as per ICH guideline as well as USP guideline.

Specificity (Selectivity):

Selectivity study is carried out to prove the ability of a method to assess unequivocally the analytes in the presence of components which may be expected to be present in sample.

To study the precision of the developed method, the diluent as a blank solution, placebo solution, Cyanoguanidine impurity solution, Melamine Impurity solution, Teneigliptin impurity A solution, Teneigliptin impurity B solution, Metformin HCl and Teneigliptin standard solutions were injected separately. The sample solutions and impurity spike sample solutions at specification level were prepared and injected in the HPLC system. The response of the individual analytes and peak purity was recorded by using the photo diode array detector.

4

Forced degradation study:

Forced degradation study was carried out to prove the selectivity of the method and to evaluate the stability, which indicate the nature of the method. Sample and placebo was being exposed under relevant stress conditions like heat, Acid, base and oxidation. These stressed samples were analyzed and record the chromatograms. Acid degradation in 0.5N hydrochloric acid for 15 hrs. at room temperature , while alkali degradation in 1N sodium hydroxide for 5hrs. at room temperature was evaluated. For thermal degradation the sample and placebo was kept at 60°C for 7 days study was conducted after 7 days, and 0.3% hydrogen peroxide used for oxidative stress condition. For photolytic degradation sample was allow expose for not less than 1.2 million lux h at 200 watt h/sq meter near ultraviolet energy.

LOD and LOQ Determination:

For determination of LOD and LOQ, a series of standard and known impurities was prepared over a range starting from 1% to at least 50 % of working concentration of known impurities. The seven concentration levels were selected like, 50%, 30%, 20%, 10%, 5%, 2%, 1% and injected in triplicate each level. The linearity graphs were plotted for the average area at each level against the concentration in PPM and determined the correlation coefficient, slope and intercept of analytes as well as known impurities. Derive the concentrations for limit of detection and limit of quantification from Linearity study by slope method.

Precision at LOQ Level:

To check the precision at LOQ level, the six solutions were prepared by spiking the Metformin Hydrochloride working standard and Teneiglipitin Hydrobromide hydrate as well as all the known impurities at LOQ level in the placebo. The solutions were injected in the HPLC system and calculated % relative standard deviations of all the impurities and principle analytes respectively. The % RSD of peak area and % results should not be more than 15.0 for all analytes.

Linearity and Range:

A series of mixed impurities and Metformin HCl and Teneiglipitin working standard solutions were prepared from the 150% to LOQ level. The concentration levels were selected as 150%, 120%, 100%, 80%, 50%, 20% and LOQ level of working concentration. The each concentration levels were injected in triplicate and plotted linearity graph of average area of individual analytes VS concentration in PPM at each level respectively. The correlation coefficient, slope and intercept, was calculated.

System Precision:

Metformin HCl and Teneiglipitin Hydrobromide hydrate working standard solution 1 and 2 were prepared and injected into the HPLC system. The % similarity factor was calculated and monitored as per system suitability criteria. The % similarity factor should be between 95 to 105% for both the standard.

Method Precision and intermediate precision:

For precision method; six sample solutions was prepared and injected in to the HPLC system, by identical analyst, and identical HPLC column. The percentage relative standard deviation was obtained for known impurities, individual unspecified impurity, and total impurities. The relative standard deviation of percentage of known impurities, individual unspecified impurities and total impurities of six sample preparations should not be more than 15%. Intermediate precision study was carried out by changing the analyst and HPLC system on different days. All the samples were synthesized by following method of analysis and injected in the sequence. The % known impurities, individual impurities and total impurities was calculated. The % relative standard deviation of results obtained from six samples were determined and monitored as per acceptance criteria as mentioned in precision study.

Accuracy

Recovery study was carried out by spiking the all the known impurities as well as Metformin Hydrochloride and Teneligliptin working standard from the stock solutions at LOQ level, and 50%, 100%, 150 % level in the placebo preparation. Prepared six preparations for LOQ Level and three preparations for each 50%, 100% and 150% Level and injected in the HPLC system. The % recovered amount was calculated for each known impurities and both principle analytes from the added amounts. The limit of Recovery was set at 80% to 120% for LOQ level and 85% to 115 % for 50% to 150% levels.

Stability of Analytical Solutions:

The Metformin HCl and Teneligliptin working standard solution and sample solution were prepared by spiking each impurity at specification level as per method. The solutions were store at room temperature and evaluate against freshly prepare standard on day 0, day 1, day 2 and day 3. The % of Known impurities, individual impurity and total impurities were calculated for the stored samples at particular time points and obtained results were compared with initial results or results obtained from the freshly prepared sample. The difference between the results from fresh sample preparation and results obtained from solution stability samples at particular time point should not be more than 15%.

Filter Validation (interference study):

Filter validation study conducted to prove the filter compatibility to the molecule and the impurities, because some time the analytes were adsorb on the filter paper resulting in the variation in results. To avoid the filter variation issue we had conducted the study by filtering the sample solution from various filters like Nylon filter, PVDF filter having 0.45μ porosity by discarding first 2 ml, 3 ml & 5 ml of filtrate and optimize the sample filtration study for precise and accurate results.

3

Robustness

It is the capability of the analytical method to stay unaffected a little but thoughtful change in method parameters, hence to prove the dependability of developed method during the routine use. This study was conducted by altering the critical method factors like, change in flow rate by ± 0.1 ml of initial flow, change in pH of mobile phase by ± 0.2 values, change in column temperature by $\pm 5^\circ\text{C}$, change in wavelength and change in gradient composition. The diluent, standard solution, sample solution and spike sample at specification levels were injected at each parameter and checked the robustness of analytical method.

3. RESULTS AND DISCUSSION

22

The developed method was validated as per ICH guideline. The results were summarized for individual parameters as below.

Specificity (Selectivity):

All known impurities, Principle analytes, placebo and diluent were prepared and injected in the HPLC system as per method of analysis and checked for any interference from placebo, and diluent solution. It was observed that no any interference occur at the retention time of known impurities and principle analytes. The entire peak were resolved from each other hence the developed method is specific.

Force degradation

As per ICH guideline the force degradation study was conducted in acid, Base, Thermal and Oxidative condition. During the stress study it was observed that the product was stable in acid,

thermal condition and photolytic degradation, while sensitive to oxidation and base degradation. The obtained results were reported in Table.

Method precision and Intermediate Precision

²⁴ Method precision was carried out by injecting six sample preparations and monitor similarity factor of standard 1 and standard 2, RT and RRT of all known impurities from spiked sample was determined. In intermediate precision a typical variance was evaluated include days, equipment, and analyst. The results were reported in tablet.

¹⁵ LOD and LOQ Determination:

Limit of detection and limit of Quantitation were determined by serial dilution of principle analytes from stock solution. The limit of detection for Metformin Hydrochloride was forum ... mcg/ml while for Teneligliptin..mcg/ml. The Limit of quantitation for Metformin HCl was found ... mcg/ml and for Teneligliptin was ... mcg/ml.

Linearity and Range:

Linearity was assessed for Metformin Hydrochloride, Teneligliptin, and known impurities from 150%, 120%, 100%, 80%, 50%, 20% and LOQ level of working concentration. It was found that the response under the curve for each analytes and impurities were linear to concentration and correlation coefficients (r^2) were minimum 0.998. The results were shown in the table.

Accuracy:

Recovery was performed spiking the all impurities and principle analytes in placebo from 50 100, and 150% of specification level. The recovery was established by dividing added ppm to recovered ppm and multiplying by 100. The obtained results were summarized in table.

Robustness

4

Robustness of the method was conducted by changing small, deliberate method variance and system suitability criteria were monitored. The study shows that no more variation occur and the method was unaffected by deliberate change.

CONCLUSIONS

An accurate and robust method was developed for organic impurity profiling for the combination drug products. The method was validated as per ICH guideline. The selectivity study showed that no interference was detected at the retention time of known impurities and analytes peak. In the stress testing the method found sensitive to oxidative and base degradation otherwise in acid, thermal and photolytic condition the no major degradation observed. The recovery at LOQ level, and 50 to 150% for all the analytes was between 90to 110%. The method was found linear from LOQ to 150% with correlation coefficient r^2 more than 0.980 for all the analytes. The method was unaffected even change in method parameters in robust ness study.

17%

SIMILARITY INDEX

PRIMARY SOURCES

1	ijpsr.com Internet	47 words — 2%
2	www.eijppr.com Internet	38 words — 1%
3	gnu.inflibnet.ac.in Internet	30 words — 1%
4	www.joac.info Internet	29 words — 1%
5	jddtonline.info Internet	28 words — 1%
6	austinpublishinggroup.com Internet	27 words — 1%
7	Kolte, B. L., B. B. Raut, A. A. Deo, M. A. Bagool, and D. B. Shinde. "Simultaneous Determination of Metformin in Combination with Rosiglitazone by Reversed-Phase Liquid Chromatography", Journal of Chromatographic Science, 2004. Crossref	24 words — 1%
8	Anvesha Vinit Ganorkar, Rekha S. Jibhkate, Krishna Radheshyam Gupta. "Development of Stability Indicating and Robust RP-HPLC Method for Determination of Teneligliptin", Asian Journal of Applied Chemistry Research, 2018 Crossref	24 words — 1%
9	www.ijpsr.info Internet	22 words — 1%

10	m.scirp.org Internet	22 words — 1%
11	Nuran Özaltın, Emirhan Nemutlu, Ceren Yardımcı, İncilay Süslü. "Application of Micellar Electrokinetic Capillary Chromatography for the Determination of Nifedipine and Its Degradation Product in Pharmaceutical Preparations", <i>Analytical Letters</i> , 2003 Crossref	21 words — 1%
12	www.rjpbcs.com Internet	21 words — 1%
13	jast-journal.springeropen.com Internet	18 words — 1%
14	rasayanjournal.co.in Internet	17 words — 1%
15	Reema H. Rupareliya, Hitendra S. Joshi. "Stability Indicating Simultaneous Validation of Telmisartan and Cilnidipine with Forced Degradation Behavior Study by RP-HPLC in Tablet Dosage Form", <i>ISRN Chromatography</i> , 2013 Crossref	15 words — < 1%
16	www.orientjchem.org Internet	12 words — < 1%
17	isindexing.com Internet	11 words — < 1%
18	pharmascope.org Internet	10 words — < 1%
19	comenius.susqu.edu Internet	10 words — < 1%
20	etheses.saurashtrauniversity.edu Internet	10 words — < 1%
21	www.pharmatutor.org	

10 words — < 1 %

22 mafiadoc.com
Internet

9 words — < 1 %

23 Jayakody, L.. "Studies on tuber and root starches. I. Structure and physicochemical properties of innala (Solenostemon rotundifolius) starches grown in Sri Lanka", Food Research International, 200507

9 words — < 1 %

Crossref

24 www.rasayanjournal.co.in
Internet

8 words — < 1 %

25 Pankaj N. Kulkarni, Alaknanda M. Dodake-Supekar, Charansingh H. Gill. "SIMULTANEOUS DETERMINATION OF MOMETASONE FUROATE AND BENZALKONIUM CHLORIDE-A STABILITY INDICATING METHOD", Rasayan Journal of chemistry, 2020

8 words — < 1 %

Crossref

26 Cholleti Vijay Kumar, Pavan Kumar Vasa, Y. Ravindra Kumar, Pasula Aparna, Padi Pratyusha. "Enantiomeric Separation of S-Epichlorohydrin and R-Epichlorohydrin by Capillary Gas Chromatography with FID Detector", American Journal of Analytical Chemistry, 2016

8 words — < 1 %

Crossref

27 ijcn.s.aizeonpublishers.net
Internet

8 words — < 1 %

28 Manchala, Madhuri. "Development of an Analytical Method for the Separation of Seven B-Complex Vitamins with Vitamin C by Hydrophilic Liquid Interaction Chromatography and Validation of Method for Vitamin B6", Northeastern Illinois University, 2021

8 words — < 1 %

ProQuest

29 www.hindawi.com
Internet

8 words — < 1 %

30

P. S. Gaikwad, S. G. Bhope, V. V. Kuber, M. J. Patil. 6 words — < 1%
"Validated TLC method for simultaneous quantitation
of kutkoside and picroside-I from Kutki extract", *Phytochemical
Analysis*, 2011

Crossref

EXCLUDE QUOTES OFF

EXCLUDE MATCHES OFF

EXCLUDE
BIBLIOGRAPHY ON

Prof.(Dr.)K.S.LOHAR

Paper 001 fpr plagiarism final.docx

Development and validation of stability indicating RP-HPLC method for Simultaneous determination of Xylometazoline Hydrochloride and Ipratropium Bromide from Nasal spray dosage form.

Abstract:

A simple, robust, precise and accurate HPLC technique was established for the instantaneous approximation of Xylometazoline Hydrochloride and Ipratropium Bromide from their Nasal spray dosage form. The effective separation was obtained by injecting 10 μ l of sample & standard solutions in to Inertsil ODS, 250x4.6, mm 5 μ column at 45°C, using phosphate buffer with 1- Pentane sulphonic acid sodium salt at pH 4.7 as a movable phase A and acetonitrile as movable phase B. The gradient was optimized with 1ml/min. flow rate and wavelength was set at 210 nm. The complete analytical method validation was carried out as per ICH guideline. The retrieval study was carried out at 50% to 150% level of working concentration, and results were observed 99 % to 101% for both the analyte. The Method was proven the linearity from 50 % to 150% of working concentration with linear regression curve $R^2=0.999$ for both analyte. The robustness study show that the developed method was found robust at various deliberate changes of different parameters like alteration in column temperature, flow rate, pH of mobile phase, mobile phase composition and gradient. Hence present developed technique can be used for estimation of Xylometazoline Hydrochloride and Ipratropium Bromide from Nasal spray dosage form in quality control department at commercial level.

Keywords:

RP_HPLC, Method validation, Nasal Spray, Ipratropium Bromide, Xylometazoline, Stability study.

Introduction:

Science and art of defining the mechanisms of materials in terms of the compound contained or elements is in general determined by the analytical chemistry. This techniques can be beneficial to classify the substances that can be resides in a material, as well as to obtain the precise quantity of the recognized substances. Moreover, analytical chemistry is significant in almost all the facets of chemistry, viz, pharmaceutical chemistry, clinical, forensic, agricultural, environmental, manufacturing metallurgical etc. These techniques govern a precise part to securing and upholding the quality of substance and critical components of quality assurance (QA), quality control (QC) etc. The reliability, utility, accuracy, interception and specificity of the measurement are the responsibility of an analytical chemist. Pharmaceutical investigation contains processes those are important to obtain the strength, identity, quality and purity of chemicals and drugs.[1]

1. Development of theory of analytical method in every possible way.
2. Improvement and scientific substantiation of the existing analytical methods.
3. Scientific elaboration of new analytical methods, which meet the requirements of advancing science and modern production.
4. Analysis of natural substances, environment and also industrial materials.[2]

Chromatography is an analytical technique which have range of applications for identification, separation and examination of chemical constituents in complex species. Such method is based on the separation of constituents in the solute because of the change in migration rates of the constituents via an immobile phase by a liquid or gaseous mobile phase. The term Chromatography (Greek: Khromatos – color and Graphos – written) means, “colour writing”. The beginning of Chromatography started with the work of botanist Micheal Tswett in the year 1896. The term chromatography and its principles were first discovered in 1903 by Micheal Tswett. [3]

In chromatographic separation method, sample is transferred in a mobile phase and subsequently pressed through an immiscible immobile phase that is secured in place on solid surface or in a column. Both the phases are discriminatory, thus the constituents of sample divided automatically among mobile and immobile phases. The compounds which are firmly held by the immobile phase transfer gently with mobile phase. On the other hand, compounds which are not firmly retained by the immobile phase transfer quickly, sample compounds separated to subtle bands which may be examined quantitatively and qualitatively.[4]

Nasal sprays are usable to provide medicines locally in the nasal cavities, such as allergic rhinitis and nasal congestion. It is significant to make sure they deliver the medicines correctly so as human body

to absorb that.

There are three easy steps, mentioned below to use the nasal spray in proper manner

1. One nostril should be blocked by finger
2. Keep the thumb at the bottom of the pump. The bottle hole at the top should be under the open nostril.
3. Squeeze the nasal pump gently and breathe slowly. Repeat the process for other nostril.

On the basis of literature survey, we were observed that there was not a significant technique for the simultaneous approximation of Xylometazoline hydrochloride and Ipratropium Bromide by RPHPLC from Nasal spray dosage form or any other dosage form. All the reported method was available for estimation of Xylometazoline hydrochloride or Ipratropium bromide individually or with combination with other drugs. Their fore we need to develop the stability representing RP HPLC technique for simultaneous estimation of Xylometazoline hydrochloride and Ipratropium Bromide in their combine nasal spray dosage form.

For the study we used marketed sample (Otrivin plus) for complete advancement and authentication of analytical technique.

Ipratropium Bromide:

The IUPAC name of Ipratropium bromide (IB) is (1R, 3R,5S,8R)-3-[(3-hydroxy-2-phenylpropanoyl)oxy]-8-methyl-8-(propane-2-yl)-8-azabicyclo[3.2.1]octane-8-ium bromide, and is a quaternary ammonium derivative of atropine which perform as an anticholinergic agent.¹ It is generally managed via breathing that permits creating a local effect deprived of giving a substantial systemic absorption. IB is usable to govern and avoid symptoms initiated by ingoing lung disease, that works by stimulating the muscles at the airways so as to breathe effortlessly. Further, IB is used since many decades for dealing of patient for symptomatic relief of rhinorrhea related with cold or seasonal allergic rhinitis in human beings.

Xylometazoline Hydrochloride:

The IUPAC name of Xylometazoline is 2-(4-tert-butyl-1, 2-dimethylbenzyl)-2-imidazoline, and is used for healing nasal blocking and minor swelling due to allergies or colds. Xylometazoline is a straightway performing sympathomimetic adrenergic alpha-agonist used to bring complete vasoconstriction, thus reducing nasal blocking. The sympathomimetic act of Xylometazoline squeezes the minor arterioles of the nasal channels, creating an elongated (8-12 hours) decongesting effect. This is a thru performing sympathomimetic drug, that perform on alpha-adrenergic receptors in the arterioles of the nasal mucosa. While creating vasoconstriction resulted in reduced blood flow in the nasal channels and accordingly reduced the nasal blocking

A nasal vaso-constricting decongestant medicine perform by binding to the same receptors as adrenaline, which is applicable as a nasal spray as well as liquid drops into the nose to comfort swelling and blocking of the nasal pathways. It fixes alpha-adrenergic receptors to trigger the adrenal organism that affects complete vasoconstriction, thus enabling nasal blocking.

Literature review shows that number of methods reported for the estimation of XYL, GC (5, 6), HPTLC (7), LC-MS (4), HPLC (10-11). Various ultraviolet spectrophotometric methods had been reported like derivative, fluorimetry (13). ICH guideline has been used for validation of developed method.

Some of the basic information's like physicochemical properties of both the APIs were summarized below which was the required for method development. From PKa values of analyte the pH of mobile phase were adjusted and it helps in selection of buffer in mobile phase preparation.

Materials and Methodology:

The liquid chromatographic system (Make-Shimadzu, Japan) LC-2010C_{HT}, with VU/visible detector is used for development and validation. Intermediate precision and selectivity study performed on Waters e 2695 with PDA detector (Model- Waters 2998). The HPLC grade reagent and chemicals for mobile phase preparation like Sodium di-hydrogen phosphate dihydrate (Rankem) , 1- Pentane sulphonic acid sodium salt(Merck) orthophosphoric acid (Rankem) Acetonitrile (Finar) were used for complete method development and validation study. The good separation between Xylometazoline and Ipratropium bromide were achieved by optimized chromatographic conditions on Inertsil ODS, 250 × 4.6 mm, 5µm column. The Marketed formulation Otrivin plus Nasal spray was used for complete study. Class A, type all glassware ware used for analysis and Calibrated weighing balance is used for weighing processes.

Mobile phase preparation:

Preparation of mobile phase A:

Dissolve 1.56 gm of Sodium di-hydrogen phosphate dihydrate, 0.5 gm of 1- Pentane sulphonic acid sodium salt in 1 L of deionized water. Observe the pH and Adjust to 4.7 if necessary with dilute orthophosphoric acid, filter and degas through 0.45 µ filter.

Preparation of mobile phase B:

Acetonitrile was taken as a mobile phase B.

Diluent: Water was choosing as diluent.

Preparation of working standard solutions:

Xylometazoline Hydrochloride Standard stock solution:

Weighed and transferred accurately ~50 mg of Xylometazoline Hydrochloride analytical grade into a 50 mL beaker. 30 mL of diluent was added and then sonicated to dissolve the mixture thoroughly. Dilute and then cooled to room temperature of entire mixture with diluent.

Ipratropium Bromide Standard stock solution:

Weighed and transferred accurately ~60 mg of Ipratropium Bromide analytical grade into a 50 mL beaker. 30 mL of diluent was added and then sonicated to dissolve the mixture thoroughly. Dilute and then cooled to room temperature of entire mixture with diluent.

Standard Solution:

Transferred 5 mL each of Xylometazoline Hydrochloride and Ipratropium Bromide in standard solution into a 50 mL beaker and then dilute to volume with diluent, mixed thoroughly.

Sample solution:

Transfer 2ml of Xylometazoline Hydrochloride and Ipratropium Bromide Nasal Spray (about 2 gm Sample) into a 10 ml volumetric flask. 3-4 ml of diluent was added and sonicated about 10 min. Cooled and diluted to entire volume with diluent, mix and filter through 0.45 μ PVDF pre-filter and use.

System Suitability:

Chromatograph the standard solution and peak responses was recorded for each analyte. Standard deviation of areas of five replicate standard injections was maintained $\leq 2.0\%$, the column efficiency was at ≥ 2000 theoretical plates and the tailing factor was > 2.0 for every analyte peak.

Procedure:

Separately injected same volume of the sample and standard solutions into the HPLC system, then chromatograms recorded, and measured the area under the curve (responses) for each analyte peak. Determined the amount of Xylometazoline Hydrochloride and Ipratropium Bromide in % w/v and % Assay by the following formulae.

Analytical method validation Plan:

The developed technique was authenticated in terms of accuracy, linearity, precision, specificity, and robustness and system suitability testing as per the ICH guidelines

1.0 Specificity – Selectivity:

1.1 Selectivity:

Prepared diluent, individual standard solutions for each analyte, placebo and sample as directed in analytical method and injected and recorded the observations.

Acceptance criteria:

In the placebo and diluent, interfering peak must not observed during the retention time of the both analyte peak and peak purity should pass for the analyte peak.

2. Precision :

The precision of an analytical process defines the goodness of agreement among the series of measurements acquired from many identical samples.

3.1 System precision:

Standard solution was obtained as described in analytical technique and vaccinated in six duplicates. The obtained result are given in Table 1.0.

Acceptance criteria:

% RSD of peak area of every analyte for six identical injections of standard solutions must not be greater than 2.0%.

Method Precision:

Six samples were prepared as per the above mentioned technique corresponding to a single batch.

A % assays of the samples were studied and the precision of the method was examined by calculating the % RSD of the results.

Method precision study has been performed for both the analyte, & results are illustrated in Table 2.0.

Acceptance criteria:

% RSD of the % assay result of these six solution samples for the analyte must not be greater than 2.0

Intermediate Precision (Ruggedness):

Intermediate precision expresses ability of method to produce reliable result under laboratories difference: such as different days, analysts, equipments etc.

Six samples were prepared as per the test process corresponding to a solitary batch. The % assay of these samples was examined and the ruggedness of the technique was estimated by calculating the % RSD of the results.

The precision of technique was validated through precision evaluation of a single batch containing six samples of different analyst, day, column and instruments as demonstrated in Table 2.0.

Intermediate precision study has been performed for both the analyte, results obtained (intermediate precision and overall precision) are given in Table 2.0

Acceptance criteria:

% RSD of the % assay outcome of six solution samples for the analyte must not be greater than 2.0.

% RSD of the % assay outcome of twelve solution samples for the analyte (six each of Intermediate Precision and Method Precision) must not be greater than 2.0

3. Accuracy:

The accuracy of an analytical process states the goodness of agreement among the results which is acceptable as a conventional true or reference value, and the value determined by the technique. Standard was spiked to placebo of various concentration levels i.e. 50, 100 and 150% of working concentration and analyzed according to the described technique.

% Recovery obtained at concentration levels 50%, 100% and 150% is reported in Table 3.0.

Acceptance criteria:

Mean %recovery for the analyte at each concentration level must be in the range of 98-102 %

% RSD of % recovery for the analyte at every level must not be greater than 2.0.

4. Linearity & Range:

The linearity of method was validated by synthesizing solutions mixture of the concentration levels in the range of 50-150 % of working concentration. These solutions injected in triplicate into the HPLC system and the area under the curve of analyte peak recorded.

Linearity graph of concentration Vs average peak area of analyte plotted separately.

The correlation co-efficient between concentration (ppm) & peak area slope and intercept evaluated.

The results are shown in Table 5.

5 Robustness:

Robustness of an analytical process measure the capacity to stay unaffected by minor, but considered differences in technique constraints and offers a suggestion of its dependability throughout usual practice.

In this study, Parameters like variation in detection wavelength, flow rate, column oven temperature, mobile phase organic composition and mobile phase buffer pH were studied.

The peak area, theoretical plates and tailing factor in each replicate injection recorded and reported the results.

Also calculated the % RSD of area of five identical injections of the standard solution and results are summarized in Table 5.0

6. Stability of Analytical Solution:

System suitability solution and sample solutions were prepared on day 0 of experiment, stored these solutions at temperature Room temperature for every time interval up to 3 days and analyzed these solutions on subsequent days. The standard solution was prepared freshly for the investigation and calculated the assay of analyte in the standard and sample solution solutions.

Acceptance criteria:

The cumulative % RSD for the average values of % assay of the analyte obtained in standard and sample solutions at periodic intervals should not be more than 2.0

The solution is considered stable, till the time point where the cumulative % RSD of the stored sample and standard solution for the analyte is not more than 2.0

7. Force degradation study:

To prove the stability indicating nature of the developed analytical method, the force degradation study was carried out at different stress condition like acid, base, oxidative and thermal degradation.

Acid degradation:

In a 10 ml volumetric flask, 2g of sample were transfer and 1 ml of 1N HCl was added. The sample was kept at room temperature for 24 Hrs, After 24 hrs, added about 1 ml of 1N NaOH to neutralize the sample, added 5 ml of solvent and processes the sample as directed in assay sample preparation method. The sample was filter and injected in HPLC system.

Base degradation:

In a 10 ml volumetric flask, 2g of sample were transfer and 1 ml of 1N NaOH was added. The sample was kept at room temperature for 24 Hrs, After 24 hrs, added about 1 ml of 1N HCL to neutralize the sample, added 5 ml of solvent and processes the sample as directed in assay sample preparation method. The sample was filter and injected in HPLC system.

Thermal degradation:

For thermal degradation study, the sample were kept in heating oven at 60°C and sample was analysed at 1day,3days, and 5 days interval.

Oxidative degradation:

For oxidative degradation, 30% Hydrogen peroxide was used.

In a 10 ml volumetric flask, 2g of sample were transfer and 1 ml of 30% Hydrogen peroxide was added. The sample was kept at room temperature for 24 hrs. After 24 hrs, about 5 ml of solvent was added and processed the sample as directed in assay sample preparation method. The sample was filter and injected in HPLC system.

Results and discussion:

Precision:

Precision study was done by injecting six identical injections of the standard preparation for both the analyte and checked the system suitability criteria as per method of analysis. During the precision study the % RSD of six replicate injections were observed < 2.0%.

Method Precision & Intermediate precision.

Method precision study was performed by synthesizing the six sample solution separately and was vaccinated in the HPLC system. The area under the curve of injected sample solution was calculated against the area under the standard curve in terms of % assay. The % assay values of six sample solutions were found within specification.

The intermediate precision carrying out by injecting the six replicate sample preparation form single batch sample, within laboratory variations like different analyst, days, column and instruments.

The % RSD of 12 sample preparation was calculated and found less than 2.0%. All the outcome of precision technique and intermediate precision are given below table.

Accuracy (% Recovery):

Accuracy was performed by spiking the both the analytes standard spiked in to a placebo at various concentration levels i.e. 50, 100 and 150% of working concentration and analyzed according to described technique.

% Recovery obtained at concentration levels 50%, 100% and 150% is reported in Table 3.0.

Linearity:

The linearity of method was validated by synthesizing solutions through the concentration levels ranging from 50-150% of working concentration. These solutions injected in triplicate into the HPLC system and the area under the curve of analyte peak recorded.

Linearity graph of concentration Vs average peak area of analyte plotted separately.

The correlation co-efficient among concentration (ppm) and peak area slope and intercept evaluated.

Force degradation study:

The force degradation analysis was done at various degradation parameters like, acid, base, Oxidative as well as thermal degradation. The 1N Sodium hydroxide used for base degradation, 0.5N HCL was used for acid degradation, and 30% H₂O₂ was used for oxidation degradation. The sample was exposed at 60°C for about 48 Hrs. The force degradation study showed that the method developed herein was found robust and can be used in quality control. The results are summarized as below.

Conclusion:

Herein a delicate, simple, precise, and exact RP HPLC with PDA detector and gradient elution technique was established for the simultaneous approximation of Xylometazoline Hydrochloride and Ipratropium bromide in Nasal spray dosage. The developed method was optimized for better separation. Forced degradation investigation was performed through conducting various stress conditions to measure the robustness and stability of the technique. The developed analytical technique was effectively both for the drugs and its degradation yields with upright determination and measures the active substances.

Hence, the developed technique may be used to routine examination in quality control laboratories.

9%

SIMILARITY INDEX

PRIMARY SOURCES

- 1** Suresh Shitole, Mukund Gurjar, Mahesh Shah, Srikant Pimple, Gobardhan Bal, Rahul Patel. "Development and Validation of Stability-Indicating RP-UPLC Method for Simultaneous Determination of Related Substances of S(-)Amlodipine and S(-)Metoprolol Succinate in Fixed Dose Combination Tablet Dosage Form", *Chromatography Research International*, 2014
Crossref 57 words — 2%
- 2** www.rroj.com
Internet 43 words — 1%
- 3** M. Barnes, R. Mansfield, S. Thatcher. "THE SELECTION OF AN ION PAIRING REAGENT FOR DEVELOPING AND VALIDATING A STABILITY-INDICATING HPLC METHOD FOR CROMOLYN SODIUM AND ITS KNOWN IMPURITIES", *Journal of Liquid Chromatography & Related Technologies*, 2007
Crossref 26 words — 1%
- 4** ajprd.com
Internet 25 words — 1%
- 5** www.sierrajournals.com
Internet 23 words — 1%
- 6** Batuk Dabhi, Hetal Jebaliya, Yashwantsinh Jadeja, Madhavi Patel, Anamik Shah, Denish Karia. "Fast Stability Indicating UPLC Method for Quantitative Analysis of Dronedarone in Pharmaceutical Dosage Form: Force Degradation Study", *ISRN Chromatography*, 2014 18 words — 1%

-
- 7 eurjchem.com
Internet 14 words — < 1%
-
- 8 Barot, Tushar Gopinath. "Analysis of some heterocyclic drugs by high performance liquid chromatography.", Proquest, 2015.
ProQuest 12 words — < 1%
-
- 9 baadalsg.inflibnet.ac.in
Internet 10 words — < 1%
-
- 10 Ghulam A. Shabir, W. John Lough, Shafique A. Arain, Tony K. Bradshaw. "Evaluation and Application of Best Practice in Analytical Method Validation", Journal of Liquid Chromatography & Related Technologies, 2007
Crossref 10 words — < 1%
-
- 11 www.abechem.com
Internet 10 words — < 1%
-
- 12 Rao, Mallikarjuna. "Investigation of Synthesis, Analytical Methods to Analyse Cefalosporin Raw Material (Ceftriaxone Sodium) Its Derivatives and Its Medical Importance.", Veer Bahadur Singh Purvanchal University, Jaunpur (India), 2019
ProQuest 9 words — < 1%
-
- 13 akademai.com
Internet 9 words — < 1%
-
- 14 es.scribd.com
Internet 8 words — < 1%
-
- 15 Flinders, Bryn. "The use of MALDI-MS for imaging drug disposition in respiratory disease models.", Sheffield Hallam University (United Kingdom), 2016
ProQuest 6 words — < 1%

EXCLUDE QUOTES OFF

EXCLUDE MATCHES OFF

EXCLUDE
BIBLIOGRAPHY ON

Manuscript.docx

By shireesh

Dr.R.H.KADAM

Strain mediated enhancement in magnetoelectric properties of sonochemically synthesized piezoelectric and piezomagnetic composites

S. S. Choudhari,^a S. R. Wadgane,^a S. S. Satpute,^a K. M. Batoo,^b Sagar E. Shirsath,^{c,d,*} R. H. Kadam^{a,*}

^a Physics Department, Shrikrishna Mahavidyalaya, Gunjoti, Omerga, Osmanabad 413606, India

^b King Abdullah Institute for Nanotechnology, King Saud University, P.O. Box 2455, Riyadh-11451, Saudi Arabia

^c Physics Department, Vivekanand College, Aurangabad 431001, MS, India

^d School of Materials Science and Engineering, University of New South Wales, Sydney, NSW 2052, Australia

ABSTRACT

Three dimensional nano-particles of the ME-composites having the general formula $(1-x)\text{CoCr}_{0.3}\text{Fe}_{1.7}\text{O}_4(\text{CCFO})+(x)\text{BaTiO}_3(\text{BTO})$ ($x = 0.0, 0.2, 0.4, 0.6, 0.8$ and 1.0) were obtained by comprising the piezoelectric-BTO and piezomagnetic-CCFO phases. The individual phases of CCFO and BTO were synthesized separately by ultrasonic irradiation assisted sonochemical and sol-gel routes. X-ray diffraction patterns confirmed the well-crystalline nature of both the phases. BTO and CCFO phases were under substantial strain as confirmed by the variation in lattice constants with varying proportion of BTO and CCFO. Crystallite size estimated from XRD data lies in the range 21.21 nm to 25.6 nm. Surface morphology of the powders confirmed the spherical shape of the particles with mostly uniform particle size. An EDAX spectrum confirmed the phase purity of the samples and stoichiometric concentration of elements. Magnetic properties were investigated by M-H loop measurements and dielectric properties by using RF impedance analyzer. The typical ferromagnetic behaviour observed in the composite reveals the presence of spontaneous polarization. Dielectric constant increases with the increasing percentage of BTO. The maximum value of ME coefficient (24.7 mV/cm·Oe) is observed for the 40%CCFO+60%BTO sample. The obtained results were discussed in the light of grain size, strain and the basic properties of the individual phases.

Keywords: Magneto-electric composites; Sonochemical synthesis; Strain; Magnetic properties; Dielectric properties; Magneto-electric coefficient

*Corresponding author: shirsathsagar@hotmail.com (SES), ram111612@yahoo.co.in (RHK)

INTRODUCTION:

Over the last decade, ³¹ efforts have been taken together to fabricate the group of materials consisting more than one ferroic orders such as ferromagnetic, ferroelectric, ferroelastic etc. Two or more phases having different structures and chemical compositions forms a composite material in which these phases do not react with each other [1]. Composite materials behave differently than that of the individual phases and show some superior properties which allow them for suitable applications in many technological devices [2-4]. Magnetolectric (ME) composites are the materials consists particularly the ferromagnetic and ferroelectric phases showing the unique property as ME effect which is difficult to obtain in the individual phase [5]. Strong mechanical coupling between piezomagnetic and piezoelectric phase within the composite produces magnetism through electric field, and magnetic field provokes the electric polarization in ³⁰ piezoelectric phase which is known as ME effect [6]. Due to the extensive use in various technological applications such as waveguides, switches, phase shifters, modulators etc.; ME composites still attracts the much attention as seen in the literature [7-9]. In concern with the practical use of ME composites, a strong ME coupling is essential at room temperature and hence the composites with BaTiO₃, PbTiO₃, SrTiO₃ as a piezoelectric phase and spinel ferrites with general formula MFe₂O₄ (A = Co²⁺, Mg²⁺, Zn²⁺, Cu²⁺, Ni²⁺ etc.) as a piezomagnetic phase have been studied widely [10-13].

²⁹ Better ME effect can be achieved by choosing the better combination of ferrite and ferroelectric phases having high piezomagnetic and piezoelectric coefficients. Magnetic and ¹⁴ electrical properties of ferrites are sensitive to the amount and type of constituent ions in the composition [14]. Cobalt ferrite which possesses inverse spinel structure have been widely used in various applications viz. phase shifters, isolators, memory cores, circulators etc. because of their low losses of eddy currents and high curie temperature [15,16]. CoFe₂O₄ is a popular choice as a piezomagnetic phase for the composite since it possess excellent magnetic

properties including high saturation magnetization, coercivity and remnant magnetization [17-19]. Notably, CoFe_2O_4 is highly magnetostrictive originated from its first order positive magnetocrystalline anisotropy and thus a perfect partner piezomagnetic candidate for ME composite. Literature reports suggests that partial substitution of Cr ions for Co enhance the magnetocrystalline anisotropy of CoFe_2O_4 [20,21]. This motivated us to use $\text{CoCr}_{0.3}\text{Fe}_{1.7}\text{O}_4$ as a piezomagnetic phase. On the other hand, BaTiO_3 was taken as a piezoelectric phase since it possess large dielectric constant, piezoelectricity and electrical resistivity ($\sim 10^9 \Omega \text{ cm}$)

The ME effect in the composites is greatly affected by ¹⁸ the grain size of the composites. The decreasing percentage of ferrite phase decreases ³³ the mean free path of electrons which in turn decreases the electrical conductivity and enhances the dielectric and ME properties of the composites [22]. Hence smaller grains in the composites are most acceptable in order to get the enhanced dielectric and ME properties [23]. Thus, in the present work CCFO phase was prepared by the sonochemical approach using ultrasonic irradiation, since this approach validated to be a timesaving to produce high-purity materials with nanoscale dimension in a accomplished way. Further, ultrasonication based sonochemical approach offers higher rate of chemical reaction, minimum waste production as well as it conserves energy [24-26].

Thus, the prepared products were composed in the form of $(1-x)\text{CoCr}_{0.3}\text{Fe}_{1.7}\text{O}_4 + (x)\text{BaTiO}_3$ (¹ $x = 0.0, 0.2, 0.4, 0.6, 0.8$ and 1.0) to investigate the structural, magnetic, dielectric and magnetoelectric properties.

MATERIALS AND METHODS:

Ultrasonic irradiation assisted sonochemical and sol-gel routes were employed to produce the pure phases of piezomagnetic ($\text{CoCr}_{0.3}\text{Fe}_{1.7}\text{O}_4$) and piezoelectric (BaTiO_3) materials. Piezomagnetic $\text{CoCr}_{0.3}\text{Fe}_{1.7}\text{O}_4$ nanoparticles were obtained by taking the AR grade $\text{Co}(\text{NO}_3)_2 \cdot 6\text{H}_2\text{O}$, $\text{Cr}(\text{NO}_3)_3 \cdot 9\text{H}_2\text{O}$ and $\text{Fe}(\text{NO}_3)_3 \cdot 9\text{H}_2\text{O}$ with their weight proportion diluted in

sufficient amount of di-ionized water. pH of the mixture was adjusted by adding the liquid ammonia. The entire solution exposed to high-intensity ultrasonic irradiation (frequency: 20 kHz and power: 70 W) for 120 min. The temperature of the solution was 90 °C during the ultrasonication process because of very high number of collisions. The synthesized product was washed several times with DI water. Finally the $\text{CoCr}_{0.3}\text{Fe}_{1.7}\text{O}_4$ powder was segregated from the liquid with outside simple magnet and dried at 100 °C for 12 h.

BaTiO_3 was prepared by sol-gel method. Titanium butoxide $\text{Ti}(\text{OC}_4\text{H}_9)_4$ was diluted in ethanol whereas barium acetate ($\text{Ba}(\text{OOCCH}_3)_2$) were dissolved in acetic acid. These solutions were stirred separately for 1 h and then mixed together. This mixed solution was stirred continuously at 100 °C till the formation of dried powder. Thus, obtained powder was ground and heat treated at 800 °C for 2 h.

The CCFO-BTO composite material was obtained by mixing the CCFO and BTO nanopowders with their weight proportion of 80-20, 60-40, 40-60 and 20-80 in percentage respectively. The mixed composites were grinded for 2-3 hours thoroughly and finally sintered at 800 °C for 6 h. By using hydraulic press, the composite powders were compressed into pellets with 1.5 to 2.5 mm thicknesses. Phase identification and structural parameters were studied by using powder X-ray diffraction patterns recorded at room temperature by using $\text{Cu-K}\alpha$ radiation ($\lambda=1.5405 \times 10^{-10}\text{m}$). Surface morphology and microstructures of the composites were investigated from scanning electron micrographs (SEM, JEOL JSM-6300) attached with energy dispersive X-ray spectroscopy (EDX). Magnetic measurements were carried by applying the magnetic field 20000 Oe at room temperature. Dielectric measurements as a function of applied frequency were taken out on a Hioki 3532-50 LCR HITESTER in the frequency range 50Hz to 50MHz. Samples were taken in the form of cylindrical pellets and placed between two electric probes to measure the dielectric properties. Dynamic method was used to measure the magneto-electric coefficient of composite samples. The measurement was

carried out by superimposing the sinusoidal magnetic field (H_{AC}) produced by Helmholtz's coils with D. C. bias magnetic field (H_{DC}) produced by electrically poled with applied electrified of 1.5 kv/cm at 200 °C for 1 h. The output ME voltage of the sample was measured as a function of bias magnetic field (H_{DC}) from 0 Oe to 8000 Oe in steps of 500 Oe with sinusoidal magnetic field ($H_{AC} = 5$ Oe, $f = 1$ kHz).

11 RESULTS AND DISCUSSION:

Figure 1 illustrates the powder X-ray diffraction patterns of all the samples of (1-x)CoCr_{0.3}Fe_{1.7}O₄+(x)BaTiO₃ (x = 0.0, 0.2, 0.4, 0.6, 0.8 and 1.0), which clearly reveals the existence of piezomagnetic and piezoelectric phases in the composites. Well distinct peaks appeared in the XRD pattern related to piezomagnetic phase are indexed by the miller indices (220), (311), (400), (422), (333), (440) and (533) corresponding to the cubic spinel structure. These XRD peaks were indexed to the Co-Cr ferrites and is confirmed by JCPDS data card no. 22-1086. The peaks indexed for piezoelectric phase confirms the perovskite structure of BaTiO₃ with space group P4mm (JCPDS card no. 05-0626) [27, 28]. It can be seen that the XRD peak intensity of CCFO planes decreased whereas BTO peaks increased with the increase in BTO percentage. Right panel in Figure 1 showed the enlarged picture of the most intensified (110) plane of BTO and (311) plane of CCFO phases. The (110) peak of BTO shifts towards higher 2θ, whereas (311) peak of CCFO shifts towards lower 2θ with the increasing percentage of BTO phase, indicating change in lattice constant of both the phases. Thus, the lattice constant (a) of CCFO and BTO phases were obtained by using the relation:

$$a = d\sqrt{h^2 + k^2 + l^2} \quad (1)$$

7 where d is the lattice spacing between the planes and (h k l) are the Miller indices. Figure 2 (left panel) shows that the calculated lattice constant of CCFO phase increased 8.3839 to 8.3864 Å, whereas lattice constant of BTO phase decreased from 4.007 Å to 3.976 Å with the

increasing percentage of BTO phase. Crystallite size (t_{XRD}) of all the samples was obtained by the Debye-Scherrer equation [29]:

$$t_{XRD} = \frac{0.9\lambda}{\beta \cos \theta} \quad (2)$$

where λ is a wavelength of incident X-ray beam and β is the full-width at half maximum intensity. Figure 2 (right panel) shows that crystallite size initially increased from 20.1 ($x = 0.0$) to 25.6 ($x = 0.6$) nm and decreased thereafter to 21.2 nm for $x = 1.0$. Variation in crystallite size and lattice parameters could be related to the; i) chemical interaction between the CCFO and BTO phases during the preparation of composite, and/or ii) strain induced by CCFO and BTO phases on each other. Williamson-Hall analysis was carried out to investigate the strain mechanism in all the composite samples using the relation [30]:

$$\varepsilon = \frac{10}{4 \tan \theta} \quad (3a)$$

The resultant broadening of the peak is a sum of broadenings due to crystallite size (β_D) and strain (β_ε):

$$\beta = \beta_\varepsilon + \beta_D \quad (3b)$$

using equations (2), (3a) and (3b):

$$\beta = 4\varepsilon \tan \theta + \frac{0.9\lambda}{D \cos \theta} \quad (3c)$$

Eq. 3c can be rearranged in following manner:

$$\beta \cos \theta = 4\varepsilon \sin \theta + \frac{0.9\lambda}{D} \quad (3d)$$

$4 \sin \theta$ versus $\beta \cos \theta$ was drawn to obtain the strain (ε) in the samples (Fig. 3). Inset of Fig. 3 shows the strain values obtained from the slope of fitted line. The tensile strain in CCFO phase increased from 1.06×10^{-4} ($x = 0.2$) to 7.89×10^{-4} ($x = 0.8$) with the increase in BTO phase. On the other hand, increase in CCFO phase composition induced the compressive strain in BTO from -2.5×10^{-4} ($x = 0.8$) to -1.7×10^{-3} ($x = 0.2$). Strain induced on the CCFO and BTO phases are consistent with their variation in lattice constant. Thus, increase in tensile strain

resulted in increment of lattice constant in CCFO phase with the increase in BTO phase. This is in contrast to the BTO phases where increase in compressive strain reduced the lattice constant.

Scanning electron micrographs obtained from the scattered secondary electrons for the various compositions of piezomagnetic-CCFO and piezoelectric-BTO phases (Fig. 4). The average grain size (D) initially increased from 38 (x = 0.0) to 60 nm (x = 0.8) and decreased thereafter to 54 nm for x = 1.0 (Fig. 2). The variation in grain size is true to the variation in crystallite size determined using the XRD data. The observed increase in grain size can be correlated with the strain. In the present work, CCFO and BTO both are polycrystalline in nature, where strain energy depends on different grain sizes and crystal orientation [31]. CCFO should possess strong anisotropy, which can introduce elastic strain energy inhomogeneously in the system which would promote abnormal grain growth. Further, CCFO is under tensile strain and this strain released on the expense of increased grain size. The asymmetry observed in the grain size may be due to the difference in crystallite sizes of the individual phases and their distribution within the composite and also the chemical homogeneity of the composition [32]. The stoichiometry percentage of elements in the composite was analyzed by using EDAX pattern for the typical sample (40)CCFO+(60)BTO (Fig. 5). Color mapping of elements (Fig. 5) confirmed the uniform distribution of elements in the sample. The analysis of EDAX pattern indicates that no loss of any constituent element is observed in the composite after sintering the sample. The observed percentage of the elements from EDAX spectra are in good agreement with their weight percentage in the composition.

FTIR spectra of CCFO-BTO composites measured in the wavenumber range of 400 - 4000 cm^{-1} are shown in Fig. 6. The strong absorption band appear around 870 cm^{-1} may be ascribed to the tetragonal structure of the BTO phase [33]. The FT-IR spectrum showed absorption bands in 1100-1300 cm^{-1} wavenumber range are related to NO_3^- ions, bands

appeared at 1400-1700 cm^{-1} are related to the carboxyl group (COO^-), vibration at 2400 cm^{-1} is related to C–O group and absorption band appeared around 3400 cm^{-1} is related to the hydrogen bonded O–H groups [34]. The absorption bands appeared around 425 cm^{-1} and 570-600 cm^{-1} were allocated to the bending vibrations of metal ions at octahedral – B and tetrahedral – A sites respectively, which is a characteristic feature of spinel ferrites.

Magneto-electric properties:

Magnetic hysteresis loops of composites with the weight percentage of CCFO and BTO phases are displayed in Fig. 7a. Hysteresis loops are showed ‘S’-type shape with saturation behavior. High coercivity was observed for all the samples. The values of coercivity (H_c), remnant magnetization (M_r) and saturation magnetization (M_s) were extracted from these loops. Figure 7b shows the variation of M_s , M_r and H_c with the variation of weight percentage of CCFO and BTO. Since the magnetic properties are only the characteristics of piezomagnetic-CCFO phase of the composite, saturation magnetization goes on decreasing from 45.53 ($x = 0.0$) to 2.371 emu/g ($x = 0.8$) with the decreasing percentage of CCFO. Apparently, remnant magnetization also decreased from 21.8 ($x = 0.0$) to 2.371 emu/g ($x = 0.8$) with the increase in BTO phase. The decreasing behaviour of M_s and M_r may be due to the dilution of ferromagnetic phase with the introduction of BTO in the composites. Similar trend in magnetic properties was also noticed in the literature reports [2, 9,13]. Interestingly, coercivity initially increased from 637 ($x = 0.0$) to 668 Oe ($x = 0.4$) and decreased thereafter with further increase in BTO phase. The variation in coercivity can be ascribed to the i) crystallite/grain size and ii) strain effects. Relation between coercivity and grain size can be interpreted through the random anisotropy model [36]:

$$Hc = \begin{cases} \rho \times \frac{K_u^4}{A^3 M_s} \times D^6 & \dots \dots \dots D < L_{ex} & 4 a \\ \rho \times \frac{K_u}{M_s} & \dots \dots \dots D \cong L_{ex} & 4 b \\ \rho \times \frac{\sqrt{AK_u}}{M_s} \times \frac{1}{D} & \dots \dots \dots D > \delta & 4 c \end{cases} \quad (4)$$

where ρ is a dimensionless quantity associated with the crystal structure, L_{ex} referred to the magnetic exchange length, δ referred to the width of domain wall, A is exchange stiffness constant and K_u is magnetocrystalline anisotropy constant. For $D < L_{ex}$, the Hc originating from the grain boundaries, and thus it is inversely proportional to the grain size. Hc follows a D^6 power law if magnetic exchange length, $L_{ex} = (A/K_1)^{1/2}$, is larger than the grain size [37] (eq. 4a). Hc is not grain size dependent for $D \cong L_{ex}$ (eq. 4b). Hc follow the grain size for $D > \delta$, as $\sim D^{-1}$. Thus, our experimental data is in good agreement with eq. 4c where Hc is directly proportional to grain size, where enhancement in anisotropy energy as a result of increase in particle size gave rise to higher Hc [38, 39]. It has also been widely reported that strain affect the variation in coercivity in ferrite materials [40-42]. It is observed that the CCFO is under tensile strain that progressively increased with BTO composition, resulted in increase in coercivity up to certain level.

The electric field (E) dependent variation in polarization (P) (P - E hysteresis loop) was studied to investigate the ferroelectric properties of $(1-x)\text{CoCr}_{0.3}\text{Fe}_{1.7}\text{O}_4 + (x)\text{BaTiO}_3$ composites samples at room temperature (Fig. 8). Pure BTO ($x = 1$) exhibit the typical PE hysteresis loop confirming its ferroelectricity, though the PE loop was not attained saturation. PE loop of CCFO is very leaky and not showed any ferroelectric characteristics. Maximum polarization (P_{max}) and remnant polarization (P_r) of composite increased with the increase in BTO composition which may related to the electromechanical coupling, polarizability and strain [43]. Ferroelectric properties of composites were diluted with higher piezomagnetic-CCFO phase.

22

Maxwell-Wagner type interfacial polarization induced dispersion was obtained in the dielectric plots of $(1-x)\text{CoCr}_{0.3}\text{Fe}_{1.7}\text{O}_4+(x)\text{BaTiO}_3$ composites. The results are well-supported by the Koop's phenomenological theory [44-46]. Frequency dependent variation in dielectric constant (ϵ') is presented in Fig. 9a. ϵ' exhibited maximum value at lower frequency which decreased rapidly with increments in frequency and almost unchanged at higher frequency region. Piezoelectric-BTO shows maximum ϵ' in contrast to the piezomagnetic-CCFO. This is consistent with the electrical properties of BTO and CCFO, where BTO possess higher resistivity ($\sim 10^9 \Omega\cdot\text{m}$) compared to CCFO ($\sim 10^7 \Omega\cdot\text{m}$). The heterogeneity at the CCFO-BTO interface could promote the space charge polarization, where space charges offered from the piezomagnetic-CCFO may stimulate to the CCFO and BTO interface (i.e. grain boundaries). This may be because of the different permittivities and resistivities values of two distinct materials [47,48]. This may lead to increment in the space charge polarization with electric field. Hence, relatively higher dielectric constant was observed in composite materials compared to the average dielectric constant of BTO and CCFO. Strong strain coupling in BaTiO_3 -based ferroelectrics is also known to lead the enhancement in the ferroelectric polarization [49, 50]. Thus, increment in ϵ' and P may also be related to the strain induced in CCFO, and BTO in particular [51]. Further, in BTO polar metal phase can be stabilized under compressive strain [52].

21

The frequency dependent variation in dielectric loss tangent ($\tan\delta$) is presented in Fig. 9b. The frequency dependent variation in $\tan\delta$ is analogues with the variation of ϵ' . Pure BTO exhibited the lowest $\tan\delta$ among all the investigated composite specimens, whereas CCFO exhibit the highest dielectric loss. The difference in dielectric loss between BTO and CCFO is related to the leakage current and resistivity. BTO has lower leakage current and high resistivity in contrast to the CCFO. A maxima is observed in the $\tan\delta$ plots, which is related to the relation:

$$\omega\tau = 1 \quad (5)$$

where τ is the relaxation time and $\omega = 2\pi f_{\max}$. Here, τ and the hopping frequency per unit time expressed as:

$$\tau = \frac{1}{2p} \quad (6)$$

Therefore the frequency of ac electric field is directly proportional to the polarization; $f_{\max} \propto p$, when the hopping frequency of electrons between $\text{Fe}^{2+} \leftrightarrow \text{Fe}^{3+}$ ions became same. Maxima in the $\tan\delta$ plots are only observed for the CCFO content and is absent in BTO content due its higher resistivity.

Dynamic method was used to measure the magnetolectric coefficient, α_{ME} , of the composite samples by using the expression [48]:

$$\alpha_{\text{ME}} = \frac{V}{H_{\text{AC}}d} \quad (7)$$

where H_{AC} , V and d are the amplitude of sinusoidal magnetic field, voltage generated due to magnetolectric effect and thickness, respectively. As dc and ac magnetic fields are superimposed over each other giving resultant field by the relation [48]:

$$H = H_{\text{DC}} + H_{\text{AC}} \sin \omega t,$$

Frequency, f ($\omega = 2\pi f$), tuned by a lock-in amplifier measure the output ME voltage [53]:

$$V \propto (\alpha + \beta H_0)h_0 = \alpha^*(H_0) \cdot h_0$$

here β is quadratic- and α is linear-coefficient of ME coupling and $\alpha^*(H_0)$ is the pseudo-linear coefficient. The obtained α_{ME} for the composite samples with dc magnetic field is presented in Fig. 10. Initially, α_{ME} increased with the increase in H_{DC} and attained a maxima. Further increase in H_{DC} decrease the value of α_{ME} . The observed behavior of α_{ME} is related to the magnetostrictive property of piezomagnetic-CCFO phase. Magnetostriction of CCFO phase increased and attained saturation with the increase in dc magnetic field [54]. Magnetization in piezomagnetic-CCFO governed by the magnetic domain and domain size which are influenced

by the strain state of piezomagnetic-CCFO. Thus, tensile-strained CCFO may require a higher H_{DC} to attain the saturation. The ¹⁹ strain induced in piezomagnetic-CCFO phase with the application of magnetic field transmitted to piezoelectric BTO phase. This would generate the ⁴ electric field in the piezoelectric BTO that produce ME voltage in the sample, which is external magnetic field dependent. (40)CCFO+(60)BTO at $H_{DC} = 1500$ Oe exhibited the maximum ME coupling coefficient, $\alpha_{ME} = 24.7$ mV/cm·Oe, among all the composite samples. (60)CCFO+(40)BTO composite sample also show comparable ME coupling coefficient of $\alpha_{ME} = 24.1$ mV/cm·Oe. The lower value of α_{ME} is associated with the higher piezomagnetic-CCFO composition since it possess lower resistivity and higher leakage current compared to piezoelectric-BTO phase.

CONCLUSIONS:

Piezomagnetic ($\text{CoCr}_{0.3}\text{Fe}_{1.7}\text{O}_4$) and piezoelectric (BaTiO_3) phases were composite in the form of $\text{CoCr}_{0.3}\text{Fe}_{1.7}\text{O}_4 + (x)\text{BaTiO}_3$ to investigate the magneto-electric properties. XRD pattern revealed that lattice constants of $\text{CoCr}_{0.3}\text{Fe}_{1.7}\text{O}_4$ increased, whereas it decreased for BaTiO_3 as a result of tensile strain in $\text{CoCr}_{0.3}\text{Fe}_{1.7}\text{O}_4$ and compressive strain in BaTiO_3 . XRD and FTIR data confirmed the presence of formation of $\text{CoCr}_{0.3}\text{Fe}_{1.7}\text{O}_4$ and BaTiO_3 phase without any signature of impurity or secondary phases. Magnetization decreased whereas polarization increased of the composite samples with the increase BTO phase. A considerably high magneto-electric coupling coefficient of $\alpha_{ME} = 24.7$ mV/cm·Oe was observed in (40)CCFO+(60)BTO composite sample at a applied magnetic field of $H_{DC} = 1500$ Oe. The observed variation in magnetic, dielectric, ferroelectric and magneto-electric properties were strongly co-related to the variation in grain size and strain induced in the composite samples.

Acknowledgement

Author K. M. Batoo is thankful to the Researchers Supporting Project (RSP-2019/148) at King Saud University for their financial support.

References:

- [1] L. S. Ashwini, R. Sridhar, S. S. Bellad; Dielectric and magnetoelectric properties of Li-Mg ferrite: Barium titanate composites; *Mater. Chem. Phys.* 200 (2017) 136-145.
- [2] A. S. Dzunuzovic; M. M. Vijatovic Petrovic, J. D. Bobic, N. I. Ilic, M. Ivanov, R. Grigalaitis, J. Banys, B. D. Stonjanovic; magneto-electric properties of $x\text{Ni}_{0.7}\text{Zn}_{0.3}\text{Fe}_2\text{O}_4$ -(1-x) BaTiO_3 multiferroic composites; *Ceram. Inter.* 44 (2018) 683-694.
- [3] S. E. Shirsath, C. Cazorla, T. Lu, L. Zhang, Y. Y. Tay, X. Lou, Y. Liu, S. Li, D. Wang, Interface-charge induced giant electrocaloric effect in lead free ferroelectric thin-film bilayers, *Nano Letters* 20 (2020) 1262-1271
- [4] S. Archary, O. Jayakumar, A. Tyagi, *Functional Materials* 159 Elsevier Insights, USA, 2012.
- [5] S. L. Kadam, C. M. Kanamadi, K. K. Patankar, B. K. Chougule; Dielectric behaviour and magnetoelectric effect in $\text{Ni}_{0.5}\text{Co}_{0.5}\text{Fe}_2\text{O}_4+\text{Ba}_{0.8}\text{Pb}_{0.2}\text{TiO}_3$ ME composites; *Mater. Lett.* 59 (2005) 215-219.
- [6] U. Salazar – Kuri, J. O. Estevez, N. R. Silva-Gonzalez, U. Pal, M. E. Mendoza; Structure and magnetic properties of the $\text{Co}_{1-x}\text{Ni}_x\text{Fe}_2\text{O}_4$ – BaTiO_3 core shell nanoparticles, *J. Magn. Magn. Mater.* 442 (2017) 247-254.
- [7] S. A. Khader, A. Parveez, A. Chaudhuri, M. S. Shekhwat, T. Sankarappa; Structural, dielectric and magnetic studies of ferrite-ferroelectric composites; *Physica B: Phys. Cond. Matter.* 584 (2020) 411665.
- [8] K. K. Patankar, V. L. Mathe, R. N. Patil, B. K. Chougule; Structural analysis, magnetic properties and magnetoelectric effect in piezomagnetic – piezoelectric composites; *Mater. Chem. Phys.* 96 (2006) 197-200.
- [9] S. R. Wadgane, S. T. Alone, A. Karim, G. Vats, S. E. Shirsath, R. H. Kadam, Magnetic field induced polarization and magnetoelectric effect in $\text{Na}_{0.5}\text{Bi}_{0.5}\text{TiO}_3$ - $\text{Co}_{0.75}\text{Zn}_{0.25}\text{Cr}_{0.2}\text{Fe}_{1.8}\text{O}_4$ multiferroic composite, *J. Magn. Magn. Mater.* 47 (2019) 388-393
- [10] C.T.M. Dung, N.H.T. Thi, K.H.T. Ta, V.C. Tran, B.T. Le Nguyen, Relaxor behaviors in $x\text{BaTiO}_3$ –(1-x) CoFe_2O_4 materials, *J. Magn.* 20 (2015) 353–359.
- [11] T. Woldu, B. Raneesh, M.R. Reddy, N. Kalarikkal, Grain size dependent magnetoelectric coupling of BaTiO_3 nanoparticles, *RSC Adv.* 6 (2016) 7886–7892.
- [12] A. Singh, I. Choudhary, S. Mehta, S. Dahiya, C.S. Walia, K. Raina, R. Chatterjee, Optimal multiferroic properties and enhanced magnetoelectric coupling in SmFeO_3 - PbTiO_3 solid solutions, *J. Appl. Phys.* 107 (2010) 084106.
- [13] A. S. Gaikwad, R. H. Kadam, S. E. Shirsath, S. R. Wadgane, J. Shah, R. K. Kotnala, A. B. Kadam; Surprisingly high magneto-electric coupling in cubic $\text{Co}_{0.7}\text{Fe}_{2.3}\text{O}_4$ - SrTiO_3 nano-composites; *J. Alloys. Comp.* 773 (2019) 564-570.
- [14] G. R. Gajula, L. R. Buddiga, K. N. C. Kumar, N. Vattikunta, M. Dasari; Effect of Gd and Nb on dielectric and magnetic transition temperature of BaTiO_3 - $\text{Li}_{0.5}\text{Fe}_{2.5}\text{O}_4$ composites; *Physica B: Cond. Matter.* 560 (2019) 1-5.

- [15] S. E. Shirsath, X. Liu, M.H.N. Assadi, A. Younis, Y. Yasukawa, S. K. Karan, J. Zhang, J. Kim, D. Wang, A. Morisako, Y. Yamauchi, S. Li, Au quantum-dots engineered room temperature crystallization and magnetic anisotropy in CoFe_2O_4 thin film, *Nanoscale Horizons*, 4, (2019) 434-444
- [16] S. E. Shirsath, X. Liu, Y. Yasukawa, S. Li, A. Morisako, Switching of magnetic easy-axis using crystal orientation for large perpendicular coercivity in CoFe_2O_4 thin film, *Scientific Reports*, 6, 30074; doi: 10.1038/srep30074 (2016)
- [17] R. N. Bhowmik, M. C. Aswathi; Modified dielectric and ferroelectric properties in the composite of ferrimagnetic $\text{Co}_{1.75}\text{Fe}_{1.25}\text{O}_4$ ferrite and ferroelectric BaTiO_3 perovskite in comparison to $\text{Co}_{1.75}\text{Fe}_{1.25}\text{O}_4$ ferrite; *Comp. Part B*; 160 (2019) 457-470.
- [18] S. M. Mane, P. M. Trimali, B. Ranjit, M. Khan, N. Khan, A. N. Tarale, S. B. Kulkarni; Studies on magnetocapacitance, dielectric, ferroelectric and magnetic properties of microwave sintered $(1-x)(\text{Ba}_{0.8}\text{Sr}_{0.2}\text{TiO}_3)-x(\text{Co}_{0.9}\text{Ni}_{0.1}\text{Fe}_2\text{O}_4)$ multiferroic composite; *Solid State Sci.* 81 (2018) 43-50.
- [19] R. Sharma, P. Pahuja, R. P. Tandon; Structural, dielectric, ferromagnetic, ferroelectric and ac conductivity studies of the $\text{BaTiO}_3\text{-CoFe}_{1.8}\text{Zn}_{0.2}\text{O}_4$ multiferroic particulate composite; *Ceram. Inter.* 40 (2014) 9027-9036.
- [20] B. G. Toksha, S. E. Shirsath, M. L. Mane, S. M. Patange, S. S. Jadhav, K. M. Jadhav, Auto-combustion high-temperature synthesis, structural and magnetic properties of $\text{CoCr}_x\text{Fe}_{2-x}\text{O}_4$ ($0 \leq x \leq 1.0$), *J. Phys. Chem. C*, 115 (2011) 20905-20912
- [21] Y. Melikhov, J. E. Snyder, C. C. H. Lo, P. N. Matlage, S. H. Song, K. W. Dennis, D. C. Jiles, The Effect of Cr-Substitution on the magnetic anisotropy and its temperature dependence in Cr-substituted cobalt ferrite, *IEEE Trans. Magn.* 42 (2006) 2861
- [22] G. N. Chavan, P. B. Belavi, L. R. Naik, B. K. Bammannavar, K. P. Ramesh, Electrical behavior of $(y)\text{Cd}_{1-x}\text{Ni}_x\text{Fe}_2\text{O}_4(1-y)\text{BaZr}_{0.2}\text{Ti}_{0.8}\text{O}_3$ composites, *Int. J. Sci. Eng. Res.* 5 (2014) 1171-1177.
- [23] D. Cao, X. Wang, L. Pan, H. Li, P. Jing, J. Wang, Q. Liu, Nonmetal sulfur-doped coral-like cobalt ferrite nanoparticles with enhanced magnetic properties, *J. Mater. Chem. C* 4 (2016) 951e957.
- [24] M.A. Almessiere, Y. Slimani, A.D. Korkmaz, N. Taskhandi, M. Sertkol, A. Baykal, S. E. Shirsath, İ. Ercan, B. Özçelik, Sonochemical synthesis of Eu^{3+} substituted CoFe_2O_4 nanoparticles and their structural, optical and magnetic properties, *Ultrason. Sonochem.* 58 (2019) 104621
- [25] Y. Slimania, M.A. Almessiere, M. Sertkol, S. E. Shirsath, A. Baykal, M. Nawaz, S. Akhtar, B. Ozcelik, I. Ercan, Structural, magnetic, optical properties and cation distribution of nanosized $\text{Ni}_{0.3}\text{Cu}_{0.3}\text{Zn}_{0.4}\text{Tm}_x\text{Fe}_{2-x}\text{O}_4$ ($0.0 \leq x \leq 0.10$) spinel ferrites synthesized by ultrasound irradiation, *Ultrason. Sonochem.* 57 (2019) 203-211
- [26] R.S. Yadav, I. Kuřitka, J. Vilcakova, J. Havlica, L. Kalina, P. Urbánek, M. Machovsky, D. Skoda, M. Masař, M. Holec, Sonochemical synthesis of Gd^{3+} doped CoFe_2O_4 spinel ferrite nanoparticles and its physical properties, *Ultrason. Sonochem.* 40 (2018) 773–783.
- [27] R.P. Mahajan, K.K. Patankar, M.B. Kothale, S.C. Choudhari, V.L. Mathe, S.A. Patil, Magnetoelectric effect in cobalt ferrite – barium titanate composites and their electrical properties; *Pramana J. Phys.* 58 (5) (6) (2002) 1115.
- [28] S. L. Kadam, K. K. Patankar, V. L. Mathe, M. B. Kothale, R. B. Kale, B. K. Chougule; Electrical properties and magnetoelectric effect in $\text{Ni}_{0.75}\text{Co}_{0.25}\text{Fe}_2\text{O}_4+\text{Ba}_{0.8}\text{Pb}_{0.2}\text{TiO}_3$ composites; *Mater. Chem. Phys.* 78 (2003) 684.

- [29] R. H. Kadam, A. R. Biradar, M. L. Mane, S. E. Shirsath, Sol-gel auto-combustion synthesis of $\text{Li}_{3x}\text{MnFe}_{2-x}\text{O}_4$ and their characterizations, *J. Appl. Phys.* 112 (2012) 043902
- [30] W.H. Hall, X-ray line broadening from field aluminium and wolfram; *Acta Metall.* 1 (1953) 22.
- [31] M. Murakami, T.-S. Kuan and I. A. Blech: Mechanical Properties of Thin Films on Substrates in *TREATISE ON MATERIALS SCIENCE AND TECHNOLOGY*, ed. by K. N. Tu and R. Rosenberg, (Academic press, New York, 1982).
- [32] R. K. Kotnala, J. Shah, B. Singh, H. Kishan, S. Singh, S. K. Dhawan, A. Sengupta, Humidity response of Li-substituted magnesium ferrite, *Sens. Actuators B Chem.* 129 (2008) 909e914.
- [33] A. Mishra, Niyati Mishra, Influence of copper doping on physical properties of barium titanate, *J. Phys. Conf.* 365 (4) (2012) 012009.
- [34] Mohd. Hashim, Alimuddin, S. Kumar, S. E. Shirsath, R. K. Kotnala, J. Shah, R. Kumar, Synthesis and characterization of Ni^{2+} substituted cobalt ferrite nanoparticles; *Mater. Chem. Phys.* 139 (2013) 364-374
- [35] P. A. Jadhav, M. B. Shelar, B. K. Chaugule; Magnetoelectric effect in three phase $y(\text{Ni}_{0.5}\text{Cu}_{0.2}\text{Zn}_{0.3}\text{Fe}_2\text{O}_4)+(1-y)(50\%\text{BaTiO}_3+50\%\text{PZT})$ ME composites; *J. Alloys Compd.* 479 (2009) 385.
- [36] R. Alben, J. J. Becker, M.C. Chi; Random anisotropy in amorphous ferromagnets; *J. Appl. Phys.* 49 (1978) 1653
- [37] G. Herzer, Grain size dependence of coercivity and permeability in nanocrystalline ferromagnets; *IEEE Trans. Magn.*, 26 (1990) 1397.
- [38] R. S. Yadav, I. Kuřitka, J. Vilcakova, J. Havlica, J. Masilko, L. Kalina, J. Tkacz, J. Švec, V. Enev and M. Hajdúchová; Impact of grain size and structural changes on magnetic, dielectric, electrical, impedance and modulus spectroscopic characteristics of CoFe_2O_4 nanoparticles synthesized by honey mediated sol-gel combustion method; *Adv. Nat. Sci.: Nanosci. Nanotechnol.* 8 (2017) 045002
- [39] S. E. Shirsath, S. S. Jadhav, B. G. Toksha, S. M. Patange, K. M. Jadhav, Influence of Ce^{4+} ions on the structural and magnetic properties of NiFe_2O_4 ; *J. Appl. Phys.* 110, (2011) 013914
- [40] B. H. Liu and J. Ding; Strain-induced high coercivity in CoFe_2O_4 powders; *Appl. Phys. Lett.* 88 (2006) 042506.
- [41] S. E. Shirsath, X. Liu, Y. Yasukawa, S. Li, A. Morisako, Stitching of magnetic easy-axis using crystal orientation for large perpendicular coercivity in CoFe_2O_4 thin film; *Sci. Rep.* 6 (2016) 30074; doi: 10.1038/srep30074 (2016)
- [42] A.S. Ponce, E.F. Chagas, R.J. Prado, C.H.M. Fernandes, A.J. Terezo, E. Baggio-Saitovitch, High coercivity induced by mechanical milling in cobalt ferrite powders, *J. Magn. Mater.* 344 (2013) 182–187
- [43] A. S. Fawzi, A. D. Sheikh, V. L. Mathe; Dielectric, electrical and magnetoelectric characterization of $(x)\text{Ni}_{0.8}\text{Zn}_{0.2}\text{Fe}_2\text{O}_4+(1-x)\text{Pb}_{0.93}\text{La}_{0.07}(\text{Zr}_{0.60}\text{Ti}_{0.40})\text{O}_3$ composites; *Mater. Res. Bull.* 45 (2010) 1000.
- [44] J. C. Maxwell, *Electricity Magnetism Vol.1*, Oxford Uni. Press, Oxford, 1954. Section 328.
- [45] K.W. Wagner; The distribution of relaxation times in typical dielectrics; *Ann. Phys.* 40 (1973) 817.

- [46] C.G. Koop; On the dispersion of resistivity and dielectric constant of some semiconductors at audiofrequencies; *Phys. Rev.* 83 (1951) 121.
- [47] R. Valenzuela, *Magnetic ceramics*, (Cambridge University Press, 1994).
- [48] A. S. Gaikwad, S. E. Shirsath, S. R. Wadgane, R. H. Kadam, J. Shah, Magneto-electric coupling and improved dielectric constant of BaTiO₃ and Fe-rich (Co_{0.7}Fe_{2.3}O₄) ferrite nano-composites; *J. Magn. Mater.* 465 (2018) 508-541.
- [49] K. J. Choi, M. Biegalski, Y. L. Li, A. Sharan, J. Schubert, R. Uecker, P. Reiche, Y. B. Chen, X. Q. Pan, V. Gopalan, L. Q. Chen, D. G. Schlom, C. B. Eom, Enhancement of ferroelectricity in strained BaTiO₃ thin films; *Science* 306, 1005 (2004).
- [50] D. G. Schlom, L.-Q. Chen, C.-B. Eom, K. M. Rabe, S. K. Streiffer, and J.-M. Triscone; Strain tuning of ferroelectric thin films; *Annu. Rev. Mater. Sci.* 37, 589 (2007).
- [51] S. Zhu, M. Yang, X. Gu, P. Zhou, C. Zhong, Strain-induced structural phase transition and the rotation of polarization in BaTiO₃ films, *Comp. Mater. Sci.* 181 (2020) 109713
- [52] C. Ma, K. Jin, C. Ge, G. Yang, Strain-engineering stabilization of BaTiO₃-based polar metals, *Phys. Rev. B* 97 (2018) 115103
- [53] J. P. Rivera, The linear magnetoelectric effect in LiCoPO₄ revisited; *Ferroelectrics* 161 (1994) 147.
- [54] S. V. Suryanarayana; Magnetolectric interaction phenomena in materials; *Bull. Mater. Sci.* 17 (1994) 1259.

Fig. 1: (Left) XRD patterns of (a) CCFO, (b) (80)CCFO + (20)BTO, (c) (60)CCFO + (40)BTO, (d) (40)CCFO + (60)BTO, (e) (20)CCFO + (80)BTO and (f) BTO. Here, # and * denotes CCFO-ferromagnetic and BTO-ferroelectric phases respectively. (Right) Expanded view of XRD patterns of all the studied samples to demonstrate the change in 2θ positions of most intense peaks of BTO (110) and CCFO (311).

Fig. 2: (Left panel) variation in lattice constants of piezomagnetic and piezoelectric phases. (Right panel) variation in crystallite size t_{XRD} obtained from XRD and grain size D obtained from SEM. Here, (A) CCFO, (B) (80)CCFO + (20)BTO, (C) (60)CCFO + (40)BTO, (D) (40)CCFO + (60)BTO, (E) (20)CCFO + (80)BTO and (F) BTO.

Fig. 3: W-H plots of piezomagnetic-CCFO and piezoelectric-BTO phases in $(x)CoCr_{0.3}Fe_{1.7}O_4+(1-x)BaTiO_3$ composites

Fig. 4: SEM micrographs of $(x)CoCr_{0.3}Fe_{1.7}O_4+(1-x)BaTiO_3$ where (a) CCFO (b) (80)CCFO + (20)BTO (c) (60)CCFO + (40)BTO (d) (40)CCFO + (60)BTO, (e) (20)CCFO + (80)BTO and (f) BTO

Fig. 5: Elemental composition analysis where (a) is EDAX pattern and (b) color mapping images of elements presented in (40)CCFO+(60)BTO composite sample.

Fig. 6: FTIR spectra of $(x)CoCr_{0.3}Fe_{1.7}O_4+(1-x)BaTiO_3$ where, (a) (80)CCFO + (20)BTO (b) (60)CCFO + (40)BTO (c) (40)CCFO + (60)BTO and (d) (20)CCFO + (80)BTO. *Left panel shows the full FTIR spectra whereas right panel shows the expanded view of low wavelength region FTIR spectra.*

Fig. 7: Magnetic properties of $(x)CoCr_{0.3}Fe_{1.7}O_4+(1-x)BaTiO_3$, (a) variation magnetization (M) with applied magnetic field (H), (b) variation in saturation magnetization (M_s), remnant magnetization (M_r), coercivity (H_c) with composition and (c) shows the expanded view of M-H loops at lower magnetic field.

Fig. 8: Variation in polarization (P) with applied electric field (E) measured at a frequency of 10 Hz for $(1-x)CoCr_{0.3}Fe_{1.7}O_4+(x)BaTiO_3$ composites

Fig. 9: (a) variation of dielectric constant (ϵ') with frequency and (b) variation in dielectric loss tangent ($\tan \delta$) with frequency of all the samples of $(x)CoCr_{0.3}Fe_{1.7}O_4+(1-x)BaTiO_3$ composites

Fig. 10: Variation of magnetoelectric coupling coefficient (α_{ME}) with applied magnetic field of $(x)CoCr_{0.3}Fe_{1.7}O_4+(1-x)BaTiO_3$ composites

11%

SIMILARITY INDEX

PRIMARY SOURCES

- 1** link.springer.com Internet 39 words — 1%
Crossref
- 2** Anil S. Gaikwad, R.H. Kadam, Sagar E. Shirsath, Santosh R. Wadgane, Jyoti Shah, R.K. Kotnala, A.B. Kadam. "Surprisingly high magneto-electric coupling in cubic $\text{Co}_{0.7}\text{Fe}_{2.3}\text{O}_4\text{-SrTiO}_3$ nano-composites", Journal of Alloys and Compounds, 2019
Crossref 36 words — 1%
- 3** aip.scitation.org Internet 35 words — 1%
- 4** Anil S. Gaikwad, Sagar E. Shirsath, Santosh R. Wadgane, R.H. Kadam, Jyoti Shah, R.K. Kotnala, A.B. Kadam. "Magneto-electric coupling and improved dielectric constant of BaTiO_3 and Fe-rich ($\text{Co}_{0.7}\text{Fe}_{2.3}\text{O}_4$) ferrite nano-composites", Journal of Magnetism and Magnetic Materials, 2018
Crossref 29 words — 1%
- 5** Sabih Qamar, Majid Niaz Akhtar, Waqas Aleem, Zia ur Rehman et al. "Corrigendum to "Graphene anchored Ce doped spinel ferrites for practical and technological applications" [Ceram. Int. 46 (2020) 7081–7088]", Ceramics International, 2020
Crossref 21 words — 1%
- 6** www.mdpi.com Internet 19 words — < 1%
- 7** Jitu Das, Vijayanand S. Moholkar, Sankar Chakma. "Structural, magnetic and optical properties of sonochemically synthesized Zr-ferrite nanoparticles", Powder 17 words — < 1%

-
- 8 Badoo, Khalid Mujasam, Dina Salah, Gagan Kumar, Arun Kumar, Mahavir Singh, M. Abd El-sadek, Feroz Ahmad Mir, Ahamad Imran, and Daler Adil Jameel. "Hyperfine interaction and tuning of magnetic anisotropy of Cu doped CoFe₂O₄ ferrite nanoparticles", Journal of Magnetism and Magnetic Materials, 2016. 17 words — < 1%
Crossref
-
- 9 jcpr.kbs-lab.co.kr 13 words — < 1%
Internet
-
- 10 A.B. Kadam, Vishwanth K. Mande, S.B. Kadam, R.H. Kadam, Sagar E. Shirsath, Rameshwar B. Borade. "Influence of gadolinium (Gd³⁺) ion substitution on structural, magnetic and electrical properties of cobalt ferrites", Journal of Alloys and Compounds, 2020 13 words — < 1%
Crossref
-
- 11 SANTOSH S. JADHAV, SAGAR E. SHIRSATH, B. G. TOKSHA, S. M. PATANGE, S. J. SHUKLA, K. M. JADHAV. " STRUCTURAL PROPERTIES AND CATION DISTRIBUTION OF – NANOFERRITES ", International Journal of Modern Physics B, 2012 13 words — < 1%
Crossref
-
- 12 Lohar, K.S., S.M. Patange, M.L. Mane, and Sagar E. Shirsath. "Cation distribution investigation and characterizations of Ni_{1-x}Cd_xFe₂O₄ nanoparticles synthesized by citrate gel process", Journal of Molecular Structure, 2013. 13 words — < 1%
Crossref
-
- 13 ethesis.nitrkl.ac.in 10 words — < 1%
Internet
-
- 14 Karimi, S., P. Kameli, H. Ahmadvand, and H. Salamati. "Effects of Zn-Cr-substitution on the Structural and Magnetic Properties of Ni_{1-x}Zn_xFe_{2-x}Cr_xO₄ Ferrites", Ceramics International, 2016. 10 words — < 1%
Crossref

-
- 15 livrepository.liverpool.ac.uk 9 words — < 1%
Internet
-
- 16 iopscience.iop.org 9 words — < 1%
Internet
-
- 17 www.socialresearchfoundation.com 9 words — < 1%
Internet
-
- 18 baadalsg.inflibnet.ac.in 9 words — < 1%
Internet
-
- 19 Kothale, M.. "Dielectric behaviour and magnetolectric effect in copper-cobalt ferrite+barium lead titanate composites", Materials Chemistry & Physics, 20030130 8 words — < 1%
Crossref
-
- 20 publikace.k.utb.cz 8 words — < 1%
Internet
-
- 21 Mehmet Kuru, Tuğba Şaşmaz Kuru, Ertuğrul Karaca, Sadık Bağcı. "Dielectric, magnetic and humidity properties of Mg–Zn–Cr ferrites", Journal of Alloys and Compounds, 2020 8 words — < 1%
Crossref
-
- 22 Sagar M. Mane, Sachin A. Pawar, Dipali S. Patil, Shrinivas B. Kulkarni, Nishant T. Tayade, Jae Cheol Shin. "Magnetolectric, magnetodielectric effect and dielectric, magnetic properties of microwave-sintered lead-free $x(\text{Co}_{0.9}\text{Ni}_{0.1}\text{Fe}_2\text{O}_4)-(1-x)[0.5(\text{Ba}_{0.7}\text{Ca}_{0.3}\text{TiO}_3)-0.5(\text{BaZr}_{0.2}\text{Ti}_{0.8}\text{O}_3)]$ particulate multiferroic composite", Ceramics International, 2020 8 words — < 1%
Crossref
-
- 23 Akshay B. Ghumare, Maheshkumar L. Mane, Sagar E. Shirsath, K. S. Lohar. "Role of pH and Sintering Temperature on the Properties of Tetragonal–Cubic Phases Composed Copper Ferrite Nanoparticles", Journal of Inorganic and Organometallic Polymers and Materials, 2018 8 words — < 1%

24 Zeng, Q.. "Soft ferromagnetism in nanostructured mechanical alloying FeCo-based powders", Journal of Magnetism and Magnetic Materials, 200711

Crossref

8 words — < 1%

25 Bhukal, Santosh, Sandeep Bansal, and Sonal Singhal. "Structural, Electrical and Magnetic Properties of Ni Doped Co-Zn Nanoferrites and their Application in Photo-Catalytic Degradation of Methyl Orange Dye", Solid State Phenomena, 2015.

Crossref

8 words — < 1%

26 Fawzi, A.S.. "Multiferroic properties of Ni ferritePLZT composites", Physica B: Physics of Condensed Matter, 20100101

Crossref

8 words — < 1%

27 www.tandfonline.com

Internet

8 words — < 1%

28 A.S. Dzunuzovic, M.M. Vijatovic Petrovic, J.D. Bobic, N.I. Ilic, M. Ivanov, R. Grigalaitis, J. Banyš, B.D. Stojanovic. "Magneto-electric properties of $x\text{Ni}_{0.7}\text{Zn}_{0.3}\text{Fe}_2\text{O}_4 - (1-x)\text{BaTiO}_3$ multiferroic composites", Ceramics International, 2018

Crossref

8 words — < 1%

29 Saha, S.K., Md. D. Rahaman, M.A. Zubair, and A.K.M. Akther Hossain. "Structural, electrical, magnetic and magnetoelectric properties of $(1-y)[\text{Ba}_{0.6-x}\text{Ca}_x\text{Sr}_{0.4}\text{Zr}_{0.25}\text{Ti}_{0.75}\text{O}_3] + (y)[(\text{Li}_{0.5}\text{Fe}_{0.5})_{0.4}\text{Ni}_{0.18}\text{Cu}_{0.12}\text{Zn}_{0.3}\text{Fe}_2\text{O}_4]$ composites", Journal of Alloys and Compounds, 2017.

Crossref

8 words — < 1%

30 Fawzi, A.S.. "Effect of magnetostrictive phase on structural, dielectric and electrical properties of $\text{NiFe}_2\text{O}_4 + \text{Pb}^{0.9}\text{La}^{0.07}(\text{Zr}^{0.6}\text{Ti}^{0.4})\text{O}_3$ composites", Solid State Sciences, 200911

Crossref

8 words — < 1%

31 Sushma Lather, Anjali Gupta, Jasvir Dalal, Vivek Verma, Rahul Tripathi, Anil Ohlan. "Effect of mechanical milling on structural, dielectric and magnetic properties of BaTiO₃-Ni_{0.5}Co_{0.5}Fe₂O₄ multiferroic nanocomposites", *Ceramics International*, 2017

8 words — < 1%

Crossref

32 A. V. Polotai, A. V. Ragulya, T. V. Tomila, C. A. Randall. "The XRD and IR Study of the Barium Titanate Nano-Powder Obtained Via Oxalate Route", *Ferroelectrics*, 2004

7 words — < 1%

Crossref

33 Pradeep Chavan, L.R. Naik, P.B. Belavi, Geeta Chavan, V.T. Muttannavar, B.K. Bammannavar, R.K. Kotnala. "Temperature Dependent Electric Properties and Magnetolectric Effects in Ferroelectric rich Ni_{0.8}Mg_{0.2}Fe₂O₄ + BaZr_{0.2}Ti_{0.8}O₃ Magnetolectric Composites", *Journal of Alloys and Compounds*, 2019

7 words — < 1%

Crossref

EXCLUDE QUOTES OFF
EXCLUDE BIBLIOGRAPHY ON

EXCLUDE MATCHES OFF

Revised Paper - 01 (todkar).doc

By Todkar

Dr.R.H.KADAM

Phase evaluation, magnetic and microwave absorbing properties of rare earth Ce-Dy doped M-type barium hexaferrite nanoparticles.

G. B. Todkar^a, R. A. Kunale^b, R. N. Kamble^c, K. M. Batoo^d, S. E. Shirsath^{e,f*}, R. H. Kadam^{a*}

^aMaterials Science research laboratory, Shrikrishhna Mahavidyalaya, Gunjoti, Tq. Omerga, Dist. Osmanabad (M.S.) India – 413606

^bPhysics Department, Kai. Rasika Mahavidyalaya, Deoni, Dist. Latur, (M.S.) India

^cDepartment of Physics, University of Mumbai, Mumbai (M.S.) India

^dKing Abdullah Institute for Nanotechnology, King Saud University, P.O. Box. 2455, Riyadh-1145, Saudi Arabia.

^eDepartment of Physics, Vivekanand College, Aurangabad, 431001, M.S. India

^fSchool of Materials Science and Engineering, University of New South Wales, Sydney, NSW 2052, Australia.

ABSTRACT

M-type barium hexaferrites (BFO) with the substitution of rare earth Ce-Dy ions have been successfully fabricated by sol-gel auto-ignition method. The structural, phase evaluation, micro-strain, morphological analysis, magnetic behaviour, microwave absorbing properties and optical properties were studied by employing the XRD, SEM, TEM, FTIR, VSM, VNA and U-V visible spectra. The refined structural parameters of Ce-Dy doped BFO hexaferrites were evaluated by using Rietveld refinement. The phase identification performed by using Rietveld refinement shows presence of single phase hexaferrite for pure BFO and presence of secondary phases, cubic CeO₂ and ortho DyFeO₃ for $x \geq 0.25$. Crystallite size obtained from W-H plots increases from 27.05 nm to 30.75 nm with an introduction of Ce-Dy ions in BFO-hexaferrites. Nanocrystalline nature of the samples was confirmed by using SEM and TEM micrographs. Fourier transform infrared spectra of all the samples were recorded in the wave number range of 400cm⁻¹ to 4000cm⁻¹. Optical studies were carried out by using UV-vis spectrophotometer. The band gap values lies in the range of 1.3725 to 1.5188 eV. Magnetic properties were investigated by using vibrating sample magnetometer for the applied magnetic field of 1000 Oe. The microwave properties were investigated by using vector network analyzer. Variation of reflection loss with sample thickness, frequency and substitution of Ce-Dy has been studied. 3mm thickness sample with high substitution $x=0.75$ were possess maximum band width of 0.7017 GHz with reflection loss -15.9273dB at Ku frequency band of 12.8648 GHz. Two-probe technique was employed to study the dielectric behaviour of the samples.

Keywords: Rietveld refinement, W-H analysis, microwave absorption, optical properties, dielectric properties.

*Corresponding Authors: shirsathsagar@hotmail.com (SES), ram111612@yahoo.co.in (RHK)

INTRODUCTION:

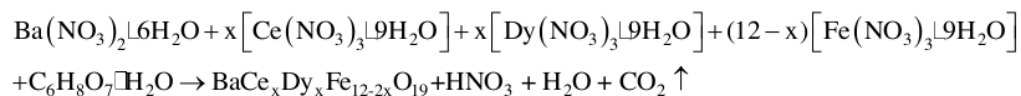
M-type barium hexaferrite have application in microwave devices, micro strip antennas, radar, memory core etc. They are widely investigated due to its unique properties like excellent chemical stability, high electrical resistivity; high coercivity, high Curie temperature and low production cost compared to other rare earth compounds [1-4]. The structure of hexaferrite is more complex compared with the other ferrites. It has magnetoplumbite crystal structure with 64 ions per unit cell. Among the 64 ions the unit cell contains 38 numbers of oxygen ions, two barium ions and 24 Fe^{3+} ions. The 24 Fe^{3+} ions distributed over five distinct sites i.e. 12k, 2a, 4f₂ octahedral site, 4f₁ tetrahedral and 2b trigonal pyramidal site [5-7]. The various iron sites and relative orientation of their spin moments are responsible for magnetism. Fe^{3+} ions at 2a, 2b, and 12k sites (a total of 16 Fe^{3+} ion) possess spin up while at 4f₁ and 4f₂ (a total of 8 Fe^{3+} ion) possess spin down. 8 spin down will cancel with 16 spin up and 8 spin up remain after cancellation with spin down. According to the electronic configuration of Fe^{3+} there are 5 unpaired electrons in the 3d orbital, each Fe^{3+} ion has magnetic momenta of $5\mu_B$ and the total magnetic moment per unit cell is $8 \times 5 = 40\mu_B$. Hence other cation substitution at Fe^{3+} site plays important role in changing magnetic properties of hexaferrite.

The magnetic properties viz. saturation magnetization, coercivity and retentivity of hexagonal ferrite can be modified by the substitution of Fe^{3+} with other ions for example Topkaya et. al. [8] found that substitution of yttrium cation improves coercivity and Chen et. al. [9] discovered a decrease in saturation magnetization as aluminium cation substitution increases. The lattice parameter, coercivity, saturation magnetization and magneton number these properties were controlled by preparation methods, sintering temperature and amount of doping at Ba and Fe site. The study of literature review suggest that there are various methods used for synthesis of hexaferrite like hydrothermal process [9], solid state reaction [10], sol gel method [11, 12], microwave adsorption method [13], co-precipitation method [14] etc. The best of our knowledge, the Ce-Dy substituted barium hexaferrite have been synthesized for the first-time using sol gel method. In the present investigation it is expected that Ce-Dy cations will affect the structural and magnetic properties of unit cell of barium hexaferrite by generating imbalance in the spin up/down. An attempt has been made to understand these structural and magnetic properties Ce-Dy substituted barium hexaferrite.

MATERIALS AND METHODS:

Synthesis:

Sol gel method was adopted to fabricate the Ce-Dy doped BFO hexaferrite nanoparticles with general chemical formula $\text{BaCe}_x\text{Dy}_x\text{Fe}_{12-2x}\text{O}_{19}$ ($x=0.00, 0.25, 0.50, 0.75$ and 1.0). High purity ($> 99\%$) (Sigma-aldrich) Barium nitrate ($\text{Ba}(\text{NO}_3)_2 \cdot 6\text{H}_2\text{O}$), Cerium nitrate ($\text{Ce}(\text{NO}_3)_3 \cdot 9\text{H}_2\text{O}$), Dysprosium Nitrate ($\text{Dy}(\text{NO}_3)_3 \cdot 9\text{H}_2\text{O}$) and Ferric nitrate ($\text{Fe}(\text{NO}_3)_3 \cdot 9\text{H}_2\text{O}$) with citric acid ($\text{C}_6\text{H}_8\text{O}_7 \cdot \text{H}_2\text{O}$) were taken as starting materials. All the starting materials were mixed in double distilled water with their desired stoichiometric proportion. The whole mixture was kept on hot plate with magnetic stirrer. The mixture was continually stirred at constant temperature of 90°C and liquid ammonia was slowly poured in order to maintain the pH a constant value 7. After continuously stirring and heating for 2-3 hours the mixture become viscous and sol was formed and after some time it converts into dried gel. By the process of self-ignition the dried gel was burnt and converted into a fine ash with dark brown colour. The homogeneous mixtures were obtained after grinding the burnt ash for one hour and sintered at 1000°C for 6 hours. After final sintering the powders were again grinded in order to obtain the fine particles of Ce-Dy doped BFO hexaferrites. The formation of Ce-Dy doped M-type BFO hexaferrites can be represented by the chemical reaction given below:



Characterization

Phase identification and structural parameters of Ce-Dy doped BFO-hexaferrites were studied by using X-ray diffraction patterns. XRD studies were performed on powder samples by using Cu-K_α radiations ($\lambda = 1.5406\text{\AA}$) in the 2θ range of 20° to 80° by keeping the scanning rate of $2^\circ/\text{min}$. Surface morphology of the samples was investigated by using scanning electron microscope (FE-SEM, JSM-6360, Jeol). Microstructure and interplanar spacing's of the prepared samples were evaluated by using transmission electron micrographs. Fourier transform infrared spectra of all the samples were recorded at room temperature in the frequency range of 400 to 4000 cm^{-1} by using Perkin Elmer spectrometer. To record the FTIR spectra, fine powder of each sample was mixed with kBr (ratio 1:250 by weight) for the uniform distribution of particles in kBr pellet. The mixture was pressed in the form of right circular pellets (thickness nearly 1 mm) by using cylindrical die. Optical measurements were

carried out by using U-V visible spectra on UV-2102 PCS spectrometer. Magnetic properties were examined by using the data obtained from vibrating sample magnetometer at room temperature for the applied field of 10000Oe. The microwave measurements, complex transmission (S21) and reflection (S11) coefficients were performed with ATM technology waveguide system and HPPNAE8364B Vector network analyzer in the frequency range of 2–18 GHz. The samples used for measurement were prepared by dispersing powder into a paraffin wax with the mass fraction of 70% and pressing the sample into a compact coaxial shape. The dielectric properties (dielectric constant and dielectric loss) were estimated with the assistance of LCR-Q meter as a function of frequency.

RESULTS AND DISCUSSION

Rietveld analysis:

Fig. 1(a-e) depicts the Rietveld refined X-ray diffraction patterns of M-type BFO samples doped by rare earth Ce-Dy ions. XRD analysis reveals that for the sample $x = 0.0$, all the Bragg's reflections are absolutely matched with pure BFO phase of standard theoretical pattern indexed by JCPDS -96-100-8842 with space group $p63/mmc$ belonging to the hexagonal structure. For the samples $X \geq 0.25$, the addition of rare earth Ce-Dy ions introduces the secondary phases of cubic CeO_2 (JCPDS card No. 96-900-9009) with space group $Fm-3m$ and orthorhombic DyFeO_3 (JCPDS card 96-200-3126) with space group $pnma$. XRD profiles of the samples were fitted for different phases by using the Full-Proof software. The small shift in the position of the peaks and variation of relative intensities may be related to the occupation of the lattice sites by substituted cations with different ionic radius. The sharpness and narrow size of the reflection peaks clearly indicates the high crystallinity and fine grain size of the hexaferrite. In Fig. 1 (a-e), the blue solid spheres represent the observed intensity, red line belongs to calculated intensity and blue vertical lines shows the Bragg's position for the refined patterns. The lowest dark orange colour solid line represents the difference in observed and calculated intensities. Majority of the peaks of all the samples are indexed to the lattice planes belonging to M-type hexagonal structure. By keeping atomic fractional positions fixed and other parameters such as lattice parameters, occupancies, scale factors, shape parameters, background etc. are as free parameters corrected by Thompson-Cox-Hasting Pseudo-Voigt function. The reliability factors such as 'R_p' (Profile factor), 'R_{wp}' (Weighted profile factor) and goodness factor (χ^2) obtained from Rietveld refinements are listed in Table 1. Similarly, the relevant lattice parameters (a, and c) obtained from XRD

analysis are given in Table 1. As seen in Table 1, the goodness factor lies between 1.010 to 1.198 indicates the good quality of the fine crystal structure of the samples. Lattice parameters 'a' and 'c' shows increasing trend with the addition of Ce-Dy rare earth ions in BFO hexaferrites. In general, these variations are related to the ionic radii of the substituted cations and their percentage in the composition. In the present case both Ce³⁺ (ionic radii 1.03 Å) [15] and Dy³⁺ (ionic radii 0.91 Å) [16] cations replaces the Fe³⁺ ions with small fraction (0.67 Å). The replacement of higher ionic radii cations in place of Fe³⁺ ions expands the crystal lattice and accordingly increases the lattice parameters. The values of c/a ratio are ranges from 3.939 to 3.929 which are lower than that of 3.98 confirms the formation of M-type hexagonal structure of the samples [17]. For the hexagonal structures, cell volume can be calculated by using $V = 0.8666a^2c$ and its values are given in Table 1. It can be seen that the cell volume increases from 694.99 to 699.99 with the addition of Ce-Dy in BFO hexaferrites.

W-H Analysis:

Williamson-Hall method was employed to study the micro-strain (ϵ) observed in the crystal lattice and crystallite size (t). Fig. 2 (a-e) shows the linearly fitted W-H plots of all the samples by using the positions and FWHM of Bragg's peaks observed in XRD plots. The slope of the W-H plots gives strain induced in the crystal lattice and y-intercept gives the crystallite sizes of the samples by using the following relation [18]:

$$\beta \cos \theta = \frac{K\lambda}{t} + 4\epsilon \sin \theta \quad (1)$$

where, K- is constant (0.95), λ - is wavelength, ϵ - is strain distribution, t - is crystallite size, θ - is Bragg's angle and β - is full width to its half maximum. Strain values increases gradually from 8.3668×10^{-5} to 1.145×10^{-3} indicating the experience of tensile type strain. The doping of Ce-Dy ions in Ba-hexaferrites increases the crystallite size from 27.05 nm to 30.75 nm and its variation is shown in Fig. 2 (f).

Surface morphology:

Scanning electron micrographs (SEM) were taken out for the different concentrations of Ce³⁺ - Dy³⁺ co-substituted M-type barium hexaferrites which are represented in Fig. 3. Particles are observed in hexagonal platelet-like shape with smooth surface and sharp edges. Close observation of the SEM images shows that the particles are agglomerated. This

agglomeration between the particles may be related to the magnetic interactions formed between them. The introduction of Ce^{3+} - Dy^{3+} cations in M-type BFO hexaferrites slightly affects on the surface morphology and grain size of the samples. Average grain size estimated by using the software (image J) is increases from 56.93 nm to 90.3 nm. The variation of average grain size with Ce-Dy substitution is presented in Fig. 2 (f), which is in accordance with the results obtained from XRD analysis. Fig 4(a, c) represents the TEM images of $\text{BaCe}_x\text{Dy}_x\text{Fe}_{12-2x}\text{O}_{19}$ respectively for the samples $x=0.00$ and $x=1.0$ along with histogram of particle size distribution. Average particle size for the sample $x = 0.0$ is obtain 49.957 nm and it increases to 53.017 nm for the sample $x = 1.0$ in which maximum percentage of Ce-Dy was doped. The variation of particle size may be related to the presence of Ce^{3+} and Dy^{3+} ions at grain boundaries [19]. Several researchers reported the particle sizes from TEM analysis in the range 45nm – 300nm [20-22]. Fig. 4 (b, d) depicts the selected area diffraction pattern (SEAD) patterns for $x=0.00$ and $x=1.00$ respectively. The superposition of bright spots with Debye rings in SEAD patterns indicating the polycrystalline nature of samples. The SEAD patterns were indexed to the lattice planes (006), (107), (203), (205), (217), (221), (2011), (317) which are found in good agreement with the planes observed in XRD patterns.

Fourier transforms infrared spectra:

The presence of different vibrational and stretching groups in the samples were investigated by using Fourier Transform Infrared spectra recorded in the wave number range of 400 cm^{-1} to 4000 cm^{-1} . Infrared spectra are very useful to find the locations of band positions inside the materials. Fig. 5 shows the FTIR spectra of all the samples of $\text{BaCe}_x\text{Dy}_x\text{Fe}_{12-2x}\text{O}_{19}$ which gives the detailed information of the structural changes occurred in the samples due to addition of Ce-Dy ions in M-type barium hexaferrites. Absorption bands at around 435 cm^{-1} represents the bending vibrations of Fe-O bonds at tetrahedral sites and stretching vibrations of Fe-O bonds at octahedral sites [23-24]. The bands that are observed for all the samples near 1350 cm^{-1} – 1480 cm^{-1} are attributed to the metal – oxygen – metal bonds (i.e. Fe-O-Fe) and the bands around the 3480 cm^{-1} represents the stretching vibrations of O-H groups [25].

Optical properties:

Optical properties of the hexaferrite were studied by UV visible diffused reflectance spectra. The UV-vis characterization was used to calculated band gap. The band gap energy values were investigated by using Tauc plot by plotting $(\alpha h\nu)^2$ versus photon energy $h\nu$. Where h is Planks constant ν is frequency and α is absorption coefficient. The values of band gap

determined by the intercepts made on X-axis by extrapolated the linear portion of graphs as shown in Fig 6. For pure BaFe₁₂O₁₉ sample (x=0.00) the observed value of band gap is 1.3725 eV. For Ce-Dy substituted sample x=0.50, 0.75, 1 the estimated band gap is 1.3775 eV, 1.3969 eV and 4.5188 eV respectively. It is observed that as a substitution increases the band gap also increases. This may be due to increase lattice parameter, grain size and presence of impurity due to substitution of Ce-Dy.

Magnetic properties:

The magnetic behaviour of the resulting samples was studied using vibrating sample magnetometer with maximum applied field 10000 Oe at room temperature. Fig 7 (a) represents variation of magnetization with applied magnetic field; the magnetization curves indicate that all the samples show hysteresis behaviour with high coercivity at room temperature. Fig. 7 (b) exhibits the variation of saturation magnetization (M_s), remnant magnetization (M_r) and coercivity with Ce-Dy substitution in M-type BFO hexaferrites. From Fig. 7 (b) it can be observed that saturation magnetization and remnant magnetization decreases and coercivity increases with the replacement of Fe³⁺ ions by Ce³⁺- Dy³⁺ ions in BFO hexaferrites. The introduction of Ce-Dy ions reduces M_s from 36.259 to 26.318 emu/g and M_r from 21.82 to 15.543 emu/g. This decreasing behaviour of M_s and M_r can be explained on the basis of weak super-exchange interaction between magnetic ions [26, 27]. Similarly, the introduction of rare earth element leads to conversion of some ferric ions into ferrous ions to maintain electronegativity. The super-exchange interaction decreases as Fe²⁺-O²⁻-Fe³⁺ exchange interactions are weaker than Fe³⁺-O²⁻-Fe³⁺ which is responsible for the dilution of saturation magnetization and remnant magnetization [28-30]. Another possibility of the dilution in M_s and M_r is may be due to spin canting. It is to be also noted that the structure of M-type hexaferrite, Fe³⁺ ion have five different interstitial sublattices, three spin up (2a, 12k, and 2b) and two spin down (4f₁ and 4f₂). The Ce³⁺ and Dy³⁺ substitution causes an unbalanced distribution of Fe³⁺ may leads to decrease in magnetization. Similar behaviour of saturation magnetization with the introduction of rare earth elements are also reported in the literature [26].

Coercivity i.e. coercive field is the magnetic field requires reducing magnetization to zero value. Coercivity is an extrinsic property of magnetic material which vary with the microstructure, particle size and particle distribution [28]. The coercivity of the samples can be expressed by using Stoner-Wolfarth [31] theory

$$H_C = \frac{2K_1}{\mu_0 M_S} \quad (2)$$

where, K_1 is magneto crystalline anisotropy constant, M_S is saturation magnetization and μ_0 is the permeability of free space. In the present investigation coercivity (Fig. 7(b)) increases from 4250-5751 Oe with addition of Ce^{3+} and Dy^{3+} ions in BFO hexaferrites. As seen from equation (2) coercivity is inversely proportional to saturation magnetization and hence it shows increasing trend. Also, this increase in coercivity related to the enhancement of magneto crystalline anisotropy. The Squareness ratio (M_{rS}) was calculated for all samples using following relation,

$$M_{rS} = \frac{M_r}{M_S} \quad (3)$$

Values of squareness ratio were obtained as 0.6018 ($x = 0.0$), 0.5994 ($x = 0.25$), 0.5979 ($x = 0.50$), 0.5925 ($x = 0.75$) and 0.5906 ($x = 1.0$). It has been suggested that squareness ratio is important for understanding the domain nature, if it has less than 0.5 then a multi-magnetic domain and if it has greater than 0.5 then a single-magnetic domain will be obtained. $M_{rS} > 0.5$, in present case clearly indicates the single-magnetic domain structure [32, 33]. High squareness ratios and coercivity make these materials suitable for the application in high density magnetic recording media and permanent magnets.

Complex permeability and permittivity:

In general, the dielectric and magnetic properties of a material can be explained by using complex permittivity (ϵ' and ϵ'') and complex permeability (μ' and μ''). Real part associates with the storage capability of electric and magnetic energies and the imaginary parts indicated the loss of energy. These parameters collectively govern the lossy characteristics of a material when an electromagnetic wave passes through it. Variations of real and imaginary permittivity are presented in Fig. 8 (a, and b). It is evident from figure that the real and imaginary part of the undoped sample is greater than those of the doped samples. This behaviour may be explained by considering the interfacial polarization and intrinsic electric dipole polarization [34]. Increasing percentage of Ce-Dy ions in M-type BFO hexaferrites decreases both real and imaginary permittivity values. From the Fig. 8 (a) it is also observed that the value of real permittivity lies in the 3.5 to 4.7 range for all the samples. At lower frequency side all sample have constant value but at higher frequency there are some resonance peaks in real permittivity which are very useful for high absorption. Here the maximum real permittivity peak value obtained are 10.7167 for the sample $x=0.75$. From Fig.

8 (b) it is observed that at lower frequency side all sample have almost same value of imaginary permittivity but at higher frequency some resonance peaks are observed. The maximum Imaginary permittivity of resonance peak is observed 5.08 for the sample x=0.75.

Fig. 9 (a, and b) respectively depicts the real (μ') and imaginary (μ'') parts of permeability within a frequency range of 2–18 GHz. It is important to note that μ' and μ'' shows significant difference among the five samples with different doping concentrations, indicating that doping exerts effect on permeability. As shown in Fig. 9 (a) the overall real part of permeability decreases with increasing substitution. Its values were lies in the range 0.8 to 1.4 for all the samples. The maximum real permeability value 2.5041 is observed for the sample x=0.50. Similarly, the maximum Imaginary permeability value 1.8078 is observed for x=0.25. At higher frequency side multi-resonance peaks in μ'' and ϵ'' may be beneficial for broad-bandwidth of microwave absorption [35].

Microwave properties:

The reflection loss (RL) can be determined by complex permittivity and permeability with given absorber thickness d by following equation according to transmission line theory [36],

$$RL = 20 \times \log \left| \frac{Z_{in} - Z_0}{Z_{in} + Z_0} \right| \quad (4)$$

$$Z_{in} = Z_0 \times \left(\frac{\mu_r}{\epsilon_r} \right)^{1/2} \times \tanh \left[j \times \frac{2\pi df}{c} \times (\mu_r \epsilon_r)^{1/2} \right] \quad (5)$$

where Z_{in} is the input impedance of the absorber material, $Z_0 = (\mu_0/\epsilon_0)^{1/2} = 377\Omega$ is the impedance of free space, ϵ_r and μ_r are the complex relative permittivity and permeability, d is the thickness of absorber layer, c is the velocity of light in vacuum, and f is frequency of the incident electromagnetic wave. According to literature there are two conditions that must possess to attain excellent absorbing (or low reflection) properties. One is that the electromagnetic wave can enter into the absorbing material at the greater extent and the second is that the electromagnetic wave coming into the materials can be almost entirely attenuated [37].

Reflection loss for different thickness 1mm, 1.1mm, 1.2mm, 1.3mm, 1.4mm, 1.5mm, 1.6mm, 1.7mm, 1.8mm, 1.9mm, 2mm, 2.5mm and 3mm of $BaCe_xDy_xFe_{12-2x}O_{19}$ with x=0.00, 0.25, 0.50, 0.75, 1.0 are shown in Fig. 10 (a-e). All the composition shows almost the same variation of reflection loss along the entire investigation at low frequency region. The various

maxima and minima of peak for all the composition occur at higher frequencies. The bandwidth give a range of frequency where the reflection loss is lower than -10dB where 90% of the microwave can be absorbed in this frequency bandwidth. Best microwave absorbing material is that which possess low reflection with wide frequency bandwidth. The reflection losses mostly depend on the thickness of the sample. In the present investigation it is observed that for all sample the peak of reflection loss is occurred at higher frequency region. The various doping composition causes variation of amplitude of reflection loss.

From Fig. 10 (a-e) it is observed that reflection loss increases with thickness and doping composition of Ce-Dy. There is no any type of absorption peak for the sample of thickness 1 mm except x=0.75 sample. The sample x=0.75 possess lower value of reflection loss due to high value of permittivity and permeability at higher frequency Ku microwave band side. As shown in 10 (a-e) at Ku frequency band the sample x=0.75 shows four absorption peaks at different thickness. Among them one peak possess maximum -10 dB bandwidth of 0.7017 GHz and reflection loss -15.9188dB at frequency 12.8648 GHz. Table 2 depicts the values of maximum reflection loss and bandwidth for 3mm thickness sample with x=0.00 to 1.0 doping composition of Ce-Dy ions. For 2mm thickness the same sample x=0.75 possess another absorption peak at 16.72 GHz with maximum reflection loss of -16.274 dB with bandwidth of 0.3546 GHz. This behavior indicates that the reflection loss strongly depend on thickness and doping content.

Dielectric measurements:

Dielectric measurements such as dielectric constant for Ce-Dy doped M-type BFO hexaferrites were studied as a function of frequency (50Hz-5MHz). Dielectric constant was calculated using the given relationship;

$$\epsilon' = \frac{cd}{A\epsilon_0} \quad (6)$$

where, c-is the capacitance, d-is the thickness and A is the area of the pellet, ϵ_0 -is the permittivity of free space (8.859×10^{-12} F/m). The variation of dielectric constant with frequency for all the samples is shown in Fig. 11 (a). As a normal behaviour of hexagonal ferrites, dielectric constant of all the samples reduces as the frequency increases. Koops' theory [38] explains the reducing behaviour of dielectric constant with frequency which imagines the dielectric medium as inhomogeneous medium with two Maxwell-Wegner type layers [39, 40]. According to this model, the dielectric material is composed of the highly conducting grains separated by the low conducting grains boundaries. Rezlescu et. al. [41]

gives the model which states that the dielectric polarization mechanism in ferrites is similar to the conduction mechanism. The ferrites conducting grains are effective on high frequency and poorly conducting grains boundaries play a major role on low frequencies and therefore responsible for the high dielectric constant at low frequencies. At low frequency region the doping of Ce and Dy causes low value of dielectric properties than $x=0.00$ (Pure Barium ferrite). Fig. 11 (b) shows the variation of dielectric loss with frequency, as dielectric loss decreases with increase in frequency and it is constant at high frequency.

CONCLUSIONS

Nanoparticles of Ce-Dy substituted M-type BFO hexaferrite were successfully obtained by sol-gel auto-ignition technique. Rietveld refinement of XRD patterns confirms the M-type hexagonal structure of all the samples with additional phases of CeO_2 and DyFeO_3 for the doped samples. The small shift in the position of the peaks with the addition of Ce-Dy ions increases the values of lattice parameters 'a' and 'c'. The sharpness and narrow size of the reflection peaks clearly indicates the high crystallinity and fine grain size of the samples. The tensile type lattice strains is observed in the samples determined by using W-H plots. Average grain size obtained from SEM analysis increases from 56.93 nm to 90.3 nm with the addition of Ce-Dy ions. The introduction of Ce-Dy ions in BFO hexaferrites reduces the saturation magnetization (M_s) and remnant magnetizations (M_r) while as increases the coercivity (H_c). The investigated squareness ratios above 0.5 confirm the single-magnetic domain structure of the samples. From UV-spectroscopy it is investigated that energy band gap increases with frequency. Highly doped $x=0.75$ sample shows reflection loss -15.9273 and large bandwidth of 0.7017 GHz at Ku- microwave frequency band of 12.8648 GHz. As a normal behaviour of hexagonal ferrites, dielectric constant of all the samples reduces as the frequency increases.

REFERENCES

- [1] S. Prathap, W. Madhuri, S.S. Meena, Effect of nan-stoichiometry in lead hexaferrites on magnetic and dielectric properties, *Material chemistry and physics* 220(2018)137-148.
- [2] Y. Yang, F. Wang, J. Shao, K. M. Batoo, D. Huang, Microstructure and magnetic properties of Zr-Mn substituted M-type Sr-La hexaferrites, *Applied Physics A*, 123(2017)1-8.
- [3] M. R. Dadfar, S. A. Seyyed Ebrahimi, S.M. Masoudpanah, *J. of superconductor Nov. Magn*, 28(2015)89-94.
- [4] N. Koga, T. Tsutaoka, Preparation of substituted barium ferrite $\text{BaFe}_{12-x}(\text{Ti}_{0.5}\text{-Co}_{0.5})\text{O}_{19}$ by citrate precursor method and compositional dependence of their magnetic properties, *J. of Magn. And Magn. Mater.* 313(2007)168-175.
- [5] M. Awawdeh, I. Bsoul, S.H. Mahmood, Magnetic properties and of Mossbauer spectroscopy on Ga, Al and Cr substituted hexaferrites, *J. of alloys and comp.* 585(2014)465-473.
- [6] M. Khan, M. U. Islam, Y. Xu, M. N. Ashiq, I. Ali, M. A. Iqbal, M. Ishaque, Structural and magnetic properties of Pr-Ni substituted $\text{Ca}_{0.5}\text{Ba}_{0.5}\text{Fe}_{12}\text{O}_{19}$ hexaferrite nanoparticles, *Ceramic Inter.* 40(2014)6487-6493.
- [7] I. Ali, M. U. Islam, M. S. Islam, M. S. Awan, M. Ahmad, Effect of Ga-Cr substitution on structural and magnetic properties of hexaferrites ($\text{BaFe}_{12}\text{O}_{19}$) synthesized by sol-gel auto-combustion, *J. of Alloys and comp.* 547(2013)118-125.
- [8] R. Topkaya, I. Auwala, A. Baykal, Effect of temperature on magnetic properties of $\text{BaY}_x\text{Fe}_{12-x}\text{O}_{19}$ hexaferrites, *Ceramic Intern.*, 42(2016)16296-16302.
- [9] D. Chen, Y. Liu, Y. Li, K. Yang, H. Zhang, Microstructure and magnetic properties of Al doped barium ferrite with sodium citrate as a chelating agent, *J. of Magn. Magn. Mater.* 337(2013)65-69.
- [10] N. Tran, H. S. Kim, T. L. Phan, D. S. Yang, B. W. Lee, Electronic structure and magnetic properties of $\text{Ba}_{1-x}\text{Sr}_x\text{CoFe}_{12}\text{O}_{19}$ hexaferrites, *ceramic Inter.* 44(2018)12132.
- [11] Y. Kang, high saturation magnetization La-Ce-Zn doped M-type Sr-hexaferrites. *ceramic Inter.*, 41 (2015)4354-4359.
- [12] M. A. Almessiere, Y. Slimani, A. Baykal, Impact of Nd-Zn cosubstitution on the microstructure and magnetic properties of $\text{SrFe}_{12}\text{O}_{19}$ nano hexaferrite, *Ceramic Inter.* 45(2019)963-969.

- [13] M. N. Ashiq, M. J. iqbal, M. N. Haq, P. H. Gomez, A. M. Qureshi, Synthesis, magnetic and dielectric properties of Er-Ni doped Sr-hexaferrite nanomaterials for application in high density recording media and microwave devices, *J. of Magn. Magn. Mater.*, 324(2012)15-19.
- [14] A. Ataie, S. Heshmati-Manesh, H. Kazempour, synthesis of barium hexaferrite by the co-precipitation method using acetate precursor, *J. of Material Science*, 37(2002)2125-2128.
- [15] C. Liu, X. Kan, F. Hu, X. Liu, S. Feng, J. Hu, W. Wang, K.M. Reshma, M. Shezad, H. Li, C. Zhang, H. Li, S. Zhou, Q. Wu, Investigation of Ce-Zn co-substituted on the crystal and ferromagnetic properties of M-type strontium hexaferrites $Sr_{1-x}Ce_xFe_{12-x}Zn_xO_{19}$ compounds, *J. Alloys and comp.* 785(2019)452-459.
- [16] D. Neupane L. Wang, H. Adhikari, J. Alam, S. R. Mishra, synthesis and characterization of co-doped $SrFe_{12-x}(DyAl)_xO_{19}$ hexaferrite, *J. Alloys and comp.*, 701(2017)138-146.
- [17] M. Shezad, X. Liu, S. Feng, X. Kan, W. Wang, C. Liu, T. J. Shezad, K. M. Rehman; Characterizations analysis of magneto-structural transitions in Ce-Co doped SrM based nano $Sr_{1-x}Ce_xFe_{12-x}Co_xO_{19}$ hexaferrite crystallites prepared by ceramic route 497 (2020) 166013.
- [18] G. A. Kaur, M. Shandilya, P. Rana, S. Thakur, P. Uniyal; Modification of structural and magnetic properties of $Co_{0.5}Ni_{0.5}Fe_2O_4$ nanoparticles embedded polyvinylidene fluoride nanofiber membrane via electrospinning method; *Nano-Stru. Nano-Obj.* 22 (2020) 100428.
- [19] R. H. Kadm, K. Desai, V. S. Shinde, M. Hasim, S. E. Shirsath, Influence of Gd^{3+} ion substitution on the $MnCrFeO_4$ for their nanoparticle shape formation and magnetic properties, *J. Alloys comp.* 657(2016)487-494.
- [20] S. S. Satpute, S. R. Wadgane, S. R. Kadam, D. R. Mane, R. H. Kadam; Y^{3+} substituted Sr-hexaferrites: sol-gel synthesis, structural, magnetic and electrical characterization; *Ceramica* 65 (2019) 274-281.
- [21] R. Parker, Ferrite; *Proc. ICF-3* (1980) 375.
- [22] S.W. Lee, S.Y. An, I.-B. Shim, C.S. Kim, Mossbauer studies of La-Zn substitution effect in strontium ferrite nanoparticles; *J. Magn. Magn. Mater.* 290 (2005) 231.
- [23] A. Baniasadi, A. Ghasemi, A. Nemati, M.A. Ghadikolaei, E. Paimozd, Effect of Ti-Zn substitution on structural, magnetic and microwave absorption characteristics of strontium hexaferrite, *J. Alloys Compd.* 583 (2014) 325-328.

- [24] S.K. Chawla, R.K. Mudsainiyan, S.S. Meena, S.M. Yusuf, Sol-gel synthesis, structural and magnetic properties of nanoscale M-type barium hexaferrites $\text{BaCo}_x\text{Zr}_x\text{Fe}_{(12-2x)}\text{O}_{19}$, *J. Magn. Magn. Mater.* 350 (2014) 23–29.
- [25] M. Rostami, M. Moradi, R. S. Alam, R. Mardani; Characterization of magnetic and microwave absorption properties of multi-walled carbon nanotubes / Mn-Cu-Zr substituted strontium hexaferrite nanocomposites; *Mater. Res. Bul.* 83 (2016) 379-386.
- [26] T. Kaur, S. Kumar, S.B. Narang, A. K. Shrivastav, Radiation loss in microwave K_a region by conducting pyrrol/barium titanate and barim hexaferrite based nanocomposite, *J. Magn, Magn, mater.*, 420(2016)336-342.
- [27] S.E. Shirsath, S. B. Jadhav, B. G. Toksha, S.M. Patange, K. M. Jadhav, Influence of Ce^{3+} ions on the structural and magnetic properties of NiFe_2O_4 , *J. App. Phys.* 110(2011)013914.
- [28] I. Ali, M. U. Islam, M. S, Awan, M. Ahmed, M. N. Ashiq, S. Naseem, Effect of Tb^{3+} substitution on the structural and magnetic properties of M-type hexaferrites synthesized by sol-gel atoconbustion technique, *J. Alloys Comp.*, 550(2013)564-572
- [29] X. Liu, W. Wang, S. Yang, Z. Yu, B. Gu, Y. Du, Structural and magnetic properties of La^{3+} substituted strontium hexaferrite particles prepared by sol-gel method. *Phys. Status Solidi A*, 193(2002)314-319.
- [30] X. Liu, W. Wang, S. Yang, Z. Yu, B. Gu, Y. Du, Influence of La^{3+} substitution on the structural and magnetic properties of M- type strontium ferrites, *J. Magn. Magn. Mater.*, 238(2002)207-214.
- [31] Z. Vakli, A. Kumar, A. Jain, K. M. Gupta, Effect of Ce^{3+} doping on the structural, magnetic and dielectric properties of barium ferrite, *IEEE-2015*.
- [32] M. N. Ashiq, A. S. Farooq, M. Najam-ul-Haq, S. Reshma, Magnetic and electrical properties of M-type nano-stontium hexaferrite prepared by sol-gel combustion method, *J. Magn. Magn. Mater.* 444(2017)426-431.
- [33] M. M. Rashad, I. A. Ibarhim, Synthesis and magnetic properties of barium hexaferrite powder using organic acid precursor method, *J. Supercond Nov. Magn.*, 26(2013)1639-1644.
- [34] C. Strgiou, Litsardakis, Design of microwave absorbing coating with new Ni and La doped hexaferrite, *IEEE*, 48(2012)1516-1519.
- [35] P. Kaur, S. Bahel, S. B. Narang, Broad Band microwave absorption of $\text{Sr}_{0.85}\text{La}_{0.15}(\text{MnZr})_x\text{Fe}_{12-2x}\text{O}_{19}$ hexagonal ferrite in 18-40 GHz frequency range, 460(2018)489-494.

- [36] F. Tabatabaie, M. H. Faith, A. Saatchi, A. Ghasemi, Microwave absorption properties of Mn and Ti doped strontium hexaferrite, *J. Alloy. Comp.*, 470(2009)332.
- [37] Z. Zhang, X. Liu, X. Wang, Y. Wu, R. Li, Effect of Nd-Co substitution on magnetic and microwave absorption properties of SrFe₁₂O₁₉ hexaferrite, *J. Alloy. Comp.*; 525(2012)114-119.
- [38] C. G. Koops; On the dispersion of resistivity and dielectric constant of some semiconductors at audio-frequencies; *Phys. Rev.* 83 (1951) 121
- [39] J. C. Maxwell, *Electricity and magnetism*; Oxford University Press, Oxford Section 328, 1 (1929).
- [40] K. W. Wagner; Zur theorie der Unvollkommenen Dielektrika, *Annalen der Physik*, Vol. 40 (1913) 817-855.
- [41] N. Rezlescu, E. Rezlescu; Dielectric properties of copper containing ferrites; *Phys. Stat. Solidi – A*; 23 (1974) 575.

32%

SIMILARITY INDEX

PRIMARY SOURCES

- 1** Li Deng, Yang Zhao, Zhaoming Xie, Zuohua Liu, Changyuan Tao, Rongrui Deng. "Magnetic and microwave absorbing properties of low-temperature sintered BaZr Fe O ", RSC Advances, 2018
102 words — 2%
Crossref
- 2** www.jcsp.org.pk
Internet
80 words — 2%
- 3** link.springer.com
Internet
43 words — 1%
- 4** Reza Shams Alam, Mahmood Moradi, Hossein Nikmanesh, Joao Ventura, Mohammad Rostami. "Magnetic and microwave absorption properties of BaMgx/2Mnx/2CoxTi2xFe12-4xO19 hexaferrite nanoparticles", Journal of Magnetism and Magnetic Materials, 2016
43 words — 1%
Crossref
- 5** Ali, Ihsan, M.U. Islam, M.S. Awan, Mukhtar Ahmad, Muhammad Naeem Ashiq, and Shahzad Naseem. "Effect of Tb³⁺ substitution on the structural and magnetic properties of M-type hexaferrites synthesized by sol-gel auto-combustion technique", Journal of Alloys and Compounds, 2013.
42 words — 1%
Crossref
- 6** Manju Sharma, Subhash C. Kashyap, H.C. Gupta. "Effect of Mg-Zr substitution and microwave processing on magnetic properties of barium hexaferrite", Physica B: Condensed Matter, 2014
41 words — 1%
Crossref
- 7** S. S. Satpute, S. R. Wadgane, K. Desai, D. R. Mane, R. H.

Kadam. "Substitution effect of Y³⁺ ions on the structural, magnetic and electrical properties of cobalt ferrite nanoparticles", *Cerâmica*, 2020

Crossref

39 words — 1%

8 M. Anis-ur-Rehman, Fatima-tuz-Zahra, Seemab Kanwal, Zeenat Khan, Anila Asif, Anam Noor Hussain, Saba Zahid. "Study of dielectric relaxations in co-precipitated Sr-Fe(Cr) nanoferrites", *Journal of Materials Science: Materials in Electronics*, 2015

Crossref

37 words — 1%

9 Reza Shams Alam, Mahmood Moradi, Mohammad Rostami, Hossein Nikmanesh, Razieh Moayedi, Yang Bai. "Structural, magnetic and microwave absorption properties of doped Ba-hexaferrite nanoparticles synthesized by co-precipitation method", *Journal of Magnetism and Magnetic Materials*, 2015

Crossref

37 words — 1%

10 www.scielo.br

Internet

34 words — 1%

11 Zeyang Zhang, Xiangxuan Liu, Xuanjun Wang, Youpeng Wu, Rong Li. "Effect of Nd-Co substitution on magnetic and microwave absorption properties of SrFe₁₂O₁₉ hexaferrites", *Journal of Alloys and Compounds*, 2012

Crossref

32 words — 1%

12 Pawandeep Kaur, Shalini Bahel, S. Bindra Narang. "Broad-band microwave absorption of Sr_{0.85}La_{0.15}(MnZr)_xFe_{12-2x}O₁₉ hexagonal ferrite in 18–40GHz frequency range", *Journal of Magnetism and Magnetic Materials*, 2018

Crossref

31 words — 1%

13 R.A. Pawar, S.S. Desai, Q.Y. Tamboli, Sagar E. Shirsath, S.M. Patange. "Ce³⁺ incorporated structural and magnetic properties of M type barium hexaferrites", *Journal of Magnetism and Magnetic Materials*, 2015

Crossref

28 words — 1%

14 Vishal Kumar Chakradhary, M.J. Akhtar. "Highly coercive strontium hexaferrite nanodisks for microwave

28 words — 1%

-
- 15 R. Topkaya, I. Auwal, A. Baykal. "Effect of temperature on magnetic properties of $Ba_{1-x}Fe_xO_{19}$ hexaferrites", *Ceramics International*, 2016 27 words — 1%
Crossref
-
- 16 Iqbal, M.J.. "Impact of Pr-Ni substitution on the electrical and magnetic properties of chemically derived nanosized strontium-barium hexaferrites", *Journal of Alloys and Compounds*, 20100903 27 words — 1%
Crossref
-
- 17 Reshma A. Nandotaria, Rajshree B. Jotania, Charanjeet Singh Sandhu, Mohd. Hashim et al. "Magnetic interactions and dielectric dispersion in Mg substituted M-type Sr-Cu hexaferrite nanoparticles prepared using one step solvent free synthesis technique", *Ceramics International*, 2018 25 words — 1%
Crossref
-
- 18 www.pagesoftools.co.uk 23 words — < 1%
Internet
-
- 19 shodhganga.inflibnet.ac.in 23 words — < 1%
Internet
-
- 20 iopscience.iop.org 19 words — < 1%
Internet
-
- 21 Z. Mosleh, P. Kameli, A. Poorbaferani, M. Ranjbar, H. Salamati. "Structural, magnetic and microwave absorption properties of Ce-doped barium hexaferrite", *Journal of Magnetism and Magnetic Materials*, 2016 18 words — < 1%
Crossref
-
- 22 Raghvendra Singh Yadav, Ivo Kuřitka, Jarmila Vilcakova, Jaromir Havlica et al. "Structural, magnetic, dielectric, and electrical properties of $NiFe_2O_4$ spinel ferrite nanoparticles prepared by honey-mediated sol-gel 18 words — < 1%

23 Varsha C. Chavan, Sagar E. Shirsath, Maheshkumar L. Mane, R.H. Kadam, Surendra S. More. "Transformation of hexagonal to mixed spinel crystal structure and magnetic properties of Co²⁺ substituted BaFe₁₂O₁₉", Journal of Magnetism and Magnetic Materials, 2016 17 words — < 1%

Crossref

24 H. Sözeri, H. Deligöz, H. Kavas, A. Baykal. "Magnetic, dielectric and microwave properties of M–Ti substituted barium hexaferrites (M=Mn²⁺, Co²⁺, Cu²⁺, Ni²⁺, Zn²⁺)", Ceramics International, 2014 17 words — < 1%

Crossref

25 pubs.rsc.org 17 words — < 1%

Internet

26 Springer Proceedings in Physics, 2013. 17 words — < 1%

Crossref

27 Sabih Qamar, Majid Niaz Akhtar, Khalid Mujasam Bato, Emad H. Raslan. "Structural and magnetic features of Ce doped Co–Cu–Zn spinel nanoferrites prepared using sol gel self-ignition method", Ceramics International, 2020 17 words — < 1%

Crossref

28 Pawandeep Kaur, Shalini Bahel, S. Bindra Narang. "Microwave absorption behavior and electromagnetic properties of Ni–Zr doped La–Sr hexagonal ferrite synthesized by auto-combustion method", Materials Research Bulletin, 2018 17 words — < 1%

Crossref

29 Pawandeep Kaur, S. Bindra Narang, Shalini Bahel. "Physical and magnetic properties of Mn–Zr doped La–Sr ferrite prepared by the auto-combustion route", Ceramics International, 2016 16 words — < 1%

Crossref

30 www.ijert.org

Internet

16 words — < 1%

31 Yan Wang, Yanbo Chen, Xinming Wu, Wenzhi Zhang, Chunyan Luo, Jinhua Li. "Fabrication of MoS₂-graphene modified with Fe₃O₄ particles and its enhanced microwave absorption performance", *Advanced Powder Technology*, 2018

Crossref

15 words — < 1%

32 Hashim, Mohd., Alimuddin, Shalendra Kumar, Sagar E. Shirsath, R.K. Kotnala, Hanshik Chung, and Ravi Kumar. "Structural properties and magnetic interactions in Ni_{0.5}Mg_{0.5}Fe₂xCr_xO₄ (0 ≤ x ≤ 1) ferrite nanoparticles", *Powder Technology*, 2012.

Crossref

15 words — < 1%

33 Lechevallier, L.. "Structural analysis of hydrothermally synthesized Sr¹-xSm¹xFe¹2O¹9 hexagonal ferrites", *Journal of Magnetism and Magnetic Materials*, 200402

Crossref

14 words — < 1%

34 Bashir Ahmad, Rabia Raissat, Saleem Mumtaz, Zahoor Ahmad, Imran Sadiq, Muhammad Naeem Ashiq, Muhammad Najam-ul-Haq. "Multiferroics BiMn_{1-x}Al_xO₃ nanoparticles: Synthesis, characterization and evaluation of various structural, physical, electrical and dielectric parameters", *Journal of Magnetism and Magnetic Materials*, 2017

Crossref

14 words — < 1%

35 aip.scitation.org

Internet

14 words — < 1%

36 S. Prathap, W. Madhuri, Sher Singh Meena. "Effect of non-stoichiometry in lead hexaferrites on magnetic and dielectric properties", *Materials Chemistry and Physics*, 2018

Crossref

14 words — < 1%

37 worldwidescience.org

Internet

38 Vakil, Z., A. Kumar, A. Jain, K. M. Gupta, Mohd. Najim, and D. Singh. "Effect of Cerium (Ce^{3+}) doping on structural, magnetic and dielectric properties of Barium Ferrite ($\text{BaFe}_{12}\text{O}_{19}$)", 2015 IEEE International Conference on Electrical Computer and Communication Technologies (ICECCT), 2015. 13 words — < 1%

Crossref

39 M. M. Rashad, I. A. Ibarhim. "Synthesis and Magnetic Properties of Barium Hexaferrite Powders Using Organic Acid Precursor Method", Journal of Superconductivity and Novel Magnetism, 2012 13 words — < 1%

Crossref

40 Alam, Reza Shams, Mahmood Moradi, Mohammad Rostami, Hossein Nikmanesh, Razieh Moayedi, and Yang Bai. "Structural, magnetic and microwave absorption properties of doped Ba-hexaferrite nanoparticles synthesized by co-precipitation method", Journal of Magnetism and Magnetic Materials, 2015. 13 words — < 1%

Crossref

41 Adel Maher Wahba, Mohamed Bakr Mohamed. "Structural, magnetic, and dielectric properties of nanocrystalline Cr-substituted $\text{Co}_{0.8}\text{Ni}_{0.2}\text{Fe}_2\text{O}_4$ ferrite", Ceramics International, 2014 13 words — < 1%

Crossref

42 Htet Kyaw Ye, S.R. Shannigrahi, C.B. Soh, S.L.W. Yang, L.S. Li, D.V.M. Repka, P. Kumar. "Development of (Zr,Mn) doped X-type hexaferrites for high frequency EMI shielding applications", Journal of Magnetism and Magnetic Materials, 2018 12 words — < 1%

Crossref

43 Mohd. Hashim, Alimuddin, Shalendra Kumar, Sagar E. Shirsath, R.K. Kotnala, Jyoti Shah, Ravi Kumar. "Influence of Cr^{3+} ion on the structural, ac conductivity and magnetic properties of nanocrystalline Ni–Mg ferrite", Ceramics International, 2013 12 words — < 1%

Crossref

44 M.A. Almessiere, Y. Slimani, H. Gungunes, M. Sertkol, M. Nawaz, N.A. Algarou, A. Baykal, I. Ercan. "Tb³⁺ substituted strontium hexaferrites: Structural, magnetic and optical investigation and cation distribution", Journal of Rare Earths, 2020
Crossref 12 words — < 1%

45 arxiv.org
Internet 12 words — < 1%

46 Chen, Daming, Yingli Liu, Yuanxun Li, Kai Yang, and Huaiwu Zhang. "Microstructure and magnetic properties of Al-doped barium ferrite with sodium citrate as chelate agent", Journal of Magnetism and Magnetic Materials, 2013.
Crossref 12 words — < 1%

47 Seyyed Salman Seyyed Afghahi, Mojtaba Jafarian, Yomen Atassi. "Microstructural and magnetic studies on BaMg_xZn_xX_{2x}Fe_{12-4x}O₁₉ (X=Zr,Ce,Sn) prepared via mechanical activation method to act as a microwave absorber in X-band", Journal of Magnetism and Magnetic Materials, 2016
Crossref 11 words — < 1%

48 Pan Shen, Juhua Luo, Yue Zuo, Zhu Yan, Kang Zhang. "Effect of La-Ni substitution on structural, magnetic and microwave absorption properties of barium ferrite", Ceramics International, 2017
Crossref 11 words — < 1%

49 Asghar, G.. "Structural, dielectric and magnetic properties of Cr-Zn doped strontium hexa-ferrites for high frequency applications", Journal of Alloys and Compounds, 20120615
Crossref 11 words — < 1%

50 Ashok V. Humbe, Prashant B. Kharat, Anant C. Nawle, K. M. Jadhav. "Nanocrystalline Ni_{0.70-x}Cu_xZn_{0.30}Fe₂O₄ with 0 ≤ x ≤ 0.25 prepared by nitrate-citrate route: structure, morphology and electrical investigations", Journal of Materials Science: Materials in Electronics, 2017
Crossref 11 words — < 1%

51 Chawla, S.K., S.S. Meena, Prabhjoyt Kaur, R.K. Mudsainiyan, and S.M. Yusuf. "Effect of site preferences on structural and magnetic switching properties of CO–Zr doped strontium hexaferrite SrCoxZrxFe(12–2x)O19", Journal of Magnetism and Magnetic Materials, 2015. 11 words — < 1%

Crossref

52 Amrin R. Kagdi, Neha P. Solanki, Francisco E. Carvalho, Sher Singh Meena, Pramod Bhatt, Robert C. Pullar, Rajshree B. Jotania. "Influence of Mg substitution on structural, magnetic and dielectric properties of X-type barium zinc hexaferrites Ba 2 Zn 2-x Mg x Fe 28 O 46", Journal of Alloys and Compounds, 2018 11 words — < 1%

Crossref

53 Ramazan Topkaya. "Effect of composition and temperature on the magnetic properties of BaBi x La x Fe(12-2x)O19 (0.0 ≤ x ≤ 0.2) hexaferrites", Applied Physics A, 2017 11 words — < 1%

Crossref

54 Shinde, U.B., Sagar E. Shirsath, S.M. Patange, S.P. Jadhav, K.M. Jadhav, and V.L. Patil. "Preparation and characterization of Co²⁺ substituted Li–Dy ferrite ceramics", Ceramics International, 2012. 11 words — < 1%

Crossref

55 F. Tabatabaie, M.H. Fathi, A. Saatchi, A. Ghasemi. "Microwave absorption properties of Mn- and Ti-doped strontium hexaferrite", Journal of Alloys and Compounds, 2009 10 words — < 1%

Crossref

56 Anil B. Mugutkar, Shyam K. Gore, Umakant B. Tumberphale, Vijaykumar V. Jadhav et al. "Role of composition and grain size in controlling the structure sensitive magnetic properties of Sm³⁺substituted nanocrystalline Co-Zn ferrites", Journal of Rare Earths, 2019 10 words — < 1%

Crossref

57 M. Yasin Shami, M. S. Awan, M. Anis-ur-Rehman. "Effect of pH Variation on Structural and Dielectric 10 words — < 1%

58 Awadallah, Ahmad, Sami H Mahmood, Yazan Maswadeh, Ibrahim Bsoul, and Aynour Aloqaily. "Structural and magnetic properties of Vanadium Doped M- Type Barium Hexaferrite (BaFe_{12-x}V_xO₁₉)", IOP Conference Series Materials Science and Engineering, 2015. 10 words — < 1%

59 Md. D. Rahaman, Md. Dalim Mia, M.N.I. Khan, A.K.M. Akther Hossain. "Study the effect of sintering temperature on structural, microstructural and electromagnetic properties of 10% Ca-doped Mn_{0.6}Zn_{0.4}Fe₂O₄", Journal of Magnetism and Magnetic Materials, 2016. 10 words — < 1%

60 Pérez-Juache, T.J., A.L. Guerrero, J.G. Cabal-Velarde, M. Mirabal-García, S.A. Palomares-Sánchez, and J.A. Matutes-Aquino. "Analysis of the structure and Mössbauer study of the neodymium substitution in the Sr-hexaferrite", Physica B Condensed Matter, 2016. 10 words — < 1%

61 R.C. Alange, Pankaj P. Khirade, Shankar D. Birajdar, Ashok V. Humbe, K.M. Jadhav. "Structural, magnetic and dielectrical properties of Al–Cr Co-substituted M-type barium hexaferrite nanoparticles", Journal of Molecular Structure, 2016. 10 words — < 1%

62 Muhammad Javed Iqbal. "Effect of annealing temperature and substitution of Zr-Cu on magnetic properties of strontium hexaferrite nanoparticles", Journal of Physics Conference Series, 03/01/2009. 9 words — < 1%

63 npl.csircentral.net. 9 words — < 1%

64 Sahu, R.C.. "Neutralization of red mud using CO₂ sequestration cycle", Journal of Hazardous Materials, 9 words — < 1%

65 Xie, Yu, Xiaowei Hong, Changlin Yu, Mingjun Li, Yan Huang, Yunhua Gao, Jie Zhao, Sifeng Yan, Lei Shi, Kai Zhang, Qiang Lai, and Yun Ling. "Preparation and magnetic properties of poly(3-octyl-thiophene) /BaFe_{11.92}(LaNd)_{0.04}O₁₉-titanium dioxide/multiwalled carbon nanotubes nanocomposites", *Composites Science and Technology*, 2013.

Crossref

66 ir.amu.ac.in 9 words — < 1%

Internet

67 E. Meher Abhinav, Anuraj Sundararaj, D. Jaison, Gopalakrishnan Chandrasekaran et al. "Influence of ERTA on magnetocaloric properties of Sr doped BaFe₁₂O₁₉ thin films", *Applied Surface Science*, 2019

Crossref

68 scienceflora.org 9 words — < 1%

Internet

69 İsa Araz. "Electromagnetic properties of Ce substituted barium hexaferrite in X band frequencies", *Journal of Materials Science: Materials in Electronics*, 2019

Crossref

70 Joshi, Rajat, Charanjeet Singh, Dalveer Kaur, Hesham Zaki, S. Bindra Narang, Rajshree Jotania, Sanjay R. Mishra, Jasbir Singh, Preksha Dhruv, and Madhav Ghimire. "Structural and magnetic properties of Co²⁺-W⁴⁺ ions doped M-type Ba-Sr hexaferrites synthesized by a ceramic method", *Journal of Alloys and Compounds*, 2016.

Crossref

71 Gholam Reza Gordani, Marzieh Mohseni, Ali Ghasemi, Sayed Rahman Hosseini. "Microstructure, magnetic and microwave absorptive behavior of doped W-type hexaferrite nanoparticles prepared by co-precipitation method",

72 Yizao Wan, Jian Xiao, Chunzhi Li, Guangyao Xiong, Ruisong Guo, Lili Li, Ming Han, Honglin Luo. "Microwave absorption properties of FeCo-coated carbon fibers with varying morphologies", Journal of Magnetism and Magnetic Materials, 2016 8 words — < 1%
Crossref

73 K.K. Gupta, S.M. Abbas, T.H. Goswami, A.C. Abhyankar. "Microwave absorption in X and Ku band frequency of cotton fabric coated with Ni–Zn ferrite and carbon formulation in polyurethane matrix", Journal of Magnetism and Magnetic Materials, 2014 8 words — < 1%
Crossref

74 www.mdpi.com 8 words — < 1%
Internet

75 Ashiq, Muhammad Naeem, Raheela Beenish Qureshi, Muhammad Aslam Malana, and Muhammad Fahad Ehsan. "Synthesis, structural, magnetic and dielectric properties of zirconium copper doped M-type calcium strontium hexaferrites", Journal of Alloys and Compounds, 2014. 8 words — < 1%
Crossref

76 Malana, Muhammad Aslam, Raheela Beenish Qureshi, Muhammad Naeem Ashiq, and Muhammad Fahad Ehsan. "Synthesis, structural, magnetic and dielectric characterizations of molybdenum doped calcium strontium M-type hexaferrites", Ceramics International, 2016. 8 words — < 1%
Crossref

77 Ihsan Ali, M. U. Islam, M. S. Awan, Mukhtar Ahmad, M. Asif Iqbal. "Structural, Electrical, and Microstructure Properties of Nanostructured Calcium Doped Ba-Hexaferrites Synthesized by Sol-Gel Method", Journal of Superconductivity and Novel Magnetism, 2013 8 words — < 1%
Crossref

78 www.setaram.com 8 words — < 1%
Internet

79 Kadam, R.H., Kirti Desai, Vishnu S. Shinde, Mohd. Hashim, and Sagar E. Shirsath. "Influence of Gd³⁺ ion substitution on the MnCrFeO₄ for their nanoparticle shape formation and magnetic properties", Journal of Alloys and Compounds, 2016.

8 words — < 1%

[Crossref](#)

80 Yujie Yang, Fanhou Wang, Xiansong Liu, Juxiang Shao, Duohui Huang. "Magnetic and microstructural properties of Al substituted M-type Ca–Sr hexaferrites", Journal of Magnetism and Magnetic Materials, 2017

8 words — < 1%

[Crossref](#)

81 M.A. Almessiere, Y. Slimani, A. Baykal. "Structural and magnetic properties of Ce-doped strontium hexaferrite", Ceramics International, 2018

7 words — < 1%

[Crossref](#)

82 Ashiq, M.N.. "Structural, magnetic and dielectric properties of Zr-Cd substituted strontium hexaferrite (SrFe₁₂O₁₉) nanoparticles", Journal of Alloys and Compounds, 20091113

7 words — < 1%

[Crossref](#)

83 Patange, S.M., Sagar E. Shirsath, S.P. Jadhav, V.S. Hogade, S.R. Kamble, and K.M. Jadhav. "Elastic properties of nanocrystalline aluminum substituted nickel ferrites prepared by co-precipitation method", Journal of Molecular Structure, 2013.

7 words — < 1%

[Crossref](#)

84 Hashim, Mohd., Alimuddin, Sagar E. Shirsath, R.K. Kotnala, Sher Singh Meena, Shalendra Kumar, Aashis Roy, R.B. Jotania, Pramod Bhatt, and Ravi Kumar. "Influence of Ni²⁺ substitution on the structural, dielectric and magnetic properties of Cu–Cd ferrite nanoparticles", Journal of Alloys and Compounds, 2013.

6 words — < 1%

[Crossref](#)

85 Gnana Praveena Nethala, Ravindar Tadi, Ganapathi Rao Gajula, K.N. Chidambara Kumar, V. Veeraiah. "Investigations on the structural, magnetic and mossbauer

6 words — < 1%

properties of cerium doped strontium ferrite", Physica B: Condensed Matter, 2018

Crossref

EXCLUDE QUOTES

OFF

EXCLUDE MATCHES

OFF

EXCLUDE
BIBLIOGRAPHY

ON

11.0%

Date: 2020-06-02 07:34 UTC

Dr.R.H.KADAM

* All sources 22 | Internet sources 22

- ✓ [0] www.researchgate.net/publication/248261219_Synthesis_and_characterization_of_nanocrystalline_BaFe_96Co_08Ti_08M_08O_19_particles
3.7% 12 matches

- ✓ [1] www.researchgate.net/publication/271893566_Dielectric_and_magnetic_properties_of_Mg-Ti_substituted_barium_hexaferrite
3.5% 12 matches

- ✓ [2] www.researchgate.net/publication/259658398_Y-Type_Hexaferrites_Structural_Dielectric_and_Magnetic_Properties
2.7% 9 matches

- ✓ [3] www.researchgate.net/publication/308888170_Modulation_of_physico-chemical_magnetic_microwave_and_electromagnetic_properties_of_nanocry
2.1% 8 matches

- ✓ [4] www.researchgate.net/publication/316303694_Microstructure_and_magnetic_properties_of_M-type_strontium_hexagonal_ferrites_with_Y-Co_substi
1.8% 7 matches

- ✓ [5] www.researchgate.net/publication/243228703_Magnetic_properties_and_microstructure_of_BaFe116-2xTixMxO19_MCo_Zn_Sn_compounds
1.4% 5 matches

- ✓ [6] www.hindawi.com/journals/jnm/2015/294239/
1.3% 4 matches

- ✓ [7] www.researchgate.net/publication/329686343_Nd3_Ion-Substituted_Co1-2xNixMnxFe2-yNdyO4_Nanoparticles_Structural_Morphological_and_Ma
1.2% 4 matches

- ✓ [8] www.researchgate.net/publication/329578128_Effect_of_bimetallic_Ca_Mg_substitution_on_magneto-optical_properties_of_NiFe2O4_nanoparticles
0.7% 2 matches

- ✓ [9] ijrbat.in/upload_papers/10032014010110Kakde_A_S.pdf
0.7% 3 matches

- ✓ [10] freepaper.me/downloads/abstract/10.1016/j.mspro.2015.06.019
0.8% 3 matches

- ✓ [11] paperity.org/p/61479368/magnetic-properties-of-cr-substituted-co-ferrite-nanoparticles-synthesized-by-citrate-gel
0.6% 3 matches

- ✓ [12] iopscience.iop.org/article/10.1088/1742-6596/1282/1/012045/pdf
0.5% 2 matches

- ✓ [13] www.researchgate.net/publication/326894259_Assesment_of_Land_Use_and_Land_Cover_change_during_2001-2016_in_Golamunda_Block_of_Kal
0.5% 2 matches

- ✓ [14] cpb.iphy.ac.cn/article/2016/1861/cpb_25_12_126102.html
0.5% 1 matches

- ✓ [15] www.researchgate.net/publication/230427025_Magnetic_properties_of_CeDy-substituted_yttrium_iron_garnet_ferrite_powders_fabricated_using_a_
0.5% 1 matches

- ✓ [16] troindia.in/journal/ijcesr/vol6iss1part3/1397-1400.pdf
0.4% 2 matches

- ✓ [17] www.researchgate.net/publication/300782244_Room_temperature_long_range_ferromagnetic_ordering_in_Ni058Zn042Co010Cu010Fe18O4_nano_
0.4% 1 matches

- ✓ [18] www.scielo.br/scielo.php?script=sci_arttext
0.5% 1 matches

- ✓ [19] www.researchgate.net/publication/316484144_Microstructures_Magnetic_Properties_and_Microwave_Absorption_Characteristics_of_Ti2_-Mn4Sub
0.3% 1 matches

- ✓ [20] www.researchgate.net/publication/300778203_Structural_and_photoluminescence_properties_of_Ce_Dy_Er-doped_ZnO_nanoparticles
0.2% 1 matches

- ✓ [21] www.iasj.net/iasj?func=fulltext
0.3% 1 matches

10 pages, 2895 words

PlagLevel: 11.0% selected / 11.0% overall

35 matches from 22 sources, of which 22 are online sources.

Settings

Data policy: *Compare with web sources, Check against my documents*

Sensitivity: *Medium*

Bibliography: *Consider text*

Citation detection: *Reduce PlagLevel*

Whitelist: --

^[0]► Influence of large ionic radii dopants Ce-Dy on structural and magnetic properties of Barium hexaferrite

Abstract:

^[3]► In this paper we reported the effect of coupled substitution of Ce-Dy for Fe³⁺ ion on structural and magnetic properties of BaCe_xDy_xFe_{12-2x}O₁₉ (x=0.00-1). Samples were synthesized via sol gel method with chelating agent citric acid. The structural, morphological and magnetic interactions of samples were investigated by XRD, SEM, TEM and VSM. XRD data confirms the formation of magnetoplumbite type hexagonal crystal structure with crystallite size ranging from 23-24 nm. From XRD calculated values of lattice parameter, volume, bulk density, X-ray density and porosity were affected by Ce-Dy dopants. The W-H plot method used to measure lattice strain induced in sample and crystallite size. The SEM investigations reveal that grain size increases with substitution.^[0]► In the present investigation it is observed that Ce-Dy substitution has significant effect on magnetic properties.^[0]► The saturation magnetization (Ms), remnant magnetization (Mr) and coercivity (Hc) were recorded from hysteresis loops.^[1]► The estimated values of saturation magnetization (Ms) and remnant magnetization (Mr) were decreases with rare earth substitution.^[3]► The reason behind this decreasing trend in Ms and Mr may be spin canting and magnetic dilution.^[3]► Squarness ratio (Mr/Ms) calculated from obtained value and it lies in the range of 0.6018-0.5994.^[1]► It was found that Ce-Dy dopant results in improving the coercivity from 4250 Oe to 5751 Oe favourable for storage devices.

Introduction:

M-type barium hexaferrite have application in microwave devices, micro strip antennas, radar, memory core etc. They are widely investigated due to its unique properties like excellent chemical stability, high electrical resistivity, high coercivity, high Curie temperature and low production cost compared to other rare earth compounds [1-4]. The structure of hexaferrite is more complex compared with the other ferrites.^[2]► It has

magnetoplumbite crystal structure with 64 ions per unit cell. Among the 64 ions, the unit cell contains 38 number of oxygen ions, two barium ions and 24 Fe³⁺ ions.^{[9]►} The 24 Fe³⁺ ions distributed over five distinct sites i.e. 12k, 2a, 4f₂ octahedral site, 4f₁ tetrahedral and 2b trigonal pyramidal site [5-7]. The various iron sites and relative orientation of their spin moments are responsible for magnetism. Fe³⁺ ions at 2a, 2b, and 12k sites (a total of 16 Fe³⁺ ion) possess spin up while at 4f₁ and 4f₂ (a total of 8 Fe³⁺ ion) possess spin down. 8 spin down will cancel with 16 spin up and 8 spin up remain after cancellation with spin down.^{[5]►} According to the electronic configuration of Fe³⁺ there are 5 unpaired electrons in the 3d orbital, each Fe³⁺ ion has magnetic momenta of 5 μ_B and the total magnetic moment per unit cell is 8×5 = 40 μ_B. Hence other cation substitution at Fe³⁺ site plays important role in changing magnetic properties of hexaferrite.

The magnetic properties viz saturation magnetization, coercivity and retentivity of hexagonal ferrite can be modified by the substitution of Fe³⁺ with other ions for example Topkaya et al. [8] found that substitution of yttrium cation improves coercivity and Chen et al [9] discovered a decrease in saturation magnetization as aluminium cation substitution increases. The lattice parameter, coercivity, saturation magnetization and magneton number these properties were controlled by preparation methods, sintering temperature and amount of doping at Ba and Fe site. The study of literature review suggest that there are various methods used for synthesis of hexaferrite like hydrothermal process [9], solid state reaction [10], sol gel method [11, 12], microwave adsorption method [13], coprecipitation method [14] etc. The best of our knowledge, the Ce-Dy substituted barium hexaferrite have been synthesized for the first-time using sol gel method.^{[10]►} In the present investigation it is expected that Ce-Dy cations will affect the structural and magnetic properties of unit cell of barium hexaferrite by generating imbalance in the spin up/down.^{[5]►} An attempt has been made to understand these structural and magnetic properties Ce-Dy substituted barium hexaferrite.

Experimental Techniques:

Sol gel method is employed to synthesize a barium hexaferrite with chemical formula $\text{BaCe}_x\text{Dy}_x\text{Fe}_{12-2x}\text{O}_{19}$ for $x=0.00, 0.25, 0.50, 0.75$ and 1 . High purity (99%) (Sigma-aldrich) Barium nitrate ($\text{Ba}(\text{NO}_3)_2 \cdot 6\text{H}_2\text{O}$), Cerium nitrate ($\text{Ce}(\text{NO}_3)_3 \cdot 6\text{H}_2\text{O}$), Dysprosium Nitrate ($\text{Dy}(\text{NO}_3)_3 \cdot 9\text{H}_2\text{O}$) and Ferric nitrate ($\text{Fe}(\text{NO}_3)_3 \cdot 9\text{H}_2\text{O}$) with citric acid ($\text{C}_6\text{H}_8\text{O}_7 \cdot \text{H}_2\text{O}$) were taken as starting materials for the synthesis. All the starting materials were mixed in desired stoichiometric amount in sufficient amount of distilled water. The whole mixture is then placed on hot plate with magnetic stirrer. The mixture was continually stirred at constant temperature of 90°C and liquid ammonia was added slowly in order to maintain the pH a constant value 7. After continuously stirring and heating at 90°C for 2-3 hr the mixture become viscous and sol was formed and after some time it converts into dried gel, by the process of self-ignition the dried gel was burnt and a fine ash was obtained. The burnt ash is grounded for two hours and then subjected to final sintering at 1000°C for 6 hours. After final sintering the powders were again grinded for two hours to obtain the fine particles of the final products. The chemical reaction given below for the formation of barium hexaferrite

Characterization

Thermal behaviour of the doped sample $\text{BaCeDyFe}_{10}\text{O}_{19}$ was examined by using thermo-gravimetric analysis technique. X-ray diffraction was carried out, using $\text{Cu-K}\alpha$ radiation source of wavelength 1.5406 \AA at the rate of 2° per minutes, to know crystal structure of annealed samples. The microstructures of sample were studied by scanning electron microscopy (SEM). The size and morphology of barium hexaferrite particles were observed by a transmission electron microscopy (TEM).^[15] The magnetic properties were investigated by using vibrating sample magnetometer (VSM) at room temperature.

Results and discussion

Thermo-gravimetric analysis

Fig 1. presents the TG plot of the sample $\text{BaCe}_x\text{Dy}_x\text{Fe}_{12-2x}\text{O}_{19}$ with $x=1.0$ in air atmosphere from room temperature to 1000 °C. The heating rate was kept at 10 °C per minute in an air atmosphere. The thermogravimetric curve exhibits a three-stage mass loss. The initial stage from room temperature to 200 °C, the weight loss is due to the removal of water content and organic compounds (citric acid) from the sample. Second stage 200-450 °C the slight (4-5%) weight loss is observed, this is may be the initial stage of formation of hexaferrites. The final weight loss is observed (5.4%) in the temperature range of 907-984 °C, which confirms the formation of M-type Ce-Dy doped Barium hexaferrite. Hence the final sintering temperature for all the samples was kept at 1000 °C.

XRD analysis

The XRD pattern of the Ce-Dy substituted barium hexaferrite in various amounts of substitution $x=0.00, 0.25, 0.50, 0.75,$ and 1 are shown in Fig. 2. All the diffraction peaks were indexed on the basis of standard magnetoplumbite hexagonal phase (JCPDS #84-0757) with a space group of $P6_3 / mmc$. The (hkl) planes (110), (107), (114), (203), (205), (2011) shows the strong reflection for pure Ba- hexaferrite and as the Ce-Dy substitution increases, the intensity of (107) and (114) decreases. The small shift in the position of the peaks and variation of relative intensities may be related to the occupation of the lattice sites by substituted cations with different ionic radius. The sharpness and narrow size of the reflection peaks clearly indicates the high crystallinity and fine grain size of the hexaferrite. Lattice parameter (a, c) and cell volume were determined by using following relations [16]

The calculated values of lattice parameter a and c and the volume V are presented in table 1. The variation of lattice parameter a and c are graphically represented in Fig. 3, it is clear that lattice parameter a increases with Ce-Dy doping in barium hexaferrite, while the values of lattice parameter c decreases. The volume is also found to be increasing

trend with substitution. The variation of lattice parameter and volume were found to be dependent on addition of Ce^{3+} and Dy^{3+} ions in barium hexaferrites. Here in the present case these changes in lattice parameter are observed due to Ce^{3+} (ionic radii 1.03 \AA) [17] and Dy^{3+} (ionic radii 0.91 \AA) [18] ions replace the host Fe^{3+} ions having relatively smaller ionic radii (0.67 \AA).

The crystallite size (D) using Scherer formula[19], X-ray density (d_x) [20], bulk density (d_B)[20] and porosity of the Ba-hexaferrites [21] are calculated by using following relations,

Where k - Scherer constant=0.9, λ - wavelength of radiation, θ - diffraction angle, β_{hkl} is full width at half maximum of the line broadening.

where d_x - X- ray density n - number of molecules per unit cell, M - molecular weight, N_A - Avogadro's number $=6.02214 \times 10^{23}$, V - volume of unit cell

Where d_B - bulk density, M is mass of pellet, V volume of sample $= \pi r^2 h$, r and h are radius and height of pellet.

The values of crystallite size as shown in table1 lies in the range of 23.037-24.817 nm. By using mass-volume relation the bulk density and x-ray density of the samples were obtained and the values presented in table 1.^[1] From table 1 it is predicted that the values of both X-ray and bulk density increases with increase in Ce-Dy substitution in the series.^[1] It can be explained on the basis that as the X-ray density proportional to molecular weight, substitution of Ce-Dy molecular weight increases hence X-ray density increases.^[16] The listed values of bulk density are less than the X-ray density due to presence of unavoidable pores during sample preparation and heat treatment [22].^[2] The voids in the material greatly affect the electrical and magnetic properties of the ferrite. To measure voids in the powders, percentage porosity was calculated by using values of X-ray and bulk density.^[0] Calculated values were in the range of 27.28-35.51 as shown in table1, which indicates that the porosity was increases with

replacement of Fe^{3+} ions by Ce-Dy ions. Fig. 4 shows the variation of porosity and X-ray density with substitution composition. It is also observed from graph that porosity and X-ray density both increases with substitution.

In the present investigation to find the crystallite size and lattice strain Williamson Hall plot (W-H) method is used. According to Williamson -Hall, for coherent scattering region the line broadening due to finite size and the internal strain in the prepared samples can be calculated. The lattice strain (ϵ) induced due to displacement of atoms from their ideal positions due to lattice imperfections i.e. dislocations, vacancies, interstitials, substitutions and similar defects in samples calculated by following equation [23-26]

From equation (3) and (4) it is found that the crystallite size inversely proportional to $\cos\theta$ and strain inversely to $\tan\theta$. Hence the total peak broadening is sum of crystal size and strain i.e.

Rearranging this we get,

Equation (8) and (9) are W-H equation

W-H plots are drawn by plotting $4\sin\theta$ against $\beta_{hkl}\cos\theta$ for all prominent peaks and applied linear fit to the data, the slope of the linear fit represents lattice strain and the reciprocal of intercept (i.e. $k\lambda/\text{Intercept}$) represents crystal size. Positive value of slope represents tensile strain whereas negative value corresponds to compressive strain. The W-H plots for different substitution were shown in Fig. 5. The crystallite size of the prepared samples evaluated with the Scherrer formula and Williamson-Hall method are listed in table 1. From table 1 it found that both the value nearly same. ^[13] The values of strain induced due to crystal imperfection and distortion is also shown in table 1. Present investigation shows the positive values of slopes, this indicates that a tensile strain is experienced by particles. ^[3] The obtained lattice strain value were lies in the range of 0.8327 - 6.1320. As the substitution increases strain decreases to

0.8327 for $x=0.25$ sample, this may be due to defects such as vacancies and imbalance in the site distribution during growth of particles.

Scanning Electron Microscope

To find the average grain size and to study changes in the surface morphology of the samples SEM characterization were used. Scanning electron micrographs (SEM images) were taken out for the different concentrations of Ce^{3+} - Dy^{3+} co-substituted M-type barium hexaferrites and the images are shown in Fig. 6. The average grain size obtained from the analysis of SEM images by using the software (image J) was found below 100 nm for all the samples and the values are given in Table 1. Close observation of the SEM images shows that the particles are agglomerated. This agglomeration between the particles may be related to the magnetic interactions formed between them.

Transmission Electron Microscopy:

The main aim of the transmission electrons microscopy was to estimate the correct particle size and to understand its variation with the addition of Ce-Dy in M-type barium hexaferrite. Fig 7(a, b) presents the TEM images of $BaCe_xDy_xFe_{12-2x}O_{19}$ for $x=0.00$ and $x=1.0$ respectively. Fig. 7 (c, d) presents the selected area diffraction pattern (SEAD) patterns for $x=0.00$ and $x=1.00$ respectively. TEM images indicate that most of the particles are found in spherical shape with some agglomeration.^[10] The average particle size obtained from TEM images is found in the range 32 nm to 78 nm. The variation of particle size may be related to the presence of Ce^{3+} and Dy^{3+} ions at grain boundaries [27]. The superposition of bright spots with Debye rings in SEAD patterns indicating the polycrystalline nature of samples. The SEAD patterns of the sample $x=0.00$ is indexed to the lattice planes (006), (107), (205), (217), (2011), (317) and for the sample $x=1.0$ lattice planes observed in SEAD pattern are in good agreement with the planes observed in XRD patterns.^[13]

[2]►

Magnetic Characterization

The magnetic properties of the resulting samples were measured using vibrating sample magnetometer with maximum applied field 12000 Oe at room temperature.^[1] Fig 8 represents variation of magnetization with applied magnetic field, the magnetization curves indicate that all the samples show hysteretic behaviour with high coercivity at room temperature. The all magnetic parameters were summarized in table 2. The magnetic parameter of hexaferrites were depends on doping element, synthesis method and sintering temperature. Fig. 9 exhibits the variation of saturation magnetization and coercivity with composition of substitution. From Fig. 9 it were observed that saturation magnetization decreases and coercivity increases with the substitution of Ce³⁺- Dy³⁺ ions at Fe³⁺ ions in barium hexaferrite.^[6] From table 2 it is seen that the values of saturation magnetization decreases from 36.259 to 26.318emu/g and remnant magnetization from 21.82 to 15.543emu/g with introduction of Ce³⁺-Dy³⁺ ions. This decrease nature is due to i) weak super-exchange interaction between magnetic ions [28, 29]. ii) The introduction of rare earth element leads to conversion of some ferric ions into ferrous ions to maintain electronegativity. The super-exchange interaction decreases as Fe²⁺- O²⁻ - Fe³⁺ exchange interactions are weaker than Fe³⁺- O²⁻ - Fe³⁺ which is responsible for the dilution of saturation magnetization and remnant magnetization [30- 32]. iii) The other possibility of the reduction in Ms and Mr is may be due to spin canting.^[2] iv) It is to be also noted that the structure of M-type hexaferrite, Fe³⁺ ion have five different interstitial sublattices, three spin up (2a,12k, and 2b) and two spin down (4f₁ and 4f₂). The Ce³⁺ and Dy³⁺ substitution causes an unbalanced distribution of Fe³⁺ may leads to decrease in magnetization. The decreasing nature of saturation magnetization was from 20 to 13.6 investigated by etal Kour [28].

Coercivity i.e. coercive field is the magnetic field requires reducing magnetization to zero value. Coercivity is an extrinsic property of magnetic material which vary with the

microstructure, particle size and particle distribution [30].^[11] The coercivity of the samples can be expressed by using Stoner-Wolfarth [33] theory

Where K_1 is magneto crystalline anisotropy constant, M_s is saturation magnetization and μ_0 is the permeability of free space. In the present investigation coercivity increases from 4250-5751 Oe with increase in concentration of Ce^{3+} and Dy^{3+} ions. As seen from equation (7) coercivity is inversely proportional to saturation magnetization and hence it shows increasing trend. Also, this increase in coercivity related to the enhancement of magneto crystalline anisotropy. The Squareness ratio (M_r) was calculated for all samples using following relation,

This value represents the squareness of hysteresis loop.^[20] The calculated values are listed in table 2.^[0] For the present investigation estimated values of squareness ratio were lies in the range of 0.5906-0.6018. It has been suggested that squareness ratio important for understanding domain nature, if it has less than 0.5 then it has multi magnetic domain and if it has greater than 0.5 then it has single magnetic domain. In present study all the values were greater than 0.5 indicating the single magnetic domain structure [34, 35].^[0] Large squareness ratios and large coercivity has applications in high density magnetic recording media and permanent magnets.

^[0] Conclusions

The M-type barium hexaferrite substituted Fe^{3+} ion with Ce-Dy successfully synthesized by sol-gel method. The structural properties and morphology of prepared sample were studied by XRD, SEM, and TEM. The values of lattice parameter 'a' increases with substitution. The crystallites size were determined by using Scherrer formula found in the range of 23.176-24.817nm. The bulk density, X-ray density and porosity also possess increasing trend with substitution. The lattice strains were determined by using W-H plot method. For $x=0.00$ sample the investigated lattice strain value is 1.3469×10^{-4} . The magnetic properties viz

saturation magnetization, remnant magnetization and coercivity were obtained from hysteresis loop. Present investigation found that coercivity were increases with substitution and obtained a maximum value of 2751 Oe for $x=1$ sample. The investigated squareness ratio values were above 0.5^[0] which is useful for application in high density magnetic recording media and permanent magnet.

001 Manuscript.doc

By Ram

Dr. R. H. KADAM

Structural, mechanical and magnetic interactions in Dy³⁺ introduced Co-Cu-Zn-Fe nanoferrites

90

P. H. Kadam,^{a,*} R. B. Borade,^b M. L. Mane,^c D. R. Mane,^d K. M. Batoo,^e S. E. Shirsath,^{f,g,*}

^aMaterials Science Research laboratory, Shrikrishna Mahavidyalaya, Gunjoti, Osmanabad, M⁹⁷ India.

^bDepartment of Physics, MSS's Arts, Science and Commerce College, Ambad, Jalna, M.S. India

^cDepartment of Physics, R. G. Shinde College, Paranda, Osmanabad, M.S. India

³⁶Department of Higher Education, Maharashtra State, Central Building, Pune M.S. India

^eKing Abdullah Institute for Nanotechnology, King Saud University, P.O. Box. 2455, Riyadh-1145, Saudi Arabia.

⁴⁶Department of Physics, Vivekanand College, Aurangabad, 431001, M.S. India

⁸School of Materials Science and Engineering, University of New South Wales, Sydney, NSW 2052, Australia.

ABSTRACT

Sol-gel synthesized Co-Cu-Zn ferrite nanoparticles diluted with Dy³⁺ ions were investigated for their structural, morphological, elastic, magnetic and dielectric properties. XRD patterns showed the formation of single phase cubic spinel structure. Concentration of Dy³⁺ ions gradually increases the lattice parameter from 8.340 Å to 8.545 Å obeying the Vegard's law. Williamson-Hall (W-H) method was employed to observe the change in lattice strain. Crystallite size obtained from W-H plots followed the similar pattern as observed by Scherrer equation. Cation distribution suggested a strong preference of Dy³⁺ ions towards octahedral – B site while Cu²⁺ and Fe³⁺ ions distributed over both A and B sites. Microstructure of the samples was observed by using TEM images. Mechanical properties such as stiffness constant (C_{11}), longitudinal and transverse wave velocity (V_l and V_t), Young's modulus (E), bulk modulus (B), rigidity modulus (G), Poisson's ratio (σ) and Debye temperature (θ_D) were investigated by FTIR spectra recorded in the range 300 cm⁻¹ to 800 cm⁻¹. Replacement of Fe³⁺ ions by strong magnetic Dy³⁺ ions increases the saturation magnetization showing the characteristics of soft magnetic materials. Dielectric constant increased with Dy³⁺ substitution whereas decreased with applied frequency.

Keywords: W-H method, lattice strain, cation distribution, elastic properties, saturation magnetization.

*Corresponding Authors: shirsathsagar@hotmail.com (SES), ram111612@yahoo.co.in (RHK)

INTRODUCTION:

Nanocrystalline spinels possessing integral properties of magnetic and electrical insulators have been intensively investigated in being the subject of great research interest [1,2]. Ferrites with spinel structure offers an enormous attention over the last few decades because of their extensive use in many technological applications such as transmitting microwave devices, computer memory chips, magnetic recording media, radio frequency coil fabrication, transformer cores, catalysis, photocatalysis, magnetically guided drug delivery, hyperthermia and many branches of telecommunication and electronic engineering [3-7]. Recently, nanoferrites have attracted much interest of academic, technical and medical fields. They have promising applications in medical applications, ferro-fluids, computer designing, sensors and microwave controls components. The spinel-nano ferrites constitute a major class of nano-materials which have nano – dimensions, where their size can vary between one to hundreds of nanometers. When their size is reduced to a few nanometers they exhibit a much different behavior from their bulk counterpart, which possesses useful ferromagnetic properties to meet the technological requirements [8-11]. Among the spinel oxides, CoFe_2O_4 is a ferrimagnetic oxide with an inverse MgAl_2O_4 (spinel)-type structure. It possess excellent magnetic properties such as; Curie temperature (T_c) ~ 870 K, saturation magnetization (M_s) ~ 80 emu/g, magnetic coercive field (H_c) $\sim 3-5$ kOe, and first-order magnetocrystalline anisotropy constant (K_1) $\sim 10 \times 10^6$ erg/cm. [12, 13] structural, electrical and magnetic properties of CoFe_2O_4 reportedly enhanced by the substitution of Cu and/or Zn ions [1, 14-16].

Apparently, properties of spinel ferrite known to modify with the substitution of rare earth (RE^{3+}) ions, since RE^{3+} ions have large magnetic moments, large magnetocrystalline anisotropy and very large magnetostriction. Rare earth ions have unpaired 4f electrons and strong spin-orbit coupling of the angular momentum. Moreover,

4f shell of RE³⁺ ions is shielded by 5s²5p⁶ and does not affected by the potential field of the surrounding metal ions. The occurrence of 4f–3d couplings which determines the magnetocrystalline anisotropy in ferrites can be improved the magnetic properties of ferrites with the substitution of RE³⁺ ions [17, 18]. RE³⁺ oxides are good electrical insulators as well and possess >10⁵ Ω-cm resistivity at room temperature [19, 20]. Among the RE³⁺ ions, substitution of Dy³⁺ ions shows marked improvement in the properties of ferrites [21, 22]. In the present article we firstly report the structural, elastic and magnetic properties of Co_{0.4}Cu_{0.1}Zn_{0.4}Dy_xFe_{2-x}O₄ (x = 0.0, 0.015, 0.03, 0.045) nanoparticles synthesized by the sol-gel combustion technique.

MATERIALS AND METHODS:

Pure, ultrafine nanopowders of Co_{0.4}Cu_{0.1}Zn_{0.4}Dy_xFe_{2-x}O₄ (x = 0.0, 0.015, 0.03, 0.045) were fabricated by sol-gel auto combustion method. Ultrapure (>99 %) metal nitrates of Co(NO₃)₂.6H₂O, Cu(NO₃)₂.6H₂O, Zn(NO₃)₂.6H₂O, Fe(NO₃)₃.9H₂O, and Dy(NO₃)₃.9H₂O were used in combination with (C₆H₈O₇·H₂O) as chelating agent in the molar ratio of 1:3. Liquid ammonia was slowly introduced in the solution in order to adjust the pH ≅ 7. Until the formation of viscous gel, the whole mixture was continuously stirred by providing a constant temperature 90 °C. After self ignition process, the burnt powders were sintered at 700 °C for 6 h and grounded as to obtain the fine nanoparticels.

Powder samples were characterized by X-ray diffraction technique (Regaku (*Miniflux II*) diffractometer) within the diffraction angles 20–80° by using Cu-K_α radiations (λ = 1.5406 Å) at 40kV. Samples were scanned slowly by maintaining the rate 2° per minute. Microstructure and surface morphology of the samples were understood by using transmission electron microscopy (JEOL JEM 2100). Elastic parameters were computed by using FTIR spectrum recorded in the range 300cm⁻¹ to 800cm⁻¹. FTIR

measurements were performed on the disc shaped samples made by using ferrite-KBr in the ratio 1:10. Magnetic characterization was carried out by applying the magnetic field upto 5T by employing a vibrating sample magnetometer. Silver pasted discs of the samples were used to understand the dielectric behaviour of the samples within the frequency range 50Hz to 50MHz by using Hioki HiTESTER 3532-50.

RESULTS AND DISCUSSION:

Structural analysis:

Bragg's reflections for the planes (220), (311), (222), (400), (422), (333), (440), (533) (indexed by ICCD # 00-008-0234) observed in the X-ray diffraction patterns of $\text{Co}_{0.4}\text{Cu}_{0.1}\text{Zn}_{0.4}\text{Dy}_x\text{Fe}_{2-x}\text{O}_4$ ($x = 0.0, 0.015, 0.03, 0.045$) as shown in Fig. 1, clearly indicating the formation of single phase cubic crystals with space group (Fd3m) [23]. No any impurity phase was observed in the XRD patterns and the addition of Dy^{3+} ions shifts the peak positions slightly towards the lower angles and decreases the peak height as depicted in Fig. 1. Lattice parameter was computed by using the equation [23] $a = d(h^2 + k^2 + l^2)^{1/2}$, where ($h k l$) are the miller indices and 'd' is the inter-atomic distance. Fig. 2 (a) shows the variation of lattice parameter with the addition of Dy^{3+} ions from which it can be understood that the replacement of Fe^{3+} ions having smaller ionic radii (0.67Å) by Dy^{3+} ions with relatively higher ionic radii (0.99Å) increases the crystal lattice and hence lattice parameter increases from 8.340 Å to 8.545 Å. Doping of Dy^{3+} ions into spinel type structure will induce uniform strain in the lattice as the material is elastically deformed. This effect causes the lattice plane spacing to change and the diffraction peaks shift to a lower 2θ -position. Crystallite diameter ' D_{XRD} ' of the powders was estimated by using the peak broadening (β) and Bragg's angle (θ) of the most intense

peak (311) in the well-known Debye-Scherrer [24] equation $D_{XRD} = (C\lambda/\beta\cos\theta)$, where $C = 0.94$ and $\lambda = 1.5406 \times 10^{-10}$ m. Addition of Dy^{3+} ions in Co-Cu-Zn nanoparticles reduces the size of the crystallites from 41.31nm to 39.57nm and its variation is shown in Fig. 2 (b). Specific surface area enhances from 34.47 m²/gm to 39.37 m²/gm shown in Fig. 2 (a) was computed by using the following relation [25],

$$S = \frac{6}{d_x D_{XRD}} \quad (1)$$

where, 6 is the shape factor. The increase in specific surface area is related to the decrease in crystallite size of the samples.

Nanocrystalline nature of the samples obtained from Debye-Scherrer relation and the micro-strain induced in the crystal lattice was studied by using Williamson-Hall (W-H) relation [26]:

$$\beta\cos\theta = \frac{C\lambda}{D_{W-H}} + 4\epsilon\sin\theta \quad (2)$$

For the nano-crystals of uniform size, $C = 0.94$, D_{W-H} is the crystallite size, λ is incident wavelength, and ϵ is the micro-strain induced in the crystal lattice. W-H analysis gives the better information of crystallite size as compared to the Debye-Scherrer relation [27]. Crystallite size and micro-strain values were obtained from y-intercept and slope of the line drawn between $4\sin\theta$ and $\beta\cos\theta$ as shown in Fig. 3. Strain values are given in the inset of Fig. 3 and the variation of crystallite size (D_{W-H}) is shown in Fig. 2 (b). Crystallite size obtained from W-H plots ranges from 34.40 nm to 31.76 nm which is consistent with the results obtained from Debye-Scherrer equation and the strain values are increased from 3.133×10^{-4} to 4.344×10^{-4} . Positive values of slopes indicating the tensile type of strain induced on the lattice which also support the variation in lattice constant.

Cation distribution:

The observed variation of lattice constant was confirmed by the use of cation distribution over tetrahedral – A and octahedral – B sites. Well-known Bertaut method [27] was used to compute the cation distribution of $\text{Co}_{0.4}\text{Cu}_{0.1}\text{Zn}_{0.4}\text{Dy}_x\text{Fe}_{2-x}\text{O}_4$. In this method few pairs of most sensitive reflections were selected according to the expression $(I_{hkl}^{\text{Obs.}}/I_{h'k'l'}^{\text{Obs.}}) = (I_{hkl}^{\text{Cal.}}/I_{h'k'l'}^{\text{Cal.}})$, where, $I_{hkl}^{\text{Obs.}}$ and $I_{hkl}^{\text{Cal.}}$ are the observed and calculated intensities for the (hkl) reflections respectively. The best information on cation distribution is achieved when comparing experimental and calculated intensity ratios for reflections whose intensities (i) are nearly independent of the oxygen parameter, (ii) vary with the cation distribution in opposite ways and (iii) do not differ significantly. The relative integrated intensity (I_{hkl}) for a given (hkl) reflection was evaluated by using the relation derived by Buerger [28]:

$$I_{hkl} = |F_{hkl}^2| P \cdot L_P \quad (3)$$

where, (F)- is the structure factor, (P)- is the multiplicity factor, (L_P)- is the Lorentz-polarization factor and was obtained by the use of following relation [24]:

$$L_P = \frac{1 + \cos^2 2\theta}{\sin^2 \theta \cos \theta} \quad (4)$$

The atomic scattering factors for various ions were taken from the literature [29]. The cation distribution for the presently studied spinel ferrite system $\text{Co}_{0.4}\text{Cu}_{0.1}\text{Zn}_{0.4}\text{Dy}_x\text{Fe}_{2-x}\text{O}_4$ obtained from X-ray diffraction technique is presented in Table 1. The results demonstrate that Cu^{2+} ions distributed over tetrahedral A and octahedral B-sites. Zn^{2+} ions shows preference towards tetrahedral A-site while as Co^{2+} ions shows preference towards octahedral B-site. Dy^{3+} preferentially replaces Fe^{3+} from octahedral sites. Further, Dy^{3+} ions predominately occupy the octahedral sites, which is consistent with the preference for large octahedral site energy. With increasing Dy^{3+} content, the fraction Dy^{3+} ions in octahedral sites increases, whereas the fraction of Fe^{3+} ions in octahedral sites decreases

linearly. Ionic radii of tetrahedral A-site (r_A) and octahedral B-site (r_B) were obtained from the cation distribution data and ionic radii of constituent ions. Fig. 4a shows that r_A and r_B both increased with the Dy^{3+} substitution. This variation is related to larger ionic radii of Dy ions compared to Fe ions which occupy both A and B sites, thus expanding both the crystallography sites. Inserting the values of $R_O = 1.32 \text{ \AA}$ (radius of oxygen ion) and r_A in the following relation, oxygen positional parameter 'u' were estimated [30]:

$$u = \left[(r_A + R_O) \frac{1}{\sqrt{3}a} + \frac{1}{4} \right] \quad (5)$$

Fig. 4b indicates that 'u' decreased from 0.3882 \AA to 0.3877 \AA with the Dy substitution. As reported by many researchers for ideal fcc packing the oxygen positional parameter 'u' should be 0.250 \AA rather than 0.375 \AA with the origin at the octahedral sites, while u is about 0.375 \AA when its origin at tetrahedral sites and crystal structure is centric [31,32]. Using XRD patterns some researcher reported $u > 0.375 \text{ \AA}$ for substituted ferrites [33, 34], for pure magnetite $u = 0.382 \text{ \AA}$ and for Zn doped ferrites $u = 0.390 \text{ \AA}$ [35]. However, in the present study, u is larger than its perfect value of 0.375 \AA , because there is a variation in the theoretical and experimental values of X-ray intensity.

The theoretical lattice parameter ' a_{th} ' was calculated using the values of tetrahedral and octahedral radii (r_A, r_B) [36]:

$$a_{th} = \frac{8}{3\sqrt{3}} \left[(r_A + R_O) + \sqrt{3}(r_B + R_O) \right] \quad (6)$$

where r_A and r_B are the radii of tetrahedral (A) site and octahedral (B) site, respectively, R_O is radius of oxygen ($R_O = 1.32 \text{ \AA}$). Fig. 4c shows the variation of theoretical lattice constant with x. Theoretical lattice constant increased from 8.543 \AA to 8.563 \AA with the increase in Dy^{3+} substitution in Co-Cu-Zn ferrite.

Shared, unshared octahedral edge (d_{BXE} , and d_{BXEU}), tetrahedral and octahedral bond lengths (d_{Ax} and d_{Bx}) and tetrahedral edge (d_{AXE}) were obtained using the relations

discussed elsewhere. Figure 4d shows that d_{BXE} , d_{BXEU} , d_{Ax} , d_{Bx} and d_{AXE} increased with Dy³⁺ substitution, which is related to the increase in lattice constant with Dy³⁺ substitution.

Transmission electron microscopy:

Fig. 5 (a) and (b) depicts the transmission electron micrographs of the typical samples $x = 0.0$ and $x = 0.045$ respectively. TEM images reveal the homogeneity of the samples with uniform size distribution of the particles. Most of the particles are observed in spherical shape which is in accordance with the fact that, to maintain the surface tension to minimum value, cubic crystals are prone to develop into spherical shape [37, 38]. The agglomerations observed in the particles may be related to the interactions of magnetic dipoles arise within the ferrite nanoparticles [39]. The main focus of the TEM images was to estimate the particle size of the samples and it was measured by using the software *ImageJ* (Version 1.52V). Fig. 5 (c) and (d) shows the histograms of particle size distribution for the samples $x = 0.0$ and $x = 0.45$ respectively. It was observed that for the sample $x = 0.0$, the particles are ranges for their sizes from 28.534nm to 97.160 nm with average value of 62.632nm. For the sample $x = 0.045$, the particle size lies in the range 41.973 nm to 114.215 nm with average value of 77.789nm.

Elastic properties:

Infrared spectra recorded in the wavenumber range of 300 cm⁻¹ to 800 cm⁻¹ for all the samples of Co_{0.4}Cu_{0.1}Zn_{0.4}Dy_xFe_{2-x}O₄ are shown in Fig. 6. The vibration bands observed near 585cm⁻¹ are related to the stretching vibrations metal ion – oxygen bond at tetrahedral site (ν_A) and bands near 375 cm⁻¹ are related to the stretching vibrations at octahedral site (ν_B) which confirms that the powders were crystallize in cubic spinels [40].

For the present series (ν_A) and (ν_B) varies with the increasing concentration of Dy³⁺ ions in Co-Cu-Zn ferrites and the values are listed in Table 2. It can be seen that the insertion of Dy³⁺ ions shifts absorption bands (ν_A) and (ν_B) slightly towards higher frequency side. This shifting of absorption bands is closely related to the crystallite size. Decreasing particle size increases the center frequency of the absorption bands [41]. Force constants K_T and K_O representing the tetrahedral – A and octahedral – B sites respectively were estimated by using the relations discussed elsewhere [42]. The values of force constants computed by using the positions of high and low frequency bands (ν_A) and (ν_B) are given in Table 2. The average force constant was obtained by the relation $K_{av} = (K_O + K_T)/2$ and the values are given in Table 2.

Force constants obtained from infrared spectra and the crystallographic parameters were used to calculate the stiffness constant and various elastic parameters. According to Waldron [41], stiffness constant $C_{11} = C_{12}$ for the materials possessing the cubic spinel crystallography and is given by $C_{11} = K_{av}/a$, where, K_{av} is average force constant and a is lattice constant. Various elastic parameters such as bulk modulus B , Young's modulus E , rigidity modulus G , Poisson's ratio σ , longitudinal wave velocity V_l , transverse wave velocity V_t , and mean wave velocity V_m were calculated by using the following relations [43]:

$$B = \frac{1}{3}(C_{11} + 2C_{12}) \quad (7)$$

$$V_l = (C_{11}/\rho)^{1/2} \quad (8)$$

$$V_t = V_l/\sqrt{3} \quad (9)$$

$$G = \rho V_t^2 \quad (10)$$

$$\sigma = \frac{3B - 2G}{6B + 2G} \quad (11)$$

$$E = (1 + \sigma)2G \quad (12)$$

$$V_m = \left[\frac{1}{3} \left(\frac{2}{V_t^3} + \frac{1}{V_l^3} \right) \right]^{-1/3} \quad (13)$$

The variation of various elastic parameters and modulus for Dy³⁺ substituted Co-Cu-Zn ferrite system are given in Table 2. It can be observed from Table 2 that stiffness constant C₁₁ and all elastic moduli (B, G, and E) increases with addition of Dy³⁺ ions in Co-Cu-Zn ferrites and the value of Poisson's constant remains constant (σ = 0.35) for all the samples. According to literature [41, 43] and the theory of isotropic elasticity [44] Poisson's ratio must lie in the range -1 to 0.5 in order to get the good elastic behaviour. In general, elastic moduli values are related to the inter-atomic bonding between the ions. As suggested by A. Bhaskar [45], strong inter-atomic bonding between the ions enhances the values of elastic moduli. In the present case increasing values of elastic moduli are may be due to the increasing inter-atomic bonding between the ions of Dy³⁺ substituted Co-Cu-Zn ferrites.

Debye temperatures (θ_D) of all the samples were estimated by using the relation suggested by Anderson [46]:

$$\theta_D = \frac{h}{k_B} \times V_m \left[\frac{3n\rho N_A}{4\pi M} \right]^{1/3} \quad (14)$$

where, h- is Planks constant, k- is Boltzmann's constant, N_A- is Avogadro's number, ρ- is density, M- is molecular weight and n- is the number of atoms per unit cell (n =8) and V_m is the mean wave velocity. Debye temperature can also be calculated by using the relation suggested by Waldron [43]:

$$\Theta_D = \frac{\hbar C}{k_B} v_{av} = 1.438 \times v_{av} \quad (15)$$

where, v_{av} is the average of absorption bands (v_A, v_B) and is given by $v_{av} = (v_A + v_B)/2$. Both the values of Debye temperatures obtained from the relations suggested by Anderson and Waldron are given in Table 2. Addition of Dy^{3+} ions increases θ_D from 539.17K to 554.97K and Θ_D varies from 678.17K to 698.28K. The variation of Debye temperature can be explained on the basis of specific heat theory [47]. Increasing P-type conduction in the materials increases the Debye temperatures. Also, the increasing rigidity of Dy^{3+} doped Co-Cu-Zn ferrites may increase the Debye temperature.

The elastic moduli (B , G and E) are not significant unless the correction will be made to zero porosity which can be calculated by using the void fraction (P) in the Hosselman and Fulrath formula [45]:

$$E_0 = \left[\frac{1}{E} \left\{ 1 - \frac{3P(1-\sigma)(9+5\sigma)}{2(7-5\sigma)} \right\} \right]^{-1} \quad (16)$$

$$G_0 = \left[\frac{1}{G} \left\{ 1 - \frac{15P(1-\sigma)}{(7-5\sigma)} \right\} \right]^{-1} \quad (17)$$

$$B_0 = \frac{E_0 G_0}{3(3G_0 - E_0)} \quad (18)$$

$$\sigma_0 = \frac{E_0}{2G_0} - 1 \quad (19)$$

Void free corrected values of Young's modulus (E_0), rigidity modulus (G_0), bulk modulus (B_0) and Poisson's ratio (σ_0) are given in Table 3. It can be observed from Table 3 that all the elastic moduli increased with the addition of Dy^{3+} ions in Co-Cu-Zn ferrites. This behaviour is analogous with the stronger inter-atomic bonding between the corresponding ions.

Magnetic properties:

¹ A-A, B-B and A-B magnetic interaction are possible between the cations by super-
exchange mechanism through the intermediate oxygen ions in spinel ferrites. ¹⁴ Among these
interactions; A-B interaction is the strongest and hence the cation-anion bond lengths are
fairly smaller. On the other hand, A-A interaction is the weakest interaction since the
cation-anion distance is large. ⁵² The interaction energies among two magnetic ions (M^I and
 M^{II}) related to the distance of these ions from the oxygen ions and the angle (θ) between
 $M^I - O - M^{II}$. The maximum angle θ of 180° among the cations gives maximum
interaction energy. The exchange energy decreased with increasing distance between
cations and the oxygen anion. ¹ The inter-ionic distances among the cations (Me – Me) (*b*,
c, *d*, *e*, and *f*) and among the cation-anion (Me – O) (*p*, *q*, *r*, and *s*) as well as bond angles
⁴ (θ_1 , θ_2 , θ_3 , θ_4 , and θ_5) among the cations and cation-anion were determined by using the
equations listed in Table 4 [48]. ¹ As evidenced from Fig. 7a-c that the Me–Me cation
distances (*b* to *f*) increased with Dy substitution in Co-Cu-Zn ferrite. In case of distances
between the Me–O cation and anion; P and S increased whereas Q and R decreased with
the Dy substitution. ⁷⁷ The substitution of larger Dy^{3+} ions for Fe^{3+} ions towards the BO_6
octahedral site resulted in the increase in the B–O bond length. On the other hand,
¹ tetrahedral- AO_4 sinks without altering the overall $\bar{4}3m$ symmetry that could further
increase the anion–anion (O–O) distances and thus resulted in an increase in the inter-
cation distances (Me–Me). It is noticed that θ_1 and θ_2 related to the A-B interaction
increased, θ_3 and θ_4 related to the B-B interaction decreased, whereas θ_5 corresponding to
the A-A interaction slightly increased with the Dy^{3+} substitution. These results suggest the
A–O–B exchange interaction mechanism strengthened than that of A–O–A and B–O–B
interactions. Such variation should increase the magnetization of Dy^{3+} substituted Co-Cu-
Zn ferrites. Thus magnetic ⁴ properties of Dy^{3+} substituted Co-Cu-Zn nano-ferrites was
⁶¹ studied by using vibrating sample magnetometer at room temperature with a peak field of

5kOe. Fig. 8 shows the hysteresis loops of all the samples which clearly indicating the saturation magnetization increases with increases in Dy³⁺ concentration. This increasing behaviour of saturation magnetization can be explained as, the overall magnetization (M_s) increased with the increase in Dy³⁺ concentration, which replaced Fe³⁺ ions at octahedral B-site predominantly. Dy³⁺ ions have larger magnetic moment (10.48μ_B) compared to Fe³⁺ (5μ_B), therefore, the introduction of Dy³⁺ ions at octahedral B-sites increase the magnetization at B-site, which resulted in increase in the saturation magnetization.

The observed magnetic moment per formula unit in the Bohr magneton (μ_B) was calculated by using the following relation [49]:

$$n_B = \frac{M_w \times M_s}{5585} \quad (20)$$

where n_B = Magnet number, M_w = Molecular weight of the compound and M_s = saturation magnetization. It has been observed that observed magnetization increased with the increase in Dy substitution. The coercivity (H_c) is related to the anisotropy constant (K₁), permeability (μ₀) and saturation magnetization through the Brown's relation [49]:

$$H_c = \frac{2K_1}{\mu_0 M_s} \quad (21)$$

The coercivity can be altered by heat treatment or deformation and thus is independent of saturation magnetization. The values of saturation magnetization, coercivity, remanance ratio, are shown in Fig. 9a-d. It is clearly observed from Fig. 9a-d, that the coercivity increased as the Dy³⁺ substitution increases. Increase in coercivity is directly related to the higher magneto-crystalline anisotropy of rare earth ions such as Dy.

Dielectric measurements:

The dielectric constant (ε') was calculated using the formula:

$$\epsilon' = \frac{Ct}{\epsilon_0 A} \quad (22)$$

where C- is the capacitance of pellet, t- is the thickness of pellet, A- is the area of sample and ϵ_0 is the permittivity in free space. Fig. 10 (a, and b) shows the variation of real part of dielectric constant (ϵ') and dielectric loss tangent ($\tan\delta$) with the frequency for all samples. The (ϵ') and ($\tan\delta$) found to decrease with the increase in frequency confirming the dispersion at lower frequency, and it almost remains constant at higher frequencies [50]. The higher value of ϵ' at lower frequency can be ascribed to the effect of heterogeneity of the samples [51]. The dielectric dispersion in ferrites can be understood via Maxwell–Wagner model [52, 53] and Koop’s [54] phenomenological theory. The exchange of 3d electrons among Fe^{2+} and Fe^{3+} which are localized at the metal ions, results in local displacement of electrons in the direction of applied electric field that determine the polarization strength. The conduction in ferrites is reported due to the hopping of electrons upon application of electric field. The variation in ϵ' and $\tan\delta$ with frequency can also be related to the fact; that at low frequency region, which corresponds to ‘grain boundary’ induced high resistivity, more energy is required for electron exchange between Fe^{2+} and Fe^{3+} ions. This contributes in observed higher value of (ϵ') and ($\tan\delta$) at lower frequency. In contrary at higher frequency region, which corresponds to low resistivity (due to grains), a small energy is required for electron exchange between the Fe ions at the octahedral site. Further, high dielectric loss at lower frequency may be related to impurities, crystal defects and moisture. The increase of Fe^{2+} concentration in the sample increases the hopping probability resulting in decrease of resistivity at higher frequencies [55]. The favorable condition of hopping between Cu^{2+} , Co^{2+} , Zn^{2+} with Fe^{3+} ions at octahedral site with the following relation is possible:





The dielectric loss tangent ($\tan\delta$) determines the energy loss within the ferrite. Dielectric loss appeared when the polarization lag behind the applied alternating field, which is caused by the various impurities and ferrite crystalline imperfections. Fig. 8b depicts the variation of $\tan\delta$ with frequency at room temperature. Relaxation peaks were observed for all the samples and can be understood by Rezlescu model [56]. The condition for maxima in the $\tan\delta$ of a dielectric material is related to the relation:

$$\omega\tau = 1 \quad (26)$$

where $\omega = 2\pi f_{max}$ and τ is the relaxation time. A relation exists between the relaxation time to the jumping probability per unit time:

$$\tau = \frac{1}{2p} \quad (27)$$

$$\text{or } f_{max} \propto p \quad (28)$$

Thus, the peaking behaviour is obtained when the frequency of charge hopping among the Fe^{2+} and Fe^{3+} ions exactly matches with the frequency of the external applied field. It can be observed that the Co-Cu-Zn ferrite samples with $x = 0.045$ showed the highest dielectric constant and lowest dielectric loss.

Conclusions:

$\text{Co}_{0.4}\text{Cu}_{0.1}\text{Zn}_{0.5}\text{Dy}_x\text{Fe}_{2-x}\text{O}_4$ for $x = 0.0, 0.015, 0.030, 0.045$ nanoparticles were successfully synthesized by sol-gel auto combustion technique. XRD patterns confirm the single phase cubic spinel structure of all the samples. The increase in lattice parameter 'a' with Dy^{3+} content 'x' is related to the difference in ionic radii of Dy^{3+} and Fe^{3+} ions. X-ray density is found to decrease with increase in Dy ions, this decrease in 'd_x' is related to ionic radii and molecular weight of Dy ions. Average Crystallite size decreases with

decrease in Dy content 'x'. Cation distribution shows that Zn²⁺ ions occupied tetrahedral – A site only and Dy³⁺ and Fe³⁺ ions shows their marked preference towards octahedral B-site, however both these ions also occupy tetrahedral A-site by small fraction. On the other hand Cu²⁺ ions distributed equally over tetrahedral A-site and octahedral B-sites while as Co²⁺ ions occupy only octahedral B-site. The increase in saturation magnetization can be deliberated to be the result of two processes: First, the overall magnetic nature is enhanced with increasing Dy³⁺ substitution in selected chemical formula, because the magnetic Dy³⁺ replaces the relatively lower magnetic Fe³⁺. When Dy³⁺ ions were introduced in Cu-Co-Zn ferrite, they replace Fe³⁺ in the B-site predominantly. Dielectric constant increased whereas dielectric loss decreased with the increase in Dy substitution.

ACKNOWLEDGEMENTS:

Author RHK is thankful to Dr. Babasaheb Ambedkara Marathwada University, Aurangabad (M.S.) for providing financial assistance under the minor research project scheme vide letter No. STAT/VI/R.G./College/2018-19/3184-85 dated 21.02.2019

REFERENCES:

- [1] S.E. Shirsath, D. Wang, S.S. Jadhav, M.L. Mane, S. Li, Ferrites obtained by sol-gel method, in: L. Klein, M. Aparicio, A. Jitianu (Eds.), Handbook of Sol-Gel Science and Technology, Springer, Cham, 2018, pp. 695-735
- [2] H. Kaur, A. Singh, V. Kumar, D. S. Ahlawat; Structural, thermal and magnetic investigations of cobalt ferrite doped with Zn^{2+} and Cd^{2+} synthesized by auto combustion method; J. Magn. Magn. Mater. 474 (2019) 505-511.
- [3] G. Mustafa, M. U. Islam, W. Zhang, Y. Jamil, A. W. Anwar, M. Hussain, M. Ahmad; (2015); Investigation of structural and magnetic properties of Ce^{3+} substituted nanosized Co-Cr ferrites for variety of applications; J. Alloys Com. 618:428.
- [4] L. Li, H. Liu, Y. Wang, J. Jang; (2008); Preparation and magnetic properties of Zn-Cu-Cr-La ferrite and its nanocomposites with polyaniline; J. Colloid. Interface Sci. 321:265.
- [5] R. Verma, S. N. Kane, S. Raghuvanshi, M. Satalkar, S. S. Modak, F. Mazaleyrat, Synthesis, structural and magnetic properties of $Mg_{0.6}Zn_{0.4}Cr_xFe_{2-x}O_4$ ($0.0 < x < 2.0$) nano ferrite, AIP Conf. Proc. 1953 (2018), 030135.
- [6] P. Jadoun, J. Sharma, S. Kumar, S. N. Dolia, D. Bhatnagar, V. K. Saxena, Structural and magnetic behavior of nanocrystalline Cr doped Co-Mg ferrite, Ceram. Int. 44 (2018) 6747.
- [7] S. E. Shirsath, R. H. Kadam, M. L. Mane, A. Ghesami, Y. Yasukawa, X. Liu, A. Morisako; Permeability and magnetic interactions in Co^{2+} substituted $Li_{0.5}Fe_{2.5}O_4$ alloys; J. Alloy. Comp. 575 (2013) 145-151.
- [8] M. A. Amer, T. M. Meaz, A. G. Mostafa, H. F. El-Ghazally; (2015); Annealing effect on the structural and magnetic properties of the $CuAl_{0.6}Cr_{0.2}Fe_{1.2}O_4$ nano-ferrites; Materials Research Bulletin 67:207.
- [9] C. N. R. Rao, P. J. Thoma, G. U. Kulkarni; (2007); Nanocrystals: Synthesis, Properties and Applications, Springer-Verlag, Berlin Hiedelberg.
- [10] B. P. Rao, O. Caltun, W. S. Cho, C. O. Kim, C. G. Kim; Synthesis and characterization of mixed ferrite nanoparticles; (2007); J. Magn. Magn. Mater; 310:e812-e814.
- [11] A. Pradeep, P. Priyadharsini, G. Chandrasekaran; (2008); Production of single phase nano size $NiFe_2O_4$ particles using sol-gel auto combustion route by optimizing the preparation conditions; Mater. Chem. Phys. 112:572.
- [12] S. E. Shirsath, X. Liu, Y. Yasukawa, S. Li, A. Morisako, Switching of magnetic easy-axis using crystal orientation for large perpendicular coercivity in $CoFe_2O_4$ thin films; Scientific Reports, 6, 30074
- [13] S. E. Shirsath, X. Liu, M.H.N. Assadi, A. Younis, Y. Yasukawa, S. Kumar Karan, J. Zhang, J. Kim, D. Wang, A. Morisako, Y. Yamauchi, S. Li; (2019); Au quantum dots engineered room temperature crystallization and magnetic anisotropy in $CoFe_2O_4$ thin films; Nanoscale Horizons, 4; 434-444.

- [14] D. R. Mane, D. D. Birajdar, S. Patil, S. E. Shirsath, R. H. Kadam, (2011); Redistribution of cations and enhancement in magnetic properties of sol-gel synthesized $\text{Cu}_{0.7-x}\text{Co}_x\text{Zn}_{0.3}\text{Fe}_2\text{O}_4$ ($0 < x < 0.5$) J. Sol-gel Sci. Technol. 58; 70.
- [15] P. P. Hankare, P. D. Kamble, M. R. Kadam, K. S. Rane, P. N. Vasambekar, (2007); Effect of sintering temperature on the properties of Cu-Co ferrites prepared by oxalate precipitation method; Mater. Lett.; 61;2769.
- [16] Mohd. Hashim, Alimuddin, S Kumar, B. H. Koo, S. E. Shirsath, E.M. Mohammed, J. Shah, R. K. Kotnala, H. K. Choi, H. Chung, Ravi Kumar; (2012) Structural, electrical and magnetic properties of Co-Cu ferrite nanoparticles; J. Alloys Compd. 518;11– 18
- [17] S. R. Naik and A. V. Salker, (2012); Change in the magneto structural properties of rare earth doped cobalt ferrites relative to the magnetic anisotropy; J. Mater. Chem., 22; 2740–2750.
- [18] S. E. Shirsath, R. H. Kadam, S. M. Patange, M. L. Mane, A. Ghasemi, A. Morisako; (2012); Enhanced magnetic properties of Dy^{3+} substituted Ni-Cu-Zn ferrite nanoparticles; Appl. Phys. Lett., 2012; 042407.
- [19] E. Rezlescu, N. Rezlescu, P. D. Mangeron, L. Rezlescu and C. Pasxick, (1997); The influence of R_2O_3 (R=Yb, Er, Dy, Tb, Gd, Sm, and Ce) on the electric and mechanical properties of a Nickel – Zinc ferrite; Phys. Status Solidi A, 162; 673.
- [20] S. E. Shirsath, S. S. Jadhav, B. G. Toksha, S. M. Patange and K. M. Jadhav, (2011); Remarkable influence of Ce^{4+} ions on the electronic conduction of $\text{Ni}_{1-2x}\text{Ce}_x\text{Fe}_2\text{O}_4$; Scr. Mater., 64, 773–776.
- [21] M.A. Almessiere, Y. Slimani, A. D. Korkmaz, S. Güner, A. Baykal, S.E. Shirsath, I. Ercan, P. Kögerler, (2020); Sonochemical synthesis of Dy^{3+} substituted $\text{Mn}_{0.5}\text{Zn}_{0.5}\text{Fe}_{2-x}\text{O}_4$ nanoparticles: Structural, magnetic and optical characterization; Ultrasonics – Sonochemistry, 61; 04836
- [22] Mohd Hashim, A. Ahmed, S. A. Ali, S. E. Shirsath, M. M. Ismail, R. Kumar, S. Kumar, S. S. Meena, D. Ravinder, (2020) Structural, optical, elastic and magnetic properties of Ce and Dy doped cobalt ferrite; J. Alloy. Comp. 834 (2020) 155089
- [23] M. V. Chaudhari, S. E. Shirsath, A. B. Kadam, R. H. Kadam, S. B. Shelke, D. R. Mane; Site occupancies of Co-Mg-Cr-Fe ions and their impact on the properties of $\text{Co}_{0.5}\text{Mg}_{0.5}\text{Cr}_x\text{Fe}_{2-x}\text{O}_4$; J. Alloy. Comp. 552 (2013) 443-450.
- [24] B. D. Cullity, 'Introduction to Magnetic Materials, Addison-Wesley, Massachusetts, 1972.
- [25] R. H. Kadam, A. R. Biradar, M. L. Mane, S. E. Shirsath; Sol-gel autocombustion synthesis of $\text{Li}_{3x}\text{MnFe}_{2-x}\text{O}_4$ and their characterization; J. App. Phys. 112 (2012) 043902
- [26] T. Tatarchuk, M. Myslin, I. Mironyuk, M. Bououdina, A. T. Pedziwiatr, R. Gargula, B. F. Bogacz, P. Kurzydło; Synthesis, morphology, crystallite size and adsorption properties of nanostructured Mg-Zn ferrites with enhanced porous structure; J. Alloy. Copm. 819 (2020) 152945.
- [27] H. Kaur, A. Sigh, V. Kumar, D. S. Ahlawat; Structural, thermal and magnetic investigations of cobalt ferrite doped with Zn^{2+} and Cd^{2+} synthesized by auto combustion method; J. Magn. Magn. Mater. 474 (2019) 505.

- [28] K. B. Modi, S. J. Shah, C. R. Kathad, D. K. Sonigra, H. P. Parmar, K. M. Jadhav; On the relationship between structural – elastic properties of Co-Zn ferrites at 300K; *Adv. Mater. Res.* 1141 (2016) 147.
- [29] I. H. Gul, A. Z. Abbasi, F. Amin, M. Anis-Ur Rehman, A. Maqsood; (2007); Structural, magnetic and electrical properties of $\text{Co}_{1-x}\text{Zn}_x\text{Fe}_2\text{O}_4$ synthesized by coprecipitation method, *J. Magn. Magn. Mater.* 311:494.
- [30] L. Weil, F. Bertaut, L. Bochirol; (1950); Propriétés magnétiques et structure de la phase quadratique du ferrite de cuivre, *J. Phys. Radium*, 11:208.
- [31] K. J. Standley, *Oxide magnetic materials*. Clarendon Press, Oxford, (1972).
- [32] J. W. Vrewey, E. L. Heilmann, (1947) Physical properties and cation arrangement of oxides with spinel structures I. Cation arrangement in spinels; *J. Chem. Phys.* 15; 174-180.
- [33] G. Fagherazzi, F. Garbassi,(1972); X-ray diffraction measurements of the cation distribution in spinel structures; *J. Appl-Crystallogr.* 5; 18-23.
- [34] R. H. Kadam, K. Desai, V. S. Shinde, Mohd. Hashim, S. E. Shirsath, (2016); Influence of Gd^{3+} ions substitution on the MnCrFeO_4 for their nanoparticle shape formation and magnetic properties; *J. Alloys Compd.* 657; 487-494
- [35] C.O. Arean, E.G. Diaz, J.M.R. Gonzalez, M.A.V. Garcia; (1988) crystal chemistry of cadmium – zinc ferrites; *Solid State Comm.* 77;275-280
- [36] R. Valenzuela, *Magnetic ceramics*, (Cambridge University Press, 1994).
- [37] K. Parikh, R.V. Upadhyay, L. Belova, K.V. Rao; (2006); Ternary monodispersed $\text{Mn}_{0.5}\text{Zn}_{0.5}\text{Fe}_2\text{O}_4$ ferrite nanoparticles: preparation and magnetic characterization; *Nanotechnology* 17;5970-5975.
- [38] T. K. Pathak, N. H. Vasoya, V. K. Lakhani, K. B. Modi; (2010); Structural and magnetic phase evolution study on needle-shaped nanoparticles of magnesium ferrite; *Ceram. Intern.* 36; 275-281.
- [39] R. H. Kadam, S. T. Alone, M. L. Mane, A. R. Birajdar, S. E. Shirsath; Phase evaluation of Li^+ substituted CoFe_2O_4 nanoparticles, their characterizations and magnetic properties; *J. Magn. Magn. Mater.* 355 (2014) 70.
- [40] R. Waldron, Infrared spectra of ferrites; *Phys. Rev.* 99 (1955) 1727.
- [41] K. B. Modi, S. J. Shah, N. B. Pujara, T. K. Pathak, N. H. Vasoya, I. G. Jhala; Infrared spectral evolution, elastic, optical and thermodynamic properties study on mechanically milled $\text{Ni}_{0.5}\text{Zn}_{0.5}\text{Fe}_2\text{O}_4$ spinel ferrite; *J. Mol. Stru.* 1049 (2013) 250.
- [42] A. A. Birajdar, S. E. Shirsath, R. H. Kadam, M. L. Mane, D. R. Mane; Permeability and magnetic properties of Al^{3+} substituted $\text{Ni}_{0.7}\text{Zn}_{0.3}\text{Fe}_2\text{O}_4$ nanoparticles; *J. App. Phys.* 112 (2012) 053908
- [43] D. Boukkeze, J. Massoudi, W. Hzez, M. Smari, A. Bougoffa, K. Khirouni, E. Dhahri, L. Bessais; Investigation of the structural, optical, elastic and electrical properties of spinel $\text{LiZn}_2\text{Fe}_3\text{O}_8$ nanoparticles annealed at two distinct temperature; *RSC Adv.* 9 (2019) 40940.
- [44] M. B. Mohamed, A. M. Wahba; Structural, magnetic and elastic properties of nanocrystalline Al-substituted $\text{Mn}_{0.5}\text{Zn}_{0.5}\text{Fe}_2\text{O}_4$ ferrite; *Ceram. Inter.* 40 (2014) 11773.

- [45] A. Bhaskar, S. R. Murthy; Effect of sintering temperature on the elastic properties of Mn(1%) added MgCuZn ferrites; *J. Magn. Magn. Mater.* 355 (2014) 100.
- [46] R. S. Yadav, I. Kuritka, J. Havlica, M. Hnatko, C. Alexander, J. Masilko, L. Kalina, M. Hajduchova, J. Rusnak, V. Enev; Structural, magnetic, elastic, dielectric and electrical properties of hot-press sintered $\text{Co}_{1-x}\text{Zn}_x\text{Fe}_2\text{O}_4$ ($x=0.0, 0.5$) spinel ferrite nanoparticles; *J. Magn. Magn. Mater.* 447 (2018) 48-57.
- [47] S. A. Mazen, S. F. Mansour, E. Dhahri, H. M. Zaki, T. A. Elmosalami; The infrared absorption and dielectric properties of Li-Ga ferrite; *J. Alloys. Comp.* 470 (2009) 294.
- [48] R. A. Pawar, S. M. Patange, A. R. Shitre, S. K. Gore, S. S. Jadhav, S. E. Shirsath; (2018) Crystal chemistry and single-phase synthesis of Gd^{3+} substituted Co-Zn ferrite nanoparticles for enhanced magnetic properties; *RSC Advances* 8; 25258–25267.
- [49] Vivek Choudhari, R. H. Kadam, M. L. Mane, S. E. Shirsath, A. B. Kadam, D. R. Mane; (2014); Effect of La^{3+} impurity on Magnetic and Electrical properties of Co-Cu-Cr-Fe nanoparticles; *J. Nanosci. Nanotech.* 14;1-8
- [50] V. G. Patil, S. E. Shirsath, S. D. More, S. J. Shukla, K. M. Jadhav; (2009); Effect of zinc substitution on structural and elastic properties of cobalt ferrite; *J. Alloys Comp.* 488; 199.
- [51] M. B. Kothale, K. K. Patankar, S. L. Kadam, V. L. Mathe, A. V. Rao, B. K. Chougule; (2002); Dielectric behaviour and magnetoelectric effect in copper-cobalt ferrite + barium lead titanate composites; *Mater.Chem and Phy.* 78; 691.
- [52] J. C. Maxwell, *Electricity Magnetism Vol.1*, Oxford Uni. Press, Oxford, 1954. Section 328.
- [53] K.W. Wagner, (1973), The distribution of relaxation times in typical dielectrics, *Am. Phys.* 40;817-819.
- [54] C. G. Koops;(1951); On the dispersion of resistivity and dielectric constant of some semiconductors at audiofrequencies; *Phys. Rev.* 83; 121.
- [55] A. Verma, R. J. Chatterjee; (2006); Effect of zinc concentration on the structural, electrical and magnetic properties of mixed Mn-Zn and Ni-Zn ferrites synthesized by the citrate precursor technique; *Magn. Magn. Mater.* 306; 313.
- [56] N. Rezlescu, E. Rezlescu; (1974); Dielectric properties of copper containing ferrites; *Phys. Status Solidi (a)* 23; 575.

45%

SIMILARITY INDEX

PRIMARY SOURCES

- 1** R. A. Pawar, Sunil M. Patange, A. R. Shitre, S. K. Gore, S. S. Jadhav, Sagar E. Shirsath. " Crystal chemistry and single-phase synthesis of Gd substituted Co–Zn ferrite nanoparticles for enhanced magnetic properties ", RSC Advances, 2018 171 words — 4%

Crossref
- 2** S. R. Kulkarni, Priyanka U. Londhe, N. B. Chaure. "Electrical and magnetic properties of Al³⁺ substituted Mn–Ni–Zn nanoferrites", Journal of Materials Science: Materials in Electronics, 2013 103 words — 2%

Crossref
- 3** M.A. Amer, T.M. Meaz, A.G. Mostafa, H.F. El-Ghazally. "Annealing effect on the structural and magnetic properties of the CuAl_{0.6}Cr_{0.2}Fe_{1.2}O₄ nano-ferrites", Materials Research Bulletin, 2015 87 words — 2%

Crossref
- 4** link.springer.com 79 words — 2%

Internet
- 5** R.H. Kadam, Suresh T. Alone, Maheshkumar L. Mane, A.R. Biradar, Sagar E. Shirsath. "Phase evaluation of Li⁺ substituted CoFe₂O₄ nanoparticles, their characterizations and magnetic properties", Journal of Magnetism and Magnetic Materials, 2014 70 words — 2%

Crossref
- 6** Le-Zhong Li, Xiao-Xi Zhong, Rui Wang, Xiao-Qiang Tu. "Structural, magnetic and electrical properties of Zr-substituted NiZnCo ferrite nanopowders", Journal of Magnetism and Magnetic Materials, 2017 55 words — 1%

-
- 7 S.K. Gurav, Sagar E. Shirsath, R.H. Kadam, D.R. Mane. "Low temperature synthesis of $\text{Li}_{0.5}\text{Zr}_x\text{Co}_x\text{Fe}_{2.5-2x}\text{O}_4$ powder and their characterizations", Powder Technology, 2013 51 words — 1%
Crossref
-
- 8 Mohd. Hashim, Alimuddin, Shalendra Kumar, B.H. Koo et al. "Structural, electrical and magnetic properties of Co–Cu ferrite nanoparticles", Journal of Alloys and Compounds, 2012 50 words — 1%
Crossref
-
- 9 M.V. Chaudhari, R.H. Kadam, S.B. Shelke, Sagar E. Shirsath, A.B. Kadam, D.R. Mane. "Combustion synthesis of Co^{2+} substituted $\text{Li}_{0.5}\text{Cr}_{0.5}\text{Fe}_2\text{O}_4$ nano-powder: Physical and magnetic interactions", Powder Technology, 2014 49 words — 1%
Crossref
-
- 10 ir.amu.ac.in 48 words — 1%
Internet
-
- 11 M.V. Chaudhari, Sagar E. Shirsath, A.B. Kadam, R.H. Kadam, S.B. Shelke, D.R. Mane. "Site occupancies of Co–Mg–Cr–Fe ions and their impact on the properties of $\text{Co}_{0.5}\text{Mg}_{0.5}\text{Cr}_x\text{Fe}_{2-x}\text{O}_4$ ", Journal of Alloys and Compounds, 2013 44 words — 1%
Crossref
-
- 12 Calvin D. Pham, Jeffrey Chang, Mark A. Zurbuchen, Jane P. Chang. "Magnetic Properties of CoFe O Thin Films Synthesized by Radical-Enhanced Atomic Layer Deposition", ACS Applied Materials & Interfaces, 2017 37 words — 1%
Crossref
-
- 13 R.H. Kadam, Kirti Desai, Vishnu S. Shinde, Mohd. Hashim, Sagar E. Shirsath. "Influence of Gd^{3+} ion substitution on the MnCrFeO_4 for their nanoparticle shape formation and magnetic properties", Journal of Alloys and Compounds, 2016 36 words — 1%
Crossref

-
- 14 Zein K. Heiba, Mohamed Bakr Mohamed, Adel Maher Wahba, M. I. Almalowi. "Effect of vanadium doping on structural and magnetic properties of defective nano-nickel ferrite", Applied Physics A, 2018
Crossref 36 words — 1%
-
- 15 D. Bouokkeze, J. Massoudi, W. Hzez, M. Smari, A. Bougoffa, K. Khirouni, E. Dhahri, L. Bessais. "Investigation of the structural, optical, elastic and electrical properties of spinel LiZn Fe O nanoparticles annealed at two distinct temperatures ", RSC Advances, 2019
Crossref 35 words — 1%
-
- 16 www.iosrjournals.org
Internet 35 words — 1%
-
- 17 Zhu Yan, Juhua Luo. "Effects of Ce Zn co-substitution on structure, magnetic and microwave absorption properties of nickel ferrite nanoparticles", Journal of Alloys and Compounds, 2017
Crossref 34 words — 1%
-
- 18 Ghulam Mustafa, M.U. Islam, Wenli Zhang, Yasir Jamil, Abdul Waheed Anwar, Mudassar Hussain, Mukhtar Ahmad. "Investigation of structural and magnetic properties of Ce³⁺-substituted nanosized Co–Cr ferrites for a variety of applications", Journal of Alloys and Compounds, 2015
Crossref 31 words — 1%
-
- 19 etheses.saurashtrauniversity.edu
Internet 30 words — 1%
-
- 20 K.B. Modi, S.J. Shah, N.B. Pujara, T.K. Pathak, N.H. Vasoya, I.G. Jhala. "Infrared spectral evolution, elastic, optical and thermodynamic properties study on mechanically milled Ni_{0.5}Zn_{0.5}Fe₂O₄ spinel ferrite", Journal of Molecular Structure, 2013
Crossref 29 words — 1%
-
- 21 Shirsath, Sagar E., Mahesh L. Mane, Yukiko Yasukawa, Xiaoxi Liu, and Akimitsu Morisako. "Self-ignited high temperature synthesis and enhanced super-exchange

interactions of Ho³⁺–Mn²⁺–Fe³⁺–O²⁻ ferromagnetic nanoparticles", Physical Chemistry Chemical Physics, 2014.

Crossref

-
- 22 aip.scitation.org 28 words — 1%
Internet
-
- 23 Ameer Azam. "Microwave assisted synthesis and characterization of Co doped Cu ferrite nanoparticles", Journal of Alloys and Compounds, 2012 27 words — 1%
Crossref
-
- 24 folk.uio.no 26 words — 1%
Internet
-
- 25 S.K. Gurav, Sagar E. Shirsath, R.H. Kadam, S.M. Patange, K.S. Lohar, D.R. Mane. "Less magnetic and larger Zr⁴⁺–Zn²⁺ ions co-substituted structural and magnetic properties of ordered Li_{0.5}Fe_{2.5}O₄ nanoparticles", Materials Research Bulletin, 2013 26 words — 1%
Crossref
-
- 26 Pranav P Bardapurkar, Sunil S Shewale, Nilesh P Barde, Kamlakar M Jadhav. "Structural, magnetic and catalytical properties of cobalt ferrite nanoparticles dispersed in silica matrix", Materials Research Express, 2019 25 words — 1%
Crossref
-
- 27 Ankam Bhaskar, S.R. Murthy. "Effect of sintering temperatures on the elastic properties of Mn (1%) added MgCuZn ferrites", Journal of Magnetism and Magnetic Materials, 2014 24 words — 1%
Crossref
-
- 28 Reshma A. Nandotaria, Rajshree B. Jotania, Charanjeet Singh Sandhu, Mohd. Hashim et al. "Magnetic interactions and dielectric dispersion in Mg substituted M-type Sr-Cu hexaferrite nanoparticles prepared using one step solvent free synthesis technique", Ceramics International, 2018 23 words — < 1%
Crossref
-
- 29 K.S. Lohar, A.M. Pachpinde, M.M. Langade, R.H. Kadam, Sagar E. Shirsath. "Self-propagating high 21 words — < 1%

temperature synthesis, structural morphology and magnetic interactions in rare earth Ho³⁺ doped CoFe₂O₄ nanoparticles", *Journal of Alloys and Compounds*, 2014

Crossref

-
- 30 O.M. Hemeda, M.Z. Said, M.M. Barakat. "Spectral and transport phenomena in Ni ferrite-substituted Gd₂O₃", *Journal of Magnetism and Magnetic Materials*, 2001
20 words — < 1%
Crossref
-
- 31 www.nanoferrite.net
18 words — < 1%
Internet
-
- 32 Mohd. Hashim, Alimuddin, Sagar E. Shirsath, R.K. Kotnala et al. "Influence of Ni²⁺ substitution on the structural, dielectric and magnetic properties of Cu–Cd ferrite nanoparticles", *Journal of Alloys and Compounds*, 2013
17 words — < 1%
Crossref
-
- 33 Ghasemi, Ali, and Mohammad Mousavinia. "Structural and magnetic evaluation of substituted NiZnFe₂O₄ particles synthesized by conventional sol-gel method", *Ceramics International*, 2013.
17 words — < 1%
Crossref
-
- 34 Hemeda, O.M.. "Effect of gamma irradiation on the structural properties and diffusion coefficient in Co-Zn ferrite", *Journal of Magnetism and Magnetic Materials*, 200301
17 words — < 1%
Crossref
-
- 35 www.inl-journal.com
17 words — < 1%
Internet
-
- 36 Anjana Sharma, Khalid Mujasam Batoo, Emad H. Raslan, Syed Farooq Adil, Gagan Kumar. "Structural and magnetic study of Mn_{0.5}Zn_{0.5}Cu_xFe_{2-x}O₄ nanoferrites synthesized via solution combustion method", *Vacuum*, 2018
17 words — < 1%
Crossref
-
- 37 www.tf.uns.ac.rs
16 words — < 1%
Internet

38 Harpreet Kaur, Amrik Singh, Vijay Kumar, Dharamvir Singh Ahlawat. "Structural, thermal and magnetic investigations of cobalt ferrite doped with Zn²⁺ and Cd²⁺ synthesized by auto combustion method", Journal of Magnetism and Magnetic Materials, 2019

16 words — < 1%

Crossref

39 S.F. Mansour, M.A. Abdo, F.L. Kzar. "Effect of Cr dopant on the structural, magnetic and dielectric properties of Cu-Zn nanoferrites", Journal of Magnetism and Magnetic Materials, 2018

15 words — < 1%

Crossref

40 Jindi Feng, Rui Xiong, Li Cheng, Yong Liu. "Effect of Chromium Substitution on Structural and Magnetic Properties of Nickel-Cobalt Ferrite Nanoparticles Synthesized by Co-precipitation Method", Journal of Superconductivity and Novel Magnetism, 2017

15 words — < 1%

Crossref

41 Chaudhari, M.V., Sagar E. Shirsath, A.B. Kadam, R.H. Kadam, S.B. Shelke, and D.R. Mane. "Site occupancies of Co–Mg–Cr–Fe ions and their impact on the properties of Co_{0.5}Mg_{0.5}Cr_xFe_{2-x}O₄", Journal of Alloys and Compounds, 2013.

15 words — < 1%

Crossref

42 Tetiana Tatarchuk, Mariana Myslin, Ivan Mironyuk, Mohamed Bououdina et al. "Synthesis, morphology, crystallite size and adsorption properties of nanostructured Mg–Zn ferrites with enhanced porous structure", Journal of Alloys and Compounds, 2020

14 words — < 1%

Crossref

43 "Advanced Nanomaterials and Nanotechnology", Springer Nature, 2013

14 words — < 1%

Crossref

44 Ram A. Pawar, Sunil M. Patange, Qudsiya Y. Tamboli, V. Ramanathan, Sagar E. Shirsath. "Spectroscopic, elastic and dielectric properties of Ho³⁺ substituted Co-Zn ferrites synthesized by sol-gel method",

14 words — < 1%

45 Gabal, M.A., Y.M. Al Angari, and F.A. Al-Agel. "Cr-substituted Ni–Zn ferrites via oxalate decomposition. Structural, electrical and magnetic properties", *Journal of Magnetism and Magnetic Materials*, 2015.

Crossref

14 words — < 1%

46 onlinelibrary.wiley.com

Internet

14 words — < 1%

47 Saffari, F., P. Kameli, M. Rahimi, H. Ahmadvand, and H. Salamati. "Effects of Co-substitution on the structural and magnetic properties of NiCo_xFe_{2-x}O₄ ferrite nanoparticles", *Ceramics International*, 2015.

Crossref

13 words — < 1%

48 T.R. Tatarchuk, M. Bououdina, N.D. Paliychuk, I.P. Yaremiy, V.V. Moklyak. "Structural characterization and antistructure modeling of cobalt-substituted zinc ferrites", *Journal of Alloys and Compounds*, 2017

Crossref

13 words — < 1%

49 Rohit Jasrotia, Pooja Puri, Ankit Verma, Virender Pratap Singh. "Magnetic and electrical traits of sol-gel synthesized Ni-Cu-Zn nanosized spinel ferrites for multi-layer chip inductors application", *Journal of Solid State Chemistry*, 2020

Crossref

13 words — < 1%

50 S.S. Bellad, S.C. Watawe, B.K. Chougule. "Some ac electrical properties of Li–Mg ferrites", *Materials Research Bulletin*, 1999

Crossref

12 words — < 1%

51 R.A. Pawar, Sagar E. Shirsath, R.H. Kadam, R.P. Joshi, S.M. Patange. "Synthesis and magnetic properties of Cu_{0.7}Zn_{0.3}Al_xFe_{2-x}O₄ nanoferrites using egg-white method", *Journal of Magnetism and Magnetic Materials*, 2013

Crossref

12 words — < 1%

52 Somnath, Indu Sharma, R.K. Kotnala, M. Singh, Arun Kumar, Pooja Dhiman, Virender Pratap Singh,

12 words — < 1%

Kartikey Verma, Gagan Kumar. "Structural, magnetic and Mössbauer studies of Nd-doped Mg-Mn ferrite nanoparticles", Journal of Magnetism and Magnetic Materials, 2017

Crossref

53 M.A. Amer, T.M. Meaz, A.G. Mostafa, H.F. El-Ghazally. "Time effect of annealing on phase transformations of Cu–Al–Cr nano-ferrites prepared by a co-precipitation method", Materials Science in Semiconductor Processing, 2015

12 words — < 1%

Crossref

54 ijiet.com

Internet

12 words — < 1%

55 R.H. Kadam, A.P. Birajdar, Suresh T. Alone, Sagar E. Shirsath. "Fabrication of $\text{Co}_{0.5}\text{Ni}_{0.5}\text{Cr}_x\text{Fe}_{2-x}\text{O}_4$ materials via sol–gel method and their characterizations", Journal of Magnetism and Magnetic Materials, 2013

12 words — < 1%

Crossref

56 S.J. Haralkar, R.H. Kadam, S.S. More, Sagar E. Shirsath, M.L. Mane, Swati Patil, D.R. Mane. "Intrinsic magnetic, structural and resistivity properties of ferromagnetic $\text{Mn}_{0.5}\text{Zn}_{0.5}\text{Al}_x\text{Fe}_{2-x}\text{O}_4$ nanoparticles", Materials Research Bulletin, 2013

12 words — < 1%

Crossref

57 www.ijarse.com

Internet

12 words — < 1%

58 M.D. Hossain, M.A. Hossain, M.N.I Khan, S.S. Sikder, M.A. Hakim. "Frequency and temperature dependent magnetic properties with structural Rietveld refinement of $\text{Co}_{0.25}\text{Zn}_{0.75}\text{Y}_x\text{Fe}_{2-x}\text{O}_4$ ferrites", Journal of Magnetism and Magnetic Materials, 2020

11 words — < 1%

Crossref

59 Vivek Chaudhari, Sagar E. Shirsath, M.L. Mane, R.H. Kadam, S.B. Shelke, D.R. Mane. "Crystallographic, magnetic and electrical properties of $\text{Ni}_{0.5}\text{Cu}_{0.25}\text{Zn}_{0.25}\text{La}_x\text{Fe}_{2-x}\text{O}_4$ nanoparticles fabricated by

11 words — < 1%

60 T.P. Poudel, B.K. Rai, S. Yoon, D. Guragain, D. Neupane, S.R. Mishra. "The effect of gadolinium substitution in inverse spinel nickel ferrite: Structural, Magnetic, and Mössbauer study", Journal of Alloys and Compounds, 2019

11 words — < 1%

Crossref

61 Pourya Motavallian, Behzad Abasht, Omid Mirzaee, Hassan Abdollah-Pour. "Correlation between structural and magnetic properties of substituted (Cd, Zr) cobalt ferrite nanoparticles", Chinese Journal of Physics, 2019

11 words — < 1%

Crossref

62 Mazen, S. A., and N. I. Abu-Elsaad. "Structural, magnetic and electrical properties of the lithium ferrite obtained by ball milling and heat treatment", Applied Nanoscience, 2014.

11 words — < 1%

Crossref

63 S.M. Patange, Sagar E. Shirsath, S.P. Jadhav, V.S. Hogade, S.R. Kamble, K.M. Jadhav. "Elastic properties of nanocrystalline aluminum substituted nickel ferrites prepared by co-precipitation method", Journal of Molecular Structure, 2013

11 words — < 1%

Crossref

64 Sagar E. Shirsath, S.M. Patange, R.H. Kadam, M.L. Mane, K.M. Jadhav. "Structure refinement, cation site location, spectral and elastic properties of Zn²⁺ substituted NiFe₂O₄", Journal of Molecular Structure, 2012

11 words — < 1%

Crossref

65 M. Vadivel, R. Ramesh Babu, K. Ramamurthi, M. Arivanandhan. "Enhanced dielectric and magnetic properties of polystyrene added CoFe₂O₄ magnetic nanoparticles", Journal of Physics and Chemistry of Solids, 2017

11 words — < 1%

Crossref

66 Raghvendra Singh Yadav, Ivo Kuřitka, Jarmila Vilcakova, Jaromir Havlica et al. "Structural, magnetic, dielectric, and electrical properties of NiFe₂O₄ spinel

11 words — < 1%

ferrite nanoparticles prepared by honey-mediated sol-gel combustion", Journal of Physics and Chemistry of Solids, 2017

Crossref

67 Mehmet Kuru, Tuğba Şaşmaz Kuru, Ertuğrul Karaca, Sadık Bağcı. "Dielectric, magnetic and humidity properties of Mg–Zn–Cr ferrites", Journal of Alloys and Compounds, 2020 11 words — < 1%
Crossref

68 baadalsg.inflibnet.ac.in 10 words — < 1%
Internet

69 www.socialresearchfoundation.com 10 words — < 1%
Internet

70 V. Jagadeesha Angadi, A.V. Anupama, R. Kumar, S. Matteppanavar, B. Rudraswamy, B. Sahoo. "Observation of enhanced magnetic pinning in Sm³⁺ substituted nanocrystalline Mn Zn ferrites prepared by propellant chemistry route", Journal of Alloys and Compounds, 2016 10 words — < 1%
Crossref

71 jmrt.com.br 10 words — < 1%
Internet

72 M.A. Almessiere, Y. Slimani, S. Guner, M. Nawaz, A. Baykal, F. Aldakheel, A. Sadaqat, I. Ercan. "Effect of Nb substitution on magneto-optical properties of Co_{0.5}Mn_{0.5}Fe₂O₄ nanoparticles", Journal of Molecular Structure, 2019 10 words — < 1%
Crossref

73 Bato, Khalid Mujasam, and M.S. Abd El-sadek. "Electrical and magnetic transport properties of Ni-Cu-Mg ferrite nanoparticles prepared by sol-gel method", Journal of Alloys and Compounds, 2013. 10 words — < 1%
Crossref

74 linknovate.com 9 words — < 1%
Internet

75 Adel Maher Wahba, Mohamed Bakr Mohamed. "Structural, magnetic, and dielectric properties of nanocrystalline Cr-substituted $\text{Co}_{0.8}\text{Ni}_{0.2}\text{Fe}_2\text{O}_4$ ferrite", *Ceramics International*, 2014

Crossref

9 words — < 1%

76 Sonal Singhal, Sheenu Jauhar, Jagdish Singh, Kailash Chandra, Sandeep Bansal. "Investigation of structural, magnetic, electrical and optical properties of chromium substituted cobalt ferrites ($\text{CoCr}_x\text{Fe}_{2-x}\text{O}_4$, $0 \leq x \leq 1$) synthesized using sol gel auto combustion method", *Journal of Molecular Structure*, 2012

Crossref

9 words — < 1%

77 Lalita Chauhan, Nidhi Singh, Ajay Dhar, Harsh Kumar, Sudhanshu Kumar, K. Sreenivas. "Structural and electrical properties of Dy³⁺ substituted NiFe_2O_4 ceramics prepared from powders derived by combustion method", *Ceramics International*, 2017

Crossref

9 words — < 1%

78 A.M. Pachpinde, M.M. Langade, K.S. Lohar, S.M. Patange, Sagar E. Shirsath. "Impact of larger rare earth Pr^{3+} ions on the physical properties of chemically derived $\text{Pr}_x\text{CoFe}_{2-x}\text{O}_4$ nanoparticles", *Chemical Physics*, 2014

Crossref

9 words — < 1%

79 www.ijert.org

Internet

9 words — < 1%

80 "Handbook of Sol-Gel Science and Technology", Springer Science and Business Media LLC, 2018

Crossref

9 words — < 1%

81 pubs.acs.org

Internet

9 words — < 1%

82 S.T. Alone, Sagar E. Shirsath, R.H. Kadam, K.M. Jadhav. "Chemical synthesis, structural and magnetic properties of nano-structured Co-Zn-Fe-Cr ferrite", *Journal of Alloys and Compounds*, 2011

Crossref

9 words — < 1%

- 83 Modi, K.B.. "Structural properties of magnesium and aluminium co-substituted lithium ferrite", Materials Letters, 200308
Crossref 8 words — < 1%
- 84 Qing Lin, Yun He, Jinpei Lin, Fang Yang, Liping Wang, Jianghui Dong. "Structural and magnetic studies of Mg substituted cobalt composite oxide catalyst Co₁-Mg Fe₂O₄", Journal of Magnetism and Magnetic Materials, 2019
Crossref 8 words — < 1%
- 85 M Manjurul Haque. "Thermal hysteresis of permeability and transport properties of Mn substituted Mg-Cu-Zn ferrites", Journal of Physics D Applied Physics, 03/07/2008
Crossref 8 words — < 1%
- 86 R.E. El-Shater, H. El Shimy, S.T. Assar. "Investigation of physical properties of synthesized Zr doped Ni-Zn ferrites", Materials Chemistry and Physics, 2020
Crossref 8 words — < 1%
- 87 K. Vijaya Babu, G. Satyanarayana, B. Sailaja, G.V. Santosh Kumar, K. Jalaiah, M. Ravi. "Structural and magnetic properties of Ni_{0.8}M_{0.2}Fe₂O₄ (M=Cu, Co) nanocrystalline ferrites", Results in Physics, 2018
Crossref 8 words — < 1%
- 88 Prita Pant Sarangi. "Development of a Novel Aqueous Solution Based Chemical Methodology for Synthesis of Ni(1-x)Zn_xFe₂O₄ Nanopowders and their Electrical and Magnetic Property", Integrated Ferroelectrics, 2010
Crossref 8 words — < 1%
- 89 www.rrcollege.org
Internet 8 words — < 1%
- 90 ethesis.nitrkl.ac.in
Internet 8 words — < 1%
- 91 Mane, M.L.. "Effects of Nd:YAG laser irradiation on structural, morphological, cation distribution and

92 Md.D. Rahaman, Tania Nusrat, Rumana Maleque, A.K.M. Akther Hossain. "Investigation of structural, morphological and electromagnetic properties of $\text{Mg}_{0.25}\text{Mn}_{0.25}\text{Zn}_{0.5-x}\text{Sr}_x\text{Fe}_2\text{O}_4$ ferrites", Journal of Magnetism and Magnetic Materials, 2018

7 words — < 1%

Crossref

93 Mane, M.L.. "Modifications in structural, cation distribution and magnetic properties of ^{60}Co gamma irradiated Li-ferrite", Nuclear Inst. and Methods in Physics Research, B, 20110915

7 words — < 1%

Crossref

94 M. A. Ahmed, A. A. Azab, E. H. El-Khawas, E. Abd EL Bast. " Characterization and Transport Properties of Mixed Ferrite System MnCuFeO ; $0.0 \leq x \leq 0.7$ ", Synthesis and Reactivity in Inorganic, Metal-Organic, and Nano-Metal Chemistry, 2015

6 words — < 1%

Crossref

95 D.M. Jnaneshwara, D.N. Avadhani, B. Daruka Prasad, B.M. Nagabhushana et al. "Effect of zinc substitution on the nanocobalt ferrite powders for nanoelectronic devices", Journal of Alloys and Compounds, 2014

6 words — < 1%

Crossref

96 R.H. Kadam, Kirti Desai, Supriya R. Kadam, Sagar E. Shirsath. "Variation in the structural and magnetic properties of heterovalent Mn^{2+} - Si^{4+} substituted MnCrFeO nanoparticles", Solid State Sciences, 2013

6 words — < 1%

Crossref

97 H.R. Lakshmiprasanna, V. Jagadeesha Angadi, B. Rajesh Babu, Mehaboob Pasha, K. Manjunatha, Shidaling Matteppanavar. "Effect of Pr^{3+} -doping on the structural, elastic and magnetic properties of Mn-Zn ferrite nanoparticles prepared by solution combustion synthesis method", Chemical Data Collections, 2019

6 words — < 1%

Crossref

EXCLUDE QUOTES OFF

EXCLUDE
BIBLIOGRAPHY ON

EXCLUDE MATCHES OFF

Dr.R.H.KADAM

123.doc



[Name of the proceedings]

34

Rietveld refinement, morphological and magnetic properties of rare earth doped Co-Zn nanoferrites.

C. U. Nikam^a, R. A. Thite^b, R. H. Kadam^b, S. S. Satpute^b, S. T. Alone^{c*}, S. E. Shirsath^d,
G. H. Kale^a

^aDepartment of Electronics, Y. C. College, Tuljapur, Dist. Osmanabad (M.S.) India

^bMaterials Science Research Laboratory, Shrikrishna Mahavidyalaya, Gutti, Dist. Osmanabad (M.S.) India

^cDepartment of Physics, Rajarshi Shahu College, Pathri, Dist. Aurangabad (M.S.) India

^dSchool of Materials Science and Engineering, University of New South Wales, Sydney, NSW 2052.

Abstract

Magnetic nanoparticles have been extensively studied in the recent past due to their long range of applications in electronics industries and biomedical fields. In the present work nano-particles of $\text{Co}_{0.9}\text{Zn}_{0.2}\text{Dy}_x\text{Fe}_{1.9-x}\text{O}_4$ were synthesized by using sol-gel auto-combustion method. The structural, morphological and magnetic properties have been investigated by using X-ray diffraction (XRD), scanning electron microscopy (SEM), energy dispersive X-ray analysis (EDAX) and vibrating sample magnetometer (VSM) techniques. Rietveld refined XRD patterns reveal the single-phase cubic spinel structure of the samples with $\text{Fd}3\text{m}$ space group. Introduction of Dy^{3+} ions in Co-Zn matrix increases the lattice lengths from 8.3641 to 8.3719 Å. Crystallite size obtained from Scherer equation varies from 15.2 to 17.3 nm. Surface morphology of the samples has been studied by using SEM images and elemental analysis was done by using EDAX spectra. The nanocrystalline nature of the samples was confirmed by using TEM images. Magnetic hysteresis loops clearly indicate the ferromagnetic nature of the samples. Introduction of higher magnetic Dy^{3+} ions increase the saturation magnetization from 62.53 to 91.03 emu/gm while as reduces the coercivity from 819 to 589 Oe.

[copyright information to be updated in production process]

Keywords: Rietveld refinement, crystallite size, saturation magnetization, coercivity.

42

1. INTRODUCTION

Magnetic nanoparticles, especially spinel ferrites with nano-scale dimensions attracts much attention due to their versatile applications in electronic and microwave devices, high density storage devices, transformer cores, recording media, magnetic fluids, high frequency devices and memory chips in computers etc. [1-4]. The physical properties of spinel ferrites strongly depend upon the factors like ionic radii of constituent ions, particle size and can be tailored by choosing the different substitute and their concentrations for desired applications. In the recent past, Co-Zn ferrites have covers remarkable space in the field of materials science due to its long-range applicability in modern technology [5-6]. They have been used as an active material for super-capacitive energy storage devices, catalysis and microwave application. It is known that introduction of rare earth (RE) ion in spinel lattice can competently modifies the electrical and magnetic properties. Due to larger ionic radii, introduction of RE ions in spinel lattice may generate the internal stress and drive the cell symmetry. RE ions have unpaired 4f electrons and possesses strong spin-orbit coupling and angular momentum. The spin coupling effect (Fe^{3+} - Fe^{2+} ion interaction) and 3d-4f coupling effect (RE-Fe ion interaction) observed in the spinel lattice due to the incorporation of RE ion governs the electrical conduction and magnetic interactions in the magnetic oxides [7-9]. This is due the unpaired 4f electrons

The noteworthy magnetic, electrical and optical properties of RE doped spinel ferrites make them capable candidate for technological applications [10-12]. Several researchers have been carried out systematic investigations on the effect of RE ion substitution in spinel lattice and studied their structural, electrical and magnetic behavior. Recently, substitution of Nd^{3+} ion in Co-Zn lattice mentioned the improvement in magnetic properties while as Gd^{3+} ions reduce the saturation magnetization and coercivity [13-14]. For a desired application, the substitution of Ce^{3+} ions have recently been used to investigate the structural and elastic properties of Ni-Mn-Zn ferrites [15]. The replacement of Fe^{3+} ions by Ho^{3+} ions enhance the structural parameters and magnetic properties of Co-Ni ferrites [16]. In the present investigation have synthesized the Dy^{3+} doped Co-Zn ferrites by using sol-gel method and systematically investigated their structural and magnetic properties. Structural profile of the prepared samples was investigated by using Rietveld Refinement done by using FullProf software.

2. MATERIALS AND METHODS

Dy^{3+} doped $\text{Co}_{0.9}\text{Zn}_{0.2}\text{Dy}_x\text{Fe}_{1.9-x}\text{O}_4$ ($x = 0.0, 0.015, 0.030, 0.045$ and 0.06) nano-ferrites were obtained by using sol-gel auto-combustion route. AR grade metal nitrates with high purity (~99 % pure) of all the constituent elements were taken as starting materials. All the starting material were taken with their weight proportion in the composition and mixed in sufficient amount of double distilled water under continuous stirring for half an hour. Citric acid acts as chelating agent and taken in the weight proportion of 1:3. Afterwards the whole mixture was kept on magnetic stirrer with hot plate and started heating for constant temperature of 90°C . The pH of the solution was maintained at 7 by adding the liquid ammonia under continuous stirring and heating. After couple of hours, the solution becomes viscous and converted into gel. At this point, after some time, the dried gel suddenly converted into brown ash by self-ignition process. After grinding and sintering at 900°C for 6 hours, the fluffy samples get converted into fine powders. Room temperature powder X-ray diffraction patterns were taken for all the samples in the scanning range of 20° to 70° by using the $\text{Cu-K}\alpha$ radiations having the wavelength 1.5405 \AA . All the XRD patterns were recorded by using an X-ray diffractometer (Bruker, Model: D8 Advance – AXS) at 360 V and 5.5 A fitted with nickel filter. Scanning electron micrographs of selected samples were collected by using ZEISS (SUPRA 55) microscope and transmission electron micrographs were collected by using a high-resolution TEM microscope (Philips make) operating to an accelerating voltage 300 kV. The magnetic behavior of the samples was studied by using a vibrating sample magnetometer as a function of applied magnetic field (up to 15000 Oe).

3. RESULTS AND DISCUSSION

Rietveld refined XRD patterns of Dy^{3+} substituted Co-Zn ferrites are depicted in Fig. 1. All the XRD patterns were analyzed by using FullProf program for Rietveld refinement. The Rietveld refinement was performed for all the samples by using all the initial input parameters of spinel cubic structure. To minimize the difference between experimental and simulated diffraction patterns, the least-square minimization procedure was carried out by monitoring the reliability factors such as weighted/unweighted profile R-factor ($R_{\text{WP}}/R_{\text{P}}$), expected R-factor (R_{EXP}) and goodness fit factor (χ^2). Thomson-Cox-Hasting pseudo-Voigt was employed to refine the XRD profiles based on cubic symmetry. Oxygen positions, lattice constant, peak shapes, and site occupancies were considered as free parameters while as atomic fractional positions were taken as free parameters. As seen in figure, all the reflections were indexed for the planes (220), (311), (222), (400), (422), (511), (440) identifying the space group $\text{Fd}\bar{3}\text{m}$. These peaks confirm the single-phase cubic spinel structure of the samples and matched well with the standard crystallographic open database (Card No. 96-900-2674) [17]. The values of goodness factor obtained from Rietveld refinement for all the samples are obtained between 1 to 2, which indicate the quality of fitting. Table 1 represents the values of goodness factor (χ^2) and the reliability factors (R_{P} , R_{WP} and R_{EXP}) and lattice parameter obtained from Rietveld refinement. It can be seen that the lattice constant increases from 8.3641 \AA to 8.3719 \AA for the substitution of Fe^{3+} ions by Dy^{3+} ions which can be explained on the basis of ionic radii differences of constituent ions. Here in the present case, larger Dy^{3+} ions (1.05 \AA) replace the Fe^{3+} ions having comparatively small ionic radii (0.64 \AA) in Co-Zn lattice and hence enhances the lattice lengths. Crystal structure obtained from Rietveld refinement for cubic spinel Co-Zn ferrites is shown in the right bottom corner of Fig. 1.

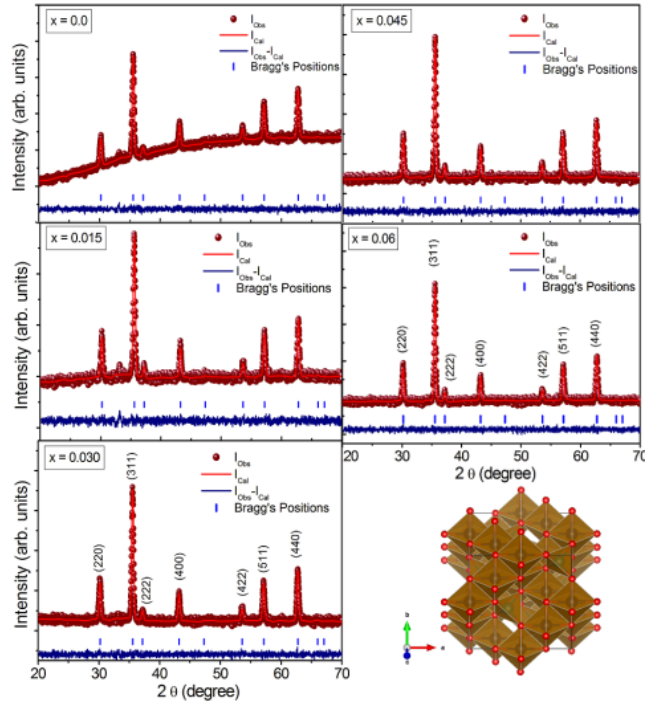


Fig. 1. Rietveld refined XRD patterns and crystal structure of $\text{Co}_{0.9}\text{Zn}_{0.2}\text{Dy}_x\text{Fe}_{1.9-x}\text{O}_4$

Sharp and intensive Bragg's lines indicate the fine crystallinity of the samples. Shifting of Bragg's positions towards lower 2θ angles enhance the lattice lengths with the substitution of Dy^{3+} ions. Bragg's positions and full width at half of the maximum of Bragg's lines were considered in Debye-Scherrer equation [18] and the values of average crystallite size were obtained.

$$t_{D-S} = \frac{0.9\lambda}{\beta_{hkl} \cos \theta_B} \quad (1)$$

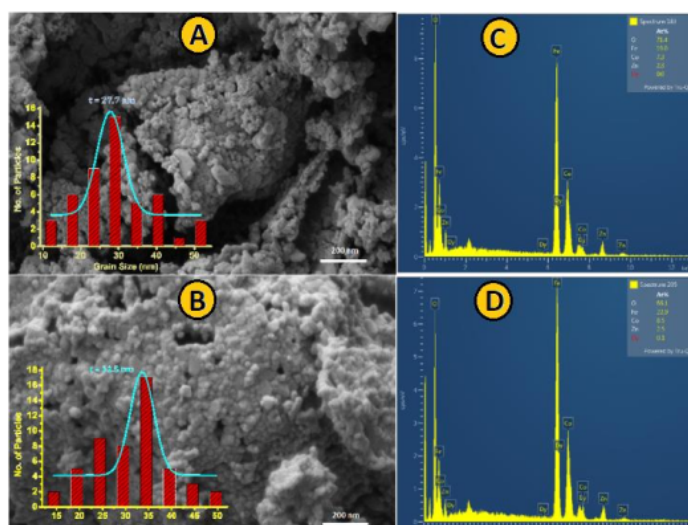
Where, t_{D-S} is the average crystallite size, λ - incident wavelength, β_{hkl} - full width at half of the maximum, θ_B - is the Bragg's position. Table 1 represents the values of average crystallite size estimated by using above relation. Crystallite size was observed in the nano-meter range and found increasing from 15.2 nm to 17.3 nm with increasing amount of Dy^{3+} ions in Co-Zn lattice.

Table 1: Lattice constant (a), Rietveld refined parameters and average crystallite size (t).

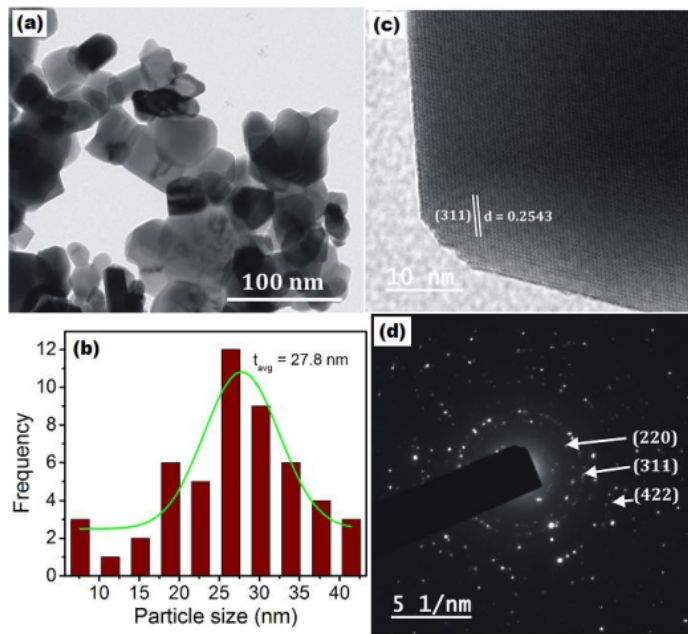
Comp. 'x'	'a' (Å)	Rietveld refined parameters				't _{D-S} ' (nm)
		R _P	R _{WP}	R _{Exp.}	χ^2	
0.0	8.3641	28.4	19.9	14.51	1.88	15.2
0.015	8.3669	18.7	19.3	14.15	1.86	15.7
0.030	8.3682	22.6	17.4	13.36	1.69	16.4
0.045	8.3694	19.1	16.2	12.62	1.64	16.7
0.060	8.3719	24.5	17.4	13.77	1.61	17.3

Fig. 2 (A, B) represents the scanning electron micrographs of the typical samples of Dy^{3+} doped $\text{Co}_{0.9}\text{Zn}_{0.2}\text{Dy}_x\text{Fe}_{1.9-x}\text{O}_4$ ($x = 0.0$ and 0.030) spinel ferrites. Surface morphology of the samples was understood by using SEM micrographs. SEM images shows that most of ferrite grains are of spherical shape with variation in size.

The grain size obtained from SEM analysis by using the software Image J for the sample $x = 0.0$ is 27.7 nm and for $x = 0.03$ is 33.5 nm which is analogous with XRD results. The grain size obtained is quite higher than that of average crystallite size obtained from XRD analysis, this may be due to the presence of small agglomerates and increases with Dy^{3+} substitution. With some limitations, EDAX is a powerful tool for elemental analysis present the composition. Fig. 2 (C, D) represents the energy dispersive X-ray spectra of the samples $x = 0.0$ and 0.03. EDAX patterns confirm the homogeneity of the samples and stoichiometric proportion of pure and doped Co-Zn ferrites.



7
Fig. 2. SEM images (A: $x=0.0$, B: $x = 0.03$) and EDAX patterns (C: $x=0.0$, D: $x=0.03$) of $Co_{0.9}Zn_{0.2}Dy_xFe_{1.9-x}O_4$



26
Fig. 3. (a) TEM image, (b) Particle size distribution histogram, (c) HRTEM, and (d) SAED pattern of typical sample $x = 0.03$ of $Co_{0.9}Zn_{0.2}Dy_xFe_{1.9-x}O_4$

Transmission electron micrograph of typical Dy³⁺ doped Co-Zn ferrites with x = 0.03, corresponding particle size distribution histogram, high resolution image (HR-TEM) and selected area electron diffraction (SAED) pattern are depicted in Fig. 3. TEM image exhibits the particles have cubic and spherical shape with nano-size distribution. The particle size distribution was evaluated by using the software Image J. As seen in Fig. 3 (b) particle size distributed from 10 nm to 40 nm with some agglomeration. Average size obtained by Gaussian fitting the chart in Origin and the mean value was obtained 27.8 nm which was found slightly higher than the XRD value. The force on the particles will rise due to the strong interaction between magnetic dipole and Van der Waals force after surface effects. Hence the aggregation of the particles will be formed and the size increases [19]. HR-TEM image shows the visible fringes with d-spacings 0.2543 nm which corresponds to the (311) plane which is a high intensity peak observed in XRD plot. SAED pattern (Fig. 3 (d)) shows the bright spots arranged in well-defined concentric rings corresponds to the cubic spinel planes (220), (311) and (422).

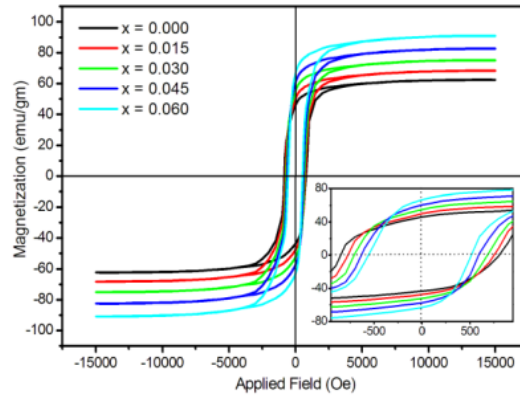


Fig. 4. Hysteresis curves for $\text{Co}_{0.9}\text{Zn}_{0.2}\text{Dy}_x\text{Fe}_{1.9-x}\text{O}_4$ where inset shows the expanded view.

The magnetic characterization of all the samples of $\text{Co}_{0.9}\text{Zn}_{0.2}\text{Dy}_x\text{Fe}_{1.9-x}\text{O}_4$ was carried out by using the hysteresis loops shown in Fig. 4 for the applied field of 1.5 kOe. S-shaped M-H loops can be more saturated after 1 kOe of applied field. Different magnetic parameter such as saturation magnetization (M_s), remanent magnetization (M_r), remanent ratio (M_r/M_s), coercivity (H_c), anisotropy constant (K) and magneton number (μ_B) in Bohr magneton were estimated by using the hysteresis loops. Copper ferrite shows the properties of semi-hard ferrites with high saturation magnetization and moderate coercivity. Generally, in ferrites, Fe^{3+} ions can be replaced by transition metal ions having less magnetic moment and hence the magnetization of the composition dropped with the addition of TM ions. On the other hand, when rare earth ion having higher magnetic moment replaces the Fe^{3+} ions at octahedral sites increases the saturation magnetization of the spinel ferrites [20].

The substitution of Dy³⁺ ions in Co-Zn lattice influences the magnetic properties of spinel ferrite. On the introduction of Dy³⁺ ions increase the saturation magnetization from 62.53 emu/gm to 91.03 emu/gm and remnant magnetization increases from 43.56 emu/gm to 66.41 emu/gm. This is because the Dy³⁺ ions has higher magnetic moment ($10.48\mu_B$) as compare to the Fe^{3+} ions ($5\mu_B$). Table 2 represents the values of M_s , M_r , M_r/M_s , H_c , K and n_B for $\text{Co}_{0.9}\text{Zn}_{0.2}\text{Dy}_x\text{Fe}_{1.9-x}\text{O}_4$.

Table 2: Magnetic Properties of $\text{Co}_{0.9}\text{Zn}_{0.2}\text{Dy}_x\text{Fe}_{1.9-x}\text{O}_4$

x	M_s (emu/gm)	M_r (emu/gm)	M_r/M_s	H_c (Oe)	$K \times 10^4$	$n_B (\mu_B)$
0.0	62.53	43.56	0.697	819	5.3342	2.645
0.015	68.37	48.25	0.706	765	5.4482	2.911
0.030	75.22	53.21	0.709	703	5.5083	3.225
0.045	82.65	59.12	0.719	646	5.5616	3.567
0.060	91.03	66.41	0.730	589	5.5850	3.954

Coercivity (H_c) of the magnetic oxides can be related through the following relation [21];

$$H_c = \frac{2K_1}{\mu_0 M_s} \quad (2)$$

Values of coercivity (H_c) with Dy^{3+} substitution decreases from 819 Oe to 589 Oe. As seen in above equation anisotropy constant is directly proportional to the product of coercivity and saturation magnetization. Here substitution of Dy^{3+} ions increase the anisotropy constant from 5.3342×10^4 to 5.3342×10^4 . Magnetic moment per formula unit in Bohr Magnetron was computed by using the following relation [22];

$$n_B(\mu_B) = \frac{M_w M_s}{5585} \quad (3)$$

Where, M_w – is the molecular weight and M_s – is the saturation magnetization. Computed values of magneton number are given in Table 2 and it was found that the magneton number increase from $2.645 \mu_B$ to $3.954 \mu_B$ with Dy^{3+} substitution.

4. CONCLUSIONS

Polycrystalline nano-particles of Dy^{3+} substituted Co-Zn ferrites have been successfully prepared by using sol-gel auto-combustion method. Sharp and well indexed XRD lines indicates the single-phase cubic spinel geometry of the samples. Goodness factor obtained from Rietveld refinement reveals the fitting quality of the XRD patterns. Substitution of Dy^{3+} ions in Co-Zn crystal lattice enhances the lattice lengths which may be due to the replacement of smaller Fe^{3+} ions by larger Dy^{3+} ions. Crystallite size obtained from Debye-Scherrer equation reveals the nanocrystalline nature of the samples. SEM and TEM images confirms the nanocrystalline nature of the samples. Introduction of higher magnetic Dy^{3+} ions in Co-Zn lattice increases the saturation magnetization and remnant magnetization and decreases the coercivity of the samples.

5. REFERENCES

- [1] M. N. Akhtar, M. Babar, S. Qamar, Z. U. Rehman, M. A. Khan, *Ceram. Inter.* 45 (2019) 10187-10195.
- [2] S. R. Wadgane, S. T. Alone, A. Karim, G. Vats, S. E. Shirsath, R. H. Kadam, *J. Magn. Magn. Mater.* 471 (2019) 388-393.
- [3] S. K. Gurav, S. E. Shirsath, R. H. Kadam, D. R. Mane, *Powd. Techn.* 235 (2013) 485 – 492.
- [4] N. Yahya, M. N. Akhtar, K. Kozoi, *J. Nanosci. Nanotech.* 12 (2012) 8116-8122.
- [5] V. More, S. Kadam, S. Shelke, P. Gaikwad, R. Kadam, S. Alone, *Biointer. Res. Appl. Chem.* 12 (2022) 5021-5030.
- [6] Y. Silmani, H. Gungunes, M. Nawaz, A. Manikandan, H. S. El Sayed, M. A. Almessiere, H. Sozeri, S. E. Shirsath, I. Ercan, A. Baykal, *Ceram. Inter.* 44 (2018) 14242-14250.
- [7] V. D. More, S. S. Kadam, S. R. Kadam, S. R. Wadgane, R. H. Kadam, S. T. Alone, *Macromole. Symp.* 400 (2021) 2100115.
- [8] R. Rani, K. M. Batoo, P. Sharma, G. Anand, G. Kumar, S. Bhardwaj, M. Singh, *Ceram. Inter.* 47 (2021) 30902-30910.
- [9] A. B. Gaikwad, T. J. Shinde, P. N. Vasambekar, *Mater. Chem. Phys.* 114 (2009) 505-510.
- [10] G. B. Todkar, R. A. Kunale, R. N. Kamble, K. M. Batoo, M. F. Ijaz, A. Imran, M. Hadi, E. H. Raslan, S. E. Shirsath, R. H. Kadam, *J. Phys. D: Appl. Phys.* 54 (2021) 294001.
- [11] C. Stergiou, *J. Magn. Magn. Mater.* 426 (2017) 629-635.
- [12] S. R. Naik, A. V. Salker, *J. Mater. Chem.* 22 (2012) 2740-2750.
- [13] P. P. Naik, R. B. Tangsali, S. S. Meena, S. M. Yusuf, *Mater. Chem. Phys.* 191 (2017) 215-224.
- [14] S. Joshi, M. Kumar, S. Chhoker, A. Kumar, M. Singh, *J. Magn. Magn. Mater.* 426 (2017) 252-263.
- [15] V. D. More, R. B. Borade, K. R. Desai, V. K. Barote, S. S. Kadam, V. S. Shinde, D. R. Kulkarni, R. H. Kadam, S. T. Alone, *Nano* 16 (2021) 2150059.
- [16] D. V. Phugate, R. B. Borade, S. B. Kadam, L. A. Dhale, R. H. Kadam, S. E. Shirsath, A. B. Kadam, *J. Supercond. Nov. Magn.* 33 (2020) 3545-3554.
- [17] H. Fjellvag, B. C. Hauback, T. Vogt, S. Stolen; *Amer. Miner.* 87 (2002) 347-349.

- [18] S. E. Shirsath, R. H. Kadam, K. M. Bato, D. Wang, S. Li; *J. Phys. D: Applied Physics*; 54 (2021) 024001
- [19] S. Li, P. Jiatong, G. Feng, Z. Deqian, Q. Feng, H. Chunlin, D. Gjergi, W. Yuezou, F. Toyohisa, *J. Mater. Sci: Mater. Electron.* 32 (2021) 13511-13526.
- [20] R. H. Kadam, R. B. Borade, M. L. Mane, D. R. Mane, K. M. Bato, S. E. Shirsath, *RSC Advances* 10 (2020) 27911.
- [21] V. Chaudhari, R. H. Kadam, M. L. Mane, S. E. Shirsath, A. B. Kadam, D. R. Mane, *J. Nanosci. Nanotech.* 14 (2014) 1-8.

20%

SIMILARITY INDEX

PRIMARY SOURCES

- 1 Vikram More, R. B. Borade, Kirti Desai, V. K. Barote, S. S. Kadam, V. S. Shinde, D. R. Kulkarni, R. H. Kadam, S. T. Alone. " Site occupancy, surface morphology and mechanical properties of Ce added Ni-Mn-Zn ferrite nanocrystals synthesized via sol-gel route ", Nano, 2021 31 words — 1%

[Crossref](#)
- 2 K.R. Desai, S.T. Alone, S.R. Wadgane, Sagar E. Shirsath et al. "X-ray diffraction based Williamson-Hall analysis and rietveld refinement for strain mechanism in Mg-Mn co-substituted CdFe₂O₄ nanoparticles", Physica B: Condensed Matter, 2021 25 words — 1%

[Crossref](#)
- 3 Gadkari, A.B.. "Structural analysis of Y³⁺-doped Mg-Cd ferrites prepared by oxalate co-precipitation method", Materials Chemistry and Physics, 20090415 21 words — 1%

[Crossref](#)
- 4 K.V. Zipare, S.S. Bandgar, G.S. Shahane. "Effect of Dy-substitution on structural and magnetic properties of Mn Zn ferrite nanoparticles", Journal of Rare Earths, 2018 21 words — 1%

[Crossref](#)
- 5 LI, L.. "Preparation and magnetic properties of Cu⁰·4Zn⁰·6Cr⁰·5Sm⁰·0⁶Fe¹·4⁴⁰4/polyaniline nanocomposites", Journal of Rare Earths, 200808 21 words — 1%

[Crossref](#)

6 Sagar M. Mane, Aviraj M. Teli, Nishant T. Tayade, Kanchan J. Pawar et al. "Correlative structural refinement-magnetic tunability, and enhanced magnetostriction in low-temperature, microwave-annealed, Ni-substituted CoFe₂O₄ nanoparticles", Journal of Alloys and Compounds, 2022 21 words — 1%

Crossref

7 Kadam, R.H., Kirti Desai, Vishnu S. Shinde, Mohd. Hashim, and Sagar E. Shirsath. "Influence of Gd³⁺ ion substitution on the MnCrFeO₄ for their nanoparticle shape formation and magnetic properties", Journal of Alloys and Compounds, 2016. 20 words — 1%

Crossref

8 Chnar Aziz, Bruska Azhdar. "Synthesis of dysprosium doped cobalt ferrites nanoparticles by solgel auto-combustion method and influence of grinding techniques on structural, Morphological, and magnetic properties", Journal of Magnetism and Magnetic Materials, 2022 18 words — 1%

Crossref

9 www.jetir.org 17 words — 1%

Internet

10 Anil B. Mugutkar, Shyam K. Gore, Rajaram S. Mane, Khalid M. Batoor, Syed F. Adil, Santosh S. Jadhav. "Magneto-structural behaviour of Gd doped nanocrystalline Co-Zn ferrites governed by domain wall movement and spin rotations", Ceramics International, 2018 16 words — 1%

Crossref

11 Ankurava Sinha, Abhigyan Dutta. "Structural, optical, and electrical transport properties of some rare-earth-doped nickel ferrites: A study on effect of ionic radii of dopants", Journal of Physics and Chemistry of Solids, 2020 15 words — 1%

Crossref

12 Filipe M. Figueiredo. "Influence of Microstructure on the Electrical Properties of Iron-Substituted Calcium Titanate Ceramics", Journal of the American Ceramic Society, 12/2004

Crossref

15 words — 1%

13 K.S. Lohar, A.M. Pachpinde, M.M. Langade, R.H. Kadam, Sagar E. Shirsath. "Self-propagating high temperature synthesis, structural morphology and magnetic interactions in rare earth Ho³⁺ doped CoFe₂O₄ nanoparticles", Journal of Alloys and Compounds, 2014

Crossref

15 words — 1%

14 Dapeng Zhu, Weiwei Liu, Rongzhi Zhao, Zhen Shi, Xiangyang Tan, Zhenhua Zhang, Yixing Li, Lianze Ji, Xuefeng Zhang. "Microscopic insights into hydrophobicity of cerium oxide: Effects of crystal orientation and lattice constant", Journal of Materials Science & Technology, 2022

Crossref

13 words — < 1%

15 R.E. Elshater, G. Kawamura, F. Fakhry, T. Meaz, M.A. Amer, A. Matsuda. "Structural phase transition of spinel to hematite of as-prepared Fe²⁺-Cr nanoferrites by sintering temperature", Measurement, 2019

Crossref

13 words — < 1%

16 P. Himakar, N. Murali, D. Parajuli, V. Veeraiah et al. "Magnetic and DC Electrical Properties of Cu Doped Co-Zn Nanoferrites", Journal of Electronic Materials, 2021

Crossref

12 words — < 1%

17 www.ijirset.com

Internet

12 words — < 1%

18 Anil B. Mugutkar, Shyam K. Gore, Rajaram S. Mane, Sunil M. Patange et al. "Structural modifications in Co-Zn nanoferrites by Gd substitution triggering to dielectric and gas sensing applications", Journal of Alloys and Compounds, 2020 11 words — < 1%
Crossref

19 S. S. Satpute, S. R. Wadgane, S. R. Kadam, D. R. Mane, R. H. Kadam. "Y³⁺ substituted Sr-hexaferrites: sol-gel synthesis, structural, magnetic and electrical characterization", Cerâmica, 2019 11 words — < 1%
Crossref

20 Atiq ur Rehman, S. F. Shaukat, Majid Niaz Akhtar, Mukhtar Ahmad. "A Study of Structural, Magnetic and Various Dielectric Parameters of Ca-Substituted W-Type Hexaferrites for Applications at 1–6 GHz Frequencies", Journal of Electronic Materials, 2019 10 words — < 1%
Crossref

21 Murli Kumar Manglam, Sushree Nibedita Rout, Suman Kumari, Sunil Kumar, Manoranjan Kar. "Structural, magnetic and optical properties of (0.45) Ni_{0.5}Zn_{0.5}Fe₂O₄ + (0.55) BaFe₁₂O₁₉ composite", Materials Today: Proceedings, 2022 10 words — < 1%
Crossref

22 R.M. Kershi. "Rare-earth ions as a key influencer on the magnetic, spectroscopic and elastic properties of EryZn_{0.2}Co_{0.8}Fe₂-yO₄ nanoparticles", Journal of Alloys and Compounds, 2021 10 words — < 1%
Crossref

23 Ravindra N. Kambale, Sunil M. Patange, R.A. Pawar, Sagar E. Shirsath, K.G. Suresh, Vaishali A. Bambole. "Magnetically recoverable CoFe_{1.9}Gd_{0.1}O₄ ferrite/polyaniline nanocomposite synthesized via green 10 words — < 1%

approach for radar band absorption", Ceramics International, 2021

Crossref

24 A. A. Kadam, K. Y. Rajpure. "Compositional variation of structural, electrical and magnetic properties of Dy substituted Ni-Co spinel ferrite", Journal of Materials Science: Materials in Electronics, 2016

9 words — < 1%

Crossref

25 G D Kulkarni, S R Patade, R R Parlikar, Gopale, R R Chilwar, T. S. Saraf, K M Jadhav. " Green synthesis of NiFe O nanoparticles using different fuels and their structural characterization ", Journal of Physics: Conference Series, 2020

9 words — < 1%

Crossref

26 Jaiswal, R., N. Patel, D.C. Kothari, and A. Miotello. "Improved visible light photocatalytic activity of TiO₂ co-doped with Vanadium and Nitrogen", Applied Catalysis B Environmental, 2012.

9 words — < 1%

Crossref

27 M. Ishaque, Muhammad Azhar Khan, Irshad Ali, Muhammad Athair, Hasan M. Khan, M. Asif Iqbal, M.U. Islam, Muhammad Farooq Warsi. "Synthesis of nickel-zinc-yttrium ferrites: Structural elucidation and dielectric behavior evaluation", Materials Science in Semiconductor Processing, 2016

9 words — < 1%

Crossref

28 journal.hep.com.cn

Internet

9 words — < 1%

29 A. Sandeep, G. Ganesh, S. Swathi, N. Rajesh et al. "Synthesis, structural, magnetic and optical studies of Eu doped Ni-Zn nano ferrites", Ceramics International, 2022

8 words — < 1%

Crossref

30 D.R. Mane, Swati Patil, D.D. Birajdar, A.B. Kadam, Sagar E. Shirsath, R.H. Kadam. "Sol-gel synthesis of Cr³⁺ substituted Li_{0.5}Fe_{2.5}O₄: Cation distribution, structural and magnetic properties", Materials Chemistry and Physics, 2011

8 words — < 1%

[Crossref](#)

31 G. Umapathy, G. Senguttuvan, L. John Berchmans, V. Sivakumar. "Structural, dielectric and AC conductivity studies of Zn substituted nickel ferrites prepared by combustion technique", Journal of Materials Science: Materials in Electronics, 2016

8 words — < 1%

[Crossref](#)

32 Kumar, Amit, Suresh Babu, Ajay Singh Karakoti, Alfons Schulte, and Sudipta Seal. "Luminescence Properties of Europium-Doped Cerium Oxide Nanoparticles: Role of Vacancy and Oxidation States", Langmuir, 2009.

8 words — < 1%

[Crossref](#)

33 M.D. Mukadam, S.M. Yusuf. "Absence of ferromagnetism in nanocrystalline", Physica B: Condensed Matter, 2008

8 words — < 1%

[Crossref](#)

34 Ritu Rani, Khalid Mujasam Batoo, Pankaj Sharma, Gagan Anand, Gagan Kumar, Sumit Bhardwaj, M. Singh. "Structural, morphological and temperature dependent electrical traits of Co_{0.9}Zn_{0.1}In_xFe_{2-x}O₄ spinel nano-ferrites", Ceramics International, 2021

8 words — < 1%

[Crossref](#)

35 S. M. Patange, Sagar E. Shirsath, G. S. Jangam, K. S. Lohar, Santosh S. Jadhav, K. M. Jadhav. " Rietveld structure refinement, cation distribution and magnetic

8 words — < 1%

properties of Al substituted NiFe O nanoparticles ", Journal of Applied Physics, 2011

Crossref

36 Vikram More, R. B. Borade, Kirti Desai, V. K. Barote, S. S. Kadam, V. S. Shinde, D. R. Kulkarni, R. H. Kadam, S. T. Alone. "Site Occupancy, Surface Morphology and Mechanical Properties of Ce³⁺ Added Ni-Mn-Zn Ferrite Nanocrystals Synthesized Via Sol-Gel Route", Nano, 2021

8 words — < 1%

Crossref

37 export.arxiv.org

Internet

8 words — < 1%

38 link.springer.com

Internet

8 words — < 1%

39 www.mysciencework.com

Internet

8 words — < 1%

40 Kumar, Hemaunt, R.C. Srivastava, Jitendra Pal Singh, P. Negi, H.M. Agrawal, D. Das, and Keun Hwa Chae. "Structural and magnetic study of dysprosium substituted cobalt ferrite nanoparticles", Journal of Magnetism and Magnetic Materials, 2016.

7 words — < 1%

Crossref

41 S.F. Mansour, N.S. Al-Bassami, M. Afifi, M.A. Abdo. "Y³⁺ substituting-adjusted mechanical, dielectric, and impedance properties of cobalt copper zinc nanoferrites for high frequency applications", Journal of Rare Earths, 2022

7 words — < 1%

Crossref

42 Hou, Wei-xiao, and Zhi Wang. "Structural and magnetic properties of Ni_{0.15}Mg_{0.1}Cu_{0.3}Zn_{0.45}Fe₂O₄ ferrite prepared by NaOH-

4 words — < 1%

precipitation method", Materials Science and Engineering B, 2015.

Crossref

EXCLUDE QUOTES OFF
EXCLUDE BIBLIOGRAPHY ON

EXCLUDE SOURCES OFF
EXCLUDE MATCHES OFF

Dr.R.H.KADAM

Nikam Paper (For Review).doc

Williamson-Hall and Size-strain plot based micro-structural analysis and evaluation of elastic properties of Dy³⁺ substituted Co-Zn nano-spinels

ABSTRACT:

Polycrystalline Co-Zn nanoferrites doped with rare earth Dy³⁺ ions having general chemical formula Co_{0.9}Zn_{0.2}Dy_xFe_{1.9-x}O₄ (x = 0.0, 0.015, 0.03, 0.045 and 0.06) were synthesized via sol-gel auto-combustion route. Powder X-ray diffraction (XRD), scanning electron microscopy (SEM) and Fourier transform Infrared Spectra (FTIR) were performed to investigate the structural, microstructural, surface morphology and elastic properties. Well indexed XRD patterns confirm the phase purity and cubic spinel structure of the samples. Fractional doping of Dy³⁺ ions shifts the Bragg's lines slightly towards the lower angles which in turn increases the lattice lengths from 8.3795 Å to 8.3834 Å. The strain induced in the crystal lattice was estimated by using Williamson-Hall and Size – Strain Plot methods. Both methods confirm that the tensile type strain was induced in the crystal lattice and increases with the substitution of Dy³⁺ ions. Surface morphology of the samples was studied by using SEM images which reveals that the grains are almost spherical in nature and the size obtained is analogous with XRD results. FTIR spectra shows the existence of two main absorption bands within the wave number range 388 – 586 cm⁻¹ which confirm the characteristics of spinel ferrites. Elastic properties were estimated by using FTIR data. Elastic moduli and Debye temperature increases with the substitution of Dy³⁺ ions which are interpreted on the basis of interatomic bondings.

1. Introduction

Mixed magnetic nano-ceramics with spinel crystallography have recently gained valuable scientific and technological interest because of its fascinating electric and magnetic properties. These materials have been successfully employed in numerous technological, biomedical and sensing applications, including magnetic recording media, antennas, computer memory chips, transformer cores, magnetic refrigeration etc. [1-5]. These nano-ferrites also applicable in biomedical applications such as hyperthermia treatments, magnetic carrier in drug delivery, biological dealings etc. [6-8]. They are also usable in gas/humidity sensors, waste water processing, catalysis process etc. [9]. Generally, two approaches can be adopted to manipulate the electric and magnetic properties of these spinel nano-ferrites to make them suitable for desired application. One can control the properties by substituting the di/trivalent ion in the spinel lattice and/or by selecting the proper synthesis route. Spinel ferrite with general formula AB₂O₄ possessing soft ferromagnetic behaviour consists of two sub-lattices, tetrahedral – A and octahedral – B sites [10].

Cobalt ferrite (CoFe₂O₄) is one of the most interesting material among the spinel ferrite family due its number of technological applications.[11] Magnetic properties of CoFe₂O₄ known to increase by the small substitution of non-magnetic Zn ions to the tetrahedral sites.[12] However, substitution of Zn in CoFe₂O₄ decrease the coercivity of the sample. Systematic manipulation of ratio of Co:Fe in CoFe₂O₄ help to enhance both magnetization and coercivity of the sample.[11] Thus, in the present work, we choose a specific parent composition; Co_{0.9}Zn_{0.2}Fe_{1.9}O₄. It is to be noted that some of the Co and Fe ions change their valency to maintain the AB₂O₄ stoichiometry.

It is reported that replacement of Fe³⁺ ions by rare-earth (RE) ions at octahedral – B site by the fractional amount induces the strain in crystal lattice which induce a distortion in crystal lattice

resulted in significant alteration in its electric as well as magnetic properties.[13] Occupation of RE ions at octahedral sites hinder the Fe^{2+} motions in conduction process which in turn increase the overall resistivity of the sample. In recent years, RE substitution for Fe^{3+} ions at octahedral site have also been broadly used to advance the compositional dependent properties of spinel ferrites [14]. Several reports are available in the literature showing the studies on RE substituted spinel ferrites [15-19]. Dysprosium (Dy^{3+}) is a RE lanthanide which has an electronic configuration $4f^{10}6s^2$. Incorporation of Dy^{3+} ions into spinel lattice starts the RE-Fe (Dy-Fe) interactions due to the existence of 4f-3d couplings which in turn lead to minor changes into magnetic properties [20].

In view of above discussion, we have synthesized Dy^{3+} substituted Co-Zn mixed spinel ferrite nanoparticles having the general compositional formula $\text{Co}_{0.9}\text{Zn}_{0.2}\text{Dy}_x\text{Fe}_{1.9-x}\text{O}_4$ ($x = 0.0, 0.015, 0.03, 0.045$ and 0.06) by using sol-gel auto-combustion technique [21]. Detailed structure, micro-structural, morphological and elastic properties have been studied by using X-ray diffraction; scanning electron microscopy and Fourier transform infrared spectroscopy.

2. Methods and Materials

Polycrystalline ferrite powders of $\text{Co}_{0.9}\text{Zn}_{0.2}\text{Dy}_x\text{Fe}_{1.9-x}\text{O}_4$ ($x = 0.0, 0.015, 0.03, 0.045$ and 0.06) were synthesized by using sol-gel auto-combustion route with citric acid as fuel. AR grade (~99% pure) Cobalt nitrate ($\text{Co}(\text{NO}_3)_2 \cdot 6\text{H}_2\text{O}$), Zinc nitrate ($\text{Zn}(\text{NO}_3)_2 \cdot 6\text{H}_2\text{O}$), Ferric nitrate ($\text{Fe}(\text{NO}_3)_3 \cdot 9\text{H}_2\text{O}$) and Dysprosium nitrate ($\text{Dy}(\text{NO}_3)_3 \cdot 9\text{H}_2\text{O}$) were mixed and dissolved in sufficient amount of the double distilled water with their weight proportion in the composition. pH of the solution was kept constant at neutral by adding the liquid ammonia drop wise. Whole mixture was kept on hot plate with magnetic stirrer for constant heating at 90°C . After couple of hours the mixture becomes viscous and converted into sol. The sol was again by heating converted into dried gel and finally burnt by self ignition process and converted into brown ash. The burnt ash was grinded and sintered at 900°C for 6 hours. The sintered powers were again grinded and finally homogeneous and fine particles of the samples were obtained. Newly prepared samples of Dy^{3+} substituted Co-Zn ferrite were characterized by using X-ray diffraction method. The XRD plots were recorded at room temperature in the scanning range of $20 - 70^\circ$ using Cu-K_α radiation ($\lambda = 1.5405 \text{ \AA}$). The surface morphology of the samples was studied by using scanning electron microscopy (ZEISS LEO SUPRA 55). FTIR measurements were carried out by using Perkin Elmer (Spectrum - 2000) spectrophotometer by KBr pallet technique within the wave number range of $350 - 4000 \text{ cm}^{-1}$.

3. Results and Discussion

2

3.1 X-ray Analysis

X-ray diffraction (XRD) technique is used to explore the structural information of the powder samples. Figure 1 shows the XRD patterns of $\text{Co}_{0.9}\text{Zn}_{0.2}\text{Dy}_x\text{Fe}_{1.9-x}\text{O}_4$ ($x = 0.0, 0.015, 0.03, 0.045$ and 0.06) spinel ferrite nanoparticles processed via sol-gel route. All the Bragg's reflections indexed for the planes (220), (311), (222), (400), (422), (511), (440) deliver a strong indication of standard structure of spinel ferrite (COD 96-900-2674) corresponding to the space group $\text{Fd}\bar{3}\text{m}$. Well resolved and intensive peaks without any trace of impurity phase confirm the polycrystalline nature and phase purity of the samples [22]. It was found that the intensity of major peak (311) decreases with the substitution of Dy^{3+} ions and also shifted the peak positions towards lower angles. It was suggested that the Dy^{3+} ions (0.99 \AA) substituted the Fe^{3+} ions (0.64 \AA) in host spinel matrix. A fractional amount of Dy^{3+} ions were substituted and hence it is successfully incorporated in the Co-Zn matrix. The higher ionic radius of Dy^{3+} ions compared to that of Fe^{3+} ions could be the reason of enhancement of lattice lengths [23, 24].

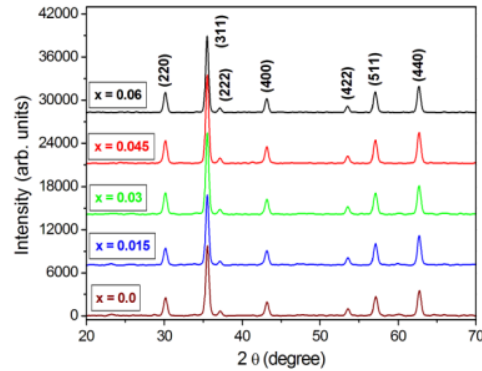


Figure 1. XRD patterns of $\text{Co}_{0.9}\text{Zn}_{0.2}\text{Dy}_x\text{Fe}_{1.9-x}\text{O}_4$

For a cubic spinel lattice, following Bragg's relation was used to estimate the lattice parameter (a) [25];

$$a = \frac{\lambda}{2\sin\theta} \sqrt{(h^2 + k^2 + l^2)} \quad (1)$$

where, λ - is incident X-ray wavelength (1.5406 Å), θ - Bragg's position and (hkl) are Miller indices. As depicted in Table 1, lattice parameter 'a' increased from 8.3795 to 8.3864 Å with the addition of larger Dy^{3+} ions in Co-Zn spinel matrix.

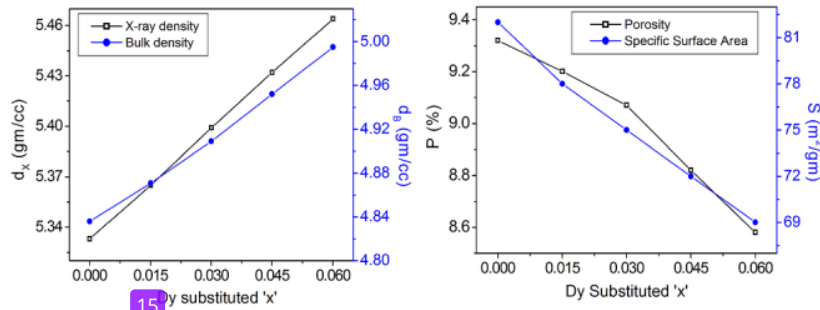


Figure 2. (Left panel) Variation of X-ray density (d_x) and bulk density (d_B), (Right panel) variation of porosity and specific surface area for $\text{Co}_{0.9}\text{Zn}_{0.2}\text{Dy}_x\text{Fe}_{1.9-x}\text{O}_4$

The X-ray density (d_x) of the samples was evaluated by using the relation discussed elsewhere and bulk density (d_B) was obtained from well known mass – volume relation [13]. Left panel of the Figure 2 depicted the variation of d_x and d_B with the substitution of Dy^{3+} ions. Figure 2 reveals that, d_x increased from 5.333 to 5.464 gm/cc and d_B from 4.836 to 4.995 gm/cc which is in agreement with the variation of 'a'. Percentage porosity (%P) of the samples in percentage and specific surface area (S) were obtained by the relations taken from literature [25]. Right panel of Figure 2 shows the variation of %P and S with the substitution of Dy^{3+} ions in Co-Zn-Fe-O crystal lattice. Porosity of the samples decreases from 9.32 to 8.58 (%) and specific surface area decreases from 82 to 69 m^2/gm .

Table 1. Lattice parameter (a), average crystallite size (t), lattice strain (ϵ) and ion jump lengths (L_A and L_B) for $\text{Co}_{0.9}\text{Zn}_{0.2}\text{Dy}_x\text{Fe}_{1.9-x}\text{O}_4$

Comp. 'x'	'a' (Å)	W-H analysis		SSP Method		Ion jump lengths	
		't _{W-H} ' (nm)	ε × 10 ⁻⁵	't _{SSP} ' (nm)	ε × 10 ⁻³	L _A (Å)	L _B (Å)
0.0	8.3795	15.2	1.97	15.2	1.65	3.6284	2.9626
0.015	8.3819	15.8	2.29	15.8	1.93	3.6295	2.9634
0.030	8.3831	16.5	4.19	16.5	2.51	3.6300	2.9639
0.045	8.3848	16.9	5.56	16.9	2.80	3.6307	2.9645
0.06	8.3864	17.6	7.37	17.5	3.32	3.6314	2.9650

The ion jump lengths 'L_A and L_B' (distance between magnetic ions) towards tetrahedral – A and octahedral – B sites were estimated by using the following relations [25];

$$L_A = \frac{a\sqrt{3}}{4} \quad (2)$$

$$L_B = \frac{a\sqrt{2}}{4} \quad (3)$$

As seen in Table 3, L_A varies from 3.6284 to 3.6314 Å and L_B varies from 2.9626 to 2.9650 Å which are attributed to the variation of lattice parameter.

3.2 Williamson – Hall and Size – Strain Plot analysis

Addition of RE ions having relatively higher ionic radius induces the strain in spinel lattice. The Scherer method, which is generally used to determine the size of nano-crystals; not considered the strain effect induced in the crystal lattice. Other approaches such as Williamson – Hall (W-H) and size – strain plot (SSP) can be employed to determine the crystallite size (t), lattice strain (ε) and other associated parameters such as energy density and stress. XRD peak widths and intensities and also the peak positions can be affected by the lattice strain induced in the crystal lattices. W-H analysis method gives the better information of contribution of micro-strains induced in the crystal lattice and crystallite size (t_{W-H}) of the samples. The modified Scherer relation given below was used to determine the t_{W-H} and lattice strain (ε) by using W-H method [26];

$$\beta_{hkl} \cos\theta = \frac{0.9\lambda}{t_{W-H}} + 4\varepsilon \sin\theta \quad (4)$$

Figure 3 (left panel) shows the W-H plots of Co_{0.9}Zn_{0.2}Dy_xFe_{1.9-x}O₄. Slope of the plot drawn between 4ε sinθ versus β_{hkl} cosθ gives the values of induced strain (ε) while as the Y-intercept gives the values of t_{W-H} (Table 1). The t_{W-H} obtained in nanometer range and varies from 15.2 to 17.6 nm with the addition of Dy³⁺ ions. Positive values of lattice strain indicate that the tensile type of strain induced in the crystal lattice and increases from 1.97 × 10⁻⁵ to 7.37 × 10⁻⁵. This variation in lattice strain is in agreement with the variation in 'a'.

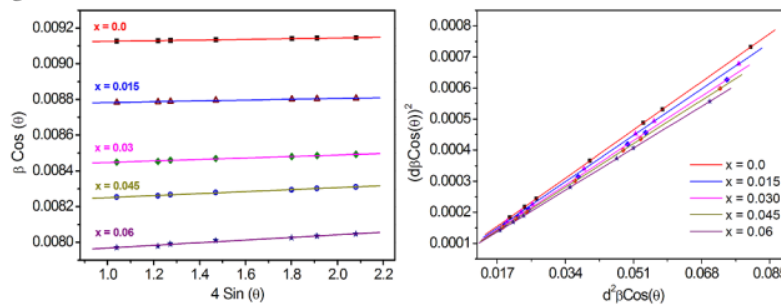


Figure 3. Williamson-Hall plots (left panel) and size – strain plots (right panel) for the series $\text{Co}_{0.9}\text{Zn}_{0.2}\text{Dy}_x\text{Fe}_{1.9-x}\text{O}_4$

Size-strain plot method is one of the best tools to study the isotropic behaviour and micro-strain contribution in the sample. The benefit of this method is that the little significance is given to the results obtained from higher reflection angles. This approximation considers that the size profile described from Lorentzian function while as the strain profile by Gaussian function [27] and the relation is given by;

$$(d\beta\cos\theta)^2 = \frac{K\lambda}{t_{SSP}}(d^2\beta\cos\theta) + \left(\frac{\varepsilon}{2}\right)^2 \quad (5)$$

Plots are drawn between $(d^2\beta\cos\theta)$ versus $(d\beta\cos\theta)^2$ for all the samples and are shown in right panel of Figure 3. The crystallite size estimated from slope of graphs and lattice strains obtained from Y-intercept are given in Table 1, which also obey the W-H analysis of the present work.

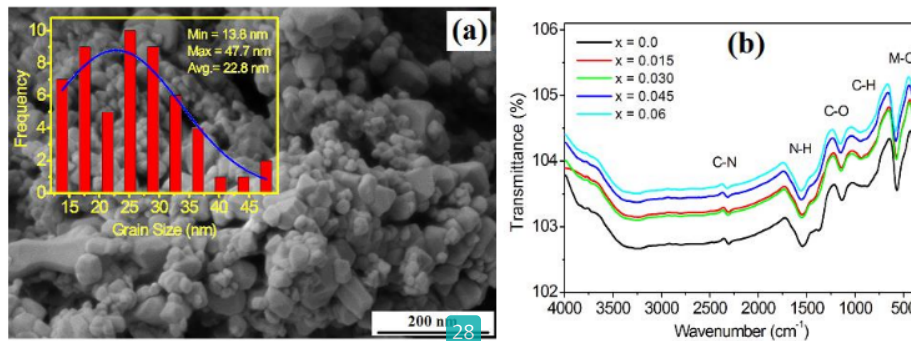


Figure 4. (a) SEM image of typical sample ($x = 0.06$), inset shows the histogram of size distribution and (b) FTIR spectra of $\text{Co}_{0.9}\text{Zn}_{0.2}\text{Dy}_x\text{Fe}_{1.9-x}\text{O}_4$

3.3 Surface morphology

Figure 4 (a) present the scanning electron microscopic (SEM) image of the typical sample $\text{Co}_{0.9}\text{Zn}_{0.2}\text{Dy}_{0.06}\text{Fe}_{1.84}\text{O}_4$. As seen in figure, most of the grains are in spherical shape with uniform size distribution with some agglomeration. The micrograph supports density and porosity calculations as very few pores are observed in the microstructure which is the indication of formation of dense samples. Inset of Figure 4 (a) shows the histogram of grain size distribution which clearly shows that the grain size of ranges from 13.8 to 47.7 nm and average grain size obtained is 22.8 nm which supports the size of the crystallites obtained from XRD data.

3.4 Elastic properties

Room temperature FTIR spectra were obtain within the wavenumber range of 350 – 4000 cm^{-1} are (Figure 4b). The analysis of FTIR spectra provides pinpoint knowledge of crystallography which helps to determine the various elastic parameters. Two absorption bands were observed in the range 388 – 586 cm^{-1} shows the characteristics interactions among the oxygen and metal cations at A and B crystallography sites [28] which confirms the formation of spinel structure. Value of band positions (ν_A and ν_B) is given in Table 2 obviously indicating that the band positions were shifted slightly towards the higher frequency region with the substitution of Dy^{3+} ions. The peaks around with wave-numbers 2300 cm^{-1} , 1570 cm^{-1} , 1130 cm^{-1} , and 940 cm^{-1} are attributed to the stretching vibrations of C-N, N-H, C-O, and C-H bands respectively [29].

Table 2. Elastic parameters of $\text{Co}_{0.9}\text{Zn}_{0.2}\text{Dy}_x\text{Fe}_{1.9-x}\text{O}_4$

	0.0	0.015	0.030	0.045	0.06
ν_A (cm ⁻¹)	571.06	573.11	577.18	581.26	585.34
ν_B (cm ⁻¹)	389.55	394.21	399.75	403.82	407.90
M_A	79.75	79.77	79.79	79.80	79.82
M_B	155.67	157.25	158.83	160.42	162.00
K_T ($\times 10^5$ dynes/cm)	198.18	199.65	202.54	205.45	208.39
K_O ($\times 10^5$ dynes/cm)	125.44	129.76	134.78	138.91	143.12
K_{av} ($\times 10^5$ dynes/cm)	161.8	164.7	168.7	172.2	175.8
C_{11} (GPa)	193.1	196.5	201.2	205.3	209.6
B (GPa)	193.11	196.54	201.19	205.35	209.57
G (GPa)	64.37	65.50	67.06	68.45	69.86
σ	0.35	0.35	0.35	0.35	0.35
E (GPa)	173.79	176.85	181.07	184.81	188.62
V_m (m/s)	3857	3879	3913	3741	3970
θ_D (K) Anderson	691	696	702	708	714

4 As suggested by Waldron, the vibration frequency of M-O bonds is directly proportional to the force constants (K_T and K_O) for A- and B-sites through the following relations [28];

$$K_T = (M_A \nu_1^2 \times 10^{-2}) \times 7.62 \quad (6)$$

$$K_O = \left(\frac{M_B}{2} \nu_2^2 \times 10^{-2} \right) \times 10.62 \quad (7)$$

here M_B and M_A are molecular weights of corresponding to [B] and [A] sites, respectively. 12 The estimated values of K_T and K_O are listed in Table 2. Both force constants are found increases with the addition of Dy^{3+} ions in Co-Zn crystal lattice. 4

To investigate the elastic constraints such as stiffness constant (C_{11}), Young's modulus (E), bulk modulus (B), modulus of rigidity (G) and Poisson's ratio (σ) for spinel ferrites; following relations were used [30];

$$C_{11} = \frac{K_{avg}}{a} \quad (B = C_{11} \text{ for cubic spinel structures}) \quad (8)$$

$$E = (1 + \sigma) 2G \quad (9)$$

$$G = \rho V_t^2 \quad (10)$$

$$\sigma = \frac{3B - 2G}{6B + 2G} \quad (11)$$

22 It can be seen that C_{11} , E , B , and G are increases with the substitution of Dy^{3+} ion Co-Zn lattice (Table 2) while as Poisson's ratio was found constant ($\sigma = 0.35$) which indicates good elastic behaviour of the samples [30]. As discussed 9 by Wooster work the increasing behaviour of elastic moduli can be related to interatomic bondings between various atoms of 26 spinel lattice [31]. For present samples the interatomic bindings between various atoms strengthens with the addition of Dy^{3+} ions and 19 hence the elastic moduli increases.

Debye temperatures (θ_D) for Dy^{3+} substituted Co-Zn ferrites were computed by using the simple Anderson formula [32];

$$\theta_D = \frac{h}{k} \left[\frac{3pqN}{4\pi M} \right]^{1/3} \times V_m \quad (12)$$

where notations have their usual meanings and V_m – average velocity ($V_m = [1/3(2/V_s^3 - 1/V_r^3)]^{-1/3}$). Debye temperature with the addition of Dy^{3+} ions in Co-Zn lattice (Table 2). The increase in Debye temperature suggests that rigidity of the samples increases with the addition of Dy^{3+} ions [32].

4. Conclusions

Single phase cubic nano-crystals of $Co_{0.52}Dy_xFe_{1.9-x}O_4$ spinel ferrites were synthesized by sol-gel method. Addition of Dy^{3+} ions increase the lattice lengths from 8.3795 Å to 8.3834 Å. W-H analysis and XRD method confirms the nano-size of the crystallites and crystal lattice experiences a tensile-strain. Crystallite size of the samples lies in the range 15.2 to 17.6 nm which is well supported by the SEM analysis. Two major absorption bands observed within the frequency region 388 – 586 cm^{-1} in FTIR spectra that also confirm the XRD analysis of crystal lattice. Incorporation of Dy^{3+} ions in Co-Zn crystal lattice increases the stiffness constant and various elastic moduli which imply that strengthen of inter-atomic bindings in the crystal. Increasing Debye temperature implies the rigidity of the samples increased by the Dy^{3+} ions addition.

References

- [1] Pubby K, Vijay Babu K, Narang S B, (2020) Magnetic, elastic, dielectric, microwave absorption and optical characterization of cobalt-substituted nickel spinel ferrites. *Mater. Sci. Engg. B* **255**: 114513.
- [2] More V D, Kadam S R, Shelke S B, Gaikwad P, Kadam R H, Alone S T, (2022) Modified structural and magnetic properties of Ni-Mn-Zn ferrite nanoparticles doped with Ce^{3+} ions. *Bioint. Res. Appl. Chem.* **12**: 5021.
- [3] Goldmann A, (2006) Modern Ferrite Technology. 2nd Edition, Springer; New York.
- [4] Wadgane S R, Alone S T, Karim A, Gaurav V, Shirsath S E, Kadam R H, (2019) Magnetic field induced polarization and magnetoelectric effect in $Na_{0.5}Bi_{0.5}TiO_3-Co_{0.75}Zn_{0.25}Cr_{0.2}Fe_{1.8}O_4$ multiferroic composites. *J. Magn. Magn. Mater.* **471**: 388.
- [5] Karimi Z, Mohmmadifar Y, Shokrollahi H, Sh. Khameneh Asl, Gh. Yousefi, Karimi L, (2014) Magnetic and structural properties of nano-sized Dy – doped cobalt ferrite synthesized by coprecipitation. *J. Magn. Magn. Mater.* **361**:150.
- [6] Bamzai K K, Kour G, Kaur B, Kulkarni S D, (2013) Effect of cation distribution on the structural and magnetic properties of Dy substituted magnesium ferrite. *J. Magn. Magn. Mater.* **327**:159.
- [7] Todkar G B, Kunale A R, Kamble R N, Batoo K M, Ijaz M F, Imran A, Hadi M, Raslan E H, Shirsath S E, Kadam R H, (2021) Ce-Dy substituted barium hexaferrite nanoparticles with large coercivity for permanent magnet and microwave absorber application. *J. Phys. D: Appl. Phys.* **54**:294001.
- [8] Ati A A, Othaman Z, Samavati A, (2013) Influence of cobalt on structural and magnetic properties of nickel ferrite nanoparticles. *J. Mole. Stru.* **1052**:177
- [9] Choudhari S S, Wadgane S R, Gaikwad B P, Satpute S S, Batoo K M, Aldossary O M, Shirsath S E, Kadam R H, (2021) Strain mediated enhancement in magnetoelectric properties of sonochemically synthesized piezoelectric and piezomagnetic composites. *Ceram. Inter.* **47**:6496.
- [10] Smith J, Wijn H P J, (1959) Ferrites, Wiley, New York **154**:157.
- [11] Gaikwad S S, Kadam R H, Shirsath S E, Wadgane S R, Shah J, Kotnala R K, Kadam A B, (2019) Surprisingly high magneto-electric coupling in cubic $Co_{0.7}Fe_{2.3}O_4-SrTiO_3$ nano-composites, *J. Alloys Compd.* **773**:564-570.

- [12] Jadhav S S, Shirsath S E, Patange S M, Jadhav K M, (2010) Effect of Zn substitution on magnetic properties of nano-crystalline Cobalt ferrite, *J. Appl. Phys.* **108**:093920
- [13] Kadam A A, Shinde S S, Yadav S P, Patil P S, Rajapure K Y, (2013) Structural, morphological, electrical and magnetic properties of Dy doped Ni-Co substitutional spinel ferrite. *J. Magn. Mater.* **329**:59-64.
- [14] Bazuev G V, Gyrdasova I O, Novikov S I, Kuznetsov A Yu, (2016) Synthesis, structure, and magnetic properties of Rare-Earth doped $\text{Ni}_{0.75}\text{Zn}_{0.25}\text{Fe}_2\text{O}_4$ nickel zinc ferrite. *Inorg. Mater.* **52**: 932.
- [15] Yehia M, Ismail S M, Hashhash A, (2014) Structural and magnetic studies of Rare-Earth substituted Nickel ferrites. *J. Supercond. Nov. Magn.* **27**:771.
- [16] Abdellatif M H, Azab A A, Salerno M, (2018) Effect of rare earth doping on the vibrational spectra of spinel Mn-Cr ferrite. *Mater. Res. Bull.* **97**:260.
- [17] More V D, Kadam S S, Kadam S R, Wadgane S R, Kadam R H, Alone S T, (2021) Complete Micro-structural analysis and elastic properties of Sm^{3+} doped Ni-Mn-Zn mixed spinel ferrite nanoparticles. *Macro. Symp.* **400**:2100115.
- [18] Satpute S S, Wadgane S R, Desai K R, Mane D R, Kadam R H, (2020) Substitution effect of Y^{3+} ions on the structural, magnetic and electrical properties of cobalt ferrite nanoparticles. *Ceram.* **66**:43.
- [19] Routry K L, Behera D, (2018) Enhancement in conductivity and dielectric properties of rare earth substituted nano-sized CoFe_2O_4 . *J. Mater. Sci.: Mater. Elect.* **29**:14248.
- [20] Phugate D V, Borade R B, Kadam S B, Dhale L A, Kadam R H, Shirsath S E, Kadam A B, (2020) Effect of Ho^{3+} ion doping on thermal, structural and morphological properties of Co-Ni ferrite synthesized by sol-gel method. *J. Supercond. Nov. Magn.* **33**:3545.
- [21] Shirsath S E, Wang D, Jadhav S S, Mane M L, Li S, (2018) Ferrites obtained by sol-gel method, in: L. Klein, M. Aparicio, A. Jitianu (Eds.), Handbook of Sol-Gel Science and Technology, Springer, Cham, pp. 695-735.
- [22] Cross W B, Affleck L, Kuznetsov M V, Parkin I P, Pankhurst Q A, (1999) Self propagating high temperature synthesis of ferrites MFe_2O_4 (M = Mg, Ba, Co, Ni, Cu, Zn) reaction in an external magnetic field. *J. Mater. Chem.* **9**:2545.
- [23] Shannon R D, (1976) Revised effective ionic radii and systematic studies of interatomic distances in halides and chalcogenides. *Acta Cryst.* **A32**:751.
- [24] Calderon-Ortiz E, Perales-Perez O, Voyles P, Gutierrez G, Tomar M S, (2009) $\text{Mn}_x\text{Zn}_{1-x}\text{Fe}_2\text{O}_4$ ($\text{R}=\text{Gd}, \text{Eu}$) ferrite nanocrystals for magnetocaloric applications. *Micro-electron. J.* **40**:677.
- [25] More V D, Borade R B, Desai K R, Barote V K, Kadam S S, Shinde V S, Kulkarni D R, Kadam R H, Alone S T, (2021) Site occupancy, surface morphology and mechanical properties of Ce^{3+} added Ni-Mn-Zn ferrite nanocrystals synthesized via Sol-gel route. *Nano* **16**:2150059.
- [26] Desai K R, Alone S T, Wadgane S R, Shirsath S E, Batoo K M, Imran A, Raslan E H, Hadi M, Ijaz M F, Kadam R H, (2021) X-ray diffraction based Williamson – Hall analysis and rietveld refinement for strain mechanism in Mg-Mn co-substituted CdFe_2O_4 nanoparticles. *Phys. B: Cond. Matter.* **614**:413054.
- [27] Balsure S D, Gurav M, Kadam R H, Haval K P, Tigote R M, Kadam A B, (2022) X-ray line profile analysis and magnetic and optical properties of $\text{Fe}_x\text{Zn}_{0.95-x}\text{Cr}_{0.05}\text{O}$ nanoparticles fabricated by sol-gel route. *Ceramica* **68**:24.
- [28] Mohamed M B, Wahba A M, (2014) Structural, magnetic and elastic properties of nanocrystalline Al-substituted $\text{Mn}_{0.5}\text{Zn}_{0.5}\text{Fe}_2\text{O}_4$ ferrite. *Ceram. Inter.* **40**:11773
- [29] Hu J, Liu X, Kan X, Feng S, Liu C, Lv O, (2014) Synthesis, analysis and characterization of Co substituted NiZnTi spinel ferrite. *J. Alloys. Comp.* **828**:154181.
- [30] Kadam R H, Borade R B, Mane M L, Mane D R, Batoo K M, Shirsath S E, (2020) Structural, mechanical, dielectric properties and magnetic interactions in Dy^{3+} substituted Co-Cu-Zn nanoferrites. *RSC Adv.* **10**:27911.

- [31] Wooster W R, (1953) Physical properties and atomic arrangements in crystals. *Rep. Prog. Phys.* **16**:62.
- [32] Shirsath S E, Patange S M, Kadam R H, Mane M L, Jadhav K M, (2012) Structure refinement, cation site location, spectral and elastic properties of Zn²⁺ substituted NiFe₂O₄. *J. Mol. Stru.* **1024**:77.

15%

SIMILARITY INDEX

PRIMARY SOURCES

- 1** Vikram More, R. B. Borade, Kirti Desai, V. K. Barote, S. S. Kadam, V. S. Shinde, D. R. Kulkarni, R. H. Kadam, S. T. Alone. " Site occupancy, surface morphology and mechanical properties of Ce added Ni-Mn-Zn ferrite nanocrystals synthesized via sol-gel route ", Nano, 2021
45 words — 1%
Crossref
- 2** www.scielo.br
Internet
41 words — 1%
- 3** Vikram More, Sanskruti Kadam, Supriya Kadam, Santosh Wadgane, Ramkrishna Kadam, Suresh Alone. " Complete Micro - Structural Analysis and Elastic Properties of Sm - Doped Ni - Mn - Zn Mixed Spinel Ferrite Nanoparticles ", Macromolecular Symposia, 2021
34 words — 1%
Crossref
- 4** www.researchgate.net
Internet
24 words — 1%
- 5** A.B. Kadam, Vishwanath K. Mande, S.B. Kadam, R.H. Kadam, Sagar E. Shirsath, Rameshwar B. Borade. "Influence of gadolinium (Gd³⁺) ion substitution on structural, magnetic and electrical properties of cobalt ferrites", Journal of Alloys and Compounds, 2020
23 words — 1%
Crossref

-
- 6 Jie Li, Ying Sun, Weiwei Kang, Pengna Wang, Huijun Zhang, Xueqin Zhang, Hong Yang, Baoping Lin. "Green synthesis of cellulose/graphene oxide/ZIF8 derived highly conductivity integrated film electrode for supercapacitor", Carbon, 2021
Crossref 20 words — 1%
-
- 7 pubs.rsc.org
Internet 20 words — 1%
-
- 8 www.ijirset.com
Internet 20 words — 1%
-
- 9 S.G. Algude, S.M. Patange, Sagar E. Shirsath, D.R. Mane, K.M. Jadhav. "Elastic behaviour of Cr³⁺ substituted Co-Zn ferrites", Journal of Magnetism and Magnetic Materials, 2014
Crossref 18 words — 1%
-
- 10 1library.net
Internet 17 words — 1%
-
- 11 www.science.gov
Internet 15 words — < 1%
-
- 12 D. El-Said Bakeer. "Elastic study and optical dispersion characterization of Fe-substituted cobalt aluminate nanoparticles", Applied Physics A, 2020
Crossref 13 words — < 1%
-
- 13 Khalid Hussain, Nasir Amin, Muhammad Imran Arshad. "Evaluation of structural, optical, dielectric, electrical, and magnetic properties of Ce³⁺ doped Cu_{0.5}Cd_{0.25}Co_{0.25}Fe_{2-x}O₄ spinel nano-ferrites", Ceramics International, 2020
Crossref 12 words — < 1%

14 B. H. Devmunde, P.S. Bhalerao, M.B. Solunke. " Structural Morphological and Infrared Properties of Cd Substitutes Nickel Ferrite Particles ", Journal of Physics: Conference Series, 2020 11 words — < 1%

Crossref

15 Hankare, P.P.. "Synthesis, characterization and studies on magnetic and electrical properties of Mg ferrite with Cr substitution", Materials Chemistry & Physics, 20090115 11 words — < 1%

Crossref

16 Hashim, Mohd., Alimuddin, Sagar E. Shirsath, S.S. Meena, R.K. Kotnala, Shalendra Kumar, Pramod Bhatt, R.B. Jotania, and Ravi Kumar. "Study of structural and magnetic properties of (Co-Cu)Fe₂O₄/PANI composites", Materials Chemistry and Physics, 2013. 11 words — < 1%

Crossref

17 Muhammad Imran Ul Haq, Atta ur Rehman, M. Asghar, Muhammad Ajaz Un Nabi, Nasir Amin, Sofia Tahir, Muhammad Imran Arshad. "Influence of Ce³⁺ and La³⁺ Substitution on Structural & Optical Parameters and Electrical Behavior on Mg-Zn Ferrites Synthesized via Co-precipitation method", Journal of Superconductivity and Novel Magnetism, 2022 10 words — < 1%

Crossref

18 Nisha Kushwah, A. Wadawale, G. Kedarnath, V. Sudarsan, R.M. Kadam. "Low temperature synthesis of wurtzite form of ZnS from single source precursor", Solid State Sciences, 2020 10 words — < 1%

Crossref

19 www.researchsquare.com 10 words — < 1%

Internet

20 P. Anjana, R.S. Arun Raj, Rosmy Jose, Manisha Kumari, P.M. Sarun, D. Sajan, Lija K. Joy. "Highly enhanced dielectric permittivity in CoFe₂O₄ by the Gd substitution in the octahedral sites", Journal of Alloys and Compounds, 2021
Crossref 9 words — < 1%

21 Sabih Qamar, Saima Yasin, Naveed Ramzan, Asim Umer, Majid Niaz Akhtar. "Structural, morphological and magnetic characterization of synthesized Co-Ce doped Ni ferrite /Graphene /BNO12 nanocomposites for practical applications", Chinese Journal of Physics, 2020
Crossref 9 words — < 1%

22 cyberleninka.org
Internet 9 words — < 1%

23 faculty.ksu.edu.sa
Internet 9 words — < 1%

24 link.springer.com
Internet 9 words — < 1%

25 K.K. Bamzai, Gurbinder Kour, Balwinder Kaur, Manju Arora, R.P. Pant. "Infrared spectroscopic and electron paramagnetic resonance studies on Dy substituted magnesium ferrite", Journal of Magnetism and Magnetic Materials, 2013
Crossref 8 words — < 1%

26 R.M. Kershi. "Rare-earth ions as a key influencer on the magnetic, spectroscopic and elastic properties of EryZn_{0.2}Co_{0.8}Fe₂-yO₄ nanoparticles", Journal of Alloys and Compounds, 2020
Crossref 8 words — < 1%

27 R.M. Kershi. "Spectroscopic, elastic, magnetic and optical studies of nanocrystallite and nanofluids Co ferrites towards optoelectronic applications", Materials Chemistry and Physics, 2020

8 words — < 1%

Crossref

28 Syed Ismail Ahmad, D. Ravi Kumar, Iizhar Ahmed Syed, Rukhsana Satar, Shakeel Ahmed Ansari. "Structural, Spectroscopic and Magnetic Study of Nanocrystalline Cerium-Substituted Magnesium Ferrites", Arabian Journal for Science and Engineering, 2016

8 words — < 1%

Crossref

29 www.scirp.org

Internet

8 words — < 1%

30 Ashok Gadkari, Tukaram Shinde, Pramod Vasambekar. "Influence of rare-earth ions on structural and magnetic properties of CdFe₂O₄ ferrites", Rare Metals, 2010

6 words — < 1%

Crossref

EXCLUDE QUOTES OFF

EXCLUDE SOURCES OFF

EXCLUDE BIBLIOGRAPHY ON

EXCLUDE MATCHES OFF

Dr.R.H.KADAM

Atul Birajdar Paper (MIT) -revised.doc

Effect of cation distribution on structural and mechanical properties of Y^{3+} substituted Co-Zn spinel ferrites nanoparticles.

C U Nikam¹, A P Birajdar², S S Kadam³, S. S. Choudhari⁴, V S Shinde⁵, S B Shelke⁶, R H Kadam^{2*}, G H Kale⁶

¹Department of Applied Science, SSBT College of Engineering and Technology, Jalgaon, (M.S.) India

²Department of Physics, BSS ASC College, Makni, Tq. Lohara, Dist. Osmanabad (M.S.) India

³Department of Physics, Jawahar College, Anadur, Tq. Tuljapur, Dist. Osmanabad (M.S.) India

⁴Department of Physics, Shrikrishna Mahavidyalaya, Gunjoti, Tq. Omerga, Dist. Osmanabad (M.S.) India

⁵Department of Chemistry, Shri Chattrapati Shivaji College, Omerga, Tq. Omerga, Dist. Osmanabad (M.S.) India

⁶Department of Physics, SMP College, Murum, Tq. Omerga, Dist. Osmanabad (M.S.) India

⁷Department of Electronics, Y. C. College, Tuljapur, Dist. Osmanabad (M.S.) India

*Corresponding Author e-mail: ram111612@yahoo.co.in

Abstract: Yttrium (Y^{3+}) substituted Co-Zn spinel ferrite nanoparticles with compositional formula $Co_{0.9}Zn_{0.2}Y_xFe_{1.9-x}O_4$ ($x = 0.0, 0.015, 0.030, 0.045, 0.06$) were synthesized by using sol-gel auto-ignition route. The structural and mechanical properties of Co-Zn ferrites were tailored by the replacement of Fe^{3+} ions by Y^{3+} ions. Rietveld refined X-ray diffraction patterns of all the samples confirm the cubic spinel structure. Lattice parameter increases with the substitution of Y^{3+} ions which may be due to the difference in ionic radii. The crystallite size obtained from XRD analysis is found in the nanometer range of 16.8 – 24.7 nm. Distribution of cations over tetrahedral – A and octahedral – B sites have been studied by using X-ray diffraction data and it is found that Y^{3+} ions prefers the octahedral – B site. Infrared spectra of all the samples were recorded in the wave number range of 300 cm^{-1} to 800 cm^{-1} which shows splitting of the two fundamental absorption bands. Two absorption bands (ν_1 and ν_2) observed in the range $380 - 610\text{ cm}^{-1}$ are belongs to tetrahedral – A and octahedral – B interstitial sites. The force constants (K_O and K_t) and corresponding elastic parameters were determined by using IR data. The stiffness constant (C_{11}), Young's modulus (E), rigidity modulus (G), bulk modulus (B) and Debye temperature (θ_D) were found increases with the addition of Y^{3+} ions.

1. Introduction

Since their discovery, nanomaterials have great interest to the scientific society due to their unique properties and uses in advanced technology. High surface to volume ratio improves the properties of nano-sized materials in comparison with their bulk counterparts leading to increase the attention of researchers to explore the materials at nanoscale level. Magnetic oxides, in particular

spinel ferrites with nano-size dimension have been comprehensively studied due their distinctive physical properties such as high magnetocrystalline anisotropy, high coercivity, very high chemical and mechanical stability, moderated saturation magnetization, low losses of eddy currents and low conductivity [1-5]. Such unique properties of nano-ferrites make them suitable for various medical and technological applications like waste water treatment [6], treatment for hyperthermia [7], drug delivery carriers [8], magnetic, humidity and biosensors [9-10], microwave devices, high density data storage devices, magnetic recording media, computer memory chips and high frequency devices [11-12]. Even after several years of their discovery, the unique combination of magnetic and electrical properties, ferrites have drawn much attention to the scientific society and still growing the interest [13].

Synthesis route, nature and concentration of dopant, and sintering conditions have a significant emphasis on the crystallographic and physico-chemical properties of the ferrites. Nano-sized spinel ferrites can be obtained by using several synthesis routes which includes sol-gel auto-ignition, micelle, reverse micelle, chemical co-precipitation, oxalate precursor, molten salt and hydrothermal etc. Among these, sol-gel technique is most feasible method as it consumes less time, economical and produces homogeneous and pure powders [14-17]. The distribution of cations in spinel ferrites also plays an important role in order to tailor the structural, electrical and magnetic properties. Ferrites with cubic spinel structure consists both divalent and trivalent cations which occupy tetrahedral – A and octahedral – B sites. According to the nature of substituted ions, they occupy tetrahedral – A and/or octahedral – B sites [18]. In the present paper we report structural and elastic properties of Y^{3+} substituted Co-Zn spinel ferrites synthesized by using sol-gel method.

2. Experimental

Y^{3+} substituted spinel ferrite nanoparticles of $Co_{0.9}Zn_{0.2}Y_xFe_{1.9-x}O_4$ were obtained by adopting the sol-gel auto-ignition method. Citric acid was used as fuel. Cobalt nitrate ($Co(NO_3)_2 \cdot 6H_2O$), Zinc nitrate ($Zn(NO_3)_2 \cdot 6H_2O$), Ferric nitrate ($Fe(NO_3)_3 \cdot 9H_2O$) and Yttrium nitrate ($Y(NO_3)_3 \cdot 9H_2O$) with high purity were used as starting materials. All the starting materials and citric acid were weighed in their weight proportion and dissolved in double distilled water. Liquid ammonia was poured in the solution in order to maintain the pH of the solution at ~ 7 . The solution was heated at constant temperature of 90° with continuous stirring by using magnetic hot plate. After two to three hours, the solution becomes denser and converted into viscous sol. Further heating converts the viscous sol into dried gel and finally self ignited with dark flints and converted into ash having dark brown colour. The burnt powders were crushed and sintered at $900^\circ C$ for 6 hours. The sintered powders were again grinded and finally homogeneous and fine particles of the samples were obtained. The prepared samples were characterized by using X-ray diffraction and Infrared spectroscopy methods. The XRD patterns were recorded at room temperature in the scanning range of $20 - 80^\circ$ by using $Cu-K_\alpha$ radiation ($\lambda = 1.5405 \text{ \AA}$). Infrared spectra of all the samples were recorded by using Perkin Elmer (Spectrum – 2000) spectrophotometer. KBr pellets were used to obtain the IR spectra within the wave number range of $350 - 800 \text{ cm}^{-1}$.

3. Results and Discussion

24

3.1 X-ray Analysis

28 Rietveld refined X-ray diffractograms of $Co_{0.9}Zn_{0.2}Y_xFe_{1.9-x}O_4$ nanoferrite samples are shown in Figure 1. All the XRD patterns were analyzed by the Rietveld refinement based programme FullProf [19]. The refinement was performed by using the initial input parameters of cubic symmetry with space group-Fd-3m and a pseudo-Voigt function as free parameter. As seen in Figure 1, all the reflection peaks are indexed for the planes (220), (311), (222), (400), (422), (333), (440), (620), (533), (622) and match well with the standard crystallography open database (COD ID: 96-900-2674) which confirmed the single phase cubic spinel structure of the samples. The fitting quality of the Rietveld patterns was assessed by using R – factors and goodness factor (χ^2). The values of goodness factor (χ^2) lies within 1 to 2 (Figure 1) indicates the best fitting quality of the XRD patterns.

Moreover, the peak positions shifted to lower 2θ angles with the substitution of Y^{3+} ions which in turn increases the lattice parameter 'a' from 8.3709 Å to 8.3811 Å (Figure 1). The difference in ionic radii of Y^{3+} (1.01 Å) and Fe^{3+} (0.645 Å) [20] increase the lattice parameter as a larger Y^{3+} ion replaces smaller Fe^{3+} ions.

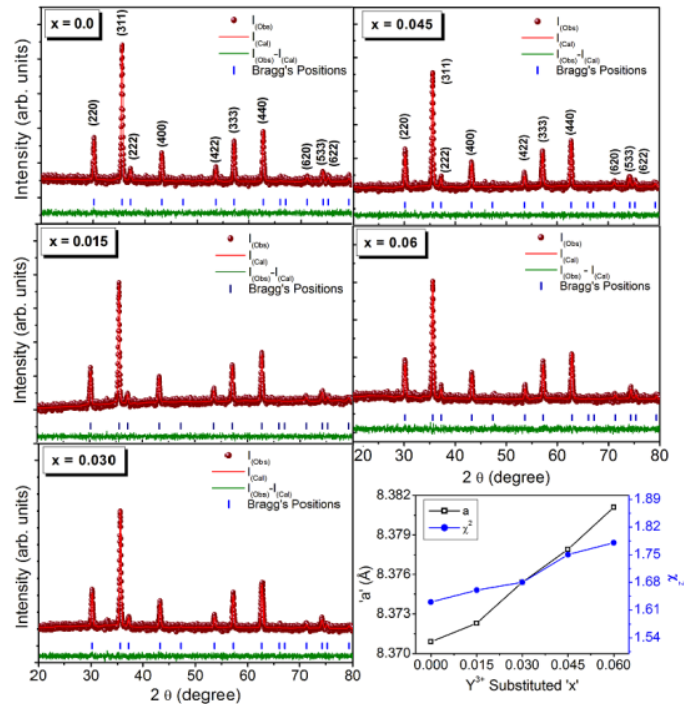


Figure 1. Rietveld refined XRD patterns of $Co_{0.9}Zn_{0.2}Y_xFe_{1.9-x}O_4$ (Figure at the bottom right display the variation of lattice parameter 'a' and goodness factor ' χ^2 ' with Y^{3+} substitution)

3.2 Cation distribution

Analysis of X-ray diffraction data by using Bertaut method provides the trustworthy information of cation distribution over tetrahedral – A and octahedral – B sites for spinel structures. To obtain the best information of cation distribution, this method selects few pairs of XRD planes which are considered sensitive and are almost independent of oxygen parameter [21]. The required formula to obtain the relative integrated intensity for a selected Bragg's line is given below;

$$I_{(hkl)} = |F_{(hkl)}|^2 P L_p \quad (1)$$

where, F – is structure factor, P – is multiplicity factor and L_p – is Lorentz polarization factor and is given by the relation $L_p = (1 + \cos^2 \theta) / (\sin^2 \theta \times \cos \theta)$. Literature values of atomic scattering factors and multiplicity factors were used for various ions in the calculations [22]. In the present investigation we have considered the typical planes (220), (400) and (440) for intensity ratio calculations. As per literature survey, the intensity ratios (I_{220}/I_{400}), (I_{400}/I_{440}) and (I_{220}/I_{440}) are found more sensitive for cation distribution [23]. The obtained cation distribution and intensity ratios are given in Table 1. The theoretical and observed intensity ratios are fairly agreed with each other and the corresponding cation distribution is taken into consideration. Due to inverse spinel structure majority of the Co^{2+} ions prefers the octahedral – B site where as normal Zn^{2+} ions occupies tetrahedral – A site. Trivalent Y^{3+} ions replaces the Fe^{3+} ions at octahedral – B site only.

Table 1: Cation distribution of $\text{Co}_{0.9}\text{Zn}_{0.1-x}\text{Fe}_x\text{O}_4$.

'x'	Cation Distribution						Intensity ratios					
	A - Site			B - Site			(18 ₂₂₀ /1400)		(1400/1440)		(1220/1440)	
	Co	Zn	Fe	Co	Y	Fe	Cal.	Obs.	Cal.	Obs.	Cal.	Obs.
0.0	0.05	0.2	0.75	0.85	0	1.15	1.4104	1.4111	0.4579	0.4583	0.6458	0.6467
0.015	0.1	0.2	0.7	0.8	0.015	1.185	1.4119	1.4124	0.4576	0.4587	0.6460	0.6479
0.030	0.15	0.2	0.65	0.75	0.030	1.22	1.4128	1.4130	0.4569	0.4556	0.6455	0.6438
0.045	0.2	0.2	0.6	0.7	0.045	1.255	1.4152	1.4155	0.4571	0.4578	0.6470	0.6480
0.06	0.25	0.2	0.55	0.65	0.06	1.29	1.4153	1.4151	0.4568	0.4558	0.6465	0.6450

3.3 Infrared spectroscopy and mechanical properties

Infrared spectroscopy is a useful characterization for the study of functional groups in the composition and local symmetry in crystalline solids. In general spinel ferrites shows two main IR active absorption bands which are originated due to the vibrations of metal ions at A- and B-sites [24]. As seen in Figure 2 (A) all the samples show two main absorption bands. Absorption bands near 556 cm^{-1} corresponds to the vibrations of Fe-Mo ions at A-site and absorption bands near 389 cm^{-1} corresponds to B-site. Variation of ν_1 and ν_2 is depicted in Figure 2 (B) which shows increasing trend with the addition of Y^{3+} ions.

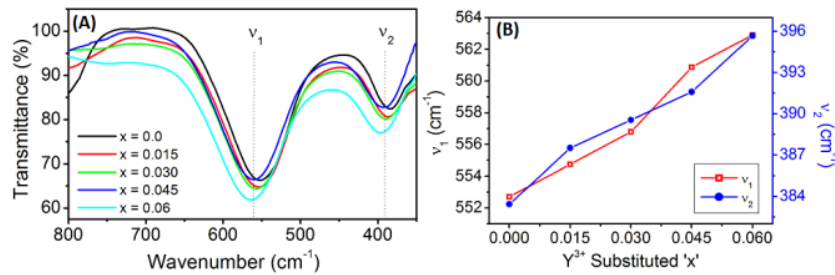


Figure 2. (A) Infrared spectra of $\text{Co}_{0.9}\text{Zn}_{0.2}\text{Y}_x\text{Fe}_{2-x}\text{O}_4$, (B) Variation of ν_1 and ν_2 with Y^{3+} doped 'x'

Force constants K_T and K_O are directly proportional to the vibration frequency and molecular weights (M_A , M_B) by the following relations as suggested by Waldron [25]:

$$\begin{aligned} K_T &= 7.62 \times M_A \times \nu_1^2 \times 10^{-2} \\ K_O &= 5.31 \times M_B \times \nu_2^2 \times 10^{-2} \end{aligned} \quad (2)$$

Cation distribution data was used to estimate the molecular weights of A- and B-sites. Figure 3 (a and b) illustrates the variation of molecular weights (M_A and M_B) and force constants (K_T and K_O) respectively. It is observed that M_A decreases from 79.91 to 78.92 g/mol and M_B increases from 155.51 g/mol to 158.48 g/mol with the substitution of Y^{3+} ions in Co-Zn matrix. Force constants K_T and K_O increases simultaneously from 186.01 to 190.56 and 124.41 to 131.75 with the substitution of Y^{3+} ions.

IR data of all the samples was used to evaluate the various elastic moduli and Debye temperature by using the relations discussed elsewhere [26]. The stiffness constant was evaluated by using the relation $C_{11} = K_A/a$ ($C_{11} = C_{12}$ for isotropic ferrite materials and thus $C_{11} = B$), where \bar{K} is the average force constant (Figure 2 B) and 'a' is lattice constant. Figure 3 shows the variation of (a) Bulk modulus 'B', (b) rigidity modulus 'G', (c) Young's modulus 'E', and (d) Poissons ration ' σ ' with Y^{3+} substituted 'x'.

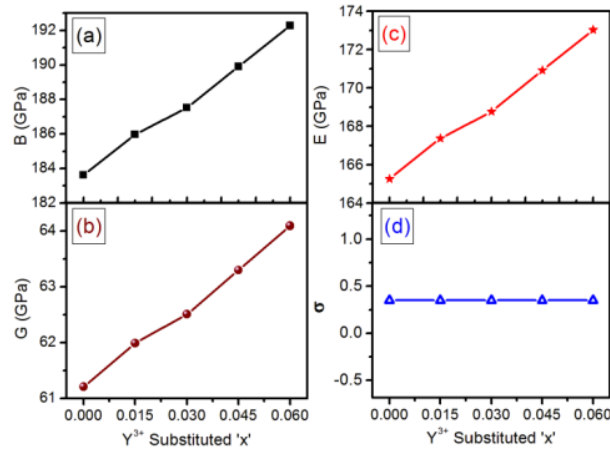


Figure 3. Variation of elastic moduli and Poisson's ratio with Y³⁺ substituted 'x'.

16

All the three elastic moduli, B, G and E are increases with the substitution of Y³⁺ ions in Co-Zn-Fe-O spinel lattice. Values of Poisson's ratio 'σ' are constant for all the samples (0.35) which lies between 0.1 to 0.5 representing the good elastic performance of the samples [27].

Longitudinal and transverse wave velocities (V_l and V_t) were evaluated by using following relations [28]:

$$V_l = \sqrt{C_{11}/d_x}; \quad V_t = V_l/\sqrt{3} \quad (3)$$

Figure 4 (a and c) shows the variation of V_l and V_t, respectively, with Y³⁺ substitutions. Both V_l and V_t shows increasing behaviour with the addition of Y³⁺ ions. By using these values in the following relation mean velocity was estimated [29].

$$V_m = \frac{1}{3} \left[\frac{2}{V_l^3} + \frac{1}{V_t^3} \right]^{-1/3} \quad (4)$$

Variation of average velocity (V_m) is presented in Figure 4 (b), indicating the increasing behaviour with the substitution of Y³⁺ ions. This behaviour of V_l, V_t and V_m can be explained on the basis of inter-atomic binding forces [30].

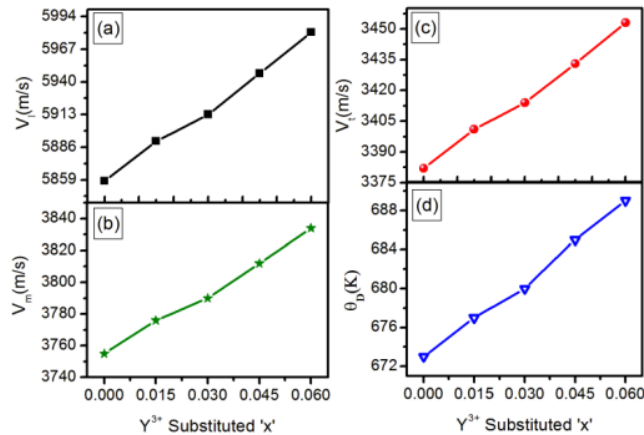


Figure 4. Variation of (a) longitudinal velocity (V_l), (b) mean velocity (V_m), (c) transverse velocity (V_t) and (d) Debye temperature (θ_D) with Y³⁺ substituted 'x'.

Debye temperature (θ_D) is a core aspect of solid materials in connection with their elastic and thermodynamic properties. Debye temperature affects some physical parameters of the solids such as mean square atomic displacement and elastic constants. Debye (θ_D) temperature was calculated by using the Anderson's formula given in literature [31] and its variation is shown in Figure 4 (d). It can be seen that the addition of Y^{3+} ions increase the values of Debye temperature which implies the increasing rigidity of the samples. This behaviour of Debye temperature suggest that the lattice vibration are hampered due to the addition of Y^{3+} ions which may occurs due the increasing bonding strength with the replacement of Fe^{3+} ions by Y^{3+} ions. Similar behaviour of Debye temperature is observed in the literature also [31-32].

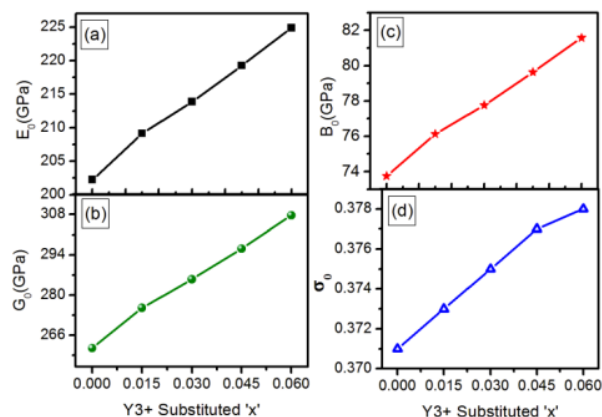


Figure 5. Variation of pore free elastic parameters.

Elastic parameters are not consistent without correction to the zero porosity i.e. void free values of elastic moduli are more reliable. Void free elastic parameters can be obtained by using the void fractions in Hosselmann and Fulrath formulae [33].

$$E_0 = 1 / \left[\frac{1}{E} \left\{ 1 - \frac{3P(1-\sigma)(9+5\sigma)}{2(7-5\sigma)} \right\} \right] \quad (5)$$

$$G_0 = 1 / \left[\frac{1}{G} \left\{ 1 - \frac{15P(1-\sigma)}{7-5\sigma} \right\} \right] \quad (6)$$

$$B_0 = \frac{E_0 G_0}{3(3G_0 - E_0)} \quad (7)$$

$$\sigma_0 = \frac{E_0}{2G_0} - 1 \quad (8)$$

Figure 5 shows the variation of void free (a) Young's modulus, (b) rigidity modulus, (c) bulk modulus and (d) Poisson's ratio with Y^{3+} substitution. All the elastic moduli increases with Y^{3+} substitution and Poisson's ratio lies between -1 to 0.5 indicating the isotropic nature of spine ferrites. Increasing values of void free elastic moduli are corresponds to the support the inter-atomic bonding to replacement of Fe^{3+} ions by Y^{3+} ions.

4. Conclusions

XRD analysis revealed the samples were formed in single phase cubic spinel structure. Obtained values of Goodness factor within 1 to 2 confirms the best fitting quality of the Rietveld refinement of XRD patterns. Cation distribution suggest that the larger Y^{3+} ions replaces smaller Fe^{3+} ions at octahedral - B site. Due to inverse spinel structure, most of Co^{2+} ions prefers octahedral - B site while

as normal Zn^{2+} ions occupies tetrahedral – A sites. IR spectra locate two main absorption bands, one corresponds to tetrahedral – A site (around 556 cm^{-1}) and other corresponds to octahedral B – site (around 389 cm^{-1}). All the elastic parameters shows increasing behaviour with Y^{3+} substitution suggesting and Poisson's ratio observed between -1 to 0.5 indicating the good elastic behaviour of the samples. Increasing values of Debye temperature confirms the increasing rigidity of the samples with Y^{3+} substitution.

References

- [1] Chakrabarty S, Dutta A, Pal M, (2018) Effect of yttrium doping on structure, magnetic and electrical properties of nanocrystalline cobalt ferrite. *J. Magn. Magn. Mater.* **461**:69.
- [2] Dunn I H, Jacobo S E, Bercoff P G, (2017) Structural and magnetic influence of yttrium – for – iron substitution in cobalt ferrite. *J. Alloys. Comp.* **691**:130.
- [3] Kadam R H, Biradar A R, Mane M L, Shirsath S E, (2012) *J. Appl. Phys.* **112**: 043902
- [4] Akhtar P, Akhtar M N, Baqir M A, Ahmad A, Khallidooon M U, Farhan M, Khan M A, (2021) Structural and magnetic evaluations of rare – earths (Tb, Pr, Ce, Gd, Y) – doped spinel ferrites for high frequency and switching applications. *J. Mater. Sci: Mater. Electron* **32**: 7692.
- [5] More V D, Kadam S R, Shelke S B, Gaikwad P, Kadam R H, Alone S T, (2022) Modified structural and magnetic properties of Ni-Mn-Zn ferrite nanoparticles doped with Ce^{3+} ions. *Bioint. Res. Appl. Chem.* **12**: 5021.
- [6] Kumar S, Akhtar M N, Batoo K M, Raslan E H, (2020) Structural and magnetic features of Ce doped Co-Cu-Zn spinel nanoferrites prepared using sol-gel self-ignition method. *Ceram. Int.* **46**: 14481.
- [7] Roman T, Asavei R L, Karkalos N E, Roamn C, Virlan C, Cimpoesu N, Istrate B, Zaharia M, Markopoulos A P, Kordatos K, Stanciu S, Pui A, (2019), Synthesis and adsorption properties of nanocrystalline ferrites for kinetic modelling development. *Int. J. Appl. Ceram. Technol.* **16**:693.
- [8] Myrovali E, Maniotis N, Makridis A, Terzopoulou A, Ntomprougkidis V, Simeonidis K, Sakellari D, Kalogirou O, Samaras T, Salikhov R, Spasova M, Farle M, Wiedwald, (2016) Arrangements at the nanoscale: effect on magnetic particle hyperthermia. *Sci. Rep.* **6**:1.
- [9] Stanciu L, Won Y H, Ganesana M, Andreescu S, (2009), Magnetic particle – based hybrid platforms for bioanalytical sensors. *Sensors* **9**:2976.
- [10] Sahoo B, Devi K S P, Dutta S, Maiti T K, Pramanik P, Dhara D, (2014) Biocompatible mesoporous silica-coated superparamagnetic manganese ferrite nanoparticles for targated drug delivery and MR imaging applications. *J. Colloid. Interface Sci.* **431**:31.
- [11] Todkar G B, Kunale R A, Kamble R N, Batoo K M, Ijaz M F, Imran A, Hadi M, Raslan E H, Shirsath S E, Kadam R H, (2021) Ce-Dy substituted barium hexaferrite nanoparticles with large coercivity for permanent magnet and microwave absorber application. *J. Phys. D: Appl. Phys.* **54**: 294001.
- [12] Wadgane S R, Alone S T, Karim A, Gaurav V, Shirsath S E, Kadam R H, (2019) Magnetic field induced polarization and magnetoelectric effect in $Na_{0.5}Bi_{0.5}TiO_3-Ce_{0.75}Zn_{0.25}Cr_{0.2}Fe_{1.8}O_4$ multiferroic composites. *J. Magn. Magn. Mater.* **471**: 388.
- [13] Akhtar M N, Babar M, Qmar S, Rehman Z, Khan M A, (2019) Structural Rietveld refinement and magnetic features of prosademedium (Pr) doped Cu nanocrystalline spinel ferrites. *Ceram. Inter.* **45**:10187.
- [14] Yehia M, Ismail S M, Hashhash A, (2014) Structural and magnetic studies of Rare-Earth substituted nickel ferrites. *J. Supercond. Nov. Magn.* **27**: 771.
- [15] Birajdar A A, Shirsath S E, Kadam R H, Mane M L, Mane D R, Shitre A R, (2012) Permeability and magnetic properties of Al^{3+} substituted $Ni_{0.7}Zn_{0.3}Fe_2O_4$ nanoparticles. *J. Appl. Phys.* **112**: 053908.
- [16] Abdellatif M H, Azab A A, Salemo M, (2018) Effect of rare earth doping on the vibrational spectra of spinel Mn-Cr ferrite. *Mater. Res. Bull.* **97**:260.

- [17] Karimi Z, Mohammadifar Y, Shokrollahi H, Sh. Khamenesh Asl, Gh. Yousefi, Karimi L, (2014) Magnetic and structural properties of nano sized Dy-doped cobalt ferrite synthesized by co-precipitation. *J. Magn. Magn. Mater.* **361**: 150.
- [18] Gurav S K, Shirsath S E, Kadam R H, Mane D R, (2013) Low temperature synthesis of $\text{Li}_{0.5}\text{Zr}_x\text{Co}_x\text{Fe}_{2.5-2x}\text{O}_4$ powder and their characterization. *Powder Techn.* **235**: 485.
- [19] Ouyahia S, Rais A, Bozzo B, Taibi K, Addou A, (2020) Cation distribution by Rietveld refinement and magnetic properties of $\text{MgCr}_x\text{Fe}_{2-x}\text{O}_4$ spinel ferrite. *Appl. Phys. A* **126**:666.
- [20] Hossain M D, Hossain M A, Khan M N I, Sikder S S, Hakim M A, (2020) Frequency and temperature dependent magnetic properties with structural Rietveld refinement of $\text{Co}_{0.25}\text{Zn}_{0.75}\text{Y}_x\text{Fe}_{2-x}\text{O}_4$ ferrites. *J. Magn. Magn. Mater.* **493**:165696.
- [21] Singhal S, Chandra K, (2007) Cation distribution and magnetic properties in chromium – substituted nickel ferrites prepared using aerosol route. *J. Solid State Chem.* **180**: 296.
- [22] Culity B D, (1956) Elements of X-ray diffraction. *Addison-Wesley Publishing Company, Inc. USA* pp. 460-485
- [23] More V D, Borade R B, Desai K R, Barote V K, Kadam S S, Shinde V S, Kulkarni D R, Kadam R H, Alone S T, (2021) Site occupancy, surface morphology and mechanical properties of Ce^{3+} added Ni-Mn-Zn ferrite nanocrystals synthesized via Sol-gel route. *Nano* **16**: 2150059.
- [24] Pubby K, Vijay Babu K, Narang S B, (2020) Magnetic, elastic, dielectric, microwave absorption and optical characterization of cobalt – substituted nickel spinel ferrites. *Mater. Sci. Engg. B.* **255**: 114513.
- [25] Shirsath S E, Patange S M, Kadam R H, Mane M L, Jadhav K M, (2012) Structure refinement, cation site location, spectral and elastic properties of Zn^{2+} substituted NiFe_2O_4 . *J. Mol. Stru.* **1024**: 77.
- [26] More V D, Kadam S S, Kadm S R, Wadgane S R, Kadam R H, Alone S T, (2021) Complete Micro-structural analysis and elastic properties of Sm^{3+} doped Ni-Mn-Zn mixed spinel ferrite nanoparticles; *Macro. Symp.* **400** : 2100115.
- [27] Desai K R, Alone S T, Wadgane S R, Shirsath S E, Batoo K M, Imran A, Raslan E H, Hadi M, Ijaz M F, Kadam R H, (2021) X-ray diffraction based Williamson – Hall analysis and rietveld refinement for strain mechanism in Mg-Mn co-substituted CdFe_2O_4 nanoparticles. *Phys. B: Cond. Matter.* **614**: 413054.
- [28] Balsure S D, Gurav M, Kadam R H, Haval K P, Tigote R M, Kadam A B, (2022) X-ray line profile analysis and magnetic and optical properties of $\text{Fe}_x\text{Zn}_{0.95-x}\text{Cr}_{0.05}\text{O}$ nanoparticles fabricated by sol-gel route. *Ceramica* **68**: 24.
- [29] Mohamed M B, Wahba A M, (2014) Structural, magnetic and elastic properties of nanocrystalline Al-substituted $\text{Mn}_{0.5}\text{Zn}_{0.5}\text{Fe}_2\text{O}_4$ ferrite. *Ceram. Inter.* **40**: 11773
- [30] Wooster W R, (1953) Physical properties and atomic arrangements in crystals. *Rep. Prog. Phys.* **16**: 62.
- [31] Abu-Elsaad N I, (2014) Elastic properties of germanium substituted lithium ferrite. *J. Mole. Stru.* **1075**: 546.
- [32] Modi K B, Chhantbar M C, Joshi H H, (2006) Study of elastic behaviour of magnesium ferri aluminates. *Ceram. Inter.* **32**: 111.
- [33] Kadam R H, Borade R B, Mane M L, Mane D R, Batoo K M, Shirsath S E, (2020) Structural, mechanical, dielectric properties and magnetic interactions in Dy^{3+} substituted Co-Cu-Zn nanoferrites. *RSC Adv.* **10**: 27911.

18%

SIMILARITY INDEX

PRIMARY SOURCES

- 1** Vikram More, R. B. Borade, Kirti Desai, V. K. Barote, S. S. Kadam, V. S. Shinde, D. R. Kulkarni, R. H. Kadam, S. T. Alone. " Site occupancy, surface morphology and mechanical properties of Ce added Ni-Mn-Zn ferrite nanocrystals synthesized via sol-gel route ", Nano, 2021
61 words — 2%
Crossref
 - 2** K.R. Desai, S.T. Alone, S.R. Wadgane, Sagar E. Shirsath, Khalid M. Batoor, A. Imran, E.H. Raslan, M. Hadi, M.F. Ijaz, R.H. Kadam. "X-ray diffraction based Williamson–Hall analysis and rietveld refinement for strain mechanism in Mg–Mn co-substituted CdFe₂O₄ nanoparticles", Physica B: Condensed Matter, 2021
23 words — 1%
Crossref
 - 3** biointerfaceresearch.com
Internet 22 words — 1%
 - 4** nopr.niscair.res.in
Internet 22 words — 1%
 - 5** N.I. Abu-Elsaad. "Elastic properties of germanium substituted lithium ferrite", Journal of Molecular Structure, 2014
20 words — 1%
Crossref
 - 6** link.springer.com
Internet 19 words — 1%
-

7 Somnath, Indu Sharma, R.K. Kotnala, M. Singh, Arun Kumar, Pooja Dhiman, Virender Pratap Singh, Kartikey Verma, Gagan Kumar. "Structural, magnetic and Mössbauer studies of Nd-doped Mg-Mn ferrite nanoparticles", Journal of Magnetism and Magnetic Materials, 2017

18 words — 1%

Crossref

8 S.A. Mazen, H.M. Elsayed, N.I. Abu-Elsaad. "A comparative study of different concentrations of (Co/Ni/Cu) effects on elastic properties of Li-Mn ferrite employing IR spectroscopy and ultrasonic measurement", Ceramics International, 2021

17 words — 1%

Crossref

9 Jalel Massoudi, Mourad Smari, Kamel Nouri, Essebti Dhahri, Kamel Khirouni, Sylvain Bertaina, Lotfi Bessais, El Kebir Hlil. "Magnetic and spectroscopic properties of Ni-Zn-Al ferrite spinel: from the nanoscale to microscale", RSC Advances, 2020

15 words — 1%

Crossref

10 www.mdpi.com

Internet

15 words — 1%

11 B. Rajesh Babu, M. S. R. Prasad, K. V. Ramesh. "Effect on structural and magnetic properties of aluminum substituted - nanoferrite system prepared via citrate-gel route ", International Journal of Modern Physics B, 2015

14 words — 1%

Crossref

12 Dalal, M., A. Mallick, A.S. Mahapatra, A. Mitra, A. Das, D. Das, and P.K. Chakrabarti. "Effect of cation distribution on the magnetic and hyperfine behaviour of nanocrystalline Co doped Ni-Zn ferrite (Ni_{0.4}Zn_{0.4}Co_{0.2}Fe₂O₄)", Materials Research Bulletin, 2016.

13 words — < 1%

Crossref

- 13 M.Z. Ahsan, M.A. Islam, A.A. Bally, F.A. Khan. "Spectroscopic analysis for electric and magnetic properties of manganese doped cobalt nanoferrite", Results in Physics, 2020
Crossref 12 words — < 1%
-
- 14 coek.info
Internet 12 words — < 1%
-
- 15 dishaedupoint.com
Internet 12 words — < 1%
-
- 16 pubs.rsc.org
Internet 12 words — < 1%
-
- 17 1library.net
Internet 11 words — < 1%
-
- 18 An-Dien Nguyen, Keith Murdoch, Norman Edelstein, L. A. Boatner, M. M. Abraham. "Polarization dependence of phonon and electronic Raman intensities in and ", Physical Review B, 1997
Crossref 11 words — < 1%
-
- 19 Environmental Science and Engineering, 2014.
Crossref 11 words — < 1%
-
- 20 www.jetir.org
Internet 11 words — < 1%
-
- 21 Rohit Jasrotia, Jyoti Prakash, Gagan Kumar, Ritesh Verma et al. "Robust and sustainable Mg_{1-x}Ce_xNi_yFe_{2-y}O₄ magnetic nanophotocatalysts with improved photocatalytic performance towards photodegradation of crystal violet and rhodamine B pollutants", Chemosphere, 2022
Crossref 10 words — < 1%

-
- 22 updatepublishing.com
Internet 10 words — < 1%
-
- 23 www.researchgate.net
Internet 10 words — < 1%
-
- 24 Farea, A.M.M.. "Structure and electrical properties of Co⁰.⁵Cd^xFe².⁵-^xO⁴ ferrites", Journal of Alloys and Compounds, 20080922
Crossref 9 words — < 1%
-
- 25 P V. Thakre, V M. Deshmukh. "Modeling, simulation and experimental investigation of closed loop MPPT based single phase stand alone photo voltaic system using particle swarm optimization technique", International Journal of Engineering & Technology, 2018
Crossref 9 words — < 1%
-
- 26 Shanmugavani, A., R.Kalai Selvan, Samar Layek, Leonid Vasylechko, and C. Sanjeeviraja. "Influence of pH and fuels on the combustion synthesis, structural, morphological, electrical and magnetic properties of CoFe₂O₄ nanoparticles", Materials Research Bulletin, 2015.
Crossref 9 words — < 1%
-
- 27 V. Lakshmi Savithri Vatsalya, G. Sunita Sundari, Ch.S.L.N. Sridhar, Ch.S. Lakshmi. "Evidence of Superparamagnetism in nano phased copper doped nickel zinc ferrites synthesized by Hydrothermal Method", Optik, 2021
Crossref 9 words — < 1%
-
- 28 www.famaf.unc.edu.ar
Internet 9 words — < 1%
-
- 29 www.infona.pl
Internet 9 words — < 1%

30 Mohamed Bakr Mohamed, Adel Maher Wahba. "Structural, magnetic, and elastic properties of nanocrystalline Al-substituted $Mn_{0.5}Zn_{0.5}Fe_2O_4$ ferrite", *Ceramics International*, 2014

8 words — < 1%

[Crossref](#)

31 S.S. More, R.H. Kadam, A.B. Kadam, A.R. Shite, D.R. Mane, K.M. Jadhav. "Cation distribution in nanocrystalline Al^{3+} and Cr^{3+} co-substituted $CoFe_2O_4$ ", *Journal of Alloys and Compounds*, 2010

8 words — < 1%

[Crossref](#)

32 Abu-Elsaad, N.I.. "Elastic properties of germanium substituted lithium ferrite", *Journal of Molecular Structure*, 2014.

7 words — < 1%

[Crossref](#)

33 Ahmad, Zahoor, Shahid Atiq, S. Kumail Abbas, Shahid Mahmood Ramay, Saira Riaz, and Shahzad Naseem. "Structural and complex impedance spectroscopic studies of Mg-substituted $CoFe_2O_4$ ", *Ceramics International*, 2016.

7 words — < 1%

[Crossref](#)

34 J.B. Shitole, S.N. Keshatti, S.M. Rathod, Santosh S. Jadhav. " Y^{3+} composition and particle size influenced magnetic and dielectric properties of nanocrystalline $Ni_{0.5}Cu_{0.5}Y_xFe_{2-x}O_4$ ferrites", *Ceramics International*, 2021

7 words — < 1%

[Crossref](#)

35 V.B Kawade, G.K Bichile, K.M Jadhav. "X-ray and infrared studies of chromium substituted magnesium ferrite", *Materials Letters*, 2000

6 words — < 1%

[Crossref](#)

EXCLUDE QUOTES OFF

EXCLUDE BIBLIOGRAPHY ON

EXCLUDE SOURCES OFF

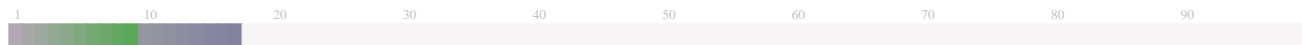
EXCLUDE MATCHES OFF

Submission Information

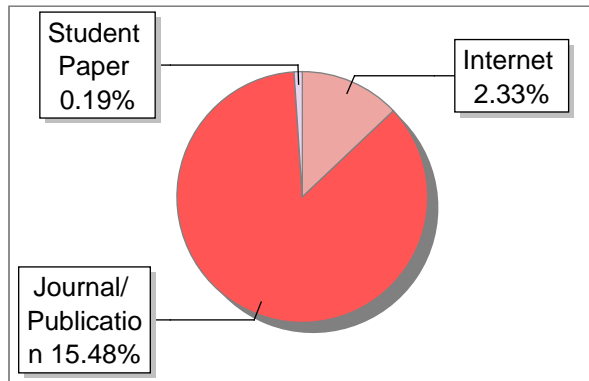
Author Name	C S Munnolli
Title	BNBT-SRYFO
Paper/Submission ID	645915
Submission Date	2022-10-31 22:05:54
Total Pages	20
Document type	Article

Result Information

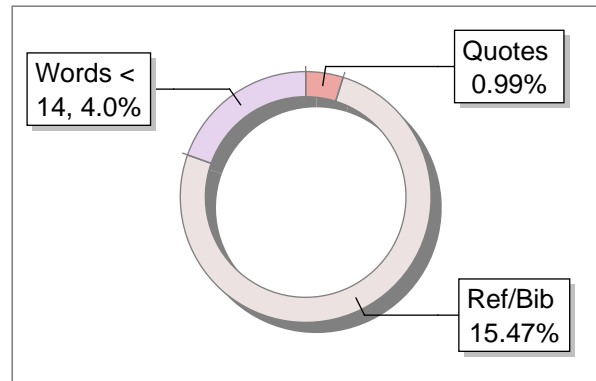
Similarity **18 %**



Sources Type



Report Content



Exclude Information

Quotes	Excluded
References/Bibliography	Excluded
Sources: Less than 14 Words Similarity	Not Excluded
Excluded Source	0 %
Excluded Phrases	Not Excluded

A Unique QR Code use to View/Download/Share Pdf File



DrillBit Similarity Report

18

SIMILARITY %

41

MATCHED SOURCES

B

GRADE

A-Satisfactory (0-10%)
B-Upgrade (11-40%)
C-Poor (41-60%)
D-Unacceptable (61-100%)

LOCATION	MATCHED DOMAIN	%	SOURCE TYPE
1	Impact of yttrium on the physical, electro-magnetic and dielectric pr, by Shekhawat, Deepshik- 2018	3	Publication
2	Effect of calcination temperature and cobalt addition on structural, optical and by Habanjar-2020	1	Publication
3	Multiferroic properties of microwave sintered BaTiO3SrFe12O19 composites by Katlakunta-2014	1	Publication
5	www.dx.doi.org	2	Publication
6	Ferroelectric and ferromagnetic properties of (by Devan-2007	1	Publication
7	Effect of calcination temperature and cobalt addition on structural, optical and by Habanjar-2020	1	Publication
8	New Family of Materials with Negative Coefficients of Thermal Expansion The Eff by Thieme-2016	1	Publication
9	Thesis submitted to shodhganga - shodhganga.inflibnet.ac.in	1	Publication
10	coek.info	1	Internet Data
12	Ferroelectric and ferromagnetic properties of (by Devan-2007	1	Publication
13	Energy-storage properties of (1x)Bi047Na047Ba006TiO3xKNbO3 lead-free cerami by Wang-2014	1	Publication

14	Influence of Samarium Substitution on the Structural and Magnetic Properties by Yasmin, Nazia Mirz- 2017	<1	Publication
15	Thesis submitted to shodhganga - shodhganga.inflibnet.ac.in	<1	Publication
16	Thesis submitted to shodhganga - shodhganga.inflibnet.ac.in	<1	Publication
17	Effect of Tool Shoulder Diameter on the Surface Hardness of Aluminum-MMC by Mahesh-2019	<1	Publication
18	Multi objective optimization of wear behaviour of Aluminum MMCs using Grey-Taguchi by Muthu-2020	<1	Publication
19	Thesis submitted to shodhganga - shodhganga.inflibnet.ac.in	<1	Publication
20	www.academia.edu	<1	Internet Data
21	The structures of metallic oxides by Wells-1948	<1	Publication
22	moam.info	<1	Internet Data
23	www.sciencedirect.com	<1	Internet Data
24	A molecular phylogeny and a revised classification of Ornithogaloideae (Hyacinth) by Manning-2009	<1	Publication
25	dspace.nwu.ac.za	<1	Publication
26	www.ajol.info	<1	Publication
27	www.researchgate.net	<1	Internet Data
28	www.dx.doi.org	<1	Publication
29	downloads.hindawi.com	<1	Publication
31	jcpr.kbs-lab.co.kr	<1	Publication
33	refubium.fu-berlin.de	<1	Publication

34	Formulating and optimizing a combustion pathways for oil shale and its by Marc-212	<1	Publication
35	Future of Water Supply and Demand in the Middle Dra Valley, Morocco, under Climate and Land Use Change	<1	Student Paper
36	High energy-storage density of lead-free BiFeO ₃ doped Na _{0.5} Bi _{0.5} by Tang-2018	<1	Publication
37	High-voltage Li ₂ SiO ₃ -LiNi _{0.5} Mn _{1.5} O ₄ hollow spheres prepared by in-situ, by Wang, Jiang Nie, P- 2018	<1	Publication
38	asbmr.onlinelibrary.wiley.com	<1	Internet Data
39	courses.lumenlearning.com	<1	Internet Data
40	Property-structure relationships in poly-urethanes Infrared studies by W-2007	<1	Publication
41	Reduced graphene oxide nanocomposites for optoelectronics applications, by Bano, N.; Hussain, - 2019	<1	Publication
42	dochero.tips	<1	Internet Data
43	Local release of siRNA using polyplex-loaded thermosensitive hydrogels by Fliervoet-2020	<1	Publication
44	On the Dispersion of Resistivity and Dielectric Constant of Some Semiconductors by Koops-1951	<1	Publication
45	repositorioslatinoamericanos	<1	Publication

Structural and magnetic investigations of (1-x) (Bi_{0.5}Na_{0.5}TiO₃)_{0.94}-(BaTiO₃)_{0.06} + (x) SrYFe₁₁O₁₉

C. S. Munnoli^{a*}, S. R. Kadam^b, S. S. Kammar^a, S. B. Kadam^c, R. H. Kadam^d, S. S. More^e

^aDepartment of Physics, HKE's A. V. Patil Degree College, Aland, Dist. Kalburgi (KA) India

^bDepartment of Physics, Jawahar College, Anadur, Dist. Osmanabad (M.S.) India

^cDepartment of Physics, LBS Senior College, Partur, Dist. Jalna (M.S.) India

^dMaterials Science Research Laboratory, Shrikrishna Mahavidyalaya, Gunjoti, Dist. Osmanabad (M.S.) India

^eDepartment of Physics, Y. C. College, Tuljapur Dist. Osmanabad (M.S.) India

*Corresponding author email: shekharm.345@gmail.com, Contact No: (Country Code) +91 7676766345

Abstract

As of now it is vital to develop a lead free multifunctional multiferroic composite for ecofriendly nature, we have developed a novel combined ferroelectric and ferrite composites with (1-x) (Bi_{0.5}Na_{0.5}TiO₃)_{0.94}-(BaTiO₃)_{0.06} + (x) SrYFe₁₁O₁₉ (x=0.00, 0.25, 0.50, 0.75 and 1) prepared separately by double solid-state sintering and sol-gel auto combustion methods. The phase formation was identified by XRD (x-ray diffraction), thus establishing the diphasic system without any impurity or secondary phase. Rietveld refinement by the FullProf suite and calculated lattice parameter shows the dual phase symmetry consisting hexagonal (P63/mmc) and tetragonal (P4bm) phases in the prepared composites. The micrographs of the magnetic powders were observed by a field emission scanning electron microscopy (FESEM) in order to understand the surface morphology of the samples. The ferroelectric and ferromagnetic grains are identified on the basis of energy dispersive spectroscopy (EDAX) studies. High resolution transmission electron microscopy (HR-TEM) was employed to determine the average particle size of the samples. The magnetic studies were conducted by using the vibrating sample magnetometer (VSM) for the applied magnetic field of 15Koe, with which the saturation magnetization (M_S), Magnetic retentivity (M_R), coercivity (H_c) and squareness ratio (Mr/Ms). The hysteresis loop reveals the ferromagnetic nature of the hexaferrite phase present in the composite.

Keywords: Composites, hexaferrites, lattice parameter, particle size, magnetization.

1. Introduction : The two-phase multiferroic composite exhibits a strong magnetoelectric interaction, a giant magnetoelectric effect above room temperature, and the simultaneous existence of electrical and magnetic coupling, and thus is considered to be an important link between magnetic composites and electrical composites. The combination of materials fascinated researchers. These connections promise to lead to the development of smarter, smaller components, memories, phase shifters, tunable filters, etc. [1-4]. Electromagnetic interactions between electrical and magnetic subsystems can be characterized by changes in magnetic anisotropy induced by the electric field or by changes in polarization due to low magnetic fields [5,6]. Coupling in multiferroic systems is the control of dielectric polarization by magnetic fields. Manipulation of magnetization by electric fields is a promising candidate for various applications such as spintronic devices, solid-state transduction and electro-magnetic optical actuators. The direct and inverse ME effects are caused by strain transfer via direct and inverse piezoelectric effects. The size of the ME output expected in single-

phase materials is small and not suitable for practical applications. It has been shown that the more composite materials containing ferrite and ferroelectric phases are considered, the greater the effect. [7,8]. Commercial applications so far have been lead-based ceramics because of their electrical properties, these materials can have a piezoelectric coefficient d_{33} up to 600-700 pC/N. However, due to toxic substances revolutionizing lead-free piezoelectric materials due to the growing demand for global environmental protection, there are more and more lead-alternative or lead-free materials with similar properties comparable to those of lead-based materials. Examples Potassium niobate (KNN - $K_{0.5} [Na]_{0.5} [NbO]_3$) and barium titanate (BT- $[BaTiO]_3$) and bismuth sodium titanate or bismuth sodium titanate (BNT - $B_{0.5} [Na]_{0.5} [TiO]_3$) [9]. The combination of BT and the starting compound NBT improves the ferroelectric and piezoelectric properties, so that the piezoelectric response d_{33} at room temperature is 120 to 180 pC/N, and the coupling Constants range from 21.2 to 36.7% and dielectric constants between 600 and 825. [10-11]. Currently, the majority of hard ferrite production is hexagonal ferrite, which is still the most practical material. They are very attractive materials with many uses. Of particular interest is strontium hexaferrite, whose unusual electromagnetic properties and applicability in the most diverse fields have aroused the curiosity of many researchers. Because it is characterized by high saturation magnetization, high coercivity, high Curie temperature, high magnetocrystalline anisotropy, high corrosion resistance, and chemical stability [12]. M-type of the general formula $[Sr]_{((1-y))} M_y [Fe]_{((12-x))} N_x O_{19}$ (where M and Z are typically 2^{+} and 3^{+} respectively) strontium hexaferrite metal). Obtained by single or double cation substitution of $[Fe]^{(3+)}$ or $[Sr]^{(2+)}$, they have attracted increasing attention from researchers [13]. SrM exhibits a hexadecimal structure with a space group of $P6_3/mm$, based on the structure of the unit cell and the distribution of ions to different sublattice sites in the unit cell. In SrM, the hexaferrite $[Fe]^{(3+)}$ is the main component that improves magnetic properties, (Sr $[Fe]_{12} O_{19}$) is considered the most important hexaferrite because it has a large amount of crystalline magnetic anisotropy, i.e. higher frequency magnetic resonance than barium hexaferrite (47.6 GHz) (196) and improve the hard magnetic properties of SrM ferrite and improve SrM hexagonal ferrites by replacing $[Sr \text{ sites}]^{(2+)}$ is equal to $[La]^{(3+)}$, $[Sm]^{(3+)}$, $[Ce]^{(3+)}$ and $[Fe]^{(3+)}$ by $[Cd]^{(3+)}$, $[Cd]^{(3+)}$, $[Zn]^{(3+)}$. Doped rare-earth elements with ionic radii similar to host cations have been found to alter the physical properties of strontium hexaferrite for a specific application. M-type hexaferrites such as Ba $[Fe]_{12} O_{19}$ and Sr $[Fe]_{12} O_{19}$ have a plumbite magnetostructure and are used as permanent magnets due to their coercive and magnetizing forces, which have low production costs for commercial production. as well as stability [13, 14, 15]. The crystal structure is characterized by the tight packing of Sr and oxygen ions with the Fe atoms in the interstitial position. M-type hexagonal ferrite is the most important multifunctional material for large-crystal magnetic anisotropy with high curie temperature and superior coercivity as well as high chemical and corrosion stability (240-340),

with an average residual of 350Mt [16-17], rare earth elements are also used to prevent particle size at high temperatures [18], they are used in the microwave range due to their strong magnetic properties. Hexagonal ferrite Sr belongs to the magnesium plumbite type material and is composed of a mixture of spinel $S = [\text{Fe}]_{-6} \text{O}_{-8}^{(2+)}$ (cubic S^*) and hexagonal Sr $[\text{Fe}]_{-6} \text{O}_{-11}^{(2-)}$ (R^* cubic) closed structure having space group P63/mmc, where Fe ions are tetrahedral (FeO4), octahedral (FeO6) and triangular tetrahedron (feo5) facilitated by oxygen ions. This structure consists of 64 ions per hexagonal unit cell across 11 base destinations. Hexagonal ferrite Sr has 24 $[\text{Fe}]^{(3+)}$ ions per unit cell distributed over five distinct crystal sites. One tetrahedral site $[\text{4f}]_{-1}$, three octahedral sites 12k, 2a and $[\text{4f}]_{-2}$, and one triangular site 2b. Of those, two have downpins and three 12k, 2a and 2b sites have upspins. Due to the spin effect, the ferromagnetic pair is preferentially exchanged between Fe-O-Fe, the bond gap becomes smaller. The distortion results in a situation where the magnetic moments of the 5 FE subnets are not parallel to each other. The sequence of the layer in the C axis is represented by the blocks RSR^{*}s^{*}(R^{*} & s^{*}) indicating that the rotation of the R and S blocks is 180 around the C axis. Electricity, magnetic and the dielectric properties of the substituted ferrics are strongly influenced by the synthesis method, the angularity ratio, the concentration, the temperature, the preference of the doping site as well as the MPB of the material.

In the present study, the goal of our work was to focus on a novel core-shell composite of sodium bismuth titanate, a rare earth metal doped with strontium (1-x) hexaferrite (Bi_{0.5}Na_{0.5}TiO₃)._{0.94}-(BaTiO₃)_{0.06} + (x) SrYFe₁₁O₁₉ is studied from the point of view of magnetic structure research. To the best of our knowledge, this is the first report on the structure as well as the electromagnetic effects in these particular composites in the core-shell form.

1.Experimental :

The magneto-electric (ME) composites with a particular composition of ferroelectric and ferrite phase having general formula $(1-x)(\text{Bi}_{0.5}\text{Na}_{0.5}\text{TiO}_3)_{0.94} - (\text{BaTiO}_3)_{0.06}$ and ferrite phase $\text{SrY}_1\text{Fe}_{12}\text{O}_{19}$ were synthesized separately via conventional solid-state method and Solgel auto-combustion method respectively, prepared samples are mixed with stoichiometric proportion for (x=0.00,0.25, 0.50, 0.75, 1) followed by double sintering method first at 900⁰ C and second at 1250⁰ C for 8hours for both phases. The above-mentioned experimental samples preparation process is as follows;

1.(a) Ceramic method: For preparation of BNBT $((1-x)(\text{Bi}_{0.5}\text{Na}_{0.5}\text{TiO}_3)_{0.94} - (\text{BaTiO}_3)_{0.06}$

The starting reagents Bi_2O_3 (99.90%), TiO_2 99.00%), BaCO_3 (99.98%), Na_2CO_3 (99.99%) were used as powders, the powders are weighed according to the stoichiometric ratio and mixed using agate mortar pestle for 6to 8 hr, the well mixed powders were dried and calcinated at 900⁰ C for 6 hr. the calcinated powder was once again mixed using agate mortar pestle for 2 hr and powder was again sintered at 1250⁰ C 8 hrs. The sintered powder was once again mixed in agate mortar pestle for 2 hours to make fine powder.

1. (b) Solgel-auto-combustion method: $SrY_1Fe_{12}O_{19}$ is our composition formula were prepared by sol gel auto-combustion method. In our case, nitrates $Sr(NO_3)_3 \cdot 9H_2O$, and $Fe(NO_3)_3 \cdot 9H_2O$ and $Y(NO_3)_3 \cdot 6H_2O$ (Analytical reagents) are used to make hexagonal ferrites of the M type. The nitrates mentioned above are used in the stoichiometric amount to prepare a distilled water solution of the compounds were combined in 2000ml beaker. The stock solution is stirred using a magnetic stirrer. Homogeneous mixture Continuous heating and stirring are used. The molar ratio of is 1:3. Citric acid is used to combine metals. The ammonia solution is then added drop by drop using the burette and stirring were maintained to keep the pH value at 7-8. Stop releasing ammonia and the solution was stirred and heated between 70 and 80 degrees Celsius until the water gets evaporated. When gel formation occurs, after forming the gel formation, the gel solution self-ignited with evaporating the large amount of gas, we started with a 200°C temperature and worked our way up to a fluffy powder. The powder crushed using agate mortar pestle for 2 hrs. The resulting powder was sintered at 900⁰ C for 6 hrs and annealed at 1250⁰ C for 6 hours. $(1-x)(Bi_{0.5}Na_{0.5}TiO_3)_{0.94}-(BaTiO_3)_{0.06} + (x) SrYFe_{11}O_{19}$

The separately prepared compounds $((1-x)(Bi_{0.5}Na_{0.5}TiO_3)_{0.94}-(BaTiO_3)_{0.06})$ and $SrY_1Fe_{12}O_{19}$ are mixed according to standard stoichiometric proportion for (x = 0.00, 0.25, 0.50, 0.75 and 1) and fine powdered by using agate mortar pestle and then sintered 1250⁰ C for 8 hours.

Characterization: An X ray diffractometer (XRD, Goniometer Ultima IV, 40KV/40MA, Cu K α radiation) XRD patterns were recorded at room temperature in the range 20 to 80 degree at radiation ($\lambda = 1.5404 \text{ \AA}$), FTIR (Fourier transformed infrared radiation) (PerkinElmer) were used to identify the phase composition in the range 440-4000 Cm^{-1} , VSM (vibrating sample magnetometer (Lakeshore 7410) were used to study the magnetic properties of the prepared sample by applying the 1.5 Tesla magnetic field, FESM (JSM 7600 F) were used to study the surface morphology of the prepared sample, EDAX were used to study the elemental composition of the sample, TEM (FEI, Tecnai G2, F30) was used to determine the grain size and interplanar spacing of the sample.

2. Results and discussion

2 (a) : XRD analysis

The XRD patterns of prepared sample $(1-x)(Bi_{0.5}Na_{0.5}TiO_3)_{0.94}-(BaTiO_3)_{0.06} + (x) SrYFe_{11}O_{19}$ (x = 0.00, 0.25, 0.50, 0.75, 1) are shown in fig.1. XRD pattern shows peaks of the both phases for BNBT and SRYFO respectively. All the XRD patterns of the prepared sample fairly matched without any external impurity. The XRD peaks were recorded in the range of 20 to 80 degree. The observed position peaks for BNBT recorded of planes (110), (111), (200), (210) and (220) and the refinement of XRD pattern was done by using Full-prof software program, peak shapes were described by Pseudo-Voigt function and refined background parameters were calculated by using Fourier cosine series to obtain detailed crystal structure information. Position peaks for SRFYO recorded planes (008), (107), (114), (201), (203), (205), (2011), (217) were indexed according to the standard match card no. For BNBT, COD Code:

2103296Reference Code:

96-210-3297and for SRFYO COD Code:

1006000Reference Code:

96-100-6001.The calculated lattice parameter **a and c** value for BNBT (5.5045\AA) and (3.8928\AA) and SRFYO lattice parameter **a and c** value (5.8816\AA) and (23.080\AA) The concentration of SrY₁ [(Fe)₁₂O₁₉] concentration showed noticeable effect on diffraction patterns peak intensity for (107),(114) planes .In the observed XRD data's it is found that the composite samples except (x=0.00 and X=1) rest of the x values indicates the coexistence of both phases and the observed group of BNBT cubic phase (crystal symmetry of space group P4bm) and SRFYO hexagonal phase (crystal symmetry of space group P63/mmc). Maximum intensity of BNBT The maximum intensity of each stage of BNBT decreased as the concentration of SRFYO increased and vice versa. The values of the network parameters a and c are calculated using the formula

$$a_{hkl} = \sqrt{\frac{4}{3} \frac{h^2 + hk + k^2}{a^2} + \frac{l^2}{c^2}}$$

and Size of the Crystal and Volume of the unit cell is calculated by below mentioned formula

$$\text{Size of the Crystal } D = \frac{0.89\lambda}{\beta \cos\theta} \text{Volume of unit cell } V = \frac{\sqrt{3}}{2} a^2 c$$

The Rietveld refinement method uses the LSM to solve the issues related to X-Ray diffraction data's such as preferred orientation, overlapped diffraction pattern and defining influential background ,etc. But present objective of this method is to enhance or gain the reduced function Δ which calculate the difference between observed $y(\text{obs})$ and calculated $y(\text{cal})$. So we used Hugo Rietveld equation to calculate Δ

$$\Delta = \sum_i W_i \left\{ y_i^{\text{obs}} - \frac{1}{c} y_i^{\text{cal}} \right\}^2$$

Where $W_i \rightarrow$ Statical weight that is equal to $1/y_i^{\text{obs}}$ and c is overall scale factor such that $C_{Y_{\text{obs}}} = C_{Y_{\text{cal}}}$ is obtained.

To determine the better quality of the process and to accomplish the convergence Profile residual R_p is calculated by the formula

$$R_p = 100 \frac{\sum y_i(\text{obs}) - y_i(\text{cal})}{\sum y_i \text{obs}}$$

And similarly weighted profile R_{wp} is calculated by the formula

$$R_p = 100 \left\{ \frac{\sum W_i y_i(\text{obs}) - y_i(\text{cal})}{(\sum W_i y_i \text{obs})^2} \right\}^2$$

The values of $y_i(\text{obs})$ and $y_i(\text{cal})$ are calculated by using intensities of the respective composition and both R-Parameters R_{wp} and R_p (less the 10% values are used) to convergence and this results the value fit parameter χ^2 .

The lattice parameter of a and c is calculated separately due to the coexistence of the two phases, the calculated values of the parameters a and c of BNBT and SRFYO change slightly, indicating the coexistence of the two phases together. The value of the calculated network parameter a for BNBT decreases with increasing SRFYO, while the SRFYO network parameter increases slightly or remains unchanged and the c value increases. This could be due to the difference in ionic radii of $[\text{Fe}]^{(3+)} [(0.63)^0]$ and $\text{Y}^{(3+)} [(0.97)^0]$ [20]. The ratio of the c/a lattice parameter increases as the SRFYO concentration increases. The c/a ratio is also an important parameter for quantifying M-type hexagonal structures, when the value is less than 3.98 [20, 21]. The c/a ratio of the calculated lattice parameter is 3.92 according to Vegard's law [22]. The crystal size was calculated using the Debye-Scherrer equation. The most intense (107) and (114) crystal peak sizes of the prepared sample increased in the range of 4.01 nm, which indicates the good quality of Hexaferrite. The unit cell volume increases as SRFYO increases [23]. The refined lattice parameter a and c , residual $R_{wp}, R_p, \chi^2 V_{cell}$ and D values are mentioned in Table .1

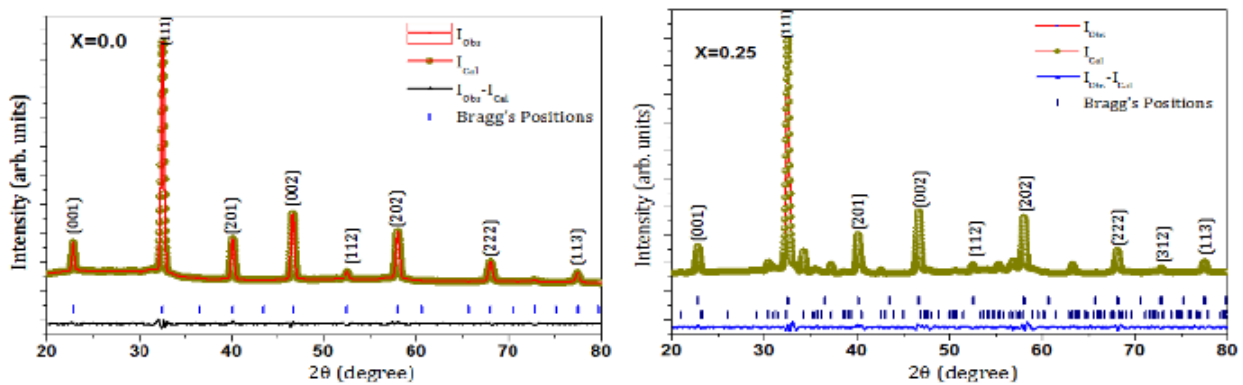


Fig. 1: X-ray diffraction Rietveld refinement pattern of prepared sample $(1-x) (\text{Bi}_{0.5}\text{Na}_{0.5}\text{TiO}_3)_{0.94}-(\text{BaTiO}_3)_{0.06} + (x) \text{SrYFe}_{11}\text{O}_{19}$ $X=0.00$ and $X=0.25$.

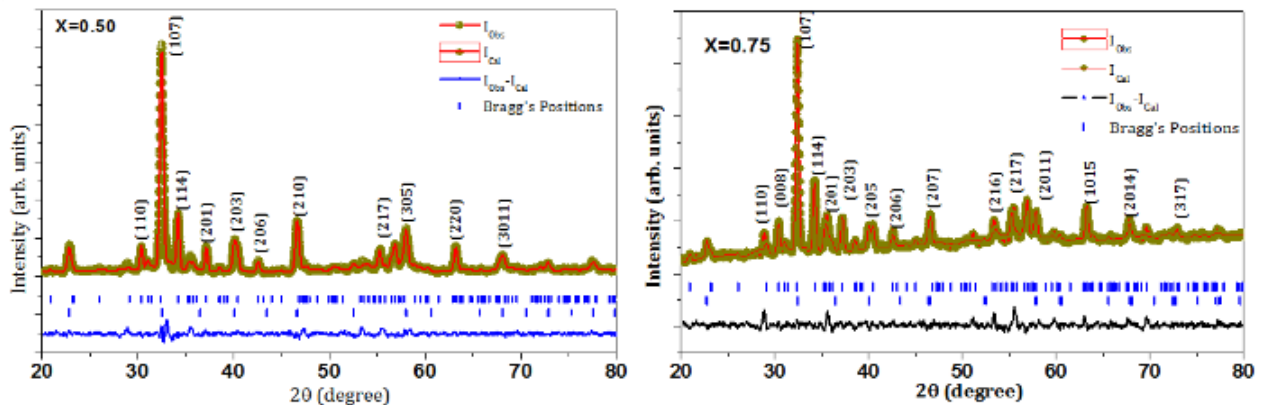


Fig. 2 : X-ray diffraction Rietveld refinement pattern of prepared sample $(1-x) (\text{Bi}_{0.5}\text{Na}_{0.5}\text{TiO}_3)_{0.94}-(\text{BaTiO}_3)_{0.06} + (x) \text{SrYFe}_{11}\text{O}_{19}$ $X=0.50$ and $X=0.75$.

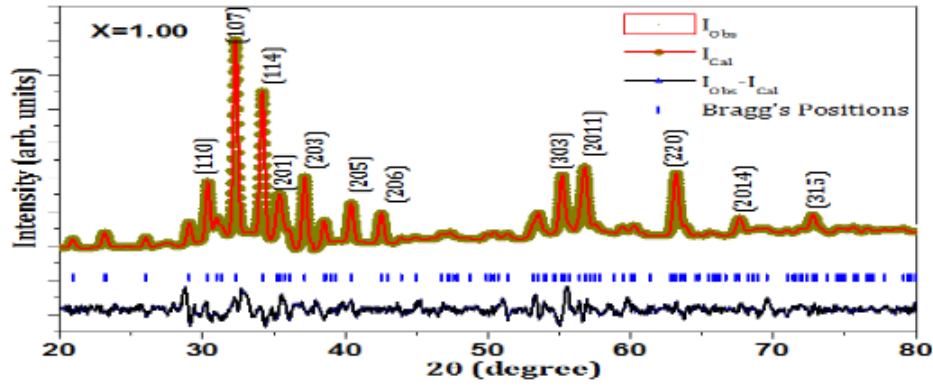


Figure 3: X-ray diffraction Rietveld refinement pattern of prepared sample $(1-x)(\text{Bi}_{0.5}\text{Na}_{0.5}\text{TiO}_3)_{0.94}-(\text{BaTiO}_3)_{0.06} + (x)\text{SrYFe}_{11}\text{O}_{19}$ ($X=1.00$)

Table 1: $(1-x)\text{BNBT}-x(\text{SRYFO})$ Structural parameters a and c , R factors, c/a , unit cell v and D values are obtained after the Rietveld refinement of the prepared samples are listed in the table

Sr No	Sample composition	Lattice constant	R- factor		R_P	R_{WP}
			χ^2	R_{Exp}		
1	0.00	BNBT (P4bm) $a = 5.511 \text{ \AA}$ $c = 3.898 \text{ \AA}$ $c/a = 0.707$ $V = 102.14 (\text{ \AA}^3)$	11.7	8.10	1.06	7.89
2	0.25	BNBT (P4bm) $a = 5.499 \text{ \AA}$ $c = 3.899 \text{ \AA}$ $c/a = 0.709$ $V = 102.12 (\text{ \AA}^3)$ SRYFO (P 63 / m m c) $a = 5.8767 \text{ \AA}$ $c = 23.0667 \text{ \AA}$ $c/a = 3.925$ $V = 689.89 (\text{ \AA}^3)$ $D = 231.683 \text{ nm}$	14.8	8.54	1.10	8.77
3	0.50	BNBT (P4bm) $a = 5.499 \text{ \AA}$ $c = 3.899 \text{ \AA}$ $c/a = 0.709$ $V = 101.99 (\text{ \AA}^3)$ SRYFO (P 63 / m m c) $a = 5.8783 \text{ \AA}$ $c = 23.0435 \text{ \AA}$ $c/a = 3.903$ $V = 689.57 (\text{ \AA}^3)$ $D = 226.665 \text{ nm}$	22.6	13.0	1.19	11.87
4	0.75	BNBT (P4bm) $a = 5.499 \text{ \AA}$ $c = 3.899 \text{ \AA}$ $c/a = 0.709$ $V = 102.65 (\text{ \AA}^3)$ SRYFO (P 63 / m m c) $a = 5.892 \text{ \AA}$ $c = 23.0422 \text{ \AA}$ $c/a = 3.9103$ $V = 692.755 (\text{ \AA}^3)$ $D = 244.003 \text{ nm}$	33.0	19.0	1.36	16.30
5	1	SRYFO (P 63 / m m c) $a = 5.8813 \text{ \AA}$ $c = 23.083 \text{ \AA}$ $c/a = 3.9248$ $V = 691.46 (\text{ \AA}^3)$ $D = 240.51 \text{ nm}$	42.9	24.7	1.59	19.61

2.(b) : FTIR :

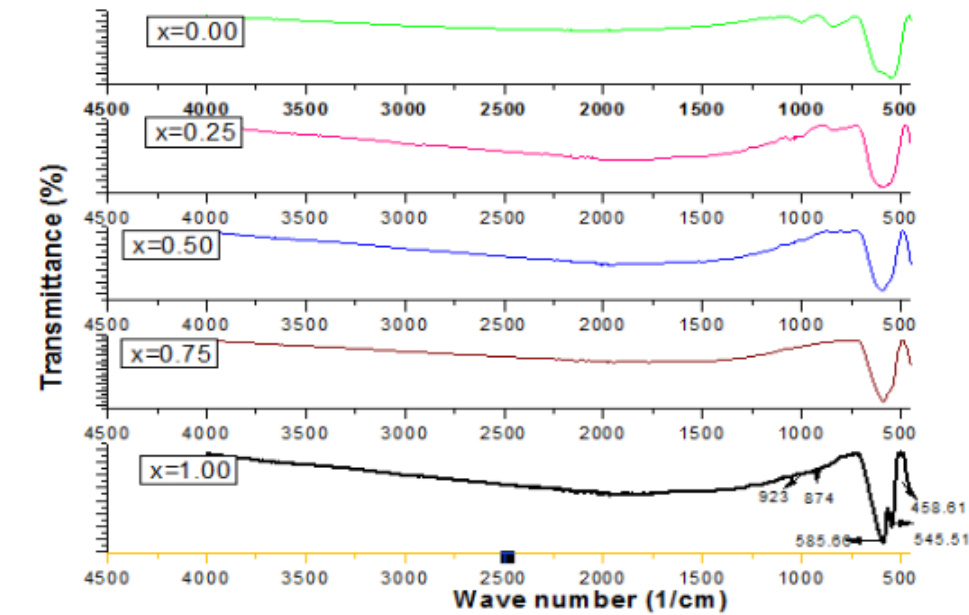


Fig: (4) FTIR Spectrum of prepared sample $(1-x) (\text{Bi}_{0.5}\text{Na}_{0.5}\text{TiO}_3)_{0.94} - (\text{BaTiO}_3)_{0.06} + (x) \text{SrYFe}_{11}\text{O}_{19}$ $x=0.0, 0.25, 0.50, 0.75, 1.0$

Figure.4:

gives the information on the dynamics of the crystal structure of spectra specially related to the vibration of the atomic bond, through which a small impurity of the sample can be detected, As reported earlier, that hexaferrite has 189 optical modes and out of them only 31 (13 $A_{2u} + 18 E_{1u}$) are IR respond modes [24] the FTIR spectra analysis of the pure and $(\text{Sr} [\text{Fe}]_{12-x} \text{Y}_x \text{O}_{19})$ and $(1-x)\text{BNBT} + x(\text{SRYFO})$ were carried out by comparative study, as well as by Spectragryph software identifier the observed FTIR spectra makes the predict the presence of the different bonds in the crystal, the above said analysis was performed at room temperature in the range of 450 to 4000 $[\text{Cm}]^{-1}$. In this study, only three are active modes the frequency of the absorption bands at 585.66 $[\text{Cm}]^{-1}$, 545.517 $[\text{Cm}]^{-1}$ and 458.61 $[\text{Cm}]^{-1}$ [24] the range of the observed band found in between 450 to 900 $[\text{Cm}]^{-1}$ are elucidated the characteristic band of $\text{Sr} [\text{Fe}]_{12} \text{O}_{19}$ [25-26]. In these bands, frequency around ν_1 (458.61 $[\text{Cm}]^{-1}$) is attributed to intrinsic elongating of the metal cation vibrations at the octahedral site and absorption frequencies around ν_2 (545.51, 585.66) are made due to intrinsic elongating of the metal cation vibrations at the tetrahedral site [24]. Coupling phenomena was found at 585.66 $[\text{Cm}]^{-1}$ and 545.517 $[\text{Cm}]^{-1}$ which changes the shape as plump peak, some other peaks observed around 874 and 923 $[\text{Cm}]^{-1}$ are Strontium carbonates [28-29] from the graph, it is also found that band position is moved to slightly shifts to lower wave number. The shift towards higher frequencies may be due to the change in bond length which can be later linked to the reduction in lattice parameters as shown by XRD. It can be also seen from the graph that the intensity of ν_1 band is decreased while broadening is increased with substitution. This shift of

the wavenumber towards the highest values is due to the contraction of the network during the substitution. Increased bonding between $[\text{Fe}]^{(3+)} - \text{O}^{(2-)}$ due to the contraction of the lattice changes the position of the peak to the higher wave numbers.

2.3 VSM: Magnetic Studies:

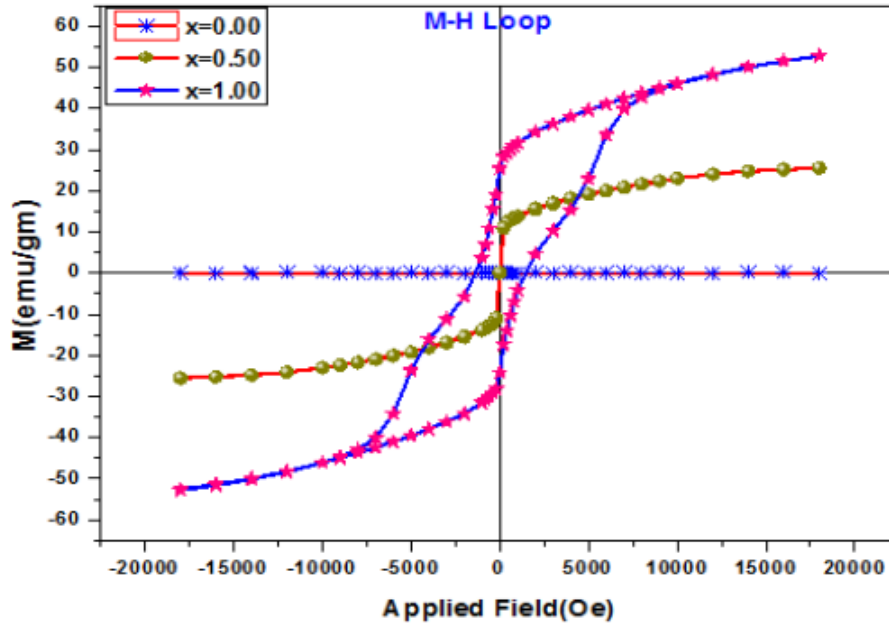


Figure 3 shows the ferromagnetic behavior of prepared sample. The magnetic characteristics of the prepared sample $(1-x)(\text{Bi}_{0.5}\text{Na}_{0.5}\text{TiO}_3)_{0.94}(\text{BaTiO}_3)_{0.06} + (x)\text{SrYFe}_{11}\text{O}_{19}$ ($x=0.00, 0.50$ and 1) composites were measured at room temperature in the range of approximately 20kOe using VSM Magnetic hysteresis loops.

Table 2. Provides the values of magnetic saturation (M_S), remanent magnetization (M_r) and coercivity (H_c), M_S/M_r of $x=0.50$ and $x=1.00$

Composition x	(M_S) in emu/gm	(M_r) in emu/gm	(H_c) in Oe	M_S/M_r
0.50	26.092	5.30	63	0.237
1.00	53.29	25.469	1393	0.4774

Table 2. Provides the values of magnetic saturation (M_S), remanent magnetization (M_r) and coercivity (H_c) of all the specimens. For $x=0.50$ reveals that the values of the (M_S) and (M_r), (H_c), M_S/M_r were 26.092, 6.12 emu/g, 52 Oe and 0.237 respectively, while the values of the (M_S) and (M_r), (H_c) and M_S/M_r for $x=1.0$ were 53.29, 25.46 emu/g, 1391Oe and 0.477

Figure 3. It was observed that the magnetic saturation (M_S) of the prepared mixture increased as the ferrite content increased. The increase in the magnetic saturation value (M_S) is due to the decrease in the volume of the ferroelectric phase. Since the magnetization in the composite is mainly due to the magnetic phase, it acts as a ferritic phase and the ferroelectric phase acts as a non-magnetic phase [30].

Values of characteristic parameters:

saturation (M_s), residual magnetization (M_r), coercivity (H_c) and M_s / M_r squared factors are reported in the table and found that the trend increases with adding the SRYFO Phase in BNBT which increases all magnetic sample parameters with an increase in the ferrite content in the ferroelectric expansion phase, the ferrite being central to the magnetization [31]. The magnetization saturation for yttrium-doped strontium hexaferrite is 53.29 emu/g compared with the commonly reported value of 49.6 emu/g [32]. The value of magnetization variation at saturation may be due to another synthesis process.

As the BNT-BT of the previously reported data is a fully ferroelectric relaxer [33], this composite exhibits ferroelectric behavior due to its paired electrons. The magnetic saturation value for the prepared sample depends on the particle size caused by the increase in the particle size. The $[[Fe]]^{(3+)}$ spin interaction in the nucleus increases more than the surface volume, increasing the magnetization [38]. When the ferrite saturates in a strong magnetic field, the magnetization vector rotates in the direction closest to the preferred field and produces strong anisotropy as the field decreases to zero, and the increase in residual magnetization values shows that most of the magnetic vectors Magnetic quenching - direction is favorable, creating a small angle with the direction of the applied stress field [34] resulting in large magnetization. Shape and stress anisotropy play an important role in the electromagnetic output of composites.

Almessiere et al. claims that a sample with a high saturation value can have a more excellent Bohr magnetic value. If the squared ratio is less than 0.50 then the particles are in the multiword domain and if equal to or greater than 0.50 the particles are in the monomagnetic domain. The square ratio of the prepared samples (SQR) M_s/M_r was found to be less than 0.5, exhibiting a multi-domain structure, the increase in parameters was due to the individual ferrite particles located at the center of the The total magnetization and their vectors are expected to produce saturation magnetization [35-36-37]. Incorporation of the non-magnetic BNBT phase into the magnetostrictive phase increases the dilution effect because these non-magnetic ions create voids between the magnetic ions and break the magnetic circuit and thus the values of the magnetic parameters are distorted. decrease (38-39) . The different B-site valence states of the BNBT lattice produced by the addition of SRYFO require charge compensation which can be achieved by converting the $[[Fe]]^{(3+)}$ ion to a $[[Fe]]^{(4+)}$ or by creating an oxygen vacancy.

2.4: Microstructure analysis (FESEM):

This page is extracted due to viral text or high resolution image or graph.

Figure. 05 (a) FESEM image and Grain size distribution after statics approximation of sample X=0.00 Figure. 05 (b) FESEM image and Grain size distribution after statics approximation of sample X=0.25 Figure. 05 (c) FESEM image and Grain size distribution after statics approximation of sample X=0.5 Figure. 05 (d) FESEM image and Grain size distribution after statics approximation of sample X=0.75

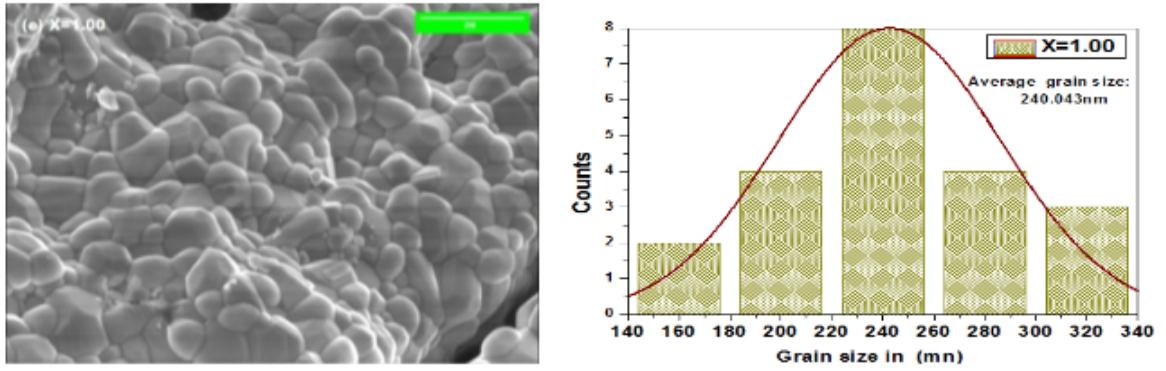


Figure. 05 (e) FESEM image and Grain size distribution after statics approximation of sample X=1.00

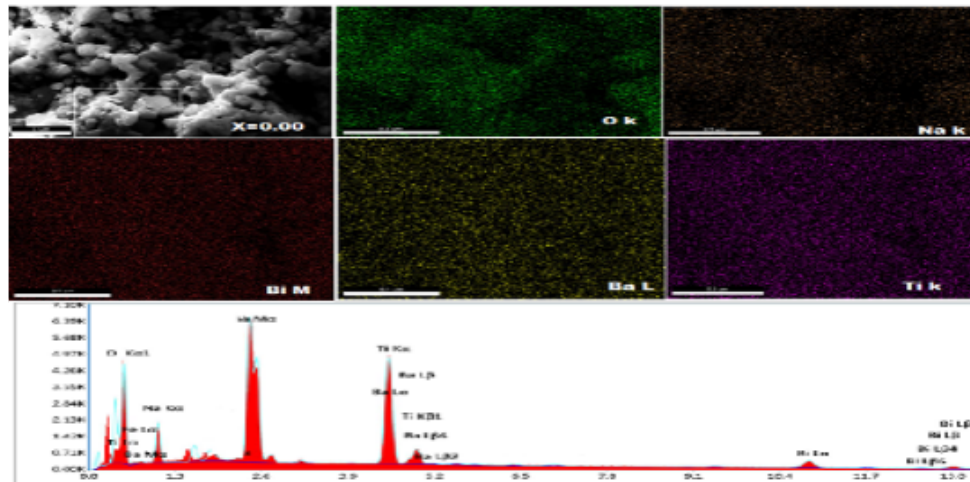


Figure 06 (a) Elemental mapping images of prepared sample X=0.00

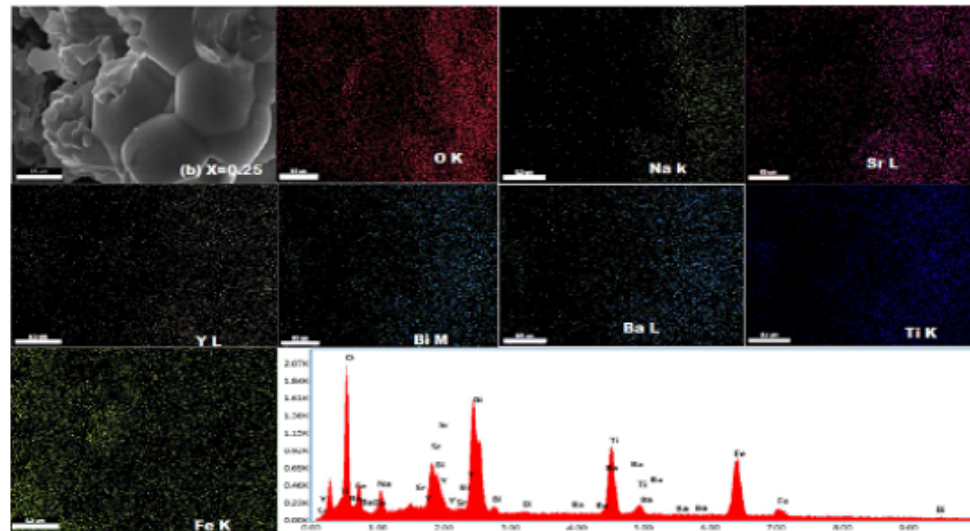


Figure 06 (b) Elemental mapping images of prepared sample X=0.25

This page is extracted due to viral text or high resolution image or graph.

Figure 06 (c) Elemental mapping images of prepared sample X=0.50 Figure 06 (d) Elemental mapping images of prepared sample X=0.75 Figure 8: Bright field TEM image (c and e) and HR-TEM image (d and f) for Pure BNBT sample with $x=0.00$ and $x=0.50$ obtained distance between the high magnification and lattice fringe found 2.84 0 and

2.64 , 2.758 \AA respectively which are in good agreement with the observed XRD plane(110) and (107) (114) respectively.

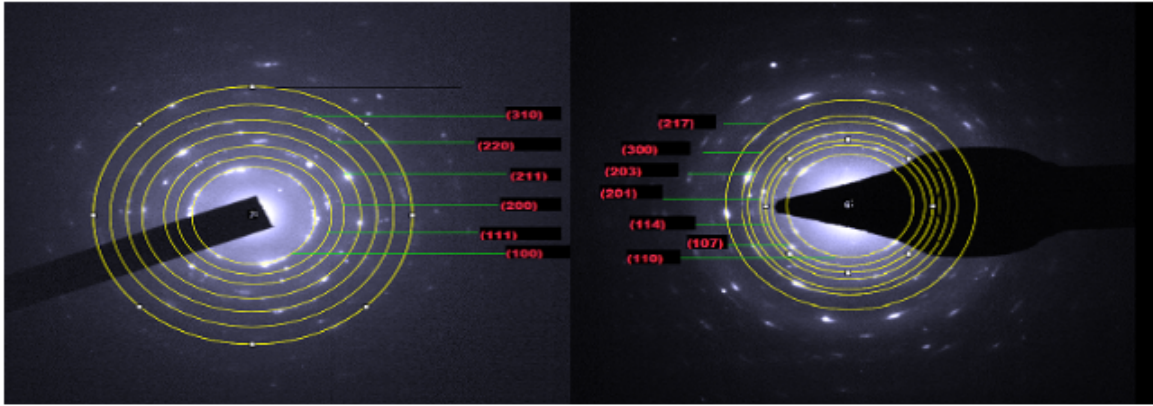


Figure.9 : SEAD pattern of sample (1-x) $(\text{Bi}_{0.5}\text{Na}_{0.5}\text{TiO}_3)_{0.94}-(\text{BaTiO}_3)_{0.06} + (x) \text{SrYFe}_{11}\text{O}_{19}$ X=0.00 and X=0.50

Table 3. Atomic percentage (at%) of Bi, Na, Ba, Ti, O, Sr, Y and Fe in sintered $(1-x) (\text{Bi}_{0.5}\text{Na}_{0.5}\text{TiO}_3)_{0.94}-(\text{BaTiO}_3)_{0.06} + (x) \text{SrYFe}_{11}\text{O}_{19}$

Composition	Elemental composition (at%)							
	Bi	Na	Ba	Ti	O	Sr	Y	Fe
X								
0.00	5.98	12.98	1.17	16.97	61.91	-	-	-
0.25	4.86	7.03	1.98	11.92	47.61	3.17	1.17	22.26
0.50	0.95	3.60	2.05	5.67	46.01	1.71	1.67	38.34
0.75	0.34	1.92	0.58	2.27	45.05	2.22	2.54	45.07

Figure 05 shows the scanning electron microscopy images with data analysis (grain size distribution obtained after static approximation) of the whole prepared sample $(1-x) (\text{Bi}_{0.5}\text{Na}_{0.5}\text{TiO}_3)_{0.94}-(\text{BaTiO}_3)_{0.06} + (x) \text{SrYFe}_{11}\text{O}_{19}$ ($x = 0.00, 0.25, 0.50, 0.75$ and 1.00) ceramic sintered at 900°C for 6 hours and incubated at 1250°C for 6 h. The beads in the form of tetragonal and hexagonal platelets correspond to BNBT and SRYFO. The magnetic phase connection is broken by the ferroelectric (non-magnetic) phase distribution in the composites and vice versa. On the contrary, this affects the magnetic and ferroelectric properties of the prepared sample. The average particle sizes of BNBT and SRYFO are 166 nm and 240,044 nm, respectively. The average particle size distribution plots and elemental mapping images are shown in Figures 5(a-e) and 6(a-d). In this study, the particle size distribution was uniform and the density was moderately high due to the preparation method and solid-state double sintering method as well as because the heating rate during the calcination process was very high compared to that of the solid-state double sintering method. with the usual heating process. ratio. In addition, heat is generated inside the material and the sampler rotates continuously, thus producing uniform heating. Compared with conventional and microwave sintering samples, solid-state double-sintering samples are homogeneously crystallized and have great advantages in terms of synthesis efficiency and energy consumption [39-40]. The average particle size of the prepared samples is shown in Fig. 5(a) to (e) were obtained using image j software and decreased with the addition of SRYFO ferrite, i.e. 166.23 nm, 202.37 nm, 237 nm, 244.04 and

240.043 nm for the modes product $x = 0.00, 0.25, 0.50, 0.75$ and 1.00 respectively. Sadhana et al. reported that the average Sr [Fe] ₁₂ O₁₉ grain is more than 200 nm annealed at 1250°C [41]. M.Rekaby et al. reported that Ba [Fe] ₁₂ O₁₉ particle size is larger than 125 nm calcined at 1050°C , K [42]. To better understand the average particle size, the prepared samples were characterized using HR-TEM figure. shows an image of a prepared sample sintered at 1250°C for ($x = 0.0, X = 0.50$). The calculated particle size obtained using (ImageJ-software) HR-TEM is 113-156 nm for $X=0.00$, 160-203 nm for $X=1.00$, the values of the grain size observed by both FESEM and HR-TEM were found to be approximately equal to the values calculated from the XRD. The overall trend of grain size increases with the addition of ferrite. The interplane distances measured from the lattice edges in the magnified HR-TEM images for $x=0.00$ were 2.84 and $x=0.50$, $x=1.00$ were 2.62 and 2.75 respectively.

These values are consistent with the indexed family plans of (107) and (114). The figure below shows schematic diagrams of BNBT and BNBT-SRYFO composites. Indexed plans (107) and (114) confirmed the BNBT-SRYFO hexaferrite formation

2.5 :Elemental composition Analysis :

To determine the elemental composition of nanocomposite $(1-x) (\text{Bi}_{0.5}\text{Na}_{0.5}\text{TiO}_3)_{0.94} (\text{BaTiO}_3)_{0.06} + (x) \text{SrYFe}_{11}\text{O}_{19}$, standard EDX spectra were recorded as shown in Figure 4. The EDX product of $X = 0.00$ nanoparticles represents the atomic percentage of 5, 98, 12, 98, 1, 17, 16, 97 and 61.91 for Bi, Na, Ba, Ti and O respectively, as shown in Figure 6 (yes). EDX analysis of nanocomposites $x = 0.25$ confirms that atomic percentages of 4.86, 7.03, 1.98, 11.92, 47.61, 3.17, 1.17 and 22.26 give elements Bi, Na, Ba, Ti, O, Sr, Y and Fe are present in the snack. Figure 6 (b). Figure 6(c) shows the EDX result of $X = 0.50$ nanocomposite with atomic percentage of 0.95, 3.60, 2.05, 5.67, 46.01, 1.71, 1.67 and 38.34 for the elements Bi, Na, Ba, Ti, O, Sr, Y and Fe. was present in the sample. Figure 6(d) shows EDX results 0.34, 1.92, 0.58, 2.27, 45.05, 2.22, 2.54 and 45.07 for elements Bi, Na, Ba, Ti, O, Sr, Y and Fe were present in the sample and did not contain any external impurities and the elemental analysis maps of the prepared samples confirmed the uniform distribution of the elements in the sample structure.

2.3 VSM: Magnetic Studies:

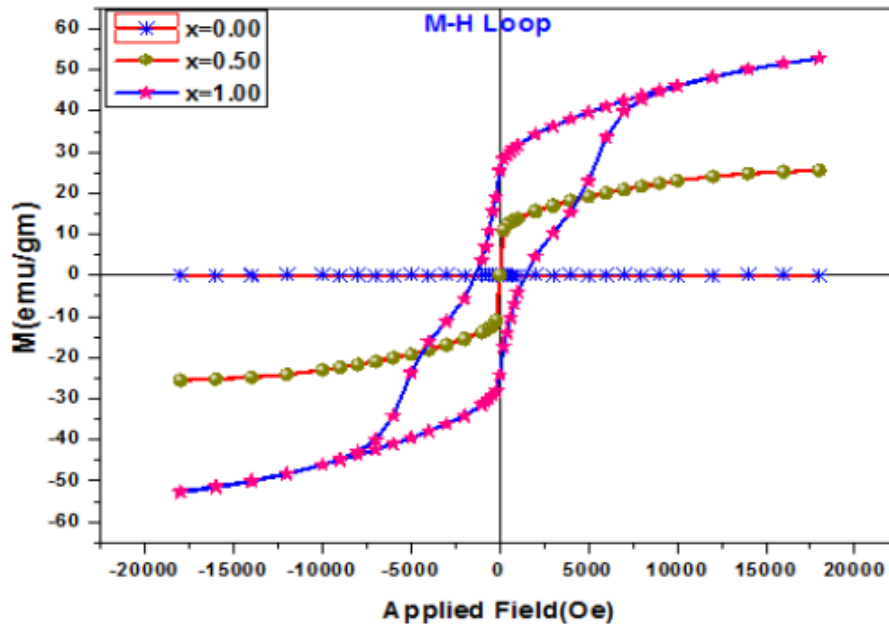


Figure 3 shows the ferromagnetic behavior of prepared sample. The magnetic characteristics of the prepared sample $(1-x)(Bi_{0.5}Na_{0.5}TiO_3)_{0.94} - BaTiO_3)_{0.06} - SrY_1Fe_{12}O_{19}$ ($x=0.00, 0.50$ and 1) composites were measured at room temperature in the range of approximately 20kOe using VSM Magnetic hysteresis loops.

Table 2. Provides the values of magnetic saturation (M_S), remanent magnetization (M_r) and coercivity (H_c), M_S/M_r of $x=0.50$ and $x=1.00$

Composition x	(M_S) in emu/gm	(M_r) in emu/gm	(H_c) in Oe	M_S/M_r
0.50	26.092	5.30	63	0.237
1.00	53.29	25.469	1393	0.4774

Table 2. Provides the values of magnetic saturation (M_S), remanent magnetization (M_r) and coercivity (H_c) of all the specimens. For $x=0.50$ reveals that the values of the (M_S) and (M_r), (H_c), M_S/M_r were 26.092, 6.12 emu/g, 52 Oe and 0.237 respectively, while the values of the (M_S) and (M_r), (H_c) and M_S/M_r for $x=1.0$ were 53.29, 25.46 emu/g, 1391 Oe and 0.477

The figure 3. It was observed that magnetic saturation (M_S) of the prepared composite increases with increase of ferrite content. The increase in the value of the magnetic saturation (M_S) is due to the fact that the volume of the ferroelectric phase decreases. As magnetization in the composite is mostly contributed by magnetic phase act as ferrite phase and ferroelectric phase acts as a non-magnetic phase [30].

Values of characteristic parameters: saturation (M_S), remanent magnetization (M_r), coercivity (H_c) and M_S/M_r squareness factors are reported in table and found that an increasing trend on adding SRYFO phase in BNBT all the magnetic samples are increased parameters with increase of ferrite content in the ferroelectric relaxor phase ferrite being the center of magnetization [31]. The magnetization saturation for pure yttrium

doped Strontium hexaferrite found 53.29 emu/g than usually reported value 49.6 emu/g [32]. The variation value of saturation magnetization may due to different synthesis process.

As previous reported data's BNT-BT is a purely ferroelectric relaxor [33], this composite shows ferroelectric behavior due to its paired electrons, The Magnetic saturation value for the prepared sample relies particle size caused by the increasing the particle size. Increase in the Fe^{3+} spin interaction in core than in the surface volume raises the magnetization [38]. When the ferrite is saturated in a strong magnetic field, the magnetization vector rotates in the direction nearest preferred field and creates a high anisotropy when the field drops to zero and increasing residual magnetization values indicates that most of the magnetizing vectors turned out of the magnetically -profitable direction, making a small angle to the direction of the applied field which experiences stress [34] resulting in large magnetization. Shape and stress anisotropy has prominent role in the Magneto electric output of the composites.

Almessiere et al. stated that the sample with a high saturation value is probable to have a more excellent value of Bohr magneton. ¹⁴ If the squareness ratio is less than 0.50, then the particles are in multi magnetic domain and if it is equal or higher than 0.50 then the particles are in a single domain. The prepared samples (SQR) M_S/M_r squareness ratio found lesser than the 0.5, which exhibits a multi domain structure, increase in the parameters are due to individual ferrite grains being center of magnetization and it is expected that their vector sum devotes the saturation magnetization [35-36-37]. Incorporation of non-magnetic phase BNBT in piezomagnetic phase increase the dilution effect as these non-magnetic ions creates pores among the magnetic ions and breaks the magnetic circuit and hence reduced values of magnetic parameters (38-39). The different valence states of B-site of BNBT Lattice created by addition of SRYFO require a charge compensation that can be attained by converting Fe^{3+} ion into Fe^{4+} ions or by generating vacant position of oxygen.

Conclusion:

Reference:

1. Y.H. Lin, N. Cai, J.Y. Zhai, G. Liu, C.W. Nan, Phys. Rev. 72 (2005) 012405.
2. R. Pattanayak, S. Raut, S. Kuila, M. Chandrasekhar, S. Panigrahi, Multiferroism of [Na_{0.5}Bi_{0.5}TiO₃-BaFe₁₂O₁₉] lead-free novel composite systems, Mater. Lett. 209(2017) 280-283.
<https://doi.org/10.1016/j.matlet.2017.08.023>.
3. A. Srinivas, T. Karthik, R. Gopalan, V. Chandrasekaran, Improved magnetoelectricity by uniaxial magnetic field pressed and sintered composites in BaTiO₃ (x)-BaFe₁₂O₁₉ (1-x) system (x = 0.8, 0.6), Mater.

Sci. Eng. B Solid-State Mater. Adv. Technol. 172 (2010)289–293.

<https://doi.org/10.1016/j.mseb.2010.05.033>. 4

4. Enhanced magnetoelectric effect in core-shell particulate composites Enhanced magnetoelectric effect in core-shell particulate composites, 503 (2014) 97–100. <https://doi.org/10.1063/1.2165147>.

5. C.-W.Nan, M.I.Bichurin, S.Dong, D.Viehland, and G.Srinivasan”, Multiferroic magnetoelectric composites: Historical perspective, status, and future directions”, J. Appl. Phys., vol. 103, pp. 031101, February 2008.

6. N.A.Spaldin and M. Fiebig, “The Renaissance of Magnetoelectric Multiferroics”, Science, vol. 309, pp.391-392, July 2005

7. N.A.Spaldin and M. Fiebig, “The Renaissance of Magnetoelectric Multiferroics”, Science, vol. 309, pp.391-392, July 2005.

8. C.A.F.Vaz, J.Hoffman, C.H.Ahn, “R.Ramesh, Magnetoelectric Coupling Effects in Multiferroic Complex Oxide Composite Structures”, Adv.Mater. vol. 22, pp. 2900-2918, July 2010.

9.. Uchino K, Nomura S, Cross LE, Jang SJ, Newnham RE. Electrostrictive effect in lead magnesium niobate single crystals. J Appl Phys 1980;51:1142–5.

10. Zhou, D.; Li, H.; Gong, S.; Hu, Y.; Han, K.: Sodium bismuth titanate-base lead-free piezoceramics prepared by aqueous gelcasting. J. Am. Ceram. Soc. 2008, 91, 2792-2796.

11. Oh, T.; Kim, M. H.: Phase relation and dielectric properties in $(\text{Bi}_{1/2}\text{Na}_{1/2})_{1-x}\text{Ba}_x\text{TiO}_3$ lead-free ceramics. Mater. Sci. Eng. B 2006, 132, 239-46

12. M. N. Ashiq, S. Shakoor, M. Najam-ul-Haq, M. F. Warsi, I. Ali and I. Shakir, J. Magn. Magn. Mater., 2015, 374, 173–178.

13. Shinde, S.R., Lofland, S.E., Ganpule, C.S., Bhagat, S.M., Ogale, S.B., Ramesh, R. and Venkatesan, T. (1999) Improvement in Spin-Wave Resonance Characteristics of Epitaxial Barium-Ferrite Thin Films by Using an Aluminum-Doped Strontium-Ferrite Buffer Layer. Applied Physics Letters, 74, 594-596. <https://doi.org/10.1063/1.123156>

14. Dho, J., Lee, E.K., Park, J.Y. and Hur, N. H. (2005) Effects of the Grain Boundary on the Coercivity of Barium Ferrite $\text{BaFe}_{12}\text{O}_{19}$. Journal of Magnetism and Magnetic Materials, 285, 164-168. <https://doi.org/10.1016/j.jmmm.2004.07.033>

15. Jean, M., Nachbaur, V., Bran, J. and Le Breton, J.M. (2010) Synthesis and Characterization of $\text{SrFe}_{12}\text{O}_{19}$ Powder Obtained by Hydrothermal Process. Journal of Alloys and Compounds, 496, 306-312. <https://doi.org/10.1016/j.jallcom.2010.02.002>

16. E.E. Riches, Ferrites Mills, Boon Technical Library, Boon, London, 1972.

17. J. Kracch, M.H. Grant, Encyclopedia of Chemical Technology, fourth ed., Wiley, 1993.

18. N. Yang, H. Yang, J.J. Jia, X.F. Pang, J. Alloy. compd. 438 (2007) 263–267.

19. El-Sayed, S., Meaz, T., Amer, M. and El Shersaby, H. (2013) Magnetic Behavior and Dielectric Properties of Aluminum Substituted M-Type Barium Hexaferrite. *PhysicaB : Condensed Matter* , 426, 137-143. <https://doi.org/10.1016/j.physb.2013.06.026>
20. Wagner, T.: Preparation and crystal structure analysis of magnetoplumbite-type BaGa₂O₁₉. *J. Solid State Chem.* **136**,120–124 (1998)
21. Auwal, I.A., Güner, S., Güngöres, H., Baykal, A.: Sr_{1-x}La_xFe₁₂O₁₉ (0.0 = x = 0.5) hexaferrites: Synthesis, characterizations, hyperfine interactions and magneto-optical properties. *Ceram. Int*
22. R.A. Pawar, S.S. Desai, Q.Y. Tamboli, S.E. Shirsath, S.M. Patange, Ce³⁺ incorporated structural and magnetic properties of M type barium hexaferrites, *J. Magn. Magn. Mater.* 378 (2015) 59–63
23. R.H. Kadam, A.A. Birajdar, S.T. Alone, S.E. Shirsath, *J. Magn. Magn. Mater.* **327** (2013) 167.
- 24.S. Mahadevan, C. Pahwa, S.B. Narang, P. Sharma, Structural, dielectric and magnetic properties of BaFe_{12-x}Al_xO₁₉hexaferrite thick films. *J. Magn. Magn. Mater.* **441**, 465–474 (2017)
25. T. Xie, L. Xu, C. Liu, Synthesis and properties of composite magneticmaterial SrCo_xFe_{12-x}O₁₉ (x = 0–0.3). *Powder Technol.* **232**, 87–92 (2012)
- 26.A. Baykal, M.S. Toprak, Z. Durmus, H. Sozeri, Hydrothermal synthesis of SrFe₁₂O₁₉ and its characterization. *J. Supercond. Nov. Magn.* **25**, 2081–2085 (2012) 182M. Jean, V. Nachbaur, J. Bran, J.-M. Le Breton, Synthesis and characterization of SrFe₁₂O₁₉ powder obtained by hydrothermal process, *J. Alloys Comp.* 496 (2010) 306-312
27. A.B. Gadkari, T.J. Shinde, P.N. Vasambekar, Structural analysis of Y³⁺ -doped Mg–Cd ferrites prepared by oxalateco-precipitation method. *Mater. Chem. Phys* **114**, 505–510 (2009)
- 28.Alange, R.C., Khirade, P.P., Birajdar, S.D., Humbe, A.V., Jadhav, K.M.: Structural, magnetic and dielectrical properties of Al–Cr Co-substituted M-type barium hexaferrite nanoparticles. *J. Mol. Struct.* **1106**, 460–467 (2016)
29. Miller, F.A., Wilkins, C.H.: Infrared spectra and characteristic frequencies of inorganic ions. *Anal. Chem.* **24**, 1253–1294 (1952)
30. D.R. Patil, S.A. Lokare, S.S. Chougule, B.K. Chougule, Dielectric and magnetic properties of x NiFe₂O₄ þ (1 - x) Ba_{0.9}Sr_{0.1}TiO₃ composites, *Phys. B* 400 (2007)77e82.
31. C.G. Koops, On the dispersion of resistivity and dielectric constant of somesemiconductors at audio frequencies, *Phys. Rev.* 83 (1951) 121e124,<https://doi.org/10.1103/PhysRev.83.121>
32. **Y³⁺ substituted Sr-hexaferrites: sol-gel synthesis, structural, magnetic and electrical characterization** <http://dx.doi.org/10.1590/0366-69132019653742582>
33. S.Dagar, A.Hooda, S. Khasa, M. Malik, “Rietveld Refinement, Dielectric and Magnetic Properties of NBT-Spinel Ferrite Composites” *Journal of Alloys and Compounds* 806 (2019) 737-752, <https://doi.org/10.1016/j.jallcom.2019.07.178>

34. R. S. Devan, S. B. Deshpande, and B. K. Chougule, "Ferroelectric and ferromagnetic properties of (x)BaTiO₃+ (1-x)Ni_{0.94}Co_{0.01}Cu_{0.05}Fe₂O₄ composite" J. Phys. D: Appl. Phys. 40(2007)1864–1868. <https://dx.doi.org/10.1088/0022-3727/40/7/004>.
35. M. Rawat, K. L. Yadav, "Electrical, magnetic and magnetodielectric properties in ferriteferroelectric particulate composites", Smart Mater. Struct. 24 (2015) 045041. doi:10.1088/0964-1726/24/4/045041
36. Manjusha, M. Rawat, K. L. Yadav, "Structural, dielectric, ferroelectric and magnetic properties of (x)CoFe₂O₄-(1-x)BaTiO₃ composite", IEEE T. DIELECT. EL. IN 22 (2015) 1462- 1469. doi:10.1109/TDEI.2015.004774.
37. N. Adhlakha, K. L. Yadav, "Study of structural, dielectric and magnetic behaviour of Ni_{0.75}Zn_{0.25}Fe₂O₄– Ba(Ti_{0.85}Zr_{0.15})O₃ composites", Smart Mater. Struct. 21 (2012) 115021. doi:10.1088/0964-1726/21/11/115021
38. K. Habanjar, H. Shehabi, A.M. Abdallah, R. Awad, Effect of calcination temperature and cobalt addition on structural, optical and magnetic properties of barium hexaferrite BaFe₁₂O₁₉ nanoparticles, Appl. Phys. Mater. Sci. Process 126 (2020), <https://doi.org/10.1007/s00339-020-03497-3>.
39. SyedMahboob, A.B. Dutta, Chandra Prakash, G. Swaminathan, S.V. Suryanarayana, G. Prasad, G.S. Kumar, Mater. Sci. Eng. B 134 (2006) 36.
40. K. Sadhana, T. Krishnaveni, K. Praveena, S. Bharadwaj, S.R. Murthy, Scr. Mater. 59 (2008) 49
41. K. Sadhana, S.R. Murthy, Jie Shang, Xia Yali, Liu Yiwei, Q. Zhang, Runwei Li, J. Appl. Phys. 3 (17) (2013) 17C731.
42. R. Pattanayak, R. Muduli, R.K. Panda, T. Dash, P. Sahu, S. Raut, S. Panigrahi, Investigating the effect of multiple grain-grain interfaces on electric and magnetic properties of [50 wt% BaFe₁₂O₁₉-50 wt% Na_{0.5}Bi_{0.5}TiO₃] composite system, Phys. B Condens. Matter 485 (2016) 67–77, <https://doi.org/10.1016/j.physb.2016.01.011> 5.

Dr. R. H. KADAM

Y paper.docx

Structural and magnetic investigations of (1-x) (Bi_{0.5}Na_{0.5}TiO₃)_{0.94}- (BaTiO₃)_{0.06} + (x) SrYFe₁₁O₁₉

C. S. Munnoli^{a*}, S. R. Kadam^b, S. S. Kammar^a, S. B. Kadam^c, R. H. Kadam^d, S. S. More^e

^aDepartment of Physics, HKE's A. V. Patil Degree College, Aland, Dist. Kalburgi (KA) India

^bDepartment of Physics, Jawahar College, Anadur, Dist. Osmanabad (M.S.) India

^cDepartment of Physics, LBS Senior College, Partur, Dist. Jalna (M.S.) India

^dMaterials Science Research Laboratory, Shrikrishna Mahavidyalaya, Gunjoti, Dist. Osmanabad (M.S.) India

^eDepartment of Physics, Y. C. College, Tuljapur Dist. Osmanabad (M.S.) India

50

*Corresponding author email: shekharm.345@gmail.com, Contact No: (Country Code) +91 7676766345

Abstract

As of now it is vital to develop a lead free multifunctional multiferroic composite for ecofriendly nature, we have developed a novel combined ferroelectric and ferrite composites with (1-x) (Bi_{0.5}Na_{0.5}TiO₃)_{0.94}-(BaTiO₃)_{0.06} + (x) SrYFe₁₁O₁₉ (x=0.00, 0.25, 0.50, 0.75 and 1) prepared separately by double solid-state sintering and sol-gel auto combustion methods. The phase formation was identified by XRD (x-ray diffraction), thus establishing the diphasic system without any impurity or secondary phase. Rietveld refinement by the FullProf suite and calculated lattice parameter shows the dual phase symmetry consisting hexagonal (P63/mmc) and tetragonal (P4bm) phases in the prepared composites. The micrographs of the magnetic powders were observed by a field emission scanning electron microscopy (FESEM) in order to understand the surface morphology of the samples. The ferroelectric and ferromagnetic grains are identified on the basis of energy dispersive spectroscopy (EDAX) studies. High resolution transmission electron microscopy (HR-TEM) was employed to determine the average particle size of the samples. The magnetic studies were conducted by using the vibrating sample magnetometer (VSM) for the applied magnetic field of 15Koe, with which the saturation magnetization (M_S), Magnetic retentivity (M_R), coercivity (H_C) and squareness ratio (Mr/M_S). The hysteresis loop reveals the ferromagnetic nature of the hexaferrite phase present in the composite.

Keywords: Composites, hexaferrites, lattice parameter, particle size, magnetization.

INTRODUCTION:

Combination of magnetic and electric composite materials have been attracting the researchers, because of the diphase multiferroic composites exhibits strong magnetoelectric interactions, giant magnetoelectric effect above the room temperature, simultaneous existence of electric and magnetic coupling, these compounds are expected to develop the smarter and small size components, memories, phase shifters and tunable filters etc. (1-2-3-4). The magnetoelectric interaction between electric and magnetic subsystem can be characterize by the change in polarization by electric fields induced change of magnetic anisotropy or by under magnetic fields(5-6) and the coupling in a multiferroic system is the control of dielectric polarization by magnetic field and manipulation of magnetization by an electric field are most promising candidates for different application like spintronic devices, solid state transformation, electro magneto optic actuators. The direct and reverse ME effects are caused by strain transfer via direct and reverse piezoelectric effects. The magnitude of ME output that is expected in single phase materials is small and is not interesting for practical applications. It has been demonstrated that the effect is greater to the extent that they can be considered for the high in composite materials that contain ferrite and ferroelectric phases. [7-8]. To date the commercial applications have been lead based ceramics due to their electrical property and these materials can exhibits d_{33} of upto 600 – 700 pC/N piezoelectric coefficient. However due to toxic material that brings revolution for lead free piezoelectric material on growing demand of global environmental protection, there is lead substituted or Pb free materials are growing which exhibits similar properties which are comparable to lead based materials. Example Potassium niobite(KNN - $K_{0.5}Na_{0.5}NbO_3$) and Barium Titanate (BT- $BaTiO_3$) and Bismuth sodium Titanate or sodium bismuth titanate (BNT - $B_{0.5}Na_{0.5}TiO_3$)(9). As the Combination of BT to the Parent compound NBT which improves the ferroelectric and Piezoelectric properties, at room temperature the piezoelectric response d_{33} is 120 to 180pC/N and coupling constant ranges from 21.2 to 36.7% and the dielectric constant is in between 600-825 (10-11).Currently, the vast majority of hard ferrite production is hexagonal ferrite, which is still by far the most practical material. They are extremely intriguing materials with numerous applications. The strontium hexaferrite, which has piqued the curiosity of many researchers due to its unusual electromagnetic characteristics and applicability in a wide variety of fields, is of special interest.. This is because it is characterized by a high saturation magnetization, a large coercive force, high Curie temperature, large magneto crystalline anisotropy, high corrosion resistance and chemical stability (12). The M-type strontium hexaferrite with general formula $Sr_{(1-y)}M_yFe_{(12-x)}N_xO_{19}$ (M and Z are 2^+ and 3^+ metals respectively) typically obtained by single or double cation substitutions for Fe^{3+} or Sr^{2+} increasingly attracts the attention of researchers (13). SrM exhibits the hexa structure with $P6_3/m$ space group, on the basis of the unit cell structure and the ion allocation at different sublattices sites in the unit cell. In the SrM

hexaferrite Fe^{3+} is the main component which enhanced the magnetic property, ($SrFe_{12}O_{19}$) considered as most prominent hexaferrite because it has large amount of magneto crystalline anisotropy i.e. highest frequency magnetic resonance than the barium Hexaferrite (47.6 GHz) (196) and the enhancement of the hard magnetic properties of the SrM ferrites and the improvement in the SrM hexagonal ferrites by the replacement of Sr^{2+} sites by $La^{3+}, Sm^{3+}, Ce^{3+}$ and Fe^{3+} ions by $Cd^{3+}, Cd^{3+}, Zn^{3+}$. Doping of rare earth elements with similar ionic radius with host cations was found changes the physical properties of Strontium hexaferrite for suitable for specific application. M-type hexaferrite like $BaFe_{12}O_{19}$ and $SrFe_{12}O_{19}$ are having magneto plumbite structure and used as a permanent magnet because of their Coercivity and magnetization, having low manufacturing cost for commercial production as well as the stability (13,14,15). Crystal structure is characterized by close packing Sr ions and Oxygen with Fe atoms at the interstitial position. The M type hexagonal ferrite is most prominent multifunctional materials for large magneto crystalline anisotropy with high curie temperature and superior coercivity as well as superior chemical stability and corrosion [240-340] having moderate remanence 350Mt (16-17), rare earth elements also used for impede the grain size at high temperature (18) these are used in hyper frequency range due to their strong magnetic properties.

Sr-hexagonal ferrite belongs to magneto plumbite type material and it is composition of mixed spinel $S = Fe_6O_8^{2+}(S^*block)$ and Hexagonal $SrFe_6O_{11}^{2-}(R^*block)$ closed -packed structure having a space group P63/mmc in which Fe ion are facilitated Tetrahedrally (FeO4), octahedrally (FeO6) and trigonal bipyramidal (feo5) by oxygen ions. This structure is comprising with 64 ions for each hexagonal unit cell on 11 fundamental destination. The hexagonal Sr-ferrite has 24 Fe^{3+} ions per unit cell which are distributed on five different distinctive crystallographic sites. One tetrahedral site 4f1, three octahedral sites 12k, 2a and 4f2 and one trigonal bipyramidal site 2b. Among them two sites have down spin and three sites 12k, 2a and 2b have up spin. Due to the spin effect the ferromagnetic couple is favoured with exchange between Fe-O-Fe the distance bond becomes smaller. The distortion leads the situation where the magnetic moment of the 5 Fe sub lattice are not mutually parallel. The sequence of the layer in C-axis is represented by RSP^*S^* (R^* & S^*) blocks denotes rotation of R and S blocks by 180 about the C- axis. The electric, magnetic and dielectric behavior of substituted ferrites are strongly affected by synthesis method, stoichiometric ratio, concentration, temperature, site preference of dopant as well as on MPB of the material.

In the present research our aim of work is to focused on the novel core-shell composite of sodium bismuth titanate rare earth metal doped with strontium hexaferrite $(1-x)(Bi_{0.5}Na_{0.5})TiO_3)_{0.94} - BaTiO_3)_{0.06} + SrY_1Fe_{12}O_{19}$ was investigated from the point of view of structural, electrical and dielectric properties. To the best of our knowledge, this is the first report on the structural as well as on the magnetoelectric effect in this particular composites in the form of the core-shell

Methods and Materials:

The magnetoelectric (ME) composites with a particular composition of ferroelectric and ferrite phase having general formula $(1 - x)(Bi_{0.5}Na_{0.5})TiO_3)_{0.94} - BaTiO_3)_{0.06}$ and ferrite phase $SrY_1Fe_{12}O_{19}$ were synthesized separately via conventional solid-state method and Solgel auto-combustion method respectively, prepared samples are mixed with stoichiometric proportion for $(x=0.00, 0.25, 0.50, 0.75, 1)$ followed by double sintering method first at $900^\circ C$ and second at $1250^\circ C$ for 8 hours for both phases. The above-mentioned experimental samples preparation process is as follows;

1. Mixing Powders: For preparation of BNBT $((1 - x)(Bi_{0.5}Na_{0.5})TiO_3)_{0.94} - BaTiO_3)_{0.06}$

The starting reagents Bi_2O_3 (99.90%), TiO_2 (99.00%), $BaCO_3$ (99.98%), Na_2CO_3 (99.99%) were used as powders, the powders are weighed according to the stoichiometric ratio and mixed using agate mortar pestle for 6 to 8 hr, the well mixed powders were dried and calcinated at $900^\circ C$ for 6 hr. the calcinated powder was once again mixed using agate mortar pestle for 2 hr and powder was again sintered at $1250^\circ C$ 8 hrs. The sintered powder was once again mixed in agate mortar pestle for 2 hours to make fine powder.

2. Solgel-auto-combustion method: $SrY_1Fe_{12}O_{19}$ is our composition formula were prepared by sol gel auto-combustion method. In our case, nitrates $Sr(NO_3)_3 \cdot 9H_2O$, and $Fe(NO_3)_3 \cdot 9H_2O$ and $Y(NO_3)_3 \cdot 6H_2O$ (Analytical reagents) are used to make hexagonal ferrites of the M type. The nitrates mentioned above are used in the stoichiometric amount to prepare a distilled water solution of the compounds were combined in 2000ml beaker. The stock solution is stirred using a magnetic stirrer. Homogeneous mixture Continuous heating and stirring are used. The molar ratio of is 1:3. Citric acid is used to combine metals. The ammonia solution is then added drop by drop using the burette and stirring were maintained to keep the pH value at 7-8. Stop releasing ammonia and the solution was stirred and heated between 70 and 80 degrees Celsius until the water gets evaporated. When gel formation occurs, after forming the gel formation, the gel solution self-ignited with evaporating the large amount of gas, we started with a $200^\circ C$ temperature and worked our way up to a fluffy powder. The powder crushed using agate mortar pestle for 2 hrs. The resulting powder was sintered at $900^\circ C$ for 6 hrs and annealed at $1250^\circ C$ for 6 hours.

The separately prepared compounds $((1 - x)(Bi_{0.5}Na_{0.5})TiO_3)_{0.94} - BaTiO_3)_{0.06}$ and $SrY_1Fe_{12}O_{19}$ are mixed according to standard stoichiometric proportion for $(x = 0.00, 0.25, 0.50, 0.75$ and $1)$ and fine powdered by using agate mortar pestle and then sintered $1250^\circ C$ for 8 hours.

Characterization: An X ray diffractometer (XRD, Goniometer Ultima IV, 40KV/40MA, Cu $K\alpha$ radiation) XRD patterns were recorded at room temperature in the range 20 to 80 degree at radiation ($\lambda = 1.5404 \text{ \AA}$), FTIR (Fourier transformed infrared radiation) (PerkinElmer) were used to identify the phase composition in the range $440-4000 \text{ cm}^{-1}$, VSM (vibrating sample magnetometer (Lakeshore 7410) were used to study the magnetic properties of the prepared sample by applying the 1.5 Tesla magnetic field, FESM (JSM 7600 F) were used to study the surface morphology of the prepared sample, EDAX were used to study the elemental

composition of the sample, TEM (FEI, Tecnai G2, F30) was used to determine the grain size and interplanar spacing of the sample and Dielectric constant ϵ' and loss ϵ'' were measured using LCR-Q meter with different of Varying frequency.

RESULTS AND DISCUSSION:

XRD analysis

The XRD patterns of prepared sample $(1-x)(Bi_{0.5}Na_{0.5})TiO_3)_{0.94} - BaTiO_3)_{0.06} + SrY_1Fe_{12}O_{19}$ ($x=0.00, 0.25, 0.50, 0.75, 1$) are shown in fig.1. XRD pattern shows peaks of the both phases for BNBT and SRFYO respectively. All the XRD patterns of the prepared sample fairly matched without any external impurity. The XRD peaks were recorded in the range of 20 to 80 degree. The observed position peaks for BNBT recorded of planes (110), (111), (200), (210) and (220) and the refinement of XRD pattern was done by using Full-prof software program, peak shapes were described by Pseudo-Voigt function and refined background parameters were calculated by using Fourier cosine series to obtain detailed crystal structure information. Position peaks for SRFYO recorded planes (008), (107), (114), (201), (203), (205), (2011), (217) were indexed according to the standard match card no. For BNBT, COD Code: 2103296 Reference Code: 96-210-3297 and for SRFYO COD Code: 1006000 Reference Code: 96-100-6001. The calculated lattice parameter a and c value for BNBT ($5.5045A^0$) and ($3.8928A^0$) and SRFYO lattice parameter a and c value ($5.8816A^0$) and ($23.080A^0$) The concentration of $SrY_1Fe_{12}O_{19}$ concentration showed noticeable effect on diffraction patterns peak intensity for (107), (114) planes. In the observed XRD data's it is found that the composite samples except ($x=0.00$ and $x=1$) rest of the x values indicates the coexistence of both phases and the observed group of BNBT cubic phase (crystal symmetry of space group P4bm) and SRFYO hexagonal phase (crystal symmetry of space group P6₃/mmc). Peak intensity of BNBT Peak intensity of individual BNBT phase decrease with increasing the SRFYO concentration and vice versa. The lattice parameter a and c values are calculated by using the formula

$$d_{hkl} = \sqrt{\frac{4h^2 + hk + k^2}{3a^2} + \frac{l^2}{c^2}}$$

and Size of the Crystal and Volume of the unit cell is calculated by below mentioned formula

$$\text{Size of the Crystal } D = \frac{0.89\lambda}{\beta \cos\theta} \text{ Volume of unit cell } V = \frac{\sqrt{3}}{2} a^2 c$$

The Rietveld refinement method uses the LSM (least square method) to solve the issues related to X-Ray diffraction data's such as preferred orientation, overlapped diffraction pattern and defining influential background etc. But present objective of this method is to enhance or gain the reduced function Δ which calculate the difference between observed $y(\text{obs})$ and calculated $y(\text{cal})$. So we used Hugo Rietveld equation to calculate Δ

$$\Delta = \sum_i W_i \left\{ y_i^{obs} - \frac{1}{c} y_i^{cal} \right\}^2$$

Where $W_i \rightarrow$ Statical weight that is equal to $1/y_i^{obs}$ and c is overall scale factor such that $C_{Yobs} = C_{cal}$ is obtained.

To determine the better quality of the process and to accomplish the convergence Profile residual R_p is calculated by the formula

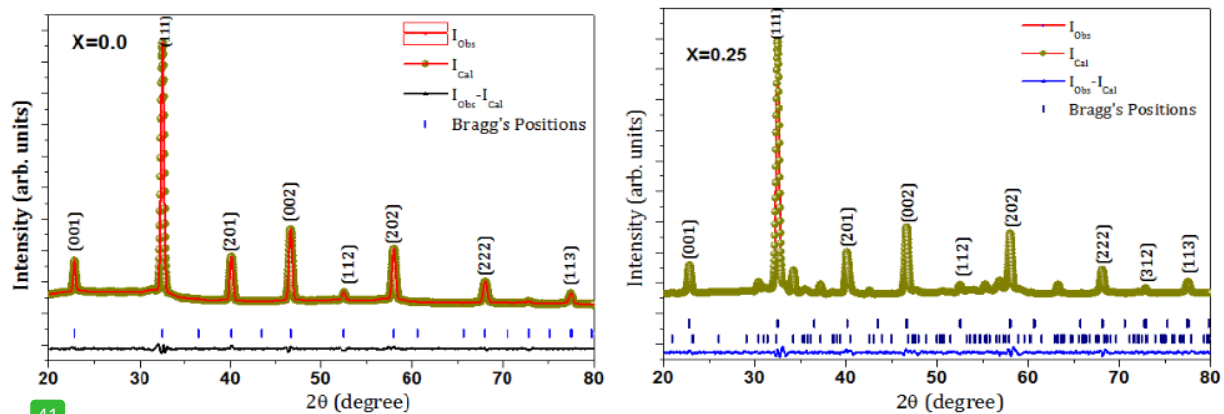
$$R_p = 100 \frac{\sum |y_i(obs) - y_i(cal)|}{\sum y_i obs}$$

And similarly weighted profile R_{wp} is calculated by the formula

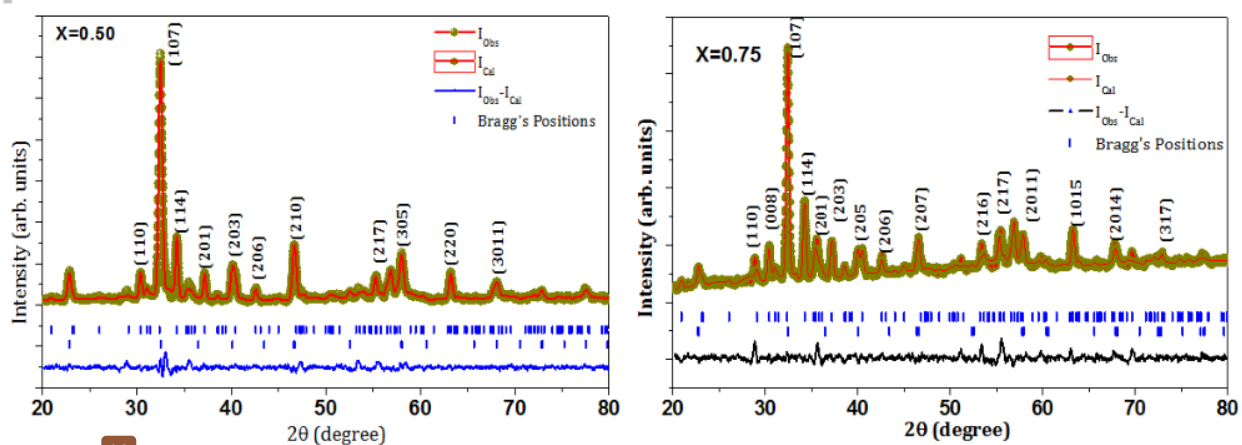
$$R_p = 100 \left\{ \frac{\sum W_i y_i(obs) - y_i(cal)}{(\sum W_i y_i obs)^2} \right\}^2$$

The values of $y_i(obs)$ and $y_i(cal)$ are calculated by using intensities of the respective composition and both R-Parameters R_{wp} and R_p (less the 10% values are used) to convergence and this results the value of goodness of fit parameter χ^2 .

The lattice parameter of a and c calculated separately because of coexistence of both phases, the calculated parameter a and c value of BNBT and SRFYO Slightly changes which indicate the coexistence of both phase with each other. The calculated lattice parameter a value for BNBT decreases with increase of the SRFYO addition, whereas SRFYO lattice parameter a slightly increase or constant and c value increases. This can be attributed to the difference in the ionic radius of Fe^{3+} (0.63⁰) and Y^{3+} (0.97⁰) (20). The ratio of lattice parameter c/a increases with increase of concentration of SRFYO. The ratio c/a is also an important parameter to quantify the M-type hexagonal structure, when the value is below 3.98 (20, 21). The calculated lattice parameter c/a ratio is found 3.92 as per Vegard's law (22). The crystallite size was calculated by Debye-Scherer equation. The most intense peak (107) and (114) the crystallite size of the prepared sample increased in the range of 4.01 nm which shows the good quality of the Hexaferrite. The unit cell volume increases with the increasing SRFYO (23). The refined lattice parameter a and c , residual R_{wp} , R_p , $\chi^2 V_{cell}$ and D values are mentioned in Table .1



41
 Fig. 1. X-ray diffraction Rietveld refinement pattern of prepared sample $(1-x)(Bi_{0.5}Na_{0.5}TiO_3)_{0.94} - BaTiO_3)_{0.06} + SrY_1Fe_{12}O_{19}$ X=0.00 and X=0.25. 46



19
 Fig. 2. X-ray diffraction Rietveld refinement pattern of prepared sample $(1-x)(Bi_{0.5}Na_{0.5}TiO_3)_{0.94} - BaTiO_3)_{0.06} + SrY_1Fe_{12}O_{19}$ X=0.50 and X=0.75. 44

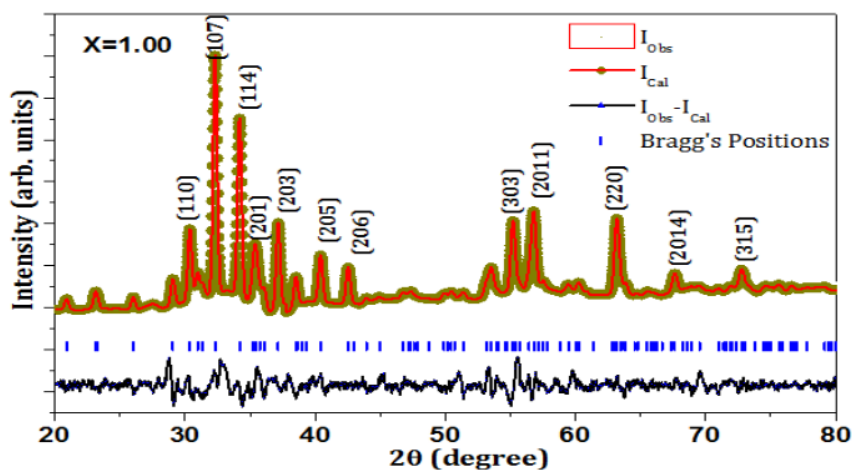


Fig. 3. X-ray diffraction Rietveld refinement pattern of prepared sample $(1-x)(Bi_{0.5}Na_{0.5}TiO_3)_{0.94} - BaTiO_3)_{0.06} + SrY_1Fe_{12}O_{19}$ (X=1.00)

40
 Table 1. $(1-x)(Bi_{0.5}Na_{0.5}TiO_3)_{0.94} - BaTiO_3)_{0.06} - SrY_1Fe_{12}O_{19}$ Structural parameters a and c, R factors, c/a, unit cell v and D values are obtained after the Rietveld refinement of the prepared samples are listed in the table 27

Sr No	Sample composition	Lattice constant	R- factor			
			R_P	R_{WP}	χ^2	R_{Exp}
1	0.00	BNBT (P4bm) a = 5.511 Å c = 3.898 Å c/a = 0.707 V = 102.14 (Å) ³	11.7	8.10	1.06	7.89
2	0.2	BNBT (P4bm) a = 5.499 Å c = 3.899 Å c/a = 0.709 V = 102.12 (Å) ³ SRYFO (P 63 / m m c) a = 5.8767 Å c = 23.0667 Å c/a = 3.925 V = 689.89 (Å) ³ D = 231.683 nm	14.8	8.54	1.10	8.77
3	0.50	BNBT (P4bm) a = 5.499 Å c = 3.899 Å c/a = 0.709 V = 101.90 (Å) ³ SRYFO (P 63 / m m c) a = 5.8783 Å c = 23.0435 Å c/a = 3.903 V = 689.57 (Å) ³ D = 226.665 nm	22.6	13.0	1.19	11.87
4	0.75	BNBT (P4bm) a = 5.499 Å c = 3.899 Å c/a = 0.709 V = 102.65 (Å) ³ SRYFO (P 63 / m m c) a = 5.892 Å c = 23.0422 Å c/a = 3.9103 V = 692.755 (Å) ³ D = 244.003 nm	33.0	19.0	1.36	16.30
5	1	SRYFO (P 63 / m m c) a = 5.8813 Å c = 23.083 Å c/a = 3.9248 V = 691.46 (Å) ³ D = 240.51 nm	42.9	24.7	1.59	19.61

FTIR :

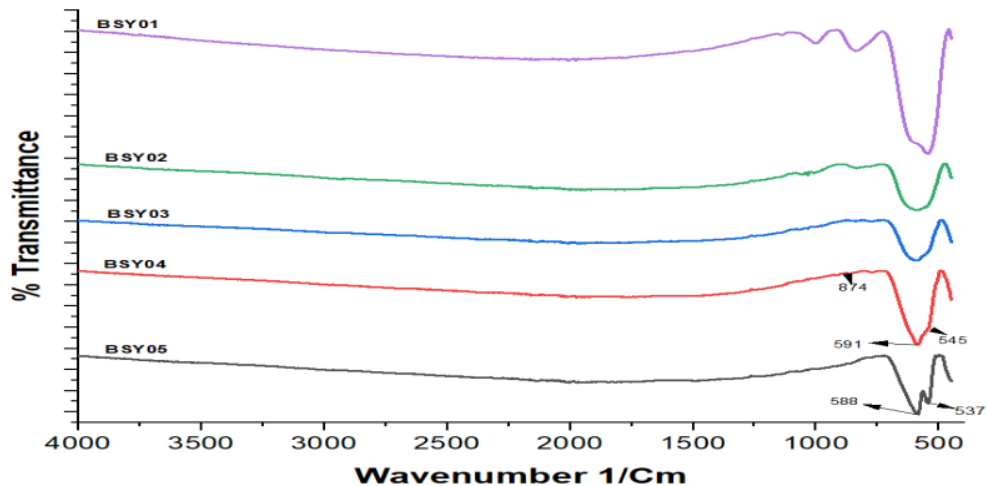


Fig: (04) FTIR Spectrum of prepared sample $(1-x)(Bi_{0.5}Na_{0.5})TiO_3)_{0.94} - BaTiO_3)_{0.06} - SrY_1Fe_{12}O_{19}(x=0.0,0.25,0.50,0.75,1.0)$

Fig: (04) FTIR Spectra of $(1-x)(Bi_{0.5}Na_{0.5})TiO_3)_{0.94} - BaTiO_3)_{0.06} - SrY_1Fe_{12}O_{19}$ ($x=0.0,0.25,0.50,0.75,1.0$) gives the information on the dynamics of the crystal structure of spectra specially related to the vibration of the atomic bond, through which a small impurity of the sample can be detected, As reported earlier, that hexaferrite has 189 optical modes and out of them only 31 (13 A_{2u} + 18 E_{1u}) are IR respond modes(24) the FTIR spectra analysis of the pure and $(SrFe_{12-x}Y_xO_{19})$ and $(1-x)(Bi_{0.5}Na_{0.5})TiO_3)_{0.94} - BaTiO_3)_{0.06} - SrY_1Fe_{12}O_{19}$ were carried out by comparative study, as well as by Spectragryph software identifier the observed FTIR spectra makes the predict the presence of the different bonds in the crystal, the above said analysis was performed at room temperature in the range of 450 to 4000 Cm^{-1} . In this study, only three are active modes the frequency of the absorption bands at 585.66 Cm^{-1} , 545.517 Cm^{-1} and 458.61 Cm^{-1} (182), the range of the observed band found in between 450 to 900 Cm^{-1} are elucidated the characteristic band of $SrFe_{12}O_{19}$ (25-26). In these bands, frequency around ν_1 (458.61 Cm^{-1}) is attributed to intrinsic elongating of the metal cation vibrations at the octahedral site and absorption frequencies around ν_2 (545.517, 585.66) are made due to intrinsic elongating of the metal cation vibrations at the tetrahedral site (24). Coupling phenomena was found at 585.66 Cm^{-1} and 545.517 Cm^{-1} which changes the shape as plump peak, some other peaks observed around 874 and 923 Cm^{-1} are Strontium carbonates (28-29) from the graph, it is also found that band position is moved to slightly shifts to lower wave number. The shift towards higher frequencies may be due to the change in bond length which can be later linked to the reduction in lattice parameters as shown by XRD. It can be also seen from the graph that the intensity of ν_1 band is decreased while broadening is increased with substitution. This shift in wave number to the higher values is due to the lattice contraction upon substitution. The increased bonding between $Fe^{3+} - O^{2-}$ due to lattice contraction shifts the peak position to the higher wave numbers.

VSM: Magnetic Studies:

The magnetic characteristics of the prepared sample $(1-x)(Bi_{0.5}Na_{0.5}TiO_3)_{0.94} - BaTiO_3)_{0.06} - SrY_1Fe_{12}O_{19}$ ($x=0.00, 0.550$ and 1) composites were measured at room temperature in the range of approximately 20kOe using VSM Magnetic hysteresis loops. Figure 3 shows the ferromagnetic behavior of prepared sample. Table 2. Provides the values of magnetic saturation (M_s), remanent magnetization (M_r) and coercivity (H_c) of all the specimens. For $x=0.50$ reveals that the values of the (M_s) and (M_r) were 21.83 and 6.12 emu/g respectively, while the values of the (M_s) and (M_r) for $x=1.0$ were 42.26 and 20.55 emu/g

The figure 3. It was observed that magnetic saturation (M_s) of the prepared composite increases with increase of ferrite content. The increase in the value of the magnetic saturation (M_s) is due to the fact that the volume of the ferroelectric phase decrease. As magnetization in the composite is mostly contributed by magnetic phase act as ferrite phase and ferroelectric phase acts as a non-magnetic phase (30).

Values of characteristic parameters: saturation (M_s), remanent magnetization (M_r) and coercivity (H_c) M_s/M_r squareness factors are reported in table and found that an increasing trend on adding SRYFO phase in BNBT all the magnetic samples are increased parameters with increase of ferrite content in the ferroelectric relaxor phase ferrite being the center of magnetization (31). The magnetization saturation for pure yttrium doped Strontium hexaferrite found 42.5 emu/g than usually reported value 49.6 emu/g (32). The variation value of saturation magnetization may due to different synthesis process.

As previous reported data's BNT-BT is a purely ferroelectric relaxor (33), this composite shows ferroelectric behavior due to its paired electrons, The Magnetic saturation value for the prepared sample relies particle size caused by the increasing the particle size. Increase in the Fe^{3+} spin interaction in core than in the surface volume raises the magnetization (38). When the ferrite is saturated in a strong magnetic field, the magnetization vector rotates in the direction nearest preferred field and creates a high anisotropy when the field drops to zero and increasing residual magnetization values indicates that most of the magnetizing vectors turned out of the magnetically -profitable direction, making a small angle to the direction of the applied field which experiences stress(34) resulting in large magnetization. Shape and stress anisotropy has prominent role in the Magneto electric output of the composites.

Almessiere et al. stated that the sample with a high saturation value is probable to have a more excellent value of Bohr magneton. If the squareness ratio is less than 0.50, then the particles are in multi magnetic domain and if it is equal or higher than 0.50 then the particles are in a single domain. Present our value found greater than 0.50 ensures the particles are in single magnetic domain with uniaxial anisotropy. The prepared samples (SQR) M_s/M_r squareness ratio found lesser than the 0.5, which exhibits a multi domain structure, increase in the parameters are due to individual ferrite grains being center of magnetization and it is expected that their vector sum devotes the saturation magnetization (35-36-37). Incorporation of non-magnetic phase BNBT in piezomagnetic phase increase the dilution effect as these non-magnetic ions creates pores among the magnetic ions and break the magnetic circuit and hence reduced values of magnetic parameters(38-39). The different valence states of B-site of BNBT Lattice created by addition of SRYFO

require a charge compensation that can be attained by converting Fe^{3+} ion into Fe^{4+} ions or by generating vacant position of oxygen.

Microstructure analysis (FESEM):

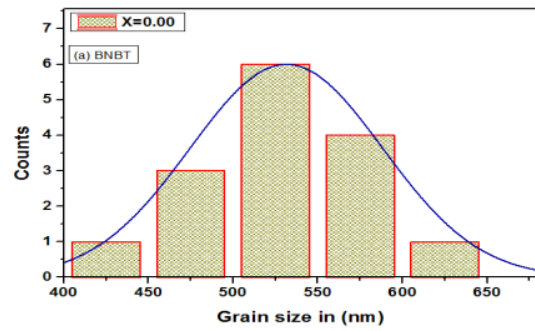
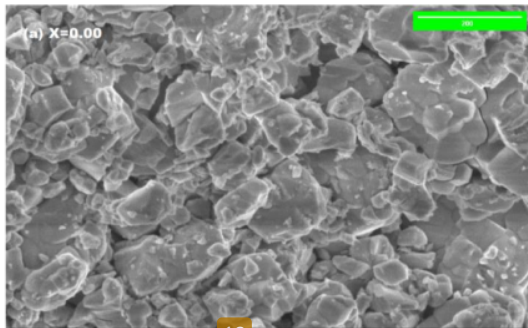


Figure. 05 (a) FESEM image and Grain size distribution after statics approximation of sample X=0.00

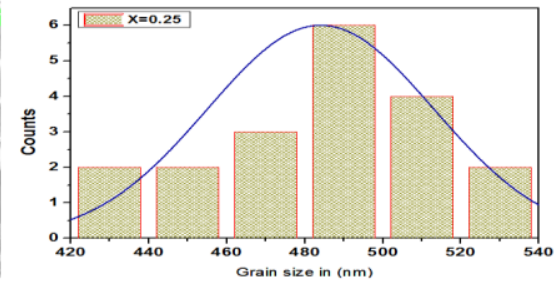
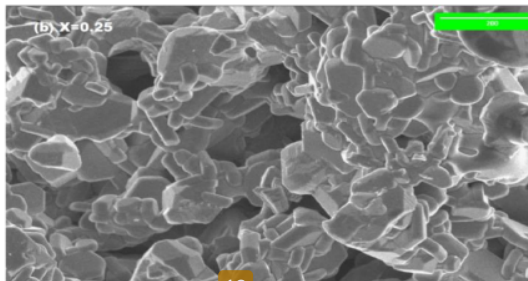


Figure. 05 (b) FESEM image and Grain size distribution after statics approximation of sample X=0.25

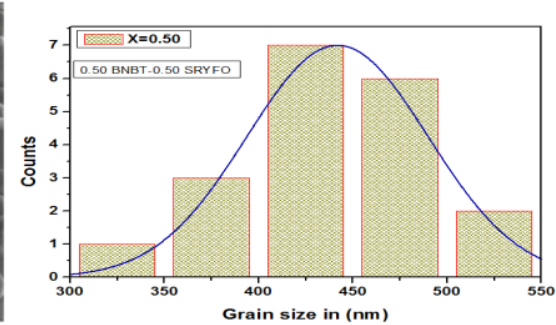
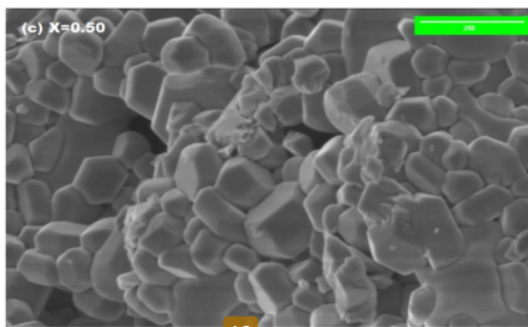


Figure. 05 (c) FESEM image and Grain size distribution after statics approximation of sample X=0.5

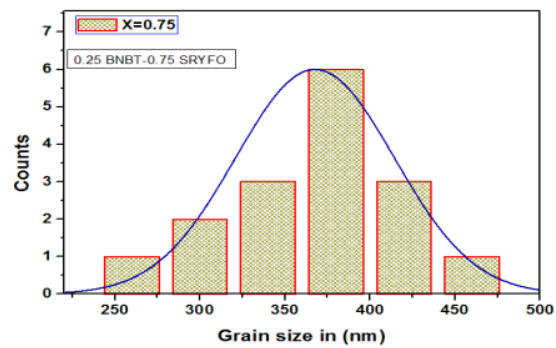
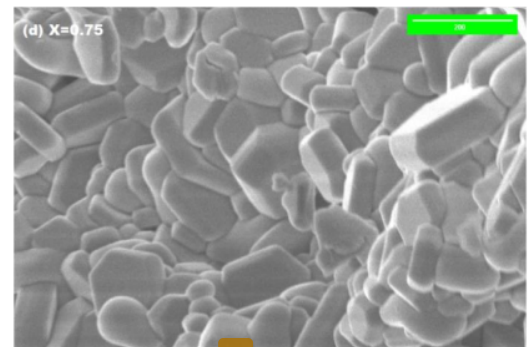
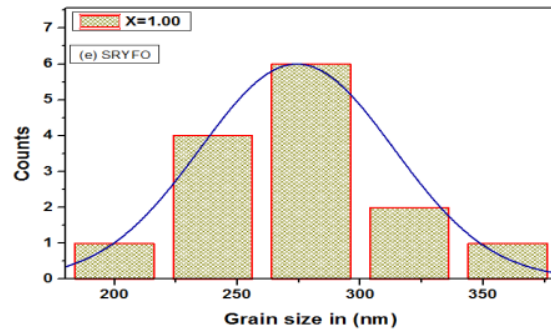
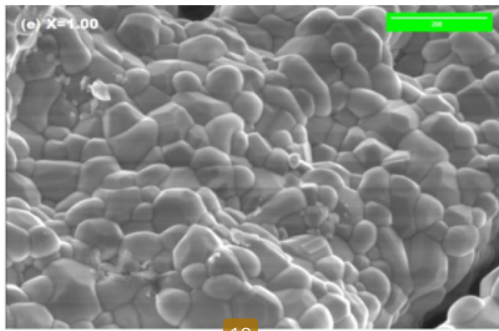
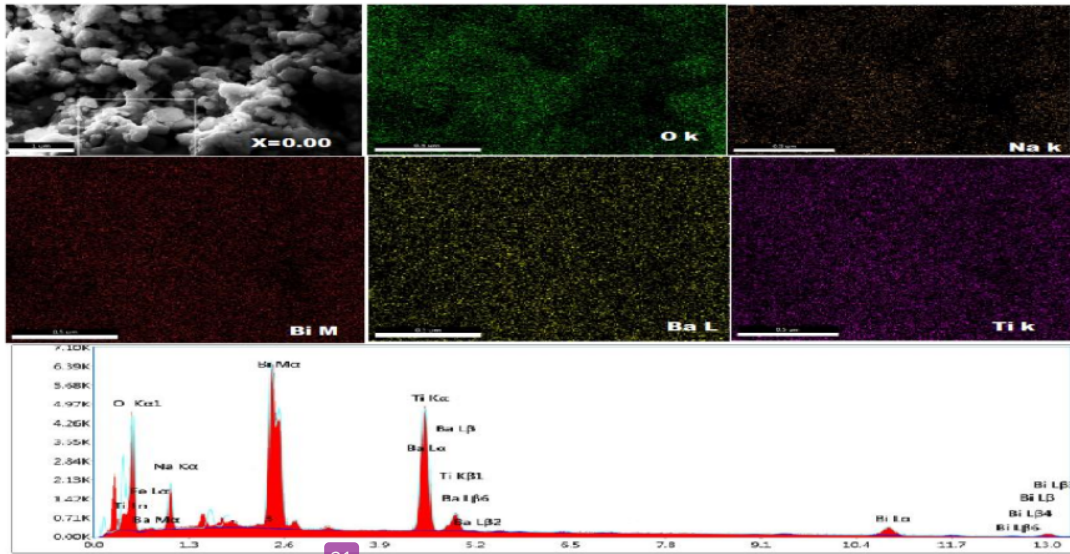


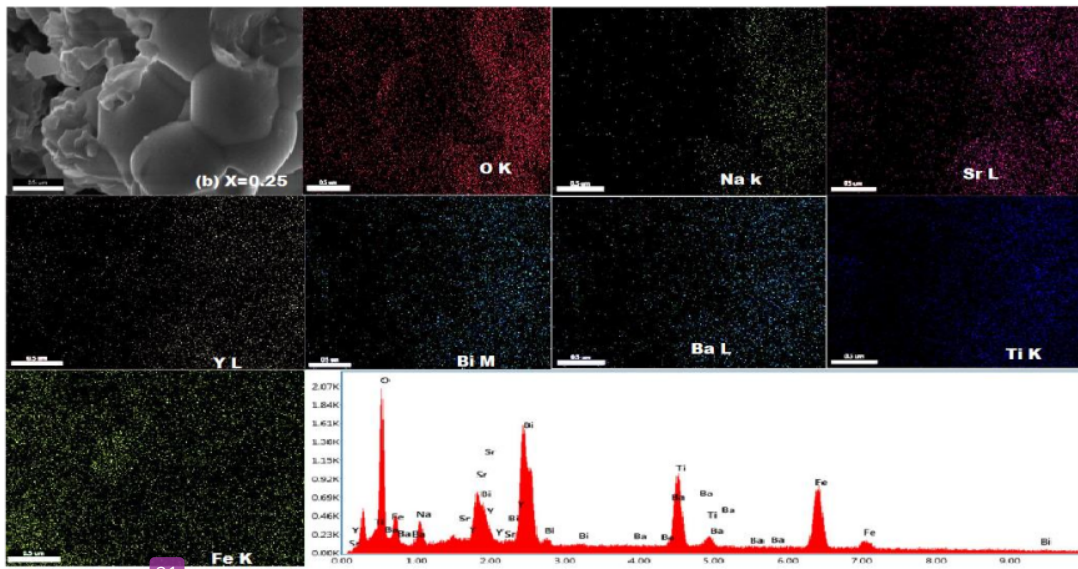
Figure. 05 (d) FESEM image and Grain size distribution after statics approximation of sample X=0.75



18
Figure. 05 (e) FESEM image and Grain size distribution after statics approximation of sample X=1.0



21
Figure 06 (a) Elemental mapping images of prepared sample X=0.00



21
Figure 06 (b) Elemental mapping images of prepared sample X=0.25

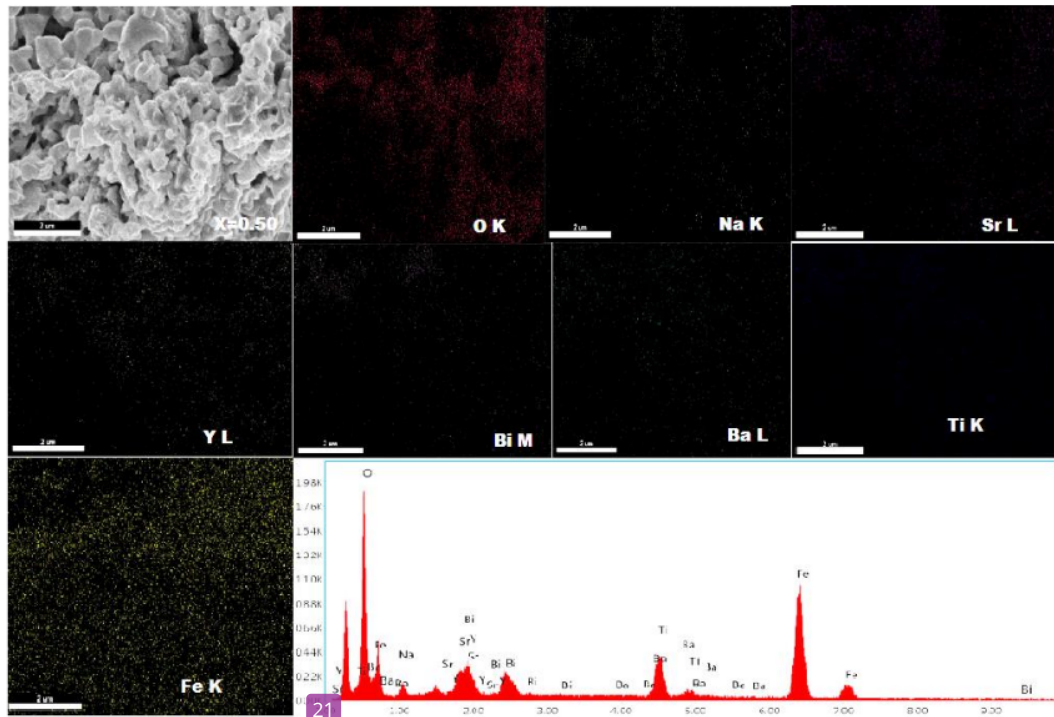


Figure 06 (c) Elemental mapping images of prepared sample X=0.50

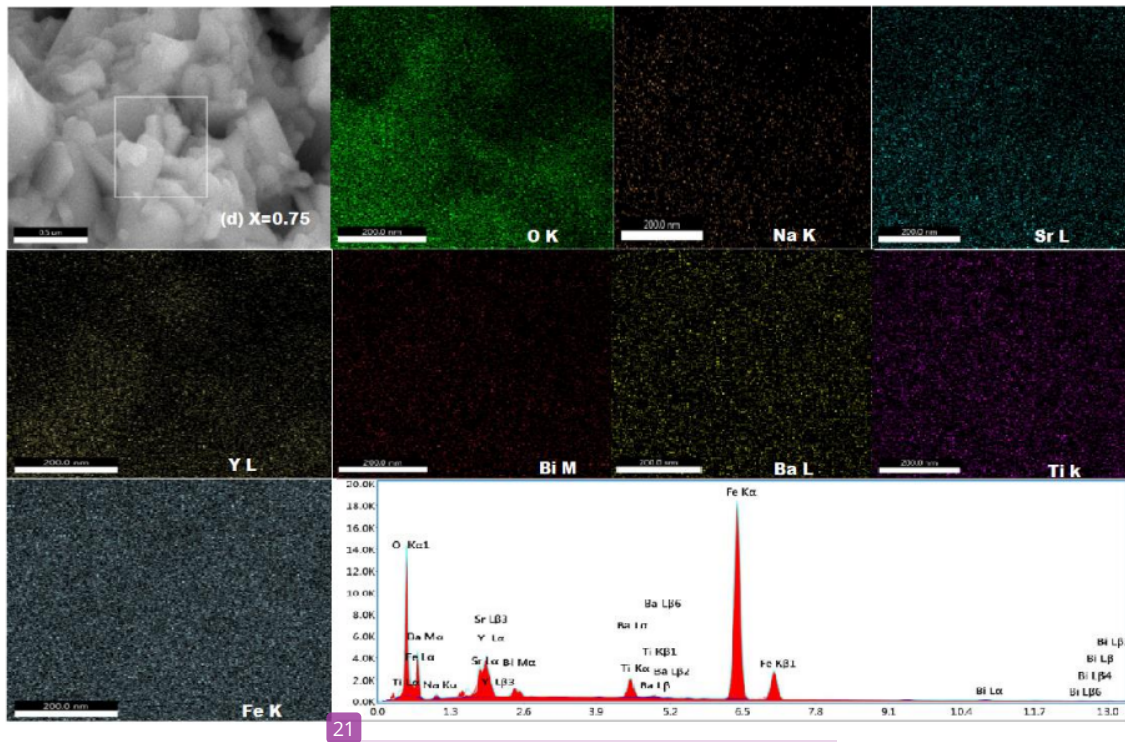
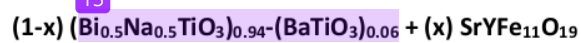


Figure 06 (d) Elemental mapping images of prepared sample X=0.75

36

Table 3. Atomic percentage (at%) of Bi, Na, Ba, Ti, O, Sr, Y and Fe in sintered



15

36

Composition	Elemental composition (at %)							
	Bi	Na	Ba	Ti	O	Sr	Y	Fe
X								
0.00	5.98	12.98	1.17	16.97	61.91	-	-	-
0.25	4.86	7.03	1.98	11.92	47.61	3.17	1.17	22.26
0.50	0.95	3.60	2.05	5.67	46.01	1.71	1.67	38.34
0.75	0.34	1.92	0.58	2.27	45.05	2.22	2.54	45.07

Elemental composition Analysis :

In order to determine the elemental composition of $(1-x) (\text{Bi}_{0.5}\text{Na}_{0.5}\text{TiO}_3)_{0.94}-(\text{BaTiO}_3)_{0.06} + (x) \text{SrYFe}_{11}\text{O}_{19}$ nanocomposites, standard EDX spectrum was recorded as shown in the Fig 4. The EDX analysis of X=0.00 nanoparticles represented the atomic percentages of 5.98, 12.98, 1.17, 16.97 and 61.91 for Bi, Na, Ba, Ti, and O respectively as shown in Fig 6(a). The EDX analysis of $x=0.25$ nanocomposites confirmed that the atomic percentages of 4.86, 7.03, 1.98, 11.92, 47.61, 3.17, 1.17 and 22.26 for Bi, Na, Ba, Ti, O, Sr, Y and Fe elements were present in the sample. Fig 6(b). Fig 6(c) shows the EDX results of X=0.50 nanocomposites with atomic percentages of 0.95, 3.60, 2.05, 5.67, 46.01, 1.71, 1.67 and 38.34 for Bi, Na, Ba, Ti, O, Sr, Y and Fe elements were present in the sample. Fig 6(d) shows the EDX results of 0.34, 1.92, 0.58, 2.27, 45.05, 2.22, 2.54 and 45.07 for Bi, Na, Ba, Ti, O, Sr, Y and Fe elements were present in the sample and did not contain any external impurities and the elemental analysis maps of prepared samples confirmed the homogeneous distribution of elements within the structure. Au signal in the EDX spectra was expected from the gold substrate itself, because the EDX analysis of the specimen was carried out on Au substrate, therefore the contribution of gold to nanocrystal could not be justified by EDX analysis in the FESEM study.

Micro- structural studies:

Figure 05 shows the scanning electron microscopy images with the data analysis (the grain size distribution obtained after the static approximation) of all the prepared sample $(1-x) (\text{Bi}_{0.5}\text{Na}_{0.5}\text{TiO}_3)_{0.94}-(\text{BaTiO}_3)_{0.06} + (x) \text{SrYFe}_{11}\text{O}_{19}$ ($x=0.00, 0.25, 0.50, 0.75$, and 1.00) ceramic being sintered at 900°C for 6h and annealed at 1250°C for 6 hours. The tetragonal and hexagonal platelet shaped grains correspond to BNBT and SRYFO respectively. The connectivity of the magnetic phase is broken by the distribution of the ferroelectric (non magnetic) phase in the composites and vice versa. Which conversely effect on the magnetic as well as ferroelectric properties of the prepared sample. The average grain size of the BNBT and SRYFO are in the range of 531.1 nm and 351.7nm respectively. The average grain size distribution plots and elemental mapping images are shown in figures 5(a to e) and 6 (a to d). In the present investigation the grain size distribution is uniform and densification is moderately high due to preparation method and solid state double sintering method as well as due to heating rate during the calcinations process is very high compare to the conventional heating rate. In addition heat generated internally within the material and the specimen set rotates continuously, so uniform heating induced. The compared to the conventional and microwave sintered samples, solid state double sintered samples are homogeneously crystallized and have tremendous advantages on synthetic efficiency and energy consumption (39-40). The average grain size of prepared samples are shown in fig. 5 (a) to (e) obtained by using image j software and found to decrease with the

addition of SRYFO ferrite i.e 531.4, 486.05, 425.91 ,383.6 and 351.75 nm for compositions $x=0.00$, 0.25, 0.50, 0.75 and 1.00 respectively. This may due to the smaller size of the grains as compared to ferroelectric grains.

Elemental composition Analysis :

In order to determine the elemental composition of $(1-x)(\text{Bi}_{0.5}\text{Na}_{0.5}\text{TiO}_3)_{0.94}(\text{BaTiO}_3)_{0.06} + (x)\text{SrYFe}_{11}\text{O}_{19}$ nanocomposites, standard EDX spectrum was recorded as shown in the Fig 4. The EDX analysis of $X=0.00$ nanoparticles represented the atomic percentages of 5.98, 12.98, 1.17, 16.97 and 61.91 for Bi, Na, Ba, Ti, and O respectively as shown in Fig 6(a). The EDX analysis of $x=0.25$ nanocomposites confirmed that the atomic percentages of 4.86, 7.03, 1.98, 11.92, 47.61, 3.17, 1.17 and 22.26 for Bi, Na, Ba, Ti, O, Sr, Y and Fe elements were present in the sample. Fig 6(b). Fig 6 (c) shows the EDX results of $X=0.50$ nanocomposites with atomic percentages of 0.95, 3.60, 2.05, 5.67, 46.01, 1.71, 1.67 and 38.34 for Bi, Na, Ba, Ti, O, Sr, Y and Fe elements were present in the sample. Fig 6 (d) shows the EDX results of 0.34, 1.92, 0.58, 2.27, 45.05, 2.22, 2.54 and 45.07 for Bi, Na, Ba, Ti, O, Sr, Y and Fe elements were present in the sample and did not contain any external impurities and the elemental analysis maps of prepared samples confirmed the homogeneous distribution of elements within the structure.

Reference:

1. Y.H. Lin, N. Cai, J.Y. Zhai, G. Liu, C.W. Nan, Phys. Rev. 72 (2005) 012405.
2. R. Pattanayak, S. Raut, S. Kuila, M. Chandrasekhar, S. Panigrahi, Multiferroism of $[\text{Na}_{0.5}\text{Bi}_{0.5}\text{TiO}_3\text{-BaFe}_2\text{O}_7]$ lead-free novel composite systems, Mater. Lett. 209(2017) 280–283.
<https://doi.org/10.1016/j.matlet.2017.08.023>.
3. A. Srinivas, T. Karthik, R. Gopalan, V. Chandrasekaran, Improved magnetoelectricity by uniaxial magnetic field pressed and sintered composites in $\text{BaTiO}_3(x)\text{-BaFe}_2\text{O}_7(1-x)$ system ($x = 0.8, 0.6$), Mater. Sci. Eng. B Solid-State Mater. Adv. Technol. 172 (2010) 289–293.
<https://doi.org/10.1016/j.mseb.2010.05.033>.
4. Enhanced magnetoelectric effect in core-shell particulate composites Enhanced magnetoelectric effect in core-shell particulate composites, 503 (2014) 97–100. <https://doi.org/10.1063/1.2165147>.

5. C.-W.Nan,M.I.Bichurin, S.Dong, D.Viehland,and G.Srinivasan”,Multiferroic magnetoelectric composites: Historical perspective, status,and future directions”, J. Appl. Phys., vol. 103, pp. 031101, February2008.
6. N.A.Spaldin and M. Fiebig, “The Renaissance of Magnetoelectric Multiferroics”, Science, vol. 309, pp.391-392, July 2005
7. N.A.Spaldin and M. Fiebig, “The Renaissance of MagnetoelectricMultiferroics”, Science, vol. 309, pp.391-392, July 2005.
8. C.A.F.Vaz , J.Hoffman, C.H.Ahn, “R.Ramesh,Magnetoelectric CouplingEffects in Multiferroic Complex Oxide Composite Structures”, Adv.Mater. vol. 22, pp. 2900-2918, July 2010.
- 9.. Uchino K, Nomura S, Cross LE, Jang SJ, Newnham RE. Electrostrictive effect in lead magnesium niobate single crystals. J Appl Phys 1980;51:1142–5.
10. Zhou, D.; Li, H.; Gong, S.; Hu, Y.; Han, K.: Sodium bismuth titanate-base lead-free piezoceramics prepared by aqueous gelcasting. J. Am. Ceram. Soc. 2008, 91, 2792-2796.
11. Oh, T.; Kim, M. H.: Phase relation and dielectric properties in $(\text{Bi}_{1/2}\text{Na}_{1/2})_{1-x}\text{Ba}_x\text{TiO}_3$ leadfree ceramics. Mater. Sci. Eng. B 2006, 132, 239-46
12. M. N. Ashiq, S. Shakoor, M. Najam-ul-Haq, M. F. Warsi, I. Aliand I. Shakir, J. Magn. Mater., 2015, 374, 173–178.
13. Shinde, S.R., Lofland, S.E., Ganpule, C.S., Bhagat, S.M., Ogale, S.B., Ramesh, R. and Venkatesan, T. (1999) Improvement in Spin-Wave Resonance Characteristics ofEpitaxial Barium-Ferrite Thin Films by Using an Aluminum-Doped Strontium-FerriteBuffer Layer. Applied Physics Letters , 74, 594-596.
<https://doi.org/10.1063/1.123156>
14. Dho, J., Lee, E.K., Park, J.Y. and Hur, N. H. (2005) Effects of the Grain Boundary on the Coercivity of Barium Ferrite $\text{BaFe}_{12}\text{O}_{19}$. Journal of Magnetism and Magnetic Materials , 285, 164-168.
<https://doi.org/10.1016/j.jmmm.2004.07.033>
15. Jean, M., Nachbaur, V., Bran, J. and Le Breton, J.M. (2010) Synthesis and Characterization of $\text{SrFe}_{12}\text{O}_{19}$ Powder Obtained by Hydrothermal Process. Journal of Alloys and Compounds , 496, 306-312.
<https://doi.org/10.1016/j.jallcom.2010.02.002>
16. E.E. Riches, Ferrites Mills, Boon Technical Library, Boon, London, 1972.
17. J. Kracch, M.H. Grant, Encyclopedia of Chemical Technology, fourth ed., Wiley,1993.
18. N. Yang, H. Yang, J.J. Jia, X.F. Pang, J. Alloy. compd. 438 (2007) 263–267.
19. El-Sayed, S., Meaz, T., Amer, M. and El Shersaby, H. (2013) Magnetic Behavior and Dielectric Properties of Aluminum Substituted M-Type Barium Hexaferrite. PhysicaB : Condensed Matter , 426, 137-143. <https://doi.org/10.1016/j.physb.2013.06.026>
20. Wagner, T.: Preparation and crystal structure analysis of magnetoplumbite-type $\text{BaGa}_{12}\text{O}_{19}$. J. Solid State Chem. **136**,120–124 (1998)

21. Auwal, I.A., Güner, S., Güngöres, H., Baykal, A.: Sr_{1-x}La_xFe₁₂O₁₉ (0.0 = x = 0.5) hexaferrites: Synthesis, characterizations, hyperfine interactions and magneto-optical properties. *Ceram. Int*
22. R.A. Pawar, S.S. Desai, Q.Y. Tamboli, S.E. Shirsath, S.M. Patange, Ce³⁺ incorporated structural and magnetic properties of M type barium hexaferrites, *J. Magn. Magn. Mater.* 378 (2015) 59–63
23. R.H. Kadam, A.A. Birajdar, S.T. Alone, S.E. Shirsath, *J. Magn. Magn. Mater.* **327** (2013) 167.
24. S. Mahadevan, C. Pahwa, S.B. Narang, P. Sharma, Structural, dielectric and magnetic properties of BaFe_{12-x}Al_xO₁₉ hexaferrite thick films. *J. Magn. Magn. Mater.* **441**, 465–474 (2017)
25. T. Xie, L. Xu, C. Liu, Synthesis and properties of composite magnetic material SrCo_xFe_{12-x}O₁₉ (x = 0–0.3). *Powder Technol.* **232**, 87–92 (2012)
26. A. Baykal, M.S. Toprak, Z. Durmus, H. Sozeri, Hydrothermal synthesis of SrFe₁₂O₁₉ and its characterization. *J. Supercond. Nov. Magn.* **25**, 2081–2085 (2012) 182M. Jean, V. Nachbaur, J. Bran, J.-M. Le Breton, Synthesis and characterization of SrFe₁₂O₁₉ powder obtained by hydrothermal process, *J. Alloys Comp.* 496 (2010) 306-312
27. A.B. Gadkari, T.J. Shinde, P.N. Vasambekar, Structural analysis of Y³⁺-doped Mg–Cd ferrites prepared by oxalate-precipitation method. *Mater. Chem. Phys* **114**, 505–510 (2009)
28. Alange, R.C., Khirade, P.P., Birajdar, S.D., Humbe, A.V., Jadhav, K.M.: Structural, magnetic and dielectrical properties of Al–Cr Co-substituted M-type barium hexaferrite nanoparticles. *J. Mol. Struct.* **1106**, 460–467 (2016)
29. Miller, F.A., Wilkins, C.H.: Infrared spectra and characteristic frequencies of inorganic ions. *Anal. Chem.* **24**, 1253–1294 (1952)
30. D.R. Patil, S.A. Lokare, S.S. Chougule, B.K. Chougule, Dielectric and magnetic properties of x NiFe₂O₄ þ (1 - x) Ba_{0.9}Sr_{0.1}TiO₃ composites, *Phys. B* 400 (2007)77e82.
31. C.G. Koops, On the dispersion of resistivity and dielectric constant of some semiconductors at audio frequencies, *Phys. Rev.* 83 (1951) 121e124, <https://doi.org/10.1103/PhysRev.83.121>
32. **Y³⁺ substituted Sr-hexaferrites: sol-gel synthesis, structural, magnetic and electrical characterization** <http://dx.doi.org/10.1590/0366-69132019653742582>
33. S. Dagar, A. Hooda, S. Khasa, M. Malik, “Rietveld Refinement, Dielectric and Magnetic Properties of NBT-Spinel Ferrite Composites” *Journal of Alloys and Compounds* 806 (2019) 737-752, <https://doi.org/10.1016/j.jallcom.2019.07.178>
34. R. S. Devan, S. B. Deshpande, and B. K. Chougule, “Ferroelectric and ferromagnetic properties of (x)BaTiO₃+ (1 - x)Ni_{0.94}Co_{0.01}Cu_{0.05}Fe₂O₄ composite” *J. Phys. D: Appl. Phys.* 40(2007)1864–1868. <https://dx.doi.org/10.1088/0022-3727/40/7/004>.
35. M. Rawat, K. L. Yadav, “Electrical, magnetic and magnetodielectric properties in ferrite ferroelectric particulate composites”, *Smart Mater. Struct.* 24 (2015) 045041. doi:10.1088/0964-1726/24/4/045041

36. Manjusha, M. Rawat, K. L. Yadav, "Structural, dielectric, ferroelectric and magnetic properties of (x)CoFe₂O₄-(1-x)BaTiO₃ composite", IEEE T. DIELECT. EL. IN 22 (2015) 1462- 1469.
doi:10.1109/TDEI.2015.004774.
37. N. Adhlakha, K. L. Yadav, "Study of structural, dielectric and magnetic behaviour of Ni_{0.75}Zn_{0.25}Fe₂O₄- Ba(Ti_{0.85}Zr_{0.15})O₃ composites", Smart Mater. Struct. 21 (2012) 115021.
doi:10.1088/0964-1726/21/11/115021
38. K. Habanjar, H. Shehabi, A.M. Abdallah, R. Awad, Effect of calcination temperature and cobalt addition on structural, optical and magnetic properties of barium hexaferrite BaFe₁₂O₁₉ nanoparticles, Appl. Phys. Mater. Sci. Process 126 (2020), <https://doi.org/10.1007/s00339-020-03497-3>.
39. SyedMahboob, A.B. Dutta, Chandra Prakash, G. Swaminathan, S.V. Suryanarayana, G. Prasad, G.S. Kumar, Mater. Sci. Eng. B 134 (2006) 36.
40. K. Sadhana, T. Krishnaveni, K. Praveena, S. Bharadwaj, S.R. Murthy, Scr. Mater. 59 (2008) 495.

36%

SIMILARITY INDEX

PRIMARY SOURCES

- 1** link.springer.com 205 words — 4%
Internet
- 2** Ehsan Naderi, Mahmoud Naseri, Dariush Souri. "The effect of SiO₂ and TiO₂ nanoparticles on physical properties of SrFe₁₂O₁₉ nanoparticle", *Current Applied Physics*, 2018 173 words — 3%
Crossref
- 3** Sunita Dagar, Ashima Hooda, Satish Khasa, Meena Malik. "Investigations of structural, enhanced dielectric and magnetic properties of NBT doped ferrite system", *Materials Chemistry and Physics*, 2020 169 words — 3%
Crossref
- 4** Sunita Dagar, Ashima Hooda, Satish Khasa. "Structural and magnetic investigations of innovative lead-free particulate composites of NBT- M-Type SrFe₁₂O₁₉ Hexaferrite", *Vacuum*, 2020 94 words — 2%
Crossref
- 5** Himani Joshi, A. Ruban Kumar. "Magnetic and dielectric response of M-type barium hexaferrite", *Journal of the Indian Chemical Society*, 2022 91 words — 2%
Crossref
- 6** Sadhana Katlakunta, Pantagani Raju, Sher Singh Meena, Sanyadanam Srinath et al. "Multiferroic 80 words — 2%

properties of microwave sintered BaTiO₃-SrFe₁₂O₁₉ composites", Physica B: Condensed Matter, 2014

Crossref

7 www.scielo.br

Internet

78 words — 2%

8 Anand Kumari, Sujata Sanghi, Ashish Agarwal, Ompal Singh. "Investigation of crystal structure, dielectric properties, impedance spectroscopy and magnetic properties of (1-x)BaTiO₃ - (x)Ba_{0.9}Ca_{0.1} Fe₁₂O₁₉ multiferroic composites", Ceramics International, 2021

Crossref

68 words — 1%

9 Sunita Dagar, Ashima Hooda, Satish Khasa, Meena Malik. "Structural refinement, investigation of dielectric and magnetic properties of NBT doped BaFe₁₂O₁₉ novel composite system", Journal of Alloys and Compounds, 2020

Crossref

66 words — 1%

10 Nazia Yasmin, Misbah Mirza, Safdar Muhammad, Maria Zahid, Mukhtar Ahmad, M.S. Awan, Altaf Muhammad. "Influence of samarium substitution on the structural and magnetic properties of M-type hexagonal ferrites", Journal of Magnetism and Magnetic Materials, 2018

Crossref

65 words — 1%

11 E. Venkata Ramana, M. P. F. Graca, J. Monteiro, S. K. Mendiratta, M. A. Valente. "Improved magnetoelectric effect in modified (Na_{0.5}Bi_{0.5})TiO₃-BaTiO₃-CoFe₂O₄ lead-free multiferroic composites", Proceedings of ISAF-ECAPD-PFM 2012, 2012

Crossref

60 words — 1%

12	pubs.rsc.org Internet	49 words — 1%
13	www.scirp.org Internet	48 words — 1%
14	coek.info Internet	44 words — 1%
15	www.tandfonline.com Internet	40 words — 1%
16	M. Elansary, M. Belaiche, C. Ahmani Ferdi, E. Iffer, I. Bsoul. "New nanosized Gd–Ho–Sm doped M-type strontium hexaferrite for water treatment application: experimental and theoretical investigations", RSC Advances, 2020 Crossref	34 words — 1%
17	www.nature.com Internet	32 words — 1%
18	Bhadra, D, Md G Masud, S K De, and B K Chaudhuri. "Large magnetoelectric effect and low-loss high relative permittivity in $0\hat{\epsilon}^3$ CuO/PVDF composite films exhibiting unusual ferromagnetism at room temperature", Journal of Physics D Applied Physics, 2012. Crossref	30 words — 1%
19	Singh, Ajay, Vishal Singh, and K.K. Bamzai. "Structural and magnetic studies on (x)PbTiO ₃ – (1 – x)SrFe ₁₂ O ₁₉ composite multiferroics", Materials Chemistry and Physics, 2015. Crossref	28 words — 1%
20	eprints-bangaloreuniversity.in Internet	27 words — 1%

21 Sung Min Cha, Goli Nagaraju, S. Chandra Sekhar, Jae Su Yu. "A facile drop-casting approach to nanostructured copper oxide-painted conductive woven textile as binder-free electrode for improved energy storage performance in redox-additive electrolyte", *Journal of Materials Chemistry A*, 2017 24 words — < 1%
Crossref

22 Ranjit Pattanayak, Surya Prakash Ghosh, Simanchalo Panigrahi. "Effect of grain size on exchange-spring mechanism of [BaFe₁₂O₁₉ (BaM)-Na_{0.5}Bi_{0.5}TiO₃ (NBT)] magnetoelectric composite system", *Journal of Magnetism and Magnetic Materials*, 2019 21 words — < 1%
Crossref

23 www.science.gov 20 words — < 1%
Internet

24 Sadhana Katlakunta, Sher Singh Meena, S. Srinath, M. Bououdina, R. Sandhya, K. Praveena. "Improved magnetic properties of Cr³⁺ doped SrFe₁₂O₁₉ synthesized via microwave hydrothermal route", *Materials Research Bulletin*, 2015 19 words — < 1%
Crossref

25 Tenorio Gonzalez, F.N., A.M. Bolarín Miró, F. Sánchez De Jesús, C.A. Cortés Escobedo, and S. Ammar. "Mechanism and microstructural evolution of polyol mediated synthesis of nanostructured M-type SrFe₁₂O₁₉", *Journal of Magnetism and Magnetic Materials*, 2016. 19 words — < 1%
Crossref

26 Xuefan Zhou, Guoliang Xue, Hang Luo, Chris R. Bowen, Dou Zhang. "Phase structure and properties of sodium bismuth titanate lead-free piezoelectric ceramics", *Progress in Materials Science*, 2021 19 words — < 1%
Crossref

27 Sunita Dagar, Ashima Hooda, Satish Khasa, Meena Malik. "Rietveld refinement, dielectric and magnetic properties of NBT-Spinel ferrite composites", *Journal of Alloys and Compounds*, 2019

18 words — < 1%

Crossref

28 Mane, Sagar, Pravin Tirmali, Snehal Kadam, Arjun Tarale, Chandrakant Kolekar, and Shrinivas Kulkarni. "Dielectric, magnetic, and magnetodielectric properties of $x[\text{Co}_{0.9}\text{Ni}_{0.1}\text{Fe}_2\text{O}_4]-(1-x)[0.5(\text{Ba}_{0.7}\text{Ca}_{0.3})\text{TiO}_3]-0.5\text{Ba}(\text{Zr}_{0.2}\text{Ti}_{0.8})\text{O}_3$ multiferroic composites", *Journal of the Chinese Advanced Materials Society*, 2016.

16 words — < 1%

Crossref

29 McQuade, Ryan R., and Michelle R. Dolgos. "A review of the structure-property relationships in lead-free piezoelectric $(1-x)\text{Na}_{0.5}\text{Bi}_{0.5}\text{TiO}_3-(x)\text{BaTiO}_3$ ", *Journal of Solid State Chemistry*, 2016.

16 words — < 1%

Crossref

30 R. Ezhil Vizhi, V. Harikrishnan, P. Saravanan, D. Rajan Babu. "Influence of Co-substitution on the structural and magnetic properties of nanocrystalline $\text{Ba}_{0.5}\text{Sr}_{0.5}\text{Fe}_{12}\text{O}_{19}$ ", *Journal of Crystal Growth*, 2016

16 words — < 1%

Crossref

31 www.ijirset.com

15 words — < 1%

Internet

32 Haiyan He. "Anisotropy and Magnetic Property of M-Type $\text{SrAl}_4\text{Fe}_8\text{O}_{19}$ Powders Prepared Via Co-Precipitation Method", *Recent Patents on Nanotechnology*, 2010

14 words — < 1%

Crossref

33 Ryan R. McQuade, Michelle R. Dolgos. "A review of the structure-property relationships in lead-free piezoelectric $(1-x)Na_{0.5}Bi_{0.5}TiO_3-(x)BaTiO_3$ ", *Journal of Solid State Chemistry*, 2016

14 words — < 1%

Crossref

34 Kaur, Prabhjyot, S.K. Chawla, S.S. Meena, S.M. Yusuf, Kunal Pubby, and S. Bindra Narang. "Modulation of physico-chemical, magnetic, microwave and electromagnetic properties of nanocrystalline strontium hexaferrite by Co-Zr doping synthesized using citrate precursor sol-gel method", *Ceramics International*, 2016.

13 words — < 1%

Crossref

35 Nazia Yasmin, Muhammad Zubair Iqbal, Maria Zahid, Saher Fatima Gillani et al. "Structural and magnetic studies of Ce-Zn doped M-type $SrFe_{12}O_{19}$ hexagonal ferrite synthesized by sol-gel auto-combustion method", *Ceramics International*, 2019

13 words — < 1%

Crossref

36 Deepshikha Shekhawat, P. K. Roy. "Impact of yttrium on the physical, electro-magnetic and dielectric properties of auto-combustion synthesized nanocrystalline strontium hexaferrite", *Journal of Materials Science: Materials in Electronics*, 2018

12 words — < 1%

Crossref

37 L. N. Pan, F. M. Gu, D. R. Cao, P. P. Jing, J. N. Li, J. B. Wang, Q. F. Liu. "Electrospun Dy-doped $SrFe_{12}O_{19}$ nanofibers: microstructure and magnetic properties", *Applied Physics A*, 2016

11 words — < 1%

Crossref

38 Ashok Gadkari, Tukaram Shinde, Pramod Vasambekar. "Influence of rare-earth ions on

10 words — < 1%

structural and magnetic properties of CdFe₂O₄ ferrites", Rare Metals, 2010

Crossref

39 Sunil Kumar, Murli Kumar Manglam, Sweety Supriya, Harendra Kumar Satyapal, Rakesh Kumar Singh, Manoranjan Kar. "Lattice strain mediated dielectric and magnetic properties in La doped barium hexaferrite", Journal of Magnetism and Magnetic Materials, 2019

10 words — < 1%

Crossref

40 www.mdpi.com

Internet

10 words — < 1%

41 Bablu Chandra Das, A.K.M. Akther Hossain. "Rietveld refined structure, ferroelectric, magnetic and magnetoelectric response of Gd- substituted Ni-Cu-Zn ferrite and Ca, Zr co-doped BaTiO₃ multiferroic composites", Journal of Alloys and Compounds, 2021

9 words — < 1%

Crossref

42 epdf.pub

Internet

9 words — < 1%

43 www.jkps.or.kr

Internet

9 words — < 1%

44 Chao, X.. "Piezoelectric, dielectric and magnetic properties of (1-x)Pb[Zr, Ti, (Mg^{1"/"2W^{1"/"2}), (Ni^{1"/"3Nb^{2"/"3})]O_{3+x}(Ni, Co, Cu)FeO₄ composites", Journal of Magnetism and Magnetic Materials, 201108}}

8 words — < 1%

Crossref

45 Jibrin Mohammed, Hafeez Yusuf Hafeez, Tchouank Tekou Carol T., Chifu E. Ndikilar et al. "Structural, dielectric, and magneto-optical properties of Cu²⁺-Er³⁺

8 words — < 1%

substituted nanocrystalline strontium hexaferrite", Materials Research Express, 2019

Crossref

46 Mudssir Shezad, Xiansong Liu, Shuangjiu Feng, Xucai Kan, Tayyab Junaid Shehzad, Arfeena Mudassir, Wei Wang, Chaocheng Liu. "Investigating the co-substitution impact of yttrium–nickel cations on lattice, morphological and magnetic parameters of SrM based ceramics", Ceramics International, 2020

8 words — < 1%

Crossref

47 Nanzhaxi Suo, Aimin Sun, Lichao Yu, Zhuo Zuo, Xiqian Zhao, Wei Zhang, Yanchun Zhang, Liqiong Shao, Tengxuan Yu. "Preparation and study of lattice structure and magnetic properties of Bi³⁺ ion-doped Ni–Mg–Co ferrites by sol–gel auto-combustion method", Journal of Sol-Gel Science and Technology, 2020

8 words — < 1%

Crossref

48 R. H. Kadam, R. B. Borade, M. L. Mane, D. R. Mane, K. M. Batoor, Sagar E. Shirsath. " Structural, mechanical, dielectric properties and magnetic interactions in Dy -substituted Co–Cu–Zn nanoferrites ", RSC Advances, 2020

8 words — < 1%

Crossref

49 Dom Lal Kunwar, Dipesh Neupane, Jiba Nath Dahal, Sanjay Raj Mishra. "Structural, Magnetic, and Electrical Properties of RE Doped Sr_{0.82}RE_{0.18}Fe_xAl_xO₁₉ (RE = Gd, Pr, Sm) Compound", Advances in Materials Physics and Chemistry, 2019

6 words — < 1%

Crossref

50 updatepublishing.com

Internet

5 words — < 1%

EXCLUDE QUOTES OFF

EXCLUDE BIBLIOGRAPHY ON













EXCLUDE SOURCES OFF















EXCLUDE MATCHES OFF

Document Information

Analyzed document	PHYSICS, MR. SHIREESH SHRIKANT CHOUDHARI Ph.D Thesis PDF.pdf (D97420033)
Submitted	3/6/2021 11:56:00 AM
Submitted by	dharmaraj veer
Submitter email	dharmaraj.veer@gmail.com
Similarity	6%
Analysis address	dharmaraj.veer.bamu@analysis.urkund.com

Sources included in the report

W	URL: http://pr.hec.gov.pk/jspui/bitstream/123456789/7593/1/PhD%28Physics%29Full%20Thes ... Fetched: 12/18/2020 7:32:17 AM		11
W	URL: https://docplayer.net/150337558-Doctor-of-philosophy.html Fetched: 12/14/2019 7:53:33 AM		10
W	URL: https://www.researchgate.net/publication/224650077_Magnetolectric_Properties_of_C ... Fetched: 2/27/2020 10:34:22 AM		3
W	URL: https://www.researchgate.net/publication/277900370_Crystal_structure_and_magnetic_ ... Fetched: 12/11/2020 4:07:06 AM		2
J	An investigation of structural and magnetic properties of Cr–Zn ferrite nanoparticles prepared by a sol–gel process URL: 0201276d-de23-493f-a933-df7286b7da30 Fetched: 11/14/2019 8:50:24 AM		4
W	URL: https://www.researchgate.net/publication/262195378_Structural_dielectric_ferromagn ... Fetched: 4/27/2020 6:12:37 PM		11
W	URL: https://www.researchgate.net/publication/229385921_Studies_on_the_Magnetic_Magneto ... Fetched: 1/7/2020 8:31:39 AM		2
W	URL: https://www.researchgate.net/publication/230928122_Magnetic_and_Magnetostrictive_P ... Fetched: 11/12/2019 10:33:19 AM		3
W	URL: https://www.researchgate.net/publication/260721358_Synthesis_and_characterization_ ... Fetched: 5/3/2020 4:56:23 PM		4
W	URL: http://pr.hec.gov.pk/jspui/bitstream/123456789/2067/2/1603S.pdf Fetched: 12/11/2020 4:39:09 PM		5
W	URL: https://serc.carleton.edu/research_education/geochemsheets/techniques/XRD.html Fetched: 3/6/2021 11:56:00 AM		5
W	URL: https://en.wikipedia.org/wiki/Fourier-transform_infrared_spectroscopy Fetched: 3/6/2021 11:56:00 AM		4

W	URL: https://www.academia.edu/33210023/STUDIES_ON_REMEDIATION_OF_CHROMIUM_CONTAINED_IND... Fetched: 3/6/2021 11:56:00 AM		1
W	URL: https://www.researchgate.net/publication/234914865_Mossbauer_spectroscopy_investig... Fetched: 11/12/2019 10:32:09 AM		1
W	URL: https://www.researchgate.net/publication/248276139_Electrical_and_dielectric_prope... Fetched: 2/10/2020 9:20:41 AM		3
W	URL: https://www.researchgate.net/publication/229315436_Optical_magnetic_and_electrical... Fetched: 1/28/2021 4:21:25 PM		1
W	URL: https://www.researchgate.net/publication/263550283_Structural_electrical_and_magne... Fetched: 3/6/2021 11:56:00 AM		2
W	URL: https://www.researchgate.net/publication/229891429_A_Ferroelectric_Ferromagnetic_C... Fetched: 10/18/2019 7:17:20 AM		2
W	URL: https://www.researchgate.net/publication/231094467_Influence_of_Thermal_Annealing_... Fetched: 10/28/2019 1:14:34 PM		3
W	URL: https://www.researchgate.net/publication/279204462_Structural_electrical_and_trans... Fetched: 10/13/2019 9:42:24 AM		3
W	URL: https://link.springer.com/article/10.1007/s10854-020-03518-0 Fetched: 3/6/2021 11:56:00 AM		1
W	URL: https://www.researchgate.net/publication/230963003_Structural_and_Magnetic_Propert... Fetched: 1/11/2021 8:09:00 AM		1
W	URL: https://www.researchgate.net/publication/229373047_Structural_and_magnetic_propert... Fetched: 3/13/2020 6:06:15 AM		3
W	URL: https://www.researchgate.net/publication/260805883_Magnetic_and_structural_propert... Fetched: 1/8/2020 11:38:51 AM		1
W	URL: https://www.x-mol.com/paper/1323383389284438016 Fetched: 3/6/2021 11:56:00 AM		1
W	URL: https://www.researchgate.net/publication/346589470_Strain_mediated_enhancement_in_... Fetched: 3/6/2021 11:56:00 AM		1

Entire Document

"PIEZOMAGNETIC-PIEZOELECTRIC COMPOSITES: STUDIES ON MAGNETOELECTRIC AND DIELECTRIC PROPERTIES"

91%

MATCHING BLOCK 1/88

W [http://pr.hec.gov.pk/jspui/bitstream/123 ...](http://pr.hec.gov.pk/jspui/bitstream/123...)

A Thesis submitted in partial fulfillment of the requirement for the degree of Doctor of Philosophy in

the subject PHYSICS under the faculty of SCIENCE AND TECHNOLOGY. By, MR. SHIREESH SHRIKANT CHOUDHARI M.Sc. Physics) Research Guide Dr. R. H. Kadam Associate Professor in Physics Shrikrishna Mahavidyalaya, Gunjoti Tq. Omerga, Dist. Osmanabad. DR. BABASAHEB AMBEDKAR MARATHWADA UNIVERSITY, AURANGABAD – 431 004 March - 2021

1 CHAPTER – I INTRODUCTION TO PIEZOMAGNETIC AND PIEZOELECTRIC MATERIALS CONTENTS 1.1 Piezomagnetic materials : 02 1.1.1 Types of piezomagnetic materials : 03 1.1.2 Classification of magnetic materials : 04 1.1.3 Novel applications of piezomagnetic materials : 09 1.2 Piezoelectric materials : 10 1.2.1 Characteristics of piezoelectric materials : 11 1.2.2 Properties of piezoelectric materials : 11 1.2.3 Applications of piezoelectric materials : 14 1.3 Introduction to M-E composites : 15 1.3.1 Merits of M-E composites : 16 1.3.2 Demerits of M-E composites : 17 1.4 Literature survey : 18 1.4.1 Cobalt – chromium ferrite (CCFO) : 18 1.4.2 Manganese-zinc ferrite (MZFO) : 21 1.4.3 Barium titanate (BTO) : 25 1.5 Aim of the present work : 28 References : 29

Chapter-I 2 1.1 PIEZOMAGNETIC MATERIALS 'Ferrites are also named as Piezomagnetic materials.' Piezomagnetism is a phenomenon simply characterized by magnetic polarization and mechanical strain coupling in the system. In such materials, application of physical stress induces the spontaneous magnetic moment. Due to various applications, ferrite (piezomagnetic) materials broadly practiced in a diverse range [1-5]. Ferrites are the novel magnetic materials that exhibit both electrical and magnetic properties and hence are commercially and scientifically important magnetic materials. Ferrites strongly behave like ferromagnetic materials as proposed by L. Neel [6]. The concise introduction of ferrite and subsequently types of magnetic materials are addressed in this chapter. The chemical composition of ferrites like spinel type, garnet type, and hexagonal type are exercised here. The deviation in properties of ferrite materials arises due to several parts such as synthesis method, sintering temperature, composition of elements, concentration of iron oxide (Fe_2O_3), divalent metal ions like metal oxide (MO) of cobalt, nickel, copper, manganese, zinc etc., amount of trivalent dopants like chromium, aluminum, R-E ions etc. and impurity arises at the time of synthesis [7]. When Ferrite material is immersed in an alternating field, eddy currents are generated in it, which dissipate energy. This waste can be lessened by lamination of ferromagnetic core to restrict the eddy current paths, since eddy current loss in magnetic material is inversely proportional to resistivity and hence magnetic material used of high resistivity [8]. Similarly ferrite shows different electric and magnetic properties i.e. extended amount of saturation magnetization (M_s), high value of permeability(μ), low coercivity, low dielectric losses, high electric resistivity and high magnetoelectric (ME) effect [9]. The electrical and magnetic properties make ferrites are useful in antenna rod, transformer core, memory chips, telecommunication, automobile,

Chapter-I 3 magnetic field sensors, transducers, electro-optic devices, magnetically tuned capacitors etc [10-12]. 1.1.1 Types of piezomagnetic materials According to the magnetic behaviour such as coercivity and remnant magnetization ferrites (Piezomagnetic) materials are generally categorized in two main types such as; i) Soft ferrites, and ii) Hard ferrites i) Soft ferrites Soft ferrite is low coercive magnetic material. When it is immersed in external magnetic field it easily magnetizes and on the removal of magnetic field it loses its magnetism. The general formula of soft ferrite is MFe_2O_4 where M stands for iron, nickel, manganese, and zinc. Soft ferrite material is used in magnetic recording media, inductor, and transformer core, vibrator due to low coercivity, low frequency and remanance. ii) Hard ferrites Magnetic hardness of ferrite is due to fine particles having shape and crystalline anisotropy. The large anisotropy is characteristics of hard ferrite. So, hard ferrite material consists of high coercivity and remanance magnetization. Fig. 1 shows the basic difference of its properties such as coercivity etc of soft and hard ferromagnetic material. The coercivity of these materials is more than 3000 Oe, which is very high compare to other magnetic material. When hard ferrite is immersed in external magnetic field it easily magnetizes and if the external field is removed it then domains will remain in the same direction. Hence resultant magnetic moment remains to its maximum value it will not lose magnetic property. So this material is used to make permanent magnet. It is used in

Chapter-I 4 different field refrigerators, loudspeakers and small electrical motors. Nickel ferrite (NiFe_2O_4), barium ferrite ($\text{BaFe}_{12}\text{O}_{19}$), cobalt ferrite CoFe_2O_4 are some commonly used hard ferrites. Fig. 1.1: Basic difference of soft and hard ferrites. 1.1.2 Classification of magnetic materials On the basis of mutual interactions or behavior of various materials in an external magnetic field, the materials are divided in five categories. i) Diamagnetic materials The orbital motion of electrons and mutual interaction between the implemented magnetic field models diamagnetism and termed as the intrinsic property of the material. Mostly it considered as the no-magnetic substance as studied. An opposing force resulting due to the applied magnetic field creates an induced magnetic field in them in the reverse direction that is to say that magnetic influence opposes the diamagnetic materials. Its magnetic susceptibility (χ) is small and negative.

Chapter-I 5 Fig. 1.2: Behaviour of diamagnetic material in external magnetic field ii) Paramagnetic materials Fig. 1.3: Behaviour of paramagnetic material in external magnetic field Materials like those have incomplete inner orbits. The electron spins continue uncoupled, thus on employing a magnetic field the magnetic moment produced because of the spin motion set and pointing towards the magnetic field and induces magnetic moment in its direction due to which the material becomes awkwardly magnetized. These materials have an odd number of electrons. Its magnetic susceptibility (χ) is positive and least. For paramagnetic material, susceptibility diminishes with ascending in temperature.

Chapter-I 6 Susceptibility varies inversely with temperature $\chi = \frac{C}{T}$; $\chi = \frac{C}{T - T_c}$ (1.1) Where C- material constant called the Curie constant, T –Absolute temperature (K) iii) Ferromagnetic materials In certain materials, the permanent atomic magnetic moments have a strong ability to adjust themselves even with no outside field. These materials denominated ferromagnetic materials. In each unmagnified ferromagnetic material, the atoms set regions inside the substance. Different domains, however, have several directions of magnetic moment and therefore the materials settle unmagnified. Besides implementing an outer magnetic field, these domains revolve and follow in the control of the magnetic field. Each ferromagnetic material has its temperature, termed the Curie temperature, or Curie point, above which it loses its ferromagnetic properties. Its magnetic susceptibility (χ) is positive and high. Fig. 1.4: Behaviour of ferromagnetic material in external magnetic field

Chapter-I 7 Table 1.1: Classification of magnetic materials on the basis of susceptibility

Sr. No.	Material	Magnetic Susceptibility (χ)	Temperature dependence
1	Diamagnetic material	Negative and small	$\chi_{\text{Au}} = -2.74 \times 10^{-6}$ $\chi_{\text{Cu}} = -0.77 \times 10^{-6}$
2	Paramagnetic material	Positive and small	$\chi_{\text{Sn}} \sim 0.16 \times 10^{-6}$ $\chi_{\text{Pt}} \sim 21.04 \times 10^{-6}$
3	Ferromagnetic material	Positive and large	$\chi_{\text{Fe}} \sim 100,000$
4	Ferrimagnetic Materials	Positive and large	Ba ferrite ~ 3
5	Antiferromagnetic Materials	Positive and small	$\chi_{\text{Cr}} \sim 3.6 \times 10^{-6}$

Fig. 1.5: Behaviour of ferrimagnetic material in external magnetic field The macroscopic magnetic characteristics of ferromagnets and ferrimagnets are similar; the distinction lies in the source of the net magnetic moments. A ferrimagnetic material is one that has populations of atoms with opposing magnetic moments, as in antiferromagnetism; however, in ferrimagnetic materials, the opposing moments are unequal and a spontaneous magnetization remains as shown in figure below.

Chapter-I 8 Ferromagnetic, ferrimagnetic, or antiferromagnetic materials possess permanent magnetization even without external magnetic field and do not have well defined zero- field susceptibility. Ferrites (widely used in household products such as refrigerator magnets) are usually ferrimagnetic ceramic compounds derived from iron oxides. Magnetite (Fe_3O_4) is a famous example. v) Antiferromagnetic Materials Fig. 1.6: Antiferromagnetic material in external magnetic field. In an antiferromagnet, unlike a ferromagnet, there is a tendency for the intrinsic magnetic moments of neighboring valence electrons to point in opposite directions. When all atoms are arranged in a substance so that each neighbor is anti-parallel, the substance is antiferromagnetic. Antiferromagnets have a zero net magnetic moment, meaning that no field is produced by them. Manganese oxide (MnO) is one material that displays this behavior. Generally, antiferromagnetic order may exist at sufficiently low temperatures, but vanishes at and above the Néel temperature. Above the Néel temperature, the material is typically paramagnetic, that is, the thermal energy becomes large enough to destroy the microscopic magnetic ordering within the material. The Néel temperature of MnO is about

Chapter-I 9 116K. Above transition temperature anti-ferromagnetic materials become paramagnetic materials, and magnetic susceptibility χ is given by equation $\chi = \frac{C}{T - \theta}$ (1.2) Where, C is Curie constant 1.1.3 Novel Applications of piezomagnetic materials Ferrites

are primarily used as inductive components in large variety of electronic circuits such as low noise amplifiers, filters, voltage controlled oscillators. [13]

Ferrites are used in radar, bubble devices, memory cores of computers, mobile phones, camera lenses, satellite communication and microwave devices. Ferrites are used as magnetic head transducer in audio-video recording. Ferrites have versatile applications in the range of microwave to radio frequencies. Ferrites are used for production of ultrasonic wave in magnetostriction method. Ferrites has attracted great deal of attention due to its good magnetic, electric properties, excellent physical-chemical stability, and mechanical strong point, and it has full of promise presentations in the fields of ferrofluids, medical care, magnetic high-density storage, gas sensors. [14] In industries, ferrite nano-particles are used in treating polluted waste water. Ferrites are used in the fields of loudspeakers, magnetic temperature converters, telephones, television, magnetrons, premagnetizing of soft magnetic cores pickup systems, high-frequency transformers, fulse transformers, television flyback transformers, deflection coils, aerials, loading coils, small dynamos and motors, logic circuits, generators and motors, couplings and retarders ,bearings, a broad field for cheap magnets, not yet mentioned, is the toy industry. [15] Ferrites are used for production of ultrasonic wave in magnetostriction method.

Chapter-I 10 1.2 PIEZOELECTRIC MATERIALS Piezoelectric materials develop a spontaneous electric polarization in response to the externally applied electric field. These ceramics are initially reported on date back to the 1920's and they followed the discovery of ferroelectricity phenomena in Seignette or Rochelle salt by Valasek [16]. Ferroelectric materials can carry a permanent electric dipole moment. All ferroelectric materials are shows the piezoelectric and pyroelectric behaviour, however, not all pyro- or piezoelectrics are ferroelectric. There are several materials showing the spontaneous polarization for which there is a non-linear relation between P and E. Such types of materials also exhibit a P-E Hysteresis. Such substances whose properties are comparable to ferromagnetics in many respects are known as Ferroelectrics. Fig.1.7: Classification of ferroelectrics into the different classes of dielectric materials Spontaneous polarization P_s is a function of temperature, decreases with increase in temperature and vanishes at the Curie temperature T_C . The temperature point at which phase of ferroelectric material changes is called the Curie point, T_C . Most of the ferroelectric materials experience a structural phase transition from a high-temperature non-ferroelectric or para-electric phase to the low-temperature ferroelectric phase. For example, $BaTiO_3$ experience a number of phase transitions into successive ferroelectric phases.

Chapter-I 11 1.2.1 Characteristics of piezoelectric materials The spontaneous polarization of ferroelectric materials varies with temperature. Ferroelectrics have very high dielectric constants at relatively low applied field frequencies. Capacitors made from these materials can be significantly smaller than capacitors made out of other dielectric materials. Curie point (T_C) is the transition temperature at which ferroelectric materials changes their phase. For the temperature higher than that of Curie point the crystal does not exhibit ferroelectric behaviour while as for the temperature lower than that of Curie point it acts as ferroelectric. Ferroelectric capacitors exhibit nonlinear properties and usually have very high dielectric constants. The polarization does not go away when the external field is removed. They exhibit distinct dependency of permittivity on the intensity of an applied electric field. The value of dielectric constant increases with increasing temperature of ferroelectric material. 1.2.2 Properties of piezoelectric materials i) Polarization Polarization is the process of inducing equal and opposite charges on the two faces of the dielectric on the application of electric field. Some dielectric material exhibits a spontaneous polarization in the absence of an applied field which can be reversed by an externally applied field; this behavior is called the ferroelectric effect Polarization is the dipole moment per unit volume and is given by, $Q = P \times V = \epsilon_0 \chi_e E \times V = \epsilon_0 \chi_e E \times C/m^2$ (1.3) It is also given by,

Chapter-I 12 $P = \epsilon_0 \chi_e E$ (1.4) where, χ_e - electric susceptibility of dielectric material. The total polarization of dielectric materials (P) is the contribution of four types of polarization namely electronic, ionic, orientation, space charge polarization can be written as $P = P_e + P_i + P_o + P_s$ (1.5) a) (P_e) Electronic polarization: The displacement of the positively charged nucleus with respect to revolving electron in opposite direction on the application of external electric field. b) (P_i) Ionic polarization: In an ionic polarization, polarization caused by relative displacement between positive and negative ions in ionic crystal. c) (P_o) Orientation polarization: Alignment of molecules in the direction of applied field It occurs only in polar substances like HCl, H_2O , N_2O molecules d) (P_s) Space Charge polarization: The ions diffuse over appreciable distance in response to the applied field giving rise to redistribution of charges in the dielectric medium. The free electrons are present but they have restriction for moving by barriers such as grain boundaries. ii) Piezoelectricity Piezoelectricity is the ability of a particular material in which electric charges will be generated due to the application of mechanical stress. In direct piezoelectric effect charge separation is due to experience of stress and in converse

piezoelectric effect the stress and strain occurs due to application of electric field which was discovered by Pierre Curie and Paul Jacques in beginning of 1880's. Electric charges will be generated within the materials when such materials experience an external stress, and conversely, generate

Chapter-I 13 the mechanical strain when subjected to external electrical field. The name 'piezo' is derived from the Greek it means that 'to press' i.e mechanical stress. Ferroelectric material is the group of piezoelectric crystal. Fig. 1.8: Schematic figure showing possible couplings between electrical, magnetic and mechanical solids In Elasticity, a stress causes a strain proportional to an elastic modulus. Here Piezoelectricity is creation of an electric charge in addition to a strain, both of which are proportional to the applied stress. iii) Phase Transition The temperature above which ferroelectric material does not show ferroelectricity is known as Curie temperature (T_C). So, at a temperature $T < T_C$ the ferroelectric crystal does not exhibit ferroelectricity, while for $T > T_C$ it is ferroelectric. By the decreasing of temperature below the Curie point, a ferroelectric undergoes a phase transition from a non-ferroelectric to a ferroelectric. If there are two or more phases observed within the single material when the temperature changes then the temperature at which the crystal changes itself from one ferroelectric phase to another is called the transition temperature. Early research works on ferroelectric transitions have been summarized by Nettleton et. al. [17]. The properties of materials such as dielectric, elastic, thermal and optical show some

Chapter-I 14 irregularities near the Curie point due to structural phase transition changes. According to Curie-Weiss law, the relative permittivity (ϵ_r) of the material falls with the temperature above the Curie point following the relation; $\epsilon_r = \epsilon_0 + \frac{C}{T - T_0}$ (1.6) where, C is Curie Constant, T_0 -be the Curie-Weiss temperature, ϵ_0 -is the dielectric permittivity in vacuum for BaTiO₃ single crystal, the phase transitions and the crystal structures can be predicted with the crystalline anisotropy constants and strain constants that depend on the temperature. [18]. 1.2.3 Applications of piezoelectric Materials The applications for ferroelectric ceramics cover all areas of our workplaces, homes, and automobiles. Ferroelectric hysteresis is used in non-volatile computer information storage, thin film capacitor, using ferroelectric material the large capacitance value are achieved in small volume capacitor devices due high dielectric constant e.g. BaTiO₃. Ferroelectrics can exhibit very high relative permittivities which means that they are widely used in capacitors. The direct piezoelectric effect is used in sensors namely as Pick-ups, Pressure sensor, force sensor, strain gauge, microphones, hydrophones, etc. The converse P-E effect is used in actuators like Loudspeaker, Piezoelectric motors, acousto-optic modulators, Valves, ultrasonic generators, resonators, filters, etc. The pyroelectric effect is widely used in un-cooled infrared detectors. The electro-optic effect is used in optical waveguides, optical memories and displays, laser Q-switches, optical shutters and integrated optical devices.

Chapter-I 15 1.3 INTRODUCTION TO M-E COMPOSITES The composite materials of the ferroelectric and the ferromagnetic phases have the ability to show the product and sum properties. In such composite materials, electro-magnetic coupling occurs and accounts for an excellent magneto-electric effect [19-21]. In the composites,

84%

MATCHING BLOCK 3/88

W

<https://www.researchgate.net/publication/...>

the magnetoelectric effect is typically generated through a mechanical strain arising under an applied magnetic or electric field at interfaces between the two constituents.

ME effect =(mechanical / magnetic) ferrite × (electrical / mechanical) ferroelectric This effect gives the results from the interaction between different properties of the two phases in the composites. The ferroelectric– ferromagnetic composites, as two-phase multiferroic materials, are desired not only for the fundamental research of magneto- electric effect, but also for the potential applications in many electronic devices, such as electromagnetic interference filters and the integration of chip inductors and capacitors [22-24]. Composite material can be well-defined as an amalgamation of two or more than two materials different in composition on a very small scale. These materials are the composition of two different phases and hence shortened to composites. These materials fabricated from two or more constituents or phases possessing different physical and chemical properties, that when amalgamated, make a material with appearances different from the individual components. In composites, porosity percentage % is increases as ferroelectric content increases. As increasing volume ratio of ferroelectric content relative to ferromagnetic content, net magnetization can be decreased whereas maximum polarization increases also coercivity increases.

Chapter-I 16 Fig.1.9: Magnetolectric effect 1.3.1 Merits of M-E composites A long range of applications of different types of M-E composites are as follows i) Nanotechnology: The Composite materials have important applications in the field of Nanotechnology. M-E nano-composites are greatly used in automotive, electronic parts and in industrial equipments etc.

ii) Aerospace: Spacecraft applications are the maximum substantial uses of composites. Commercial aircrafts experiences greater stress on safety and weight. A modern civil aircraft designed with application the glass and carbon reinforced hybrid composites for the factor of power and safety. iii) Wind Power Generation: Wind power generation is ecologically the safest way to generate energy. So hybrid fibres (carbon, glass) are largely used for fabrication of simple power element blades. iv) Telecommunication: Hybrid cable made up of composites is the advanced product class used in the requirement of powerful transmission of data in telecommunication industries. Hybrid Composite Cable, aerial are requirements of a period, primarily to support for Power transmission for always ON (Interrupt free) telecom needs.

Chapter-I 17 v) Electrical: The composites have important properties like high quality electric insulation, spark-free and good antimagnetic agents, good adhesion toward glue & paint due to which it is used for the construction of distribution pillars, link boxes and profiles for the separation of current-carrying phases to prevent short circuits etc. vi) Orthopaedic Aids: People who were born with physically challenged. Artificial substitutes are used in the human body to utility such as original parts. Composite materials have been known as the innovative class of synthetic bio-materials. Composite material are light- weight, comfortable to work with and more durable such as lighter prosthesis needs less energy consumption for the period of running, walking and other activities, weight is very important in an artificial leg. vii) Nuclear Industry: Composite materials are used widely in nuclear industries due to its nuclear fuels. The ceramic fuels used in fast reactors have been sensibly successful in stainless steel matrix as used in plutonium uranium dioxide solid solution in steel cermets. 1.3.2 Demerits of M-E composites Some disadvantages of composites are given below; Challenge to fabricate low cost composites [25]. More complex mechanical characterization as compare with metal structure. Complicated reuse process as compared to that of metals. Composites materials do not have the quality of high combination of strength and fracture toughness compared to metals. It is not compulsory that composites give greater performance in all the properties used for material in corrosion resistance, join ability, strength, and toughness. Transverse properties may be weak.

Chapter-I 18 1.4 LITERATURE SURVEY The origin of the magnetoelectric (ME) effect in ME composites is the coupling between ferromagnetic (magnetostrictive) and ferroelectric (piezoelectric) phases [26-28]. Ferrite material will be prepared by sol-gel method & ferroelectric phase will be obtained by sol-gel method. Finally, the composite materials will be synthesized by using solid state reaction method Hence the possibility of impurity phases being present and affecting the signal [29]. The two phases ferromagnetic (magnetostrictive) and ferroelectric (piezoelectric) must be in equilibrium to obtain higher output of ME conversion [30] Composites have been synthesized by various synthesis techniques 1.4.1 Cobalt-chromium ferrite (CCFO) Cobalt ferrite CoFe_2O_4 (CFO) has a cubic spinel-type crystal structure, in which the O²⁻ ions form a FCC like lattice, and the Co²⁺ and Fe³⁺ cations reside in interstitial sites, of which there are two types: tetrahedral A sites and octahedral B sites. There are 8 tetrahedral sites and 16 octahedral sites in the unit cell [31]. It possesses interesting physical properties such as high sensitivity of magnetization to applied stress, excellent chemical stability, and a large magneto-optic effect. Recently cobalt ferrite based composites have received attention because of their high magnetostriction, high sensitivity of magnetic induction to applied stress, chemical stability and low cost [32-35]. S. Mohan et al. 2019 [36]: High purity Fe_2O_3 , CoCO_3 , BaCO_3 and TiO_2 were used as starting materials in synthesis of CoFe_2O_4 (CFO) and BaTiO_3 (BTO) by the conventional solid-state method. For preparation of CFO, a stoichiometric mixture of Fe_2O_3 and CoCO_3 was initially calcined at 1000 °C for 24 h with an instant grinding. The resulting powder was further calcined at 1100 °C for 72 h with three instant grindings. For preparation of BTO, the mixed powder of BaCO_3 and TiO_2 was initially calcined at 1000 °C for 6 h, then

Chapter-I 19 at 1200 °C for 6 h, and finally at 1300 °C for 6 h, with intermediate grindings. Composites of CFO and BTO were prepared by mixing the corresponding component powders taken in different weight percentages according to formula $(100-x)\text{CoFe}_2\text{O}_4 - (x)\text{BaTiO}_3$ ($x=0, 10, 20, 80, 90$ and 100 percentage of weight). Magnetization, as well as Curie temperature of the ferrite phase, is found to be decreased with increasing sintering temperature for a particular composite and with increasing ferroelectric BTO content for composites sintered at a particular temperature. L. Kumar et al. [37]: Initially Nano crystalline $\text{CoFe}_{2-x}\text{Cr}_x\text{O}_4$ samples with $0.0 \leq x \leq 0.4$ were prepared by the standard citrate precursor method. The coercivity and Neel's temperature decrease with the addition of chromium (Cr) concentration in cobalt ferrite. The increase in temperature increases the magneto crystalline anisotropy of the samples. Average crystallite size reduces with the addition of Cr³⁺ ions in CFO lattice. R. K. Panda et. al. [38]: When Cr substituted in CFO results in reduction in particle size and surface anisotropy which is responsible for decrease in coercivity but material resistivity increases AC conductivity analysis disclosed that the overlapping large polaron tunnelling (OLPT) mechanism takes place in Cr substituted cobalt ferrite nanoparticles. Till Walther et. al. [39]: T. Walther and co-workers have studied magnetoelectric properties of CFO-BTO composites. Sometimes, chemicals were used as purchased without further purification so they have synthesized five samples of $(\text{CoFe}_2\text{O}_4)_x - (\text{BaTiO}_3)_{(1-x)}$ composites were with $(x)\text{CFO} = 0.1,$

0.2, 0.3, 0.4 and 0.5 with moderate purity. A modified polyol mediated process was used to prepare the precursor powders for the composites. A. Aubert et. al. [40]: In the year 2018, a group of A. Aubert published their work on the role of cobalt ferrite in M-E composites. They have prepared two different kinds of polycrystalline cobalt ferrites, one exhibiting isotropic properties and the other presenting

Chapter-I 20 a uniaxial anisotropy. The starting materials in synthesis of cobalt ferrite are nano sized (>50 nm) oxides Fe_2O_3 and Co_3O_4 (Sigma-Aldrich) in a molar ratio of 3:1. Powders were mixed in a planetary ball mill for 30 min at 400 rpm and then grounded for 1 h at 600 rpm. For the first type, the synthesis of the spinel phase of CFO is achieved by the usual calcination at 900 °C for 12 h. After grinding the cobalt ferrite powder at 550 rpm for 1 h was sintered using spark plasma sintering (SPS). Here composite material was prepared by the isotropic cobalt ferrite as CFOI, and the anisotropic one as CFOA. Another method to manufacture magnetoelectric composites, cobalt ferrite disks are bonded on 1-mm-thick and 10-mm diameter commercial lead zirconate titanate (PZT) disks (Ferropem PZ27) using silver epoxy. The piezoelectric samples are polarized along the thickness direction. The magnetoelectric bilayers becomes disks with a thickness of 3 mm and a diameter of 10 mm. Measurements are also performed on a tri-layer CFO/PZT/CFO with layer thicknesses of 0.4 mm=0.75 mm=0.4 mm, and with a diameter of 10 mm. Y. Liu et. al. [41]: The magnetic hysteresis loops of two samples showed that anisotropic sample CFOI exhibits a higher coercive field ($H_c = 51$ kA/m) than the isotropic one CFOA ($H_c = 18$ kA/m). The isotropic sample appears to be more sensitive to the field and exhibits a higher susceptibility than the anisotropic one tri-layer composite is known to enhance the mechanical coupling factor and reduce the demagnetizing effect, which contributes to enhancing the magnetoelectric effect. It could also be enhanced by co-sintering both magnetic and piezoelectric phases instead of bonding them, hence increasing the mechanical coupling. The co-sintering was recently achieved in bulk CFO= $BaTiO_3$ composites. T. Ramesh et. al. [42]: Cobalt Ferrite ($CoFe_2O_4$) powders were synthesized using cobalt nitrate [$Co(NO_3)_2 \cdot 6H_2O$] (98% Sigma-Aldrich) and ferric nitrate [$Fe(NO_3)_3 \cdot 9H_2O$] (98% Sigma-Aldrich) as starting chemicals. For barium titanate ($BaTiO_3$) powder, barium

Chapter-I 21 chloride ($BaCl_2 \cdot 2H_2O$) (99% Alfa Aesar) and titanium (IV) chloride ($TiCl_4$) (99.0% Alfa Aesar) solutions were taken as starting materials. pure, single-phase $CoFe_2O_4$ and $BaTiO_3$ nanoparticles are successfully synthesized by microwave hydrothermal method.

87%

MATCHING BLOCK 4/88

W

[https://www.researchgate.net/publication/...](https://www.researchgate.net/publication/)

Composites of $(1 - x)CoFe_2O_4 + (x)BaTiO_3$ (where $x = 0, 0.25, 0.50, 0.1$) were prepared by

mixing the microwave hydrothermal synthesized $CoFe_2O_4$ (CFO) and $BaTiO_3$ (BTO) powders in a ball mill [Retsch Co] for 3 h. it is found that with increasing ferroelectric content $BaTiO_3$ content, the dielectric constant of the composite samples increases and resonance frequency decreases Magnetoelectric coefficient (dE/dH) of composite materials increases with increasing ferroelectric phase $BaTiO_3$ and is due to the reduction in higher conductivity magnetic phase as compared to ferroelectric phase causes. M. Raghasudha et. al. [43]: Nanoferrites $CoFe_2O_4$ and $CoCr_0.9Fe_{1.1}O_4$ were prepared through citrate-gel auto-combustion technique using Co(

87%

MATCHING BLOCK 6/88

J

0201276d-de23-493f-a933-df7286b7da30

$NO_3)_2 \cdot 6H_2O$, $Fe(NO_3)_3 \cdot 9H_2O$,
 $Cr(NO_3)_3 \cdot 9H_2O$, $C_6H_8O_7 \cdot H_2O$

and NH_3 as starting materials of high purity The values of saturation magnetization(M_s) of the samples at 310K are 43emu/g (for $CoFe_2O_4$) and 12emu/g(for $CoCr_0.9Fe_{1.1}O_4$). It was also found that substitution of 0.9 mol of Cr³⁺ in Cobalt ferrite has decreased the coercivity from 1760 to 338 Oe at room temperature, making the material magnetically very soft favoring its application in high frequency transformers. 1.4.2 Manganese-Zinc ferrite (MZFO) Manganese-Zinc ferrite is soft ferrite used in many applications. It is primarily used for frequencies less than 2 MHz. This composition of Mn and Zn gives optimum performance for saturation flux density (B_s), low losses (Q) and high initial permeability (μ_s). It identifies the temperature lines for 100 and 250°C. Mg-Zn ferrites are used in

Chapter-I 22 various applications like power transformers, microwave devices, and telecommunications due to their high permeability and electrical resistivity [44]. Rongli Gao et. al. [45]: The comparative study of properties like structural, dielectric, ferroelectric, magnetic properties as well as coupling effect for $(1-x)Mn_{0.5}Zn_{0.5}Fe_2O_4 - xBa_{0.85}Sr_{0.15}Ti$

0.9 Hf 0.1 O₃ ((1-x)MZFO- (x)BSTHO) (x = 0.2, 0.35, 0.5, 0.65, 0.8) composite ceramics prepared by combining co-precipitation process with sol-gel method. The composite particles in the stoichiometric ratio were ball milled again for 8 h, mixed thoroughly with a PVA binder solution and then pressed at 12 MPa for 10 min into disk samples with the size of 10 mm diameter and 1mm thickness. The disk samples were finally sintered at 1150 °C for 4 h in a chamber furnace in air to form the required composite ceramics. Using XRD patterns of the prepared composite ceramics main diffraction peaks of magnetic/ferroelectric phase can be observed magnetolectric coupling coefficient (1420 mV/cm Oe) are obtained for the specimen x =0.65 due to its stronger interface interaction between ferroelectric and ferromagnetic phases.. The MZFO/BSTHO composites exhibit multiferroic properties at room temperature which is confirmed by the observations of ferroelectric and magnetic hysteresis loops. MZFO has been chosen as the magnetic phase for this particulate composite because it has high permeability, high saturation magnetization, low coercivity, high resistivity and low high frequency loss, high (time, temperature) stability, high permeability frequency characteristics [46]. K. Praveena et. al. [47]: Fabrication of composites is obtained by taking NBT and MFO powders in different mole percent ratios and ground thoroughly for 3 h and sintered at 900 °C for 4 h. The structural characteristics of the composites were carried out by X-ray diffraction (XRD) using Phillips PAN analytical X'pert powder diffractometer with Cu-K α radiation (λ= 1.5406 Å) Morphological characteristics were studied by field emission

Chapter-I 23 scanning electron microscope (FSEM). The ME output of the samples was obtained by static method. It is known that the distribution of the ferrite and the ferroelectric phases in composites plays a most essential role not only in the combination properties (magnetization, dielectric constant, resistivity, etc.) but also in the product properties such as the ME output. The saturated magnetization values of the composites increased almost linearly with increasing ferrite concentration. These composites exhibited ME effect at room temperature, which is strongly dependent on ferrite content in the composite. Kiran et al 2020 [48]:

77%

MATCHING BLOCK 5/88

W

[https://www.researchgate.net/publication/ ...](https://www.researchgate.net/publication/...)

lead-free magnetolectric composites (x)K_{0.5}Na_{0.5}NbO₃ – (x)MnFe₂O₄ (x = 0, 0.2, 0.4, 0.6, 0.8, and 1) synthesized by solid-state reaction

route have been studied for their structural, dielectric, and magnetolectric properties. The micro- structural analysis (XRD, FESEM, EDX, FTIR, and RAMAN spectroscopy) indicates the coexistence of diphas in the composites. Compared to the individual phases, composites exhibit better electrical properties such as low leakage current, high resistivity, high dielectric constant, and low dielectric loss. I–V characteristics reveal that the conduction behavior of the composites is ohmic in nature in whole tested electric field range at room temperature. The maximum value of dielectric constant is noticed for composite with 20 wt% of MnFe₂O₄ among the composites. The magnetic measurements indicate that the magnetic behaviour of the composites lies on the mass content of MnFe₂O₄ phase. The magnetization increases with MnFe₂O₄ weight percentage which provides information regarding the magnetolectric effect (ME) coupling between the magnetostrictive ferromagnetic and ferroelectric phases. Furthermore, ME effect is evaluated as a function of applied magnetic field. The highest ME response of 2.02 mV/cm-Oe is observed for composite with 80 wt% content of MnFe₂O₄. These composites are worthy material for environment-friendly ME device applications.

Chapter-I 24 Phuong-Linh Nguyen et. al. [49]:

93%

MATCHING BLOCK 7/88

W

[https://www.researchgate.net/publication/ ...](https://www.researchgate.net/publication/...)

The successful realization of multifunctional systems consisting of ferrimagnetic Mn_{0.7}Fe_{2.3}O₄ spinel platelets, of controlled sizes and nanometric thicknesses, embedded in an epitaxial ferroelectric BaTiO₃ perovskite thin film. The embedded platelets experience a much higher iso-static strain than that obtained for single layers.

There was

98%

MATCHING BLOCK 9/88

W

[https://www.researchgate.net/publication/ ...](https://www.researchgate.net/publication/...)

successfully achieved nanometer-thick composite layers, with identical composition, having either in-plane or out-of-plane electric polarization orientations. The optimal samples combine several functionalities: (i) the magnetoelectric nature of the full oxide artificial structures is confirmed, (ii) semiconducting diode behaviors are obtained when contacted with a metal electrode, and (iii) marked (eightfold) electro-resistance transport properties with respect to the electric polarization orientation are revealed. The embedded platelets configuration enhances significantly interface and two-dimensional effects and is thus believed of high interest to realize functional device structures.

S. Satapathy et. al. [50]: MgFe_2O_4 (MFO) and $(\text{Ba}_{0.85}\text{Ca}_{0.15})(\text{Zr}_{0.1}\text{Ti}_{0.9})\text{O}_3$ (BCZT) was prepared by solid state route and are found to be ferromagnetic and ferroelectric at room temperature respectively. MFO/BCZT composite (50:50 M concentration of MFO and BCZT) was also prepared by solid state route. Scanning electron micrograph confirms the distribution of small grains of MFO around large grain of BCZT for proper surface interaction. MFO/BCZT composite exhibits saturated magnetization of 12 emu/gm, which reduce to 10 emu/gm on electrical poling at 2.5 kV/cm indicating magneto-electric coupling between MFO and BCZT through interface interaction. The transverse magnetoelectric coupling coefficient ($\text{aV}/31$) for this composite is found to be 7.97 mV/cm 1 Oe 1 at 10 kHz. MFO/BCZT ceramic composite exhibit multiferroic and magnetoelectric coupling properties for 50:50 M concentration at room temperature may be suitable for device applications.

Chapter-I 25 1.4.3 Barium Titanate (BaTiO_3) Barium Titanate (BaTiO_3) is the first polycrystalline ceramic material which exhibits high ferroelectricity and resistivity of the order of $10^9 \Omega\text{cm}$. BTO has extremely high relative permittivity. Ferroelectrics are polar materials that possess at least two equilibrium orientations of spontaneous polarization in the absence of an electric field. Under the application of an electric field, the direction of the polarization vector can be reoriented. Hence, ferroelectric materials are both piezoelectric and pyroelectric and exhibit nonlinear phenomena associated with polarization reversal. Barium titanate- based materials are the preferred choice for capacitor applications Kuldeep Chand Verma et. al. [51]:

100%

MATCHING BLOCK 11/88

W

[https://www.researchgate.net/publication/ ...](https://www.researchgate.net/publication/...)

The MFO/BTO thin films were prepared by metallo-organic decomposition method. The MFO/BTO nanocomposite stoichiometric ratio has been analyzed with X-ray fluorescence elemental analysis. X-ray diffraction reveals the formation of both spinel MFO and perovskite BTO phases with crystallite size lies in the range of 25-137 nm. The lattice strain observed in MFO/BTO nanocomposite is due to tetragonal distortion of BTO unit cell and lattice mismatch with ferrite MFe_2O_4 . The crystallite size is also depicted with atomic force microscopy. The observed ferromagnetism of MFO/BTO nanocomposite is highly influenced by inversion degree of MFO ferrite and oxygen vacancies formation. All MFO/BTO nanocomposites have well saturated ferroelectric hysteresis polarization. This has been discussed based on lattice strain, leakage current and the degree of lattice mismatch. The chemical valence states of Fe and O and their influence on the magnetic and ferroelectric properties have been analyzed with X-ray photoelectron spectroscopy. The capacitance versus bias voltage characteristics under the influence of applied dc magnetic field indicates ferroelectric behavior and the presence of magneto-electric/dielectric effects. The dielectric permittivity reduces with applied dc magnetic field which is responsible for negative

magneto-

Chapter-I 26 dielectric

effect. The higher longitudinal magnetoelectric coupling coefficient is obtained in $M(1/4\text{Co, Ni, Zn})\text{FO/BTO}$ nanocomposite which is correlated with piezoelectric coefficient, d_{33} value measurement.

Chiranjib Nayek et. al. [52]: The magnetoelectric properties of $\text{La}_{0.7}\text{Sr}_{0.3}\text{MnO}_3 - \text{BaTiO}_3$ core-shell nanostructure synthesized by sol-gel method. X-ray diffraction analysis suggests that the BaTiO_3 undergoes large strain in the core-shell structure which can be attributed to lattice induced strain. Interestingly, the core-shell nanoparticle exhibits enhanced magnetization (143 emu/g) compared to the ferromagnetic $\text{La}_{0.7}\text{Sr}_{0.3}\text{MnO}_3$ bare core (20 emu/g). The core-shell structure also exhibits inherent magnetoelectric coupling which is reflected as an anomaly at the ferroelectric transition in the magnetization measurement. The direct magnetoelectric measurement on $\text{La}_{0.7}\text{Sr}_{0.3}\text{MnO}_3 - \text{BaTiO}_3$ nanocomposite revealed the magnetoelectric voltage coefficient value is 54.5 mV/cm Oe at 1 kOe, which is a promising result as compared to the other perovskite based nanocomposites. Vandana Kuldeep et. al. [53]: Nano-structural fabrication of both multiferroic BTO and DMS ZnO depends upon the synthesis method, type of dopant material, stoichiometric proportion, and sintering conditions. In perovskites, the multiferroicity appears as the superposition of two phenomena formally independent (TN $6\frac{1}{4}$ TFE), magnetism generally emerges in structures that already present some distortions (including ferroelectric). The ferromagnetism in Fe-doped BTO and ZnO systems is explained due to F-centre exchange (FCE) and the BMP model. The survey from multiferroic studies has demonstrated that the ME coupling may enhance effectively from the multilayered heterostructures of BTO, BFO, and ferrite nano composites. Guo Yu et. al. [54]: Nano-composites BTO-MZF films have been grown on (001)- oriented SrTiO_3 substrates by a pulsed laser deposition method with composition

Chapter-I 27 $0.6\text{BaTiO}_3 - 0.4\text{Mn}_{0.4}\text{Zn}_{0.87}\text{Fe}_2\text{O}_4$ demonstrated by a PLD method at $>850^\circ\text{C}$ in spite of very large lattice mismatch between the two phases. Bulk MZF generally has a low saturation field, however, the measured saturation field of BTO-MZF is ~ 2000 Oe, which limits the maximum permeability. MZF may not be fully decomposed from BTO matrix even after annealing at 1020°C for one hour. Zhenhua Shi et. al. [55]: The NFO-BTO PC was obtained by the two-step approach, as confirmed by XRD, TEM and EDX analysis. The interface phase has been observed in the PC, and the M_s of NFO in PC significantly lower than purely NFO, thanks to the presence of interface phase. The ac magnetic susceptibility shows an abnormal around the ferroelectric phase transition temperature. The PC exhibits remarkable ME effect through both static measurement and dynamic measurement. Notably, the PC exhibits giant ME voltage coupling coefficient without dc magnetic field, this is beneficial for application in high frequency devices. D. Zhou et. al. [56]: The structural, ferroelectric, ferromagnetic, resonance and magnetoelectric (ME) properties of multilayered ME composites fabricated using tape casting method. The compositions corresponding to CoFe_2O_4 (CFO) with particle size of ~ 150 nm and BaTiO_3 (BTO) with particle size of ~ 100 nm were chosen as ferromagnetic and ferroelectric phases, respectively. Delamination was found at the interface between CFO and BTO layers, which was related to the residual stress due to the difference in thermal expansion coefficient between the two layers. The largest direct magnetoelectric and converse magnetoelectric coefficients of the multilayered ME composite were, respectively, $36 \mu\text{V}/\text{cm Oe}$ at a bias magnetic field of 2,800 Oe and $1.16 \times 10^{-3} \text{ G}/\text{V}$ at a frequency of 30 kHz. For the multilayered ME composite, a resonance frequency of 4.96 MHz and a bandwidth of 40 kHz were obtained using capacitance-frequency spectrum method.

Chapter-I 28 1.5 AIM OF THE PRESENT WORK In order to probe the magnetoelectric coefficient (ME) of composite material, the ferromagnetic phase Cr substituted Co ferrite with a chemical formula $\text{CoCr}_{0.3}\text{Fe}_{1.7}\text{O}_4$ has been made composite with ferroelectric BaTiO_3 phase. Here, the composition of ferromagnetic $\text{CoCr}_{0.3}\text{Fe}_{1.7}\text{O}_4$ phase varies with ferroelectric BaTiO_3 phase with the following formula $(1-x)\text{CoCr}_{0.3}\text{Fe}_{1.7}\text{O}_4 + (x)\text{BaTiO}_3$. Similarly, $\text{Mn}_{0.7}\text{Zn}_{0.3}\text{Fe}_2\text{O}_4$ is a new type of single phase room temperature multiferroic material having spinel structure is combining with ferroelectric BaTiO_3 phase with increasing the concentration of ferroelectric phase having chemical composition is $(1-x)\text{Mn}_{0.7}\text{Zn}_{0.3}\text{Fe}_2\text{O}_4 + (x)\text{BaTiO}_3$. Following are the main objectives of the present study; Synthesis of CCFO $(1-x) + (x)$ BTO and $(1-x)$ MZFO $+ (x)$ BTO by employing ultrasonic assisted irradiation assisted sonochemical sol-gel route to obtain the ferromagnetic phases and sol-gel route for the fabrication of ferroelectric phase of BTO. Use of ceramic route to obtain the M-E composites. Identification of individual phases in M-E composites and phase purity by X-ray diffraction method. Study of surface morphology and determination of grain size by scanning electron microscopy. Determination of stoichiometry percentage of elements in the composite by using EDAX patterns uniform distribution of elements in the sample by color mapping. Study of absorption bands in the M-E crystals by FTIR spectra. Investigations of magnetic

properties by VSM technique. Investigations of ferroelectric properties by P-E loops. Frequency dependent dielectric properties by two probe technique. Study of M-E coefficient of the composites by dynamic method.

Chapter-I 29 REFERENCES [1] M. V. Chaudhari, R. H. Kadam, S. B. Shelke, S. E. Shirsath, A. B. Kadam, D. R. Mane; Combustion synthesis of Co²⁺ substituted Li_{0.5}Cr_{0.5}Fe₂O₄ nano-powder: physical and magnetic interactions; Powder Tech. 259 (2014) 14-21 [2] A. Rajeshwari, I. K. Punithavathy, S. J. Jeyakumar, N. Lenin, B. Vigneshwaran; Dependence of lanthanum ions on structural, magnetic and electrical of manganese based spinel nanoferrites; Ceram. Inter. 46 (2020) 6860-6870. [3] S. E. Shirasth, R. H. Kadam, S. M. Patange, M. L. Mane, A. Ghesami, A. Morisako; Enhanced magnetic properties of Dy³⁺ substituted Ni-Cu-Zn ferrite nanoparticles; Appl. Phys. Lett. 100 (2012) 042407. [4] V. Prasad, K. V. Ramesh, A. Srinivas;

100%

MATCHING BLOCK 12/88

W

[https://www.researchgate.net/publication/ ...](https://www.researchgate.net/publication/)

Structural and magnetic studies of Nano-crystalline ferrites MFe₂O₄ (M = Zn, Ni, Cu, and Co) synthesized via citrate gel

auto combustion method; J. Super. Nov. Magn. 30 (2017) 3523-3535. [5] Z. Liu, Z. Peng, X. Fu; Structural and electromagnetic properties of Ni_{0.5}Zn_{0.5}HoxFe_{2-x}O₄ ferrites; Ceram. Inter. 43 (2017) 14938-14944. [6] L. Neel, Magnetic properties of ferrites: ferrimagnetism and antiferromagnetism; Ann.de Phys. 3 (1948)137. [7] S. E. Shirsath, R. H. Kadam, A. S. Gaikwad, A. Ghesami, A. Morisako; Effect of sintering temperature and the particle size on the structural and magnetic properties of nanocrystalline Li_{0.5}Fe_{2.5}O₄; J. Magn. Magn. Mater. 323 (2011) 3104-3108. [8] V. Choudhari, S. E. Shirsath, M. L. Mane, R. H. Kadam, S. B. Shelke, D. R. Mane; Crystallographic, magnetic and electrical properties of Ni_{0.5}Cu_{0.25}Zn_{0.25}La_xFe_{2-x}O₄ nanoparticles fabricated by sol-gel method; J. Alloys. Comp. 549 (2013) 213-220 [9] M. Sugimoto; The past, present and future of ferrites; J. Am. Ceram. Soci. 82 (1999) 269-280.

Chapter-I 30 [10] M. P. Horvath; Microwave applications of soft ferrites; J. Magn. Magn.

95%

MATCHING BLOCK 10/88

W

<https://docplayer.net/150337558-Doctor-of ...>

Mater. 215 (2000) 171-183.

[11] N. Rezlescu, E. Rezlescu; Dielectric properties of copper containing ferrites; Phys.

Stat. Solid. (a); 23 (1974) 575-582. [12] J. L. Dormann, M. Nogus; Magnetic structures in substituted ferrites; J. Phys.: Cond. Matter. 02 (1990) 1223. [13] R. Valenzuela; Novel applications of ferrites; Adv. Mag. Mater. 2012 (2011) 591839. [14] M. Amiri, K. Eskandari, M. S. Niasari; Magnetically retrievable ferrite nanoparticles in the catalysis application; Adv. Coll. Inter. Sci. 271 (2019) 101982. [15] J. M. Haspers; Ferrites: Their properties and applications; Mod. Mater. 3 (1962) 259-341. [16] J. Valasek, Piezo-electric and allied phenmena in Rochell Salt, Physical Review, 17 (1921) 475. [17] R. E. Nettleton, Ferroelectric phase transitions a review of theory and experiment; Ferroelectrics; 1(1970) 127-135. [18] H. Zhang; A theory of structural phase transitions in BaTiO₃ single crystal and PbZrO₃-xPbTiO₃ solid solutions; AIP advances; 3 (2013) 042118. [19] V. F. Janas and A. Safari; Overview of Fine-Scale Piezoelectric Ceramic/Polymer Composite Processing; J. Am. Ceram. Soc. 78 (1995) 2945. [20] J. Zhai, N. Cai, Z. Shi, Y. Lin, C. W. Nan; Magnetic-dielectric properties of NiFe₂O₄/PZT particulate composites; J. Phys. D: Appl. Phys. 37 (2004)823-7. [21] J. Ryu, A. V. Carazo, K. Uchino, H. E. Kim; Magnetoelectric Properties in Piezoelectric and Magnetostrictive Laminate Composites; Japan. J. Appl. Phys. 40 (2001) 4948.

Chapter-I 31 [22] R. S. Devan, S. A. Lokare, D. R. Patil, S. S. Chougule, Y. D. Kolekar, B. K. Chougule; Electrical conduction and magnetoelectric effect of (x) BaTiO₃ + (1-x) Ni_{0.92}Co_{0.03}Cu_{0.05}Fe₂O₄ composites in ferroelectric rich region; J. Phys. Chem. Solids 67 (2006) 1524-30. [23] J. H. Shen, Y. Bai, J. Zhou, L. T. Li; Magnetic Properties of a Novel Ceramic Ferroelectric-Ferromagnetic Composite; J. Am. Ceram. Soc. 88 (2005) 3440. [24] S. Lopatin, I. Lopatina, I. Lisnevskaya; Magnetoelectric PZT/ferrite composite material; Ferroelectrics 162 (1994) 63. [25] K. K. Patankar, V. L. Mathe, R. P. Mahajan, S. A. Patil, R. M. Reddy, K. V. Sivakumar; Dielectric behaviour and magnetoelectric effect in CuFe₂O₄ - Ba_{0.8}Pb_{0.2}TiO₃ composites; Mater. Chem. Phys. 72 (2001) 23. [26] P. Thori, P. Sharma, M. Bhargava; An approach of composite materials in industrial machinery: advantages, disadvantages and applications; IJRET Volume: 2 (2013) 350-355 [27] J. Van Suchetelene; Product properties : a new application of composite materials; Philips Res. Rep. 27 (1972) 28 [28] K. Zhao, Y. R. Dai, J. G. Wan, Z. F. Zhang, J. S. Shu; The study of magnetic field- induced strain of Ni₂MnGa/Pb(Zr_{0.52}Ti_{0.48})O₃ composite; Mater. Sci. Eng.; A 438 (2006) 1019-1021 [29] S. Lopatin, I. Lopatina, I. Lisnevskaya; Magnetoelectric PZT/ferrite

composite material; Ferroelectrics 162 (1994) 63–68. [30] K. K. Patankar, V. L. Mathe, A. N. Patil, S. A. Patil, S. D. Lotke, Y. D. Kolekar, P. B. Joshi; Electrical Conduction and Magnetolectric Effect in $\text{CuFe}_{1.8}\text{Cr}_{0.2}\text{O}_4 - \text{Ba}_{0.8}\text{Pb}_{0.2}\text{TiO}_3$ Composites; J. Electroceram. 6 (2001)115–122

Chapter-I 32 [31] J. V. D. Boomgaard, D. R. Terre, R. A. J. Born, H. F. J. Giller; An in situ grown eutectic magnetolectric composite material; J. Mater. Sci. 9 (1974) 1705 [32] G. A. Sawatzky, F. van der Woude, and A. H. Morrish; Mössbauer Study of Several Ferrimagnetic Spinel; Phys. Rev. 187 (1969) 747. [33] K. Kriehle, T. Schaeffer, J. A. Paulsen, A. P. Ring, C. C. H. Lo, and J. E. Snyder,;

75%

MATCHING BLOCK 13/88

W

<https://www.researchgate.net/publication/...>

Mössbauer spectroscopy investigation of Mn-substituted Co-ferrite ($\text{CoMn}_x\text{Fe}_{2-x}\text{O}_4$); J. Appl. Phys. 97 (2005) 10

F101. [34] K. Kriehle, C. C. H. Lo, Y. Melikhov, and J. E. Snyder;

Investigation of Cr substitution in Co ferrite ($\text{CoCr}_x\text{Fe}_{2-x}\text{O}_4$) using Mossbauer spectroscopy; J. Appl. Phys. 99 (2006) 08M912. [35]

100%

MATCHING BLOCK 14/88

W

<https://www.researchgate.net/publication/...>

Y. Melikhov, J. E. Snyder, D. C. Jiles, A. P. Ring, J. A. Paulsen, C.

C. H. Lo, and K. W. Dennis;

80%

MATCHING BLOCK 15/88

W

<https://www.researchgate.net/publication/...>

Temperature dependence of magnetic anisotropy in Mn-substituted cobalt ferrite; J. Appl. Phys. 99 (2006) 08

R102. [36] S. Mohan, Magnetic properties of sintered $\text{CoFe}_2\text{O}_4 - \text{BaTiO}_3$ particulate magnetolectric composites; Ceram. Inter. 45 (2019) 12307-12311. [37] L. Kumar, P. Kumar, V. Kuncser, S. Greculeasa, B. Sahoo, M. Kar; Strain induced magnetism and super exchange interaction in Cr substituted nano crystalline cobalt ferrite; Mater. Chem. Phys. 211 (2018) 54-64. [38] R. K. Panda, R. Muduli; Effect of Cr^{3+} substitution on electric and magnetic properties of cobalt ferrite nano particles; J. Alloys Comp. 669 (2016) 19-28. [39] T. Walther, U. Straube, R. Kofenstein, S. G. Ebbinghaus; Hysteretic magneto electric behaviour of $\text{CoFe}_2\text{O}_4 - \text{BaTiO}_3$ composites prepared by reductive sintering and reoxidation, J. Mater. Chem. C 4 (2016) 4792-4799.

Chapter-I 33 [40] A. Aubert, V. Loyau, Y. Pascal, F. Mazaleyrat, M. Loue; Dynamic Magnetostriction of CoFe_2O_4 and Its Role in Magnetolectric Composites; Phys. Rev. Appl. 9 (2018) 044035. [41] Y. Liu, G. Xu, Y. Xie, H. Lv, C. Huang, Y. Chen, Z. Tong, J. Shi, R. Xiong; Magnetolectric behaviours in $\text{BaTiO}_3 / \text{CoFe}_2\text{O}_4 / \text{BaTiO}_3$ laminated ceramic composites prepared by spark plasma sintering, Ceram. Int. 44 (2018) 9649-9655. [42] T. Ramesh, D. Rejendar, S. R. Murthy;

81%

MATCHING BLOCK 22/88

W

<https://www.researchgate.net/publication/...>

$\text{CoFe}_2\text{O}_4 - \text{BaTiO}_3$ multi ferroic composites: role of ferrite and ferroelectric phases on the structural, magneto dielectric properties; J Mater Sci. 28 (2017) 11779-11788. [43]

M. Raghasudha, D. Ravinder, P. Veersomaiah; Investigation of super- paramagnetism in pure and chromium substituted cobalt nanoferrites; J. Magn. Mater. 420 (2016) 45. [44] K. A. Mohammed, A. D. Al-Rawas, A. M. Gismelseed, A. Sellai, H. M. Widatallah, A. Yousif, M. E. Elzain, M. Shongwe; Infrared and structural studies of $\text{Mg}_{1-x}\text{Zn}_x\text{Fe}_2\text{O}_4$ ferrites; Phys. B. 407 (2012) 795-804. [45] R. Gao, X. Qin, Q. Zhang, Z. Xu, Z. Wang, C. Fu, G. Chen, X. Deng, W. Cai; Enhancement of magnetolectric properties of $(1-x)\text{Mn}_{0.5}\text{Zn}_{0.5}\text{Fe}_2\text{O}_4 - x\text{Ba}_{0.85}\text{Sr}_{0.15}\text{Ti}_{0.9}\text{Hf}_{0.1}\text{O}_3$ composite ceramics; J. Alloys Comp. 795 (2019) 501-512. [46] A. Srinivas, R. V. Krishnaiah, T. Karthik, P. Suresh, S. Asthana, S.V. Kamat; Observation

of direct and indirect magnetoelectricity in lead free ferroelectric (Na 0.5 Bi 0.5 TiO 3)–magnetostrictive (CoFe 2 O 4) particulate composite; Appl. Phys. Lett. 101 (2012) 082902. [47] K. Praveena, K. B. R. Varma; Improved magneto-electric response in Na 0.5 Bi 0.5 TiO 3 –MnFe 2 O 4 composites; Mater Sci. Mater Electron. 25 (2014) 111– 116

Chapter-I 34 [48] Kiran, K. Thakur, S. Kumar, S. Kimar, N. Thakur; Investigation of structural, dielectric, and magnetoelectric properties of K 0.5 Na 0.5 NbO 3 – MnFe 2 O 4 lead free composite system; J. Alloys Comp. 857 (2021) 158251. [49] P. L. Nguyen, B. Sarpi, F. Petronio, C. Mocuta, P. Ohressser, D. Stanescu; J. B. Moussy, A. Vlad, A. Resta, E. Otero, R. Bbelkhou, N. Jedrecy, A. Bbrbier;

100% **MATCHING BLOCK 16/88** **W** <https://www.researchgate.net/publication/...>

Mn 0.7 Fe 2.3 O 4 Nanoplatelets Embedded in BaTiO 3 Perovskite Thin Films for Multifunctional Composite Barriers;

ACS Appl; Nano Mater. 3 (2020) 327-341. [50] S. Satapathy, G. Prudhavi, A. A. Khan, P. Deshmukh, A. Ahlawat, K. R. S. Preethi Meher, A. K. Karnal; MgFe 2 O 4 /(Ba 0.85 Ca 0.15) (Zr 0.1 Ti 0.9)O 3 lead free ceramic composite: A study on multiferroic and magnetoelectric coupling properties at room temperature ; J. Alloys Comp. 853 (2021) 156960. [51] K. C. Verma, D. Singh;

100% **MATCHING BLOCK 17/88** **W** <https://www.researchgate.net/publication/...>

Multiferroic effects in MFe 2 O 4 /BaTiO 3 (M ¼ Mn, Co, Ni, Zn) nanocomposites;

J. Alloys Comp. 709 (2017) 344-355. [52] C. Nayek, K. Kumar Sahoo, P. Murugavel; M-E in La 0.7 Sr 0.3 MnO 3 –BaTiO 3 core– shell nano composite; Mater. Res. Bull. 48 (2013) 1308. [53] K. C. Verma, R. K. Kotnala, N. Goyal; Multi-Functionality of Spintronic Materials; Nanoelectronics (2019) 153-215 [54] G. Yu, F. Bai, H. Zhang; Self-Assembled BaTiO 3 -MnZnFe 2 O 4 Nanocomposite Films; Adv. Mater. Sci. Eng. 2012 (2012)109856. [55] Z. Shi, J. Zhang, D. Gao, Z. Zhu, Z. Yang, Z. Zang; Giant magnetoelectric coupling observed at high frequency in NiFe 2 O 4 –BaTiO 3 particulate composite; RSC Advances 10 (2020) 27242-27248. [56] D. Zhou, L. Hao; S. Gong, Q. Fu, F. Xue, G. Jian; Magnetoelectric effect of the multilayered CoFe 2 O 4 /BaTiO 3 composites fabricated by tape casting; J Mater Sci. Mater Electron. 23 (2012) 2098–2103

35 CHAPTER – II CRYSTAL STRUCTURE AND THEORETICAL BACKGROUND CONTENTS 2.1 Introduction : 36 2.2 Classification of ferrites : 36 2.2.1 Spinel : 37 2.2.2 Magnetoplumbites : 37 2.2.3 Garnets : 38 2.3 Classification of spinel ferrites : 39 2.3.1 Normal spinel : 40 2.3.2 Inverse spinel : 40 2.3.3 Random spinel : 40 2.4 Crystal structure of ferroelectrics : 41 2.5 Properties of ferrites : 43 2.5.1 Magnetic properties : 44 2.5.2 Magnetic induction : 46 2.5.3 Permeability : 46 2.5.4 Magnetization : 48 2.5.5 Magnetic hysteresis loop : 49 2.5.6 Anisotropy : 50 2.5.7 Energy losses : 52 2.5.8 Electrical conductivity : 52 2.6 Properties of ferroelectrics : 53 2.6.1 Spontaneous polarization : 54 2.6.2 Piezoelectric effect : 54 2.6.3 Ferroelectric hysteresis loop : 55 2.7 Properties of M-E Composites : 57 2.7.1 Magneto-electric effect : 57 References : 58

Chapter-II 36 2.1 Introduction The various properties of ferrites and ferroelectric materials like moderate saturation magnetization, low dielectric losses, high permeability, high magnetic saturation, low coercivity, more stable, less expensive etc makes them useful in many applications in research field. So it has wide range of application in electronic industries. The ferrite materials are synthesis by various techniques at different composition and conditions. Ferrites are classified into two type's soft and hard ferrite. The material shows both ferromagnetism and ferroelectric are known as multiferroic. Ferrite exhibits different structures like cubic, hexagonal, tetragonal etc. out of these cubic spinal structure is one of the most essential class of magnetic oxide. 2.2 CLASSIFICATION OF FERRITES Ferrites are the important class of magnetic materials which can be classified on the basis of their crystal structure and magnetic properties as, Fig. 2.1: Classification of ferrites

Chapter-II 37 2.2.1 Spinel Spinel ferrites are also called as cubic ferrites. Spinel ferrites are described by the chemical formula MFe 2 O 4 where M stands for divalent metal ions like Cobalt (Co 2+), Zinc (Zn 2+), Magnesium (Mg 2+), Copper (Cu 2+), Cadmium(Cd 2+) etc. A complete substitution of the divalent metal ion by a combination of ions with an average valency of two is known to exist for the combinations Li + -Fe 3+ and Cu + -Fe 3+ in Li 0.5 Fe 2.5 O 4 and Cu 0.5 Fe 2.5 O 4 . However, the Cu + -Fe 3+ valences are only stable at high temperature (1200-1350°C) at which the spinel

phase is formed [1]. The crystal structure of spinel ferrite possess two interstitial sites namely octahedral [B] to tetrahedral (A) sites are in the ratio 2:3. Fig. 2.2: Crystal structure of Spinel ferrite 2.2.2 Magnetoplumbites 'Magnetoplumbites are also known as hexagonal ferrites.' Magnetoplumbites, hexagonal or rhombohedral ferromagnetic oxides are described by the chemical formula $MFe_{12}O_{19}$ where the M occupied by divalent ions with large ionic radius (Ca^{2+} , Sr^{2+} , Pb^{2+} , and Ba^{2+}) The hexaferrite contain octahedral and tetrahedral sites occupied by iron ions [2].

Chapter-II 38 Fig. 2.3: Crystal structure of strontium hexagonal ferrite 2.2.3 Garnets The chemical formula for ferrimagnetic garnet is $Me_3Fe_5O_{12}$ where, Me is a trivalent ion such as rare earth or yttrium The unit cell is cubic and contains eight molecules of $Me_3Fe_5O_{12}$ i.e. (160 atoms). The metal ions are distributed over three types of sites. The Me ions occupy the dodecahedral sites (called c sites), where they are surrounded by eight oxygen ions, the Fe^{3+} ions distributed over the tetrahedral and octahedral sites in the ratio 3:2. Thus, the cation distribution of $Me_3Fe_5O_{12}$ can be written as $Me_3cFe_2aFe_3dO_{12}$. Fig. 2.4: Schematic octant of a garnet crystal structure showing only cation positions.

Chapter-II 39 Fig. 2.5: An octant of a garnet crystal structure. 2.3 CLASSIFICATION OF SPINEL FERRITES The spinel construction of ferrites is gotten from the mineral spinel (MA_2O_4), whose structure enlightened by Bragg in 1915. This spinel construction of ferrite is made out of 32 shut pressed oxygen atoms as demonstrated in Fig. 2.2. In the middle of the layer of these oxygen particles, there are a few interstices. These interstices are called as 'A' site or 'B' site. In the spinel design of ferrite there are 64 tetrahedral locales 'A' and 32 octahedral destinations (B). The site (A) is composed with 4 closest adjoining oxygen particles and structures a tetrahedron. In this way, 'A' sites are called tetrahedral destinations. The 'B' sites are facilitated 6 closest neighbor oxygen particles and whose lines associating focus to depict an octahedron. Subsequently, the 'B' sites are called as octahedral destinations. In cubic spinel design of ferrites, there are 64 tetrahedral destinations and 32 octahedral sites. Incidentally, out of the 64 tetrahedral destinations; just 8 sites are involved by divalent particles and out of 32 octahedral sites; just 16 are involved by trivalent particles. The all out certain charge would be $8 \times (+2) = +16$ or more the $16 \times (+3) = +48$ or an aggregate of +64 which is expected to adjust the $32 \times (- 2) = - 64$ for the oxygen particles [3, 4]. Fig. 2.2 addresses the area of oxygen and metal particles in

Chapter-II 40 four neighboring octants of a solitary unit cell of spinel ferrite. Substitute number of the octants possesses the tetrahedral site 'A' and staying nearby octants involves the octahedral site 'B'. In view of the cation conveyance, spinel ferrites are ordered into three types: 2.3.1 Normal spinel In ordinary spinel ferrite, the di-valent particles possess the A- sites and the trivalent particles involve the B- sites. The cation dispersion is given by: $[M^{2+}]_A[Fe^{3+}]_B O_4^{2-}$ where, M is the divalent metal particle for example $ZnFe_2O_4$ 2.3.2 Inverse spinel In opposite spinel ferrite, the trivalent (Fe^{3+}) particles possess all the A- sites and other trivalent particles involve a large portion of the quantity of B-destinations and the excess B- sites are involved by the divalent (M^{2+}) metal particles. The cation circulation is given by, $[Fe^{3+}]_A[M^{2+}]_B O_4^{2-}$ These materials show ferromagnetic properties. for example $NiFe_2O_4$, $CoFe_2O_4$, $CuFe_2O_4$ etc. 2.3.3 Random spinel At the point when the divalent (M^{2+}) and trivalent (Fe^{3+}) particles are haphazardly disseminated over tetrahedral and octahedral sites, the spinel are known as irregular spinel ferrites. The cation circulation is given by, $[M_xFe_{(1-x)}]_A[M_{(1-x)}Fe_{(1+x)}]_B O_4^{2-}$ where, $0 \leq x \leq 1$ with $x = 1$ ordinary spinel and $x = 0$ backwards spinel ferrite is gotten.

Chapter-II 41 Sometimes, the divalent particle might be supplanted by monovalent and trivalent particles, while as yet holding the spinel structure like $Li_{0.5}Fe_{0.5}O_4$ [Fe₂³⁺]O₄ [3,4]. 2.4 CRYSTAL STRUCTURE OF FERROELECTRICS "Perovskite" was initially the name of the mineral perovskite $CaTiO_3$. Ideally, the crystal structure of perovskite can be described as ABX_3 . The ABX_3 perovskite structure stands out by a wide margin compared with other structures. Since, it can produce an incredibly wide array of phases with totally different functions and various chemical manipulations. In this family, the perovskite group of oxides with the chemical formula of ABO_3 . It can be visualized as a simple cubic unit cell with large cations 'A' located at eight corners and smaller cations 'B' located in the body center and oxygen atoms in the face center, as shown in Fig. 2.2. The resulting perovskite structure can also be described as consisting of corner sharing $[BO_6]$ octahedral with the 'A' cation occupying the 12-fold coordination site formed in the middle of the cube of eight such octahedral as shown in Fig. 2.6. However, in the perovskite crystal structure the unit cell is temperature dependent. Fig. 2.6: $BaTiO_3$ Perovskite crystal structure

Chapter-II 42 Fig. 2.7: Polyhedra model of perovskite structure The $BaTiO_3$ is one class of Perovskite crystal structure in which the Ti is a '3d' transition element and has the 'd' orbital for electrons to form covalent bonds with its neighbors. The radius of Ti^{4+} ion is about 0.68 Å and that of Ba^{2+} is about 1.35 Å. These ions form nice octahedral cages, with the O^{2-} ions held apart. At temperatures higher than the Curie temperature (<120°C), Ti^{4+} stays in the cage, rattling around it to make the unit cell maintain a symmetrical cubic structure. At a certain transition temperature, the particular structure of the unit cell becomes unstable and must transform to a more stable one. So, at the Curie temperature (T_c), the

octahedral cages distort and the positive ions move to off- center positions. The crystal takes a tetragonal form, resulting from the stretching of the cubic unit cells along one edge, as shown in Fig. 2.5. In fact, the Ba 2+ ions shift 0.05 Å upward from their original position in the cubic structure; Ti 4+ ions shift upward by 0.1 Å and the O 2- ions shift downward by 0.04 Å to form the tetragonal structure. As a result of the ion shifts, the centroid of the

Chapter-II 43 positive charges no longer coincides with the centroid of the negative charges; therefore, the unit cells become permanently polarized and behave as permanent dipoles, leading to spontaneous polarization. The direction of the displacement can be reversed by a sufficiently high electric field of opposite polarity. This possibility of dipole reversal distinguishes ferroelectric materials from non ferroelectric ones [5]. Fig. 2.8: The ion displacements due to the cubic-tetragonal distortion in BaTiO 3

2.5 PROPERTIES OF FERRITES The magnetic properties of ferrites, such as saturation magnetization(M_s), magnetic induction, initial permeability (μ), Curie temperature (T_c), coercivity (H_c) and Magnetolectric (ME) effect these properties depends upon the concentration of divalent metal ions on both tetrahedral and octahedral sites. Hence the properties are known as "intrinsic properties". On the other hand, the hysteresis loop, resistivity, AC conductivity and dielectric constant depend on the structure of ferrites and hence are called as "structure sensitive proportion". The magnetic properties are strongly dependent on the chemical composition, sintering atmosphere, sintering temperature, sintering time, grain size, crystal structure, cations distribution and porosity of the materials.

Chapter-II 44 2.5.1 Magnetic properties The spontaneous magnetization in ferrite materials was firstly given by Neel in 1948; where he stated that these materials show distinctly different magnetic structures than previously reported magnetic materials. Table 2.1: Comparative properties of soft and hard magnetic materials.

Sr. No.	Soft ferrite	Hard ferrite
1	High saturation magnetization(1-2T)	High saturation magnetization(0.3-6T)
2	Low coercivity (H C)	High coercivity (H C)
3	High permeability	Not important but low
4	Low anisotropy	High anisotropy
5	Low magnetostriction	Not important
6	High curie temperature	High curie temperature
7	High electrical resistivity	Not important
8	Low losses	High energy product

Ferrites avail ferrimagnetism because of superexchange interaction among electrons of metal and oxygen ions. The various factors that determine the magnetic properties of ferrites include the nature of cations, heat treatment, preparative method, site preference, energy of cations, and Madelung energy. Theory of Heisenberg's exchange forces is used by Neel to explain the magnetization in ferrites; according to this theory, the exchange energy between two adjacent atoms having spin angular momentum is given by following equation. $E_{ex} = - 2 J_{ex} S_i S_j$ (2.1) where, E_{ex} is the exchange energy, S_i and S_j are the total spins of adjacent atoms, J_{ex} is the exchange integral (probability of exchange of electron).

Chapter-II 45 In spinel ferrites, there are three kinds of magnetic interactions between the magnetic ions. The magnetic ions are present in two crystallographically distinct lattice sites and magnetic interaction is through intermediate O 2 ions through a super exchange mechanism [8]. In a spinel, these magnetic moments interact through the anions (super exchange), resulting in a situation where, the moments of both A- and B-site ions are aligned, i.e., A- A and B-B parallel, but A-B antiparallel a ferrimagnetic ordering. The exchange force acted between an ion on A-site and an ion on B-site is governed by above equation. The value of J_{ex} determines the ferri, ferro, or antiferromagnetism. It has been experimentally proved that the interaction energy for spinel ferrites is negative and hence induces an antiparallel orientation. However, magnetizations magnitude of A and B sublattices are not equal which produces a resultant net magnetization in ferrites.

82% **MATCHING BLOCK 18/88** **W** <http://pr.hec.gov.pk/jspui/bitstream/123 ...>

The distance from magnetic ions to the oxygen ion (through which the interaction occurs) and the angle

Φ between the magnetic ions are the key factors in determining the magnitude of the interaction energy between two magnetic ions [9]. An angle of 180 o will give rise to the greatest exchange energy and it tends to decrease very rapidly with increasing the distance. Based on

84% **MATCHING BLOCK 19/88** **W** <http://pr.hec.gov.pk/jspui/bitstream/123 ...>

the values of the distance and the angle Φ , it may be inferred that of the three interactions, the A-B interaction

is of the greatest magnitude and the A-A interaction is the weakest. A-B interaction is predominant, and

83%

MATCHING BLOCK 20/88

W

[http://pr.hec.gov.pk/jspui/bitstream/123 ...](http://pr.hec.gov.pk/jspui/bitstream/123...)

the spins of the A- and B-site ions in ferrite will be oppositely magnetized

in the A and B

100%

MATCHING BLOCK 21/88

W

[http://pr.hec.gov.pk/jspui/bitstream/123 ...](http://pr.hec.gov.pk/jspui/bitstream/123...)

sublattices, with a resultant magnetic moment equal to the difference between those of A- and B-site ions [10].

Generally, the value of saturation magnetic moment for the B lattice (M_B) is greater than that of the A lattice (M_A) so that the resultant saturation magnetization (M_s) may be given as $M_s = M_B - M_A$. Magnetic moment of ferrites can be systematically altered by chemical substitutions. Magnetic moment in mixed Mn-Zn ferrites and Ni-Zn ferrites need to be high for important industrial applications.

Chapter-II 46 Introduction of Zn ions in Mn-ferrite or Ni-ferrite helps in increasing net magnetic moment [11]. It occupies A-sites, and Zn $2+$ ions are nonmagnetic, thus reducing the A- sublattice magnetization on increasing the total net magnetic moment. Addition of small amount of Zn follows the expected relationship, but at higher content, net moments tend to decrease because some of the Fe $3+$ ions no longer have magnetic neighbors and interactions break up. Increased temperature also decreases the degree of magnetic moment because of influence of thermal agitation. At a certain temperature, the Curie temperature T_c , the magnetic ordering completely vanishes. 2.5.2 Magnetic induction If the performance of a magnetic component or device depends on the magnetization of the ferromagnetic material involved, induction, rather than magnetization is used to assess the performance. This is so because the definition of induction, $B = \mu_0 (H + M)$ (2.2) It has made it inherently structure-sensitive static property through the permeability of free space (μ_0), magnetic intensity (H) term and therefore induction is more useful than magnetization in practice. 2.5.3 Permeability In an unmagnetized state, magnetic material contains a large number of small magnetic domains with parallel spin. These domains are oriented in all possible directions, so the net moment is zero. Between two adjacent domains, a thin transition zone exists in which the orientation gradually changes from the first to that of the second domain. Such a transition zone is called as domain wall. If external magnetic field with sufficient strength is applied to the magnetic material, then all domains are oriented in the direction of

Chapter-II 47 applied magnetic field. There are two possible mechanisms given for such orientations [12-13]: (1) rotation, in which all domains are turned along with external magnetic field, and (2) domain wall displacement, in which domains with same orientation are enlarged at the expense of neighbors by moving domain wall between them. In metals, at a low field only wall displacements take place but in ferrites the domain walls are more fixed and more difficult to move than in metals, perhaps because of the voids present in the material. In ferrites, μ_i is simply the result of rotation and for displacement contribution H requirement is very high. The amount to which each of the two mechanisms contributes to μ_i depends on different parameters such as frequency of H-field, chemical composition, ceramic microstructure, temperature, stress, etc. Pinning of domain walls is affected by microstructure and grain boundaries, and the effective initial permeability depends more or less linearly on grain size [14, 15]. In small grains, the rotational contribution dominates, whereas at higher grain size, the wall contribution becomes more and more important [16]. Permeability, $\mu = dB/dH$, is plotted as a function of H, for $H = 0$ is called the initial permeability, μ_i increases with increasing H to a maximum value, μ_{max} , and then decreases again to saturation value of 1. For ferrites, the ratio of $\mu_{max} : \mu_i$ is 2 to 4. For a static small magnetic field, metals can reach up to $\mu_i = 10^5$ and ferrites have maximum μ_i , which is approximately 10^5 . If an alternating magnetic field of increased frequency is applied, then μ_i of metals decreases because of eddy current losses; but, for ferrites μ_i remains constant into the high frequencies, which leads to many applications. However, μ_{max} decreases with frequency and asymptotically approaches μ_i because the walls are inclined to "freeze" in the material and can no longer follow the alternating field. This absence of wall displacements leads, for high frequencies saturation is rather independent of H, resulting in a low distortion [17].

Chapter-II 48 Magnetic permeability (μ) is defined as ratio of magnetic induction (B) to magnetic field (H) or strength of applied field. The ratio of flux density and applied field is called as absolute permeability. $B/H = \mu (1 + M/H) = \mu_{absolute}$ (2.3) This absolute permeability is the product of the magnetic constant of free space and the relative permeability, $B/H = \mu_r \mu_0$ (2.4) There are several versions of μ_r depending on conditions 2.5.4 Magnetization Magnetic materials experience

change in the dimensions during magnetization. The major effect in a change in a shape, with the volume remains approximately constant. This phenomenon is known as magnetostriction. These changes occur, when the material is cubic but the magnetic order is non-cubic. If material shrinks in the direction of applied magnetic field, the magnetostriction is considered to be negative and it expands, then termed as positive magnetostriction. The saturation magnetization of a material decreases on heating towards the Curie temperature due to the decrease in the degree of alignment of the atomic magnetic moments. As this alignments and the saturation magnetization decreases so does the volume expansion caused by the spontaneous magnetostriction and hence the materials contracts. In the case of inverse this contraction due to loss of spontaneous magnetostriction is equal to the expansion caused by normal thermal vibration processes and hence the material shows no change in dimensions [18]. However, above the Curie temperature there is no longer any magnetic ordering and thermal expansion occurs normally. Field induced magnetostriction occur when the magnetic domains align and the dimension change caused by the ordering of the

Chapter-II 49 atomic magnetic moments all combine to give a dimensional change to the block of material. 2.5.5 Magnetic Hysteresis loop When ferromagnetic material, consisting of magnetic domain with spins oriented at random, is subjected to an external magnetic field, the domain start orienting in the direction of the magnetic field and the net magnetization may vary between zero and saturation value. Under the influence of an external field, the domain wall experiences a pressure and grows at the expense of unfavorably oriented domains. Due to the irreversible domain wall movements, the magnetization will always lag behind the field and an open loop will be traced. This phenomenon is known as magnetic hysteresis and the loop is called a hysteresis loop. The nature of hysteresis loop as shown in Fig.2.9. Fig. 2.9: Magnetic Hysteresis loop of ferrite At certain magnetic field the material attains a saturation value i.e. saturation magnetization (M_s) and after reduction of the magnetic field, certain magnetization is

Chapter-II 50 retained which is termed as residual or remnant magnetization (M_r). When the direction of magnetic field is reversed, the remnant magnetization reduces and finally becomes zero at certain magnetic field, called as coercive field (H_c). The loop provides information about the work done in cycle of magnetization, coercivity and saturation magnetization. Extensive work has been done on the magnetization of ferrites through hysteresis measurements. The shape of hysteresis loop provides the information about the domain state of grains inside the sample. Based on the hysteresis phenomenon, Bean has classified the magnetic particles into single domain, multi domain and super magnetic domain [19]. 2.5.6 Anisotropy The magnetization behavior of spinel ferrites is majorly affected by anisotropy, and the most common types of anisotropies are magneto crystalline anisotropy, shape anisotropy and stress anisotropy. The effortless orientation of spins in a certain direction depends on the position with respect to the crystallographic axis [20]. Magnetocrystalline anisotropy occurs due to spine-orbit coupling and energetically favors alignment of the magnetization along a specific crystallographic direction. The direction preferred by the magnetocrystalline anisotropy is known as the easy axis of the material. A polycrystalline sample with no preferred grain orientation presents no net crystal anisotropy due to averaging over all orientations. The magnetocrystalline anisotropy is specific to a given material and independent of particle shape. It can be considered as anisotropy of the exchange energy in the various crystal directions [21]. Exchange energy is lowered by the addition of Zn ferrite, which at the same time lowers the Curie point. For a cubic spinel lattice, the energy of a certain orientation is $E_c = K (\alpha_1^2 \alpha_2^2 + \alpha_1^2 \alpha_3^2 + \alpha_2^2 \alpha_3^2)$, where, α_1 , α_2 and α_3 are angles of the orientation with the crystallographic axes. For all cubic ferrites, the magnetocrystalline anisotropy, K , is

Chapter-II 51 negative, so that E_c is a minimum for the cube diagonal direction where $\alpha_1 = \alpha_2 = \alpha_3$. A symmetric shape like sphere does not have any shape anisotropy while nonspherical polycrystalline specimen has shape anisotropy. A cylindrical sample is easier to magnetize along the long direction than along the short directions. Shape anisotropy is predicted to produce high coercive forces. Stress anisotropy is associated to the phenomenon of magnetostriction that indicates the changes in shape of magnetic material. Various internal and external stresses such as rapid cooling, application of external pressure, annealing in a magnetic field, plastic deformation, or ion beam irradiation are responsible for stress anisotropy [22, 23]. Magnetostriction is an elastic change in the shape of a magnetic body on magnetization. If the length is increased in the direction of the magnetization, the magnetostriction becomes positive; if it is decreased, the magnetostriction becomes negative. On increase of the field, the magnetostriction, like the magnetization, arrives at a saturation value. This specific change in length at saturation is negative for all cubic ferrites (Mn ferrites, -2×10^{-6} ; Ni ferrite, -27×10^{-6}) with the exception of ferrous ferrite, Fe_3O_4 , where it is 40×10^{-6} . When a ferromagnet is in close proximity to an antiferromagnet or ferrimagnet, it leads to exchange anisotropy. Magnetic coupling at the interface of these two materials can form a special direction in the ferromagnetic phase, which takes the form of a unidirectional anisotropy [24, 25]. This type of anisotropy is mostly observed in type-B particles when an antiferromagnetic or ferrimagnetic oxide forms around a ferromagnetic core. Magnetocrystalline anisotropy, magnetostriction, and magnetic permeability depend markedly on chemical composition.

Chapter-II 52 2.5.7 Energy Losses The losses in a soft magnetic material under certain conditions can be defined as the amount of energy from a high-frequency magnetic field is converted into a heat. Usually, these losses are expressed in different ways for weak and strong magnetic fields. At elevated frequencies, spinel ferrites show energy losses. There are various physical mechanisms responsible for these losses and occur at different frequencies with heat dissipation. Hysteresis losses are responsible for major heat dissipation and are generated because of irreversible domain wall jumps. The loss per cycle (cycle of the H- and B- fields corresponds to one hysteresis loop) is greater when the area of loop is higher. Hysteresis losses can be reduced by preventing the domain wall jumps by reducing the number of inhomogeneities, magnetocrystalline, and stress anisotropy. Addition of Co²⁺ and Ti⁴⁺ ions or use of ceramic microstructures of smaller grains also reduces the domain wall jump [26, 27]. Eddy current losses are second important loss contributor, which is induced by alternating magnetic fluxes. Eddy current losses can be restricted by providing a high electrical resistivity [28]. Magnetic resonances are also responsible for energy losses usually at above ~ 1 MHz. In ferrites, the eddy current loss is usually negligible because of the high ρ , which is about 10¹² times that for metals. Only for Mn-Zn ferrites containing ferrous ions, the resistivity lower, in the neighborhood of 0.5 to 1 Mc/sec, thereby, the losses can no longer be neglected. In metals, eddy current losses are usually the biggest loss source [29]. 2.5.8 Electrical conductivity Spinel ferrites occupy special a place among the other conventional magnetic materials because of their wide variety of applications. It has very low conductivity as compared with other magnetic materials and hence, they are frequently used at microwave

Chapter-II 53 frequencies. Spinel ferrites are basically semiconductors having conductivity in the range between 10⁻² and 10⁻¹¹ Ohm⁻¹ cm⁻¹. Fe²⁺ and metal ions (M³⁺) are responsible for semi- conductivity in which Fe²⁺ shows an n-type and M³⁺ p-type behavior. The conductivity arises because of the mobility of the extra electron or the positive hole through the crystal lattice. Hopping mechanism best describes the movement of charge carrier jump from one ionic site to the other. Electrostatic interaction between conduction electron (hole) and nearby ions may result into a displacement of the latter and polarization of the surrounding region, so that the carrier is situated at the center of a polarization potential well. If potential well is deep enough, then the carrier is trapped at a lattice site and its transition to a neighboring site is determined by thermal activation. Mobility of the jumping electrons or holes is proportional to $e^{-Q/KT}$, where Q is the activation energy, K-Boltzmann's constant and T the temperature in degree absolute [30]. 2.6 PROPERTIES OF FERROELECTRICS Ferroelectric materials have a spontaneous electric polarization, they have been studied since over a century ago when large piezoelectric constant were observed. The ferroelectric have received a great amount of interests because of their various use in a range of applications, including transducers, actuators, capacitors and memory applications. A ferroelectric material possesses at least two equilibrium orientations of the spontaneous polarization vector in the absences of an external electric field, and the spontaneous polarization can be switched by an electric field. The polar character of the orientation state should represent an absolutely stable configuration in null field.

Chapter-II 54 2.6.1 Spontaneous polarization Spontaneous polarization (P_s) is defined as the magnitude of polarization within a single ferroelectric domain in the absence of an external electric field. Spontaneous polarization is a fundamental property of all pyroelectric crystals, but it is reversible and reorientationable in ferroelectrics only. Most ferroelectric phase originates from a non- polar prototypic phase and all of the polarization is reorientationable. However, if the prototypic phase is polar, only a proportion of the total spontaneous polarization may be reoriented, the reorientationable or reversible process is commonly called as the spontaneous polarization. The magnitude of P_s in a single crystal is directly related to the atomic displacements that occur in ferroelectric reversal and may be calculated from the atomic positions within the unit cell if known. Designating Δ_i as the component of the atomic displacement vectors joining the ith atom positions in the original and reversed orientations along the direction of P_s, Z_i the effective charge on the ith ion and V as the unit cell volume, then $P = (1/2V)\sum_i \Delta_i Z_i$. The spontaneous polarization of single-domain materials usually lie within the range 10⁻⁷ and 10⁻⁴ Coulomb/cm [31-32]. The spontaneous polarization can be calculated directly from charge density obtainable by X-ray diffraction structural measurements, corrected for the charge transferred across unit cell boundaries. 2.6.2 Piezoelectric effect The piezoelectricity is the property of crystal to exhibit electric polarity when subjected to the stress. It is termed as a flow of charges in certain direction after application of pressure to the piezoelectric crystal. Basically the word 'piezo' means 'pressure' hence the original meaning of the word piezoelectricity implies 'pressure electricity'. If the pressure is replaced by tension, the charge will flow in the opposite

Chapter-II 55 direction. Also if we apply an electric field to the crystal plate, it will get stretched and if we reverse the field direction the crystal will get compressed i.e. under an applied electric field, the cations are drawn in the direction of electric field, and the anions in the opposite direction, leading to the relative change in the inter-ionic distance and depending on the applied electric field contraction and expansion occurs. This is termed as the converse piezoelectric effect. Certain materials produce electric charges on the surface after application of mechanical stress. The charges

induced are proportional to the mechanical stress. This is called the direct piezoelectric effect. 2.6.3 Ferroelectric hysteresis loop Fig. 2.10: The P-E hysteresis loop of ferroelectric material where P_{max} is the saturation polarization, P_r means remnant polarization and E_c shows Coercive field

Chapter-II 56 Considering a crystal, which initially has an overall polarization equal to zero, i.e., the sum of the vectors representing the dipole moments of the individual domain vanishes. When an electric field is applied to the crystal, the domains with polarization components along the applied field direction grow at the expense of the "anti-parallel" domains; thus the polarization increases. When all domains are aligned in the direction of the applied field the polarization saturates and the crystal becomes a single domain. A further increase in the polarization with increasing applied field results from "normal polarization" effects; rotation of domain vectors may also be involved if the external field does not coincide with one of the possible directions of spontaneous polarization. The hysteresis loop the saturation polarization is plotted along Y-axis and electric field along X-axis the nature of graph as shown in fig. When positive and negative domains are equal in the crystal, then overall polarization is zero. When electric field is applied on crystal the domain tend to be polarized along the positive direction for sufficiently large electric field all the domain are polarized to the applied electric field indicating the state of saturation polarization and crystal becomes single domain. When we reducing the applied electric field, then polarizations decreases but not return to zero when field applied field back to zero value it means that material is spontaneously polarized is called as remnant polarization (P_r) and it refers to the crystal as a whole. To remnant polarization can be removed only when the applied field is move in reverse direction. The field at which saturation polarization is zero that field is called as coercive field (E_c) [33]. The continuing decreasing the electric field in negative direction the material again reaches saturation with its entire domain polarized but in negative direction. The plot of P verses E is called as dielectric hysteresis loop it is similar to the B-H curve in ferromagnetic material.

Chapter-II 57 2.7 PROPERTIES OF M-E COMPOSITES 2.7.1 Magnetolectric effect (ME) The Magnetolectric (ME) property of the piezoelectric-piezomagnetic composite is known as product property of the composites which is achieved from the interaction between different properties of the two phases in composites. Both phases have not ME effect, but when they combined together, the composite show remarkable ME effect. Thus ME effect is a result of product of piezomagnetic effect (magnetic/mechanical effect) in the ferromagnetic phase and the piezoelectric effect (mechanical/electric effect) in the ferroelectric phase, namely [34]. ME Effect = Magnetic Mechanical X Mechanical Electrical (2.5) This is coupled electrical and magnetic phenomenon by elastic interaction. This effect would make the conversion between electric energy and magnetic energy possible, which provides opportunities for potential applications as ME memories, waveguides, transducer, actuators and sensors [35-37]. This effect in composites is due to strain induced in the ferrite phase, thereby resulting in polarization of the ferroelectric phase due to piezoelectric effect [38]. Thus the ME effect is result of inherent properties such as magnetostriction and piezoelectric effect of the constituent phases present in the composite. In spite of the low value observed in dE/dH such composites has scientific and technological interest. The study of such composites provides a unique tool to characterize the material simultaneously in single phase and in composite form.

Chapter-II 58 REFERENCES [1] J. Maxmain; Contribution to the study of copper ferrite and its solid solution with copper ferrite; Ann. Chem. 6 (1971) 297-307 [2] V. Bilovol, R. Martínez-García; Phase transformation of strontium hexagonal ferrite; J. Phys. Chem. Solid. 86 (2015)131-137. [3] L. Neel; Magnetic properties of ferrites; Ferrimagnetism and antiferromagnetism; Ann. phys 12 (1948) 137-198. [4] J. J. Went, E. W. Gorter; The magnetic and electrical properties of ferrite materials; Philips Tech. Rev. 13 (1952) 181-193. [5] M. B. Smith, K. Page, T. Siegrist, P. L. Redmond, E. C. Walter, R. Seshadri, L. E. Brus, M. L. Steigerwald; J. Am. Chem. Soc. 130 (2008) 6955-6963. [6] L. Kumar, M. Kar; Influence of Al³⁺ ion concentration on the crystal structure and magnetic anisotropy of nanocrystalline spinel cobalt ferrite; J. Magn. Magn. Mater. 323 (2011) 2042-2048. [7] A. N. Birgani, M. Niyafar, A. Hasanpour; Study of cation distribution of spinel zinc nano - ferrite by X-ray; J. Magn. Magn. Mater. 374 (2015) 179-181. [8] D. L. Leslie-Pelecky, R. D. Rieke; Magnetic properties of nanostructured materials; Chem. Mater. 8 (1996) 1770-1783. [9]

100%

MATCHING BLOCK 23/88

W

[http://pr.hec.gov.pk/jspui/bitstream/123 ...](http://pr.hec.gov.pk/jspui/bitstream/123...)

J. Smit, H. P. J. Wijn; Ferrites, Philips' Technical Library, Eindhoven,

The Netherlands (1959). [10]

E.W. Gorter; Some properties of ferrites in connection with their chemistry; Proc. IRE 43 (1955) 1945. [11] J. Smit, H. P. J. Wijn; Physical properties of ferrites. Adv. Electron. Electron. Phys. 6 (1954) 69-136. [12]

100%

MATCHING BLOCK 24/88

W <http://pr.hec.gov.pk/jspui/bitstream/123 ...>

J. Smit, H.P.J. Wijn, Ferrites; Wiley; New York (1959).

Chapter-II 59 [13] H.P.J. Wijn, E.W. Gorter, C.J. Esveldt, P. Geldermans; Conditions for square hysteresis loops in ferrites; Philips Tech. Rev. 16 (2) (1954) 49. [14] E. Ross, I. Hanke, E. Moser; Ferrites with initial permeability exceeding 20 000 and their microstructures; Z. Angew. Phys. 17 (1964) 504. [15] D. J. Perduijn, H. P. Peloschek; MnZn ferrites with very high permabilities; Proc. Br. Ceram. Soc. 10 (1968) 263. [16] E.G. Visser, M.T. Johnson, P.J. van der Zaag; Proceedings of the 6th International Conference on Ferrites (ICF-6); The Jap. Soc. Powd. Metal.; Tokyo (1992). [17] H.P.J. Wijn; Ph.D. Thesis ; Leiden (1953). [18] L. F. Brailsford; "Physical Properties of Magnetism" D.Van Nostrand Comp. Ltd. London 120 (1966). [19] E. P. Wohlfarth, K. H. J. Buschow;

100%

MATCHING BLOCK 26/88

W <http://pr.hec.gov.pk/jspui/bitstream/123 ...>

Ferromagnetic materials: A handbook on the properties of magnetically ordered substances; North-Holland

Pub. Comp. (1980) [20]

100%

MATCHING BLOCK 25/88

W <http://pr.hec.gov.pk/jspui/bitstream/123 ...>

B. D. Cullity; Introduction to Magnetic Materials; Addison-Wesley Publishing Company;

Reading, MA (1972) . [21] S. Chikazumi; Physics of Magnetism; John Wiley & Sons, Inc.; New York, 1978. [22] A. Broese van Groenou, P.F. Bongers, A. L. Stuyts; Magnetism, microstructure and crystal chemistry of spinel ferrites; Mater. Sci. Eng. 3 (1968-1969) 317-392. [23] K. Ohta, N. Kobayashi; Magnetostriction constants of Mn-Zn-Fe ferrites; Jpn. J. Appl. Phys. 3 (1964) 576. [24] H. Samuda, N. Sugita, M. Maekawa, N. Nagai; Magnetic properties of modified Ba- ferrite particles; J. App. Phys. 75 (1994) 5559. [25] A. L. Stuyts, G. W. Rathenau, G. H. Weber; Ferroxdure II and III; anisotropic permanent magnet materials; Philips Tech. Rev. 16 (5/6) (1954) 141.

Chapter-II 60 [26] T. G. W. Stijntjes, J. J. Roelofsma, F. F. Y. Wang (Eds.); Proceedings of the 4th International Conference on Ferrites (ICF-4); Pt. II, San Francisco (1985) p. 493. [27] E. G. Visser, J. J. Roelofsma, G. J. M. Aaftink; Domain wall loss and rotational loss in high frequency powerferrites; in: Proceedings of the 5th Int. Conf. On Ferrites; Bombay In: Crystal Properties and Preparation pp. 605-609 (1989) 27-30. [28] T. Sano, A. Morita, and A. Matsukawa; The magnetization in domains and bulk materials; Power Electronics PCIM 19 (July 1988) and Ref. 45 (1989) p. 595. [29] K. Ishino, Y. Narumiya; Development of magnetic ferrites: control and application of losses; Am. Cer. Bull. 66 (1987) 1469. [30] J.C.M. Li; Microstructure and Properties of Materials; world scientific; Singapore, 1996. [31] C. Kittel; Introduction to Solid State Physics; Wlley Eastern; New York (1977). [32] J. S. Black more; Solid State Physics; Camb. University Press; Cambridge (I- 985). [33] H. V. Keer ; Principles of Solid State Physics;Wiley Eastern, New York (1993). [34] S. Lopatin, I. Lopatin, I. Lisnevskaya; Magnetolectric PZT/ferrite composite material; Ferroelectrics, 162 (1994). [35] C. W. Nan; Magnetolectric effect in composites of piezoelectricity and piezomagnetic phases; Phy. Rev.B 50 (1994) 6082. [36] C. W. Nan, D. R. Clarke; Effective properties of ferroelectric and/or ferromagnetic composites: a unified approach and application; J. Am. Ceram. Soc. 80 (1997) 1333. [37] K. H. Shin, M. Inoue, K. I. Arai; Elastically coupled magneot-electric elements with highly magnetostrictive amorphous films and PZT substrates; Smart Mater. Struct. 9 (2000) 357. [38] J. Ryu, S. Priya, K. Uchino, H. E. Kim; Magnetolectric effect in composites of magnetostrictive and piezoelectric materials; J. Electroceram 8 (2002) .

61 CHAPTER – III CHARACTERIZATION TECHNIQUES CONTENTS 3.1 Introduction : 62 3.2 X-ray diffraction : 62 3.2.1 Inter-planner spacing : 64 3.2.2 Lattice constant : 64 3.2.3 X-ray density and bulk density : 65 3.2.4 Porosity : 65 3.2.5 Crystallite size : 66 3.3 Scanning electron microscopy : 66 3.4 Energy dispersive X-ray spectroscopy : 68 3.4.1 Wavelength dispersive X-ray analysis : 68 3.4.2 Energy dispersive X-ray analysis : 69 3.5 Fourier transform infrared spectroscopy : 69 3.6 Vibrating sample magnetometer : 70 3.6.1 Saturation magnetization : 72 3.6.2 Coercivity : 73 3.7 Dielectric properties : 73

3.7.1 Dielectric constant : 74 3.7.2 Dielectric loss and tangent : 75 3.8 P-E loop tracer : 75 3.9 Magneto-electric effect : 76
References : 79

Chapter-III 62 3.1 INTRODUCTION In the present era fabrication and characterization of nano size particles has attracted the much attention of the peoples from science and technology. The physical and chemical properties show dramatic modifications at smaller scale and their applications in various fields. Chemical routes provide a convenient process for the fabrication of nanostructured ceramics at comparatively low cost, temperature, and time [1]. Newly prepared samples can be characterized by various techniques in order to understand the structural, electric and magnetic behaviour under certain conditions. This chapter gives the details of various characterization methods used to study the structural, electrical and magnetic properties of CCFO-BTO and MZFO-BTO M-E composites. 3.2 X-RAY DIFFRACTION X-ray diffraction technique is one of the most important characterization tool used in solid state chemistry and material science to study the atomic and molecular structure of crystalline substances. Crystal structure and phase are some way helps to find physical properties of solid. A crystal lattice is a periodically arranged in three-dimensional array (cubic, rhombic, hexagonal) of atoms in space. They are shaped in such a way that they form a series of parallel planes separated from one another by a distance d (inter-planar or inter-atomic distance) which varies according to the nature of the material. In a crystal, planes are found in a number of different orientations each with its own specific d -spacing.

85%

MATCHING BLOCK 27/88

W

[https://serc.carleton.edu/research_educat ...](https://serc.carleton.edu/research_educat...)

X-ray diffractometer contains of three basic elements: an X-ray tube, a sample holder, and an X-ray detector.

Productions of electrons by heating filament

52%

MATCHING BLOCK 28/88

W

[https://serc.carleton.edu/research_educat ...](https://serc.carleton.edu/research_educat...)

in a cathode ray tube, X-rays are generated. Highly energetic electrons are accelerated toward a target by applying a voltage, and penetrate the target material. When penetrated electrons have enough energy to dislocate inner shell electrons of the target material, characteristic X-

rays are

Chapter-III 63

100%

MATCHING BLOCK 34/88

W

[https://serc.carleton.edu/research_educat ...](https://serc.carleton.edu/research_educat...)

produced [2]. These spectra consist of several components, the most common being

$K\alpha$, $K\beta$, and $K\gamma$. Characteristic of the target material (Cu, Fe, Mo, and Cr) have specific wavelengths. Most common target material used for single-crystal diffraction is copper having $K\alpha$ radiation of wavelength 1.5418

68%

MATCHING BLOCK 29/88

W

[https://serc.carleton.edu/research_educat ...](https://serc.carleton.edu/research_educat...)

Å. These X-rays are collimated and directed to the sample [3]. The intensity of the reflected X-rays is recorded, when the sample and detector are rotated. When the geometry of the incident X-ray impinging the sample satisfies the Bragg condition, constructive interference occurs and intensive peaks observed [4]. A detector records and processes this X-ray signal and turns the signal to a count rate which is then output to a device such as a printer or computer monitor.

The

experimental arrangement

77%

MATCHING BLOCK 30/88

W

[https://serc.carleton.edu/research_educat ...](https://serc.carleton.edu/research_educat...)

of an X-ray diffractometer is such that the specimen rotates in the path of the collimated X-ray beam by an angle θ while the X-ray detector is fixed on an arm to detect the diffracted X-rays and rotates at an angle of 2θ . The instrument used to rotate the sample by a specific angle is called a goniometer. For typical powder patterns, data is collected at 2θ from $\sim 10^\circ$ to 80° angles that are preset in the X-ray scan (Fig. 3.1). Powder X-ray diffraction technique is

useful to understand the following parameters of the material. Fig. 3.1: XRD experimental setup

Chapter-III 64 3.2.1 Inter-planer spacing (d) A plane in a crystal is specified in terms of Miller indices (hkl). The inter-planar spacing (d) for the planes of indices (hkl) is equal to the distance between the nearest parallel planes of crystalline lattice. Bragg's law gives the equation which is used to calculate inter planer distances between two planes in the crystalline lattice [5]; $n d \sin \lambda = \theta$ (3.1) Where, n – is order of spectrum, λ - is the incident wavelength, d is inter-planer distance and θ - is the Bragg's angle. 3.2.2 Lattice constant (a)

86%

MATCHING BLOCK 31/88

W

[https://docplayer.net/150337558-Doctor-of ...](https://docplayer.net/150337558-Doctor-of...)

Unit cell parameters, i.e. lattice constant were determined by indexing the detected reflections of the

X-ray diffraction patterns. Lattice constant or lattice parameter, refers to the constant distance between unit cells in a crystalline lattice. As lattice constant (a) have the dimension of length, its SI unit is meter. Lattice constant is typically of the order of several angstroms (Å). The Lattice constant (a) was determined by using following relations for different crystal structures [6], A) For Cubic Crystals $\frac{a}{\sqrt{h^2 + k^2 + l^2}} = \frac{d}{\sin \theta}$ (3.2) Where, (hkl) is the miller indices, λ is the wavelength of X-ray radiation and θ is the Bragg's angle. B) For tetragonal Structure $\frac{a}{\sqrt{h^2 + k^2}} = \frac{d}{\sin \theta}$ (3.3)

Chapter-III 65 3.2.3

84%

MATCHING BLOCK 32/88

W

[http://pr.hec.gov.pk/jspui/bitstream/123 ...](http://pr.hec.gov.pk/jspui/bitstream/123...)

X-ray density (d X) and Bulk density (d B)
The method of

preparation, sintering temperature and sintering conditions affects on change in

100%

MATCHING BLOCK 33/88

W

[http://pr.hec.gov.pk/jspui/bitstream/123 ...](http://pr.hec.gov.pk/jspui/bitstream/123...)

the X-ray density (d X) and bulk density (d B)

may be due the existence of pores in the samples. The mass of many particles of the material divided by the total volume they occupied is known as Bulk density (d B) . Bulk density is an extrinsic property of a material; it can change depending on how the material is handled [7]. A) Bulk Density $\frac{M}{V} = \frac{M}{\pi r^2 h} = \frac{M}{\pi d^2 h}$ (3.4) Where, d B – is the Bulk density, M – is mass of pellet, V – is volume of sample ($\pi r^2 h$), r – radius of pellet, and h – thickness of pellet B) X-ray density $\frac{d_x}{d_B} = \frac{M}{M_0} \frac{N_A}{N_A} \frac{V_0}{V} = \frac{M}{M_0} \frac{V_0}{V}$ (3.5) Where, d x = X-ray density, M = Molecular weight of the composition, n = Number of molecules per unit volume (8 for cubic structure), N_A = Avogadro's Number = 6.02214×10^{23} , V = Volume = a^3 (for cubic) and $a^2 c$ (for tetragonal) 3.2.4 Porosity Porosity in spinel ferrite nano-particles is a measure of voids (empty) spaces in the materials. It is a fraction of the volume of voids out of total volume, as percentage porosity (P) between 0–100%. The magnetic and electric properties of ferrites are nearly related with porosity. Hence, the by using the following relation 'P' of the nano-particles can be determined [8], $\frac{d_x}{d_B} = \frac{M}{M_0} \frac{V_0}{V} = \frac{M}{M_0} \frac{V_0}{V} (1 - P)$ (3.6)

Chapter-III 66 3.2.5 Crystallite size The broadening of x-ray diffraction lines exhibited by material are indication of crystalline size of crystals. So, the crystalline size is usually measured from X-ray diffraction patterns. The crystallite size (t)

was determined by using the line broadening of the most intense diffraction peak by using the well-known Debye Scherrer equation [9]. $FWHM = 0.9 \lambda / t \cos \theta$ (3.7) Where, t – is crystalline size, λ - Wavelength of incident radiation, B FWHM – Full width at Half Maximum intensity in radian, θ - Bragg's angle. 3.3 SCANNING ELECTRON MICROSCOPY (SEM) Fig. 3.2: Schematic representation of SEM analysis [10]

Chapter-III 67 Rather than visible light electrons are used in this class of microscopes to produce magnified images, especially of objects having dimensions smaller than the wavelengths of visible light, with linear magnification approaching or exceeding a million (10^6). An electron microscope forms a three dimensional image on a cathode ray tube by moving a beam of focused electrons across an object and reading both the electrons scattered by the object and the secondary electrons produced by it. High powered indirect microscope produces an image by bombarding a sample with a beam of high energy electrons. The electrons emitted from the sample are then scanned to form a magnified image which allows the examination of the structure, relief and morphology of materials. In addition to its high magnification, the SEM also has a high depth of field. Scanning electron microscopy (SEM) used to study microstructures of prepared samples. Fig. 3.3: SEM experimental setup The surface morphology of the sample was studied using HITACHI S-4800 microscope having accelerating voltage is about 20 KV. The samples of material were deposited on carbon tape on sample holder to study the micro structure and grain boundary

Chapter-III 68 also particle size of sample is determined. SEM gives the detail information of samples has the dense, homogeneous and fine grain structure and distinguished grain boundaries of the material. Fig. 3.2 shows the schematic representation of SEM analysis and Fig. 3.3 shows the experimental setup of scanning electron microscope. 3.4 ENERGY DISPERSIVE X-RAY SPECTROSCOPY (EDAX) Elemental compositions were predicted using X-ray electron diffraction analysis (EDAX) or also called as energy –dispersive X-ray spectroscopy (EDS). The EDS is an analytical technique used to identify the elemental composition of samples and used in combination with scanning electron microscopy (SEM). The energy dispersive X-rays analysis is used for elemental detection and quantization for compositional analysis. The beam electron is hit on the surface of conducting sample. Energy of the beam is specifically in the range of 10 -20 keV. The beam of x-ray is moving the across the sample of the material and image of each element in the sample can be obtained. The elements having high atomic number are easy to detect by EDAX analysis but the element of low atomic number are difficult to detect by using this techniques. The EDAX spectra are recorded by focusing the beam at different regions of the same specimen to verify the spatially homogeneous composition of materials [11]. 3.4.1 Wavelength dispersive X-ray Analysis (WDAX) or (WDS) The characteristics X-ray are identified by their wavelengths by diffracting them on a crystal monochromator of known 'd' spacing and following Bragg's law (Eq. 2.6). In totally focusing spectrometer sample, crystal and detector all are lies on the same circle known as Rowland circle such that Bragg's law satisfied in all cases. The crystal moves on

Chapter-III 69 a linear path in order to maintain constant take off angle. The centre of Rowland circle moves on arc with X-ray source as centre. 3.4.2 Energy dispersive X-ray analysis (EDAX) or (EDS) Here, the characteristics X-rays are identified by their energy using solid state detectors. It consists of semiconductor Si (Li) counter and FET preamplifier this two are cooled by liquid nitrogen and multichannel analyzer (MCA). The utility of this kind of spectrometer is based on two properties. The excellent energy resolution of Si (Li) counters. The ability of MCA is to perform rapid pulse height analysis. 3.5 FOURIER TRANSFORM INFRARED SPECTROSCOPY (FTIR) The aim of absorption Fourier transform infrared spectroscopy is to measure the absorption percentage of a sample at different wavelengths. Rather than a monochromatic light, this method focuses a beam simultaneously

75%

MATCHING BLOCK 35/88

W

[https://en.wikipedia.org/wiki/Fourier-tra ...](https://en.wikipedia.org/wiki/Fourier-tra...)

containing many frequencies of light and measures how much of that beam is absorbed by the sample. Next, the beam is customized to have a different group of frequencies which gives a second data point.

In a very short time span, the same

71%

MATCHING BLOCK 38/88

W

[https://en.wikipedia.org/wiki/Fourier-tra ...](https://en.wikipedia.org/wiki/Fourier-tra...)

process is repeated several times. A simulated computer collects all this data and works backward to infer what the absorption is at each wavelength. The beam as explained above is generated by a broadband light source which consist the full spectrum of wavelengths. The beam enters into a Michelson interferometer through a certain configuration of mirrors, one of which is moved by a motor. As this mirror moves, each wavelength of light in the beam is repeatedly blocked and transmitted by the interferometer, due to

phenomena of

76%

MATCHING BLOCK 43/88

W

[https://en.wikipedia.org/wiki/Fourier-tra ...](https://en.wikipedia.org/wiki/Fourier-tra...)

wave interference. Different wavelengths are modulated at different rates and hence at each moment the beam emerging out of the interferometer has a different spectrum. As

explained above, a computer processing is

Chapter-III 70 required to process the raw data into the desired result.

100%

MATCHING BLOCK 36/88

W

[https://en.wikipedia.org/wiki/Fourier-tra ...](https://en.wikipedia.org/wiki/Fourier-tra...)

The Fourier transform converts one domain (in this case displacement of the mirror in cm) into its inverse domain (wavenumbers in cm^{-1}). The raw data is called an "interferogram" [12].

Fig. 3.4: Schematic diagram of FTIR 3.6 VIBRATING SAMPLE MAGNETOMETER The magnetic behavior of magnetic materials is measured by using vibrating sample magnetometer (VSM). VSM operates on the principal of

51%

MATCHING BLOCK 37/88

W

[https://docplayer.net/150337558-Doctor-of ...](https://docplayer.net/150337558-Doctor-of...)

Faraday's law of induction; a change in magnetic field will generate an electric field. This electric field give us information about the changing magnetic field

by measure it. The sample to be studied is kept in constant magnetic field. If the sample is magnetic, this constant magnetic field will magnetize the sample by aligning the magnetic domains, or the individual magnetic spins, with the field. The magnetization will be higher, when the value of the applied constant magnetic field is higher. A magnetic field around the sample will create by the magnetic dipole moment of the sample; sometimes it called the magnetic stray field. As the sample is moved up and down, this magnetic stray field changes as a function of time and can be sensed by a set of pickup coils. Due to alternating magnetic field, an electric

Chapter-III 71 field generate in the pick-up coils according to Faraday's law of induction. This current will be proportional to the magnetization of the sample. Induced current will be higher if the sample possesses higher magnetization. Fig. 3.5: Schematic representation of VSM analysis [13]. In order to investigate the ferromagnetic properties of the multiphase multiferroic composite, VSM measurements were performed on all samples at room temperature, indicating magnetic hysteresis loops with a maximum field of 0.5 kOe. The magnetic properties such as saturation magnetization, magneton number, coercivity, remanence ratio etc. were studied by using vibrating sample magnetometer. Fig. 3.5 shows the schematic representation of VSM analysis and Fig. 3.6 shows experimental set-up of vibrating sample magnetometer.

Chapter-III 72 Fig. 3.6: Experimental set-up of vibrating sample magnetometer 3.6.1 Saturation magnetization (M_s) The maximum attainable intensity of magnetization per unit volume is called as saturation magnetization of ferromagnetic

material and is shown by (Ms). The powerful

71%

MATCHING BLOCK 39/88

W

<https://docplayer.net/150337558-Doctor-of ...>

tool to study the different parameter such as domain wall motion, anisotropy, magnetic hardness or softness of material, magnetic ordering etc

is magnetization. The experimental method for the determination of saturation magnetization has reviewed by Mc Guire and Flanders. The saturation magnetization can be examined by using high field hysteresis loop technique. When the

88%

MATCHING BLOCK 40/88

W

<https://docplayer.net/150337558-Doctor-of ...>

magnetic field is applied to the ferromagnetic material, the magnetization may vary from zero to saturation value. This

behavior is expressed by Weiss introducing the idea of existence of domains. By using the molecular weight and saturation magnetization data of the samples, the magneton number (n B) was calculated by using the following relation [14], $W S B M M n 5585 \times = (3.8)$

Chapter-III 73 Where, B n = Magneton number; M W = Molecular weight of the compound, M S = Saturation magnetization, 5585 is Constant related to molecular weight of nickel. The specific saturation magnetization is computed by using the following relation; $() S S 1 P M d \sigma = - \times (3.9)$ Where, S σ = specific saturation magnetization; P = porosity; d = thickness 3.6.2 Coercivity (Hc) The intensity of the magnetic field which must be applied in order to lower the magnetization of a ferromagnetic material to zero after the magnetization of the sample has been driven to saturation Coercivity generally used to determine whether a material is soft or hard. The (Hc) less than 400 Am⁻¹ (5 Oe) indicate that material is soft magnetic material and Hc with values higher 8000 Am⁻¹ (100 Oe) indicates hard magnetic materials. 3.7 DIELECTRIC PROPERTIES LCR-Q meter used to study the frequency dependence dielectric properties of ferrite material. The dielectric properties are very useful to know the various polarization phenomenon in crystallography of material i.e. space charge polarization, atomic polarization, electronic polarization and orientation polarization. The different parameter of sample impedance, resistance, capacitance, inductance, dielectric loss and tangent of ferrite material are measure by using LCR meter. Fig. 3.7 shows the experimental setup to measure the dielectric properties of the materials in the present work. The pellets of sample were kept in a removable sample holder. The sample holder has two rods which move up and down through a spring mechanism and pressure. The pellets are sandwiched between top and bottom electrodes. Pellet's top and bottom surface is coated by silver paste to make good ohmic contact

Chapter-III 74 between two electrodes. The two rods were connected to LCR meter through the clip wire system. The data was collected using a data acquisition system which consists of a computer interfaced with LCR meter. The dielectric properties of ferrite material in terms of frequency dependence parameters are measures such as dielectric constant and dielectric loss with the frequency range of 1 kHz to 120 MHz Fig. 3.7: Dielectric measurement set up 3.7.1 Dielectric Constant It is used to determine the ability of an insulator to store the electrical energy. It

45%

MATCHING BLOCK 41/88

W

<https://docplayer.net/150337558-Doctor-of ...>

is the ratio of induced capacitance of metallic plates with insulator to the induced capacitance of the plates with air or vacuum

medium. Dielectric constant is also depends upon the polarization produced in the sample. The dielectric constant of ferrite material is determined by using following equation [15]: $0 C d A ' \epsilon = \epsilon (3.10)$ Where, ' ϵ = dielectric constant, C = capacitance of the material, d = thickness of pellet; A = surface area of pellet; 0ϵ = absolute permittivity = 8.854×10^{-12} F/m.

Chapter-III 75 3.7.2 Dielectric loss and loss tangent The electric energy that is converted into heat energy in dielectric material when it is subjected to frequency variation is known as dielectric loss. The dielectric loss tangent is also known as dissipation factor D and is the ratio at any particular frequency between the real and imaginary parts of impedance of the capacitor. Following are the formulas for dielectric loss and loss tangent given by equations (3.11) and (3.12) respectively

[15]; $0.2 f \sigma \epsilon = \pi \cdot \epsilon$ (3.11) Where, σ = a.c. conductivity; f = frequency $\tan \delta = \epsilon$ (3.12) Where, ϵ = dielectric loss, ϵ = dielectric constant

3.8 P-E LOOP TRACER Fig. 3.8: Ferroelectric hysteresis loop experimental setup The Automatic P-E Loop tracer is designed for characterization of materials such as ferroelectrics. The system measures the hysteresis loops for these materials. For

Chapter-III 76 ferroelectric's materials polarization is plotted against the electric Field. Measurements are done at line different frequencies of 20 Hz to 10 KHz nominal in different steps. Fig. 3.8 shows the experimental setup of P-E loop tracer. The basic P-E test system is based on sawyer tower circuit. The principle is simple when two capacitors are connected in series and AC voltage is applied on both in series, the charge on both will be same. In order to get complete saturation the internal capacitance must be higher than the sample capacitance. The thickness of sample used to measured electronic polarization is less than the 1mm also all the pellet of 10mm diameter so we can determine the area of sample. The pellets of ferrite or ferroelectric material is coated with silver paste on both the sides and place the pellets in sample holder and insert in silicon oil it must be moisture free or bubble free to avoid the spark. After all the setup applies the electric field on sample always starts with lower fields such as 2 kv/cm or 5 kv/cm. Here you can raise/ lower the field according to the requirement to seek saturation In case of overload decrease the voltage level and press reset switch and do not raise the voltage level and run the P-E loop software to plot the hysteresis loop of sample.

3.9 MAGNETO-ELECTRIC EFFECT The magnetoelectric effect is the phenomenon it consist suitable combination of two phases such as ferroelectric material with ferromagnetic material. There are basically two types of material exhibit magnetoelectric effect namely single phase material and composite material. In single phase material due to the interaction between the magnetic and ferroelectric sub-lattice ME-effect occur, in other hand composite material shows ME signal as a product property is essentially due to the interaction between two participating phases. The ME effect is the phenomenon where a magnetic field (H) produces an electric polarization or electric field produces a magnetization. The study of ME effect one of the

Chapter-III 77 most popular area in the field of material science and it offers new idea for multifunctional material suitable for new generation potential application in various areas like magnetic field sensors, transducer, electro-optic devices and memory devices (RAM and D-RAM). Fig. 3.9: Helmholtz coil experimental setup of ME effect The Helmholtz coil used to measure the ME coefficient by experimental set-up as shown in Fig. 3.9. The ME voltage coefficient α_{ME} (dE/dH) (direct magnetoelectric effect, DME) measurement was carried out as follows: a ME composite was kept in a Helmholtz coils. A charge signal from the surface of the sample can induce by Helmholtz coils which generated AC magnetic field. The direction of DC bias magnetic field and AC magnetic field was perpendicular to the electrode surface of the sample. Static, quasi-static, dynamic and pulsed dynamic method is one of the different methods to measure ME effect of composite sample. To measure the ME coefficient of any sample it is necessary to pole the sample both electrically or magnetically to achieve the dipole orientation of sub lattice or different constituent phases in composite material to produce the polarization it shows the voltage output across the sample. In dynamic method the sample is subjected to the action of superimposed AC electric field in variable of DC

Chapter-III 78 magnetic field which generates at the ends of the material a voltage drop generated across the sample is nothing but the ME signal is generated. The ME coefficient of sample is calculated by using following formula, $\alpha_{ME} = \frac{V_{out}}{H_{ac} \times T}$ (3.13) where, T - thickness of the sample, V_{out} - ME voltage measured across the samples; and H_{ac} - applied AC magnetic fields by Helmholtz coil

Chapter-III 79 REFERENCES [1] M. J. Iqbal,

75%

MATCHING BLOCK 42/88

W

[http://pr.hec.gov.pk/jspui/bitstream/123 ...](http://pr.hec.gov.pk/jspui/bitstream/123...)

Z. Ahmad, T. Meydan, Y. Melikhov; Physical, electrical and magnetic properties of nano-sized Co-Cr substituted magnesium

ferrite; J. App. Phys. 111 (2012) 033906. [2]

https://serc.carleton.edu/research_education/geochemsheets/techniques/XRD.html [3] B. C. Giessen, G. E. Gordon; X-ray diffraction: New high speed technique based on X-ray spectroscopy; Science 159 (1968) 973-975. [4] <https://www.>

76%

MATCHING BLOCK 47/88

W

<https://www.academia.edu/33210023/STUDIES ...>

academia.edu/33210023/STUDIES_ON_REMEDIATION_OF_CHRO
MIUM_CONTAINED_INDUSTRIAL_EFFLUENTS_USING_HYBRID_

REACTO R [5] G. Mustafa, M. U. Islam, W. Zhang, Y. Jamil, A. W. Anwar, M.

77%

MATCHING BLOCK 44/88

J

0201276d-de23-493f-a933-df7286b7da30

Hussain, M.

Ahmad; Investigation of structural and magnetic properties of Ce³⁺ substituted Co-Cr ferrite for variety of applications; J.

Alloy. Comp. 618 (2015) 428-436. [6] R. A. Pawar, S. E. Shirsath, R. H. Kadam, R. P. Joshi, S. M. Patange; Synthesis and magnetic properties of Cu_{0.7}Zn_{0.3}Al_xFe_{2-x}O₄ nanoferrite using egg-white method; J. Magn. Mater. 339 (2013) 138-141. [7] Vivek Choudhari, S. E. Shirsath, M. L. Mane, R. H. Kadam, S. B. Shelke, D. R. Mane; Crystallographic, magnetic and electrical properties of Ni_{0.5}Cu_{0.25}Zn_{0.25}La_xFe_{2-x}O₄ nanoparticles fabricated by sol-gel method; J. Alloy. Comp. 549 (2013) 213-220. [8] S. J. Haralkar, R. H. Kadam, S. S. More, S. E. Shirsath, M. L. Mane, Swati Patil, D. R.

87%

MATCHING BLOCK 45/88

J

0201276d-de23-493f-a933-df7286b7da30

Mane; Substitutional effect of Cr³⁺ ions on the properties of Mg-Zn ferrite nanoparticles; Physica B:

Condensed Matter; 407 (2012) 4338-4346.

Chapter-III 80 [9] R. H. Kadam, A. P. Birajdar, S. T. Alone, S. E. Shirsath; Fabrication of Co_{0.5}Ni_{0.5}Cr_xFe_{2-x}O₄

91%

MATCHING BLOCK 46/88

W

<https://www.researchgate.net/publication/ ...>

materials via sol-gel method and their characterizations; J.

Magn. Mater. 327 (2013) 167-171.

[10]

B. J. Inkson; Materials characterization using nondestructive evaluation (NDE) methods; Elsevier B. V. (2016) p. 17-43. [11]

M. Shabbir, S. Ahmed, J. N. Sheikh; Frontiers of textile materials; John Wiley & Sons, (2020). [12]

https://en.wikipedia.org/wiki/Fourier-transform_infrared_spectroscopy [13] E. Gupta, R. R. Yadav, M. Sharma; Hardware

implementation of a vibrating sample magnetometer circuitry; Int. J. Soft. Hard. Res. Engg. 2 (2014) 124-127. [14] S. S.

More, R. H. Kadam, A. B. Kadam, D. R. Mane, G. K. Bichile; Structural properties and magnetic interactions in Al³⁺ and Cr

³⁺ co-substituted CoFe₂O₄ ferrite; Cent. Euro. J. Chem.; 8 (2010) 419-425. [15] S. T. Alone, S. E. Shirsath, R. H. Kadam,

D. R. Mane, K. M. Jadhav; Dielectric behaviour in nanocrystalline Al doped Co-Zn ferrite; Opto. Adv. Mater. Rap. Commu. 3

(2009) 1200-1203.

81 CHAPTER – IV SYNTHESIS AND CHARACTERIZATION OF CCFO AND MZFO FERRITES CONTENTS 4.1 Introduction :

82 4.2 Experimental : 83 4.3 Results and discussion : 83 References : 88 This part of the thesis is communicated with

Journal of Materials Science: Materials in electronics (ISSN: 1662-8985)

Chapter-IV 82 4.1 INTRODUCTION Polycrystalline ferrites show excellent dielectric and magnetic properties and therefore, they have wide-spread applications in the area of research and technology [1-3]. As these materials used in various industrial and medical applications such as cores in transformers, magnetic data storage device, rod antennas, microwave devices, and drug delivery, it is very important to synthesis and characterize the new materials by considering their utility in particular application [4]. In particular spinel ferrites represented by general formula AB₂O₄ shows interesting magnetic and electrical behaviour which originates mainly from the distribution of metal cations over tetrahedral – A and octahedral B-sites [5]. Co-Cr and Mn-Zn ferrites belongs to the important category of magnetic ceramics with long-range technological/industrial applications, in devices that in the broadest sense can be characterized

as transformers, inductors or absorbers [6, 7]. Because of very good magnetic behavior Co-Cr ferrites can be used in magnetic applications and due to low resistivity Mn-Zn ferrites can be used at low frequencies [8]. Literature survey shows that several researchers have been investigated the structural, magnetic and electrical properties of Co-Mn-Zn ferrite [9], zinc ferrite [10], nickel ferrite [11], nickel – BTO [12], BaFe₁₆O₂₇ [13] barium hexaferrite [14] etc. The synthesis approach greatly affects the crystallite size of the samples which in turn alters the physical and chemical properties. Traditional synthesis methods involve several stages including multiple grinding and sintering at high temperatures [15]. Ultrafine particles at nano-scale dimension can be obtained at sufficiently low temperature by wet-chemical methods like co-precipitation, sol-gel auto-ignition and ultrasonic irradiation assisted sonochemical method. [16]. Magnetolectric composites simultaneously possess both ferroelectric and ferromagnetic ordering within a single compound. The occurrence of multiphase

Chapter-IV 83 behaviour within a single material makes them suitable for next generation multifunctional electronic device and integrated circuits [17]. These M-E composites consists one phase as AB₂O₄ ferromagnetic material and other consists perovskite oxides. In the present chapter we have reported the XRD, IR and elastic properties of CCFO and MZFO nanoparticles produced via ultrasonic irradiation assisted sono-chemical method and used as ferromagnetic phase in next generation M-E composites. 4.2 EXPERIMENTAL Ultrasonic irradiation assisted sono-chemical route was employed to produce the pure phases of CoCr_{0.3}Fe_{1.7}O₄ (CCFO) and Mn_{0.7}Zn_{0.3}Fe₂O₄ (MZFO) materials. A.R.

72%	MATCHING BLOCK 48/88	W https://www.researchgate.net/publication/ ...
grade (99% purity) Co(NO ₃) ₂ ·6H ₂ O, Cr(NO ₃) ₃ ·9H ₂ O, Mn(NO ₃) ₂ ·3H ₂ O, Zn(NO ₃) ₂ ·6H ₂ O		

and Fe(NO₃)₃·9H₂O were mixed in sufficient amount of double distilled water. Monohydrate citric acid was used as chelating agent and liquid ammonia was poured slowly in the mixture to maintain the pH of the solution at 7. The entire solution exposed to high- intensity ultrasonic irradiation (frequency: 20 kHz and power: 70 W) for 120 min at constant temperature 90 °C. The powders were finally sintered at 800 °C for six hours. The final powders were then characterized by X-ray diffraction technique and Infrared spectroscopy. 4.3 RESULTS AND DISCUSSION X-ray diffraction patterns of CCFO and MZFO ferrite nano-particles are shown in Fig. 4.1. All Bragg's lines are sharp and no impurity peaks are observed. The broadening of these lines shows well crystalline nature of the samples with nano sized dimension. The peaks are indexed for the planes (220), (311), (222), (400), (422), (333), (440) and (533) which corresponds to the cubic spinel structure of the samples. Peak intensity of the

Chapter-IV 84 sample CCFO is observed higher than that of the MZFO while peak broadening is higher for MZFO sample. Fig. 4.1: XRD patterns of (A) CCFO sample and (B) MZFO sample. Lattice constant of both the samples was estimated by using the relation given below [18]; $2d = \frac{a}{\sqrt{h^2 + k^2 + l^2}}$ (4.1) Where, d hkl – is the interplanar spacing and hkl are the miller indices. Lattice constant for the sample CCFO was observed 8.3730 Å and for MZFO sample it was 8.431Å. Size of unit cell is closely related to the ionic radii of the constituent elements. Here in the present case, for CCFO crystal, Co (0.78Å) and Cr (0.64Å) have relatively smaller ionic radii than the Mn (0.89Å) and Zn (0.83Å) which in turn reduces the unit cell length. X-ray density of the samples was obtained from the relation discussed elsewhere [18]. For the sample CCFO, X-ray density is obtained 5.401 gm/cc and for the sample MZFO it was 5.318 gm/cc.

Chapter-IV 85 Well known Scherrer equation is used to estimate the average crystallite size of both samples. Peak width of all the major peaks was considered for the calculation of average crystallite size by using following relation [19]; $\beta = \frac{K \lambda}{D \cos \theta}$ (4.2) Where, K is constant (preferably 0.95 for simple crystals), $\lambda = 1.5405 \text{ \AA}$, β hkl – is the full width of half maxima, θ – Bragg's angle. For the sample CCFO, average crystallite size was obtained 20.1 nm and for the sample MZFO it was 15.36 nm. Infrared spectra of both the samples were collected at room temperature in the wavenumber range 300 cm⁻¹ to 800 cm⁻¹ as shown in Fig. 4.2. Fig. 4.2: IR spectra of CCFO and MZFO samples. The vibration bands are observed near 420 cm⁻¹ related to the stretching vibration of metal ion and oxygen bond at octahedral – B site and near 600 cm⁻¹ are related to tetrahedral – B site. The positions of vibration bands confirm the cubic crystal structure of the samples [20]. Vibration bands shifts for higher frequencies for MZFO sample is may

Chapter-IV 86 be due to the crystallite size and cation distribution [20]. The force constants K_T (tetrahedral – A site) and K_O (octahedral – B site) were computed by using the relations discussed in literature [21]. The average force constant (K_{av}) was obtained from the average of K_T and K_O and the values are given in Table 4.1. Table 4.1: Band positions (ν₁, ν₂) and force constants (K_T, K_O, K_{av}) for CCFO and MZFO samples. Sample ν₁ (cm⁻¹) ν₂ (cm⁻¹) K_T × 10⁵ (dynes/cm) K_O × 10⁵ (dynes/cm) K_{av} × 10⁵ (dynes/cm) CCFO 584.45 420.49 239.40 175.32 207.36 MZFO

611.45 424.35 225.57 153.71 189.64 Elastic parameters like stiffness constant (C₁₁), elastic moduli (B, G and E), Poisson's constant (σ) and Debye temperature (θ_D) were calculated by using the molecular weight and force constants of the samples at tetrahedral – A and octahedral – B sites in the following relations [18]. $\nu = \frac{1}{2\pi} \sqrt{\frac{K}{m}}$ (4.3) $B = \frac{1}{3} \frac{C_{11} + 2C_{12} + C_{33}}{3}$ (4.4) $G = \frac{1}{2} \frac{C_{11} - C_{12} + 3C_{44}}{3}$ (4.5) $\sigma = \frac{C_{12}}{C_{11}}$ (4.6) $E = \frac{3BG}{B+2G}$ (4.7) The obtained elastic parameters are tabulated in Table 4.2. It can be seen that stiffness constant and all elastic parameters shows lower values for MZFO samples than the CCFO samples. The stiffness constant (C₁₁), modulus of rigidity (B), bulk modulus

Chapter-IV 87 (G) and Young's modulus (E) are obtained higher for CCFO sample and lower for MZFO sample. The higher values of elastic parameters are attributed to the increased ionic bonding between the metal ions. In order to achieve good elastic behaviour, Poisson's ratio must lie in the range -1 to 0.5 [22]. In the present case it is constant (0.35) for both samples. As described by Anderson [23], Debye temperature (θ_D) was calculated by using the following relation; $\theta_D = \frac{h}{k} \left(\frac{6\pi^2 N}{V} \right)^{1/3} \frac{v_m}{2\pi}$ (4.8) Where, k – is Boltzmann's constant and h – is Plank's constant, N – is Avagadro's number, n – is number of atoms per unit cell (n = 8, for cubic crystals), ρ - is density of the sample, V – is the mean wave velocity, and M- is the molecular weight. Calculated values of Debye temperature for both samples are given in the following Table 2. The Debye temperature is observed higher for MZFO sample which is may be related to the increasing P-type conduction in the material [24]. Table 4.2: Elastic properties of CCFO and MZFO samples. Sample C 11 (GPa) B (GPa) G (GPa) σ σ σ σ E (GPa) θ θ θ θ D (K) CCFO 247.33 247.33 82.44 0.35 222.60 722.55 MZFO 225.17 225.17 75.06 0.35 202.65 744.74

Chapter-IV 88 REFERENCES [1] S. T. Alone, S. E. Shirsath, R. H. Kadam, D. R. Mane, K. M. Jadhav; Dielectric behaviour in nanocrystalline Al doped Co-Zn ferrite; Opt. Elect. Adv. Mater. 3 (2009) 1200-1203. [2] S. S. More, R. H. Kadam, A. B. Kadam, A. R. Shitre, D. R. Mane, K. M. Jadhav; Cation distribution in nanocrystalline Al³⁺ and Cr³⁺ co-substituted CoFe₂O₄; J. Alloy. Comp. 502 (2010) 477-479. [3] H. Yang, L. Shen, L. Zhao, L. Song, J. Zhao, Z. Wang, L. Wang, D. Zhang; Magnetic properties of nanocrystalline Li_{0.5}Fe_{2.1}Cr_{0.4}O₄ ferrite; Mater. Lett. 57 (2003) 2455-2459. [4] M. Mozaffari, J. Amighian; Preparation of Al-substituted Ni ferrite powders via mechanochemical processing;

100% **MATCHING BLOCK 51/88** **W** <https://www.researchgate.net/publication/...>

J. Magn. Mater.; 260 (2003) 244-249.
[5] T. M. Meaz, S. M. Attia; A. M. Abo El Ata;

86% **MATCHING BLOCK 52/88** **W** <https://www.researchgate.net/publication/...>

Effect of tetravalent titanium ions substitution on the dielectric properties of Co-Zn ferrite; J. Magn. Mater. 257 (2003) 296-305.
[6]

D. R. Mane, D. D. Birajdar, S. E. Shirsath, R. H. Kadam; Combustion synthesis and magnetic characterizations of Mn-Substituted Ni-Zn ferrite nanoparticles; NSTI- Nanotech 01 (2010) 539-542. [7] S. Gubbala, H. Nathania, K. Kozolb, R. D. K. Mishra; Magnetic properties of nanocrystalline Ni-Zn, Zn-Mn and Ni-Mn ferrites synthesized by reverse micelle technique; Physica B: Cond. Mater. 348 (2004) 317. [8] S. Son, M. Taheri, E. Carpenter, V. G. Harris, M. E. McHenry; Synthesis of ferrite and nickel ferrite nanoparticles using radio-frequency thermal plasma torch; J. Appl. Phys. 91 (2002) 7589.

Chapter-IV 89 [9] J. Xiang, X. Shen, X. Meng; Preparation of Co-substituted MnZn ferrite fibers and their magnetic properties; Mater. Chem. Phys. 114 (2009) 362-366. [10] H. Akther, K. K. Kabira, M. Sekib, T. Kawaib, H. Tabata; Structural, AC, and DC magnetic properties of Zn_{1-x}Co_xFe₂O₄; J. Phys. Chem. Solid. 68 (2007) 1933-1939. [11] M. K. Shobna, S. Sankar; Synthesis and characterization of Ni_{1-x}Co_xFe₂O₄; J. Magn. Mater. 321 (2009) 3132-3137. [12] X. Shen, Z. Zhou, F. Song; Synthesis and magnetic properties of nanocomposite Ni_{1-x}Co_xFe₂O₄-BaTiO₃ fibers by organic gel-thermal decomposition process; J. Sol. Gel. Sci. Techn. 53 (2010) 405-411 [13] H. Zhang, Z. Liu, X. Yao, L. Zhang, M. Wu; The synthesis, characterization and microwave properties of znco-substituted W-type barium hexaferrite, from a sol-gel precursor; J. Sol. Gel. Sci. Tech. 27 (2003) 277-285. [14] J. Bursik, Z. Simsa, M. Cernansky; Magneto-optical characteristics of Co, Ti- substituted barium hexaferrite films deposited by the dip-coating method; J. Sol. Gel. Sci. Tech. 8 (1997) 947-951. [15] E. A. Schawabe, D. A. Campbell, Influence of Grain size on square – loop properties of lithium ferrites; J. Appl. Phys. 34 (1963) 1251. [16] Z. Yue, J. Zhao, X. Wang, Z. Gui, L. Li; Preperation and magnetic properties of titanium –

substituted LiZn ferrites via a sol-gel auto-combustion process; J. Eur. Ceram. Soc. 23 (2003) 189. [17] S. R. Wadgane, S. E. Shirsath, A. S. Gaikwad, S. S. Satpute, A. B. Kadam, R. H. Kadam; Ferro-and magneto-electric characteristics in $YFeO_3 - Y_3Fe_5O_{12}$ nanocomposites; J. Magn. Mater. 457 (2018) 103-109.

Chapter-IV 90 [18] R. H. Kadam, R. B. Borade, M. L. Mane, D. R. Mane, K. M. Batoor, S. E. Shirsath; Structural, mechanical, dielectric properties and magnetic interactions in Dy^{3+} substituted Co-Cu-Zn nanoferrites; RSC Advances 10 (2020) 27911 [19] D. R. Mane, D. D. Birajdar, S. Patil, S. E. Shirsath, R. H. Kadam; Redistribution of cations and enhancement in magnetic properties of sol-gel synthesized $Cu_{0.7-x}Co_xZn_{0.3}Fe_2O_4$; J. Sol. Gel. Sci. Techn. 58 (2011) 70 [20] R. Waldron, Infrared spectra of ferrite; Phys. Rev. 99 (1955) 1727. [21]

90% **MATCHING BLOCK 49/88** **W** [https://www.researchgate.net/publication/ ...](https://www.researchgate.net/publication/)

A. A. Birajdar, S. E. Shirsath, R. H. Kadam, M. L. Mane, D. R. Mane;

83% **MATCHING BLOCK 50/88** **W** [https://www.researchgate.net/publication/ ...](https://www.researchgate.net/publication/)

Permeability and magnetic properties of Al^{3+} substituted $Ni_{0.7}Zn_{0.3}Fe_2O_4$ nanoparticles; J. Appl. Phys. 112 (2012) 053908.

91

CHAPTER – V RESULTS AND DISCUSSION ON $(1-x)CoCr_{0.3}Fe_{1.7}O_4 + (x)BaTiO_3$ CONTENTS 5.1 Introduction : 92 5.2 Materials and Methods : 94 5.2.1 Synthesis of CCFO Phase : 94 5.2.2 Synthesis of BTO Phase : 94 5.2.3 Synthesis of CCFO-BTO composites : 95 5.2.4 Characterization techniques : 95 5.3 Results and discussion : 96 5.3.1 XRD analysis : 96 5.3.2 W-H analysis : 99 5.3.3 Scanning electron microscopy : 100 5.3.4 FTIR spectroscopy : 101 5.3.5 Magnetic properties : 102 5.3.6 P-E loop measurements : 103 5.3.7 Dielectric measurements : 104 5.3.8 M-E measurements : 106 References : 108 Figures : 115 Tables : This part of the thesis is published in Ceramics International 47 (2021) 6496-6504. (ISSN: 0272-8842)

Chapter-V 92 5.1 INTRODUCTION Since the last few years, efforts have been taken together to produce the group of materials consisting two or more ferroic orders such as ferromagnetic, ferroelectric, ferroelastic etc. More than one phase with different crystallography and chemical compositions forms a composite material in which these phases remains present without any chemical reaction [1]. Such materials show some superior properties than the individual phases and behave differently than that of the individual and make them suitable for many technological applications and devices [2-4]. Magnetolectric (ME) composites particularly composed by ferromagnetic and ferroelectric phases shows the unique property as ME effect which cannot be observed in individual phase [5]. Single phase materials are unable to produce the M-E effect at room temperature. Piezomagnetic and piezoelectric phases produces strong mechanical coupling within the composite material which magnetize the material after application of electric field, and induced magnetization provokes the dielectric polarization in piezoelectric phase which is termed as M-E effect [6]. When the M-E composites placed in a magnetic field they can be electrically polarized and when they are subjected to electric field becomes magnetized. As seen in the literature, M-E composites have attracted significant attention of the researchers in recent years due to their extensive use in various technological devices such as waveguides, switches, phase shifters, modulators etc [7-9]. The condition for the practical use of ME composites is to simultaneous occurrence of piezoelectricity and magnetic ordering within the same material. Hence a strong mechanical coupling is required at room temperature which is possible when the composites with $BaTiO_3$, $PbTiO_3$, $SrTiO_3$ as a piezoelectric phase and spinel ferrites with general formula MFe_2O_4 ($A = Co^{2+}$, Mg^{2+} , Zn^{2+} , Cu^{2+} , Ni^{2+} etc.) as a piezomagnetic phase can be synthesized. Such types of M-E composites have been widely produced and characterized [10-13].

Chapter-V 93 Superior M-E effect can be achieved by combining the suitable ferrite and ferroelectric phases which are having high piezomagnetic and piezoelectric coefficients. Magnetization and dielectric polarization of piezomagnetic material is sensitive to the type of constituent ions and their concentration in the composition [14]. Cobalt ferrite which is

the example of inverse spinels have been extensively used in various technologically important devices like RF phase shifters, electrical isolators, magnetic core memory, circulators etc. as they possess low losses of Foucault's currents and high Curie point [15,16]. Excellent magnetic properties like high saturation magnetization, high coercivity and high remnant magnetization make cobalt ferrite very popular for the piezomagnetic phase of composite [17-19]. Moreover due to high magnetostriction observed in cobalt ferrite from its first order positive magnetocrystalline anisotropy makes it a perfect piezomagnetic partner for ME composite. Previously published literature suggests that partial substituted chromium ions in cobalt ferrite improve the magnetocrystalline anisotropy [20, 21]. This motivated us to choose the piezomagnetic phase as $\text{CoCr}_{0.3} \text{Fe}_{1.7} \text{O}_4$. On the other hand, the second phase (piezoelectric) was taken as BaTiO_3 due to its high value of dielectric constant, large piezoelectricity and electrical resistivity ($\sim 10^9 \Omega\text{cm}$). Grain size and porous structure of the composites significantly affected the ME effect. Decreasing mean free path of electrons due to the dilution of piezomagnetic phase decreases the electrical conductivity and increases the magnetoelectric and dielectric properties of the composites [22]. In order to enhance the dielectric and magnetoelectric properties of M-E composites, grains with small size are most acceptable [23]. In the present investigation chromium doped cobalt ferrite (CCFO) phase was synthesized by sonochemical method using ultrasonic irradiation. This method is timesaving and produces high-purity grains with nanoscale dimension in a simplistic way. Also ultrasonication

Chapter-V 94 based sonochemical method offers superior rate of chemical reaction, lower waste production and lower energy consumption [24-26]. Thus, the synthesized phases were mixed in the form of $(1-x)\text{CoCr}_{0.3}\text{Fe}_{1.7}\text{O}_4 + (x)\text{BaTiO}_3$ ($x = 0.0, 0.2, 0.4, 0.6, 0.8$ and 1.0) and investigated for their structural, morphological, magnetic, dielectric and magnetoelectric properties.

5.2 MATERIALS AND METHODS

5.2.1 Synthesis of CCFO phase CCFO phase of CCFO-BTO composites were obtained individually by ultrasonic irradiation assisted sonochemical sol-gel route. AR grade $\text{Co}(\text{NO}_3)_2 \cdot 6\text{H}_2\text{O}$, $\text{Cr}(\text{NO}_3)_3 \cdot 9\text{H}_2\text{O}$ and $\text{Fe}(\text{NO}_3)_3 \cdot 9\text{H}_2\text{O}$ with high purity (99%) were taken as starting materials to produce the piezomagnetic $\text{CoCr}_{0.3}\text{Fe}_{1.7}\text{O}_4$ nano particles. All the metal nitrates of constituent elements were diluted in double distilled water with their weight proportion. In order to get more stable piezomagnetic phase with high purity, pH of the solution was maintained at neutral by pouring the liquid ammonia in the mixture. The temperature of the entire solution was increased by exposing it to high-intensity ultrasonic irradiation (frequency: 20 kHz and power: 70 W) for 120 min. During ultrasonication process, due to very large number of collisions, the temperature of the solution was raised 90 °C. The synthesized precursor was washed several times with DI water and finally, the $\text{CoCr}_{0.3}\text{Fe}_{1.7}\text{O}_4$ powder was segregated from the viscous liquid with outside simple magnet and dried at 100 °C for 12 h.

5.2.2 Synthesis of BTO phase Nanoparticles of BTO phase (BaTiO_3) was obtained by employing the sol-gel route. Ethanol was used to dilute titanium butoxide $\text{Ti}(\text{OC}_4\text{H}_9)_4$ while acetic acid was used

Chapter-V 95 to dissolve barium acetate ($\text{Ba}(\text{OOCCH}_3)_2$). Both the solutions were separately stirred for one hour and then mixed together. This mixture was continuously stirred at 100 °C up to the formation of dried powder. Thus, obtained powder was subjected to grinding and heat treatment at 800 °C for 2 h.

5.2.3 Synthesis of CCFO-BTO composites The CCFO-BTO M-E composite materials were fabricated by mixing the CCFO and BTO nanopowders with their weight proportion in percentage of (80%)CCFO+(20%)BTO, (60%)CCFO+(40%)BTO, (40%)CCFO+(60%)BTO and (20%)CCFO+(80%)BTO respectively. Mixed solid-solutions of M-E composites were thoroughly grinded for 2-3 hours and finally sintered at 800 °C for 6 h. By using hydraulic press, the composite powders were compressed into pellets with 1.5 to 2.5 mm thicknesses. Flow chart of the synthesis of CCFO-BTO composites is shown in Fig. 5.1.

5.2.4 Characterization techniques Room temperature X-ray diffraction patterns of all the samples were recorded by using $\text{Cu-K}\alpha$ radiation ($\lambda = 1.5405 \times 10^{-10} \text{ m}$). XRD patterns were used to identify the individual phase in the composite and to study the structural parameters. Scanning electron micrographs (SEM, HITACHI S-4800) of all the samples were taken to study the grain size distribution and surface morphology of the composites. Energy dispersive X-ray spectroscopy (EDX) with color mapping images was employed to study the elemental analysis. Magnetic parameters such as saturation magnetization, remnant magnetization, and coercivity were investigated by using vibrating sample magnetometer in the applied magnetic field up to 20000 Oe at room temperature. Hioki 3532-50 LCR HITESTER was used to understand the dielectric behaviour of

64%

MATCHING BLOCK 54/88

W

[https://www.researchgate.net/publication/ ...](https://www.researchgate.net/publication/...)

all the samples as a function of applied

Chapter-V
96

frequency in the range 50Hz to 50MHz.

For this, composite powders were converted in the form of right circular cylindrical pellets and placed between two electric probes. Dynamic method was employed to investigate the magneto-electric coefficient of M-E composites. The measurements were carried out by superimposing the sinusoidal magnetic field (H_{AC}) produced by Helmholtz's coils with D. C. bias magnetic field (H_{DC}) produced by electrically poled with applied electric field of 1.5 kv/cm at 200 °C for 1 h. The output ME voltage of the sample was measured as a function of bias magnetic field (H_{DC}) from 0 Oe to 8000 Oe in steps of 500 Oe with sinusoidal magnetic field ($H_{AC} = 5$ Oe, $f = 1$ kHz). 5.3 RESULTS AND DISCUSSION 5.3.1 XRD analysis Rietveld refinement of all the samples of $(1-x)\text{CoCr}_2\text{Fe}_2\text{O}_4 + x\text{BaTiO}_3$ ($x = 0.0, 0.2, 0.4, 0.6, 0.8$ and 1.0) composites was done by using the software FullProf suite. Rietveld refined

88%

MATCHING BLOCK 57/88

W

[https://www.researchgate.net/publication/ ...](https://www.researchgate.net/publication/...)

X-ray diffraction patterns of all the samples are illustrated in Fig. 5.2 (a)

which clearly indicating the existence of both piezomagnetic as well as piezoelectric phases in the composites. Well distinct and intensive peaks indexed by the planes (220), (311), (400), (422), (333), and (440) observed in the XRD patterns related to piezomagnetic phase. These miller indices are belongs to the cubic spinel structure of the CCFO samples. According to standard JCPDS data card no. 22-1086, all the peaks indexed for piezomagnetic phase are related to the Co-Cr ferrites. The typical crystal structure of the cubic spinel CCFO phase is shown in Fig. 5.2 (b). The peaks indexed for the Miller indices (100), (110), (111), (200), (210) and (211) are related to piezoelectric phase. All these peaks are well matched with the standard JCPDS card no. 05-0626 confirms the perovskite structure of BaTiO_3 with space group $P4mm$ [27, 28]. A general crystal structure of perovskite BTO phase is illustrated in Fig. 5.2(c). It can be seen that, as

Chapter-V 97 the concentration of BTO grains increases in the composite, peak intensity of CCFO phase decreases and BTO phase increases. A keen observation of XRD patterns indicate that the peak (110) related to BTO phase slightly shifted towards higher 2θ angles with the increasing percentage of BTO grains in the composite. Whereas the peak (311) related to CCFO phase slightly shifted towards lower 2θ angles for the composition up to $x = 0.4$ with the increasing percentage of BTO grains and thereafter further increase of BTO phase concentration shifted the peak position (311) towards higher 2θ . This change in peak intensity and peak position clearly indicates the variation in lattice parameter of both phases and crystallite size of the composite. By using the interplaner spacing's obtained from XRD data and Miller indices in the following relation, lattice constant (a) of both CCFO and BTO phases were calculated individually. $\frac{1}{d^2} = \frac{h^2}{a^2} + \frac{k^2}{b^2} + \frac{l^2}{c^2}$ (5.1) Fig. 5.3 represents the variation of lattice parameters for piezomagnetic CCFO and piezoelectric BTO phase and the values are given in Table 5.1. It can be seen from of Fig. 5.3 and Table 5.1 that the lattice constant of piezomagnetic phase increased from 8.373 Å to 8.3774 Å up to $x = 0.4$ and thereafter decreases to 8.3738 Å for $x = 1.0$ with the increasing concentration of BTO phase. Simultaneously, lattice constant of BTO phase decreased from 4.021 Å to 4.005 Å with the increasing concentration of BTO phase. Other Rietveld parameters such as χ^2 , R_{EXP} , R_{WP} , R_P are listed in Table 5.1. X-ray density ' d_x ' of CCFO-BTO M-E composites was obtained by using the following relation [29]; $d_x = \frac{Z \cdot M}{N_A \cdot a^3}$ (5.2) where, ' N_A ' is Avogadro's number and ' a ' is the lattice parameter and M is the molecular weight of the composition. Calculated values of X-ray density ' d_x ' were computed in Table 5.1 and the variation with BTO concentration is shown in Fig. 5.4. As seen in Table

Chapter-V 98 5.1, increasing piezoelectric (BTO) phase in the composite increases the values of X-ray density ' d_x ' from 5.401 gm/cc to 6.015 gm/cc. Porosity of the samples in percentage was estimated by using the bulk density values obtained from simple mass-volume relation and X-ray density in the following equation [29]; $P\% = \left(1 - \frac{d_b}{d_x}\right) \times 100$ (5.3) Computed values of percentage porosity were listed in Table 5.1 and its variation with BTO concentration is shown

in Fig. 5.4. It can be seen that the porosity of the samples decreased from 13% to 8.9% for the samples $x \geq 0.8$ and again increased for $x = 1.0$ to 9.1%. Crystallite size and grain size directly relates to the porous structure of the sample as porosity is inversely proportional to crystallite size. Debye – Scherrer relation was employed to determine the average crystallite size (t XRD) of all the samples [30]; $XRD \ 0.9 \ t \ \cos \ \lambda = \ \beta \ \theta \ (5.4)$ where, 0.9

62%

MATCHING BLOCK 53/88

J

0201276d-de23-493f-a933-df7286b7da30

is the constant, λ - is the wavelength of incident radiation (X-ray) and β is the full-width at half

of the maximum intensity of peak. Calculated values of crystallite size from XRD data are given in Table 5.2 and its variation is shown in Fig.5.5. It is observed from Table 5.2 that the average crystallite size increased initially from 20.1 nm (Pure CCFO phase) to 25.6 nm ((40%) CCFO+(60%)BTO) and decreased thereafter to 21.2 nm for pure BTO phase. Variation in lattice parameter and average crystallite size may be related to the; i) chemical interaction occurred between the CCFO phase and BTO phase during the synthesis process of M-E composite, and/or ii) strain induced by both CCFO and BTO phases on each other.

Chapter-V 99 5.3.2 Williamson-Hall analysis The micro-strain induced in individual CCFO and BTO phases was investigated by using Williamson-Hall equation [31]: $4 \tan \beta \ \epsilon = \ \theta \ (5.5)$ Actually, total width of the peak is a combined effect of peak width due to strain induced in the crystallite and due to crystallite size, $D \ \epsilon \ \beta = \ \beta \ + \beta \ (5.6)$ using equations (5.4), (5.5) and (5.6) $0.9 \ 4 \ \tan \ D \cos \ \lambda \ \beta = \ \epsilon \ \theta + \ \theta \ (5.7)$ Rearranging equation (5.7) we get; $0.9 \ \cos \ 4 \ \sin \ D \ \lambda \ \beta \ \theta = \ \epsilon \ \theta + \ (5.8)$ Figs. 5.6 (a, b) shows the W-H plots of CCFO and BTO phases respectively. Plots are drawn between $4 \ \sin \theta$ versus $\beta \ \cos \theta$. Slope of linearly fitted lines gives the values of strain induced in the crystallites which are given in the inset of Figs. 5.6 (a, b) and are also given in Table 5.2. Positive values of lattice strains induced in CCFO phases indicating the tensile type of strain. The increasing BTO concentration in M-E composite initially increases the tensile strain in CCFO phase from 4.68×10^{-4} to 7.89×10^{-4} and thereafter further increase of BTO concentration decreases the tensile strain to 1.069×10^{-4} ($x = 0.8$). Simultaneously, the tensile strain in piezoelectric BTO phase reduces from 1.67×10^{-3} to 2.5×10^{-4} with the increasing concentration of BTO grains. This can be explained as increasing concentration of piezomagnetic CCFO phase induces positive tensile strain on piezoelectric BTO phase. The variation in strain values induced on both CCFO and BTO phase is in accordance with the variation of lattice parameters of individual phases. In

Chapter-V 100 other words, increasing increase in lattice strain in BTO phase due to increasing percentage of CCFO grains increases the lattice constant of BTO phase as illustrated in Fig. 5.3. Fig. 5.6 (c and d) illustrates the strain mechanism observed in CCFO+BTO M-E composites. The lattice constant of CCFO phase is observed twice than that of BTO phase and hence it was expected to induce comprehensive type strain on CCFO phase by BTO phase and due to larger lattice parameter CCFO phase was expected to exert tensile type strain on BTO crystallite (Fig. 5.6d). This expectation becomes true for BTO phase where tensile type of strain is observed for all compositions. In contrast, tensile strain was also observed for CCFO phase with a higher value of 7.89×10^{-4} for the composition (60%)CCFO+(40%)BTO. Majority of CCFO grains surrounds the BTO grains at lower BTO concentrations. Thus, there is a possibility of Ba and Ti ions to enter in the CCFO spinel lattice, where comparatively higher ionic radii of Ba ions may increase the lattice length of CCFO phase (Fig. 5.6c). 5.3.3 Scanning electron microscopy Secondary scattered electrons generated scanning electron micrographs of CCFO- BTO composites are shown in Fig. 5.7. Average grain size of all the samples from SEM micrographs was evaluated by using the software Image J. Variation of average grain size with BTO composition is depicted in Fig. 5.5 and the values are given in Table 5.2. From Table 5.2, it can be observed that for the samples $x \geq 0.8$, the average grain size (D) increases from 38 nm to 60 nm and for pure BTO phase it reduces to 54 nm. This variation of grain size with BTO concentration is analogues with the variation of average crystallite size obtained from the XRD analysis. The strain induced in CCFO-BTO phases is related to the increase in grain size of the composites. In the present M-E composites, both CCFO and BTO phases are polycrystalline in nature, where strain energy depends on crystal

Chapter-V 101 orientation and different grain sizes [32]. The CCFO phase may possess strong anisotropy in the elastic constants, which can set up inhomogeneous elastic strain energy in the composition which would promote abnormal growth of grain size. Here, CCFO phase experiences tensile strain and this strain released on the expense of increased grain size. The difference in crystallite sizes of the individual phases of the CCFO-BTO composite and chemical inhomogeneity of the composition may affect the grain size of the composite [33]. The distribution of individual phases within the composite also plays an important role in grain growth. The stoichiometric elemental analysis of the composite was done by using EDAX spectra for the selected samples (100%)CCFO and (40%)CCFO +(60%)BTO. EDAX spectra of

both (100%)CCFO and (40%)CCFO+(60%)BTO are shown in Fig. 5.8. Color mapping images of same samples were taken and are shown in Fig. 5.9 (a, b) respectively. Color mapping images confirms that the elements are uniformly distributed in the samples. EDAX spectra reveal that all the constituent elements in the composition are observed with their stoichiometric proportion and no loss of any constituent element is observed. The observed percentage of the elements from the analysis of EDAX spectra are given in Table 5.3 which are found in good agreement with their weight percentage in the composition. 5.3.4 Fourier transforms infrared spectroscopy Fig. 5.10 (a) represents the FTIR spectra of CCFO-BTO M-E composites recorded in the wavenumber range of 400 to 4000 cm⁻¹ and Fig. 5.10 (b) shows the expanded view of FTIR spectra at lower frequency range. Absorption band appeared near wavenumber 870 cm⁻¹ may be related to the perovskite tetragonal structure of the BTO phase [34]. Absorption bands observed in the wavenumber region 1100-1300 cm⁻¹ are attributed to the stretching vibrations of 3 NO⁻ ions and absorption bands in the range 1400-1700 cm⁻¹

Chapter-V 102 are related to the carboxyl group (COO⁻). Vibrations at 2400 cm⁻¹ are related to C-O group and absorption band near 3400 cm⁻¹ is corresponding to hydrogen bonded O-H groups [35]. Absorption bands observed around the wavenumber 425 cm⁻¹ and 570-600 cm⁻¹ as seen in expanded view (Fig. 5.10 (b)) are represents the bending vibrations of metal ions at octahedral – B and tetrahedral – A sites respectively, which is a characteristic feature of spinel ferrites. 5.3.5 Magnetic properties Fig. 5.11 depicts the magnetic hysteresis loops of CCFO-BTO M-E composites with the increasing percentage of BTO concentration. High coercive field and well saturated magnetization is observed in the hysteresis loops. By using these hysteresis curves,

87%	MATCHING BLOCK 55/88	W https://www.researchgate.net/publication/ ...
values of saturation magnetization (Ms), remnant magnetization (Mr) and coercivity (Hc) were		

obtained. Fig. 5.12(a) represents the variation of saturation magnetization, remnant magnetization and coercivity with the varying weight percentage of CCFO and BTO phases and the observed values are given in Table 5.4. It can be observed that the saturation magnetization and other parameters decreases with the increasing concentration of BTO phase in the composite because magnetic properties are only the characteristics of piezomagnetic-CCFO phase. Saturation magnetization gradually decreases from 45.53 (x = 0.0) to 2.371 emu/g (x = 0.8) with the increasing percentage of BTO phase. It can also be seen that the increasing BTO phase in CCFO-BTO composites reduces the remnant magnetization from 21.8 (x = 0.0) to 2.371 emu/g (x = 0.8). The reducing behaviour of Ms and Mr may be related to the decreasing percentage of ferromagnetic grains with the substitution of BTO grains in the composites. This type of magnetic behavior has also been observed in the literature reports [2, 9, 13, 36]. Surprisingly, coercive field increased initially from 637 Oe to 668 Oe for the samples x ≥

Chapter-V 103 0.4 and reduced thereafter with further increase in BTO concentration. Such type of variation in coercivity is may be related to the i) size of the crystallite and/or grains, and ii) lattice strain induced in the crystal lattice. Random anisotropy model can be employed to interpret the relation between coercivity and grain size [37]: $4 \mu_0 M_s K H_c \approx \frac{2 \mu_0 M_s K}{\delta} \left(\frac{L}{D} \right)^2$ (5.9) Where μ_0 is a dimensionless factor related to the crystal lattice, L is the magnetic exchange length, δ is the domain wall width, A is the exchange stiffness constant and K_u is the magnetocrystalline anisotropy constant. For $D > L$, the coercivity arising from grain boundaries is inversely proportional to the grain size. When the grain size is smaller than the magnetic exchange length, $L = (A/K_u)^{1/2}$, then H_c follows a D^{-6} power law [38] (eq. 5.9a). H_c is independent of D for $D \approx L$ (eq. 5.9b). If $D < \delta$, the coercivity follow the grain size as $\sim D^{-1}$ (eq. 5.9c), this is consistent with our experimental data. The increase in coercivity is result of increase of anisotropy energy with increase of crystallite size [39, 40]. Reports are available in the literature which shows that lattice strain also affects the variation in coercivity in ferrite materials [41-43]. It is observed that the tensile strain experienced by CCFO phase gradually increased with increase in BTO concentration which results in the increase in coercivity up to certain limit. 5.3.6 P-E loop measurements Variation in polarization (P) with electric field (E) (P-E hysteresis loop) measurement was taken for the investigation the room temperature ferroelectric properties of (1-x)CoCr_{0.3}Fe_{1.7}O₄ + (x)BaTiO₃ composites and is shown in Fig. 5.13. Pure

Chapter-V 104 piezoelectric phase (x = 1) exhibit the typical P-E hysteresis loop which confirms the ferroelectricity in the sample, but the P-E loop was not saturated. P-E loop of CCFO phase is very absorbent and not showing any ferroelectric characteristics. Maximum polarization (P_{max}) and remnant polarization (P_r) of M-E composites increased with the addition of BTO grains in CCFO-BTO composites which may be related to the electro- mechanical coupling, polarization

effect and lattice strain [44]. The higher order of CCFO phase dilutes the ferroelectric properties of composites. 5.3.7 Dielectric measurements Dielectric measurements of all the samples of CCFO-BTO composites

85%

MATCHING BLOCK 56/88

W

[https://www.researchgate.net/publication/...](https://www.researchgate.net/publication/)

were taken as a function of applied frequency in the range 50Hz to 50MHz.

The dielectric dispersion is observed in the dielectric plots. This dispersion may be occurs due to the Maxwell- Wagner type interfacial polarization which is also in good agreement with the Koop's phenomenological theory [45-47]. Variation in dielectric constant (ϵ') with applied frequency is shown in Fig. 5.14. Dielectric constant attends maximum value at lower frequency region and decreased rapidly with increase in frequency and almost remains constant at higher frequency region. Higher dielectric constant is observed in pure piezoelectric-BTO phase in contrast to the pure piezomagnetic-CCFO phase. This is closely related to the electrical conductivity of BTO and CCFO phases, where BTO phase possess relatively higher resistivity ($\sim 10^9 \Omega.m$) as compared to CCFO phase ($\sim 10^7 \Omega.m$). The observed maximum values of dielectric constant for CCFO-BTO composites are given in Table 5.5. The heterogeneous nature of CCFO-BTO phases at the interface could increase the space charge polarization, where space charges provided by the piezomagnetic-CCFO phase may stimulate at the CCFO and BTO interface due to the difference in permittivity's and resistivity's [48,49]. This may lead to increase in the space

Chapter-V 105 charge polarization with the applied electric field. Hence, as compared to the average dielectric constant of BTO and CCFO phase, higher dielectric constant was observed in composite materials. Strong strain coupling in BaTiO₃-based ferroelectrics is also acknowledged to direct the enhancement in the ferroelectric polarization [50, 51]. Thus, increase in dielectric constant and polarization could also be related to the strain induced CCFO and BTO in particular [52]. Further, under comprehensive strain polar metal phase can be stabilized in BTO phase [53]. The frequency dependent dielectric loss tangent ($\tan\delta$) is shown in Fig. 5.15. Variation of loss tangent as a function of frequency is analogues with the variation of dielectric constant. Pure BTO shows the lowest dielectric loss among all the investigated composite samples, whereas CCFO show the highest dielectric loss. The difference in dielectric loss between BTO and CCFO is may be related to the leakage current and electrical conductivity. In contrast to CCFO phase, BTO has least leakage current and lower electrical conductivity. The maxima observed in the $\tan\delta$ plots can be explained by using the relation: $\omega\tau = 1$ (5.10) where τ is the relaxation time and $\omega = 2\pi f$ max. Here, τ and the jumping probability per unit time are expressed as: $1/2p\tau =$ (5.11) Therefore the frequency of ac electric field; $f \text{ max} \propto p$ when the hopping frequency of electrons between Fe²⁺ ↔ Fe³⁺ ions became same. Maxima in the $\tan\delta$ plots are only observed for the CCFO content and is absent in BTO content due its higher resistivity.

Chapter-V 106 5.3.8 Magneto-electric measurements Dynamic method was employed to estimate the magnetoelectric coefficient, α_{ME} , of the CCFO-BBTO composite samples by using the following relation [49]: $ME_{AC} = V_{HD} / d \alpha =$ (5.12) where H_{AC} , V and d are the amplitude of sinusoidal magnetic field, voltage generated due to magnetoelectric effect and thickness of the specimen, respectively. Superimposed dc and ac magnetic fields give resultant field by the relation given below [49]: $H = H_{DC} + H_{AC} \sin \omega t$, (5.13) Frequency, f ($\omega = 2\pi f$), adjusted by a lock-in amplifier measure the output M-E voltage [53]: $V_{ME} = H_{DC} \alpha + H_{AC} \beta \sin \omega t$ (5.14) where β and α are quadratic and linear coefficient of ME coupling, respectively and $\alpha(H_{DC})$ is pseudo-linear coefficient. The obtained higher values of α_{ME} for the composite samples with dc magnetic field are given in Table 5.5 and its variation is shown in Fig. 5.16. It can be seen that, α_{ME} increased initially from 15.1 mV/Cm-Oe ($x = 0.2$) with the increase in H_{DC} and attained a maxima at 24.7 mV/Cm-Oe ($x = 0.6$). Further increase in H_{DC} decrease the value of α_{ME} . This behavior of α_{ME} is associated with the magnetostrictive property of piezomagnetic-CCFO phase. Magnetostriction of CCFO phase increased and attained saturation with the increase in dc magnetic field [55]. Magnetization in piezomagnetic-CCFO is controlled by the magnetic domain and domain size which can be influenced by the strain type of piezomagnetic-CCFO. Thus, tensile- strained CCFO may require a higher H_{DC} to reach the saturation. The external applied magnetic field transmits the strain induced in piezomagnetic-CCFO phase to piezoelectric BTO phase. This may generate the electric field in the piezoelectric BTO phase that

Chapter-V 107 produces ME voltage in the composite. The ME voltage generated in the ME composite is totally dependent on external magnetic field. Among all the compositions, the sample (40%)CCFO+(60%)BTO possess higher ME voltage coefficient $\alpha_{ME} = 24.7 \text{ mV/cm}\cdot\text{Oe}$ for the applied dc magnetic field of 1500 Oe. Comparable value of ME coefficient ($\alpha_{ME} = 24.1 \text{ mV/cm}\cdot\text{Oe}$) is observed for the composition (60%)CCFO+(40%)BTO. Values of ME coupling

coefficient α ME are given in Table 5.5. The lower value of α ME is observed for higher piezomagnetic-CCFO composition since it possess higher conductivity and leakage current compared to piezoelectric-BTO phase.

Chapter-V 108 REFERENCES [1] L. S. Ashwini, R. Sridhar, S. S. Bellad;

92%

MATCHING BLOCK 59/88

W

[https://www.researchgate.net/publication/...](https://www.researchgate.net/publication/)

Dielectric and magnetoelectric properties of Li-Mg ferrite: Barium titanate composites; Mater. Chem. Phys. 200 (2017) 136-145. [2]

A. S. Dzunuzovic; M. M. Vijatovic Petrovic, J. D. Bobic, N. I. Ilic, M. Ivanov, R. Grigalaitis, J. Banys, B. D. Stonjanovic;

100%

MATCHING BLOCK 63/88

W

[https://www.researchgate.net/publication/...](https://www.researchgate.net/publication/)

magneto-electric properties of $x\text{Ni}_{0.7}\text{Zn}_{0.3}\text{Fe}_2\text{O}_4-(1-x)\text{BaTiO}_3$ multiferroic composites;

Ceram. Inter. 44 (2018) 683-694. [3] S. E. Shirsath, C. Cazorla, T. Lu, L. Zhang, Y. Y. Tay, X. Lou, Y. Liu, S. Li, D. Wang, Interface-charge induced giant electrocaloric effect in lead free ferroelectric thin-film bilayers, Nano Letters 20 (2020) 1262-1271 [4] S. Archary, O. Jayakumar, A. Tyagi, Functional Materials 159 Elsevier Insights, USA, 2012. [5] S. L. Kadam, B. K. Chougule; Dielectric behaviour and magnetoelectric effect in $\text{Ni}_{0.5}\text{Co}_{0.5}\text{Fe}_2\text{O}_4+\text{Ba}_{0.8}\text{Pb}_{0.2}\text{TiO}_3$ ME composites; Mater. Lett. 59 (2005) 215-219. [6] U. Kuri, U. Pal, M. E. Mendoza;

95%

MATCHING BLOCK 58/88

W

[https://www.researchgate.net/publication/...](https://www.researchgate.net/publication/)

Structure and magnetic properties of the $\text{Co}_{1-x}\text{Ni}_x\text{Fe}_2\text{O}_4-\text{BaTiO}_3$ core shell nanoparticles, J. Magn. Magn. Mater. 442 (2017) 247. [7]

S. A. Khader, A. Parveez, A. Chaudhuri, M. S. Shekhawat, T. Sankarappa; Structural, dielectric and magnetic studies of ferrite-ferroelectric composites; Physica B: Phys. Cond. Matter. 584 (2020) 411665. [8] K. K. Patankar, V. L. Mathe, R. N. Patil, B. K. Chougule; Structural analysis, magnetic properties and magnetoelectric effect in piezomagnetic – piezoelectric composites; Mater. Chem. Phys. 96 (2006) 197-200. [9] S. R. Wadgane, S. T. Alone, A. Karim, G. Vats, S. E. Shirsath, R. H. Kadam,

95%

MATCHING BLOCK 60/88

W

[https://www.researchgate.net/publication/...](https://www.researchgate.net/publication/)

Magnetic field induced polarization and magnetoelectric effect in $\text{Na}_{0.5}\text{Bi}_{0.5}\text{TiO}_3-\text{Co}_{0.75}\text{Zn}_{0.25}\text{Cr}_{0.2}\text{Fe}_{1.8}\text{O}_4$ multiferroic composite, J. Magn. Magn. Mater. 47 (2019) 388-393

Chapter-V 109 [10] C.T.M. Dung, N.H.T. Thi, K.H.T. Ta, V.C. Tran, B.T. Le Nguyen, Relaxor behaviors in $x\text{BaTiO}_3-(1-x)\text{CoFe}_2\text{O}_4$ materials, J. Magn. 20 (2015) 353–359. [11] T. Woldu, B. Raneesh, M.R. Reddy, N. Kalarikkal, Grain size dependent magnetoelectric coupling of BaTiO_3 nanoparticles, RSC Adv. 6 (2016) 7886–7892. [12] A. Singh, I. Choudhary, S. Mehta, S. Dahiya, C.S. Walia, K. Raina, R. Chatterjee, Optimal multiferroic properties and enhanced magnetoelectric coupling in $\text{SmFeO}_3-\text{PbTiO}_3$ solid solutions, J. Appl. Phys. 107 (2010) 084106. [13] A. S. Gaikwad, R. H. Kadam, S. E. Shirsath, S. R. Wadgane, J. Shah, R. K. Kotnala, A. B. Kadam; Surprisingly high magneto-electric coupling in cubic $\text{Co}_{0.7}\text{Fe}_{2.3}\text{O}_4-\text{SrTiO}_3$ nano-composites; J. Alloys. Comp. 773 (2019) 564-570. [14] G. R. Gajula, L. R. Buddiga, K. N. C. Kumar, N. Vattikunta, M. Dasari; Effect of Gd and Nb on dielectric and magnetic transition temperature of $\text{BaTiO}_3-\text{Li}_{0.5}\text{Fe}_{2.5}\text{O}_4$ composites; Physica B: Cond. Matter. 560 (2019) 1-5. [15] S. E. Shirsath, X. Liu, M.H.N. Assadi, A. Younis, Y. Yasukawa, S. K. Karan, J. Zhang, J. Kim, D. Wang, A. Morisako, Y. Yamauchi, S. Li, Au quantum-dots engineered room temperature

crystallization and magnetic anisotropy in CoFe₂O₄ thin film, *Nanoscale Horizons*, 4, (2019) 434-444 [16] S. E. Shirsath, X. Liu, Y. Yasukawa, S. Li, A. Morisako, Switching of magnetic easy-axis using crystal orientation for large perpendicular coercivity in CoFe₂O₄ thin film, *Scientific Reports*, 6 (2016) 30074 [17] R. N. Bhowmik, M. C. Aswathi; Modified dielectric and ferroelectric properties in the composite of ferrimagnetic Co_{1.75}Fe_{1.25}O₄ ferrite and ferroelectric BaTiO₃ perovskite in comparison to Co_{1.75}Fe_{1.25}O₄ ferrite; *Comp. Part B*; 160 (2019) 457- 470.

Chapter-V 110 [18] S. M. Mane, P. M. Trimali, B. Ranjit, M. Khan, N. Khan, A. N. Tarale, S. B. Kulkarni; Studies on magnetocapacitance, dielectric, ferroelectric and magnetic properties of microwave sintered (1-x)(Ba_{0.8}Sr_{0.2}TiO₃)-x(Co_{0.9}Ni_{0.1}Fe₂O₄) multiferroic composite; *Solid State Sci.* 81 (2018) 43-50. [19] R. Sharma, P. Pahuja, R. P. Tandon;

100%

MATCHING BLOCK 61/88

W [https://www.researchgate.net/publication/ ...](https://www.researchgate.net/publication/)

Structural, dielectric, ferromagnetic, ferroelectric and ac conductivity studies of the BaTiO₃-CoFe_{1.8}Zn_{0.2}O₄ multiferroic particulate

composite; *Ceram. Inter.* 40 (2014) 9027-9036. [20]

91%

MATCHING BLOCK 62/88

W <https://docplayer.net/150337558-Doctor-of ...>

B. G. Toksha, S. E. Shirsath, M. L. Mane, S. M. Patange, S. S. Jadhav, K. M. Jadhav,

Auto-combustion high-temperature synthesis, structural and magnetic properties of CoCr_xFe_{2-x}O₄ (0 ≤ x ≤ 1.0), *J. Phys. Chem. C*, 115 (2011) 20905- 20912 [21] Y. Melikhov, J. E. Snyder, C. C. H. Lo, P. N. Matlage, S. H. Song, K. W. Dennis, D. C. Jiles, The Effect of Cr-Substitution on the magnetic anisotropy and its temperature dependence in Cr-substituted cobalt ferrite, *IEEE Trans. Magn.* 42 (2006) 2861 [22] G. N. Chavan, P. B. Belavi, L. R. Naik, B. K. Bammannavar, K. P. Ramesh, Electrical behavior of (y)Cd_{1-x}Ni_xFe₂O₄ (1-y)BaZr_{0.2}Ti_{0.8}O₃ composites, *Int. J. Sci. Eng. Res.* 5 (2014) 1171-1177. [23] D. Cao, X. Wang, L. Pan, H. Li, P. Jing, J. Wang, Q. Liu, Nonmetal sulfur-doped coral-like cobalt ferrite nanoparticles with enhanced magnetic properties, *J. Mater. Chem. C*. 4 (2016) 951-957. [24] M.A. Almessiere, Y. Slimani, A.D. Korkmaz, N. Taskhandi, M. Sertkol, A. Baykal, S. E. Shirsath, İ. Ercan, B. Özçelik, Sonochemical synthesis of Eu³⁺ substituted CoFe₂O₄ nanoparticles and their structural, optical and magnetic properties, *Ultrason. Sonochem.* 58 (2019) 104621

Chapter-V 111 [25] Y. Slimania, M.A. Almessiere, M. Sertkol, S. E. Shirsath, A. Baykal, M. Nawaz, S. Akhtar, B. Ozcelik, I. Ercan, Structural, magnetic, optical properties and cation distribution of nanosized Ni_{0.3}Cu_{0.3}Zn_{0.4}Tm_xFe_{2-x}O₄ (0.0 ≤ x ≤ 0.10) spinel ferrites synthesized by ultrasound irradiation, *Ultrason. Sonochem.* 57 (2019) 203-211 [26] R.S. Yadav, I. Kuřitka, J. Vilcakova, J. Havlica, L. Kalina, P. Urbánek, M. Machovsky, D. Skoda, M. Masař, M. Holec, Sonochemical synthesis of Gd³⁺ doped CoFe₂O₄ spinel ferrite nanoparticles and its physical properties, *Ultrason. Sonochem.* 40 (2018) 773–783. [27] R. P. Mahajan, K. K. Patankar, M. B. Kothale, S. C. Choudhari, V. L. Mathe, S. A. Patil,

83%

MATCHING BLOCK 65/88

W [https://www.researchgate.net/publication/ ...](https://www.researchgate.net/publication/)

Magnetolectric effect in cobalt ferrite – barium titanate composites and their electrical properties; *Pramana J. Phys.* 58 (5) (6) (2002) 1115. [28]

S. L. Kadam, K. K. Patankar, V. L. Mathe, M. B. Kothale, R. B. Kale, B. K. Chougule; Electrical properties and magnetolectric effect in Ni_{0.75}Co_{0.25}Fe₂O₄ + Ba_{0.8}Pb_{0.2}TiO₃ composites; *Mater. Chem. Phys.* 78 (2003) 684. [29] A. M. Abdeen, O. M. Hemeda, E. E. Asssem, M. M. El-Sehly;

100%

MATCHING BLOCK 67/88

W [https://www.researchgate.net/publication/ ...](https://www.researchgate.net/publication/)

Structural, electrical and transport phenomena of Co ferrite substituted by Cd;

J. Magn. Magn. Mater. 238 (2002) 75-83. [30] R. H. Kadam, A. R. Biradar, M. L. Mane, S. E. Shirsath, Sol-gel auto-combustion synthesis of $\text{Li}_{3x}\text{MnFe}_{2-x}\text{O}_4$ and their characterizations, J. Appl. Phys. 112 (2012) 043902 [31] W.H. Hall, X-ray line broadening from field aluminium and wolfram; Acta Metall. 1 (1953) 22. [32] M. Murakami, T.-S. Kuan and I. A. Blech: Mechanical Properties of Thin Films on Substrates in TREATISE ON MATERIALS SCIENCE AND TECHNOLOGY, ed. by K. N. Tu and R. Rosenberg, (Academic press, New York, 1982).

Chapter-V 112 [33] R. K. Kotnala, J. Shah, B. Singh, H. Kishan, S. Singh, S. K. Dhawan, A. Sengupta, Humidity response of Li-substituted magnesium ferrite, Sens. Actuators B Chem. 129 (2008) 909e914. [34] A. Mishra, Niyati Mishra, Influence of copper doping on physical properties of barium titanate, J. Phys. Conf. 365 (4) (2012) 012009. [35] Mohd. Hashim, Alimuddin, S. Kumar, S. E. Shirsath, R. K. Kotnala, J. Shah, R. Kumar, Synthesis and characterization of Ni²⁺ substituted cobalt ferrite nanoparticles; Mater. Chem. Phys. 139 (2013) 364-374 [36] P. A. Jadhav, M. B. Shelar, B. K. Chaugule;

86%

MATCHING BLOCK 64/88

W

[https://www.researchgate.net/publication/ ...](https://www.researchgate.net/publication/...)

Magnetoelectric effect in three phase $y(\text{Ni}_{0.5}\text{Cu}_{0.2}\text{Zn}_{0.3}\text{Fe}_2\text{O}_4)_{1-y}(50\%\text{BaTiO}_3 + 50\%\text{PZT})$ ME composites; J. Alloys Compd. 479 (2009) 385. [37]

R. Alben, J. J. Becker, M.C. Chi; Random anisotropy in amorphous ferromagnets; J. Appl. Phys. 49 (1978) 1653 [38] G. Herzer, Grain size dependence of coercivity and permeability in nanocrystalline ferromagnets; IEEE Trans. Magn., 26 (1990) 1397. [39] R. S. Yadav, I. Kuřitka, J. Vilcakova, J. Havlica, J. Masilko, L. Kalina, J. Tkacz, J. Švec, V. Enev and M. Hajdúchová;

100%

MATCHING BLOCK 68/88

W

[https://link.springer.com/article/10.1007 ...](https://link.springer.com/article/10.1007...)

Impact of grain size and structural changes on magnetic, dielectric, electrical, impedance and modulus spectroscopic characteristics of CoFe_2O_4 nanoparticles synthesized by honey mediated sol-gel combustion method; Adv. Nat. Sci.: Nanosci. Nanotechnol. 8 (2017) 045002 [40]

S.

100%

MATCHING BLOCK 66/88

W

[https://docplayer.net/150337558-Doctor-of ...](https://docplayer.net/150337558-Doctor-of...)

E. Shirsath, S. S. Jadhav, B. G. Toksha, S. M. Patange, K. M. Jadhav,

Influence of Ce⁴⁺ ions on the structural and magnetic properties of NiFe_2O_4 ; J. Appl. Phys. 110, (2011) 013914 [41]

100%

MATCHING BLOCK 70/88

W

[https://www.researchgate.net/publication/ ...](https://www.researchgate.net/publication/...)

B. H. Liu and J. Ding; Strain-induced high coercivity in CoFe_2O_4 powders; Appl. Phys. Lett. 88 (2006) 042506.

Chapter-V 113 [42] S. E. Shirsath, X. Liu, Y. Yasukawa, S. Li, A. Morisako, Stitching of magnetic easy-axis using crystal orientation for large perpendicular coercivity in CoFe_2O_4 thin film; Sci. Rep. 6 (2016) 30074. [43] A.S. Ponce, E.F. Chagas, R.J. Prado, C.H.M. Fernandes, A.J. Terezo, E. Baggio-Saitovitch, High coercivity induced by mechanical milling in cobalt ferrite powders, J. Magn. Magn. Mater. 344 (2013) 182-187 [44] A. S. Fawzi, A. D. Sheikh, V. L. Mathe; Dielectric, electrical and magnetoelectric characterization

80%

MATCHING BLOCK 71/88

W

[https://www.researchgate.net/publication/ ...](https://www.researchgate.net/publication/...)

of (x)Ni 0.8 Zn 0.2 Fe 2 O 4 +(1-x)Pb 0.93 La 0.07 (Zr 0.60 Ti 0.40)O 3 composites;

Mater. Res. Bull. 45 (2010) 1000. [45] J. C. Maxwell, Electricity Magnetism Vol.1, Oxford Uni. Press, Oxford, 1954. Section 328. [46] K.W. Wagner; The distribution of relaxation times in typical dielectrics; Ann.

81%

MATCHING BLOCK 69/88

W

[https://docplayer.net/150337558-Doctor-of ...](https://docplayer.net/150337558-Doctor-of-...)

Phys.
40 (1973) 817.

[47] C.G. Koop; On the dispersion of resistivity and dielectric constant of some semiconductors at audiofrequencies; Phys. Rev. 83 (1951) 121.

[48]

R. Valenzuela, Magnetic ceramics, (Cambridge University Press, 1994). [49] A. S. Gaikwad, S. E. Shirsath, S. R. Wadgane, R. H. Kadam, J. Shah, Magneto- electric coupling and improved dielectric constant of BaTiO 3 and Fe-rich (Co 0.7 Fe 2.3 O 4) ferrite nano-composites; J. Magn. Mater. 465 (2018) 508-541. [50] K. J. Choi, M. Biegalski, Y. L. Li, A. Sharan, J. Schubert, R. Uecker, P. Reiche, Y. B. Chen, X. Q. Pan, V. Gopalan, L. Q. Chen, D. G. Schlom, C. B. Eom, Enhancement of ferroelectricity in strained BaTiO 3 thin films; Science 306, 1005 (2004).

Chapter-V 114 [51] D. G. Schlom, L.-Q. Chen, C.-B. Eom, K. M. Rabe, S. K. Streiffer, and J.-M. Triscone; Strain tuning of ferroelectric thin films; Annu. Rev. Mater. Sci. 37, 589 (2007). [52] S. Zhu, M. Yang, X. Gu, P. Zhou, C. Zhong, Strain-induced structural phase transition and the rotation of polarization in BaTiO 3 films, Comp. Mater. Sci. 181 (2020) 109713 [53] C. Ma, K. Jin, C. Ge, G. Yang, Strain-engineering stabilization of BaTiO 3 -based polar metals, Phys. Rev. B 97 (2018) 115103 [54] J. P. Rivera, The linear magnetoelectric effect in LiCoPO 4 revisited; Ferroelectrics 161 (1994) 147. [55] S. V. Suryanarayana; Magnetoelectric interaction phenomena in materials; Bull. Mater. Sci. 17 (1994) 1259.

Chapter-V 115 Fig. 5.1: Flow chart of CCFO-BTO composite synthesis.

Chapter-V 116 Fig.5.2: (a) Rietveld refined XRD patterns of CCFO+BTO composites, (b) crystal structure of CCFO cubic spinel ferrite and (c) crystal structure of perovskite BTO.

Chapter-V 117 Fig. 5.3: Variation in lattice constants of piezomagnetic and piezoelectric phases. Here, (A) CCFO, (B) (80%)CCFO + (20%)BTO, (C) (60%)CCFO + (40%)BTO, (D) (40%)CCFO + (60%)BTO, (E) (20%)CCFO + (80%)BTO and (F) BTO.

Chapter-V 118 Fig. 5.4: Variation of X-ray density (d_x) and percentage porosity (P) with composition 'x' for CCFO+BTO composites.

Chapter-V 119 Fig. 5.5: Variation in crystallite size t XRD obtained from XRD and grain size D obtained from SEM. Here, (A) CCFO, (B) (80%)CCFO + (20%)BTO, (C) (60%)CCFO + (40%)BTO, (D) (40%)CCFO + (60%)BTO, (E) (20%)CCFO + (80%)BTO and (F) BTO.

Chapter-V 120 Fig. 5.6: W-H plots of (a) piezomagnetic-CCFO phase and (b) piezoelectric – BTO phase in (x)CoCr 0.3 Fe 1.7 O 4 + (1-x)BaTiO 3 composites, (c)perovskite BTO structure embedded in cubic spinel lattice, and (d) strain mechanism in cubic spinel CCFO and perovskite BTO structures.

Chapter-V 121 Fig. 5.7: SEM micrographs of (x)CoCr 0.3 Fe 1.7 O 4 +(1-x)BaTiO 3 where (a) CCFO (b) (80%)CCFO + (20%)BTO (c) (60%)CCFO + (40%)BTO (d) (40%)CCFO + (60%)BTO, (e) (20%)CCFO + (80%)BTO and (f) BTO

Chapter-V 122 Fig. 5.8: EDAX patterns of (1-x) CoCr 0.3 Fe 1.7 O 4 + (x) BaTiO 3 (x = 0.0, and 0.4)

Chapter-V 123 Fig. 5.9(a): Color mapping of (1-x) CoCr 0.3 Fe 1.7 O 4 + (x) BaTiO 3 (x = 0.0)

Chapter-V 124 Fig. 5.9(b): Color mapping of (1-x) CoCr 0.3 Fe 1.7 O 4 + (x) BaTiO 3 (x = 0.4)

Chapter-V 125 Fig.5.10: (a) FTIR spectra of (x)CoCr 0.3 Fe 1.7 O 4 +(1-x)BaTiO 3 where, (a) (80%)CCFO + (20%)BTO (b) (60%)CCFO + (40%)BTO (c) (40%)CCFO + (60%)BTO and (d) (20%)CCFO + (80%)BTO. (b) Expanded view of low

wavelength region FTIR spectra.

Chapter-V 126 Fig.5.11: Variation magnetization (M) with applied magnetic field (H).

Chapter-V 127 Fig. 5.12: (a) Variation in saturation magnetization (Ms), remnant magnetization (Mr), coercivity (Hc) with composition and (b) shows the expanded view of M-H loops at lower magnetic field.

Chapter-V 128 Fig. 5.13: Variation in polarization (P) with applied electric field (E) measured at a frequency of 10 Hz for (1-x)CoCr 0.3 Fe 1.7 O 4 +(x)BaTiO 3 composites

Chapter-V 129 Fig. 5.14: Variation of dielectric constant (ε') with frequency for (1-x) CoCr 0.3 Fe 1.7 O 4 + (x) BaTiO 3

Chapter-V 130 Fig. 5.15: Variation of dielectric loss tangent (tan δ) with frequency for (1-x) CoCr 0.3 Fe 1.7 O 4 + (x) BaTiO 3

Chapter-V 131 Fig. 5.16: Variation of magnetoelectric coupling coefficient (α ME) with applied magnetic field of (x)CoCr 0.3 Fe 1.7 O 4 +(1-x)BaTiO 3 composites

Chapter-V 132 Table 5.1: Rietveld parameters, lattice constant (a), X-ray density (d x) and porosity (P) for CCFO-BTO composites. 'x' Rietveld Parameters Lattice Constant 'a' (Å) d x (gm/cc) P (%) XXXX 2 R EXP (%) R WP (%) R P (%) Ferrite Phase Ferroelectric Phase
 0.0 1.12 0.823 0.901 0.591 8.3730 --- 5.401 13.0 0.2 1.09 1.008 1.057 0.665 8.3749 4.021 5.521
 12.3 0.4 1.21 1.194 1.374 0.903 8.3774 4.015 5.634 11.7 0.6 1.13 1.509 1.603 1.153 8.3746 4.009 5.766 10.4 0.8 1.44 1.842
 2.213 1.653 8.3738 4.006 5.893 8.9 1.0 1.93 2.520 3.500 2.420 --- 4.005 6.015 9.1

Chapter-V 133 Table 5.2: Crystallite size (t) and lattice strain induced in CCFO-BTO composites. Comp. 'x' Crystallite Size 't' (nm) Lattice strain (εεεε) XRD SEM CCFO BTO 100%(CCFO) 20.1 38 --- --- 80%(CCFO)+20%(BTO) 21.4 42 4.68x10 -4 1.67x10 -3 60%(CCFO)+40%(BTO) 23.2 46 7.89x10 -4 1.12x10 -3 40%(CCFO)+60%(BTO) 25.6 55 6.24x10 -4 6.09x10 -4 20%(CCFO)+80%(BTO) 24.7 60 1.069x10 -4 2.5x10 -4 100%(BTO) 21.2 54 --- ---

Chapter-V 134 Table 5.3: Observed elemental composition in atomic weight % of constituent ions observed from EDAX patterns for (1-x) CoCr 0.3 Fe 1.7 O 4 + (x) BaTiO 3. Composition Elemental composition in atomic weight (%) Co Cr Fe O Ba Ti 100%(CCFO) 28.59 4.74 38.56 28.12 --- ---- 60%(CCFO)+40%(BTO) 16.00 2.53 27.21 22.06 20.02 12.18

Chapter-V 135

Table 5.4:

95% **MATCHING BLOCK 74/88** **W** [https://www.researchgate.net/publication/...](https://www.researchgate.net/publication/)

Saturation magnetization (M S), Remnant magnetization (M r), coercivity (H C)

and remnant ratio (M r /M S) of (1-x) CoCr 0.3 Fe 1.7 O 4 + (x) BaTiO 3. Comp. 'x' '

73% **MATCHING BLOCK 72/88** **W** [http://pr.hec.gov.pk/jspui/bitstream/123 ...](http://pr.hec.gov.pk/jspui/bitstream/123...)

M S '
 (emu/gm)
 'M r '
 (emu/gm)
 (M r /M S)
 'H C '
 (Oe)
 100%(

CCFO) 45.53 21.8 0.479 637 80%(CCFO)+20%(BTO) 25.84 12.02 0.465 641 60%(CCFO)+40%(BTO) 16.727 7.7 0.460 668
 40%(CCFO)+60%(BTO) 7.8 3.25 0.417 635 20%(CCFO)+80%(BTO) 2.371 1.12 0.472 631

Chapter-V 136 Table 5.5: Dielectric constant (ε') and Magnetoelectric Conversion factor (dE/dH) of (1-x) CoCr 0.3 Fe 1.7 O 4 + (x) BaTiO 3. Composition Dielectric Constant (ε) Magnetoelectric Conversion factor [dE/dH] H (mV/Cm-Oe) 100%

(CCFO) 208.2 --- 80%(CCFO)+20%(BTO) 527.1 15.1 60%(CCFO)+40%(BTO) 923.4 24.1 40%(CCFO)+60%(BTO) 1011.5 24.7
20%(CCFO)+80%(BTO) 1019.12 22 100%(BTO) 1289.25 ---

137 CHAPTER – VI RESULTS AND DISCUSSION ON (1-x)Mn 0.7 Zn 0.3 Fe 2 O 4 +(x)BaTiO 3 CONTENTS 6.1 Introduction :
138 6.2 Materials and methods : 139 6.2.1 Synthesis of MZFO : 139 6.2.2 Synthesis of BTO : 140 6.2.3 Synthesis of MZFO-
BTO : 140 6.2.4 Characterization techniques : 140 6.3 Results and discussion : 141 6.3.1 XRD analysis : 141 6.3.2 W-H
analysis : 143 6.3.3 Scanning electron microscopy : 144 6.3.4 Elemental analysis : 145 6.3.5 Fourier transform infrared
spectra : 145 6.3.6 Magnetic properties : 145 6.3.7 Dielectric measurements : 146 6.3.8 Magneto-electric properties : 147
References : 149 Figures : 154 Tables : 170 This part of the thesis is accepted for publication in Journal of Materials:
Materials in electronics (Accepted) (ISSN: 1573-482X)

Chapter-VI 138 6.1 INTRODUCTION Now days, the term multiferroic composites covers the materials which simultaneously possesses any type of ferromagnetic, ferroelectric and/or ferroelastic properties [1]. Composites particularly consisting piezomagnetic and piezoelectric phases are known as magnetoelectric composites in which the ME effect is predominant. Single phase materials have several drawbacks to show the ME effect at room temperature and hence can be observed only in composite structure and absent in the constituent phases [2]. Magnetoelectric effect is a combine property of material in which dielectric polarization occurs in piezoelectric material due to the application dc/ac magnetic field and magnetization occurs in piezomagnetic material due to presence of dc/ac electric field due to the interaction between the magnetic and electric dipole [3-6]. In the present era ME composites have attracted much more attention because of their unique properties and wide applications in multifunctional devices viz. sensors, isolators, phase shifters, modulators, wave guides, transducers, etc. [7-11]. High ME effect in magnetoelectric composites can be attained by using the proper piezomagnetic and piezoelectric phases and their weight proportion in the composite. The mechanical coupling formed between piezoelectric-piezomagnetic phases produces the ME effect in the composites [12-13]. When ME-composite is placed in the external magnetic field, strain is developed in piezomagnetic phase due to magnetostriction phenomena which in turn induces the stress in piezoelectric material and as a result due to electrostriction phenomena an electric polarization is induced in piezoelectric phase [14]. It is very important to select the piezomagnetic and piezoelectric phases in order to produce the ME composite with enhanced magnetoelectric and dielectric properties. Numerous papers have been published on ME composited by changing the ferrite and ferroelectric phases and their concentrations in the composites [15-19]. Ferrites with spinel

Chapter-VI 139 structure are known for their high magnetic permeability and high resistivity having widespread applications in high frequency range [20]. Properties of ferrites can be modified by choosing the appropriate dopant and by changing the synthesis routs and sintering conditions [21-23]. BaTiO 3 , PbTiO 3 and SrTiO 3 are most commonly used piezoelectric phases for the preparation of ME composites. In the present investigation we have prepared the series of ME composite consisting Mn 0.7 Zn 0.3 Fe 2 O 4 (MZFO) as piezomagnetic phase and BaTiO 3 (BTO) as piezoelectric phase. Composites were obtained by mixing the MZFO and BTO phases with their weight proportion in the series (1-x) Mn 0.7 Zn 0.3 Fe 2 O 4 + (x) BaTiO 3 (x = 0.0, 0.25, 0.50, 0.75 and 1.0).

100%

MATCHING BLOCK 73/88

W [http://pr.hec.gov.pk/jspui/bitstream/123 ...](http://pr.hec.gov.pk/jspui/bitstream/123...)

X-ray diffraction,
scanning electron microscopy, energy dispersive X-ray

analysis, infrared spectra, vibrating sample magnetometer, ME effect measurement technique and two-probe technique were employed to study the structural, magnetic and dielectric behaviour of MZFO-BTO composites. 6.2 MATERIALS AND METHODS 6.2.1 Synthesis of MZFO MZFO (Mn 0.7 Zn 0.3 Fe 2 O 4) nanoparticles were produced by using the sol-gel auto- combustion technique. AR grade metal nitrates of the constituent elements were taken with their stoichiometric proportion in the composition and mixed thoroughly in 100ml distilled water. Anhydrous citric acid was used as chelating agent. pH=7 of the solution was maintained by adding the liquid ammonia drop wise. The whole mixture was subjected to hot plate with magnetic stirrer for continuous stirring at constant temperature 90 0 C. After couple of hours the mixture is converted into viscous sol and within few minutes becomes dried gel. The dried gel was suddenly burnt by self ignition process and an ash was obtained. The burnt ash was then pre-sintered at 600 0 C for 4 hours.

Chapter-VI 140 6.2.2 Synthesis of BTO BTO phase of the ME composite was also obtained by using sol-gel technique. Titanium butoxide Ti(OC 4 H 9) 4 and barium acetate Ba(OOCCH 3) 2 were used as starting materials and dissolved separately in ethanol and acetic acid separately. The mixtures were stirred individually for 1 hour and then mixed together. The mixture is then subjected for continuous stirring at 100 0 C. Nearly after 2 hours, the mixture is converted into dried

powder. Finally the powder was pre-sintered at 800 °C for 4 hours. 6.2.3 Synthesis of MZFO-BTO Standard ceramic route is employed to obtain the MZFO-BTO composites. Individual phases MZFO and BTO were mixed with their weight proportion in the composites and grounded for 2.5 hours in order to obtain the homogeneous mixture. The grounded mixtures were finally sintered at 800 °C for 4 hours and again grinded to obtain the fine particles of MZFO-BTO composites. Fig. 6.1 represents the flow chart of synthesis steps involved in the fabrication of MZFO-BTO composites. 6.2.4 Characterization techniques Crystallographic structure of the ME composites and identification of constituent phases was done by using room temperature X-ray diffraction technique. All the XRD patterns were recorded on powder X-ray diffractometer (Rigaku, Ultima - IV) by using Cu-K α radiation ($\lambda=1.5406 \times 10^{-10}$ m). The scanning rate was maintained at 2° per minute in the 2θ range of 20° to 80°. Backscattered electron images produced by scanning electron microscope (FE-SEM; HITACHI S-4800) were used to study the surface morphology of the samples and to estimate the average grain size of the composites. Energy dispersive X-ray analysis technique was employed to obtain the elemental

Chapter-VI 141 percentage in the composition. Fourier transform infrared spectra of all

100%

MATCHING BLOCK 79/88

W

[https://www.researchgate.net/publication/...](https://www.researchgate.net/publication/)

the samples were recorded in the wave number range of 300cm⁻¹

to 4000cm⁻¹ at room temperature on the infrared spectrometer (Model 783, Perkin Elmer). Powder samples were mixed with KBr in the ratio 1:250 by weight. The mixture was then pressed with the help of hydraulic press in a cylindrical die to obtain disc shaped samples of about 1 mm thickness. By varying the magnetic field from 0 Oe to 20000 Oe in vibrating sample magnetometer, hysteresis loops of all the samples were traced at room temperature. Disc shaped samples were used to obtain the dielectric data by using two-probe technique. A silver paste is applied on both circular faces of the disc in order to get the good ohmic contact with electrodes of the LCR – Q meter. As a function of applied frequency, all the dielectric measurements were taken out on a Hioki 3532-50 LCR HITESTER in the frequency range 50Hz to 50MHz. The ME coefficient of composite material (at $H_{ac} = 50$ Oe, voltage 1.4 V and $f = 999$ Hz) measurement was carried out with DC magnetic field in the range of (0 – 8000 Oe.) with interval of 500 Oe. All the samples are poled at 5 kV/cm before the ME analysis. 6.3 RESULTS AND DISCUSSION 6.3.1 XRD analysis Fig. 6.2 shows the room temperature X-ray diffraction patterns of the samples of (1-x) Mn_{0.7}Zn_{0.3}Fe₂O₄ + (x) BaTiO₃ (x = 0.0, 0.25, 0.50, 0.75 and 1.0) recorded in the 2θ range of 20° to 80° by using Cu-K α radiations ($\lambda=1.5406 \times 10^{-10}$ m). All the diffraction peaks observed in the XRD patterns are well indexed by their constituent phases. Sharpness and well-broadening Bragg's lines confirms the nano-crystallinity of the samples. Bragg's lines observed for piezomagnetic phase (MZFO) are indexed by the planes (220), (311), (222), (400), (422), (440) belongs to the cubic spinel structure and well matched to the international database (ICCD No. 01-074-2401, Space group-Fd-3 m).

Chapter-VI 142 It is observed that peaks referred to MZFO phase shifted slightly towards the higher 2θ angles and peak intensity decreased with the increasing percentage of BTO phase in the composite which in turn decreases the lattice parameter. Similarly, for the piezoelectric phase, reflections are observed for the planes (100), (110), (111), (200), (210), (211), (220), (300) and (310) which confirms the perovskite structure of BTO (ICDD No. 01-078-2738, Space group – P 4 m m). As seen in the XRD patterns, absence of undesired and un-indexed peaks confirms the successful formation pure bi-phase composition of each sample. Individually calculated lattice parameters of both piezomagnetic and piezoelectric phases by using the relation discussed elsewhere [24] shows decreasing trend with the dilution of MZFO concentration (Fig. 6.3). The lattice constant of piezomagnetic MZFO phase 8.431 Å to 8.413 Å with the addition of BTO phase in the composite. While as the lattice parameter of BTO phase reduce from 4.021 Å to 4.005 Å and the computed values are listed in Table 6.1. This small decrement in lattice lengths of both phases may be related to the stress developed within the composite material due to the strain induced by distinct phases on each other and the chemical interaction occurred within the distinct phases during synthesis [23, 25]. X-ray density of all the samples of MZFO-BTO composites was estimated by using the molecular weight and cell volume in the equation discussed elsewhere [26]. The computed values of X-ray density as a function of BTO concentration are given in Table 6.1 and its variation is illustrated in Fig. 6.4. It can be seen that X-ray density increases from 5.318 gm/cc to 6.027 gm/cc with the addition of BTO phase in MZFO phase. The porosity observed in the samples was estimated by using following relation [26]; $(\rho) (\rho) X B B d d P \% 100 d - = \times (6.1)$

Chapter-VI 143 Fig. 6.4 illustrates the variation of percentage porosity with the increasing concentration of BTO phase in the composite and the computed values are listed in Table 6.1. Porous structure of the sample is directly related to the

size of crystallites in the inverse proportion and hence decreases from 28.80% to 20.25% with the increasing percentage of BTO phase in the composite. Average size of MZFO-BTO crystallites was determined by taking the peak broadenings (FWHM) and Bragg's positions (θ) in the well-known Debye Scherrer relation [27] given below: $\text{avg. FWHM} = \frac{0.9 \lambda}{t \cos \theta}$ (6.2) Average crystallite size (t avg.) obtained from XRD analysis for all the compositions of MZFO-BTO varies from 15.36 nm to 21.94 nm (Table 6.1) and the variation is shown in Fig. 6.5. 6.3.2 W-H analysis The lattice distortion and imperfection in crystal induces an internal strain which may causes the XRD line broadening [28]. The strain developed in the crystal lattice due to defects and distortion can be given by [29]; $\epsilon = \frac{4 \tan \beta}{hkl} \theta$ (6.3) In addition to the crystallite size, induced strain modifies the Scherrer equation by summing and rearranging the equations (6.2) and (6.3), we get; $\frac{0.9 \lambda}{4 \cos \theta} \frac{1}{\sin^2 \theta} = \frac{1}{t} + \epsilon \theta$ (6.4) Equation (6.4) is well – known Williamson – Hall equation in which an assumption was made that the all crystallographic planes experiences uniform micro-

Chapter-VI 144 strain. The strain induced within the crystal lattice was obtained from slope of the linearly fitted graph plotted between $\frac{hkl \cos \theta}{4 \sin^2 \theta}$ and $4 \sin \theta$. Fig. 6.6 represents the W-H plots of individual piezomagnetic (left panel) and piezoelectric (right panel) phases of MZFO- BTO composites for which all intensive peaks were considered. The lattice strain observed for MZFO phase shows negative values and ranges from -2.01×10^{-4} to -8.36×10^{-6} which indicating that piezomagnetic phase experiences a compressive type strain which gradually increases with increasing percentage of BTO in the composite. While as, BTO phase experience positive (tensile type) strain which reduces from 9.30×10^{-4} to 5.40×10^{-4} with the decreasing percentage of MZFO in the composite [30]. Induced strain in both MZFO and BTO phases is in accordance with the decreasing behaviour of lattice parameter. 6.3.3 Scanning electron microscopy SEM images and grain size distribution histograms of $\text{Mn}_{0.7} \text{Zn}_{0.3} \text{Fe}_2 \text{O}_4 + x \text{BaTiO}_3$ for the samples $x = 0.0, 0.25, 0.50,$ and 0.75 are presented in Fig. 6.7. Average grain size was estimated by taking into account the linear dimensions of several grains and by using the software Image Scanning electron micrographs indicates that the agglomeration of smaller particles have been formed and hence the grain size varies. The average grain size obtained from histograms is found in the range 36.066 nm to 54 nm and the variation is shown in Fig. 6.5 which is in consistent with the variation of average crystallite sizes obtained from XRD analysis. The chemical homogeneity of the sample and different crystallite sizes of the individual phases may affects the distribution of grain size and hence asymmetric grains are observed in the SEM images [31].

Chapter-VI 145 6.3.4 Elemental analysis In order to confirm the stoichiometric proportion of constituents in MZFO-BTO composites, EDAX spectra of typical samples (100%)MZFO and (25%)MZFO + (75%)BTO were collected and are shown in Fig. 6.8 and also, the color mapping images of same compositions are shown in Fig. 6.9 (a and b). Analysis of EDAX spectra and color mapping images confirms that, all the constituent elements are present in the compositions and their percentage observed from EDAX spectra is analogous with the stoichiometric proportion in the composites. The observed weight percentage of constituent elements is given in Table 6.2. 6.3.5 Fourier Transform Infrared spectra Fig. 6.10 represents the FTIR spectra of MZFO-BTO composites recorded in the wavenumber range of 400 cm^{-1} to 4000 cm^{-1} . Five strong absorption peaks were observed for all the samples out of them two between 400 cm^{-1} to 700 cm^{-1} , and other three at around 1400 cm^{-1} , 2275 cm^{-1} and 3400 cm^{-1} respectively. The two fundamental bands observed within the range 400 cm^{-1} to 700 cm^{-1} are attributed to the stretching vibrations of metal ions and oxygen ions at tetrahedral – A and octahedral – B sites [32]. The absorption bands observed around 1400 cm^{-1} are related to the vibrations of NO_3^- ions and COO^- (Carboxyl group), the absorption bands around 2275 cm^{-1} are related to the vibrations of C-O group and the absorption bands observed around 3400 cm^{-1} are related to the O-H groups [33]. 6.3.6 Magnetic properties Magnetic hysteresis loops of MZFO-BTO composites were recorded at room temperature as a function of applied field H and are illustrated in Fig. 6.11. Well saturated

Chapter-VI 146 magnetic ordering at room temperature in all samples (except pure BTO) is observed exhibiting the typical behaviour of ferromagnetic material. The observed hysteresis curves are basically representing ferromagnetic phase in the composite. As the MZFO concentration in composites decreases,

100%

MATCHING BLOCK 75/88

W

[https://www.researchgate.net/publication/ ...](https://www.researchgate.net/publication/)

the saturation magnetization decreases from 33.12 emu/gm to 4.54 emu/gm

and found zero for pure BTO phase. The variation

of saturation magnetization (M_s), remnant magnetization (M_r) and coercivity (H_c)

is illustrated in Fig. 6.12. The lesser values of M_s in composites than the pure MZFO are due to the increasing voids among the grains breaking the magnetic ordering between the grains which in result decreases the magnetic parameters [34]. The decreasing MZFO grains in the composites also decreases the magnetic parameters of the composite with increase in BTO phase. The remnant magnetization (M_r) decreases from 10.58 emu/gm to 0.49 emu/gm and coercivity decreases from 565 Oe to 23 Oe for the composite materials with the increasing percentage of nonmagnetic BTO grains (Table 6.3). The increase in average grain size with the increasing concentration of nonmagnetic piezoelectric phase dilutes the net magnetization and hence the magnetic moment [34].

6.3.7 Dielectric measurements

Frequency dependent variation of dielectric constant and dielectric loss measured at room temperature for all the samples of MZFO-BTO composites are shown in Fig. 6.13 and 6.14 respectively. The combine effect of electronic, ionic, dipolar and interfacial polarization gives the dielectric constant of a material. Due to charge transport relaxation, dielectric constant varies with applied frequency. The decrease in ionic polarization is expected and hence the dielectric constant is also decreases. It is observed that the dielectric constant of all the samples rapidly decreases at low frequency region indicating the usual dielectric dispersion. At high frequency region both dielectric constant and

Chapter-VI 147 dielectric loss shows almost linear trend. Such type of dielectric dispersion can be explained by using Maxwell-Wagner theory of interfacial polarization [35]. In case of composite materials, when two distinct phases with different conductivities connected with each other then uncompensated charges increases at the interface which in turn produces the interfacial polarization. The decrease in polarization at higher frequency region is independent to the externally applied field. It is also observed that the dielectric constant and loss factor is higher for the pure BTO phase and decreases with increase in MZFO content in the composite (Table 6.4). This maximum value of dielectric constant is closely related to the grain size. Increasing grain boundary area with grain size increases the possibility of space – charge polarization at the grain boundaries which in turn increases the value of dielectric constant [36].

6.3.8 Magneto electric properties

Magneto electric voltage coefficient assisted by magnetic field for MZFO-BTO composites was measured to study the magneto electric coupling within the material. All the measurements were carried out on disc shaped samples by measuring the electrical response in lock in amplifier when the applied magnetic field varies [37]. By measuring core-shell voltage drop, the magneto electric voltage coefficient (α_{ME}) can be obtained by using the relation [38]; $ME = dV/dh$ where $\alpha = \frac{dV}{dh} \times t$ (6.5) where 't' – represents the thickness of the specimen, and 'h' – representing the applied magnetic field. Fig. 6.15 represents the variation of magneto electric coupling coefficient as a function of applied magnetic field. As the applied magnetic field increases, initially, the magneto electric coupling coefficient increases and reaches to a maximum value. Further

Chapter-VI 148 increase of applied magnetic field decreases the values of α_{ME} . Magnetostriction of the magnetic sub-lattice generates the M-E interactions and the piezomagnetic coefficient which is dependent on applied magnetic field is linearly proportional to α_{ME} [39]. In the absence of applied magnetic field most of the multiferroic composites have piezomagnetic coefficient close to zero which in turn shows the very low values of α_{ME} . Hence, a sufficient magnitude of applied magnetic field is required to achieve the maximum value of magneto electric coupling coefficient [40]. Among all the composite samples, (25%)MZFO-(75%)BTO shows maximum M-E coefficient ($\alpha_{ME} = 20.45 \text{ mVcm}^{-1} \text{ Oe}^{-1}$) and decreases with the higher percentage of MZFO phase and shows lower M-E coefficient for the sample (75%)MZFO-(25%)BTO ($\alpha_{ME} = 17.41 \text{ mVcm}^{-1} \text{ Oe}^{-1}$). Table 6.4 represents the values of M-E voltage coefficient for MZFO-BTO composites.

Chapter-VI 149 REFERENCES [1] N. A. Spaldin, M. Fiebig; The renaissance of magneto electric multi-ferroics, *Science* 309 (2005) 391–392. [2] V. Suchtelen; Product properties: A new approach of composite materials; *Philips Res. Rep.* 27 (1972) 28. [3] M. Mahesh Kumar, A. Srinivas, S. V. Suryanarayana, G. S. Kumar, T. Bhimasankaram; An experimental setup for dynamic measurement of magneto electric effect; *Bull. Mater. Sci.* 21 (3) (1998) 251. [4] S. Lopatin, I. Lopatin, I. Lisnevskaya; Magneto electric PZR/ferrite composite material; *Ferroelectrics* 162 (1994) 63. [5] S. V. Suryanarayana; Magneto electric interaction phenomena in materials; *Bull. Mater. Sci.* 17 (7) (1994) 1259. [6] S. L. Kadam, C. M. Kanamadi, K. K. Patankar, B. K. Chougule; Dielectric behaviour and magneto electric effect in $\text{Ni}_{0.5} \text{Co}_{0.5} \text{Fe}_2 \text{O}_4 + \text{Ba}_{0.8} \text{Pb}_{0.2} \text{TiO}_3$ ME composites; *Mater. Lett.* 59 (2005) 215-219. [7] A. S. Gaikwad, S. E. Shirsath, S. R. Wadgane, R. H. Kadam, J. Shah; R. K. Kotnala, A. B. Kadam, Magneto electric coupling and improved dielectric constant of BaTiO_3 and Fe-rich ($\text{Co}_{0.7} \text{Fe}_{2.3} \text{O}_4$) ferrite nano-composites; *J. Magn. Mater.* 465 (2018) 508-514. [8] N. A. Spaldin, M. Fiebig; The renaissance of

magnetolectric multiferroics; Science 309 (2005) 391. [9] W. Eerenstein, N. D. Mathur; Multiferroic and magnetolectric materials; J. F. Scott, Nature 442 (2006) 759. [10] J. F. Scott; Multiferroic memories; Nat. Mater. 6 (2007) 256.

Chapter-VI 150 [11] S. Lee, A. Pirogrove, M. Kang, K.H. Jang, M. Yonemura, T. Kamiyama, S.W. Cheong, F. Gozzo, N. Shin, H. Kimura, Y. Noda, J.G. Park; Giant magneto-elastic coupling in multiferroic hexagonal manganites; Nature 451 (2008) 805. [12] H. F. Zhang, S. W. Or, H. L. W. Chan; Electrical, magnetic, and magnetolectric characterization of fine-grained $\text{Pb}(\text{Zr}_{0.53}\text{Ti}_{0.47})\text{O}_3$ -($\text{Ni}_{0.5}\text{Zn}_{0.5}$) Fe_2O_4 composite ceramics; J. Alloys Comp. 509 (2011) 6311. [13] A. M. J. G. Van Run, D. R. Terrel, J. H. Scholling; An insitu grown eutectic magnetolectric composite material; J. Mater. Sci. 9 (1974) 1710. [14] M. A. Ahmed, S. F. Mansour, M. Afifi; Structural, electric and magnetolectric properties of $\text{Ni}_{0.85}\text{Cu}_{0.15}\text{Fe}_2\text{O}_4$ / $\text{BiFe}_{0.7}\text{Mn}_{0.3}\text{O}_3$ multiferroic nanocomposites; J. Alloys Comp. 578 (2013) 303. [15] A. Dzunuzovic, M. Vijatovic Petrovic, B. Stojadinovic, N. Ilic, J. Bobic, C. Foschini, M. Zaghete, Multiferroic (NiZn) Fe_2O_4 - BaTiO_3 composites prepared from nanopowders by auto-combustion method, Ceram. Int. 41 (2015) 13189-13200. [16] R. Mondal, B. Murty, V. Murthy, Dielectric, magnetic and enhanced magnetolectric response in high energy ball milling assisted BST-NZF particulate composite, Mater. Chem. Phys. 167 (2015) 338-346. [17] G. Srinivasan, E. Rasmussen, R. Hayes,

94%

MATCHING BLOCK 77/88

W

[https://www.researchgate.net/publication/...](https://www.researchgate.net/publication/)

Magnetolectric effects in ferrite-lead zirconate titanate layered composites: the influence of zinc substitution in ferrites, Phys. Rev. B 67 (2003) 1-10. [18]

Z. Yu, C. Ang,

82%

MATCHING BLOCK 78/88

W

[https://www.researchgate.net/publication/...](https://www.researchgate.net/publication/)

Maxwell-Wagner polarization in ceramic composites BaTiO_3 - ($\text{Ni}_{0.3}\text{Zn}_{0.7}$) Fe_2O_4 , J. Appl. Phys. 91 (2002) 794-797. [19]

A. S. Dzunuzovic, M. M. Vijatovic Petrovic, J. D. Bobic, M. Ivanov, R. Grigalaitis, J. Banys, B. D. Stojanovic; Magnetolectric

100%

MATCHING BLOCK 80/88

W

[https://www.researchgate.net/publication/...](https://www.researchgate.net/publication/)

properties of $x\text{Ni}_{0.7}\text{Zn}_{0.3}\text{Fe}_2\text{O}_4$ - (1-x) BaTiO_3 multiferroic composites;

Ceram. Inter. 44 (2018) 683-694.

Chapter-VI 151 [20] R. F. Soohoo, Theory and Application of Ferrites, Presentice-Hall, New-Jersey, 1960. [21] M. H. Abdellatif, G. M. El-Komy, A. A. Azab, Magnetic characterization of rare earth doped spinel ferrite, J. Magn. Mater. 442 (2017) 445-452. [22] P. P. Hankare, R. P. Patil, K. M. Garadkar, R. Sasikala, B. K. Chougule, Synthesis, dielectric behavior and impedance measurement studies of Cr-substituted Zn-Mn ferrites, Mater. Res. Bull. 46 (2011) 447-452. [23]

68%

MATCHING BLOCK 81/88

W

<https://www.x-mol.com/paper/1323383389284...>

S. S. Choudhari, S. R. Wadgane, B. P. Gaikwad, S. S. Satpute, K. M. Batoo, O. M. Aldossary, S. E. Shirsath, R. H. Kadam;

88%

MATCHING BLOCK 86/88

W

[https://www.researchgate.net/publication/...](https://www.researchgate.net/publication/)

Strain mediated enhancement in magnetolectric properties of snochemically synthesized piezoelectric and piezomagnetic composites;

Ceram. Inter. 47 (2021) 6496-6504. [24] R. H. Kadam, A. R. Biradar, M. L. Mane, S. E. Shiirsath; Sol-gel auto-combustion synthesis of $\text{Li}_{3x}\text{MnFe}_{2-x}\text{O}_4$ and their characterizations; J. Appl. Phys. 112 (2012) 043902. [25] A. S. Fawzi, A. D. Sheikh, V. L. Mathe, Multiferroic properties of Ni ferrite—PLZT composites, Physica B 405 (2010) 340-344. [26] A. M. Abdeen, O. M. Hemeda, E. E. Asssem, M. M. El-Sehly;

100%

MATCHING BLOCK 82/88

W

[https://www.researchgate.net/publication/ ...](https://www.researchgate.net/publication/)

Structural, electrical and transport phenomena of Co ferrite substituted by Cd;

J. Magn. Magn. Mater. 238 (2002) 75-83. [27] S. E. Shiirsath, R. H. Kadam, M. L. Mane, A. Ghesami; Y. Yasukawa, X. Liu, A. Morisako; Permeability and magnetic interactions in Co²⁺ substituted $\text{Li}_{0.5}\text{Fe}_{2.5}\text{O}_4$ alloys; J. Alloy. Comp. 575 (2013) 145-151. [28] S. Debnath, R. Das; Cobalt doping on nickel ferrite nanocrystals enhances the micro- structural and magnetic properties: shows a correlation between them; J. Alloy. Comp. 852 (2021) 156884.

Chapter-VI 152 [29] S. Gaba, A. Kumar, P. S. Rana, M. Arora; Influence of La³⁺ ion doping on physical properties of magnesium nanoferrites for microwave absorption application; J. Magn. Magn. Mater. 460 (2018) 69-77. [30] K. L. Routrary, D. Behera;

86%

MATCHING BLOCK 83/88

W

[https://www.researchgate.net/publication/ ...](https://www.researchgate.net/publication/)

Enhancement in conductivity and dielectric properties of rare-earth (Gd³⁺) substituted nano-sized CoFe_2O_4 ; J. Mater. Sci. Mater.

Elect. 29 (2018) <https://doi.org/10.1007/s10854-018-9558-2> [31] R. K. Kotnala, J. Shah, B. Singh, H. Kishan, S. Singh, S. K. Dhawan, A. Sengupta; Humidity response of Li-substituted magnesium ferrite; Sensor. Actu. B. Chem. 129 (2008) 909-914. [32] N. S. Al-Bassami, S. F. Mansour, M. A. Abdo; The magneto-mechanical properties of cobalt substituted Mg-Zn nanoferrites; J. Super. Nov. Magn. 33 (2020) 3086. [33] M. Hashim, Alimuddin, S. Kumar, S. E. Shiirsath, R. K. Kotnala, J. Shah, R. Kumar; Synthesis and characterization of Ni²⁺ substituted cobalt ferrite nanoparticles; Mater. Chem. Phys. 139 (2013) 364-374. [34] P. B. Belavi, G. N. Chavan, L. R. Naik;

100%

MATCHING BLOCK 84/88

W

[https://www.researchgate.net/publication/ ...](https://www.researchgate.net/publication/)

Grain size dependent dielectric and magnetic properties of (Y) NCCF + (1-Y) BTO particulate

composites; Int. J. Nano. 11 (2012) 1240007 [35] K. W. Wagner; The distribution of relaxation times in typical dielectrics; Ann. Phys. 40 (1973) 817. [36] S. Priya, R. Islam, S. Dong, D. Viehland; Recent advancement in magnetoelectric particulate and laminate composites; J. Elect. Ceram. 19 (2007) 149-166. [37] P. Kaviraj, R. Pramanik, A. Arockiarajan; Influence of individual phases and temperatures on the properties of CoFe_2O_4 – BaTiO_3 magnetoelectric core-shell nanocomposites; Ceram. Inter. 45 (2019) 12344-12352.

Chapter-VI 153 [38] T. Parida, A. Kumar, B. S. Murty, C. Makandeyulu; Magnetic and magnetoelectric response of Gd doped nickel ferrite and barium titanate nanocomposites; J. App. Phys. 127 (2020) 114104. [39] C. S. Park, A. Khachatryan, S. Priya, Giant magnetoelectric coupling in laminate thin film structure grown on magnetostrictive substrate, Appl. Phys. Lett. 100 (2012), 192904-4. [40] T. Nan, Y. Hui, M. Rinaldi, N.X. Sun, Self-biased 215 MHz magnetoelectric NEMS resonator for ultra-sensitive DC magnetic field detection, Sci. Rep. 3(2013) 1985- 1986.

Chapter-VI 154 Fig. 6.1: Flow chart for sol-gel synthesis of $(1-x)\text{Mn}_{0.7}\text{Zn}_{0.3}\text{Fe}_2\text{O}_4 + (x)\text{BaTiO}_3$ ($x = 0.0, 0.25, 0.50, 0.75$ and 1.0)

Chapter-VI 155 Fig. 6.2: XRD patterns of MZFO-BTO composites

Chapter-VI 156 Fig. 6.3: Variation of lattice parameter of cubic MZFO and pervoskite BTO phases in $(1-x)\text{Mn}_{0.7}\text{Zn}_{0.3}\text{Fe}_2\text{O}_4 + (x)\text{BaTiO}_3$ ($x = 0.0, 0.25, 0.50, 0.75$ and 1.0)

Chapter-VI 157 Fig. 6.4: Variation X-ray density (d_x) and percentage porosity (P) for $(1-x) \text{Mn}_{0.7} \text{Zn}_{0.3} \text{Fe}_2 \text{O}_4 + (x) \text{BaTiO}_3$ ($x = 0.0, 0.25, 0.50, 0.75$ and 1.0)

Chapter-VI 158 Fig. 6.5: Variation Crystallite size (t) and grain size (D) for $(1-x) \text{Mn}_{0.7} \text{Zn}_{0.3} \text{Fe}_2 \text{O}_4 + (x) \text{BaTiO}_3$ ($x = 0.0, 0.25, 0.50, 0.75$ and 1.0)

Chapter-VI 159 Fig. 6.6: W-H plots of piezomagnetic-MZFO and piezoelectric-BTO phases in $(1-x) \text{Mn}_{0.7} \text{Zn}_{0.3} \text{Fe}_2 \text{O}_4 + (x) \text{BaTiO}_3$ composites.

Chapter-VI 160 Fig. 6.7: SEM micrographs of $(1-x) \text{Mn}_{0.7} \text{Zn}_{0.3} \text{Fe}_2 \text{O}_4 + (x) \text{BaTiO}_3$ (a) MZFO, (b) (75%)MZFO + (25%)BTO, (c) (50%)MZFO + (50%)BTO, and (d) (25%)MZFO + (75%)BTO

Chapter-VI 161 Fig. 6.8: EDAX spectra of (a) MZFO and (b) (25%)MZFO+(75%)BTO samples.

Chapter-VI 162 Fig. 6.9 (a): Color mapping images of pure MZFO sample.

Chapter-VI 163 Fig. 6.9 (b): Color mapping images of (25%)MZFO+(75%)BTO sample.

Chapter-VI 164 Fig. 6.10: FTIR spectra of $(1-x) \text{Mn}_{0.7} \text{Zn}_{0.3} \text{Fe}_2 \text{O}_4 + (x) \text{BaTiO}_3$ composites.

Chapter-VI 165 Fig. 6.11: Variation magnetization (M) with applied magnetic field (H) for the composite series $(1-x) \text{Mn}_{0.7} \text{Zn}_{0.3} \text{Fe}_2 \text{O}_4 + (x) \text{BaTiO}_3$.

Chapter-VI 166 Fig. 6.12: Variation in saturation magnetization (M_s), Remnant magnetization (M_R) and coercivity (H_c) with composition for $(1-x) \text{Mn}_{0.7} \text{Zn}_{0.3} \text{Fe}_2 \text{O}_4 + (x) \text{BaTiO}_3$.

Chapter-VI 167 Fig. 6.13: Variation of dielectric constant (ϵ') with frequency for $(1-x) \text{Mn}_{0.7} \text{Zn}_{0.3} \text{Fe}_2 \text{O}_4 + (x) \text{BaTiO}_3$ composites.

Chapter-VI 168 Fig. 6.14: Variation of dielectric loss (ϵ'') with frequency for $(1-x) \text{Mn}_{0.7} \text{Zn}_{0.3} \text{Fe}_2 \text{O}_4 + (x) \text{BaTiO}_3$ composites.

Chapter-VI 169 Fig. 6.15: Variation of magnetoelectric coupling coefficient (α_{ME}) with applied magnetic field of $(1-x) \text{Mn}_{0.7} \text{Zn}_{0.3}$

32%

MATCHING BLOCK 85/88

W

[http://pr.hec.gov.pk/jspui/bitstream/123 ...](http://pr.hec.gov.pk/jspui/bitstream/123...)

$\text{Fe}_2 \text{O}_4 + (x) \text{BaTiO}_3$ composites

Chapter-VI
170

Table 6.1: Lattice Constant (a), X-ray density (d_x), Bulk Density (d_B), Porosity (P) and Particle Size (t) for $(1-x) \text{Mn}_{0.7} \text{Zn}_{0.3} \text{Fe}_2 \text{O}_4 + (x) \text{BaTiO}_3$.

Comp.

'x'

Lattice constant 'a'

(Å)

X-ray

Density

' d_x '

(gm/cc)

Bulk

Density

' d_B '

(

gm/cc) Percentage Porosity 'P' (%) Particle Size 't' (nm) Ferrite Phase Ferroelectric Phase XRD SEM 0.0 8.431 --- 5.318
 4.129 28.80 15.36 36.066 0.25 8.424 4.021 5.487 4.318 27.07 16.25 43.8 0.50 8.420 4.014 5.662 4.521 25.24 17.9 52.093
 0.75 8.413 4.009 5.842 4.758 22.78 19.48 53.88 1.0 --- 4.005 6.027 5.012 20.25 21.94 54.01

Chapter-VI 171 Table 6.2: Elemental composition in atomic weight % of constituent ions observed from EDAX patterns for (1-x) Mn 0.7 Zn 0.3 Fe 2 O 4 + (x) BaTiO 3. Comp. 'x' Elemental composition in atomic weight (%) Mn Zn Fe O Ba Ti 0.0
 16.452 8.391 47.780 27.333 --- --- 0.75 3.19 1.95 10.9 23.51 44.27 16.18

Chapter-VI 172

Table 6.3:

95%	MATCHING BLOCK 87/88	W https://www.researchgate.net/publication/ ...
Saturation magnetization (M S), Remnant magnetization (M r), coercivity (H C)		

and remnant ratio (M r /M S) of (1-x) Mn 0.7 Zn 0.3 Fe 2 O 4 + (x) BaTiO 3. Comp. 'x' '

73%	MATCHING BLOCK 88/88	W http://pr.hec.gov.pk/jspui/bitstream/123 ...
M S ' (emu/gm) 'M r ' (emu/gm) (M r /M S) 'H C ' (Oe) 0.0 33.12 10.58 0.319 565 0.25 23.89 6.78 0.284 338 0.50 14.17 1.23 0.087 112 0.75 4.54 0.49 0.108 23 1.0 --- --- --- ---		

Chapter-VI 173 Table 6.4: Dielectric constant (ε') and Magnetoelectric Conversion factor (dE/dH) of (1-x) Mn 0.7 Zn 0.3 Fe 2 O 4 + (x) BaTiO 3 Comp. 'x' Series Dielectric Constant (ε) Magnetoelectric Conversion factor [dE/dH] H (mV/Cm-Oe) 0.0

100%(Mn 0.7 Zn 0.3 Fe 2 O 4) 220.60 --- 0.25 75%(Mn 0.7 Zn 0.3 Fe 2 O 4)+25%(BaTiO 3) 242.23 17.41 0.50 50%(Mn 0.7 Zn 0.3 Fe 2 O 4)+50%(BaTiO 3) 251.76 19.12 0.75 25%(Mn 0.7 Zn 0.3 Fe 2 O 4)+75%(BaTiO 3) 273.54 20.45 1.0 100% (BaTiO 3) 292.12 ---

174 CHAPTER – VII CONCLUSIONS CONTENTS 7.1 Conclusions on CCFO and MZFO ferrites : 175 7.2 Conclusions on CCFO-BTO composites : 175 7.3 Conclusions on MZFO-BTO composites : 177

Chapter-VII 175 7.1 CONCLUSIONS ON CCFO AND MZFO FERRITES CoCr 0.3 Fe 1.7 O 4 (CCFO) and Mn 0.7 Zn 0.3 Fe 2 O 4 (MZFO) nanoparticles were successfully obtained by using ultrasonic irradiation assisted sono-chemical route. Cubic spinel structure of the samples was confirmed by using X-ray diffraction method. The higher ionic radius of the Mn and Zn ions enhances the lattice parameter. Two absorption bands observed in the infrared spectra reveals the typical ferromagnetic behaviour of the samples. The stiffness constant and elastic parameters are observe higher for CCFO sample while as Debye temperature is found maximum for MZFO sample. Value of Poisson's ratio reveals the good elastic behaviour of both the samples. 7.2 CONCLUSIONS ON CCFO-BTO COMPOSITES CoCr 0.3 Fe 1.7 O 4 nano particles were obtained by ultrasonic irradiation assisted sonochemical sol-gel route. Nanoparticles of BTO phase (BaTiO 3) was obtained by employing the sol-gel route. The CCFO-BTO M-E composite materials were fabricated by mixing the CCFO and BTO nanopowders with their weight proportion by using solid – state reaction method. Rietveld refinement of all the samples of (1-x)CoCr 0.3- Fe 1.7 O 4 +(x)BaTiO 3 (x = 0.0, 0.2, 0.4, 0.6, 0.8 and 1.0) composites was done by using the software FullProf suite. XRD evaluation suggests that the CCFO phase possess cubic spinel structure while as BTO phase possesses perovskite structure. Lattice constant of piezomagnetic phase increased from 8.373 Å to 8.3774 Å up to x = 0.4 and thereafter decreases to 8.3738 Å for x = 1.0 with the increasing concentration of BTO phase. Simultaneously, lattice constant of BTO phase decreased from 4.021 Å to 4.005 Å with the increasing concentration of BTO phase. The average crystallite size increased initially from 20.1 nm (Pure CCFO phase) to 25.6 nm ((40%) CCFO+(60%)BTO) and decreased thereafter to 21.2 nm for pure BTO phase. Positive values of lattice strains induced in

Chapter-VII 176 CCFO phases indicting the tensile type of strain. Simultaneously, the tensile strain in piezoelectric BTO phase reduces from 1.67×10^{-3} to 2.5×10^{-4} with the increasing concentration of BTO grains. From SEM analysis, it can be observed that for the samples $x \geq 0.8$, the average grain size (D) increases from 38 nm to 60 nm and for pure BTO phase it reduces to 54 nm. EDAX spectra reveal that all the constituent elements in the composition are observed with their stoichiometric proportion and no loss of any constituent element is observed. Color mapping images confirms that the elements are uniformly distributed in the samples. FTIR spectra of CCFO-BTO M-E composites recorded in the wavenumber range of 400 to 4000 cm^{-1} . Absorption band appeared near wavenumber 870 cm^{-1} may be related to the pervoskite tetragonal structure of the BTO phase. Saturation magnetization and other parameters decreases with the increasing concentration of BTO phase in the composite because magnetic properties are only the characteristics of piezomagnetic-CCFO phase. The increase in coercivity is result of increase of anisotropy energy with increase of crystallite size. Pure piezoelectric phase (x = 1) exhibit the typical P-E hysteresis loop which confirms the ferroelectricity in the sample, but the P-E loop was not saturated. P-E loop of CCFO phase is very absorbent and not showing any ferroelectric characteristics. The dielectric dispersion is observed in the dielectric plots. This dispersion may be occurs due to the Maxwell-Wagner type interfacial polarization which is also in good agreement with the Koop's phenomenological theory. Pure BTO shows the lowest dielectric loss among all the investigated composite samples, whereas CCFO show the highest dielectric loss. The difference in dielectric loss between BTO and CCFO is may be related to the leakage current and electrical conductivity. In contrast to CCFO phase, BTO has least leakage current and lower electrical conductivity. It can be seen that, α ME increased initially from 15.1 mV/Cm-Oe (x = 0.2) with the increase in H DC and attained a maxima at 24.7

Chapter-VII 177 mV/Cm-Oe (x = 0.6). Further increase in H DC decrease the value of α ME . This behavior of α ME is associated with the magnetostrictive property of piezomagnetic-CCFO phase. Magnetostriction of CCFO phase increased and attained saturation with the increase in dc magnetic field [55]. Magnetization in piezomagnetic-CCFO is controlled by the magnetic domain and domain size which can be influenced by the strain type of piezomagnetic- CCFO. Thus, tensile-strained CCFO may require a higher H DC to reach the saturation. 7.3 CONCLUSIONS ON MZFO-BTO COMPOSITES Composites of piezomagnetic MZFO and piezoelectric BTO have been investigated for their structural, magnetic, permittivity and M-E effect measurements. Both individual cubic spinel (piezomagnetic) and pervoskite (piezoelectric) phases were identified by XRD investigations. Average crystallite size obtained from XRD analysis shows similar behaviour that are obtained from SEM micrographs. The micro-strain observed from W-H plots shows gradually increasing comprehensive type strain from -2.01×10^{-5} to -8.36×10^{-6} for MZFO phase and decreasing tensile type strain from 9.30×10^{-4} to 5.40×10^{-4} for BTO phase with the increasing percentage of BTO in the composite. Magnetic parameters such as saturation magnetization, remnant magnetization and coercivity reduced with the dilution of MZFO content in

composite which is related to the reduction of magnetic grains and increasing grain size. Frequency dependent real and imaginary parts of permittivity showed higher values for pure BTO phase and decreases with more number of MZFO particles. M-E coefficient has maximum value for higher concentration of BTO grains and lower value for higher concentration of MZFO grains in the composites. The obtained results are very interesting and thus making MZFO-BTO composite a promising candidate for electronic devices where ME effect does play an important role.

Hit and source - focused comparison, Side by Side

Submitted text As student entered the text in the submitted document.

Matching text As the text appears in the source.

1/88	SUBMITTED TEXT	18 WORDS	91% MATCHING TEXT	18 WORDS
<p>A Thesis submitted in partial fulfillment of the requirement for the degree of Doctor of Philosophy in</p>		<p>A thesis submitted in partial fulfillment of the requirement for the Degree of Doctor of Philosophy in</p>		
<p>W http://prh.hec.gov.pk/jspui/bitstream/123456789/7593/1/PhD%28Physics%29Full%20Thesis%20Hasan.pdf</p>				

2/88	SUBMITTED TEXT	25 WORDS	73% MATCHING TEXT	25 WORDS
<p>are primarily used as inductive components in large variety of electronic circuits such as low noise amplifiers, filters, voltage controlled oscillators. [13]</p>		<p>are widely used as inductive components in a huge variety of electronic circuits as in low noise amplifiers, filters, voltage-controlled oscillators,</p>		
<p>W https://docplayer.net/150337558-Doctor-of-philosophy.html</p>				

3/88	SUBMITTED TEXT	25 WORDS	84% MATCHING TEXT	25 WORDS
<p>the magnetoelectric effect is typically generated through a mechanical strain arising under an applied magnetic or electric field at interfaces between the two constituents.</p>		<p>the ME effect is normally generated through a mechanical strain arising under an applied magnetic or electric field at the interfaces between the two constituent</p>		
<p>W https://www.researchgate.net/publication/224650077_Magnetoelectric_Properties_of_CoFe_O_-BaTiO_Co ...</p>				

4/88	SUBMITTED TEXT	28 WORDS	87% MATCHING TEXT	28 WORDS
<p>Composites of $(1 - x)\text{CoFe}_2\text{O}_4 + (x)\text{BaTiO}_3$ (where $x = 0, 0.25, 0.50, 0.1$) were prepared by</p>		<p>composites of $(1-x)\text{CoFe}_2\text{O}_4+(x)\text{BaTiO}_3$ ($0.0 \leq x \leq 1.0$) were prepared by</p>		
<p>W https://www.researchgate.net/publication/224650077_Magnetoelectric_Properties_of_CoFe_O_-BaTiO_Co ...</p>				

6/88	SUBMITTED TEXT	58 WORDS	87% MATCHING TEXT	58 WORDS
<p>NO₃)₂·6H₂O, Fe(NO₃)₂·9H₂O, Cr(NO₃)₂·9H₂O, C₆H₈O₇·H₂O</p>		<p>NO₃)₃·9H₂O, Zn(NO₃)₂·6H₂O, Cr(NO₃)₃·9H₂O and C₆H₈O₇·H₂O (</p>		
<p>J 0201276d-de23-493f-a933-df7286b7da30</p>				

5/88	SUBMITTED TEXT	37 WORDS	77% MATCHING TEXT	37 WORDS
<p>lead-free magnetoelectric composites (x)K_{0.5}Na_{0.5}NbO₃ – (x)MnFe₂O₄ (x = 0, 0.2, 0.4, 0.6, 0.8, and 1) synthesized by solid-state reaction</p>		<p>Lead-free magnetoelectric composites (1-x)K_{0.5}Na_{0.5}NbO₃–(x)BaFe₁₂O₁₉ (x = 30, 40, and 50 wt%) are synthesized using solid state reaction</p>		
<p>W https://www.researchgate.net/publication/277900370_Crystal_structure_and_magnetic_properties_of_t...</p>				

7/88	SUBMITTED TEXT	57 WORDS	93% MATCHING TEXT	57 WORDS
<p>The successful realization of multifunctional systems consisting of ferrimagnetic Mn_{0.7}Fe_{2.3}O₄ spinel platelets, of controlled sizes and nanometric thicknesses, embedded in an epitaxial ferroelectric BaTiO₃ perovskite thin film. The embedded platelets experience a much higher iso-static strain than that obtained for single layers.</p>		<p>the successful realization of multifunctional systems consisting of ferrimagnetic Mn_{0.7}Fe_{2.3}O₄ spinel platelets, of controlled sizes and nanometric thicknesses, embedded in an epitaxial ferroelectric BaTiO₃ perovskite thin film. The embedded platelets experience a much higher isostatic strain than that obtained for single layers.</p>		
<p>W https://www.researchgate.net/publication/262195378_Structural_dielectric_ferromagnetic_ferroelect...</p>				

successfully achieved nanometer-thick composite layers, with identical composition, having either in-plane or out-of-plane electric polarization orientations. The optimal samples combine several functionalities: (i) the magnetoelectric nature of the full oxide artificial structures is confirmed, (ii) semiconducting diode behaviors are obtained when contacted with a metal electrode, and (iii) marked (eightfold) electro-resistance transport properties with respect to the electric polarization orientation are revealed. The embedded platelets configuration enhances significantly interface and two-dimensional effects and is thus believed of high interest to realize functional device structures.

successfully achieved nanometer-thick composite layers, with identical composition, having either in plane or out of plane electric polarization orientations. The optimal samples combine several functionalities: (i) the magnetoelectric nature of the full oxide artificial structures is confirmed; (ii) semiconducting diode behaviors are obtained when contacted with a metal electrode and (iii) marked (8 fold) electro-resistance transport properties with respect to the electric polarization orientation are revealed. The embedded platelets configuration enhances significantly interface and two-dimensional effects and is thus believed of high interest to realize functional device structures.

W [https://www.researchgate.net/publication/262195378_Structural_dielectric_ferromagnetic_ferroelect ...](https://www.researchgate.net/publication/262195378_Structural_dielectric_ferromagnetic_ferroelect...)

The MFO/BTO thin films were prepared by metallo-organic decomposition method. The MFO/BTO nanocomposite stoichiometric ratio has been analyzed with X-ray fluorescence elemental analysis. X-ray diffraction reveals the formation of both spinel MFO and perovskite BTO phases with crystallite size lies in the range of 25-137 nm. The lattice strain observed in MFO/BTO nanocomposite is due to tetragonal distortion of BTO unit cell and lattice mismatch with ferrite MFe_2O_4 . The crystallite size is also depicted with atomic force microscopy. The observed ferromagnetism of MFO/BTO nanocomposite is highly influenced by inversion degree of MFO ferrite and oxygen vacancies formation. All MFO/BTO nanocomposites have well saturated ferroelectric hysteresis polarization. This has been discussed based on lattice strain, leakage current and the degree of lattice mismatch. The chemical valence states of Fe and O and their influence on the magnetic and ferroelectric properties have been analyzed with X-ray photoelectron spectroscopy. The capacitance versus bias voltage characteristics under the influence of applied dc magnetic field indicates ferroelectric behavior and the presence of magneto-electric/dielectric effects. The dielectric permittivity reduces with applied dc magnetic field which is responsible for negative

The MFO/BTO thin films were prepared by metallo-organic decomposition method. The MFO/BTO nanocomposite stoichiometric ratio has been analyzed with X-ray fluorescence elemental analysis. X-ray diffraction reveals the formation of both spinel MFO and perovskite BTO phases with crystallite size lies in the range of 25–137 nm. The lattice strain observed in MFO/BTO nanocomposite is due to tetragonal distortion of BTO unit cell and lattice mismatch with ferrite MFe_2O_4 . The crystallite size is also depicted with atomic force microscopy. The observed ferromagnetism of MFO/BTO nanocomposite is highly influenced by inversion degree of MFO ferrite and oxygen vacancies formation. All MFO/BTO nanocomposites have well saturated ferroelectric hysteresis polarization. This has been discussed based on lattice strain, leakage current and the degree of lattice mismatch. The chemical valence states of Fe and O and their influence on the magnetic and ferroelectric properties have been analyzed with X-ray photoelectron spectroscopy. The capacitance versus bias voltage characteristics under the influence of applied dc magnetic field indicates ferroelectric behavior and the presence of magneto-electric/dielectric effects. The dielectric permittivity reduces with applied dc magnetic field which is responsible for negative

W [https://www.researchgate.net/publication/262195378_Structural_dielectric_ferromagnetic_ferroelect ...](https://www.researchgate.net/publication/262195378_Structural_dielectric_ferromagnetic_ferroelect...)

8/88	SUBMITTED TEXT	27 WORDS	100% MATCHING TEXT	27 WORDS
	effect. The higher longitudinal magnetoelectric coupling coefficient is obtained in $M(\frac{1}{4}\text{Co}, \text{Ni}, \text{Zn})\text{FO/BTO}$ nanocomposite which is correlated with piezoelectric coefficient, d_{33} value measurement.		effect. The higher longitudinal magnetoelectric coupling coefficient is obtained in $M(=\text{Co}, \text{Ni}, \text{Zn})\text{FO/BTO}$ nanocomposite which is correlated with piezoelectric coefficient, d_{33} value measurement.	
	<p>W https://www.researchgate.net/publication/262195378_Structural_dielectric_ferromagnetic_ferroelect ...</p>			

12/88	SUBMITTED TEXT	27 WORDS	100% MATCHING TEXT	27 WORDS
	Structural and magnetic studies of Nano-crystalline ferrites MFe_2O_4 ($\text{M} = \text{Zn}, \text{Ni}, \text{Cu}, \text{and Co}$) synthesized via citrate gel		Structural and Magnetic Studies of Nano-crystalline Ferrites MFe_2O_4 ($\text{M} = \text{Zn}, \text{Ni}, \text{Cu}, \text{and Co}$) Synthesized Via Citrate Gel	
	<p>W https://www.researchgate.net/publication/229385921_Studies_on_the_Magnetic_Magnetostrictive_and_E ...</p>			

10/88	SUBMITTED TEXT	17 WORDS	95% MATCHING TEXT	17 WORDS
	Mater. 215 (2000) 171-183. [11] N. Rezlescu, E. Rezlescu; Dielectric properties of copper containing ferrites; Phys.		Mater. Struct. 15(2006) [50] N. Rezlescu, E. Rezlescu, Dielectric properties of copper containing ferrites, Phys.	
	<p>W https://docplayer.net/150337558-Doctor-of-philosophy.html</p>			

13/88	SUBMITTED TEXT	23 WORDS	75% MATCHING TEXT	23 WORDS
<p>Mössbauer spectroscopy investigation of Mn-substituted Co-ferrite (CoMnxFe_{2-x}O₄); J. Appl. Phys. 97 (2005) 10</p>		<p>Mössbauer spectroscopy investigation of Mn-substituted Co-ferrite (CoMnxFe_{2-x}O₄)</p> <p>Article</p> <ul style="list-style-type: none"> • May 2005 • J APPL PHYS • 		
<p>W https://www.researchgate.net/publication/230928122_Magnetic_and_Magnetostrictive_Properties_of_Ma ...</p>				

14/88	SUBMITTED TEXT	16 WORDS	100% MATCHING TEXT	16 WORDS
<p>Y. Melikhov, J. E. Snyder, D. C. Jiles, A. P. Ring, J. A. Paulsen, C.</p>		<p>Y Melikhov</p> <ul style="list-style-type: none"> • J E Snyder • D C Jiles • A P Ring • J A Paulsen • C 		
<p>W https://www.researchgate.net/publication/230928122_Magnetic_and_Magnetostrictive_Properties_of_Ma ...</p>				

16/88	SUBMITTED TEXT	27 WORDS	100% MATCHING TEXT	27 WORDS
<p>Mn 0.7 Fe 2.3 O 4 Nanoplatelets Embedded in BaTiO 3 Perovskite Thin Films for Multifunctional Composite Barriers;</p>		<p>Mn 0.7 Fe 2.3 O 4 Nanoplatelets Embedded in BaTiO 3 Perovskite Thin Films for Multifunctional Composite Barriers</p>		
<p>W https://www.researchgate.net/publication/262195378_Structural_dielectric_ferromagnetic_ferroelect ...</p>				

17/88	SUBMITTED TEXT	23 WORDS	100% MATCHING TEXT	23 WORDS
<p>Multiferroic effects in MFe 2 O 4 /BaTiO 3 (M ¼ Mn, Co, Ni, Zn) nanocomposites;</p>		<p>Multiferroic effects in MFe 2 O 4 /BaTiO 3 (M = Mn, Co, Ni, Zn) nanocomposites</p>		
<p>W https://www.researchgate.net/publication/262195378_Structural_dielectric_ferromagnetic_ferroelect ...</p>				

18/88	SUBMITTED TEXT	18 WORDS	82% MATCHING TEXT	18 WORDS
<p>The distance from magnetic ions to the oxygen ion (through which the interaction occurs) and the angle</p>		<p>the distances from these ions to the oxygen ion through which the interaction occurs and the angle</p>		
<p>W http://pr.hec.gov.pk/jspui/bitstream/123456789/7593/1/PhD%28Physics%29Full%20Thesis%20Hasan.pdf</p>				

19/88	SUBMITTED TEXT	22 WORDS	84% MATCHING TEXT	22 WORDS
<p>the values of the distance and the angle Φ, it may be inferred that of the three interactions, the A-B interaction</p>		<p>the values of the distance and the angle ϕ, it may be concluded that of the three possible interactions, the A-B interaction</p>		
<p>W http://pr.hec.gov.pk/jspui/bitstream/123456789/7593/1/PhD%28Physics%29Full%20Thesis%20Hasan.pdf</p>				

20/88	SUBMITTED TEXT	15 WORDS	83% MATCHING TEXT	15 WORDS
<p>the spins of the A- and B-site ions in ferrite will be oppositely magnetized</p>		<p>the spins of the A and B-site ions, in ferrimagnets will be</p> <p style="text-align: center;">Chapter.1</p> <p style="text-align: center;">Page 30</p> <p style="text-align: center;">oppositely magnetized</p>		
<p>W http://pr.hec.gov.pk/jspui/bitstream/123456789/7593/1/PhD%28Physics%29Full%20Thesis%20Hasan.pdf</p>				

21/88	SUBMITTED TEXT	19 WORDS	100% MATCHING TEXT	19 WORDS
<p>sublattices, with a resultant magnetic moment equal to the difference between those of A- and B-site ions [10].</p>		<p>sublattices, with a resultant magnetic moment equal to the difference between those of A and B site ions.</p> <p style="text-align: center;">1.9</p>		
<p>W http://pr.hec.gov.pk/jspui/bitstream/123456789/7593/1/PhD%28Physics%29Full%20Thesis%20Hasan.pdf</p>				

23/88	SUBMITTED TEXT	12 WORDS	100% MATCHING TEXT	12 WORDS
<p>J. Smit, H. P. J. Wijn; Ferrites, Philips' Technical Library, Eindhoven,</p>		<p>J. Smit, H. P. J. Wijn, Ferrites, Philips Technical Library, Eindhoven, (1959). [6]</p>		
<p>W http://pr.hec.gov.pk/jspui/bitstream/123456789/7593/1/PhD%28Physics%29Full%20Thesis%20Hasan.pdf</p>				

24/88	SUBMITTED TEXT	12 WORDS	100% MATCHING TEXT	12 WORDS
<p>J. Smit, H.P.J. Wijn, Ferrites; Wiley; New York (1959).</p>		<p>J. Smit, H.P.J. Wijn, Ferrites, Wiley, New York, 1959. [66]</p>		
<p>W http://pr.hec.gov.pk/jspui/bitstream/123456789/7593/1/PhD%28Physics%29Full%20Thesis%20Hasan.pdf</p>				

51/88

SUBMITTED TEXT

20 WORDS

100% MATCHING TEXT

20 WORDS

J. Magn. Magn. Mater.; 260 (2003) 244-249.
[5] T. M. Meaz, S. M. Attia; A. M. Abo El Ata;

J.

Magn.

Magn.

Mater.

204

(1999)

36.

[5]

T.M.

Meaz,

S.M.

Attia,

A.M.

Abo

El

Ata,

W [https://www.researchgate.net/publication/248276139_Electrical_and_dielectric_properties_of_nano_c ...](https://www.researchgate.net/publication/248276139_Electrical_and_dielectric_properties_of_nano_c...)

52/88	SUBMITTED TEXT	22 WORDS	86% MATCHING TEXT	22 WORDS
--------------	-----------------------	----------	--------------------------	----------

Effect of tetravalent titanium ions substitution on the dielectric properties of Co-Zn ferrite; J. Magn. Magn. Mater. 257 (2003) 296-305. [6]

Effect of tetravalent titanium ions substitution on the dielectric properties of Co-Zn ferrites

Article

- Feb 2003
- J MAGN MAGN MATER

•

W [https://www.researchgate.net/publication/248276139_Electrical_and_dielectric_properties_of_nano_c ...](https://www.researchgate.net/publication/248276139_Electrical_and_dielectric_properties_of_nano_c...)

49/88	SUBMITTED TEXT	16 WORDS	90% MATCHING TEXT	16 WORDS
--------------	-----------------------	----------	--------------------------	----------

A. A. Birajdar, S. E. Shirsath, R. H. Kadam, M. L. Mane, D. R. Mane;

A.A. Birajdar, Sagar E. Shirsath, R.H. Kadam, M.L. Mane, D.R. Mane,

W [https://www.researchgate.net/publication/260721358_Synthesis_and_characterization_of_nanocrystall ...](https://www.researchgate.net/publication/260721358_Synthesis_and_characterization_of_nanocrystall...)

50/88	SUBMITTED TEXT	38 WORDS	83% MATCHING TEXT	38 WORDS
	Permeability and magnetic properties of Al ³⁺ substituted Ni _{0.7} Zn _{0.3} Fe ₂ O ₄ nanoparticles; J. Appl. Phys. 112 (2012) 053908.		Permeability and Magnetic Properties of Al ³⁺ Substituted Ni _{0.7} Zn _{0.3} Fe ₂ O ₄ Nanoparticles	
91			Article Full-text available • Oct 2012 • J APPL PHYS •	
				W https://www.researchgate.net/publication/260721358_Synthesis_and_characterization_of_nanocrystall ...

54/88	SUBMITTED TEXT	110 WORDS	64% MATCHING TEXT	110 WORDS
	all the samples as a function of applied		all the samples have been studied as a function of	
Chapter-V 96	frequency in the range 50Hz to 50MHz.		frequency in the range 600 Hz to 1 MHz	
				W https://www.researchgate.net/publication/229315436_Optical_magnetic_and_electrical_investigation_ ...

57/88

SUBMITTED TEXT

14 WORDS

88% MATCHING TEXT

14 WORDS

X-ray diffraction patterns of all the samples are illustrated in Fig. 5.2 (a)

X-

ray

diffraction

patterns

of

all

the

samples

are

shown

in

Fig.

1(a)-(

61/88	SUBMITTED TEXT	29 WORDS	100% MATCHING TEXT	29 WORDS
<p>Structural, dielectric, ferromagnetic, ferroelectric and ac conductivity studies of the BaTiO₃-CoFe_{1.8}Zn_{0.2}O₄ multiferroic particulate</p>		<p>Structural, dielectric, ferromagnetic, ferroelectric and ac conductivity studies of the BaTiO₃-CoFe_{1.8}Zn_{0.2}O₄ multiferroic particulate</p>		
<p>W https://www.researchgate.net/publication/262195378_Structural_dielectric_ferromagnetic_ferroelect...</p>				

62/88	SUBMITTED TEXT	19 WORDS	91% MATCHING TEXT	19 WORDS
<p>B. G. Toksha, S. E. Shirsath, M. L. Mane, S. M. Patange, S. S. Jadhav, K. M. Jadhav,</p>		<p>B. G. Toksha, Sagar E. Shirsath, M. L. Mane, S. M. Patange, S. S. Jadhav, K. M. Jadhav,</p>		
<p>W https://docplayer.net/150337558-Doctor-of-philosophy.html</p>				

65/88	SUBMITTED TEXT	23 WORDS	83% MATCHING TEXT	23 WORDS
<p>Magnetoelectric effect in cobalt ferrite – barium titanate composites and their electrical properties; Pramana J. Phys. 58 (5) (6) (2002) 1115. [28]</p>		<p>Magnetoelectric effect in cobalt ferrite-barium titanate composites and their electrical properties</p>		
<p>Article</p> <p>Full-text available</p> <ul style="list-style-type: none"> • May 2002 • PRAMANA-J PHYS • 				
<p>W https://www.researchgate.net/publication/231094467_Influence_of_Thermal_Annealing_on_the_Dielectr...</p>				

67/88	SUBMITTED TEXT	12 WORDS	100% MATCHING TEXT	12 WORDS
<p>Structural, electrical and transport phenomena of Co ferrite substituted by Cd;</p>		<p>Structural, electrical and transport phenomena of Co ferrite substituted by Cd </p>		
<p>W https://www.researchgate.net/publication/279204462_Structural_electrical_and_transport_phenomena_ ...</p>				

64/88	SUBMITTED TEXT	40 WORDS	86% MATCHING TEXT	40 WORDS
<p>Magnetoelectric effect in three phase $y(\text{Ni}_{0.5}\text{Cu}_{0.2}\text{Zn}_{0.3}\text{Fe}_2\text{O}_4) + (1-y)(50\%\text{BaTiO}_3 + 50\%\text{PZT})$ ME composites; J. Alloys Compd. 479 (2009) 385. [37]</p>		<p>Magnetoelectric effect in three phase $y(\text{Ni}_{0.5}\text{Cu}_{0.2}\text{Zn}_{0.3}\text{Fe}_2\text{O}_4) + (1 - y) (50\% \text{BaTiO}_3 + 50\% \text{PZT})$ ME composites</p>		
		<p>Article</p> <ul style="list-style-type: none"> • Jun 2009 • J ALLOY COMPD • 		
<p>W https://www.researchgate.net/publication/262195378_Structural_dielectric_ferromagnetic_ferroelect ...</p>				

68/88	SUBMITTED TEXT	43 WORDS	100% MATCHING TEXT	43 WORDS
<p>Impact of grain size and structural changes on magnetic, dielectric, electrical, impedance and modulus spectroscopic characteristics of CoFe_2O_4 nanoparticles synthesized by honey mediated sol-gel combustion method; Adv. Nat. Sci.: Nanosci. Nanotechnol. 8 (2017) 045002 [40]</p>		<p>Impact of grain size and structural changes on magnetic, dielectric, electrical, impedance and modulus spectroscopic characteristics of CoFe_2O_4 nanoparticles synthesized by honey mediated sol-gel combustion method. Adv. Nat. Sci.: Nanosci. Nanotechnol. 8(4), 045002 (2017)</p>		
<p>W https://link.springer.com/article/10.1007/s10854-020-03518-0</p>				

74/88	SUBMITTED TEXT	21 WORDS	95% MATCHING TEXT	21 WORDS
<p>Saturation magnetization (M S), Remnant magnetization (M r), coercivity (H C)</p>		<p>saturation magnetization (M s), remnant magnetization (M r) and coercivity (H c)</p>		
<p>W https://www.researchgate.net/publication/229373047_Structural_and_magnetic_properties_of_Co1-xMnx ...</p>				

72/88	SUBMITTED TEXT	28 WORDS	73% MATCHING TEXT	28 WORDS
<p>M S ' (emu/gm) 'M r ' (emu/gm) (M r /M S) 'H C ' (Oe) 100%(</p>		<p>M s (emu/g) 38 35 30.4 32.3 37.0 39.3 Remanence M r (emu/g) 22.6 18.7 16.5 16.4 18.9 19.3 M r /M s 0.59 0.54 0.54 0.52 0.55 0.53 Coercivity H c (Oe) 1634 1778 1831 1940 1985 2134</p>		
<p>W http://pr.hec.gov.pk/jspui/bitstream/123456789/7593/1/PhD%28Physics%29Full%20Thesis%20Hasan.pdf</p>				

73/88	SUBMITTED TEXT	9 WORDS	100% MATCHING TEXT	9 WORDS
<p>X-ray diffraction, scanning electron microscopy, energy dispersive X-ray</p>		<p>X-ray diffraction, scanning electron microscopy, energy dispersive X-ray</p>		
<p>W http://pr.hec.gov.pk/jspui/bitstream/123456789/7593/1/PhD%28Physics%29Full%20Thesis%20Hasan.pdf</p>				

79/88	SUBMITTED TEXT	15 WORDS	100% MATCHING TEXT	15 WORDS
<p>the samples were recorded in the wave number range of 300cm⁻¹</p>		<p>the samples were recorded in the wave number range of 400– 4000 cm ?1</p>		
<p>W https://www.researchgate.net/publication/260805883_Magnetic_and_structural_properties_of_nano_siz ...</p>				

75/88	SUBMITTED TEXT	11 WORDS	100% MATCHING TEXT	11 WORDS
<p>the saturation magnetization decreases from 33.12 emu/gm to 4.54 emu/gm</p>		<p>The saturation magnetization decreases from 91emu/gm to 44emu/gm</p>		
<p>W https://www.researchgate.net/publication/231094467_Influence_of_Thermal_Annealing_on_the_Dielectr ...</p>				

76/88	SUBMITTED TEXT	23 WORDS	100% MATCHING TEXT	23 WORDS
<p>of saturation magnetization (M S), remnant magnetization (M R) and coercivity (H C)</p>		<p>of saturation magnetization (M s), remnant magnetization (M r) and coercivity (H c)</p>		
<p>W https://www.researchgate.net/publication/229373047_Structural_and_magnetic_properties_of_Co1-xMnx ...</p>				

77/88	SUBMITTED TEXT	23 WORDS	94% MATCHING TEXT	23 WORDS
<p>Magnetolectric effects in ferrite-lead zirconate titanate layered composites: the influence of zinc substitution in ferrites, Phys. Rev. B 67 (2003) 1–10. [18]</p>		<p>Magnetolectric Effects in Ferrite-Lead Zirconate Titanate Layered Composites: The Influence of Zinc Substitution in Ferrites</p> <p>Article</p> <ul style="list-style-type: none"> • Jan 2003 • Phys Rev B • 		
<p>W https://www.researchgate.net/publication/262195378_Structural_dielectric_ferromagnetic_ferroelect ...</p>				

81/88	SUBMITTED TEXT	25 WORDS	68% MATCHING TEXT	25 WORDS
	S. S. Choudhari, S. R. Wadgane, B. P. Gaikwad, S. S. Satpute, K. M. Batoo, O. M. Aldossary, S. E. Shirsath, R. H. Kadam;		S.S. Choudhari; S.R. Wadgane; Bharatratna P. Gaikwad; S.S. Satpute; Khalid Mujasam Batoo; Omar M. Aldossary; Sagar E. Shirsath; R.H. Kadam	
	<p>W https://www.x-mol.com/paper/1323383389284438016</p>			

86/88	SUBMITTED TEXT	14 WORDS	88% MATCHING TEXT	14 WORDS
	Strain mediated enhancement in magnetoelectric properties of sonochemically synthesized piezoelectric and piezomagnetic composites;		Strain mediated enhancement in magnetoelectric properties of sonochemically synthesized piezoelectric and piezomagnetic composites	
	<p>W https://www.researchgate.net/publication/346589470_Strain_mediated_enhancement_in_magnetoelectric ...</p>			

82/88	SUBMITTED TEXT	12 WORDS	100% MATCHING TEXT	12 WORDS
	Structural, electrical and transport phenomena of Co ferrite substituted by Cd;		Structural, electrical and transport phenomena of Co ferrite substituted by Cd	
	<p>W https://www.researchgate.net/publication/279204462_Structural_electrical_and_transport_phenomena_ ...</p>			

83/88	SUBMITTED TEXT	29 WORDS	86% MATCHING TEXT	29 WORDS
	Enhancement in conductivity and dielectric properties of rare-earth (Gd 3+) substituted nano-sized CoFe 2 O 4 ; J. Mater. Sci. Mater.		Enhancement in conductivity and dielectric properties of rare-earth (Gd3+) substituted nano-sized CoFe2O4	
			Article	
			Full-text available	
			• Jun 2018	
			• J MATER SCI-MATER	
	<p>W https://www.researchgate.net/publication/231094467_Influence_of_Thermal_Annealing_on_the_Dielectr ...</p>			

84/88	SUBMITTED TEXT	15 WORDS	100% MATCHING TEXT	15 WORDS
	Grain size dependent dielectric and magnetic properties of (Y) NCCF + (1-Y) BTO particulate		Grain size dependent dielectric and magnetic properties of (y) NCCF+(1 - Y) BTO particulate	
	<p>W https://www.researchgate.net/publication/263550283_Structural_electrical_and_magnetic_properties_ ...</p>			

M S '
 (emu/gm)
 'M r '
 (emu/gm)
 (M r /M S)
 'H C '
 (Oe)
 0.0 33.12 10.58 0.319 565
 0.25 23.89 6.78 0.284 338
 0.50 14.17 1.23 0.087 112
 0.75 4.54 0.49 0.108 23
 1.0 -----

M s (emu/g)
 38 35 30.4 32.3 37.0 39.3
 Remanence
 M r (emu/g)
 22.6 18.7 16.5 16.4 18.9 19.3
 M r /M s 0.59 0.54 0.54 0.52 0.55 0.53
 Coercivity H c (Oe) 1634 1778 1831 1940 1985 2134

W <http://pr.hec.gov.pk/jspui/bitstream/123456789/7593/1/PhD%28Physics%29Full%20Thesis%20Hasan.pdf>

Dr.S.M.Patange

Impact of Zn^{2+} - Zr^{4+} ions on
mechanical and opto-electrical
properties of cobalt ferrites
prepared by sol-gel route

by S Desai

Submission date: 16-Jul-2018 08:43PM (UTC+0530)

Submission ID: 982901434

File name: ZnZr_paper_New_2.docx (35.47K)

Word count: 2312

Character count: 12422

Abstract:

In the present report, the doping effect of Zn-Zr on optical, electrical and mechanical properties of cobalt ferrite are examined. The nanocrystalline cobalt ferrites, $\text{CoZn}_x\text{Zr}_x\text{Fe}_{2-2x}\text{O}_4$ ($x = 0.0$ to 0.4 , $\Delta x = 0.1$), were synthesized using sol-gel route. The FT-IR spectra showed two major absorption bands at frequencies $580 - 610 \text{ cm}^{-1}$ and $375 - 400 \text{ cm}^{-1}$ related to spinel ferrite structure. Elastic constants were determined using Ultrasonic Pulse Transmission (UPT) method at room temperature. The values of elastic constants decreases with increase in the Zn-Zr composition 'x'. The dielectric constant (ϵ') and dielectric loss tangent ($\tan\delta$) were studied as a function of Zn-Zr composition and frequency. Both ϵ' and $\tan(\delta)$ decreased with increase in frequency and Zn-Zr substitution. The behaviour of ϵ' and $\tan(\delta)$ is explained on the basis of Maxwell-Wagner interfacial polarization which is in accordance with the Koops phenomenological theory. The Curie temperature and activation energy values were estimated from plots of thermal variation of DC resistivity.

Keywords: Ferrites; Sol-gel method; FT-IR; Elastic Properties; Dielectric properties; D.C. resistivity; Curie temperature.

1. Introduction:

Spinel ferrites are versatile magnetic ceramics materials having special magnetic and electric properties. The complex structures of spinel owe their feasibility to make large compositional variability with number of solid solutions of various metal cations. Spinel ferrite is close packed cubic crystal structure with anions (O^{2-}) amalgamate with cations (Fe^{3+} and divalent metal ions) in two sub-lattices such as tetrahedral (A), and octahedral [B] sites. Many attempts have been made to modify the electrical and elastic properties of the ferrites, by the

substitution of divalent, trivalent and tetravalent cations for replacing divalent metal ions or trivalent Fe^{3+} ions [1-3]. The substitution of Zr^{4+} modified the magnetic and structural properties of the cobalt ferrite [4, 5]. Significant modification in saturation magnetization, coercivity and magnetic anisotropy of the cobalt ferrite due to substitution of Zr^{4+} was obtained by M.V. Reddy et. al. [6]. The Zr^{4+} substituted cobalt ferrite is a suitable magnetostrictive material for magnetostriction applications [7]. The Zn-Zr doped cobalt ferrites have many technological applications for high frequency due to low magnetic losses [8-9]. In spinel ferrites, Zn^{2+} ions occupy tetrahedral (A) sites [10] while Zr^{4+} occupy both (A) and [B] sites [11]. The combinations of divalent and tetravalent ions such as Zn - Ti [12], Zn - Sn [13] and Zn - Mo [14] were doped in different ferrite systems by the investigators. The simultaneous doping of Zr-Mg by replacing Fe^{3+} ions modified electrical and structural properties of the cobalt ferrite [15].

The various methods are used to prepare nano ferrites such as, co-precipitation [16], mechano chemical reaction [17], citrate gel method [18], precursor method [19], sol-gel [20], hydrothermal methods [21] and chemical spray method [22]. Among these methods sol-gel auto combustion method is a most suitable, effective and less costly [23] for preparation of ferrite nano particles.

The mechanical behaviour of ferrites has great importance to understand the nature of inter-atomic and ionic forces in the ferrite. The mechanical properties of ferrite help to select suitable ferrite for industrial applications [24]. Basically, the elastic behaviour of material is important to illustrate the nature of binding forces and thermal properties such as specific heat and Debye temperature of the materials. The mechanical properties of ferrite such as strength of material under various strained conditions are important [25]. In the present work an attempt has been made to study the impact of Zn- Zr doping on mechanical and electrical properties cobalt ferrites.

2. Experimental Method:

2.1 Synthesis

Fig. 1 shows the flowchart of sol-gel auto combustion route for synthesis of Zn-Zr substituted cobalt ferrites of chemical formula $\text{CoZn}_x\text{Zr}_x\text{Fe}_{2-2x}\text{O}_4$ (CZ^2FO) where $x = 0.0$ to 0.4 . All chemicals are of AR grade which includes nitrates of compositional elements, ammonia solution and citric acid. The solutions are prepared in deionised water by dissolving metal nitrate salts in stoichiometric amount for all elements. The molar ratio 1:2 were kept for divalent and trivalent ions. The citric acid were mixed with aqueous solutions of metal nitrates. The mixed solution was continuously stirred for 30 min on magnetic stirrer. The solution was maintained with 7 pH by adding ammonium hydroxide solution [26]. The solution was stirred and heated simultaneously at 100°C to get thick solution called sol. The continuous heating of sol converts it into viscous gel that automatically ignited to yield the precursors, known as xerogel. These precursors are converted into powder by grinding it in an agate mortar. This powder was annealed at 650°C for 5h in furnace at constant temperature in air atmosphere to give the dense ceramic material of the ferrite.

2.1 Measurements

The structural characterization of the ferrites was performed by X-ray diffraction (XRD) and fourier transform infrared spectroscopy (FTIR). The XRD patterns were recorded in 2θ range 20° to 80° on XRD model; Philips X'Pert instrument with $\text{Cu-K}\alpha$ radiations of $\lambda = 1.54056\text{\AA}$ with scanning rate of 10° per sec at room temperature. The FT-IR spectra were recorded in the range of $300\text{--}1100\text{ cm}^{-1}$ wave number using Perkin Elmer (model 783) infrared spectrometer. The mechanical property was measured by using the Ultrasonic Pulse Transmission (UPT) method. The longitudinal and shear wave velocities (V_L & V_S) for all the samples were obtained at the room temperature. In this method ultrasonic waves are generated by using 124.6 kHz PZT crystals. The measurements were carried out with an accuracy of $\pm 5\text{ m/s}$ with interferometer. The LCR-Q meter (HIOKI 3532-50) was used for electrical measurements in the frequency range 50 Hz to 5 MHz at room temperature. The sample pellet was applied with silver paste on both sides and dried before taking the measurements. The disc shaped pellet of 10 mm diameter and 3 mm thickness were prepared. The two probe method was used to measure DC resistivity in temperature range of 300 K to 700 K .

3. Results:

3.1 XRD Analysis

The typical XRD patterns of CZ²FO for x = 0 and 0.3 are shown in Fig. 2. The peaks observed in XRD patterns were indexed using Bragg's law. The sequence and Miller indices of the peaks match with the JCPDS file No. 22-1086 for cobalt ferrite. Thus formation of cubic crystals of spinel phase ferrites with space group fd3m is revealed. The XRD analysis was performed to calculate the lattice parameters (a) of the ferrites. Table 1 exhibits that lattice parameter increased with the Zn-Zr substitution (x). The replacement of two Fe³⁺ (0.67 Å) ions by two ions Zn²⁺ (0.82 Å) and Zr⁴⁺ (0.80 Å) of larger radii creates swelling in the unit cell which was responsible for the increasing values of 'a'. The bond lengths (tetrahedral and octahedral), tetrahedral edges, octahedral edges (shared and unshared) were calculated using formula reported [27] in literature. The increase in bond lengths and edges with increasing Zn-Zr content due to increase in lattice parameters.

3.2 FTIR Analysis

The synthesized samples infrared absorption spectra were measured by using KBr pellet method in the range 300–1100 cm⁻¹ at room temperature. The FT-IR spectra of all the samples are shown in Fig. 3. The transmission bands ν_1 around 600 and ν_2 around 400 cm⁻¹ were observed. These measured bands shows ferro-spinels bands characteristics due to stretching vibration while interacting oxygen atom and cations in tetrahedral and octahedral sites. The significant changes were seen in the ν_1 band and it shifts from lower to higher frequencies with increasing Zn-Zr ions doping due to the stretching of Fe–O bonds. This shifting of band position may be due to replacing Fe with Zn-Zr [28]. The absorption band ν_2 of lower frequency can be related to oxygen- metal (octahedral) vibrations. The band position and their values are as given in Table 2. It is observed from Table 2 that bands ν_1 and ν_2 shifting gradually towards the higher frequency side due to Zn²⁺ ions solely occupied tetrahedral A-site in ferrite lattice.

The ratio of line positions of v_1 and v_2 is given by relation [28],

$$\frac{v_1}{v_2} = \frac{K_t}{K_o} \sqrt{2} \quad (1)$$

where K_t and K_o are force constants with displacement of cations–oxygen at the (A) and (B) site. The ratio of force constants was calculated using eqn (1) and the corresponding values are given in Table 2. The ratios of force constants are ≈ 1 , which means that expansion of octahedral (B) sites and compression of tetrahedral (A) sites are not same. The splitting of bands indicates the replacement of (A) and (B) site cations.

3.2 Mechanical Properties:

The longitudinal (V_l) and shear (V_s) ultrasonic wave velocities were measured with UPT technique at room temperature. Figure 4 shows variation of longitudinal wave velocities and mean velocity with Zn-Zr composition. It is cleared that the wave velocity decreased with increase in composition 'x'. This decreased wave velocity is due to increase in bulk density of material. Shearing wave velocity is less than longitudinal velocity. The mean sound velocity was calculated by the relation reported in Algude et. al. [29]. It is evident that mean velocity decreased with increase in the content 'x'.

Longitudinal modulus (L), rigidity modulus (G), Young's modulus (E), Poisson's ratio and bulk modulus (K), (σ) were calculated using the experimental values of V_L , V_S and bulk density with the help of the relation reported elsewhere [30]. The variations of all moduli with Zn-Zr content 'x' are shown in Fig. 5. It is clear that all moduli decreased with increasing Zn-Zr content x. This is due to the replacement of Fe ions having high values of all moduli by Zn-Zr ions having comparatively low values of moduli. The elastic properties of material are dependent on crystal structure and bonding stiffness, hardness and strength of material. The elastic moduli decrease slightly as the lattice expands. The lattice expands due to Fe ions replaced by the Zn-Zr ions. Table 2 shows the values of Poisson ratio. It also shows that these values are almost constant ($\sigma \approx 0.26$) for all tested

samples similar to other ferrites as reported [14]. The σ varies in the range -1 to 0.5 which is a theoretical evidence of isotropic elasticity.

The Debye temperatures of all tested samples were obtained from mean velocities. Figure 6 shows variation of Debye temperature with composition 'x'. It is seen that Debye temperature decreased with increase in Zn-Zr content 'x', due to decreased mean velocity.

3.3 Electrical Properties

3.3.1 Dielectric Properties

Dielectric properties such as dielectric loss tangent ($\tan\delta$) and dielectric constant (ϵ') were calculated from the measured values of capacities of the material in the range 50Hz to 5MHz frequency. The variations of ϵ' with frequency of electric field are shown in Fig. 7. From Fig. 7 it is clear that ϵ' decreased with increasing frequency

and remains almost constant for higher frequencies. Similar results are reported in Zr-Co doped in Co-Ni ferrites [30]. The decreased dielectric constant at higher frequency can be as per Maxwell Wagner mechanisms. The ferrite material consists conducting grains with non-conducting grain boundaries. The grains in conducting layer are more than non-conducting layer. In ferrites polarization and conduction happens due to hopping of electrons from Fe^{2+} and Fe^{3+} ions. The dielectric polarization decreased with increase in applied electric field frequency and reached a constant value at certain frequency beyond which hopping of electrons could not follow the applied field [32].

Figure 8 shows variation of dielectric loss tangent ($\tan\delta$) with frequency of the electric field. The $\tan\delta$ decreased with increasing applied electric field frequency. Again the Maxwell–Wagner model can be used to explain the variation of loss tangent. The Zn-Zr doped in place of Fe^{3+} decreases the hopping mechanism from Fe^{2+} and Fe^{3+} ions. The dielectric loss tangent appears due to lagging of polarization behind the applied electric

field. The $\tan\delta$ values depend upon the structural inhomogeneties and the impurities present in the ferrite samples. The maximum value of $\tan\delta$ obtained is 0.8. Such smaller values of loss tangent reveal the structural perfection in the ferrite samples synthesized by sol gel route [33].

3.3.1 DC Resistivity

Figure 9 shows thermal variation in d.c. resistivity of the Zn-Zr doped cobalt ferrites. The high value of conductivity in ferrites is due to both ferrous and ferric ions in the crystallographically equivalent sites. The low resistivity in ferrites is related with the occupancy of divalent metal ions and trivalent iron ions on octahedral B-site. The activation energy was calculated using Arrhenius equation ($\rho = \rho_0 \exp [\Delta E / kT]$) and Curie temperature was calculated from the $\log\rho$ versus $1000/T$ plots. The activation energy and Curie temperature are given in Table 3. It is clear that both values decrease with Zn-Zr increase in content 'x'. This behaviour of activation energy and Curie temperature may be due to electron hopping and occupancy of cations in tetrahedral and octahedral site. The Zn^{2+} ion occupy the tetrahedral site and Zr^{4+} ions occupy octahedral site. Similar results are reported in the literature [34-35].

4. Conclusions:

The Zn^{2+} and Zr^{4+} doped cobalt ferrites were prepared successfully by sol-gel route. The XRD analysis confirms formation of spinel phase in the ferrite crystals. The variation of lattice parameter with Zn-Zr composition was according to Vegard's law. FT-IR spectra showed two main bands corresponding to spinel structure of ferrite. Both frequencies of bands are improved slightly with increasing Zn-Zr content. This variations in bands of frequencies is because of the distribution of Co^{2+} , Zn^{2+} , Zr^{4+} and Fe^{3+} ions over tetrahedral (A) and octahedral (B) sites. The elastic constants were decreased with the addition of Zn-Zr content. The result showed with addition of Zn-Zr content elastic moduli magnitude decreased which reflects the strengthening of inter-atomic bonding. The Dielectric constant and dielectric loss tangent were also decreased with increase in applied electric field frequency. The calculated values of activation energies reveal the hopping of electrons can lead to the conduction in ferrites. The occupancy of tetrahedral site by Zn^{2+} and octahedral by Zr^{4+} ions reduces the Curie temperatures of the ferrites with increasing Zn-Zr content.

Impact of Zn²⁺- Zr⁴⁺ ions on mechanical and opto-electrical properties of cobalt ferrites prepared by sol-gel route

ORIGINALITY REPORT

16%

SIMILARITY INDEX

4%

INTERNET SOURCES

15%

PUBLICATIONS

4%

STUDENT PAPERS

PRIMARY SOURCES

- 1 R.A. Pawar, S.S. Desai, S.M. Patange, S.S. Jadhav, K.M. Jadhav. "Inter-atomic bonding and dielectric polarization in Gd³⁺ incorporated Co-Zn ferrite nanoparticles", *Physica B: Condensed Matter*, 2017
Publication 4%
- 2 Bhosale, Ravil R., R. S. Barkule, D. R. Shengule, and K. M. Jadhav. "Synthesis, structural, electrical and dielectric properties of Zn-Zr doped strontium hexaferrite nanoparticles", *Journal of Materials Science Materials in Electronics*, 2013.
Publication 2%
- 3 nanoscalereslett.springeropen.com
Internet Source 2%
- 4 B.M. Sahanashree, E. Melagiriappa, M. Veena, G.J. Shankaramurthy, H.M. Somashekarappa. "Influence of Neodymium and gamma rays irradiation on structural electrical and magnetic properties of Co-Zn nanoferrites", *Materials* 1%

Chemistry and Physics, 2018

Publication

5

Submitted to Üsküdar Üniversitesi

Student Paper

1%

6

Algude, S.G., S.M. Patange, Sagar E. Shirsath, D.R. Mane, and K.M. Jadhav. "Elastic behaviour of Cr³⁺ substituted Co–Zn ferrites", Journal of Magnetism and Magnetic Materials, 2014.

Publication

1%

7

file.scirp.org

Internet Source

1%

8

Birajdar, Shankar D., Pankaj P. Khirade, Tukaram S. Saraf, R.C. Alange, and K.M. Jadhav. "Sol-gel auto combustion synthesis, electrical and dielectric properties of Zn_{1-x}Co_xO (0.0 ≤ x ≤ 0.36) semiconductor nanoparticles", Journal of Alloys and Compounds, 2017.

Publication

1%

9

Avazpour, L., M.A. Zandi khajeh, M.R. Toroghinejad, and H. Shokrollahi. "Synthesis of single-phase cobalt ferrite nanoparticles via a novel EDTA/EG precursor-based route and their magnetic properties", Journal of Alloys and Compounds, 2015.

Publication

1%

10

Gurav, S.K., Sagar E. Shirsath, R.H. Kadam, and D.R. Mane. "Low temperature synthesis of $\text{Li}_{0.5}\text{Zr}_x\text{Co}_x\text{Fe}_{2.5-2x}\text{O}_4$ powder and their characterizations", Powder Technology, 2013.

Publication

1%

11

Submitted to Higher Education Commission Pakistan

Student Paper

1%

12

S.A. Mazen, N.I. Abu-Elsaad. "Temperature dependence of electrical conductivity and dielectric properties in Li–Mn ferrite", Canadian Journal of Physics, 2014

Publication

1%

13

www.academicconcepts.net

Internet Source

1%

14

S.G. Algude, S.M. Patange, Sagar E. Shirsath, D.R. Mane, K.M. Jadhav. "Elastic behaviour of Cr^{3+} substituted Co–Zn ferrites", Journal of Magnetism and Magnetic Materials, 2014

Publication

<1%

15

Singh, N.. "Dielectric relaxation, conductivity behaviour and magnetic properties of Mg substituted Ni-Li ferrites", Journal of Alloys and Compounds, 20110707

Publication

<1%

16

Zeng, Qianpu Wang, Chong Luo, Yaoling Yu.

"Effect of temperatures on TSA in cement mortars under electrical field.(thaumasite form of sulfate a", Construction and Building Materials, Feb 20 2018 Issue

<1%

Publication

17

Khalid MUJASAM Bato. "Low temperature fired Ni-Cu-Zn ferrite nanoparticles through auto combustion method for multilayer chip inductor applications", Nanoscale Research Letters, 2012

<1%

Publication

Exclude quotes Off

Exclude matches Off

Exclude bibliography Off

Dr. S.M.PATANGE



Plagiarism Checker X Originality Report

Similarity Found: 26%

Date: Wednesday, December 04, 2019

Statistics: 1173 words Plagiarized / 4545 Total words

Remarks: Medium Plagiarism Detected - Your Document needs Selective Improvement.

Study Of Structural and Electromagnetic Properties of Co Substituted Mg-Cu-Zn Ferrite Synthesized by Citrate Gel combustion Method. S.R.Kamble¹, R.S. Ramshetti²

L.M.Thorat¹, S.M.Patange^{3*} ¹ Dept of Physics, S.M.Dnyandeo Mohekar Mahavidyalaya Kallam Dist-Osmanabad. ²Dept. of Physics, Adarsh College, Omerga Dist. Osmanabad (M.S.) India ³ Dept. of Physics, Shrikrishna Mahavidyalaya Gunjoti Dist-Osmanabad.

Abstract A polycrystalline Mg_{0.25-x} Co_x Cu_{0.25} Zn_{0.5} Fe₂O₄ system (for $x = 0.0, 0.05, 0.10, 0.15, 0.20, 0.25$) have been synthesize by citrate gel combustion method and studied by using X-ray diffraction (X R D) technique. The XRD data confirms the formation of signal phase cubic structure.

The temperature dependence of DC electrical resistivity of all the samples of the series was study by two – probe methods. The increase in resistivity with increase in Co content x was reported. The result is in reduction of Fe²⁺ ions that may be formed during preparation therefore electron exchange between the iron–iron ions at B-site is reduced and hence resistivity increased was reported in the present study. Key Words: Ferrite, Co, Mg – Cu – Zn, electrical resistivity, X-ray diffraction. 1.

Introduction In recent years, the advancement in microwave technology like the wireless telecommunication systems, radar, microwave oven, medical equipment, Bluetooth technologies etc. induced a serious problem of electromagnetic pollution in this frequency range. Therefore, the demands to develop electromagnetic wave absorbers with wider absorbing bandwidths have been increased [1-8]. The electromagnetic pollution can be controlled by making use of electromagnetic absorbers and extensive studies have been carried out in this concern [9,10].

Electromagnetic wave energy can be completely absorbed and dissipated into heat through magnetic losses and dielectric losses when the impedance of free space is matched with the input characteristic impedance of an absorber [11]. Spinel ferrites have been widely utilized as electromagnetic wave absorbing materials in VHF/UHF region, due to their large magnetic losses and large resistivities [12-14]. Among the various spinel ferrites Ni-Cu-Zn ferrites have been intensively studied due to their high resistivity, low dielectric losses, high Curie temperature and excellent microwave-absorbing properties [15].

They have also been widely employed in both low and high frequency devices that play a vital role in many technological applications, such as microwave equipments, power transformers in electronics, rod antennas and read/write heads for high speed digital tape, etc [16-19]. However, the Ni-Cu-Zn ferrites have been facing certain inherent problems like sensitivity to stress, high magnetostriction constant, carcinogenic nature of nickel and its compounds etc [20, 21]. Numerous methods have been employed for the synthesis of mixed ferrites which includes sol gel [24], hydrothermal [25], mechanochemical [26], precursor [27] and auto-emulsion method [28].

We have adopted the citrate gel combustion method for the synthesis of $Mg_{0.25-x}Ni_xCu_{0.25}Zn_{0.5}Fe_2O_4$ ferrites. This method is a promising technique for the preparation of fine ferrite powders with high-sintering activity which can ultimately lead to reduction in sintering temperature [29-31]. In addition the citrate gel combustion method is simple, inexpensive and less time consuming as compared to other wet chemical methods. The present paper is focused on the structural, morphological, and magnetic properties of citrate gel synthesized $Mg_{0.25-x}Co_xCu_{0.25}Zn_{0.5}Fe_2O_4$ with $X=0, 0.05, 0.10, 0.15, 0.20, 0.25$ ferrites. 2 Experimental details 1 Synthesis of nanocrystalline $Mg_{0.25-x}Co_xCu_{0.25}Zn_{0.5}Fe_2O_4$ powders The $Mg_{0.25-x}Ni_xCu_{0.25}Zn_{0.5}Fe_2O_4$ ($x=0, 0.05, 0.1, 0.15, 0.2$ and 0.25) ferrites were synthesized using the citrate gel combustion method. The citrate gel combustion method is a single step, easy and economical way of synthesis of single and multicomponent oxides.

This method has certain inherent advantages like low processing temperature, good stoichiometric control, homogeneous distribution of reactants and production of ultra fine particles with narrow size distribution. The fuel citric acid is a weak acid and has three carboxylic and one hydroxyl group. These groups coordinate metal ions which enhances the homogeneous mixing of the reactants. The citric acid suppresses the precipitation of metal nitrates during water dehydration.

It has electronegative oxygen atoms which interact with electropositive metal ions and

therefore homogeneous single phase powders can be prepared at a relatively low temperature. Analytical reagent grade magnesium nitrate, cobalt nitrate, copper nitrate, zinc nitrate and ferric nitrate were used as starting precursors. The ratio of metal nitrates to fuel (citric acid) was kept at 3:5 moles. As per the molar composition of the investigated systems the precursor solution was prepared and further it was heated on hot plate. Continuous heating on the hot plate converted the precursor into the gel which gets auto ignited.

The auto ignition causes a rapid evolution of large volume of gases to produce voluminous powder. The as prepared powders were collected and calcinated at 700°C for 2 h to remove traces of undecomposed fuel, nitrates (if any), and their decomposition products to obtain the pure and well crystalline powder. The toroids of samples were fabricated using a die having outer diameter 2 cm, inner diameter 1 cm with average height of 0.3 cm by applying a pressure of 1.5 ton/cm² using hydraulic press machine.

All the samples in present study were sintered at 950 °C for 4 hrs in air atmosphere. 2 Experimental measurements The X-ray diffraction (XRD) pattern of the samples were obtained on BRUKER D8 advanced X-ray diffractometer using Cu-Ka ($\lambda = 1.54056 \text{ \AA}$) radiation at 2θ values between 20° to 80°. The interplanar distance d (\AA) was calculated using Bragg's law. The lattice parameter of sintered samples was calculated using the formula (1) for interplanar spacing [32] _ (1) The average particle size, D , was calculated from the Scherrer formula _.

(2) The X-ray density, bulk density and relative density were calculated by _ (3) _ (4) Surface morphology of the samples was studied using scanning electron microscope (Model SEM-JEOL) operating at 5 kV. Percentage porosity (P) of the samples was calculated from ρ_m and ρ_x values using the expression: _ (5) Transmission electron microscope (TEM) images were taken by using a Philips CM 200 FEG microscope equipped with a field emission gun at an accelerating voltage of 200 kV, with a resolution of 0.24nm.

A vibrating sample magnetometer (Lake Shore 7410 VSM) was used to study the magnetization measurements of the samples and the magnetic hysteresis loops were obtained with an applied magnetic field of 20 kOe. The double coil set up [33] was used to study the susceptibility measurements on powder sample. The inductance measurements were carried out on toroid samples from room temperature to 350 °C at 1 kHz using a computer controlled impedance analyzer (Hioki Model 3532-50 LCR HiTester, Japan).

Also the frequency dispersion of initial permeability was studied in frequency range 100 Hz to 5 MHz at room temperature. The initial permeability of the various samples was calculated using the inductance data and the standard formula for initial permeability [34]. The dielectric measurements at room temperature were carried using LCR-Q meter (HP 4284). The temperature variation curves of susceptibility and initial permeability were referred for the determination of the Curie temperature values. **3 Results and discussion**

A Analysis of Structural properties 1.

X-ray diffraction X-ray diffraction (XRD) was used to study the structural properties of samples in the present study. The X-ray diffraction patterns of different compositions of sintered $\text{Mg}_{0.25-x}\text{Co}_x\text{Cu}_{0.25}\text{Zn}_{0.5}\text{Fe}_2\text{O}_4$ ferrites are shown in Fig. 1. The spectra revealed the presence of peaks corresponding to (3 1 1), (2 2 0), (2 2 2), (4 0 0), (4 2 2), (5 1 1), (4 4 0) and (5 3 1) planes for cubic spinel structure [23]. The peaks in the X-ray diffraction pattern were indexed using standard JCPDS File No. 08-0234. The lattice parameter (a) for various compositions is given in Table 1. No prominent effect of Co addition on the values of lattice parameter was observed.

However the lattice parameter values for different samples are in close agreement with earlier reported values [18, 21]. The crystallite size for different sample varies in the range of 49 nm to 51 nm and it does not shown any systematic dependency on the Co content. The bulk density, X-ray density and relative density values for different samples in the present study are given in Table 1. Relative density increased with Co addition exhibiting maximum for $x= 0.05$ and 0.25 . The relative density of sample with $x=0.00$ (Mg-Cu-Zn) is lower as compared to sample with $x=0.25$ (Co-Cu-Zn) which is attributed to the fact that magnesium has lower atomic weight (24.30 amu) than the cobalt (58.93 amu) atom.

The replacement of Mg atoms by cobalt causes the increase in the relative density. It can also be noticed from the Table 1 that X-ray density of each sample is higher than the corresponding bulk density of sintered samples. This is attributed to the existence of the pores, which depends on sintering conditions [35].

2. Scanning electron Micrograph (SEM) and EDS

The grain growth occurring in any material is specifically due to the replacement of solid–vapour surface of the crystals by solid–solid interface via solid state diffusion, in order to, reduce overall surface energy. Diffusion of atoms through the grain boundary and grain boundary migration causes the grains to grow in size [36–38]. The microstructure of samples in the present study was observed using scanning electron microscopy (SEM).

SEM micrographs for different samples of sintered $\text{Mg}_{0.25-x}\text{Co}_x\text{Cu}_{0.25}\text{Zn}_{0.5}\text{Fe}_2\text{O}_4$ ferrites are shown in Fig. 2. The formation of compact microstructure was observed for

all Co added samples. The microstructure was significantly affected by the addition of cobalt. The average grain size determined using the line intercept method list in Table 1. Enhancement in the grain size was observed with the addition of Co to $\text{Mg}_{0.25-x}\text{Ni}_x\text{Cu}_{0.25}\text{Zn}_{0.5}\text{Fe}_2\text{O}_4$ ferrite. The SEM images of Co doped samples show the formation of distinct grains, however no particular shape and size was observed. The maximum size was observed for the sample with $x=0.10$.

The non-uniformity in grain size and shape observed in the present study is mainly due to the presence of Cu in the ferrite. The presence of copper strongly affects the microstructure of the ferrite sample because it facilitates the liquid phase sintering. The grain growth can be considered as competition between the driving force for grain boundary movement and the retarding force exerted by pores [39]. During the sintering, the thermal energy generates a force that drives the grain boundaries to grow over pores, thereby decreasing the pore volume and making the material dense.

If the driving force on each grain is homogeneous then we observed uniform distribution of the grain size. However if the driving force is non homogenous then one observes abnormal grain growth. The non uniformity of the grain size in the present study might be due to the non homogeneous driving force on the grains [40]. The observed microstructure of the samples in present study is useful for attaining good electromagnetic properties like permeability and magnetization. The elemental composition of the samples in the present study was confirmed using the EDS analysis.

Fig. 3 shows the typical EDS spectra for $\text{Mg}_{0.25-x}\text{Co}_x\text{Cu}_{0.25}\text{Zn}_{0.5}\text{Fe}_2\text{O}_4$ ferrites with $x=0.15$. The EDS data given in the Table 2 confirmed the elemental composition as per the initial concentration. Similar type of observations were reported in earlier studies [41]. 3. TEM and SAED studies The TEM images of the different compositions of sintered $\text{Mg}_{0.25-x}\text{Co}_x\text{Cu}_{0.25}\text{Zn}_{0.5}\text{Fe}_2\text{O}_4$ ferrites are shown in Fig. 4. No typical shape of the particles was observed for all samples, however from TEM images it is vivid that particles are aggregated however the sample with $x=0.25$ exhibited spherical shape.

The average crystallite size for different compositions is given in Table 1. The average particle size was influenced by addition of Co and no particular variation of particle size with Co content was observed. The maximum particle size was observed sample with $x=0.05$. The aggregates of the particles may be formed due to the interfacial surface tension, which arises from the magnetostatic or exchange interactions between particles [42]. Inset of Fig. 4 shows the SAED pattern for various samples of sintered $\text{Mg}_{0.25-x}\text{Co}_x\text{Cu}_{0.25}\text{Zn}_{0.5}\text{Fe}_2\text{O}_4$ ferrites.

The SAED pattern confirmed the presence of bright spots corresponding to various

planes as represented in XRD pattern and confirmed the polycrystalline nature of the samples B. Analysis of Magnetic properties The magnetic properties of soft ferrites are influenced by the composition, additives, and microstructures of the materials. Among these factors, the microstructures have great effect on magnetic properties. Generally ferrites possessing large saturation magnetization, initial permeability with low coercivity find useful technological applications. 1. A. C. susceptibility The normalized AC susceptibility of the sintered $\text{Mg}_{0.25-x}\text{Co}_x\text{Cu}_{0.25}\text{Zn}_{0.5}\text{Fe}_2\text{O}_4$ ferrite samples as a function of temperature is depicted in Fig. 10.

The normalized susceptibility for all samples almost remained constant upto certain temperature and thereafter all the samples showed a sharp decrease in normalized AC susceptibility with temperature near Curie temperature, indicating absence of impurity phases in the samples which was confirmed from XRD studies. The room temperature susceptibility was not influenced significantly by the addition of Co. The constant behavior of normalized susceptibility upto Curie temperature is because of the available thermal energy is not sufficient to disturb the aligned moments of spins.

This behavior has confirmed the ferrimagnetic nature of the material under investigation. However above the Curie temperature the decrease in susceptibility is attributed to the disturbance of moment's alignment due to the thermal energy provided by that temperature and this is the indication of the transition of material from ferrimagnetic state to paramagnetic state. The temperature invariance of normalized AC susceptibility up to Curie temperature for all samples confirmed that the compositions contain multi domain particles in predominance.

In general, magnetic grains tens of microns are known as multi domain (MD), small grains up to about a hundred of angstroms are called as super paramagnetic (SP) and those which are few hundred angstroms are called as single domain (SD) [43]. The Curie temperature values for all samples are given in Table 3. The Curie temperature was found to increase with increase in cobalt content. The increase in the Curie temperature with addition of Co is mainly due to the replacement of nonmagnetic Mg^{2+} by Co^{2+} which causes the increase in ferrimagnetic region at the same time the decrease in paramagnetic region.

It is due to the fact that the Co has preference occupancy at octahedral site and when it replaces the Mg at octahedral site enhancement in magnetic interaction at octahedral site occurs. Similar type of behavior was also reported by some researchers [44, 45]. Above the Curie temperature a complete disordered state as well as the magnetization destruction is obtained. The strong exchange interaction in case of sample with $x=0.25$ due to high content of Co resulted into highest Curie temperature compared to other

samples [46]. 2.

Magnetization (VSM) The preferential occupancy of the cations, composition, microstructure and density of ferrites strongly influences their magnetic properties like saturation magnetization, coercivity and remanence. The room temperature hysteresis loops for various samples of sintered $\text{Mg}_{0.25-x}\text{Co}_x\text{Cu}_{0.25}\text{Zn}_{0.5}\text{Fe}_2\text{O}_4$ ferrites are shown in Fig. 11. The magnetic hysteresis in case of all samples exhibited a typical shape and confirmed that the samples are magnetically ordered. The values of saturation magnetization, coercivity and remanence for all compositions are given in Table 1.4. It is observed from the Table 1.4 that the increase in Co content has resulted into the increase in the value of saturation magnetization.

Maximum value of saturation magnetization was exhibited by the $\text{Mg}_{0.25-x}\text{Co}_x\text{Cu}_{0.25}\text{Zn}_{0.5}\text{Fe}_2\text{O}_4$ ferrite with $x = 0.25$. The enhancement in saturation magnetization is mainly due to the substitution of nonmagnetic Mg^{2+} ions with highly magnetic Co^{2+} . The observed variation in saturation magnetization can be explained on the basis of cation distribution and the exchange interactions between A and B-sites. It is known that the Mg ferrite is a spinel with an inversion degree of about 0.8 [47]. In Mg-Cu-Zn ferrite, the stable Zn^{2+} ions occupy the A-sites only. By substituting Co^{2+} ions for Mg^{2+} (which has a magnetic moment of 3.7

μ_B) on the octahedral sites (B-sites), an increase in the magnetization of B sublattice takes place, leading to the increase in the saturation magnetization of the ferrite [48]. Squareness or remnant ratio (M_r/M_s) is a characteristic parameter of the material and is dependent on anisotropy. It indicates the ease with which the magnetization direction is reoriented to the nearest easy axis magnetization direction after the magnetic field is removed. The lower is its value, the more isotropic the material will be [49].

The knowledge of squareness ratio plays an essential role in the development of new materials. The values of experimental magnetic moment and probable cation distribution are given in Table 1.5. The experimental magnetic moment was increased with increase in Co content however the a_y-k was decreased. The decrement in a_y-k is attributed to the replacement of nonmagnetic Mg by magnetic Co which lead to enhancement in exchange interaction. 3. Initial permeability The initial permeability is a very sensitive parameter, which depends on various factors like temperature, grain size, method of preparation etc. For MLCI applications, the temperature dependence of initial permeability is very important.

It is recognized that the permeability of polycrystalline ferrite is associated with two magnetizing mechanisms: spin rotation and domain wall motion. According to Globus

[50], the domain walls normally remain pinned to the grain boundary and bulge when subjected to a small magnetic field. The initial permeability is mainly due to reversible motion of the domain walls. Globus assumed that the permeability due to the wall motion is likely to be linearly dependent on the grain size, while the permeability contribution due to spin rotation was assumed to be independent of grain size.

The initial permeability for various samples of sintered $\text{Mg}_{0.25-x}\text{Co}_x\text{Cu}_{0.25}\text{Zn}_{0.5}\text{Fe}_2\text{O}_4$ ferrites at room temperature were measured in the frequency range of 100 Hz–5 MHz. Fig. 1.12 shows the variation of initial permeability as a function of frequency. The initial permeability for various samples of sintered $\text{Mg}_{0.25-x}\text{Co}_x\text{Cu}_{0.25}\text{Zn}_{0.5}\text{Fe}_2\text{O}_4$ ferrites exhibited a constant behavior upto a certain frequency and then initial permeability increased with further increase in the frequency. However the variation of initial permeability with Co substitution was not consistent with the variation of saturation magnetization, coercivity, density and microstructure.

This behavior of initial permeability seems to be in accordance with the magnetocrystalline anisotropy as the maximum permeability was recorded for the sample at which the magnetocrystalline anisotropy constant changes its sign [51]. Table 1.6. Shows the initial permeability values (μ_i), measured at room temperature, for 1 KHz frequency. As revealed in Table 1.6, the initial permeability increased with the addition of Co and showed maximum value for sample with $x=0.05$ and then decreased with further increase in Co content. It was observed that for Co content more than $X=0.05$ the initial permeability decreases and this decrease is mainly attributed to the increase in magnetostriction constant due to substitution of Mg by Co and similar type of results were reported earlier [52].

As mentioned above, the variation of initial permeability of Mg-Cu-Zn ferrite was influenced not only by microstructures, but also by magnetostriction, inner stress and other factors. Fig. 1.13 shows the variation of initial permeability as a function of temperature for different compositions of sintered $\text{Mg}_{0.25-x}\text{Co}_x\text{Cu}_{0.25}\text{Zn}_{0.5}\text{Fe}_2\text{O}_4$ ferrites. The initial permeability exhibited a steady behavior upto a particular temperature, achieves a peak value and then suddenly drops to a minimum value at Curie temperature.

The sudden fall in initial permeability at Curie temperature is the sign of transition from ferrimagnetic state to the paramagnetic state. The $\text{Mg}_{0.25-x}\text{Co}_x\text{Cu}_{0.25}\text{Zn}_{0.5}\text{Fe}_2\text{O}_4$ ferrite with $x=0.05$ exhibited maximum initial permeability and with further increase in Co content decrease in permeability was observed. The Curie transition temperature (T_c) was measured from Fig. 1.13 and the values are presented in Table 1.6. The magnitude of Curie temperature increased with Co content. This increase in Curie transition

temperature is due to the substitution of magnetic Co^{2+} in place of nonmagnetic Mg^{2+} at octahedral site [53].

The rotational and wall permeability values were calculated using the formula ($\mu_r = 1 + 2(M_2s / l k_1)$, ($w = (i - (\mu_r - 1))$ respectively. The rotational permeability and wall permeability values are given in Table 1.6. From Table 1.6 it is clearly seen that the magnitude of wall permeability (w is very large in comparison with rotational permeability (μ_r for all compositions of $\text{Mg}_{0.25-x}\text{Co}_x\text{Cu}_{0.25}\text{Zn}_{0.5}\text{Fe}_2\text{O}_4$ ferrite. Thus, it is concluded that the main contribution to the initial permeability is due to domain wall motion. The initial permeability values during heating and cooling cycles and μ_i are given in Table 1.7.

All the samples have exhibited the thermal hysteresis of initial permeability and μ_i increased with addition of Co. In ferrite materials magnetic losses are due to phase lag of domain wall motion with respect to the applied AC magnetic field. The variation of magnetic loss factor with temperature is shown in Fig. 1.14. For all the samples the loss factor almost remain constant up to a certain temperature thereafter a drastic increase in the loss factor was observed. It is well known that higher the value of initial permeability lower is the value of loss factor and accordingly the sample with $x=0.05$ exhibited lowest value of loss factor at room temperature. 4. Conclusions The fine particles of $\text{Mg}_{0.25-x}\text{Co}_x\text{Cu}_{0.25}\text{Zn}_{0.5}\text{Fe}_2\text{O}_4$ with $X= 0, 0.05, 0.10, 0.15, 0.20, 0.25$ ferrites were successfully synthesized using citrate gel combustion method. The structural properties were found to be influenced by addition of Co. SEM study revealed formation of compact microstructure.

All the samples have exhibited the dielectric dispersion phenomena. The addition of Co has shown strong impact on the magnetic properties. Initial permeability studies confirmed the multi-domain nature of the grains. To conclude with, $\text{Mg}_{0.25-x}\text{Co}_x\text{Cu}_{0.25}\text{Zn}_{0.5}\text{Fe}_2\text{O}_4$ at $X=0.05$ is the potential candidate for EMI and MLCI applications. Figure Caption ; Fig 1: X-ray diffraction patterns of the sintered $\text{Mg}_{0.25-x}\text{Co}_x\text{Cu}_{0.25}\text{Zn}_{0.5}\text{Fe}_2\text{O}_4$ ferrites. Fig2: The SEM images of all compositions of sintered $\text{Mg}_{0.25-x}\text{Co}_x\text{Cu}_{0.25}\text{Zn}_{0.5}\text{Fe}_2\text{O}_4$ ferrites. Fig 3: Typical EDAX spectra for sintered $\text{Mg}_{0.25-x}\text{Co}_x\text{Cu}_{0.25}\text{Zn}_{0.5}\text{Fe}_2\text{O}_4$ ferrites with $x=0.15$. Fig4: The TEM images of all compositions of sintered $\text{Mg}_{0.25-x}\text{Co}_x\text{Cu}_{0.25}\text{Zn}_{0.5}\text{Fe}_2\text{O}_4$ ferrites. Fig.

5: AC susceptibility of all samples as function of Temperature Fig 6: Magnetic hysteresis loops of sintered $\text{Mg}_{0.25-x}\text{Co}_x\text{Cu}_{0.25}\text{Zn}_{0.5}\text{Fe}_2\text{O}_4$ ferrites. Fig7: Frequency dependency of initial permeability for different compositions of sintered $\text{Mg}_{0.25-x}\text{Co}_x\text{Cu}_{0.25}\text{Zn}_{0.5}\text{Fe}_2\text{O}_4$ ferrites. Fig.8: Temperature dependency of permeability for different compositions of sintered $\text{Mg}_{0.25-x}\text{Co}_x\text{Cu}_{0.25}\text{Zn}_{0.5}\text{Fe}_2\text{O}_4$ ferrites. Fig.9:

Temperature dependency of loss factor for different compositions of sintered $\text{Mg}_{0.25-x}\text{Co}_x\text{Cu}_{0.25}\text{Zn}_{0.5}\text{Fe}_2\text{O}_4$ ferrites. 5 References [1] _H. Bayrakdar, J. Magn. Magn. Mater. 323 (2011) 1882. _ [2] _V.G. Harris, IEEE Trans. Magn. 48 (2012) 1075–1104. _ [3] _J. L. Xie, M. Han, L. Chen, R. xiong Kuang, Long jiang Deng, J. Magn. Magn. Mater. 314 (2007) 37. _ [4] _M.R.

Meshram, N.K. Agrawal, B. Sinha, P.S. Misra, J. Magn. Magn. Mater. 271 (2004) 207. _ [5] _M. Yu Ou Long jiang Deng, J. Magn. Magn. Mater. 321 (2009) 1125. _ [6] _K. Matsumoto, A. Kondo, T. Habu, K. Hayashi, O. Hashimoto, Microwave Opt. Technol. Lett. 48 (2006) 2065. _ [7] _L. Ma, G. Wang, L. Liu, B. Li, J. Alloys Comp. 505 (2010) 374. _ [8] _Y.N. Kazantsev, A.V. Lopatin, N.E. Kazantseva, A.D. Shatrov, V.P. Maltsev, J. Vilcakova, P. Saha, IEEE Trans. Antennas Propag. 58 (2010) 1227. _ [9] _J.J. Siddiqui, K. Zhu, J. Qiu, H. Ji, Mater. Res. Bull. 47 (2012) 1961. _ [10] _R.S. Meena, S. Bhattacharya, R. Chatterjee, Mater. Sci. Eng., B 171 (2010) 133. _ [11] _S.P. Gairola, V. Verma, V. Pandey, Ravi, L.P. Purohit, R.K. Kotnala, Int. J.

119 (2010) 151. _ [12] _Y. Nie, H. He, Z. Zhao, R. Gong, H. Yu, J. Magn. Magn. Mater. 306 (2006) 125. _ [13] _M. Matsumoto, Y. Miyata, IEEE Trans. Magn. 33 (1997) 4459. _ [14] _L. Deng, M. Han, Appl. Phys. Lett. 91 (2007) 0231191. _ [15] _Y. Hwang, Mater. Lett. 60(27) (2006) 3277. _ [16] _A Verma, D. C. Dube. J. Am. Ceram. Soc. 88(3) (2005) 519. _ [17] _M. P. Reddy, W. Madhuri, N. R. Reddy, K.V.S. Kumar, V.R.K. Murthy, R.R. Reddy. J Electro. Ceram. 28(1) (2012) 1. _ [18] _S.A. Ghodake, U.R. Ghodake, S.R. Sawant, S.S. Suryavanshi, P.P. Bakare, J. Magn. Magn. Mater. 305 (2006) 110. _ [19] _M. Yan, J. Hu, W. Luo, W.Y. Zhang, J. Magn. Magn. Mater. 303 (2006) 249. _ [20] _H. Su, H. Zhang, X. Tang, B. Liu, Z.

Zhong, Journal of Alloys and Compounds 475 (2009) 683. _ [21] _A. Daigle, J. Modest, A.L. Geiler, S. Gillette, Y. Chen, M. Geiler, B. Hu, S. Kim, K. Stopher, C. Vittoria, V.G. Harris, Nanotechnology 22 (2011) 305708. _ [24] _A. Xia, C. Zuo, L. Chen, C. Jin, Y. Lv, J. Magn. Magn. Mater. 332 (2013) 186. _ [25] _H. Yang, X. Zhang, W. Ao, G. Qiu, Mater. Res. Bull. 39 (2004) 833. _ [26] _M. Penchal Reddy, W. Madhuri, G. Balakrishnaiah, N. Ramamanohar Reddy, K.V. Siv Kumar, V.R.K. Murthy, R. Ramakrishna Reddy, Curr. Appl. Phys. 11(2011) 191. _ [27] _R. Ali, M. A. Khan, A. Mahmood, A. H. Chughtai, A. Sultan, M. Shahid, M. Ishaq, M. F. Warsi, Ceram. Int. 40 (2014) 3841. _ [28] _A. Mahmood, M. Farooq Warsi, M. Naeem Ashiq, M. Ishaq, J. Magn.

Magn. Mater. 327 (2013) 64. _ [29] _S. Yan, W. Ling, E. Zhou. J. Cryst. Growth 273(2004)226. _ [30] _M.R. Barati, S.A. Seyyed Ebrahimi, A. Badiei, Key Eng. Mater. 368–372 (2008) 598. _ [31] _J. Azadmanjiri, H.K. Salehani, M.R. Barati, F. Farzan, J. Mater. Lett. 61 (2007) 84. _ [32] _B.D. Cuility, Elements of X-ray Diffraction, Addison Wesley

Pub. Co. Inc., London-Wesley London, 1956, pp. 42. _ _[33] _D.N. Bhosale, V.M.S. Verenkar, K.S. Rane, P.P. Bakare, S.R. Sawant, *Materials Chemistry and Physics* 59 (1999) 57. _ _[34] _N. Varalaxmi, K.V. Sivakumar, *Mater. Sci. Eng. B* 184 (2014) 88. _ _[35] _M. P. Reddy, I.G. Kim, D. S. Yoo, W. Madhuri, M. V. Ramana, A. Shaaban, N. R. Reddy, K.V. S. Kumar, R. R.Reddy, *Superlatt.*

Micros. 56 (2013) 99. _ _[36] _H. Su, X. Tang, H. Zhang, Z. Zhong, J. Shen, *J. Appl. Phys.* 109 (2011)07A501. _ _[37] _T.K. Gupta, R.L. Coble, *J. Am. Ceram. Soc.* 51 (1968) 521. _ _[38] _R.L. Coble, T.K. Gupta, in: G.C. Kuczynski, N.A. Hroton, C.F. Gibbon (Eds.), *Sintering and Related Phenomena*, Gordon and Breach, New York, 1967, p. 423. _ _[39] _M. Manjurul Haque, M. Huq, M.A. Hakim, *J. Magn. Magn. Mater.* 320 (2008) 2792. _ _[40] _Ch. Sujatha, K. Venugopal Reddy, K. Sowri Babu, A. Rama Chandra Reddy, K.H. Rao, *Ceram. Int.* 38 (2012) 5813. _ _[41] _M. P. Reddy, W. Madhuri, N. R. Reddy, K.V. S. Kumar, V.R.K. Murthy, R. R.Reddy, *Mat. Sci. Eng. C* 30 (2010) 1094. _ _[42] _H. Bahirae, M. Z. Shoushtari, K. Gheisari, C.K. Ong, *Mater. Lett.*

122 (2014) 129. _ _[43] _C. Radhakrishnamurthy, *J. Geol. Soc. India* 26 (1985) 640. _ _[44] _M.A. Ahmed, S.T. Bishay, *J. Magn. Magn. Mater.* 279 (2004) 178. _ _[45] _G. Singh, V.S. Darshane, *J. Mater. Sci.* 29 (1994) 1540. _ _[46] _M.A. Ahmed, S.F. Mansour, S.I. El-Dek, *Solid State Ionics* 181 (2010)1149. _ _[47] _J. Smit, H.P.J. Wijn, *Les Ferrites*, Dunod, Paris, 1961. _ _[48] _H. Su, H. Zhang, X. Tang, *J. Magn. Magn. Mater.* 302 (2006) 278. _ _[49] _A.R. Bueno, I.M. Gregori, M.C.S. Nobrega, *Mater. Chem. Phys.* 105 (2007) 229. _ _[50] _M. P. Reddy, W. Madhuri, M. V. Ramana, N. R. Reddy, K.V. S. Kumar, V.R.K. Murthy, K. S. Kumar, R. R. Reddy, *J. Magn. Magn. Mater.* 322 (2010) 2819. _ _[51] _Ohta K.: *J. Phys. Soc. Japan*, 18 (1963) 685. _ _[52] _J.H.

Nam, W.G. Han, J.H. Oh, *J. Appl. Phys.* 81 (8) (1997)4794. _ _[53] _M. Naeem, N.A. Shah, I.F. Gul, A. Maqsood, *J. Alloys Compd.* 487 (2009) 739. _ _

INTERNET SOURCES:

<1% - <https://www.sciencedirect.com/science/article/pii/S0272884213015198>

<1% -

https://www.researchgate.net/publication/243230846_Temperature_dependence_of_the_electrical_resistivity_of_amorphous_Co_80-x_Er_x_B_20_alloys

1% - <https://www.sciencedirect.com/science/article/pii/S0304885307002338>

<1% - <https://www.sciencedirect.com/science/article/pii/S0925838818305176>

<1% - <https://www.sciencedirect.com/science/article/pii/S0304885313007890>

3% - <https://link.springer.com/content/pdf/10.1007%2Fs40145-018-0272-6.pdf>

1% -

<http://english.sic.cas.cn/rh/RD/skl/rf/sj/publications/201504/W020150504536510373509.pdf>

2% -

https://www.researchgate.net/publication/328196668_Co2_substituted_Mg-Cu-Zn_ferrite_Evaluation_of_structural_magnetic_and_electromagnetic_properties

<1% - <https://www.sciencedirect.com/science/article/pii/S0928493118315856>

<1% - <https://www.sciencedirect.com/science/article/pii/S0022369717320474>

<1% - <https://www.sciencedirect.com/science/article/pii/S0955221903005247>

<1% -

https://www.researchgate.net/publication/222737290_Effect_of_Preparation_Conditions_on_Formation_of_Nanophase_Ni-Zn_Ferrites_Through_Hydrothermal_Technique

<1% -

https://www.researchgate.net/publication/229732158_Magneto-Dielectric_Properties_of_Mg-Cu-Co_Ferrite_Ceramics_I_Densification_Behavior_and_Microstructure_Development

<1% -

https://www.researchgate.net/publication/284084616_Bulk_synthesis_of_nanocrystalline_uranium_powders_by_citrate_gel-combustion_method

2% - <https://www.sciencedirect.com/science/article/pii/S0272884214005471>

<1% -

https://www.researchgate.net/publication/229246442_Nanocrystalline_Thoria_Powders_Via_Glycine-Nitrate_Combustion

<1% - <https://www.sciencedirect.com/science/article/pii/S0921452618300425>

<1% - <https://www.sciencedirect.com/science/article/pii/S0304885304001313>

1% -

https://www.researchgate.net/publication/314292994_Solution_combustion_synthesis_of_Ca_hexaferrite_using_glycine_fuel

<1% -

<https://www.intechopen.com/books/sintering-applications/development-of-a-stress-insensitive-mgcu-zn-nicu-zn-composite-ferrite-useful-for-microinductors-applications>

<1% -

<https://epdf.pub/physics-and-technology-of-thin-films-iwtf-2003-proceedings-of-the-international-.html>

<1% -

https://www.researchgate.net/publication/330523405_Synthesis_and_Characterization_of_Cadmium_Sulfide_Nanoparticles_by_Chemical_Precipitation_Method

<1% - <https://www.sciencedirect.com/science/article/pii/S0272884212001885>

<1% - <https://nanoscalereslett.springeropen.com/articles/10.1186/1556-276X-8-446>

<1% - <https://www.sciencedirect.com/science/article/pii/S0167577X00000082>

1% - <https://www.sciencedirect.com/science/article/pii/S0928493112003876>

<1% -

https://www.researchgate.net/publication/316342080_gamma_irradiation_study_of_zinc_ferrite_nanoparticles_using_Mossbauer_spectroscopy_and_X-ray_diffraction

<1% - http://www.ukm.my/mjas/v18_n3/Sundari_18_3_1.pdf

<1% - <https://www.science.gov/topicpages/x/xrd+diffraction+peaks>

<1% -

<http://nanojournal.ifmo.ru/en/wp-content/uploads/2013/06/NPCM2013-43P430.pdf>

<1% - <https://www.sciencedirect.com/science/article/pii/S0955221919306077>

<1% -

https://www.researchgate.net/publication/6773001_Analysis_of_Amorphous_and_Nanocrystalline_Solids_from_Their_X-Ray_Diffraction_Patterns

1% - <https://www.sciencedirect.com/science/article/pii/S0925838809016223>

<1% -

https://www.researchgate.net/publication/259781835_Sintering_Densification_Grain_Growth_Microstructure

<1% - <https://www.sciencedirect.com/science/article/pii/S0026271419302343>

<1% - <https://www.sciencedirect.com/science/article/pii/S0925838819303354>

<1% -

https://www.researchgate.net/publication/223622944_Structural_analysis_of_nickel_doped_cobalt_ferrite_nanoparticles_prepared_by_coprecipitation_route

<1% - <https://www.chemweb.com/articles/SV11661/0004700006>

<1% - <http://me.buet.ac.bd/icme/icme2011/Proceedings/PDF/ICME%2011-RT-021.pdf>

1% -

https://www.researchgate.net/publication/229384869_Influence_of_CuO_and_Sintering_Temperature_on_the_Microstructure_and_Magnetic_Properties_of_Mg-Cu-Zn_Ferrites

<1% - <https://www.sciencedirect.com/science/article/pii/S0272884212003355>

<1% - <https://www.sciencedirect.com/science/article/pii/S0079642510000290>

<1% - <https://link.springer.com/article/10.1007%2Fs42452-019-0258-1>

2% - <https://www.sciencedirect.com/science/article/pii/S0304885302008545>

<1% -

https://www.researchgate.net/publication/323637277_Magnetoreflexion_and_Magnetotriaxion_in_Ferrimagnetic_Spinels_CoFe2O4

<1% -

https://www.researchgate.net/publication/257152549_Magnetic_properties_and_cation_distribution_study_of_nanocrystalline_Ni-Zn_ferrites

1% -

https://www.researchgate.net/publication/229366738_Thermal_hysteresis_and_domain_states_in_Ni-Zn_ferrites_synthesized_by_oxalate_precursor_method

<1% -

<http://nopr.niscair.res.in/bitstream/123456789/9295/1/IJEMS%2011%284%29%20289-29>

4.pdf

1% -

https://www.researchgate.net/publication/257150895_The_role_of_Dy3_ions_and_sintering_temperature_on_the_magnetic_characterization_of_LiCo-Ferrite

<1% - <https://www.chemweb.com/articles/09258388/061500S1>

<1% - <https://www.sciencedirect.com/science/article/pii/S0022286013000318>

<1% - <https://www.sciencedirect.com/science/article/pii/S0022286011004704>

<1% - <https://www.sciencedirect.com/science/article/pii/S0304885397004952>

<1% -

https://www.researchgate.net/publication/272171533_IR_and_Magnetic_Studies_of_Al3_Substituted_Co-Mn-FeO4_Nano_Ferrites

2% - <https://www.sciencedirect.com/science/article/pii/S0928493110001372>

1% - <https://www.sciencedirect.com/science/article/pii/S0304885308007099>

<1% - <https://www.sciencedirect.com/science/article/pii/S0304885318300283>

<1% - <https://www.sciencedirect.com/science/article/pii/S0301479718304134>

<1% - <https://www.sciencedirect.com/science/article/pii/S0304885314006027>

<1% -

https://www.academia.edu/3630486/Microwave_Sintering_of_NiCuZn_ferrites_for_Multilayer_Chip_Inductors

<1% -

https://www.academia.edu/3496325/Influence_of_copper_substitution_on_magnetic_and_electrical_properties_of_MgCuZn_ferrite_prepared_by_microwave_sintering_method

<1% -

https://www.researchgate.net/publication/225449564_Effect_of_Manganese_Substitution_on_the_Magnetic_Properties_of_Nickel-Zinc_Ferrite

<1% - <https://www.sciencedirect.com/science/article/pii/S0304885305011595>

<1% - <https://www.sciencedirect.com/science/article/pii/S0025540810002618>

<1% - <https://www.sciencedirect.com/science/article/pii/S0272884212009376>

<1% - <https://www.sciencedirect.com/science/article/pii/S0304885317312088>

<1% -

https://www.researchgate.net/publication/327675007_Structural_magnetic_and_elastic_properties_of_Mn03-xMgxCu02Zn05Fe3O4_nanoparticles

DR.S.M.PATANGE

122144

by 89 145

Submission date: 05-Feb-2020 02:20PM (UTC+0530)

Submission ID: 1251880367

File name: 8781788.doc (82K)

Word count: 2678

Character count: 14725

Influence of Crystalline size on Structural, Magnetic, Mechanical and Dielectric properties of Ni-Cu-Zn nano ferrites

Abstract

The sol-gel auto combustion method was used to prepare $\text{Ni}_{0.3}\text{Cu}_{0.2}\text{Zn}_{0.5}\text{Fe}_2\text{O}_4$ Nano spinel ferrite. The synthesized samples annealed with different temperatures such as as-prepared, 400°C and 600°C for 4 hr and there are characterized by XRD, TEM, V.S.M., Elastic and Dielectric properties. Analysis of x-ray diffraction patterns shows as temperature increases, the crystallinity increases and XRD pattern shows the single phase cubic structure. The lattice constant 'a' increases with increase in annealed temperature. TEM images revealed that crystalline size is in the range of 8 to 12 nm. As annealing temperature increases, Saturation magnetization and coercivity are also increased. Room temperature values of shearing velocity (V_s) and longitudinal velocity (V_L) are obtained from the Ultrasonic Pulse transmission method, are employed to determine the elastic moduli such as young's (E), Bulk (K), longitudinal (L), Rigidity (G) and Poisson's ratio. With increase in annealing temperature the values of these moduli are increased, which predict bonding force between atoms. The dielectric properties such as dielectric constant (ϵ') and dielectric loss (ϵ'') are explained on the basis of hopping mechanism.

Keyword : NiCuZn Ferrite; TEM; V.S.M.; Mechanical Properties; Dielectric properties.

1. Introduction:

The polycrystalline Ni-Zn ferrites (NZFOs) are soft magnetic materials, which have wide application in electrical and electronic industries [1], multi-layer LC filters [2], magnetic temperature sensors [3] and humidity sensors [4]. Now a day's, from technological point of view soft magnetic material having particle size in nanometer scale are of research interest due to their unique magnetic properties significantly vary from those of bulk materials. The NiCuZn ferrite was widely used to fabricate Multilayer Ferrite Chip Inductor (MLFCI). Multilayer Ferrite Chip Inductor (MLFCI) is an electronic component for the electronic products such as Video Cameras, Cellular Phone, Notebook, and Computer etc. [5,6]. In recent year Multilayer Chip Inductor

[MLCI] is used as key surface mounting devices [7, 8]. The NiCuZn ferrite sintered at low temperature is significant magnetic material for multi-layer chip inductors (MLCIs) applications due to their chemical stability, high electrical resistivity, high permeability in a high frequency region and low sintering temperatures [9,10]. The traditional standard ceramic method is the generally used method for production of Ni-Cu-Zn ferrites, which has disadvantages of coarser particle size, chemical inhomogeneity etc. [11, 12].

Engineers have been researching high strength and ductile materials for decade. These two properties often behave differently when composition and structure are varied [13]. The mechanical properties of the base materials are enhanced by two basic processes viz. deformation and heat treatment. Annealing induces dislocation rearrangement, allowing stress relief. This may lead to improved ductility properties [14]. The size distribution of the grain and contamination in the grain boundaries can play an important role. It is well established that reducing the grain size is beneficial to the mechanical properties of poly-crystalline bulk materials [15]. Very small grain size improved metallic material strength and toughness at low temperature. Optimal grain size is usually found in the range of 5 to 10 nm [16].

The present paper is an account of the results of a meticulous study of elastic behavior of NiCuZn ferrite nanoparticles produced by self-propagation route. However, according to the knowledge of the authors a study on the specific composition $Ni_{0.3}Cu_{0.2}Zn_{0.5}Fe_2O_4$ of Ni-Cu-Zn system is not reported. In most of the technological applications ferrites are used as a dielectric material hence it is crucial to study their dielectric properties at varying frequencies. The present investigation is aimed to study frequency and annealed temperature dependent dielectric properties of nanocrystalline Ni^{2+} substituted Cu-Zn ferrite prepared by sol-gel auto-combustion technique. In this paper, we report on the synthesis process, the structural characterization, the elastic properties of as prepared and annealed temperature ferrite powder and dielectric behavior of $Ni_{0.3}Cu_{0.2}Zn_{0.5}Fe_2O_4$ ferrites nano-sized powder.

2. Experimental

2.1 Synthesis method

The nanocrystals of $Ni_{0.3}Cu_{0.2}Zn_{0.5}Fe_2O_4$ (NCZ ferrites) were synthesized by self-propagating way. The AR grade metal nitrates having chemical formulae $Cu(NO_3)_2$, $Zn(NO_3)_2$, $Ni(NO_3)_2$, and $Fe_2(NO_3)_2$ were utilized to prepare the precursor solution. The hydrous solutions of these nitrates were prepared separately by dissolving the chemicals in the distilled

water and stirring for 15 minutes at 80 °C. These solutions were then added together and stirred continuously for 30 min. at the temperature of 100 °C to obtain the precursor solution. The aqueous solution citric acid was added to the precursor solution and the pH of solution was adjusted to 7 with slow addition of ammonia solution. Then this solution was put on to a hot plate and stirred continually at 100°C. The solution then transformed to the thick viscous gel. The continuous heating of few minutes ignites the gel automatically which burns with glowing flints.

The burning called auto combustion complete within a minute and the brown colored ashes known as precursor were produced. These precursors were crushed well in a mortar to obtain the powders. These powders were annealed at 400°C and 600°C for 4 hours to obtain ferrite which is the final product. The ferrite pellets of 10 mm diameter were prepared by pressing the powder in the hydraulic press under the pressure of 60 kg/ cm² for two minutes. The polyvinyl alcohol was used as a binding material. The sintering of the pellets at 400° C for two hours was performed to remove the binder.

2.2 Characterization

The X- ray diffraction (XRD) patterns of the ferrite powders were obtained by using the X- ray diffractometer (Model: Bruker D8), with Cu-K α irradiation ($\lambda = 1.5405 \text{ \AA}$). The scanning step was 2 °/min and scanning rate was 0.02°. 1-D detector was used for the XRD measurement. The XRD data were used to obtain the values of crystallite (grain) size, lattice parameter of investigated samples.

Morphology, structure and crystalline size of the powder samples were studied using transmission electron microgram (TEM). V.S.M. measurements were performed at room temperature.

The ultrasonic pulse transmission method was used to calculate values of shear (V_s) and longitudinal (V_l) wave velocities of the studied ferrite samples. In this method 124.6 KHz PZT crystals and calibrated range of Interferometer were used with an accuracy of error ± 5 m/s in velocity measurements. The dielectric parameters, ϵ' (dielectric constant), ϵ'' (dielectric loss) and $\tan\delta$ (dielectric loss tangent) were measured with varying frequency using LCR-Q meter (Hioki model 3532-50).

3. Results and Discussion

3.1 Structural analysis

The analysis of XRD patterns have revealed the spinel phase within all the ferrite samples. The XRD patterns of $\text{Ni}_{0.3}\text{Cu}_{0.2}\text{Zn}_{0.5}\text{Fe}_2\text{O}_4$ ferrites are displayed in Fig. 1. These diffraction peaks is the evidence of the formation of ferrite phase in synthesized powder samples. Table 1: Values of atomic coordinates (x, y, z) and occupancy (g) determined from Rietveld refinement of XRD pattern of $\text{Ni}_{0.4}\text{Cu}_{0.1}\text{Zn}_{0.5}\text{Fe}_2\text{O}_4$.

Atom	Sample (S1)		Sample (S2)		Sample (S3)	
	x=y=z	Occ(g)	x=y=z	Occ(g)	x=y=z	Occ(g)
Ni	0.1250	0.1885 (2)	0.1250	0.1645 (2)	0.1250	0.1423 (3)
Cu	0.1250	0.0500 (2)	0.1250	0.0452 (1)	0.1250	0.0325 (2)
Zn	0.1250	0.5000 (2)	0.1250	0.5000 (2)	0.1250	0.5000 (2)
Fe	0.1250	0.2615 (2)	0.1250	0.2903(1)	0.1250	0.3252(2)
Ni	0.5000	0.2115(2)	0.5000	0.2355(1)	0.5000	0.2577(2)
Cu	0.5000	0.0500(1)	0.5000	0.0548(1)	0.5000	0.0675(1)
Fe	0.5000	1.7385(2)	0.5000	1.7097(2)	0.5000	1.6748(2)

The relative intensity and position of peaks in diffraction pattern are good agreed with standard powder diffraction data [17]. From most intense peak average particle size for selected composition of ferrite was obtained by using Scherrer formula [18]. The Table 1 represents the values of lattice parameters and crystallite size of all prepared samples. Upon substitution of Ni^{2+} ions, the lattice parameter and crystallite size were increased with the increasing annealing temperature which is confirmed from the TEM data.

The calculated values of lattice parameter and Miller indices are the characteristic values of the spinel structure; thus confirming the formation of cubic spinel structure within the synthesized ferrites [19-21]. The values of crystalline size are shown in Table 1. These values are in between 8 to 15 nm. The crystalline size increases with increase in temperature which is in agreement with TEM data. Fig 2 shows crystal structure of sample annealed at 600°C .

3.2 Morphological analysis

Fig. 3 and Fig. 4 shows micrographs of TEM of nanocrystalline ferrite for as prepared and annealed samples at 600°C. According to Fig. 4 the particles are seen to be in spherical form with crystallite size of 10 to 12 nm and electron diffraction pattern confirm the spinel structure of ferrite with several lines (220), (311), (400), (511) and (440) depicted from TEM data.

The x-ray densities of the samples are obtained from formula given by Smith and Wijn [22],

$$d_x = \frac{8M}{Na^3} \quad (1)$$

where d_x is the X-rays density, M is molecular weight of the sample, ' a^3 ' is volume of unit cell, N is the Avogadro's number.

The calculated values of d_x are listed in Table 1.

The x-ray density falls with rise in annealing temperature, which is in consistent with rise in unit cell volume i.e rise in lattice parameter (a).

The porosity 'P' is determined from the equation [23].

$$\% \text{Porosity} = \frac{\rho_x - \rho_a}{\rho_x} \times 100 \quad (2)$$

where ρ_x and ρ_a are X-ray density and bulk density respectively of the nano ferrites. The specific surface area 'S' was calculated in g/cm^3 using equation [24],

$$S = \frac{6000}{D\rho_m} \quad (3)$$

Where D is the diameter of the particle and ρ_m is the measured density. The porosity 'P' is important parameter in deciding a material for gas sensing applications. The values of porosity are shown in Table 1. It is seen that as the annealing temperature increases, porosity decreases due to decrease in x-ray density. Values of specific surface area are also tabulated in Table 1, which shows that specific surface area (S) lies in the range from 53.93 gm/cm^3 to 21.12 gm/cm^3 . It is found that values of specific surface area are reduced due to increase in particle size.

3.3 Magnetic Properties

Magnetic properties like coercivity (H_c), saturation magnetization (M_s) are influenced by particle size, lattice constant, micro structure and bulk density of the ferrites [25]. Fig. 5 illustrates room temperature hysteresis loops for all studied samples annealed at different temperatures.

From the hysteresis loop coercivity (H_c) and saturation magnetization (M_s) values are investigated and are represented in Fig 6.

It is observed that both the magnetic properties are increased with annealing temperature was attributed to improved grain size, crystallinity of samples similar results observed in NiCuZn ferrites [26, 27].

3.4 Elastic properties

Ultrasonic pulse transmission technique was used to obtain values of shear (V_s) and longitudinal (V_L) wave velocities at room temperature of all prepared samples [28] and are represented in Fig 7. It is seen that V_L and V_s increases with rise in annealing temperature.

Using these values Young's modulus (E), Rigidity modulus (G), Bulk modulus (K), Longitudinal modulus (L) and Poisson's ratio (σ) were calculated [29]. The values of elastic moduli and annealing temperature are represented in Fig 8. It can be observed from Fig 8 that the values of

Rigidity modulus (G), Bulk modulus (K), Young's modulus (E) and longitudinal modulus (L) increases with increase in temperature. This performance of elastic moduli is attributed to inter atomic binding between Ni, Zn, Cu and Fe ions in material. As the annealing temperature increases the bonding force increases and results into inter molecular forces which cause to increase the elastic moduli.

In the present system, the possible cause behind increase in the elastic constants and densities with temperature may be the increasing size of grains. Such type of results is shown for other ferrites system [30].

It is also observed that for all samples Poisson's ratio (σ) values are constant ($\sigma = 0.249$), similar result are reported for other ferrites [31]. The values of Poisson ratio lies in the range from -1 to 0.5 which is consistent with the theory of isotropic elasticity [27]. The mean velocity was used to calculate the Debye temperature (θ_E):

$$\theta_E = \frac{h}{k} \left(\frac{3\rho q N}{4\pi M} \right)^{\frac{1}{3}} \times V_m \quad (4)$$

Where N is Avogadro's number, k is Boltzmann's constant, h is Planck's constant, q is number of atoms in molecule, ρ is density of the sample, M is Molecular weight of the specimen and V_m is the mean sound velocity. The variation of Debye temperature with annealing temperature is shown in Fig. 9, which depicts that there is increase in Debye temperature with annealing temperature.

3.5 Dielectric properties

The values of the electrical capacities of the ferrite pellets measured using impedance analyser were used for calculation of the dielectric constant (ϵ') using equation,

$$\epsilon' = \frac{Ct}{\epsilon_0 A} \quad (5)$$

where, A is the area of sample, ϵ_0 is the permittivity in free space, t is the thickness of pellet, and C is electrical capacity of the pellet.

The calculated dielectric constant (ϵ') varies with frequency as shown in the Fig. 10 for all samples of the ferrite. As shown in the figure, ϵ' falls with frequency and dispersion is observed in the frequency range.... The values of ϵ' remains constant in spite of the further increase in frequency. As annealing temperature increases dielectric constant also increases similar result obtained for other ferrite [32]. The effect of heterogeneity plays an important role at low frequencies, due to which the highest value of ϵ' is reported for the lowest frequency applied [33]. The dispersion observed in the frequency range ... can be explained using Maxwell–Wagner model [34] and Koop's [35] phenomenological theory. dielectric constant falls at low frequencies; the fall is being rapid for the NCZ ferrite possessing the higher value of the constant. Thus the large dispersion exhibits the

was used to describe dielectric dispersion in ferrite. At low frequencies, ϵ' falls rapidly for the composition having higher value of dielectric constant indicates the large dispersion in the composition with large value of ϵ' . The strength of the polarization is determined by the local displacement of electrons in the ferrites which is due to the exchange of 3d electrons between localized Fe^{3+} and Fe^{2+} ions.

The exchange of 3d electrons between Fe^{3+} and Fe^{2+} which are localized at the metal ions, results in local displacement of electrons in the direction of field which determines the strength of polarization. The low value of dielectric constant could be due to the preparation method which suppresses the formation of Fe^{2+} ions.

At low frequency, the $\tan \delta$ value was found to be greater and it decreases with increasing frequency and temperature. The physical significance of $\tan \delta$ is the loss of energy in the dielectric system. The energy loss disappears at greater frequency range and the dipole orientation contributes to the polarization. As reported by researcher hopping of electrons by the application of electric field results into conduction in ferrites. Due to increase in Fe^{2+}

concentration in selected samples the hopping probability increases, which results decrease in resistivity at higher frequencies [36]. Similar observations are reported for Cu–Zn ferrites by Sattar et al. [37] and El-Syed [38] suggested the conduction mechanism could be predominantly due to hopping of electrons or ions. The variation of dielectric loss (ϵ'') against logarithm of frequency at room temperature is represented in Fig. 11 for all ferrite samples. It can be seen that, all the samples shows a normal dielectric behaviour with frequency where, the dielectric loss decreases exponentially with increase in frequency.

4. Conclusions:

Nano particles of polycrystalline $\text{Ni}_{0.3}\text{Cu}_{0.2}\text{Zn}_{0.5}\text{Fe}_2\text{O}_4$ ferrites, with an average crystalline size between 7 and 13 nm, were synthesized through auto combustion method. The XRD peak indicates formation of nano ferrites. The observed lattice parameter and specific indices are characteristics of spinel structure with no any secondary peak. The results of XRD pattern show that the lowest annealing temperature is around 400°C . The TEM images together with SAED pattern shows that after annealing and metals substitution, the nano particles are combined. The equivalent lattice outer boundary is found elongated, pores and grains edges also deviate for samples heated at 600°C which indicates that by distributing symmetrical planes, the nano particles are arranged into a similar oriented structure. The elastic constant increases with increasing Ni^{2+} content. The increase in magnitude in elastic moduli with increase in annealing temperature suggest that the strengthening of inter atomic bonding. The low value of dielectric constant is attributed to the method of synthesis which suppresses the formation of Fe^{2+} ion.

ORIGINALITY REPORT

31%

SIMILARITY INDEX

12%

INTERNET SOURCES

26%

PUBLICATIONS

12%

STUDENT PAPERS

PRIMARY SOURCES

- 1** S. R. Kulkarni, Priyanka U. Londhe, N. B. Chaure. "Electrical and magnetic properties of Al³⁺ substituted Mn–Ni–Zn nanoferrites", Journal of Materials Science: Materials in Electronics, 2013
Publication 6%
- 2** ijcps.org
Internet Source 3%
- 3** Submitted to Higher Education Commission Pakistan
Student Paper 3%
- 4** S.G. Algude, S.M. Patange, Sagar E. Shirsath, D.R. Mane, K.M. Jadhav. "Elastic behaviour of Cr³⁺ substituted Co–Zn ferrites", Journal of Magnetism and Magnetic Materials, 2014
Publication 3%
- 5** Sagar E. Shirsath, B.G. Toksha, R.H. Kadam, S.M. Patange, D.R. Mane, Ganesh S. Jangam, Ali Ghasemi. "Doping effect of Mn²⁺ on the magnetic behavior in Ni–Zn ferrite nanoparticles 2%

prepared by sol–gel auto-combustion", Journal of Physics and Chemistry of Solids, 2010

Publication

6

S.J. Haralkar, R.H. Kadam, S.S More, Sagar E. Shirsath, M.L. Mane, Swati Patil, D.R. Mane. "Substitutional effect of Cr³⁺ ions on the properties of Mg–Zn ferrite nanoparticles", Physica B: Condensed Matter, 2012

Publication

2%

7

S. M. Patange, S. S. Desai, S. S. Meena, S. M. Yusuf, Sagar E. Shirsath. " Random site occupancy induced disordered Néel-type collinear spin alignment in heterovalent Zn –Ti ion substituted CoFe O ", RSC Advances, 2015

Publication

2%

8

aip.scitation.org

Internet Source

1%

9

Algude, S.G., S.M. Patange, Sagar E. Shirsath, D.R. Mane, and K.M. Jadhav. "Elastic behaviour of Cr³⁺ substituted Co–Zn ferrites", Journal of Magnetism and Magnetic Materials, 2014.

Publication

1%

10

link.springer.com

Internet Source

1%

11

S. S. Desai, R. A. Pawar, S. S. Jadhav, Sagar E. Shirsath, S. M. Patange. "Role of Coupling Divalent and Tetravalent Metal Ions on the

1%

Elastic and Electric Properties of CoFe₂O₄ Ferrites Prepared by Sol–Gel Method", Journal of Superconductivity and Novel Magnetism, 2016

Publication

12 Submitted to Rajarambapu Institute of Technology 1%
Student Paper

13 Lin-Wei Ruan, Yu-Jun Zhu, Ling-Guang Qiu, Yu-Peng Yuan, Yun-Xiang Lu. "First principles calculations of the pressure affection to g-C₃N₄", Computational Materials Science, 2014 1%
Publication

14 Yue, Z.. "Preparation and magnetic properties of titanium-substituted LiZn ferrites via a sol-gel auto-combustion process", Journal of the European Ceramic Society, 200301 1%
Publication

15 Submitted to Panjab University 1%
Student Paper

16 d-nb.info <1%
Internet Source

17 paccon2015.kmutt.ac.th <1%
Internet Source

18 Vijay V. Warhate, Dilip S. Badwaik. "Structural, magnetic and thermo-magnetic properties of

NiMn Y-Type strontium nano-hexaferrites",
Journal of Alloys and Compounds, 2020

Publication

19

downloads.hindawi.com

Internet Source

<1%

20

Submitted to King Mongkut's Institute of
Technology Ladkrabang

Student Paper

<1%

21

"Physics of Semiconductor Devices", Springer
Science and Business Media LLC, 2014

Publication

<1%

22

D.-H. Hong, S. Park, H.-S. Oh, B.-K. Lee, S.-Y.
Hong, T.-D. Lee. "Dependence of Sputtering
Power and Soft Underlayer on Magnetic
Properties in CoCrPtO Perpendicular Recording
Media", IEEE Transactions on Magnetics, 2004

Publication

<1%

23

Chaudhari, Vivek, Sagar E. Shirsath, M.L.
Mane, R.H. Kadam, S.B. Shelke, and D.R.
Mane. "Crystallographic, magnetic and electrical
properties of Ni_{0.5}Cu_{0.25}Zn_{0.25}LaxFe_{2-x}O₄
nanoparticles fabricated by sol-gel method",
Journal of Alloys and Compounds, 2013.

Publication

<1%

24

Sagar E. Shirsath, S.M. Patange, R.H. Kadam,
M.L. Mane, K.M. Jadhav. "Structure refinement,
cation site location, spectral and elastic

<1%

properties of Zn²⁺ substituted NiFe₂O₄",
Journal of Molecular Structure, 2012

Publication

25

S.S. Chougule, B.K. Chougule. "Response of dielectric behaviour on ferroelectric rich (y) Ni_{0.8}Zn_{0.2}Fe₂O₄+(1-y) PZT ME composites", Materials Chemistry and Physics, 2008

<1%

Publication

26

R.H. Kadam, Suresh T. Alone, Maheshkumar L. Mane, A.R. Biradar, Sagar E. Shirsath. "Phase evaluation of Li⁺ substituted CoFe₂O₄ nanoparticles, their characterizations and magnetic properties", Journal of Magnetism and Magnetic Materials, 2014

<1%

Publication

27

K. S. Deepa, P. Shaiju, M. T. Sebastian, E. Bhoje Gowd, J. James. " Poly(vinylidene fluoride)–La Sr CoO composites: the influence of LSCO particle size on the structure and dielectric properties ", Phys. Chem. Chem. Phys., 2014

<1%

Publication

Exclude quotes On

Exclude matches Off

Exclude bibliography On

DR.S.M.PATANGE

pppp

by Fgh Fghj

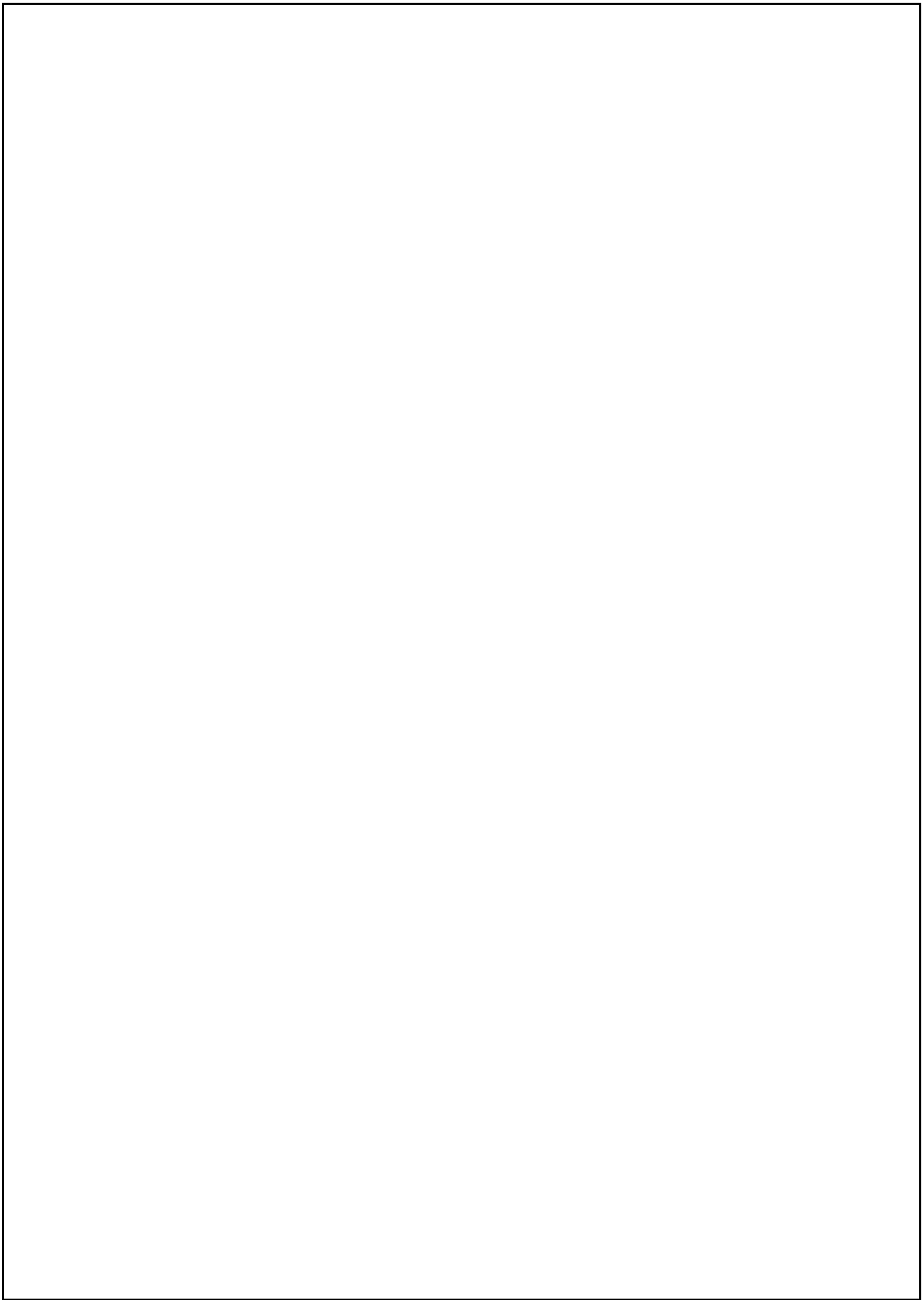
Submission date: 13-Jul-2019 05:57PM (UTC+0530)

Submission ID: 1151503079

File name: Manucript_-plagarism_13.7.19.docx (72.67K)

Word count: 4886

Character count: 26195



1 Introduction :

Nano-structured materials are being extensively investigated due to their novel and versatile physicochemical properties that are not exhibited by the bulk materials of same composition [1]. Among a variety of nano-structures, the transition metal oxide-based nanomaterials have attracted the significant portion of engineers and materials scientists. These nanomaterials have a broad spectrum of applications ranging from medical diagnosis and therapy to energy harvesting and storage technology [2,3]. Further the nano-crystalline ferrites are being explored because of their vital role in advanced technological devices fabrication [4]. The unique properties of ferrite nanopowders have generated more interest in the science community because high surface to volume ratio resulting in novel phenomena's of nanomagnetism such as superparamagnetic, magnetic quantum tunneling and spin-glasslike behavior etc. [5]. It is well established that method of preparation, nature and concentration of dopants and their site preferences modify various magnetic properties of ferrites. Extensive research is currently being carried out on new mixed valent dopants where it is possible to independently monitor coercivity (H_c) while retaining high and almost constant saturation magnetization (M_s) – a prime requirement for data recording. The most extensively used techniques for the bulk preparation of ferrites are the conventional solid-state reactions such as ceramic method, high energy ball milling and flash combustion. These methods involve milling and firing of the reaction mixture at about 1200°C or above and thus result in the incorporation of impurities, generation of lattice strain and irregularity in particle shape. Moreover, at high temperature, their particle size tends to be larger due to agglomeration of fine particles [6-9].

R.S. Alam et al. [10] reported $\text{BaCo}_{0.2}\text{Zn}_{0.2}\text{Zr}_{2x}\text{Fe}_{(12-4x)}\text{O}_{19}$ ferrites synthesized by Co-precipitation method and doped up to $x = 0.5$ level and concluded that saturation magnetic and magnetic resonance (M_r) first decrease and then increase with dopant concentration. This may be due to the dopant occupancy at five different sites of hexagonal ferrite system. Authors concluded that the composition $\text{BaCo}_{0.5}\text{Zn}_{0.5}\text{ZrFe}_{10}\text{O}_{19}$ has desired reflection loss and band-width in order to be used as a potential single layer absorber material with microwave absorption greater than 90% ($\text{RL} < -10$ dB) with in the 8–12 GHz frequency range. Similarly P. Kaur et al. [11] also synthesized tri-substituted strontium hexaferrites $\text{SrFe}_{(12-2x)}\text{Cu}_x\text{Co}_x\text{Zr}_x\text{O}_{19}$ ($x = 0.0-1.0$, $\Delta x = 0.2$) by sol-gel auto-combustion route and observed that magnetic parameters have been first increased and

then decreases with dopant concentration. Ghasemi and Morisako [12] prepared $\text{SrFe}_9(\text{Mn}_{0.5}\text{Co}_{0.5}\text{Zr})_{3/2}\text{O}_{19}$ by applying sol-gel method and observed that doping leads to a large decrease in H_c from 3251 Oe to 42.72 Oe. The authors find these compounds have been suitable for applications in filters, antennas, isolator, circulators etc. [13].

Magnetic as well as electrical properties ferrites are sensitive to the processing conditions and the type of (partial) substitution of Fe by other divalent, trivalent, or the combination of divalent-tetravalent ions. The combination of divalent and tetravalent ion has been substituted in ferrite by many other workers, with the combination of $\text{Zn}^{2+}\text{-Ti}^{4+}$ [14-17], $\text{Zn}^{2+}\text{-Sn}^{4+}$ [18], $\text{Zn}^{2+}\text{-Mo}^{4+}$ [19], $\text{Co}^{2+}\text{-Zr}^{4+}$ [20].

Divalent zinc (Zn^{2+}) substitution plays a decisive role in determining the ferrite properties. Non-magnetic Zn^{2+} doped ferrites are of interest in fundamental understanding of the properties and variety of applications such as radiofrequency circuits, transformer cores, antennas and read/write heads for high speed digital tape and in high quality filters [21-23]. In the present work we have substituted Zr^{4+} ions along with Zn^{2+} ions in cobalt ferrite. The basic requirement of ferrites is high resistivity and low eddy current losses. The substitution of tetravalent ions has paved a way to increase the resistivity of ferrites [24]. Tetravalent Zr^{4+} is a kind of nonmagnetic ions and has an ionic radius larger than that of Fe^{3+} [25].

Considering all above facts, it would be worth to study the structural and magnetic properties of Zn^{2+} and Zr^{4+} substituted CoFe_2O_4 with a chemical composition of $\text{CoZn}_x\text{Zr}_x\text{Fe}_{2-2x}\text{O}_4$ ($x=0.0$ to 0.4 in step 0.1) by sol-gel method.

2 Experimental procedures :

Zirconium nitrate ($\text{Zr}(\text{NO}_3)_4 \cdot 5\text{H}_2\text{O}$), zinc nitrate ($\text{Zn}(\text{NO}_3)_2 \cdot 6\text{H}_2\text{O}$) and iron nitrate ($\text{Fe}(\text{NO}_3)_3 \cdot 9\text{H}_2\text{O}$) were used as starting materials to prepare the samples of $\text{CoZn}_x\text{Zr}_x\text{Fe}_{2-2x}\text{O}_4$ ($x=0.0$ to 0.4 in step 0.1) by sol-gel method. Reaction procedure was carried out in air atmosphere without protection of inert gases. The solutions of the compositional elements were prepared by dissolving stoichiometric amount of nitrate salts in deionized water. Molar ratios of divalent and trivalent ions were kept 1:2. The aqueous solutions of nitrates were mixed using magnetic stirrer and citric acid is simultaneously added. This mixed solution was magnetically stirred for 30 min. The solutions were then neutralized by adding ammonia solution to set the $\text{pH}=7$. The heating of the solution at 100°C is then stirred and after 2 h of continuous heating and stirring the solution converted into viscous gel which then automatically converted in to fluffy powder by self-combustion. This powder is annealing at

650 °C for 5 h in temperature-controlled furnace in air atmosphere. The chemical reaction of prepared samples as show the Fig 1.

The phase formation identification of samples prepared was characterized by X-ray diffraction (XRD, Philips X'Pert instrument) with Cu K α radiation (wave length $\lambda = 1.54056$ Å) at room temperature. Transmission electron microscope (TEM) measurements were recorded on Philips (Model CM 200). Magnetic measurements were performed at room temperature using a commercial PARC EG&G vibrating sample magnetometer VSM 4500. Magnetic hysteresis loops were measured at room temperature with maximum applied magnetic fields up to 1T.

Mössbauer spectra of all the samples were recorded at BARC Mumbai at room temperature using a Mössbauer spectrometer (Nucleonix Systems Pvt. Ltd., Hyderabad, India) operated at a constant acceleration mode (triangular wave) in transmission geometry at room temperature. The source employed was Co⁵⁷ in Rh matrix of strength 50 mCi. The calibration of the velocity scale is done by using an enriched α -⁵⁷Fe metal foil. The line width (inner) of calibration spectrum is 0.23 mm/s.

3. Results:

3.1 Structural properties

The structural characteristic of cobalt ferrite nanoparticles synthesized at different concentration of Zn-Zr ions was determined with the help of powder X-ray diffractometer (Figure 2). XRD data were processed to software program FULLPROF for the Rietveld structure refinement, with goodness fit index value close to one. Rietveld refined discrepancy factors such as weighted profile R-factor (R_{wp}), expected R factor (R_{exp}) and goodness fit factor (χ^2) are given in Table 1. The diffraction patterns revealed that the investigated samples for $x \leq 0.2$ were formed in a single cubic phase. The main reflection planes (220), (311), (400), (422) (511) and (440) of the spinel structure appear in all the patterns. However, at higher substitution level of Zn-Zr ($x > 0.2$), some other peaks at (012), (104) and (024) were also seen which indicates the formation of α Fe₂O₃ phase [26,27]. Further for $x > 0.2$, the percentage of ferrite phases reduced and forms other phases of ZrO₂ like monoclinic phase at (-111) and (111) and tetragonal phase at (022) and (140) [27, 28].

The lattice parameter (a) was also calculated from XRD analysis data using the following equation:

$$a = d_{hkl} [h^2 + k^2 + l^2]^{1/2} \quad (1)$$

18

where d is the lattice spacing between the planes and $(h k l)$ are the miller indices. The extrapolation function $F(\theta)$ i.e., the Nelson–Riley function, for each reflection of the studied nanoferrites was calculated by using following relation:

$$F(\theta) = \frac{1}{2} \left[\left(\frac{\cos^2 \theta}{\sin \theta} \right) + \left(\frac{\cos^2 \theta}{\theta} \right) \right] \quad (2)$$

60

Fig. 3 shows the Nelson–Riley plots for all the samples under investigation. The true values of the lattice parameter ' a_0 ' are determined by extrapolating $F(\theta) = 0$ or $\theta = 90^\circ$.

18

It is observed from Fig. 4 that the lattice parameter increases with Zr^{4+} - Zn^{2+} substitution. The increase in lattice parameter is attributed to difference in ionic radii of the Zr^{4+} - Zn^{2+} ions along with Fe^{3+} ions. In the present series smaller Fe^{3+} ions (0.67Å) are replaced by larger Zr^{4+} and Zn^{2+} ions having the ionic radii of 0.80 Å and 0.83 Å respectively, and hence it is observed that lattice parameter increases with increasing Zr^{4+} - Zn^{2+} content x .

The X-ray density (d_x) of all the samples was obtained by the following relation:

$$d_x = \frac{8M}{Na^3} \quad (3)$$

where M is molecular weight, N is Avogadro's number and a is lattice constant. Values of X-ray density are presented in Fig. 4. It can be seen from Fig. 5.3 that like lattice parameter, X-ray density also increases with increasing Zr^{4+} and Zn^{2+} content x . This increase was expected since the Zr^{4+} - Zn^{2+} ions are heavier than the Fe ion, and this increase in weight which causes an increase in the X-ray density.

The average crystallite diameter ' D_{XRD} ' of powder estimated from the most intense (311) peak of XRD and using the Scherrer method [29]. The values of crystallite diameter are presented in table 1. The values are of the order of few nano meter dimension. The specific surface area (S) was calculated in gm/cm^3 using the relation discussed elsewhere [30]. It is also cleared from table 1 that specific surface area (S) decreases with increase in Zr^{4+} and Zn^{2+} content x . The decrease in S is due to increase in particle size.

The hopping length for A-site (L_A) and B-sites (L_B) are calculated using the values of lattice constant. The variation of hopping lengths with Zr^{4+} and Zn^{2+} content x is shown in Table 1. It is observed from that the distance between the magnetic ions (hopping length) increases as Zr^{4+} and Zn^{2+} content x increases. This behavior of hopping length with x is analogous with the behavior of ' a ' with x . This variation may be attributed to the deference in

the ionic radii of the constituent ions, which makes the magnetic ions become larger to each other and the hopping length increases.

The allied parameters such as tetrahedral and octahedral bond length (d_{Ax} and d_{Bx}), tetrahedral edge, shared and unshared octahedral edge (d_{AXE} , d_{BXE} and d_{BXEU}) were calculated:

$$d_{Ax} = a\sqrt{3}\left(u - \frac{1}{4}\right) \quad (4)$$

$$d_{Bx} = a\left[3u^2 - \left(\frac{11}{4}\right)u + \frac{43}{64}\right]^{\frac{1}{2}} \quad (5)$$

$$d_{AXE} = a\sqrt{2}\left(2u - \frac{1}{2}\right) \quad (6)$$

$$d_{BXEshared} = a\sqrt{2}(1 - 2u) \quad (7)$$

$$d_{BXEunshared} = a\left(4u^2 - 3u + \frac{11}{16}\right)^{\frac{1}{2}} \quad (8)$$

where 'a' is the experimental values of lattice constant and 'u' is oxygen positional parameter. The values are presented in Table 2, which indicates that the tetrahedral and octahedral bond lengths increase as Zn-Zr ion substitution increases. The tetrahedral and shared and unshared octahedral edges increase with Zn-Zr substitution and may be due to the comparatively larger ionic radii of Zn-Zr as compared to Fe^{3+} ions.

TEM images (Fig. 5) shows that, as the amount of Zn-Zr substituent increased, the size of particles increased from ~45 nm ($x = 0.2$) to ~80 nm ($x = 0.4$). The nano-size range of the particles starts some agglomeration at high Zn-Zr substituent level. This is may be due to the start of some another phase that affecting the crystal lattice of cobalt ferrite. As a result, the lattice parameters and crystallinity will be distorted at high Zn-Zr substituent levels which signify the change in morphology of the crystalline phase.

3.2 Cation distribution

The cation distribution in the present system was obtained from the Rietveld refinement of XRD patterns [31]. Considering the site preference energy of the cations, Zn^{2+} ions have strong preference towards tetrahedral (A) site. It can be seen from Table 3 that Zn^{2+} ions predominately occupy the tetrahedral sites, which is consistent with the preference for large tetrahedral site energy. As far as lattice site preference energy is concerned, Zr^{4+} ions have no particular site preference as Zr^{4+} have d^0 configuration. According to previous work

Zr⁴⁺ can occupy both octahedral and tetrahedral coordination [32,33]. Though, EXAFS studies have demonstrated that Zr⁴⁺ ions occupy tetrahedral site more in certain systems [32]. Table 3 shows that Zr⁴⁺ ions distribute evenly among the octahedral and tetrahedral sites at lower concentration. Due to the strong preference of Zn²⁺ ions for the tetrahedral (A) coordination, Zn²⁺ ions pushes Zr⁴⁺ ions to octahedral site at higher values of *x*. Fe³⁺ has no definite site preference and occupies both tetrahedral and octahedral sites.

The mean ionic radius of the tetrahedral A- 'r_A' and octahedral B-site 'r_B' can be calculated by using cation distribution and modifying the relation discussed elsewhere [34]. The variation of mean ionic radius of the A-site (r_A) and of the B-site (r_B) with Zn²⁺ and Zr⁴⁺ are presented in Table 4. The r_A increases for Zn²⁺ and Zr⁴⁺ substitution, this is due the increase in concentration of larger Zn²⁺ (0.83 Å) ions to A site and resultant decrease in smaller Fe³⁺ (0.67 Å) ions at A site. The increase in octahedral radii (r_B) is associated with increase in larger Zr⁴⁺ (0.80 Å) ions which replace Fe³⁺ (0.67 Å) ions. Using the values of 'a', the radius of oxygen ion R_O = 1.32 Å and r_A in the following expression, the oxygen positional parameter 'u' can be calculated [35],

$$u = \left[(r_A + R_O) \frac{1}{\sqrt{3}a} + \frac{1}{4} \right] \quad (9)$$

Table 4 shows decreasing value of oxygen positional parameter 'u' from 0.3837- 0.3886 Å. In most oxide spinels the oxygen ions are apparently larger than the metallic ions. In spinel like structure the oxygen positional parameter has a value in the neighbourhood of 0.375 Å for which the arrangement of O²⁻ ions are equals exactly a cubic closed packing but in actual spinel lattice, this ideal pattern is slightly deformed. The structure of the spinel has space group *Fd3m(O₇^h)* and can be described as 32 oxide ions in nearly closed packing with eight of the 64 tetrahedral sites and 16 of the 32 octahedral sites normally occupied by cations. Taking origin at one of the octahedral site, the oxygen positional parameter has a value equal to 0.250 instead of 0.375 Å (for ideal *fcc* packing) as conventionally reported by many authors [36,37]. The *u* has a value 0.375 Å when the origin is chosen on the tetrahedral sites but the structure is a centric and the structure factor calculation is less direct [38]. For pure magnetite *u* = 0.382 Å and even higher values like 0.384 Å for Ga-substituted ferrites [38, 39] and *u* = 0.390 Å for Cd-Zn [40] using XRD techniques are reported. Our value of *u* is larger than its ideal value (*u*= 0.375 Å), this larger value may probably be due to many reasons, including experimental or measurement errors, e.g. precision of the observed X-ray intensity and the theoretical data used for the scattering model of the system. As mentioned earlier that in most

spinels $u > 0.375$ is obtained because of the small displacement of anions due to the expansion of the tetrahedral and octahedral interstices. However, in the present work $u > 0.375$ may be due to anion displacement from the ideal situation so that it forms expanded tetrahedral interstices. The lattice disturbance is confirmed from the data for lattice constant and the oxygen positional parameter 'u'.

The theoretical lattice parameter ' a_{th} ' was calculated using the values of tetrahedral and octahedral radius (r_A, r_B) [41]. Table 4 shows the variation of theoretical lattice constant with x. Theoretical lattice constant increases with increase in Zr^{4+} and Zn^{2+} substitution.

3.3 Magnetic measurements by VSM

The magnetic properties are the most important properties for ferrites depending on the processing conditions, microstructure, chemical composition and the type of the additives. As it can be seen from the Fig. 6 the magnetic characteristics of cobalt ferrite are significantly influenced by substitution of Zn^{2+} - Zr^{4+} ions instead of Fe^{3+} cations.

The values of saturation magnetization (M_s) and coercivity (H_c) obtained from magnetization plots are given in Table 4. It is observed from Fig. 6 and Table 4 that saturation magnetization and coercivity decreased with increase in Zn^{2+} - Zr^{4+} substitution. Generally, the magnetic behavior of the cobalt ferrite is notably governed by the distribution of Fe^{3+} ions on the crystallographic lattice sites. A decrease in magnetization is expected when Zn^{2+} - Zr^{4+} is added to the cobalt ferrite lattice since paramagnetic Zn^{2+} and Zr^{4+} is known to occupy tetrahedral and octahedral sites respectively and reduce the density of magnetic Fe ions in A and B sublattice. Thus reducing not only the magnetic moment of the sublattice but also the exchange interaction. According to Neel's molecular-field model [42], the A-B super exchange interaction predominate the intra sublattice A-A and B-B interactions. Therefore, the net magnetic moment is given by the sum of the magnetic moments of the A and B sublattices.

The magnetic moment per formula unit (n_B) was calculated from Neel's sub-two-lattice model using the relation,

$$n_B^N = M_B(x) - M_A(x) \quad (10)$$

where M_B and M_A are the B and A sub-lattice magnetic moments in μ_B . The n_B^N (μ_B) values for $CoZn_xZr_xFe_{2-2x}O_4$ were calculated using cation distribution and ionic magnetic moment of Fe^{3+} , Co^{2+} , Zn^{2+} , Zr^{4+} with their respective values $5\mu_B$, $3\mu_B$, $0\mu_B$ and $0\mu_B$. In the present

ferrite system the Fe^{3+} ions are replaced by Zn^{2+} - Zr^{4+} ions, leading to a decrease in the A and B -site sublattice magnetization, which leads to a decrease in the net magnetization.

Coercivity in the ferrite samples is shown in Fig. 6. It decreases with the increase in Zr^{4+} and Zn^{2+} concentration. This is due to the reason that H_c decreases with the decrease in magnetocrystalline anisotropy. The magnetocrystalline anisotropy constant (K_1) is negative for Zn ferrites. The absolute value of K_1 is larger for Fe^{3+} than that of Zr^{4+} and Zn^{2+} ferrites. The total anisotropy is equal to the sum of their individual anisotropies. So K_1 and hence coercivity decreases with the increase in Zr^{4+} and Zn^{2+} concentration.

3.4 Field cooled (FC) and Zero Field Cooled (ZFC) measurements

Field cooled (FC) and zero field cooled (ZFC) magnetization curves in applied fields of 100 Oe for all the samples (except $x = 0.1$) were measured in temperature range of 2–300 K (Fig. 7). A divergence between ZFC and FC curve can easily be observed from the FC-ZFC plots, which is a characteristic feature of ferromagnetic behavior, which is attributed to the temporal relaxation. Such a divergence originates from the anisotropy barrier blocking of the magnetization orientation in the nano-particles cooled with a ZFC process [43]. A peak in the magnetization is evident in each case with the position of the peak varies with Zn^{2+} - Zr^{4+} substitution. It is understood that in the ZFC mode the magnetization of a collection of nanoparticles may go through a peak as the particles' moments become blocked along the anisotropy axes. The blocking temperature (T_B) is defined as the temperature at which maximum magnetization is achieved. It is observed that the blocking temperature do not vary much with increase in Zn^{2+} - Zr^{4+} substitution.

3.5 Mössbauer spectroscopy

Mössbauer spectra of $\text{Ni}_{0.5}\text{Mg}_{0.5}\text{Fe}_{2-x}\text{Cr}_x\text{O}_4$ ferrites were recorded at room temperature (300 K). The spectra of all the samples are shown in Fig. 8, spectra could be resolved into two well defined sextets each. One of the sextets is attributed to Fe^{3+} ions at tetrahedral (A) site due to its smaller isomer shift and smaller hyperfine field of the Zeeman pattern and the second sextet has been attributed to Fe^{3+} ions at octahedral [B] site due to its larger isomer shift and larger hyperfine field of the Zeeman pattern [44]. The presence of six finger pattern in the spectra of all the samples shows that the samples are magnetically ordered. The values of the Line width (Γ), isomer shift (IS), quadruple splitting (QS) and hyperfine field (BHF) corresponding to tetrahedral (A) and octahedral (B) sites for all the samples are given in Table 5. The line width of the tetrahedral sites becomes broader than that of the octahedral

site with the increase of the Zn^{2+} - Zr^{4+} contents at the tetrahedral and octahedral sites respectively. Such broadening is, in fact, expected due to a distribution of the hyperfine fields at the A-site caused principally by a random distribution of Co^{2+} , Fe^{3+} and Zr^{4+} ions at the B-site, since the Fe^{3+} A-sites would feel different configurations of Co^{2+} , Fe^{3+} and Zn^{2+} ions occupying the 12 nearest neighbors B-sites [45]. The observed values of isomer shift show, within experimental error, an insignificant change with increasing substitution of Zn^{2+} - Zr^{4+} ions. It implies that the s-electron charge density of Fe^{3+} ions is not influenced by increased Zn^{2+} - Zr^{4+} substitution in cobalt ferrites. It is observed from Table 5 that isomer shift value for octahedral sites is greater than that for tetrahedral sites. In cubic spinel ferrites, the bond separation Fe^{3+} - O^{2-} is larger for octahedral sites when compared to that for tetrahedral sites. Due to this, overlapping of orbital of Fe^{3+} ions is small at B-sites and thus a larger isomer shift at B-sites was expected [46, 47]. The range of values of isomer shift indicates that iron exists in Fe^{3+} valence state with high spin configuration in the prepared samples [48]. The values of quadrupole splitting (Table 5) for hyperfine spectra of all the samples are found to be negligibly small and attributed to the fact that overall cubic symmetry is maintained between Fe^{3+} ions and their surroundings with the substituted Zn^{2+} - Zr^{4+} ions in the present cobalt ferrites. The variations in hyperfine magnetic field at tetrahedral (A) and octahedral [B] sites as a function of Zn^{2+} - Zr^{4+} substitutions in cobalt ferrites are given in Table 5. In most of the ferrites, B-site hyperfine magnetic field, is generally larger than that of A-site, which is attributed to the dipolar field resulting due to deviation from cubic symmetry and covalent nature of tetrahedral bonds [47]. The observed variations in hyperfine magnetic field at A- and B-sites with increasing Zn^{2+} - Zr^{4+} substitutions in cobalt ferrites can be qualitatively explained using Neel's super-exchange interactions [42]. According to Neel's model, inter sublattice exchange interactions, i.e., AB exchange interactions are stronger than intra sublattice exchange interactions, i.e., AA or BB exchange interactions. As both A and B sites are occupied by Fe^{3+} ions, so the interaction of Fe^{3+} is possible with Co^{3+} , Zn^{2+} and Zr^{4+} ions. The net magnetic field is mainly due to strong $Fe_A^{3+} - O - Fe_B^{3+}$ interactions. In the present series Fe^{3+} ions with larger magnetic moment (i.e. $5\mu_B$) are replaced by non-magnetic Zn^{2+} - Zr^{4+} ions. This results in decrease of magnetic linkages in $Fe_A^{3+} - O - Fe_B^{3+}$, $Fe_A^{3+} - O - Mg_A^{2+}$ and $Fe_A^{3+} - O - Ni_B^{2+}$ and consequently Fe^{3+} ion experience a decrease in the magnetic field at A and B sites. Therefore, hyperfine magnetic field is expected to decrease with increase of Zn^{2+} - Zr^{4+} concentration. Usually the saturation magnetization is proportional to the hyperfine field which agrees well with

hysteresis measurements. Therefore, the magnetization is lowered due to the decrease in hyperfine field.

4. Conclusion:

Zr⁴⁺ and Zn²⁺ substituted nano-size cubic ferrites of CoFe₂O₄ with a chemical formula CoZn_xZr_xFe_{2-2x}O₄ were successively prepared through sol-gel auto combustion route. The X-ray diffraction study reveals the formation of cubic spinel structure with linear increase in lattice constant. At higher substitution level of Zn-Zr (x > 0.2), some other peaks at (012), (104) and (024) were also seen which indicates the formation of α-Fe₂O₃ phase. The crystallite size increases from 24 nm to 55 nm with increasing of Zr⁴⁺ and Zn²⁺ content. The cation distribution suggests that Zr⁴⁺ shows its preference towards octahedral A site though it occupies tetrahedral A site as well by small fraction. Zn²⁺ prefers tetrahedral A site, whereas Fe³⁺ occupies both A and B sites. In the present work oxygen parameter $u > 0.375$ and may be due to anion displacement from the ideal situation so that it forms expanded tetrahedral interstices. The lattice disturbance is confirmed from the data for lattice constant and the oxygen positional parameter 'u'. Saturation magnetization and coercivity of cobalt ferrite decreased with the increase in Zn-Zr content. The net magnetic field is mainly due to strong Fe_A³⁺-O-Fe_B³⁺ interactions. In the present series Fe³⁺ ions with larger magnetic moment (i.e. 5μ_B) are replaced by non-magnetic Zn²⁺-Zr⁴⁺ ions. This results in decrease of magnetic linkages in Fe_A³⁺-O-Fe_B³⁺, Fe_A³⁺-O-Mg_A²⁺ and Fe_A³⁺-O-Ni_B²⁺ and consequently Fe³⁺ ions experience a decrease in the magnetic field at A and B sites. A divergence between ZFC and FC curve can easily be observed from the FC-ZFC plots, which is a characteristic feature of ferromagnetic behaviour.

5 Reference:

- [1] C. Liu, F. Li, L.P. Ma, H.M. Cheng, *Advanced materials for energy storage*, *Adv. Mater.*, 22 (2010), pp. E28-E62
- [2] M.F. Warsi, R.W. Adams, S.B. Duckett, V. Chechik, *Gd-functionalised Au nanoparticles as targeted contrast agents in MRI: relaxivity enhancement by polyelectrolyte coating*, *Chem. Commun.*, 46 (2010), pp. 451-453.
- [3] A.S. Arico, P. Bruce, B. Scrosati, J.M. Tarascon, W. van Schalkwijk, *Nanostructured materials for advanced energy conversion and storage devices*, *Nat. Mater.*, 4 (2005), pp. 366-377.
- [4] M.N. Akhtar, A.B. Sulong, M. Ahmad, M.A. Khan, A. Ali, M.U. Islam, *Impacts of Gd-Ce on the structural, morphological and magnetic properties of garnet nanocrystalline ferrites synthesized via sol-gel route*, *J. Alloy. Compd.* 660 (2016)486-495.
- [5] Le-Zhong Li, Xiao-Xi Zhong, Rui Wang, Xiao-Qiang Tu, *Structural, magnetic and electrical properties of Zr-substituted NiZnCo ferrite nanopowders*, *J. Magn. Magn. Mater.* 435 (2017) 58-63
- [6] R.A. Pawar, S.S. Desai, Q.Y. Tamboli, S.E. Shirsath, S.M. Patange, *J. Magn. Magn. Mater.*, 378 (2015), 59
- [7] S. Kanagesan, M. Hashim, T. Kalaivani, I. Ismail, N. Rodziah, I.R. Ibrahim, N.A. Rahman, *J. Mater. Sci.: Mater. Electron.*, 26 (2015), 1363
- [8] Z. Durmus, A. Durmus, H. Kavas, *J. Mater. Sci.*, 50 (2015), 1201
- [9] T. Tsutaoka, N. Koga, *J. Magn. Magn. Mater.*, 325 (2013), 36
- [10] R.S. Alam, M. Moradi, M. Rostami, H. Nikmanesh, R. Moayedi, Y. Bai, *J. Magn. Magn. Mater.*, 381 (2015), p. 1
- [11] P. Kaur, S.K. Chawla, S.B. Narang, K. Pubby, *J. Supercond. Nov. Magn.*, 30 (2017) 635
- [12] A. Ghasemi, A. Morisako, *J. Magn. Magn. Mater.*, 320 (2008), p. 1167
- [13] A. K.Jassal, R.K. Mudsainiyan, S.K.Chawla, Anu, S. B.Narange, K.Pubby, *Sol-gel route approach and improvisation in physico-chemical, structural, magnetic and electrical properties of $BaCo_{x/2}Zn_{x/2}Zr_xFe_{(12-2x)}O_{19}$ ferrites*, *J. Magn. Magn. Mater.* 447 (2018) 32-41
- [14] O. Kubo, T. Ido, H. Yokoyama, *IEEE Trans. Magn.* 18 (1982) 1122.
- [15] Ji-Chyun Liu, Chin-Yen Liu, Yaw-Shun Hong, Ching-Yang Wu, Der-Chyuan Lou, *Micro. Opt. Technol. Lett.* 49 (2007) 201-203.

- [16] ⁴⁶ A. G. Belous, V. A. Elshanskii, E. V. Pashkova, and V. P. Ivanitskii, *Inorg. Mater.* 35 (1999) 170.
- [17] ³² P. Wartewig, M.K. Krause, P. Esquinazi, S. Rösler and R. Sonntag, *J. Magn. Magn. Mater.* 192 (1999) 83.
- [18] ² R. K. Puri and Usha Varshney, *J. Phys. Chem. Solids* 44, (1983) 655-661.
- [19] ²⁰ D.G. Agresti, T.D. Shelfer, Y.K. Hong, Y. J. Paig, *IEEE Trans. Magn.* 25 (1989) 4069
- [20] R. Ali, M. Azhar Khan, A. Manzoor, M. Shahid, S. Haider, A. S. Malik, M. Sher, I. Shakir, M. F. Warsi, Investigation of structural and magnetic properties of Zr-Co doped nickel ferrite nanomaterials, *J. Magn. Magn. Mater.* 429 (2017) 142-147
- [21] ³⁰ M. U. Rana, T. Abbas, *J. Magn. Magn. Mater.* 246 (2002) 110.
- [22] A.C.F.M. Costa, M. R. Morelli, R.H.G.A. Kiminami, *J. Mater. Sci.* 42 (2007) 779-783
- [23] ¹⁹ I. Kulikowski, *J. Magn. Mater.* 41 (1984) 56.
- [24] ² R.B. Pujar, S.N. Kulkarni, S.S. Bellad, B.K. Chougule, *J. Mater. Sci. Lett.* 16 (1997) 1668-1669.
- [25] ⁷ M. Javed Iqbal, Barkat-ul-Ain, *Mater. Sci. Engg. B* 164 (2009) 6-11.
- [26] F.B. Li, X.Z. Li, C.S. Liu, T.X. Liu, Effect of alumina on photocatalytic activity of iron oxides for bisphenol a degradation, *J. Hazard. Mater.*, 149 (2007), 199–207
- [27] C. Lin, C. Zhang, J. Lin, Phase transformation and photoluminescence properties of nanocrystalline ZrO₂ powders prepared via the pechini-type sol-gel process, *J. Phys. Chem. C*, 111 (2007), 3300–3307
- [28] J.R. De la Rosa, A. Hernandez, F. Rojas, J.J. Ledezma, Sol-gel synthesis and characterization of novel La, Mn and Fe doped zirconia: catalytic combustion activity of trichloroethylene, *Colloids Surf. A Physicochem. Eng. Asp.*, 315 (2008), 147–155.
- [29] ⁵⁰ C. Caizer, M. Stefanescu, *J. Phys. D. Appl. Phys.* 35 (2002) 3035.
- [30] ³¹ I.H. Gul, A.Z. Abbasi, F. Amin, M. Anis-Ur Rehman, A. Maqsood, *J. Magn. Magn. Mater.* 311 (2007) 494.
- [31] ²² S. M. Patange, Sagar E. Shirsath, G. S. Jangam, K. S. Lohar, S. S. Jadhav, K. M. Jadhav, Rietveld structure refinement, cation distribution and magnetic properties of Al³⁺ substituted NiFe₂O₄ nano particles, *J. Appl. Phys.* 109 (2011) 053909
- [32] ⁴ K. Okasaka, H. Nasu, K. Kamiya, *J. Non Cryst. Solids* 136 (1991) 103.
- [33] F.A. Khalifa, Z.A. El-Keshen, F.A. Moustafa, *Ind. J. Pure Appl. Phys.* 34 (1996) 201.
- [34] R. K. Sharma, Varkey Sebastian, N. Lakshmi, K. Venugopalan, R. V. Reddy, Ajay Gupta, *Phys. Rev. B* 75 (2007) 144419-1-6.

- [35] ² K. J. Standley, Oxide magnetic materials. Clarendon Press, Oxford, (1972).
- [36] I. W. Vrewey, E. L. Heilmann, J. Chem. Phys. 15 (1947) 174-180.
- [37] ⁴⁵ T. Abbas, Y. Khan, M. Ahmad, S. Anwar, Solid State Comm. 82 (1992) 701-703.
- [38] ³³ G. Fagherazzi, F. Garbassi, J. Appl-Crystallogr. 5 (1972) 18-23.
- [39] ⁴ C. O. Arean, J. L. R. Blanco, J. M. R. Gonzalez, M. C. T. Fernez, J. Mater. Sci. Letts. 9 (1990) 229-230.
- [40] C.O. Arean, E.G. Diaz, J.M.R. Gonzalez, M.A.V. Garcia, Solid State Comm. 77 (1988) 275-280
- [41] ⁴¹ R. Valenzuela, Magnetic ceramics, (Cambridge University Press, 1994).
- [42] Neel L. Magnetic properties of ferrites: ferrimagnetism and antiferromagnetism, Ann Phys Paris, 1948;3:137.
- [43] ²⁶ A. J. Rondinone, A.C. S. Samia, Z. J. Zhang, Superparamagnetic relaxation and magnetic anisotropy energy distribution in CoFe₂O₄ spinel ferrite nanocrystallites, J. Phys. Chem. B103 (1999) 6876-6880.
- [44] ¹⁶ N.N. Greenwood, T.C. Gibb, Mossbauer Spectroscopy, (Chapman & Hall, London, 1971, p. 259).
- [45] Abbasher M. Gismelseed and Ali A. Yousif, Physica B 370 (2005) 215.
- [46] K.H. Rao, S.B. Raju, R.G. Mendiratta, J.P. Eymery, Solid State Commun. 45 (1983) 919.
- [47] A. Lakshman, P.S.V. Subba Rao, K.H. Rao, Mater. Lett. 60 (2006) 7.
- [48] D.P.E. Dickson, F.J. Berry, Mossbauer Spectroscopy, (Cambridge University Press, London, 1986, p. 22).

Figure Captions:

Fig 1 : Chemical reaction of $\text{CoZn}_x\text{Zr}_x\text{Fe}_{2-2x}\text{O}_4$ Ferrites

Fig 2: XRD pattern of $\text{CoZn}_x\text{Zr}_x\text{Fe}_{2-2x}\text{O}_4$ Ferrites.

Fig 3: Nelson–Riley plot of $\text{CoZn}_x\text{Zr}_x\text{Fe}_{2-2x}\text{O}_4$ Ferrites.

Fig 4 : X-ray density and lattice parameter of $\text{CoZn}_x\text{Zr}_x\text{Fe}_{2-2x}\text{O}_4$ Ferrites.

Fig 5 : TEM images of $\text{CoZn}_x\text{Zr}_x\text{Fe}_{2-2x}\text{O}_4$ Ferrites (a) for $x=0.2$ and (b) for $x=0.4$.

Fig 6 : Variation of magnetization with applied magnetic field for $\text{CoZn}_x\text{Zr}_x\text{Fe}_{2-2x}\text{O}_4$ spinel ferrites.

Fig 7: Temperature dependent variation in FC/ZFC of $\text{CoZn}_x\text{Zr}_x\text{Fe}_{2-2x}\text{O}_4$

Fig 8 : Room temperature Mossbauer spectra of all the samples of $\text{CoZn}_x\text{Zr}_x\text{Fe}_{2-2x}\text{O}_4$

84%

SIMILARITY INDEX

42%

INTERNET SOURCES

84%

PUBLICATIONS

36%STUDENT PAPERS

PRIMARY SOURCES

- 1** Amanpreet Kaur Jassal, R.K. Mudsainiyan, S.K. Chawla, Anu, Sukhleen Bindra Narang, Kunal Pubby. "Sol-gel route approach and improvisation in physico-chemical, structural, magnetic and electrical properties of $\text{BaCo}_{x/2}\text{Zn}_{x/2}\text{Zr}_x\text{Fe}_{(12-2x)}\text{O}_{19}$ ferrites", Journal of Magnetism and Magnetic Materials, 2018
Publication **10%**
- 2** S.K. Gurav, Sagar E. Shirsath, R.H. Kadam, S.M. Patange, K.S. Lohar, D.R. Mane. "Less magnetic and larger Zr^{4+} - Zn^{2+} ions co-substituted structural and magnetic properties of ordered $\text{Li}_{0.5}\text{Fe}_{2.5}\text{O}_4$ nanoparticles", Materials Research Bulletin, 2013
Publication **10%**
- 3** Mohd. Hashim, Alimuddin, Shalendra Kumar, Sagar E. Shirsath, R.K. Kotnala, Hanshik Chung, Ravi Kumar. "Structural properties and magnetic interactions in $\text{Ni}_{0.5}\text{Mg}_{0.5}\text{Fe}_{2-x}\text{Cr}_x\text{O}_4$ ($0 \leq x \leq 1$) ferrite nanoparticles", Powder Technology, 2012 **10%**

4

S.K. Gurav, Sagar E. Shirsath, R.H. Kadam, D.R. Mane. "Low temperature synthesis of $\text{Li}_{0.5}\text{Zr}_x\text{Co}_x\text{Fe}_{2.5-2x}\text{O}_4$ powder and their characterizations", Powder Technology, 2013

7%

Publication

5

D. R. Mane, D. D. Birajdar, Swati Patil, Sagar E. Shirsath, R. H. Kadam. "Redistribution of cations and enhancement in magnetic properties of sol-gel synthesized $\text{Cu}_{0.7-x}\text{Co}_x\text{Zn}_{0.3}\text{Fe}_2\text{O}_4$ ($0 \leq x \leq 0.5$)", Journal of Sol-Gel Science and Technology, 2010

6%

Publication

6

Rajjab Ali, Muhammad Azhar Khan, Alina Manzoor, Muhammad Shahid et al. "Investigation of structural and magnetic properties of Zr-Co doped nickel ferrite nanomaterials", Journal of Magnetism and Magnetic Materials, 2017

4%

Publication

7

Jitu Das, Vijayanand S. Moholkar, Sankar Chakma. "Structural, magnetic and optical properties of sonochemically synthesized Zr-ferrite nanoparticles", Powder Technology, 2018

4%

Publication

8

R.A. Pawar, S.S. Desai, S.M. Patange, S.S. Jadhav, K.M. Jadhav. "Inter-atomic bonding and

2%

dielectric polarization in Gd³⁺ incorporated Co-Zn ferrite nanoparticles", Physica B: Condensed Matter, 2017

Publication

9

Hashim, Mohd., Alimuddin, Shalendra Kumar, Sagar E. Shirsath, R.K. Kotnala, Hanshik Chung, and Ravi Kumar. "Structural properties and magnetic interactions in Ni_{0.5}Mg_{0.5}Fe_{2-x}Cr_xO₄ (0 ≤ x ≤ 1) ferrite nanoparticles", Powder Technology, 2012.

Publication

2%

10

Chaudhari, M.V., Sagar E. Shirsath, A.B. Kadam, R.H. Kadam, S.B. Shelke, and D.R. Mane. "Site occupancies of Co–Mg–Cr–Fe ions and their impact on the properties of Co_{0.5}Mg_{0.5}Cr_xFe_{2-x}O₄", Journal of Alloys and Compounds, 2013.

Publication

2%

11

Hashim, Mohd., Alimuddin, Shalendra Kumar, Sagar E. Shirsath, R.K. Kotnala, Jyoti Shah, and Ravi Kumar. "Influence of Cr³⁺ ion on the structural, ac conductivity and magnetic properties of nanocrystalline Ni–Mg ferrite", Ceramics International, 2013.

Publication

2%

12

Patange, S. M., S. S. Desai, S. S. Meena, S. M. Yusuf, and Sagar E. Shirsath. "Random site

2%

occupancy induced disordered Néel-type collinear spin alignment in heterovalent Zn^{2+} – Ti^{4+} ion substituted $CoFe_2O_4$ ", RSC Advances, 2015.

Publication

13

R.H. Kadam, A.P. Birajdar, Suresh T. Alone, Sagar E. Shirsath. "Fabrication of $Co_{0.5}Ni_{0.5}Cr_xFe_{2-x}O_4$ materials via sol–gel method and their characterizations", Journal of Magnetism and Magnetic Materials, 2013

Publication

14

Mohd. Hashim, Alimuddin, Sagar E. Shirsath, S.S. Meena, R.K. Kotnala, Shalendra Kumar, Pramod Bhatt, R.B. Jotania, Ravi Kumar. "Study of structural and magnetic properties of (Co–Cu) Fe_2O_4 /PANI composites", Materials Chemistry and Physics, 2013

Publication

15

Gurav, S.K., Sagar E. Shirsath, R.H. Kadam, S.M. Patange, K.S. Lohar, and D.R. Mane. "Less magnetic and larger Zr^{4+} – Zn^{2+} ions co-substituted structural and magnetic properties of ordered $Li_{0.5}Fe_{2.5}O_4$ nanoparticles", Materials Research Bulletin, 2013.

Publication

16

Mohd. Hashim, S.S. Meena, R.K. Kotnala, Sagar E. Shirsath et al. "Study of structural,

1%

1%

1%

1%

electrical and magnetic properties of Cr doped Ni–Mg ferrite nanoparticle", Journal of Alloys and Compounds, 2014

Publication

17

prc.hec.gov.pk

Internet Source

1%

18

Khalid Mujasam Batoo, Gagan Kumar, Yujie Yang, Y. Al-Douri, Mahavir Singh, Rajshree B. Jotania, Ahmed Imran. "Structural, morphological and electrical properties of Cd²⁺doped MgFe_{2-x}O₄ ferrite nanoparticles", Journal of Alloys and Compounds, 2017

Publication

1%

19

Hankare, P.P.. "Effect of zinc substitution on structural and magnetic properties of copper ferrite", Journal of Alloys and Compounds, 20100702

Publication

1%

20

S.R. Bhongale, H.R. Ingawale, T.J. Shinde, Kunal Pubby, Sukhleen Bindra Narang, P.N. Vasambekar. "Nano-crystalline Magnesium Substituted Cadmium Ferrites as X-band Microwave Absorbers", Journal of Magnetism and Magnetic Materials, 2017

Publication

1%

21

Xu Wu, Ruonan Wang, Yali Du, Chunlei Zou, Hao Meng, Xianmei Xie. "Performance

1%

enhancement of NH₃-SCR via employing hydrotalcite-like precursor to induce the decoration of NiO by TiO₂ phase", *Molecular Catalysis*, 2019

Publication

22

Submitted to University of Dhaka

Student Paper

1%

23

Le-Zhong Li, Xiao-Qiang Tu, Rui Wang, Long Peng. "Structural and magnetic properties of Cr-substituted NiZnCo ferrite nanopowders", *Journal of Magnetism and Magnetic Materials*, 2015

Publication

1%

24

Kadam, R.H., Kirti Desai, Supriya R. Kadam, and Sagar E. Shirsath. "Variation in the structural and magnetic properties of heterovalent Mn²⁺-Si⁴⁺ substituted MnCrFeO nanoparticles", *Solid State Sciences*, 2013.

Publication

1%

25

K.Vijaya Babu, B. Sailaja, K. Jalaiah, Paulos Tadesse Shibeshi, M. Ravi. "Effect of zinc substitution on the structural, electrical and magnetic properties of nano-structured Ni_{0.5}Co_{0.5}Fe₂O₄ ferrites", *Physica B: Condensed Matter*, 2018

Publication

1%

26

rd.springer.com

1%

27

S. Ounnunkad, P. Winotai. "Properties of Cr-substituted M-type barium ferrites prepared by nitrate–citrate gel-autocombustion process", *Journal of Magnetism and Magnetic Materials*, 2006

Publication

<1%

28

Ram A. Pawar, Sunil M. Patange, Sagar E. Shirsath. " Spin glass behavior and enhanced but frustrated magnetization in Ho substituted Co–Zn ferrite interacting nanoparticles ", *RSC Advances*, 2016

Publication

<1%

29

S.J. Haralkar, R.H. Kadam, S.S More, Sagar E. Shirsath, M.L. Mane, Swati Patil, D.R. Mane. "Substitutional effect of Cr³⁺ ions on the properties of Mg–Zn ferrite nanoparticles", *Physica B: Condensed Matter*, 2012

Publication

<1%

30

dspace.nitrkl.ac.in

Internet Source

<1%

31

Birajdar, A.A.. "Role of Cr³⁺ ions on the microstructure development, and magnetic phase evolution of Ni⁰.₇Zn⁰.₃Fe₂O₄ ferrite nanoparticles", *Journal of Alloys and Compounds*, 20120125

<1%

32

P.A. Mariño-Castellanos, J.C. Somarriba-Jarque, J. Anglada-Rivera. "Magnetic and microstructural properties of the BaFe(12-(4/3)x)SnxO19 ceramic system", Physica B: Condensed Matter, 2005

Publication

33

Mazhar U Rana, Misbah-ul Islam, Tahir Abbas. "Cation distribution and magnetic interactions in Zn-substituted CuFe2O4 ferrites", Materials Chemistry and Physics, 2000

Publication

34

S. M. Patange, Sagar E. Shirsath, G. S. Jangam, K. S. Lohar, Santosh S. Jadhav, K. M. Jadhav. " Rietveld structure refinement, cation distribution and magnetic properties of Al substituted NiFe O nanoparticles ", Journal of Applied Physics, 2011

Publication

35

export.arxiv.org

Internet Source

36

L. Wang, B.K. Rai, S.R. Mishra. "Structural and magnetic study of Al³⁺ doped Ni_{0.75}Zn_{0.25}Fe_{2-x}Al_xO₄ nanoferrites", Materials Research Bulletin, 2015

Publication

Dhanraj R. Mane. "Structural and magnetic

<1%

<1%

<1%

<1%

<1%

37 characterizations of MnNiZn ferrite nanoparticles", physica status solidi (a), 07/15/2010 <1%
Publication

38 www.socialresearchfoundation.com <1%
Internet Source

39 Nikam, Dipali S., Swati V. Jadhav, Vishwajeet M. Khot, R. A. Bohara, Chang K. Hong, Sawanta S. Mali, and S. H. Pawar. "Cation distribution, structural, morphological and magnetic properties of $\text{Co}_{1-x}\text{Zn}_x\text{Fe}_2\text{O}_4$ ($x = 0-1$) nanoparticles", RSC Advances, 2014. <1%
Publication

40 F. Saffari, P. Kameli, M. Rahimi, H. Ahmadvand, H. Salamati. "Effects of Co-substitution on the structural and magnetic properties of $\text{NiCo}_x\text{Fe}_{2-x}\text{O}_4$ ferrite nanoparticles", Ceramics International, 2015 <1%
Publication

41 www.scielo.br <1%
Internet Source

42 onlinelibrary.wiley.com <1%
Internet Source

43 Mohd. Hashim, Alimuddin, Shalendra Kumar, Sagar E. Shirsath, R.K. Kotnala, Jyoti Shah, Ravi Kumar. "Synthesis and characterizations of

Ni²⁺ substituted cobalt ferrite nanoparticles",
Materials Chemistry and Physics, 2013

Publication

44

R.A. Pawar, S.S. Desai, Q.Y. Tamboli, Sagar E. Shirsath, S.M. Patange. "Ce³⁺ incorporated structural and magnetic properties of M type barium hexaferrites", Journal of Magnetism and Magnetic Materials, 2015

<1%

Publication

45

Vivek Verma, Vibhav Pandey, Sukhveer Singh, R.P. Aloysius, S. Annapoorni, R.K. Kotanala. "Comparative study of structural and magnetic properties of nano-crystalline Li_{0.5}Fe_{2.5}O₄ prepared by various methods", Physica B: Condensed Matter, 2009

<1%

Publication

46

www.maik.rssi.ru

Internet Source

<1%

47

Zhong, W.. "Key step in synthesis of ultrafine BaFe¹²O¹⁹ by sol-gel technique", Journal of Magnetism and Magnetic Materials, 19970401

<1%

Publication

48

Vivek Chaudhari, Sagar E. Shirsath, M.L. Mane, R.H. Kadam, S.B. Shelke, D.R. Mane. "Crystallographic, magnetic and electrical properties of Ni_{0.5}Cu_{0.25}Zn_{0.25}La_xFe_{2-x}O₄ nanoparticles fabricated by sol-gel method",

<1%

49

K. Rajasekhar Babu, M. Purnachandra Rao, P. S. V. Subba Rao, K. Rama Rao, B. Kishore Babu, B. Rajesh Babu. "Structural and Magnetic Properties of Cu²⁺ Substituted Co–Zn Ferrite Nanoparticles, Synthesized by Sol–Gel Combustion Method", Journal of Inorganic and Organometallic Polymers and Materials, 2017

Publication

<1%

50

dyuthi.cusat.ac.in

Internet Source

<1%

51

A. A. Birajdar, Sagar E. Shirsath, R. H. Kadam, S. M. Patange, D. R. Mane, A. R. Shitre. "Rietveld Structure Refinement and Cation Distribution of Substituted Nanocrystalline Ni-Zn Ferrites", ISRN Ceramics, 2012

Publication

<1%

52

M.K. Kokare, Nitin A. Jadhav, Yogesh Kumar, K.M. Jadhav, S.M. Rathod. "Effect of Nd³⁺ doping on structural and magnetic properties of Ni_{0.5}Co_{0.5}Fe₂O₄ nanocrystalline ferrites synthesized by sol-gel auto combustion method", Journal of Alloys and Compounds, 2018

Publication

<1%

53

Submitted to Rajarambapu Institute of

Technology

Student Paper

<1%

54

A D Patil, S B Kondhalkar, S G Algude, Sagar E Shirsath, Vishnu S Shinde, S M Patange. "Influence of Ta O additive on the structural, optical and magnetic properties of Ni-Cu-Zn nanocrystalline spinel ferrites ", Materials Research Express, 2019

Publication

<1%

55

Kumar, Gopathi Ravi, Katrapally Vijaya Kumar, and Yarram Chetty Venudhar. "Synthesis, Structural and Magnetic Properties of Copper Substituted Nickel Ferrites by Sol-Gel Method", Materials Sciences and Applications, 2012.

Publication

<1%

56

Le-Zhong Li, Xiao-Xi Zhong, Rui Wang, Xiao-Qiang Tu, Lei He, Rong-Di Guo, Zhi-Yong Xu. "Structural, magnetic and electrical properties in Al-substitued NiZnCo ferrite prepared via the sol-gel auto-combustion method for LTCC technology", RSC Advances, 2017

Publication

<1%

57

opus.bibliothek.uni-augsburg.de

Internet Source

<1%

58

Submitted to Higher Education Commission
Pakistan

Student Paper

<1%

59

Submitted to Universiti Kebangsaan Malaysia

Student Paper

<1%

60

Gagan Kumar, R. K. Kotnala, Jyoti Shah, Vijay Kumar, Arun Kumar, Pooja Dhiman, M. Singh. "Cation distribution: a key to ascertain the magnetic interactions in a cobalt substituted Mg–Mn nanoferrite matrix", Physical Chemistry Chemical Physics, 2017

Publication

<1%

61

Gul, I.H.. "Structural, magnetic and electrical properties of $\text{Co}^{1-x}\text{Zn}^x\text{Fe}_2\text{O}_4$ synthesized by co-precipitation method", Journal of Magnetism and Magnetic Materials, 200704

Publication

<1%

62

"ICAME 2007", Springer Nature, 2009

Publication

<1%

63

Abdeen, A.. "Electric conduction in Ni-Zn ferrites", Journal of Magnetism and Magnetic Materials, 19980604

Publication

<1%

64

Submitted to Jawaharlal Nehru Technological University

Student Paper

<1%

65

Mitra, Arijit, J. Mohapatra, S. S. Meena, C. V. Tomy, and M. Aslam. "Verwey Transition in Ultrasmall-Sized Octahedral Fe_3O_4

<1%

Nanoparticles", The Journal of Physical Chemistry C

Publication

66

Submitted to Panjab University

Student Paper

<1%

67

R. L. Dhiman. "Preparation and Characterization of Manganese Ferrite Aluminates", Advances in Condensed Matter Physics, 2008

Publication

<1%

Exclude quotes Off













Exclude matches Off

Exclude bibliography Off

Document Information

Analyzed document	Physics Asha Dattatray Patil Ph.D theses.pdf (D98513385)
Submitted	3/16/2021 12:31:00 PM
Submitted by	dharmaraj veer
Submitter email	dharmaraj.veer@gmail.com
Similarity	3.6%
Analysis address	dharmaraj.veer.bamu@analysis.arkund.com

Sources included in the report

W	URL: https://www.researchgate.net/publication/282545713_Electrical_and_Dielectrical_Pro ... Fetched: 10/4/2019 1:10:07 PM		10
W	URL: https://docplayer.net/150337558-Doctor-of-philosophy.html Fetched: 12/14/2019 7:53:33 AM		13
W	URL: http://pr.hec.gov.pk/jspui/bitstream/123456789/2067/2/1603S.pdf Fetched: 12/11/2020 4:39:09 PM		2
W	URL: https://www.researchgate.net/profile/Carlos_Arean/post/What_the_types_of_ferrites/ ... Fetched: 3/16/2021 12:33:00 PM		1
W	URL: http://repository.sustech.edu/bitstream/handle/123456789/9342/Catalytic%20Activity ... Fetched: 3/16/2021 12:33:00 PM		1
W	URL: http://www.jetir.org/papers/JETIR2010314.pdf Fetched: 3/5/2021 12:08:43 PM		5
W	URL: https://www.researchgate.net/publication/256770513_Investigation_of_structural_mag ... Fetched: 10/6/2019 1:22:52 PM		1
W	URL: https://www.researchgate.net/publication/223682590_Electrical_conductivity_of_nick ... Fetched: 2/18/2020 7:13:37 AM		1
W	URL: https://www.researchgate.net/publication/269564409_Temperature_and_Frequency_Depen ... Fetched: 3/16/2021 12:33:00 PM		1
W	URL: https://www.researchgate.net/publication/223349848_Preparation_of_nanocrystalline_ ... Fetched: 3/16/2021 12:33:00 PM		1
W	URL: https://core.ac.uk/download/pdf/35351804.pdf Fetched: 3/16/2021 12:33:00 PM		1
W	URL: https://www.researchgate.net/publication/292073468_Dielectric_Complex_Impedance_an ... Fetched: 3/16/2021 12:33:00 PM		1

W	URL: https://www.researchgate.net/publication/229570579_Structural_magnetic_and_electr... Fetched: 11/3/2019 9:45:17 AM		1
W	URL: https://www.researchgate.net/publication/229484169_Dielectric_and_magnetic_propert... Fetched: 3/16/2021 12:33:00 PM		1
W	URL: https://www.researchgate.net/publication/221930315_Structural_electrical_and_magne... Fetched: 11/1/2019 9:19:44 AM		1
W	URL: https://www.researchgate.net/publication/322333655_Structural_optical_dielectric_a... Fetched: 9/30/2019 12:03:38 PM		1
W	URL: https://www.researchgate.net/publication/251616003_Enhancement_of_the_magnetic_pro... Fetched: 5/18/2020 9:26:16 PM		2

Entire Document

Dr. Babasaheb Ambedkar Marathwada University, Aurangabad A Ph.D. Thesis on "EFFECT OF ADDITIVES ON THE STRUCTURAL AND MAGNET PROPERTIES OF NANO CRYSTALLINE SPINEL FERRITES" For the Award of Ph.D. Degree in Physics Submitted by Smt. Asha Dattatray Patil M.Sc. Assistant Professor, Department of Physics D.A.B.N. Arts & Science College, Chikhali, Tal-Shirala, Dist. Sangli. Under the Guidance of Dr. Sunil M. Patange M.Sc., Ph.D. Head, Department of Physics Shrikrishna Mahavidhyalay Gunjoti, Tal: Omarga, Dist: Osmanabad March 2021

i Abstract The NiCuZn ferrite composition is an exceptional spinel ferrite having very high permeability and electrical resistivity and employed in the fabrication of multilayer chip inductors. The present work is intended to investigate structural, dielectric, electrical and magnetic properties of ferrite by doping additive. The doping of tetravalent and pentavalent metal ions is endeavored in order to create the understanding of different properties of NiCuZn ferrite composition. With this broad scene in mind, we have prepared nanocrystalline spinel ferrite with formula $Ni_{0.4}Cu_{0.3}Zn_{0.3}Fe_2O_4 + xTa_2O_5$ and $Ni_{0.4}Cu_{0.3}Zn_{0.3}Fe_2O_4 + xTiO_2$ (for $x = 0, 1, 2, 3, 5$ and 10 wt. %) employing sol gel method and studied structural, dielectric and magnetic properties of pure and doped ferrite. $Ni_{0.4}Cu_{0.3}Zn_{0.3}Fe_2O_4 + xTa_2O_5$ (for $x = 0, 1, 2, 3, 5$ and 10 wt. %) The compositions $Ni_{0.4}Cu_{0.3}Zn_{0.3}Fe_2O_4 + xTa_2O_5$ for all the selected concentrations of dopant were synthesized by using the Sol gel method. The XRD data was subjected for structural analysis of all the investigated samples with the help of Rietveld refinement using FULLPROF software. The result shows a cubic spinel structure and also forms a secondary phase of $FeTaO_4$ with increasing Ta_2O_5 composition. The lattice constant found to decrease with the increase in Ta_2O_5 doping content. The crystallite size was obtained using Debye-Scherrer's formula. The crystallite size of the prepared samples was increased with an increase in content of Ta_2O_5 additive. Spinel structure of the samples under investigation was confirmed the presence of two main absorption bands in FTIR spectrum. There is variation in force constant values as well as bond length values of cations and oxygen ions at the tetrahedral and octahedral site in NiCuZn ferrite with the Ta_2O_5 additive. Also, there was no systematic

ii variation in the ratio μ_1 / μ_2 which shows that Ta_2O_5 additive do not considerably alter the site occupancy of cations present in the NiCuZn ferrite system. The morphological study carried out with the help of SEM image analysis shows spherical shaped particles with some agglomeration. The bandgap energies of synthesized ferrite samples were obtained from UV-Visible diffused reflectance spectra and increased with the Ta_2O_5 additive concentration of ≤ 5 wt%, however, further increase in Ta_2O_5 doping concentration of < 5 wt% decrease the band gap energy. There was decrement in saturation magnetization with enhancement in Ta_2O_5 additive concentration in NiCuZn ferrite samples. DC electrical resistivity values were recorded to decrease with increment in temperature. The computed values of activation energy were found to be higher for the paramagnetic region than the ferromagnetic region. The results for the dielectric constant and dielectric loss tangent were decreased with increase in frequencies for all Ta_2O_5 doped samples. Further, the estimated AC conductivity values were increased with Ta_2O_5 additive composition. $Ni_{0.4}Cu_{0.3}Zn_{0.3}Fe_2O_4 + xTiO_2$ (for $x = 0, 1, 2, 3, 5$ and 10 wt. %) TiO_2 (0–10 wt. %) doped nanocrystalline $Ni_{0.4}Cu_{0.3}Zn_{0.3}Fe_2O_4$ (Ni-Cu-Zn) ferrite compositions were synthesized using sol gel route of synthesis. The cubic spinel structure having $Fd\bar{3}m$ space group of the ferrite compositions under consideration was revealed from the analysis of Rietveld refined X-ray diffraction (XRD) data. The secondary phase with a space group of $I41/amd$ was observed within the ferrites with TiO_2 doping, $x < 3$ wt. %. The values of lattice parameter were increased with the addition of TiO_2 up to 5 wt. % and reduced further for the highest experimental doping of 10 wt. %. Field emission scanning electron microscope (FESEM) images exhibit the spherical shape of the synthesized particles with some agglomeration while compositional purity of prepared ferrite samples was confirmed from energy dispersive X-ray spectroscopy (EDX) and elemental mapping. The cubic spinel structure of the prepared ferrite sample was confirmed from the Raman and Fourier transform infra-red (FTIR) spectra. UV– visible diffuse reflectance spectroscopy was utilized to study the optical properties of the ferrites. The value of band gap energy for the pristine sample was less than those of the

iii doped samples and there was a decrement in band gap energy values with the increase in TiO_2 doping which specifies the semiconducting nature of prepared ferrite samples. Magnetic study performed by means of vibrating sample magnetometer (VSM) demonstrates that the values of saturation magnetization of the ferrites goes on decreasing with the addition of TiO_2 content and all investigated ferrites show the characteristics of soft magnetic materials at room temperature. The Mössbauer study confirms the decrease in the magnetic behavior of the doped ferrites due to the non-magnetic secondary phase of TiO_2 . The ultrasonic pulse transmission method was employed to determine the elastic properties of the ferrites.

The elastic constants initially increased with an increase in TiO_2 up to 1 wt. % and then

declined with the further addition of TiO₂. The dielectric properties were studied within 50 Hz to 5 MHz frequency range with the help of LCR-Q meter. The values of dielectric constant (ϵ') as well as dielectric loss tangent were observed to be continuously decreasing trend with increase in

frequency for all the selected samples at room temperature revealing normal dielectric behavior of ferrites. Also, the AC conductivity was increased with an increase in the frequency of all the selected samples. Cole-Cole plots were obtained for all

the investigated samples and showed a

single semicircle which indicates that the electrical conduction process appears only due to grain boundaries.

Keywords: TiO₂ doping; Ni-Cu-Zn ferrite; Rietveld refinement; Raman spectra; Mössbauer spectroscopy; UV Vis spectra.

Chapter 1 1 A.D.Patil Ph.D. Thesis Introduction to Ferrites Chapter 1 Introduction to Ferrites 1.1 Introduction to Nanomaterials Nanoscience is an interdisciplinary and rising field of science which includes the study of matter at nano (10⁻⁹ m) scale. The phenomena of nanotechnology initially explained by Richard Feynman in 1959, gave a speech entitled "There's Plenty of Room at the Bottom" at Caltech. In his lecture he put forward the opportunity of manipulating things at very small scale [1]. The word „Nano" obtained from „dwarf" a Greek word and is utilized as a prefix for any measurement unit like meter (nanometer), or second (nanosecond). Therefore one billionth of meter or 10⁻⁹ m is referred as a nanometer (nm). The materials having particle size less than 100 nm are generally known as nanomaterials. Nanotechnology plays important role in modern science and technology. In the past few years nano science and technology is a wide and interdisciplinary area for research which is rising worldwide. Nanomaterials have broadly different properties from those of the bulk materials because of their large surface to volume ratio, spatial confinement, high surface energy and imperfections are decreased which are not present in related bulk materials [2]. Depending upon the shape of grains or crystallites, generally nanomaterials are categorized into four groups such as (a) Zero dimensional nanomaterials for example quantum dots, (b) One dimensional nanomaterials for example quantum rod / quantum wire, (c) Two dimensional nanomaterials for example thin films and quantum well and (d) Three dimensional nanomaterials for example zeolites or molecular sieves with cage like nanopores [3]. Nanomaterials are produced by two methods such as top-down approach and bottom-up approach. In top-down approach, the bulk material is disintegrated into smaller nanomaterials whereas in bottom-up approach, molecules or atoms are assembled to form nanomaterials. Also

Chapter 1 2 A.D.Patil Ph.D. Thesis Introduction to Ferrites there are various methods to manufacture nanomaterials, some well-known methods such as (1) Wet synthesis (liquid phase synthesis), (2) Microwave processing (plasma phase synthesis), (3) Gas phase synthesis, (4) Mechanical grinding (Solid Phase synthesis). Nanomaterials have gained utmost interest in recent years due to their significant chemical, magnetic, mechanical, optical, biological and electrical properties which are predictable to provide for different potential applications such as in optical devices, treatment and prevention of many diseases, magnetic devices, chemical and biological sensors, and so on [4]. 1.2 Magnetic materials and Magnetization The word magnetism is obtained from Magnesia, a Greek town in the area of Asia Minor. The name magnet is originated in Greek civilization. According to etymology meaning of the word magnet is that "the stone from Magnesia" which have property of attracting iron as well as pieces of same materials [5]. The use of magnetic materials is so widespread that a world without magnetic materials is difficult to visualize. Magnetic materials play a vital role in progress of modern technology. In number of electronic and electromechanical devices magnetic materials are employed such as high frequency transformers, electromagnetic gadgets, memory or disc storage devices, electromagnetic interference (EMI) suppressors, actuators, broad band pulse transformers, sensors, switches, power inductors etc. Magnetic materials exhibit the property by which it can experience force of attraction or repulsion among each other or through applied field. This magnetic interaction depends on atomic magnetic moment. The materials which have total magnetic moment are known as magnetic materials. Also, the requirement of efficient generation of electricity and use of electricity depends on enhancement and design in magnetic materials. As soon as external magnetic field (H) is applied to a material, dipole moments which are randomly oriented get oriented in the direction of H so that material has non zero magnetic moment. To explain magnetic state of material, a term introduced is magnetization (M) and is described as magnetic moment per unit volume [6]. The magnetic field which is applied to a material is known as applied field (H) and Magnetic induction (B), is nothing but magnetic flux density and these three are related by relation, $B = \mu_0 (H + M)$

Chapter 1 3 A.D.Patil Ph.D. Thesis Introduction to Ferrites Where, μ_0 is the permeability of free space. Further, the magnetic susceptibility is defined as termed as χ and given as, $\chi = M/H$

H The relative permeability is given by the ratio of the magnetic permeability to that of free space $\mu_r = \mu/\mu_0$

Paramagnetism and diamagnetism are the general types of magnetism and are related to room temperature magnetic properties of the elements of periodic table. Fig 1.1: The periodic table highlighting the type of magnetic behavior of each element at room temperature. 1.3 Classification of Magnetic Materials According to magnetic dipole moments arrangement in a material, the magnitude and the sign of magnetic susceptibility (χ), there are five types such as 1. Diamagnetism. 2. Para-magnetism. 3. Ferromagnetism. 4. Anti-ferromagnetism. 5. Ferrimagnetism.

Chapter 1 4 A.D.Patil Ph.D. Thesis Introduction to Ferrites 1.3.1 Diamagnetic Materials The elements like copper, lead, sulfur, mercury, bismuth, silver, zinc etc and materials like wood, water are repelled by a magnet are termed as diamagnetic materials. These materials are weakly magnetized when kept in strong magnetic field and magnetic dipoles in these materials are tried to align in opposite direction to the applied magnetic field. For diamagnetic materials the value of permeability is less than one. These materials have no permanent magnetic dipoles. The susceptibility of diamagnetic materials is negative and almost temperature independent [7]. 1.3.2 Paramagnetic Materials In case of paramagnetic materials individual dipole moments are randomly oriented and hence total magnetic dipole moment for these materials is zero. The elements like Titanium, Oxygen, Aluminum, Sodium, and Chromium are the paramagnetic materials. These materials are magnetized only in presence of applied strong magnetic field and once the applied magnetic field is removed then magnetization vanishes. The relative permeability of these materials is greater than one. Paramagnetic materials possess positive and small susceptibility values. 1.3.3 Ferromagnetic Materials The well-known ferromagnetic materials are Nickel, Iron, Neodymium, Cobalt and alloys of these materials which are strongly attracted by magnet and also magnetized. These materials possess very larger value of relative permeability. The susceptibility of ferromagnetic materials besides being temperature dependent, demonstrates very large and positive value. In case of ferromagnetic materials unpaired electrons are present so they acquire net magnetic moment. The ferromagnetic materials possess magnetic properties because of magnetic domains. Inside the domain dipole moments of atoms are aligned parallel to each other so there is strong magnetic force within the domain. For ferromagnetic material when magnetic field is not applied, domains are randomly oriented and hence material as a whole does not show any magnetism. On the other hand, when magnetic field is applied to ferromagnetic material, all the domains are oriented in the direction of applied field and generate strong magnetic field within the material. On removal of applied field, majority of domains are still aligned in the direction of applied field and

Chapter 1 5 A.D.Patil Ph.D. Thesis Introduction to Ferrites hence magnetic field of the materials maintain even after removal of applied magnetic field. Such a property of these materials is employed to construct permanent magnets. With rise in temperature, there is reduction in ferromagnetism owing to increase in thermal agitations. The temperature at which ferromagnetic material loses their property and turns into paramagnetic. This temperature is termed as Curie temperature [8] $\chi = C T^{-2}$. 1.3.4 Antiferromagnetism Chromium is only one element in the periodic table which at room temperature shows antiferromagnetism. In case of antiferromagnetic materials dipole moments of adjacent atom align antiparallel so the total magnetic moment of the material is zero which means that no magnetic field is produced by them. Above Neel temperature antiferromagnetic materials converts into paramagnetic materials (T_N). 1.3.5 Ferrimagnetism Ferrimagnetic materials have spin arrangement opposite in direction. However, these spins do not cancel each other as in case of antiferromagnetism. As a result there is net magnetic moment. The iron oxide is most well-known example and a number of other magnetic oxide materials exhibit ferrimagnetic because they have unequal anti-parallel spin moments and hence having net magnetic moment. Further, the compounds having complex crystal structure as compare to pure elements exhibits ferrimagnetism. 1.4 Ferrites Ferrite materials play a vital role in modern technology due to their applications in computer systems, nuclear power engineering, electrical engineering etc. Now a day's huge amount of work is going on by many researchers on various ferrite compositions for different device applications owing to their excellent chemical stability, mechanical hardness and high resistivity. This group of magnetic materials is termed as ferrimagnetic materials and the most crucial ferrimagnetic materials are ferrites. Ferrites have main components as iron oxide and metal oxides.

Chapter 1 6 A.D.Patil Ph.D. Thesis Introduction to Ferrites Fundamentally, ferrites are ceramic substances appeared black or dark grey in color and they are brittle, electrically nonconductive and very hard in physical character. Commonly, ferrites behave as ferrimagnetic ceramic compounds obtained from iron oxides for example Magnetite (Fe_2O_4) or hematite (Fe_2O_3) also oxides of other metals. In 1930, first ferrite compounds were prepared by Yogo Kato and Takeshi Takei in the Tokyo Institute of Technology. Ferrites show ferrimagnetism because of the super-exchange interaction among the electrons of oxygen and metal ions. Due to presence of opposite spins in ferrite magnetization decreases as compare to ferromagnetic metals as there are parallel spins. Further, as compared to ferromagnetic metal ferrite has large resistivity owing

to the intrinsic atomic level interaction among metal ions and oxygen. This enables the ferrite to find out applications at maximum frequencies and

hence from technological point of view ferrites are very precious. 1.5 Types of Ferrites According to crystal structure they are categorized into three groups 1) Spinel Ferrite 2) Garnet 3) Hexagonal ferrite 1.5.1 Spinel ferrites Bragg and Nishikawa [9] in 1915 first determined the spinel ferrites crystal structure. Also spinel ferrites are termed as cubic ferrite and are soft magnetic materials. The eddy current losses are low as well as electrical resistivity values are higher for spinel ferrite. For this reason they are used at microwave frequencies. Generally spinel ferrites have chemical formula MFe_2O_4 . Where M represents divalent metal ions such as Cd^{2+} , Mg^{2+} , Fe^{2+} , Ni^{2+} , Cu^{2+} , Zn^{2+} , Co^{2+} etc. or combination of these metal ions [10,11]. The spinel ferrite resides in FCC crystal structure having two interstitial sites, one is tetrahedral (A) and other is octahedral (B). Metallic cations are occupied among these sites. In one unit cell 96 interstitial sites are present. Out of which 32 are at octahedral (B) sites and 64 at tetrahedral (A) sites.

Chapter 17 A.D.Patil Ph.D. Thesis Introduction to Ferrites 1.5.2 Garnet The common formula to represent garnets is $M_3Fe_5O_{12}$, where M stands for rare earth metal ions or yttrium ion. The garnet have cubic unit cell with eight molecules of $M_3Fe_5O_{12}$. There is distribution of metal ions among three sites such as octahedral, tetrahedral and dodecahedral. Due to larger ionic radius rare earth ions are occupied only at dodecahedral site having bigger space and not occupied at tetrahedral and octahedral sites. 1.5.3 Hexagonal ferrite The Hexagonal ferrites was first recognized by Rathenau, Gorter, Went, and Van Oostershout in 1952 [12] and in 1956 by Jnker, Braun and Wijn. Hexagonal ferrites are extensively employed as permanent magnets. The crystal structure of hexagonal ferrite is hexagonal and rhombohedral with chemical formula $MFe_{12}O_{19}$, where M corresponds to divalent ion having large ionic radius like barium, lead or strontium. Further these ferrites are categorized into M, W, Y, X, Z and U. This class of ferrite materials possesses high coercivity and is useful at very high frequency applications. In comparison with garnet ferrite, hexagonal ferrites contain larger ions such as barium, lead or strontium. 1.6 Applications of Ferrites Ferrites have extensive applications from microwaves to radio frequencies Ferrites are considered as good magnetic materials as compared to pure metals since they have lower cost, easy to manufacture, high resistivity and better magnetization properties. Mostly ferrites are employed in fly back transformer in TV picture tube, telephone exchange, memory cores of computers audio-video and digital recording, broad band transformer, in radar and antenna cores in radio receivers [13-15]. Soft and hard ferrites are two categories of ferrites which are superior magnetic materials. Soft ferrites are used in core materials such as transformers, inductors, data storage devices, magnetic audio heads, radio/television, amplifiers, telecommunications, switching elements in microwave devices, and core memory in electronic data processing equipments, etc [16]. Hard ferrites have various applications such as in sensor technology, segment magnets in motors, toy magnets, watch industries, household appliances, generators for magnetic clutches, etc. The

Chapter 18 A.D.Patil Ph.D. Thesis Introduction to Ferrites electrical conductivity of ferrites is small than that of ferromagnetic materials and hence are applicable at high frequency due to no eddy current losses. Generally ferrite devices used at higher frequency such as circulator, phase shifters and isolators [17- 20]. Nano materials of Ferrites are also used in the treatment of hyperthermia [21], radiotherapy, drug delivery and AC magnetic field assisted cancer therapy [22- 24]. Mostly in large number of electronic circuit's as impedance matching networks, voltage controlled oscillators, filters and low noise amplifiers ferrite as inductive component is used. Ferrites are also exploited as multilayer chip inductor, in surface mounting devices electromagnetic wave absorber transformer core electro-magnetic interference (EMI) suppression [25-28]. The most significant properties of ferrites at lower and higher frequency applications are initial permeability (μ_i), saturation magnetization (M_s), losses and coercive force (H_c). By changing the compositions or preparation method or by adding additives, everyone can control the majority factors for any particular applications. 1.7 Review of Literature Many researchers used different additives in various spinel ferrites to study their effect on the properties of ferrites. Additives play very significant role in the contribution to magnetic properties of sintered ferrites. Addition of small amount of additives can improved the electromagnetic properties while too much amount of additives may decline magnetic properties. The impact of different additives in Ni- Cu-Zn ferrite along with some different ferrites is reviewed below. K. Yazhou Wang et al [29] observed the influence of additives Nb_2O_5 and MoO_3 on NiCuZn ferrites. It was reported that the additives Nb_2O_5 and MoO_3 shows progress in the densification, grain growth and increase in magnetic properties. The influence of Ta_2O_5 doping in MnZn ferrite were investigated by Znidarsic et al [30] and showed that Ta^{5+} present in grain boundaries and hence magnetic loss decreases. Li et al [31] found that when addition of Ta_2O_5 is up to 0.04 wt. %, enhancement in grain size and if it is larger than 0.04 wt. % then there was abnormal grain growth and porosity. Ke Sun et al [32] worked on Ni MgCuZn ferrites by co doping Ta_2O_5 - Co_2O_3 additives and found that, there was decrement in sintering density by inhibiting the

Chapter 1 9 A.D.Patil Ph.D. Thesis Introduction to Ferrites grain growth with the increase in doping of additives. Sea –Fue Wang et al [33] studied Ni_{0.38} Cu_{0.12} Zn_{0.50} Fe₂ O₄ by adding Bi₂ O₃ additive. The result indicated that a smaller amount of Bi₂ O₃ addition as well as low sintering temperature are needed for attaining same densification for ferrites synthesized by wet chemical coating process as compared with solid state mixing. Further, higher values of B_r and B_s and lower value of H_c are gained by the samples produced by wet chemical coating method than that of solid state mixing process. Jeong et al [34] observed the impact of Bi₂ O₃ additive on the electromagnetic and microstructure properties of Ni Cu Zn ferrite. They found that there was enhancement in bulk density and grain growth with raise in content of Bi₂ O₃. If content of Bi₂ O₃ greater than 0.5wt. % then there was abnormal grain growth. Also the sample having 0.25wt. % Bi₂ O₃ additive exhibits uniform microstructure, good quality factor and maximum value of initial permeability. N. Chu et al [35] worked on Ni Cu Zn ferrite by low Mn doping and found that there was reduction in saturation magnetization of the samples with enhancement in Mn²⁺ concentration. For toroidal samples B_r and B_s reduced with Mn²⁺ concentration equal to 0.02. Also, there was increment in values of B_s and B_r with increase in sintered temperature whereas reduction in coercivity (H_c). Further, secondary maximum and low frequency permeability enhanced with sintering temperature. Rathi et al [36] investigated properties of NiCuZn ferrite by Titanium doping and observed the reduction in values of x ray density and lattice constant with rise in concentration of titanium. Average crystallite size were observed in between 35-45nm. Decrement in dielectric constant with enhancement in frequency and at higher values of frequency it remains constant. Further, saturation magnetization reduced with increment in temperature as well as content of titanium. Y. Yang et al [37] synthesized NiCuZn ferrite from solid state method with doping TiO₂ additive. They found that with TiO₂ doping there was decrement in permeability while increment in permittivity values. The DC resistivity increases, dielectric loss tangent reduced with the increase in composition of TiO₂ in NiCuZn ferrite. The SEM analysis revealed compact and uniform ferrites with small grains were formed by controlling grain growth. Finally, they reported that Synthesized NiCuZn ferrite ceramics having high equivalent values of permittivity and

Chapter 1 10 A.D.Patil Ph.D. Thesis Introduction to Ferrites permeability and low dielectric loss tangent are superior for very small scale antenna substrate materials. Wang et al [38] studied Ni_{0.38} Cu_{0.12} Zn_{0.50} Fe₂ O₄ ferrites with the doping of different wt% of Bi₂ O₃, PbO: SiO₂ and PbO: B₂ O₃ and by changing sintering temperature. The result showed that initial permeability and density enhanced while quality factor and resistivity reduced with increment in sintering temperature. Also, with the variation in concentration of additives the performance of other factors was noted. The influence of Ti⁴⁺ doping on Magnetic, Electrical and Structural Properties of Ni_{0.4} Cu_{0.2} Zn_{0.4} Fe_{2-x} Ti_x O₄ Ferrites were reported by S. Mazumdar et al [39]. They observed that theoretical density (ρ_{th}) values are higher than bulk density (ρ_B) which specified that the pores are formed inside the bulk sample. There was decrement in average grain size and Saturation magnetization (M_s) with the addition of Ti concentration whereas coercivity (H_c) and remanent magnetization (M_r) enhanced with Ti. For the sample having composition x = 0.02 showed higher value of real part of the initial permeability owing to maximum density and homogeneity of the sample. Further, dielectric loss and dielectric constant are found to be reduced with rise in frequency. They suggested that such material were useful for biomedical applications and data storage. Cu²⁺ doped Zn_{0.5} Cu_x Mg_{0.5-x} Fe₂ O₄ Nano-ferrites produced by Co-precipitation method were investigated by B. Ali et al [40]. The result revealed that with increment in copper concentration lattice parameter enhanced. The measured values of grain size from the XRD data analyses are in between 15.97 to 28.33 nm. Spinel ferrite structure of manufactured ferrites were confirmed from FTIR spectroscopy. The computed values of energy band gap for studied samples are in between 4.04 to 4.67 eV. The impact of the additive V₂ O₅ on the magnetic and structural properties of Ni-Zn ferrite was reported by M. Patil et al [41]. They found that prepared samples exhibits single phase cubic spinel structure. Both x- ray as well as bulk density enhances with the V⁵⁺ doping while porosity reduced. There is decrement in magneton number and saturation magnetization with increment in content V⁵⁺ than undoped Ni-Zn spinel ferrite. A. Bhaskar et al. [42] synthesized polycrystalline samples of MgCuZn ferrites doped with 1 % Mn by using conventional solid-state method and observed the impact of sintering temperature on their properties such as dielectric and electrical. The result

Chapter 1 11 A.D.Patil Ph.D. Thesis Introduction to Ferrites indicated that Lattice constant, grain size, bulk density initial permeability and dielectric constant rises with enhancement in sintering temperature whereas DC electrical resistivity declined. Shuoqing Yan et al [43] studied properties NiCuZn ferrite by doping V₂ O₅ additive. The investigation reveals that better amount of V₂ O₅ additive considerably rises homogeneous and dense microstructure and the magnetic properties enhanced. At 0.5 wt. % V₂ O₅ additive doping in NiCuZn ferrite shows excellent properties. They suggest that such material is better for high-frequency WPC applications. Magnetic and electrical properties of TiO₂ doped Ni_{0.35} Zn_{0.12} Zn_{0.35} Fe₂ O₄ were studied by K. Praveena et al [44]. They found that variation in particle size in between 18 to 35 nm. There was increment in bulk densities, dielectric properties as well as imaginary part of permeability of produced

samples with the TiO₂ content. Further, all the composites shows resonant frequency above 1GHz. 1.8 Aim of The Present Work Technologically spinel ferrites play very important role owing to low dielectric and eddy losses and high electrical resistivity. These significant properties make NiCuZn ferrites important in many high frequency, electronic, electrical, microwave devices, telecommunication and gas sensing applications.

The properties of spinel ferrites depend on distribution of cations between the

tetrahedral (A) and octahedral [B] sites, composition of chemicals used, amount of doping of additives and preparation method. Nanosize spinel ferrite is found to be better as compare to corresponding bulk form and the soft magnetic materials have extended applications in future[45]. Therefore the collection of all above information and existing knowledge in this specific trail, the aim of our work is to fabricate additives doped NiCuZn spinel ferrite by the sol-gel method and study their influence on the properties of NiCuZn Spinel ferrite. The proposed chemical compositions of the present work are Ni_{0.4} Cu_{0.3} Zn_{0.3} Fe₂ O₄ + X Ta₂ O₅ (X = 0 to 10 wt %) and Ni_{0.4} Cu_{0.3} Zn_{0.3} Fe₂ O₄ + X TiO₂ (X = 0 to 10 wt %). The structural, magnetic, elastic and electrical properties of selected ferrite samples will be investigated systemically by doping these additives in NiCuZn Spinel ferrite by using standard characterization techniques.

Chapter 1 12 A.D.Patil Ph.D. Thesis Introduction to Ferrites References [1] P. R. Feynman "Miniaturization. Reinhold" New York, (1961) [2] G. Cao, Nanostructures and Nanomaterials. Synthesis, Properties and Applications. Imperial College Press, London, (2004) [3] C. Suryanarayana, Bull. Mater. Sci., 17 (1994) 307 [4] A Alagarasi, Introduction To Nanomaterials (2011) [5] K. H. J. Buschow, F. R. de Boer, Physics of Magnetism and Magnetic Materials, Kluwer Academic Publishers, New York, (2004) [6] J. David Griffiths, Introduction to electrodynamics, Pentice Hall of India, New Delhi, (2007) [7] M.E. Lines, A. M. Glass, "Principles and Applications of Ferroelectric and Related Materials", Clarendon Press, Oxford, (1997) [8] C. Kittel, Introduction to Solid State Physics (8thEd.), John Wiley & Sons, Inc., New Jersey, (2005) [9] R. Valenzuela, Magnetic ceramics, Cambridge University Press, New York, (2005) [10] R. Valenzuela. Magnetic Ceramics. Cambridge University Press, (1994) [11] E. S. Murdock, R. F. Simmons, R. Davidson. Roadmap for 10 Gbit/in² Media: Challenges. IEEE Trans. Magnet, 28(1992) 3078 [12] K.J. Standley, "Oxide Magnetic Materials" 2 ed., Oxford University Press, (1972) [13]

A. Hagfeldth, M. Gratzel, Chem. Rev., 95(1995) 49 [14] S. Prasad, N. S. Gajbhiye, J. Alloys Compd., 265 (1998) 87 [15] B. Viswanathan, V.R.K. Murthy: Ferrite Materials. Springer Verlag, Berlin, (1990) [16]

R. Valenzuela, Novel Applications of Ferrites, Phys. Res. Inter., (2012) [17] Ernst Schloemann, J. Magn. Magnet. Mater., (2000) 15 [18] A. J. B. Fuller, Ferrites at Microwave Frequencies. London: Peter Peregrinus, (1987) [19] Martha Pardavi-Horvath, J. Magn. Magn. Mater., 215, 216 (2000) 171 [20] Vincent G. Harris, Anton Geiler, Yajie Chen, Soack Dae Yoon, Mingzhong Wu, Aria Yang, Zhaohui Chen, Peng He, Patanjali V. Parimi, Xu Zuo,

Chapter 1 13 A.D.Patil Ph.D. Thesis Introduction to Ferrites Carl E. Patton, Manasori Abe, Olivier Acher, Carmine Vittoria, J. Magn. Magn. Mater., 321 (2009) 2035 [21] J. Chandradass and K. H. Kim, J. Alloys Compd., 509 (2011) L59 [22] A. T. Raghavender Ph.D thesis, S. R. T. M. University, (2000) [23] Hariharan Shrikant, James Gass Rev. Adv. Mat. Sci., 10 (2005) 398 [24] M. Kinoshita, J. Alloy Compd., 365 (2004) 281 [25] S. C. Watawe, U. A. Bamane, S. P. Gonbare, R. B. Tangsali, Mater. Chem. Phys., 103 (2007) 323 [26] J. Azadmanjiri, H. K. Salehani, M. R. Barati, F. Farzan, Mater. Lett., 61 (2007) 84 [27] B K Vijaya Kumar, D. Ravinder, Mater. Lett., 52 (2002) 166 [28] A. A. Goldman, Modern Ferrite Technology Springer US, (2006) 375 [29] Yazhou Wang, Hongqing Zhou, Hongqing Qi, Luchao Ren, Zhiming Xu, Zhenxing Yue, Ceram. Int., 41 (2015) 12253 [30] A Zdinarsic, M Lempel and M Drogenik, IEEE Trans. Magn. 31 (1995) 950 [31] Li Lezhong, Lan Zhongwen, Yu Zhong, Sun Ke, Luo Ming, Xu Zhiyong, Ji Haining, J. Magn. Magn. Mater. 321 (2009) 438 [32] Sun Ke, J Wang, Y Yang, Y Li, Z Yu, Z Lan, X Jiang, R Guo, C Wu, Phys. B: Cond. Matt., 476 (2015) 122 [33] S. F. Wang, Y. R. Wang, T. C. K. Wang, C. F. Chen, C. A. Lu, C. Y. Huang, J. Magn. Magn. Mater., 220 (2000) 129 [34] Jaill Jeong, Young Ho Han, Mater. In elect., 15 (2004) 303 [35] N. Chu, X. Wang, Y. Liu, H. jin, Q. Wu, L. Li, Z. Wang, H. Ge, J. Alloys compds., 470 (2009) 438 [36] R. Rathi, R. Neogi, Mater. Today; proced., 3 (2016) 2437 [37] Yan Yang, Jie Li, Huaiwi Zhang, Gang Wang, Yiheng Rao, Gongwen Gan, J. Magn. Magn. Mater., 487 (2019) 165318 [38] S. F. Wang, Y. R. Wang, T. C. K. Wang, P. J. Wang, C. A. Lu, J. Magn. Magn. Mater., 217 (2000) 35 [39] S. C. Muzumdar, F. Alam, U. H. Tanni, K. Kali, B. C. Das, M. N. Khan, J. Mater. Sci. and Applns., 10 (2019) 733 [40] B. M. Ali, M. A. Siddig, Y. A. Al Sabah, Abdelrahman A. Elbadawi 1, Abdalrawf I. Ahmed, J. Adv. in Nanoparticles, 7 (2018) 1

Chapter 1 14 A.D.Patil Ph.D. Thesis Introduction to Ferrites [41] M.S. Patil, M. N. Sarnaik, V.D. Murumkar, A. A. Pandit, Inter. J. Inov. Sci., Eng. and technol., 4 (2017) 91 [42] A. Bhaskar, S. R. Murthy, Indian J. Phys., 88 (2014) 151 [43] Shuoqing Yan, Sheng Liu, Longhui He, Jun He, Shengxiang Huang, Lianwen Deng, J. Mater. Res. Exp., (2019) [44] K. Praveena, K. Sadhana, S. Srinath, S. R. Murthy, J. Phys. Chem. Solids, 74 (2013) 1329 [45] Barbara Pacakova, Simona Kubickova, Alice Reznickova, Daniel Niznansky and Jana Vejpravova, Spinel Ferrite Nanoparticles: Correlation of Structure and Magnetism, Magnetic Spinel - Synthesis, Properties and Applications, Mohindar Singh Seehra, Intech. Open, (2017)

Chapter 2 15 A. D. Patil Ph.D. Thesis Chapter 2 Crystal Structure and properties of ferrites 2.1 Crystal Structure of ferrite There are different kinds of ferrite material, out of them spinel ferrite is the imperative class of magnetic materials since they have outstanding magnetic and electrical properties. Mainly, spinel ferrites are illustrated by formula MFe_2O_4 where M corresponds to divalent cations. Spinel ferrite having closed packed cubic crystal structure was initially explained by Bragg [1] and Nishikawa [2]. The crystal structure of spinel is decided mostly from oxygen ions lattice. In such formulations, as compare to metallic ions radii, oxygen ions radii are quite greater. Therefore crystal structure can be considered to be formed by close packed layer of oxygen atoms, with the metal ions acquire interstitial position such as octahedral (B) and tetrahedral (A) sites. The octahedral and tetrahedral sites are surrounded by six and four oxygen ions which are located at corners of octahedron and tetrahedron respectively. The unit cell has 96 interstitial sites (32 octahedral sites and 64 tetrahedral sites), out of 96 interstitial sites, metal cations occupies at 16 octahedral and at 8 tetrahedral sites. According to Neel [3], magnetic oxides exhibit ferromagnetic nature. The spinel ferrite arrogate $O_h^7 (Fd\bar{3}m)$ cubic space group [4]. Figure1 depicts the spinel ferrites crystal structure with the oxygen ions are represented by white circles whereas metal ions are represented by the black and hatched circles.

Chapter 2 16 A. D. Patil Ph.D. Thesis Fig.2.1: Schematic of spinel structure unit cell showing tetrahedral and octahedral sites As per the distribution of metal cations between octahedral [B] and tetrahedral (A) sites [5], there are three types of spinel ferrites. 1. Normal Spinel 2. Inverse Spinel 3. Random Spinel 2.1.1 Normal spinel In normal spinel ferrite type, at tetrahedral A sites all the divalent metal ions are occupied while at octahedral B sites all the trivalent ions are occupied. The inversion parameter in these spinels is zero. The tendency to form normal spinel nature primarily comes from crystal field stabilization energy. The distribution of cations in normal spinel ferrite is given by formula $[M^{2+}]_A [Fe^{3+}]_B O_4$ e.g. Zinc ferrite and Cadmium ferrite

Chapter 2 17 A. D. Patil Ph.D. Thesis 2.1.2 Inverse Spinel In inverse spinel ferrite type, there is equal distribution of trivalent ions between octahedral and tetrahedral sites while at the octahedral sites divalent ions are occupied. The inversion parameter in these spinels has the value „one“. The formula for distribution of cations in an inverse spinel is represented as $[Fe^{3+}]_A [M^{2+}]_B O_4$ e.g. $CoFe_2O_4$, Fe_3O_4 and $NiFe_2O_4$ 2.1.3 Random Spinel The random spinel ferrite type have random distribution of trivalent ions as well as divalent metal ions at octahedral [B] site and tetrahedral (A) sites. The inversion parameter in these spinels has the value „2/3“. The distribution of cations is given as $(M^{3+})_A [M^{2+}]_B O_4$ e.g. $MgFe_2O_4$, $CuFe_2O_4$. 2.2 Magnetic Properties The magnetization is a dominant tool for study of the various factors such as magnetic hardness or softness of material, magnetic ordering, domain wall rotation, anisotropy etc. The properties of ferrites and ferromagnetic materials are similar in various aspects. In ferromagnetic material, variation in magnetization from zero to saturation value is due to application of magnetic field and such performance can be explained by Weiss [6] on the basis of the concept of existence of domains. According to Weiss, material consists of small regions, called as domain. There exists random orientation of all the domains and hence material has zero net magnetic moment. When magnetic field is applied to such a material, all the domains are magnetized towards the applied field. Magnetization varies from one domain to other domain. Therefore net magnetic moment of material is nothing but addition of magnetic moments of all the domains and hence magnetization values lies in between zero to saturation.

Chapter 2 18 A. D. Patil Ph.D. Thesis The study of magnetic hysteresis phenomena of ferrites gives us information regarding remanence ratio (M_r / M_s), coercive force (H_C), saturation magnetization (M_s), and permeability. The ferrite materials are categorized into two types as soft and hard ferrites depending upon values of these magnetic factors. This classification depends on the magnetic behavior of the material and has no relevance with the physical properties of the material. Soft ferrites have small coercive force, high magnetic permeability, low remanent magnetization and low hysteresis losses therefore these ferrites are easily magnetized and demagnetized, while the hard ferrites have high hysteresis energy losses, high remanence, high saturation flux density as well as high coercivity. Hard ferrites are difficult to magnetize/demagnetize and are employed in the permanent magnet. The ferrite materials have a particular temperature termed as Curie temperature (T_c) above which spins are randomly oriented destroying spontaneous magnetization and material becomes paramagnetic. The permeability achieves maximum value just below Curie temperature and above which the permeability disappears sharply. Further, ferrites magnetic properties can be divided into two groups as structure sensitive and intrinsic. Hysteresis and permeability structure sensitive whereas anisotropy, magnetostriction, Curie temperature and Saturation magnetization are the intrinsic properties [7, 11] 2.2.1 Magnetic Ordering and Interactions The metal ions are located at the tetrahedral (A) as well as octahedral [B] sites in ferrite. There are three categories of the magnetic interactions among the metal ions occupied at the tetrahedral (A) as well as octahedral [B] sites, through the intermediate magnetically neutral O^{2-} ions by super exchange mechanism such as A-B interaction, A-A interaction and B-B interaction. During these interactions an anti-parallel orientation of spins are induced since

interaction energies are negative which was proved experimentally. Generally extent of the interaction energy among the magnetic ion, Me I and Me II depends upon- i) the distances between magnetic ions and oxygen ion ii) an angle θ between Me I - O - Me II as represented in figure 2.2. The exchange energy should be maximum for the angle 180° and there is a rapid decrement in energy with enhancement in distances. Gorter [8] predicted the different probable configurations of

Chapter 2 19 A. D. Patil Ph.D. Thesis the ions pairs in spinel ferrites with favorable distances and angle for which magnetic interaction is effective as shown in figure 2.2. Fig.2.2: Angle θ between Me I and Me II with oxygen ion The theory developed on the basis of sub-lattice interaction depending upon the angles and distances, Neel [3] suitably explained magnetic saturation data calculated and the magnetic susceptibility values observed experimentally for ferrites. The spinel ferrite material with various configurations of the ion pairs with possibly various distances and angles primarily decide the effective magnetic interactions. Depending on the values of the angle θ and the distance, it may be considered that, A-B interaction has maximum magnitude as compare to A-A and B-B interactions. For A-B interaction, there are two configurations having relatively high values of angle θ and small distances (p,q and q,r).The B-B interaction have also two configurations but only first is effective because in other configuration, for effective interaction distance, "s" is very much large. In case of A- A interaction the angle $\theta = 180^\circ$ and distance r is quite large and hence it is weakest interaction [9]. The most significant interaction is A-B interaction and two sublattices A and B are oppositely magnetized making the net magnetic moment nothing but difference between magnetic moments at two sub lattice A and B. Usually, saturation magnetic moment value at A lattice (M_A)

is smaller than that of the B lattice (M_B). Therefore net saturation magnetization (M_s) is represented as $M_s = |M_B - M_A|$

Chapter 2 20 A. D. Patil Ph.D. Thesis A-B interaction B-B interaction A-A interaction $\theta = 126^\circ \theta = 154^\circ \theta = 90^\circ \theta = 125^\circ \theta = 79^\circ$
 Fig.2.3: Configuration of ion pairs in spinel ferrites with favorable distance and angles for effective magnetic interaction.
 2.2.2 Soft and Hard ferrites 2.2.2.1 Soft ferrites The soft ferrite materials do not retain significant values of magnetization and possess low value of coercive force. A low coercive force value means there was easy movement of domain walls under the influence of magnetic field which changes in direction or magnitude. Soft ferrite materials are those which can be easily magnetized and demagnetized without loss of much energy. Further, soft ferrites possess low values of saturation magnetization and permeability. The soft ferrite materials have relatively very small losses at greater frequencies and hence they are widely employed in the cores of inductors and radio frequency (RF) transformers. Nickel-zinc ferrite (Ni-Zn) and Manganese-zinc ferrite (Mn-Zn) are most frequently used soft ferrites. Ni-Zn ferrite possess maximum resistivity than Mn-Zn ferrite so they are most appropriate above 1 MHz frequencies. Mn-Zn ferrites exhibit higher saturation magnetization and permeability than the Ni-Zn ferrites.

Chapter 2 21 A. D. Patil Ph.D. Thesis 2.2.2 Hard ferrites The ferrite materials which essentially retain the magnetization and possess high resistance to demagnetization are termed as hard ferrites. For the fabrication of permanent magnets hard ferrites are employed. After magnetization they acquire high remanence and coercivity. For the synthesis of hard ferrites strontium or barium carbonate and iron oxides are used. Also they possess high value of magnetic permeability therefore they are known as ceramic magnets and are cheap. Hard ferrites have wide applications in household products such as electrical motors, loudspeakers, refrigerator magnets, magnets in radios. They have greater hysteresis energy losses. Barium and Strontium ferrite are usually used hard ferrite material for permanent magnet applications while Cobalt ferrite employed in some media for magnetic recording. 2.3 Transport properties 2.3.1 Resistivity The ferrite material possesses better electric properties with high resistivity and wide range of frequency applications. Resistivity is most significant property of any material under consideration for applications and it depends on temperature. In general, the resistivity increases with increment in temperature in case of metals and decreases in case of insulators and semiconductors. The decrement in resistivity of ferrite with rise in temperature reveals the fact that ferrites are semiconductor in behavior and room temperature resistivity varies from 10^{-3} to 10^{11} ohm-cm [10]. The parameters such as amount of doping, sintering condition, distribution of cations among A and B sites, preparation method and grain size influences the electrical properties of ferrites. The electrical conductivity of spinel ferrites is smaller than other magnetic materials and hence they are employed at microwave frequency applications. In ferrite material, the conductivity is due to existence of Fe^{2+} to Fe^{3+} ions which are located at octahedral

Chapter 2 22 A. D. Patil Ph.D. Thesis site. The occurrence of Fe^{2+} and Fe^{3+} ions results in n-type and p-type behavior respectively [11,12]. The variation in resistivity behavior in ferrite was explained on the basis of Verwey hopping mechanism [13]. According to this empirical model, the jumping of electrons among Fe^{2+} and Fe^{3+} ions which are situated at octahedral sites causes the conductivity mechanism [14] and resistivity is temperature sensitive. Dependence of resistivity on temperature is represented by the expression $\rho = \rho_0 \exp(\frac{E}{kT})$ Where T is absolute temperature, k is Boltzmann constant and E is

the activation energy. Generally, conduction in ferrites is described with the help of hopping mechanism as below [15]. $Fe^{2+} + Fe^{3+} \rightleftharpoons Fe^{3+} + Fe^{2+} + ?E$ Where, $?E$ is the activation energy, necessary for conduction of electron from Fe^{2+} to Fe^{3+} and vice versa. Electrical properties of ferrites were explained with various models such as the „small polaron“ model which is based on the phonon induced tunneling and hopping of electron. 2.3.2 Dielectric constant Spinel ferrite covers extensive range of applications in microwave and radio frequencies. Ferrites have low conductivity, which means that they are useful at microwave applications. Dielectric properties of ferrites depend on various factors such as grain structure or size, chemical composition and preparation method [16]. Polycrystalline ferrites possess high value of dielectric constant at low frequencies. The AC resistivity values follow the trend of DC resistivity, reducing with rise in temperature, while dielectric constant enhances with increment in temperature. Number of researchers worked on low frequency dielectric performance of ferrites. To name a few, are Moltgen [17], Rezlescu [18,19], Iwauchi et al. [20], Josyolu [21], and Koops [22]. The

Chapter 2 23 A. D. Patil Ph.D. Thesis mechanism of dielectric polarization process in ferrite resembles to that of conduction process [23]. Koops [22] proposed a phenomenological theory of dispersion in which dielectric structure is composed of two layers, specifically non conducting grain boundaries and good conducting grains as discussed by Maxwell-Wagner [24,25]. Grains having high conductivity are formed during the process of preparation of ferrite whereas insulating grain boundaries are formed during the process of sintering. At lower frequencies insulating grain boundaries are more active while the conducting grains are found to be more active at higher frequencies. Due to applied electric field, movement of electrons among Fe^{+2} and Fe^{+3} ions at B site takes place which is termed as hopping mechanism of transfer of electrons. Therefore at the grain boundaries electrons are pile up and polarization is produced. At higher frequency beyond particular frequency of applied electric field, jumping of electrons among Fe^{+2} and Fe^{+3} cannot follow applied field and hence polarization reduced. Thus in case of polycrystalline ferrites size of grains in the composition is related to dielectric constant.

Chapter 2 24 A. D. Patil Ph.D. Thesis References [1] W. H. Bragg, Phil. Mag. ,30 (1915) 305 [2] S. Nishikawa, Proc. Tokyo Math. Phys. Soc.,8(1915) 199 [3] L. Neel, Ann. Phys.,3(1948) 137 [4] R. W. G. Wyckoff, Crystal structures, Interscience, New York, 1 and 2(1963) [5] M. K. Shobana, V. Rajendran, M. Jeyasubramanian, N. S. Kumar. Mater. Lett.,612 (2007) 2616 [6] P. Weiss, J. Phys., 6 (1907) 667 [7] C. Beatrice, F. Filorillo, F. J. Landgraf, V. Lazaro-Colan, S. Janasi and J. Leicht, J. Magn. Mater. ,320 (2008) 865 [8] E. W. Gorter, Phillips Res. Rept. ,9 (1954) 321 [9] B. Vishwanathan and V.R.K. Murthy, Ferrite Material Science and Technology Narosa Publishing House, New Delhi, (1990) [10] M. S. Vijaya, G. Rangarajan, "Materials Science", McGraw-Hill Publishing Company Limited, New Delhi, (1999-2000) [11] S.L. Snoek, "New Development in ferromagnetic material" Elsevier publishing co. New York, Amsterdam ,(1947) [12] F.J. Morin, Phys. Rev. ,93 (1954) 1195 [13] D. Elwell, B. A. Griffiths and R. Parker, Brit. J. Appl. Phys. ,17(1966) 249 [14] E. J. W. Verwey, P. W. Haaijman and F. R. Romeyn, G. W. Van.Oostehout J. Phil. Res. Rep. ,5(1950) 173 [15] G. H. Jonker, J. Phys. Chem. Solids, 9 (1959)165 [16] S.

E. Shirsath, B. G. Toksha, M. L. Mane, V. N. Dhage, D. R. Shengule, K. M. Jadhav,

Powder Technology, 212 (2011) 218 [17] S.

Moltgen, Zh. Fur. Ang. J. Phys. ,4(1952) 216 [18] N. Rezlescu and E. Rezlescu, J. Phys. Stat. Sol (a), 23(1974) 575

Chapter 2 25 A. D. Patil Ph.D. Thesis [19] N. Rezlescu, E. Cucioreanu and V. Petrescu, J. Rev. Mod. Phys. ,15(1970) 965 [20] K. Iwauchi, J. Jap. Appl. Phys. ,10(1971)1520-46 [21] O. S. Josyulu and J. Sobhanadri, J. Phys. Stat. Sol. (a), 36K (1976) 133 [22] C. G. Koop, Phys. Rev., 83(1951) 121 [23] L. I. Rabkin and Z. I. Novikova, Ferrites IZS Acad. Nauk Mink, (1960) 146 [24] J.C. Maxwell, A Treatise on

Electricity and Magnetism, Oxford University Press. New York, 1(1973)828 [25] K.W. Wagner,

Zur Theories der Unvollkommenen Dielektrika. Annalen der Physik, 40(1913)817

Chapter 3 26 A.D. Patil Ph.D. Thesis Chapter 3 Synthesis and Characterization of ferrite material 3.1 Preparation Method The ferrite material with iron oxide framework are relatively easy, involves lesser processing steps and cheap to synthesize. The family of ferrites is stable under a wide range of conditions and some family members' exhibit low toxicity and no concerns for living organisms. Preparation of material is the most critical step in fabricating novel materials with varying properties. There are various methods for the production of various materials being explored and practiced. The selection of synthesis method mainly depends on the question that whether the produced material is yielding well-dispersed particles having uniform size and better crystallinity. The availability of choice of tuning the structure and properties of the materials by simple modification of the conditions is also highly desirable. Among different methods sol gel method is

most convenient method. This method is used in an extensive variety of fields of materials science to produce nano particles of metal oxides. It is a wet chemical route and multistep process which involves both physical and chemical processes. This synthesis process could produce the tiny materials since highly homogeneous starting materials or the nitrates are employed for the preparation of materials. The main advantages of the sol gel method are- 1. The process involves cheap and easy steps to produce metal oxides 2. It requires low temperature

Chapter 3 27 A.D.Patil Ph.D. Thesis 3. Good homogeneity and high-purity products are obtained 4. Also, it is capable of obtaining small sized particles, and uniform powder Flow chart for the steps involved in sol gel process is represented in figure 3.1. Fig.3.1: Flow chart displays the steps of sol-gel method. Weighing the High Purity Nitrates in Stiochiometric Ratio Dissolve Nitrates in Double Distilled Water. water Add Citric Acid in Molar Ratio with Metal Nitrates (3:1) Add Drop Wise Liquid Ammonia in the Solution to Maintain pH Constant Stirring on Hot Plate At Temperature 80°C Dry gel formation overnight at 100°C Grind the Powder and Perform Calcination at Suitable Temperature Compact By Using Hydraulic Press and Then Sintered

Chapter 3 28 A.D.Patil Ph.D. Thesis 3.2 Characterization Techniques In present study to obtain various properties of ferrites, various characterization techniques are used, some of which gives information about physical and chemical properties and others about morphology and structure. The various characterization techniques selected in the present work are as below: (1)

X-rays diffraction (2)

Scanning Electron Microscope (SEM) (3) Energy Dispersive Spectroscopy (EDX) (4) Infrared spectroscopy (IR) (5) Raman Spectroscopy (6) Vibrating Sample Magnetometer (VSM) (7)

LCR Meter 3.2.1 X-ray Diffraction

Now a day, X-ray diffraction is a usual technique for the study of samples in the bulk, powder and thin film form. From this technique, we can get the information concerning the crystallite size, lattice constant, phase analysis and crystalline nature of the selected sample material [1, 2]. X-rays are electromagnetic radiation having wavelengths in between 0.01 to 10 nanometers employed in diffraction. X-rays are produced by the reducing speed of fast moving electrons hitting the metal target which gives rise to broad continuous spectrum and X-rays are named as 'bremsstrahlung' or breaking of radiation. If the incident electrons have high energy they eject an electron from inner shell of the target atom, then the vacancy is created which is filled by jumping of electrons from higher shell to lower shell and emits X-rays known as characteristic X-rays [3]. The Bragg's law illustrates a correlation between X-rays wavelength, inter-planar spacing of the crystal plane and the diffraction angles (Bragg angle). According to the

Chapter 3 29 A.D.Patil Ph.D. Thesis Bragg, the X-rays are reflected from a series of crystallographic planes as revealed in Figure 3.2. Fig.3.2: Illustration of Bragg's law for crystal The path difference between the two waves travelled through the adjacent crystallographic planes is investigated by the inter-planar spacing. If the path difference between the two waves is equal to $n\lambda$ (n is an integer), the constructive interference will take place and diffraction peaks were observed which gives a spectrum known as X-ray diffraction spectrum or pattern. The Bragg's law can be represented by equation – $2d \sin \theta = n\lambda$ (1) Here ' λ ' is the wavelength of the radiations used, ' d ' is the distance between two adjacent lattice planes, ' θ ' is angle of diffraction and ' n ' is an integer. Furthermore, this technique is employed to obtain the average crystallite size of the synthesized nanocrystalline materials. Generally, in case of nano materials a peak broadening is observed and is used to determine average crystallite size of the particles in material. The crystallite size in the prepared ferrite material was estimated from the Debye Scherrer's equation [4] $D = \frac{0.9 \lambda}{\beta \cos \theta}$ (2) Where θ is the Bragg's angle, β is the full-width half-maximum (FWHM), and λ is the wavelength of X-rays. The values of lattice constant can be investigated by using relation

Chapter 3 30 A.D.Patil Ph.D. Thesis $\frac{1}{d^2} = \frac{h^2}{a^2} + \frac{k^2}{b^2} + \frac{l^2}{c^2}$ (3) Where, hkl d is the inter-planar distance and (h, k, l) are the Miller indices of planes 3.2.2

Field Emission Scanning Electron Microscopy (FE-SEM) Scanning electron microscopy (

SEM) is a prominent and multipurpose tool for characterization of materials which is able to get a high-quality complete profile of the sample under consideration [5]. Scanning electron microscope (SEM) is an electron microscope and image is acquired by scanning the converged electron probe across surface of the sample in a raster scan pattern. The electrons after traversing the vacuum chamber interact with the sample and generate different types of signal which includes back scattered electrons (BSE), transmitted electrons and sample current, secondary electrons and characteristic X-rays. These signals are utilized to get information regarding morphology, composition, orientation of grains, crystallographic

information, topography, chemistry etc. of a material. These various signals are collected by detectors and with the help of computer processed image is investigated for further analysis. The most commonly used signal to form image in SEM is secondary electron emission signal generated by interaction of electron beam with the sample which have small amount of energy about 3-5eV and hence provide topographic information with fine resolution. One more important method of obtaining image in SEM is with the help of finding of back scattered electrons (BSE) which gives topographic and compositional information of the sample. Further Characteristic X-rays are produced from the interaction of electron beam with the sample. When an inner shell electron is ejected by collision with incident electron, vacancy is formed which is filled by falling of electrons from higher shell to lower shell and emits X-rays known as characteristic X-rays. The characteristic X-rays are employed to receive the chemical and elemental information in the sample. The experimental arrangement of Scanning electron microscopy is depicted in figure 3.3. In the present work, the JEO JSM 6360 Field Emission Scanning Electron Microscope is employed for microstructure analysis of the fabricated samples.

Chapter 3 31 A.D.Patil Ph.D. Thesis Fig.3.3: Scanning electron microscope (SEM) diagram 3.2.3 Energy Dispersive X-ray Spectroscopy: Energy dispersive X-ray spectroscopy (EDX) is a chemical nondestructive technique used along with scanning electron microscopy (SEM). Analysis of constituent elements of material or specimen was done by using energy dispersive X-ray spectroscopy [6]. When an electron beam is incident on sample, X-rays are emitted which are detected by EDX techniques. As electrons are incident on the sample, electrons knock out from the atoms of the sample surface and vacancies are created. These vacancies are filled by jumping of electrons from higher state and the X-rays are emitted having energy equal to energy difference between the lower energy state and the higher-energy state. The energy of x rays and number of x rays released from the sample are analyzed by an EDX-detector to obtain constituent elements of the sample and hence to measure percentage of elements .

Chapter 3 32 A.D.Patil Ph.D. Thesis 3.2.4 Fourier Transform Infrared Spectroscopy (IR) Fourier transform infrared spectroscopy (IR) is most extensive spectroscopic technique which is used in the field of organic and inorganic materials studies owing to its knack in investigating and identifying the structures of compounds. In FTIR, a beam of infrared part of electromagnetic spectrum is selected. After passing through an interferometer and then through the sample directly a signal is formed, called an 'interferogram' then a spectrum can be obtained by performing a Fourier transform on the interferogram. The diagram of FTIR is shown in figure 3.4. Fig.3.4: Schematic representation of FTIR In present study, Fourier transform infrared spectra of all the samples in KBr medium were obtained between 3500-1000 cm^{-1} at room temperature on Jasco model 310 spectrophotometer. From Waldron [7] analysis the force constant values of ions at tetrahedral (F_t) and octahedral sites (F_0) were calculated. With help of Gorter [8] formula, bond lengths R_B and R_A for octahedral [B] and tetrahedral (A) sites in a cubic crystal were investigated from IR spectra. 3.2.5 Raman Spectroscopy Raman spectroscopy is most significant scattering technique which is based on Raman Effect. Raman Effect was first discovered by Indian scientist C. V. Raman in 1928. Raman Effect - when monochromatic rays are incident on the material, they interact with the molecules of the material and gets scattered in all directions. The

Chapter 3 33 A.D.Patil Ph.D. Thesis scattering process can be divided depending upon the difference in frequency of incident and scattered rays. If the incident rays and scattered rays have same frequency, the scattering process is called Rayleigh scattering and if scattered rays have different frequency from that of incident one, such scattering process is known as Raman scattering. Further, the frequency of scattered rays is either greater or lower than the frequency of the incident rays depends upon special scattering process. The energy of incident rays (photon) is ' $h\nu$ '. If the scattered light radiations have energy equal to $h\nu - \Delta E$ then this scattering process is termed Stokes Raman Scattering. In Stokes Raman scattering ΔE amount of energy is used by the molecule or material system in order to get transitions among rotational or vibrational energy levels in the system. On the other hand if the scattered light radiations will have the energy equal to $h\nu + \Delta E$ then this type of scattering is called as Anti-stokes Raman scattering. Hence rays scattered with greater frequency than that of incident rays frequency are known as anti-stokes' radiations whereas rays scattered with low frequency are called as Stokes radiations [9-11]. Figure 3.5 represents energy level diagram and energy transitions for Infrared, Rayleigh, Stokes and Anti-Stokes Raman scattering. Fig.3.5: Energy level diagram for Raman scattering; (a) Stokes Raman scattering (b) anti-Stokes Raman scattering The Raman Spectrometer consists of monochromatic source (Laser) of light. The radiations from the laser source are incident on the sample and gets scattered. These scattered radiations are directed towards the lens and passed into a grating monochromator. CCD camera or photomultiplier tube measures the signal further it is

Chapter 3 34 A.D.Patil Ph.D. Thesis analyzed by a computer and it provides the Raman spectra. Figure 3.6 reveals the diagram of a Raman spectrometer. Fig. 3.6: Schematic diagram of Raman Spectrometer 3.2.6 Ultraviolet Visible Diffuse Reflectance Spectroscopy (UV- Vis.DRS) Diffused reflectance spectroscopy is a widespread technique in which reflection of light in near-infrared (NIR), visible (VIS) and ultraviolet (UV) region takes place by sample in powder or in crystalline form and if the sample is in liquid state then UV- visible spectroscopy method were employed. Diffuse reflectance

spectroscopy is much related to UV-visible spectroscopy because in these methods visible light is utilized for excitation of valence electrons to vacant orbital's inside the sample. The simple difference is that in diffused reflectance spectroscopy, variation in amount of reflected light from the sample surface is considered while in UV-visible spectroscopy transmitted light is measured after passing through solution. In addition, to trace absorption spectra of the sample dispersion medium is essential in UV-Vis spectroscopy whereas in DRS it is not necessary to record spectra. Along with the UV-visible instrument an integrated sphere is organized for measurement of diffused reflectance spectra. An integrated sphere is layered by white standard and is made to receive reflected light by the sample and the standard. The suitable selection of coating material for the integration sphere and

Chapter 3 35 A.D.Patil Ph.D. Thesis reference standard is also important in DRS measurement [12]. The figure 3.7 shows diffuse reflectance spectrophotometer with integrated spheres. Fig. 3.7: Schematic diagram of diffuse reflectance spectroscopy. In present study UV-visible diffuse reflectance spectra of the sample were done on UV-Vis. DRS Jasco spectrophotometer Model V-670. 3.2.7 Vibrating Sample Magnetometer (VSM) The working of vibrating sample magnetometer (VSM) is based on Faraday's law of electromagnetic induction. This device is employed to study magnetic properties of various materials. In 1959, Simon Foner designed the first Vibrating sample Magnetometer in laboratories of Lincoln [13]. In the VSM the sample under investigation is placed in constant magnetic field which is produced in between the poles of electromagnet. Due to this constant magnetic field, sample will be magnetized by aligning dipole moment in the direction of field. If the applied constant field is stronger, then the magnetization will be larger. The dipole moment of the studied sample will produce magnetic field around the sample which is known as magnetic stray field. At the same time sample is kept under sinusoidal vibrations, and in the set of stationary pick-up coils an electrical signal is induced which is related to magnetic moment of the sample. The magnetic moment of the sample depends upon induced current. If the induced current will greater then magnetic moment will also higher. Figure 3.8 displays the diagram of VSM. In the present study, magnetic properties of prepared samples were done on vibrating sample magnetometer (VSM) (Quantum Design PPMS-VSM) at 2K and room temperature.

Chapter 3 36 A.D.Patil Ph.D. Thesis Fig. 3.8: Schematic system overview of VSM

The relationship between induced magnetic flux density (B) and magnetizing force (H)

can be illustrated from hysteresis curve which is considered as M-H or B-H loop. Figure 3.9 shows hysteresis loop for spinel ferrite which gives information about magnetic properties of ferrites such as remanence magnetization (M_r), coercivity (H_c), magnetization (M_s) etc. Fig. 3.9: Hysteresis curve for a spinel ferrite.

Chapter 3 37 A.D.Patil Ph.D. Thesis 3.2.8 DC Resistivity Four probe and two probe methods are two well – known methods employed for the determination of the DC resistivity of samples [14]. Electrical properties such as activation energy and DC resistivity of the samples were studied by two probe method. This method is very simple as compare to four probe method. The DC resistivity of the ferrite samples with variation in temperature was investigated by two probe method. The samples in the form of cylindrical pellets were polished and for fine ohmic contact silver coating were applied on both the surfaces. The sample is fixed in a sample holder and the sample holder is kept in temperature controlled muffle furnace. With the help of a stabilized power supply unit 3V constant voltage is supplied and the current corresponding to the variation in temperature is measured in a digital nano /micro ammeter. The figure 3.10 represents diagram of two probe method. The DC resistivity of the samples were obtained from the equation $\rho = R \times A / t$ (4) Where t is the thickness of the sample, A is cross-sectional area of the sample, ρ is the resistivity and R is the resistance of the sample. The graphs of $\log \rho$ versus $1000/T$ were plotted and the activation energy of the samples were investigated from the relation, $\rho = \rho_0 \exp(-E/KT)$ (5) Where, K is Boltzmann constant, ρ is the resistivity of the sample, T is absolute temperature, ρ_0 is constant and E is activation energy

Chapter 3 38 A.D.Patil Ph.D. Thesis Fig. 3.10: Diagram of DC resistivity measurement method 3.2.9 Dielectric Properties LCR meter were used to measure the inductance, resistance, impedance, loss factor, capacitance etc. of the materials. The LCR-Q meter Hioki (3250) was used to compute

dielectric constant (ϵ'), loss tangent ($\tan \delta$) and AC conductivity as a function of frequency

in

the range 50 Hz

to 5 MHz

at room temperature.

The

synthesized pellets form a parallel plate capacitor by using silver coating on either side to make good ohmic contacts and dielectric material as a ferrite material for measurement of ac impedance and dielectric. 3.2.9.1 Dielectric Constant: The dielectric constant (ϵ') was obtained from the equation $\epsilon' = C \times d / \epsilon_0 \times A$ (6) Where, A is area

of the pellet, ϵ_0 is the permittivity of the free space,

d is thickness of pellet and C is capacitance of the material.

Chapter 3 39 A.D.Patil Ph.D. Thesis 3.2.9.2 Dielectric Loss tangent ($\tan \delta$) There is loss of energy in a dielectric material in a changeable electric field is considered as dielectric loss. As soon as the polarization lags behind the applied electric field, the dielectric loss occurs and is because of imperfections and impurities in the crystal lattice. The dielectric loss tangent were computed from the equation $\tan \delta = \epsilon'' / \epsilon'$. (7) 3.2.9.3 AC conductivity AC conductivity represents the capacity of material to conduct electric current. Across a conductor if potential difference is applied then movable charges flow through the conductor which gives an electric current. The reciprocal of electrical resistivity is the conductivity. Further, depending of electrical conductivity the materials are divided into metals, semiconductors and insulators. Metals have high conductivity and hence are good conductors while the semiconductors are in-between metals and insulators whereas insulators are bad conductors. The sum of dc conductivity and ac conductivity of any material is nothing but total conductivity and represented by relation $\zeta_{tot}(\omega) = \zeta_{dc} + \zeta_{ac}(\omega)$ (8) Where, $\zeta_{ac}(\omega)$ is the ac conductivity, ζ_{dc} is the dc conductivity and $\zeta_{tot}(\omega)$ is the total conductivity. The relation to obtain the values of ac electrical conductivity ζ_{ac} was given as $\zeta_{ac} = 2\pi f \tan \delta \epsilon' \epsilon_0$ (9)

Chapter 3 40 A.D.Patil Ph.D. Thesis References [1] A. Michel. Van Hove, Surface physics of materials, Academic Press, New York, (1975) [2] D. Liu, Q. Wang, H.L.M. Chang, H. Chen, J. Mater. Res. 10 (1995) 1516 [3] B. D. Cullity, Elements of X – ray diffraction, Reading, Mass Addison– Wesley Pub.Co. ,(1956) [4] C. Kittel, Introduction to Solid State Physics, John Wiley and Sons (Asia), Singapore, (1996) [5] J.I. Goldstein, D.E. Newbury, P. Echlin, D. C. Joy, C. Fiori, E. Lifshin, Scanning Electron Microscopy and X-ray Microanalysis, Plenum Press, New York, (1981) [6] W. Zhou and Z. L. Wang, Scanning Microscopy for nanotechnology: Technique and Application, Springer,(2006) 31 [7] R.D.Waldron, Phys. Rev., 99 (1955) 1727 [8] E.W. Gorter, Philips Res. Rep., 9 (1954) 295 [9] D. A. Long, Raman Scattering, Mcgraw Hill Book Company, New York,(1977) [10] A. R. Barron, Surface-Enhanced Raman Spectroscopy for the Study of Surface Chemistry, (2010) [11] A.Z. Zymanski, Raman Spectroscopy Theory and Practice, Plenum Press, New York, (1970) [12] J.D. Han, S.I. Woo, Korean J. Chem. Eng., 8 (1991) 235 [13] S. Foner, Rev. Sci. Inst., 30 (1959) 548 [14] S. M. Sze, Physics of Semiconductor Devices, 2 nd edition, John Wiley and Sons,(1981) 30

Chapter 4 41 A. D. Patil Ph.D. Thesis Chapter 4 Result and Discussion on Ni_{0.4} Cu_{0.3} Zn_{0.3} Fe₂ O₄ +xTa₂ O₅ (X=0-10 wt.%) 4.1.

Introduction

The study of spinel ferrite is of great importance from both fundamental and

technological point of view because of their excellent structural, electrical and magnetic properties. There are different types of spinel ferrites among them NiCuZn ferrite is a unique spinel ferrite possessing high permeability and high electrical resistivity [1, 2]. Therefore, NiCuZn ferrite is considered as one of the most interesting soft magnetic materials for high frequency applications. However, preparation of these NiCuZn ferrites at low temperature with high bulk density is vitally important for their practical application. The properties of ferrites are depend upon various factors such as method of preparation, pH value, sintering temperature, amount and type of substitution, and most important being the distribution of metal cations at the tetrahedral and octahedral sites in the spinel lattice [3, 4]. It is known that, introduction of a relatively small amount of additive such as CaO, ZrO₂, Ta₂ O₅ Na₂ O, V₂ O₅, and Bi₂ O₃ can brought an important modification in structural and electro-magnetic properties of ferrites [5–7]. N Rezlescu et al. [8] reported that Na₂ O and CaO increase the sintering density and electrical resistivity whereas ZrO₂ increases permeability of Ni-Zn ferrite. Jun Xiang et al [9] studied NiCuZn ferrite and observed variation in the magnetic properties at room temperature and at 77 K. Yazhou Wang et al [10] studied Nb₂ O₅ and MoO₃ additives effect on the NiCuZn ferrites and observed that these additives promote the uniform grain growth that further improve the densification and enhanced the magnetic properties. Sea-

Chapter 4 42 A. D. Patil Ph.D. Thesis Fue Wang et al [11] used the $PbO.SiO_2$, $PbO.B_2O_3$ as well as glass former (i.e. $PbO:SiO_2$, or $PbO: B_2O_3$ ratio) and noted some changes in the structural and magnetic properties of the NiCuZn ferrite. Xiaohui Wang et al [12] reported that there is an increase in permeability in NiCuZn ferrite with optimized amount of Mn doping. The Ta_2O_5 is one of the additives used by Znidarsic et al [13] and Li et al [14]. Znidarsic et al reported that doping of Ta_2O_5 in MnZn ferrite reduce the magnetic loss due to presence of Ta^{5+} in the grain boundaries. Li et al observed that when Ta_2O_5 doping is less than 0.04 wt%, the grain size of the sample increases, and if it is greater than 0.04% porosity and grain growth show abnormal growth. K Sun et al [15] investigated the influence of $Ta_2O_5 - Co_2O_3$ co doping in NiMgCuZn ferrites. The result shows that by addition of additives the sintering density reduces via inhibiting the grain growth. Nagaraj et al. synthesized Ta_2O_5 nanoparticles [16] by the ultrasound-assisted method. It is observed that Ta_2O_5 nanoparticles superior for the biological activities against breast cancer cell line and the human pathogens and important in the pharmaceutical industries. Ta_2O_5 nanoparticles [17] are prepared by laser ablation method and its antibacterial properties are studied. It was reported that Ta_2O_5 nanoparticles have orthorhombic crystal structure with outstanding antibacterial performance against Escherichia coli bacteria. Liu et al [18] investigated doping of Nitrogen in Ta_2O_5 and result showed that sample doped at $650^\circ C$ have maximum photo catalytic hydrogen production efficiency than all the prepared samples. Kao et al. [19] reported that the Ti-doped high-k Ta_2O_5 have larger breakdown electric field, greater dielectric constant and smaller gate voltage shift than of undoped Ta_2O_5 dielectric. Seetha Rama Raju studied Ta_2O_5 and PbO doping in MgCuZn [20]. It was presented that addition of PbO into ferrite improves sintered density, bulk density and elastic wave velocity as compared with Ta_2O_5 . Yamamoto et al. [21] investigated effect of Ta doping in MnZn ferrite. It is seen that small amount of addition Ta to the ferrite increases electrical resistivity, while excessive amount of Ta decreases resistivity without grain growth [15, 22]. There are reports available on Ta_2O_5 doping in MgCuZn ferrite mentioning that with increase in Ta_2O_5 there is increase in cation vacancy and decline resistivity of the sample. Seetha Rama Raju [23] studied Ta_2O_5 added MgCuZn ferrites and found that with the addition of Ta_2O_5 resistivity decreases without grain growth. The

Chapter 4 43 A. D. Patil Ph.D. Thesis value of ϵ' and $\tan\delta$ initially decreased up to 100 kHz and nearly remains constant up to 300 MHz and further increased with increase in frequency up to 1 GHz for all prepared samples 4.2. Methodology The selected NiCuZn ferrite was prepared with a composition of Ni 0.4 Cu 0.3 Zn 0.3 Fe $2O_4$ using sol-gel method. A. R. grade nickel, zinc, copper and ferric nitrates and citric acid were considered as starting materials. The known concentration of metal nitrates as well as citric acid was dissolved in 200 ml double distilled water to form clear solution. The pH 7 of the solution was adjusted by drop-wise addition of ammonia. The prepared solution was heated to $80^\circ C$ on the hot plate with vigorous stirring to form the powder. Formed loose powder was grinded in an agate mortar and calcinated at $400^\circ C$ for 5 h. This powder was mixed with selected additive Ta_2O_5 (0 to 10 wt. %) and again grinded for 45 min before calcinating at $600^\circ C$ for 2 h. The pellets of size 10 mm diameter and 2 to 3 mm thick were prepared and sintered at $950^\circ C$ for 4.30 h before used for characterization. The ferrites sintered at $900^\circ C$ possess high density and permeability and hence suitable for the applications such as multilayered chips [47]. Therefore, in the present study, the final sintering temperature of $950^\circ C$ was applied. The XRD patterns for samples were taken at room temperature using X-ray diffractometer (Philips X'Pert instrument) in 2θ range of $20-80^\circ$ with Cu-K α radiation (wavelength $\lambda = 1.54056 \text{ \AA}$). SEM was carried out to analyze microstructure of samples on JEOJSM 6360 SEM. Fourier transform infrared (FTIR) spectroscopic analysis was performed in KBr medium using Jasco model 310 spectrophotometer. Magnetic hysteresis loops were measured at 2K and 300K using vibrating sample magnetometer (Quantum Design PPMS-VSM). Absorption measurements were carried out using UV-Visible diffuse reflectance spectroscopy (UV-Vis. DRS Jasco spectrophotometer Model V-670). The DC electrical resistivity properties of all ferrite samples were measured by using two probe method in the temperature range 300 K to 700 K with silver as a good Ohmic contact material. The frequency dependent dielectric properties such as dielectric constant, the dielectric loss tangent, and the AC conductivity are also measured at room

Chapter 4 44 A. D. Patil Ph.D. Thesis temperature using Hioki (32-50) LCR-Q meter. The variation in frequency was measured

in the range 50 Hz to 5 MHz. The dielectric constant was estimated using formula; $A d C_p \epsilon' \epsilon'' \epsilon_0 \epsilon'' \epsilon'$ (1) Where C_p is parallel capacitance, d is thickness

of sample, and A is area of pellet. 4.3. Result and discussion 4.3.1. Structural properties Rietveld refinement using FULLPROF software [24] was carried out for the phase analysis of all the synthesized ferrite samples (Figure 4.1). Rietveld refined parameters such as weighted profile R-factor (R_{wp}), expected R values (R_{exp}) and goodness fit factor (χ^2) are given in Table 4.1. It is observed from Figure 4.1 that the refined XRD pattern shows two phases; one is the cubic spinel structure with space group $Fd\bar{3}m$ and other with space group $P4_2/mnm$. Small percent of the secondary phase is observed in the XRD pattern which is indexed as $FeTaO_4$ phase (space group $P4_2/mnm$). The lattice constant (a) was

calculated using the relation: $a = d_{hkl} \sqrt{h^2 + k^2 + l^2}$ (2) Where d_{hkl} is the interplanar distance and h, k, l are the Miller indices of planes. Values of lattice constants are given in Table 4.2. The lattice constant decreased with the increase in Ta₂O₅ doping and obeying Vegard's law [25]. The similar nature of lattice constant for various dopant additions in different types of ferrites were reported by several investigators [26–28]. There is possibility that Ta ions enter into the spinel lattice of NiCuZn ferrite causing change in the lattice constant. It is known that

the variation

in the lattice constant may be due to the difference in ionic radii of

Ta, Ni, Cu, Zn and Fe ions. The ionic radii of

Ta⁵⁺ (0.64 Å) less than that of Ni²⁺ (0.69 Å) and Fe³⁺ (0.67 Å). The average crystallite size (D) for ferrite were calculated using the most intense (311)

peak in XRD and using Debye–

Scherrer's formula [29] $D = 0.9 \lambda / \beta \cos \theta$ (3) Where λ is the wavelength of x-rays, β is the full width at half-maximum (FWHM)

and θ is the

Bragg's angle. The calculated values of crystallite size lie in range of

Chapter 4 45 A. D. Patil Ph.D. Thesis 36–55 nm (Table 4.2) indicating the nano size of the prepared ferrite particles. Bulk density (ρ_B) was calculated using the mass and volume of the pellet samples. Table 4.2 shows the variation in the X-ray density and bulk density with Ta₂O₅ additive. The x-ray density increased with the increase of Ta₂O₅ additive concentration which is attributed to the fact that the density of the Ta ions (16.69 g cm⁻³) is greater than that of Zn (7.14 g cm⁻³), Fe (7.87 g cm⁻³), Ni (8.908 g cm⁻³) and Cu (8.96 g cm⁻³). The bulk density increased with Ta₂O₅ additive concentration. This may be due to the fact that Ta ions (180.94 a.m.u.) having a greater atomic weight than that of Ni (58.69 a.m.u.), Fe (55.84 a.m.u.), Cu (63.54 a.m.u.) and Zn (65.38 a.m.u.) atoms. It is also observed that X-ray density is greater than bulk density. The change in X-ray density and bulk density may be because of the existence of pores in the sample, which is dependent upon the method of preparation, sintering temperature and sintering condition. The allied parameters further, the structural related parameters such as tetrahedral and octahedral hopping length (L_A and L_B), tetrahedral and octahedral bond lengths (d_{AX} and d_{BX}), tetrahedral edge, octahedral shared and unshared edges (d_{AXE} , d_{BXE} and d_{BXEU}) for Ni_{0.4}Cu_{0.3}Zn_{0.3}Fe₂O₄ doped with Ta₂O₅ additive were synthesized by sol gel method can be obtained by using oxygen positional parameter 'u' and lattice constant 'a' values in the following relations [30, 31]. $a = 3.4$ (4) $a = 3.2$ (5) $a = 3.1$ (6) $a = 3.2 - 11.4 + 43.64$ (7) $a = 2.2 - 1.2$ (8) $a = 2.1 - 2$ (9) $a = 4.2 - 3 + 11.16$ (10) The investigated values are summarized in Table 4.3, which shows that the tetrahedral and octahedral hopping lengths as well as tetrahedral edge and octahedral

Chapter 4 46 A. D. Patil Ph.D. Thesis shared and unshared edges reduced with Ta₂O₅ additive doping. This is owing to less ionic radii of Ta⁵⁺ (0.64 Å) than that of Ni²⁺ (0.69 Å) and Fe³⁺ (0.67 Å) ions. 4.3.2. Field Emission Scanning Electron Microscopy The FESEM characterization is used to identify the surface morphology of ferrite. Figure 4.2 shows FESEM images for 0, 1, 3 and 10 wt. % Ta₂O₅ additive concentrations. It is observed that the particles and grains are uniformly distributed. Some of the particles were agglomerated due to the presence of the magnetic interactions among the grains/particles. Figure 4.3 shows energy dispersive x-ray (EDX) spectroscopy patterns. The peaks observed in EDX patterns are related to the constituent ions in the samples where no impurity phases/elements were detected. This confirms the purity of the samples for composition of the Ni_{0.4}Cu_{0.3}Zn_{0.3}Fe₂O₄ with Ta₂O₅ additive. 4.3.3. Fourier Transform Infrared (FTIR) Spectroscopy FTIR is used to investigate the structural properties and distribution of cations among the tetrahedral and octahedral sites of spinel NiCuZn ferrites. Figure 4.4 shows the FT-IR spectra of all the samples in the frequency range of 800–350 cm⁻¹. In FTIR spectra two major absorption bands (ν_1 and ν_2) are observed near 600 cm⁻¹ and 400 cm⁻¹ corresponding to tetrahedral and octahedral sites respectively. These bands are a common characteristic feature of spinel ferrites [32]. Values of absorption bands (ν_1 and ν_2) are listed in Table 4.4. Waldron [33] attributed these ν_1 and ν_2 bands observed at around 600 cm⁻¹ and 400 cm⁻¹ to the intrinsic vibration of tetrahedral and octahedral metal oxygen complexes respectively. It has been observed from Figure 4.4 and Table 4.4 that the frequency of tetrahedral and octahedral bands varies with the Ta₂O₅ additive. In order to elaborate the spectra, we have calculated the ratio of tetrahedral to octahedral (ν_1 / ν_2) (Table 4.4). The force constant of ions at the tetrahedral and octahedral sites can be calculated using frequencies of ν_1 and ν_2 in the following relation [34]: $k = 4 \pi^2 \nu^2$

(11) Where F is the force constant, c is the light velocity $2.99 \times 10^8 \text{ m s}^{-1}$, ν is the vibration frequency of the tetrahedral and octahedral sites, μ is the reduced mass for the Fe^{3+} and O^{2-}

Chapter 4 47 A. D. Patil Ph.D. Thesis ions ($\sim 2.065 \times 10^{-26} \text{ kg mol}^{-1}$). The variation in force constant indicates variation in bond lengths of cations and oxygen ions at the tetrahedral and octahedral site in Ta_2O_5 additive spinel NiCuZn ferrite. No systematic trend of variation is observed in the ν_1 / ν_2 ratio indicating that the Ta_2O_5 additive does not significantly alter the site occupancy of cations present in the $\text{Ni}_{0.4}\text{Cu}_{0.3}\text{Zn}_{0.3}\text{Fe}_2\text{O}_4$ ferrite system.

4.3.4 The UV-Vis. Diffused Reflectance Spectroscopy The optical properties of NiCuZn ferrite with Ta_2O_5 additives were studied by UV-Vis. Diffused reflectance spectra. Figure 4.5 shows the absorbance spectra of the synthesized NiCuZn ferrites with the different concentration of Ta_2O_5 additive. It is observed that all the samples show optical properties in the visible region. As evident the broad absorption observed in the blue region of 500–600 nm and interestingly the absorption increased with Ta_2O_5 additive. The increase in absorption is related to increase in Ta_2O_5 , bulk density and particle/grain size. It is observed that all samples in the visible region the absorption in the range 700–800 nm. The absorption edge in the visible region of ferrite nanoparticles is in relation with the electron excitation from $\text{O}^{2-} 2p$ level into the $\text{Fe}^{3+} 3d$ level for the ferrites. The Kubelka-Munk function was used to calculate the equivalence absorption coefficient by converting the diffused reflectance as given by: $[35] = \frac{1 - R}{2R}$ (12) Where $F(R)$ is Kubelka-Munk function, α is absorption coefficient and R is reflectance value. Furthermore, the absorption coefficient values are used to estimate band gap energy by using Tauc relation: $h\nu = (h\nu_g - E_g)^2$ (13) Where $h\nu$ is photon energy and E_g is the activation energy. Figure 4.6 shows the band gap energy estimated by plotting a graph of $(h\nu)^2 = [F(R)h\nu]^2$ versus $h\nu$. Band gap energy of the sample was calculated by extrapolating $(h\nu)^2 = [F(R)h\nu]^2$ in linear regions. The calculated values of band gap energy of present samples are ranging from 2.55 to 2.90 eV. Further, it is observed that band gap increased for $\leq 5 \text{ wt}\%$ Ta_2O_5 additive concentration, further increase in Ta_2O_5 for $< 5 \text{ wt}\%$ decrease the band gap energy.

Chapter 4 48 A. D. Patil Ph.D. Thesis 4.3.5 Magnetic properties Magnetic properties were characterized by a vibrating sample magnetometer (VSM) at 2 K and 300 K. The Figure 4.7(a) for VSM the typical samples for 2 wt%, 3 wt% of Ta_2O_5 at temperature 2 K and Figure 4.7(b) for all samples at temperature 300 K the value of magnetic parameter that is saturation magnetization (M_s), coercivity (H_c) and remanence magnetization (M_r) are listed in Table 4.5. It is found that for lower magnetic field, magnetization increases rapidly and attains saturation at higher magnetic field. It is also observed that saturation magnetization (M_s) decreased with the increase in Ta_2O_5 additive concentration. The gradual decrease in the saturation magnetization by increasing Ta_2O_5 additive may be related to the fact that; Ta_2O_5 could form a magnetic insulating layer over the grain surfaces. This magnetic insulating layer possibly prevents the inter-particle magnetic interactions [36]. Further, considering the fact that Ta_2O_5 is diamagnetic in nature, therefore, increase in Ta_2O_5 diamagnetic volume fraction in ferrimagnetic degrades the saturation magnetization of $\text{Ni}_{0.4}\text{Cu}_{0.3}\text{Zn}_{0.3}\text{Fe}_2\text{O}_4$. Similar behavior in magnetization was observed in Ta_2O_5 additive MnZn ferrite [14]. The reduction in saturation magnetization

can also be justified on the basis of exchange interactions between tetrahedral and octahedral

sub-lattice [37]. Ta_2O_5 additive could change some of Fe^{3+} ions into Fe^{2+} ions, this valence change then weakens the ferrimagnetic $\text{Fe}^{3+} - \text{O}^{2-} - \text{Fe}^{3+}$ super exchange interactions [38]. Saturation magnetization is also affected by extrinsic factors such as microstructure, bulk density and grain size of the ferrites [39]. In present work, crystallite size increased with addition of Ta_2O_5 . The coercivity of the samples is very small confirming the soft magnetic nature of the prepared samples.

4.3.6 DC Electrical Resistivity The nanocrystalline $\text{Ni}_{0.4}\text{Cu}_{0.3}\text{Zn}_{0.3}\text{Fe}_2\text{O}_4$ spinel ferrite samples are studied for 0 to 10 wt% Ta_2O_5 additive doping. Figure 4.8 shows the variation of the DC electrical resistivity with inverse of temperature for all samples. It is observed that resistivity is decreased with increase in the temperature for all samples. It indicates the semiconducting

Chapter 4 49 A. D. Patil Ph.D. Thesis nature and obeys the Arrhenius relation. The plot was divided into two separate regions one as ferrimagnetic and another as paramagnetic regions at particular temperature. This particular temperature is called Curie temperature. The change in slope of curve shows phase transition from ferromagnetic to paramagnetic. According to Verwey, in ferrite the conduction mechanism is mostly due to hopping of charge carriers among Fe^{2+} and Fe^{3+} ions in the octahedral (B) site [40]. The Arrhenius relation is given as $\rho = \rho_0 \exp(\frac{E}{kT})$ (14) Where, ρ_0 is constant, E activation energy, k Boltzmann constant and T absolute temperature. Table 4.6 shows calculated values of activation energy of ferrite samples and Curie temperature. It is seen that activation energy is higher in paramagnetic region than ferrimagnetic region. Curie temperature is decreased with increase in Ta_2O_5 additive doping.

4.3.7 Dielectric Properties Dielectric properties are very important from the application point of view. The dielectric constant is measured at room temperature for 50 Hz to 5 MHz frequencies. The pellets were made up of disc shape. Figure 4.9 shows variation

in dielectric constant and frequency for different composition of Ta₂O₅ additive. It is seen that with increase in frequency there is decrement in dielectric constant for all samples doped with Ta₂O₅ additive. It indicates the normal behavior of the ferrites. The dielectric constant decreases rapidly at lower frequencies showing dispersion whereas almost constant at higher frequencies. Similar behavior for dielectric constant is reported by Reddy et al. and Wang et al. [41, 42] where the values of ϵ' are in the range of 25 to 225. According to interfacial polarization of Maxwell's Wagner and Koop's theory [43-45] dielectric material is made of conducting grains which are separated by non-conducting grain boundaries. These grain boundaries are effective at lower frequencies. Also at higher frequencies grains are more effective. Therefore, due to the effect of grain boundaries, the dielectric constant is decreased rapidly in lower frequency regions. At high frequency the grain comes into

Chapter 4 50 A. D. Patil Ph.D. Thesis action hence there is almost no change in dielectric constant According to Debye equation [46], dielectric constant decreased with increased frequencies. The selected sample results also show similar nature of dielectric constant variation with frequencies. Figure 4.10 shows the variation of dielectric loss tangent and frequency at room temperature for 0 to 10 wt. % Ta₂O₅ additive doping. The results are similar in nature to that of dielectric constant. Result shows that the dielectric loss tangent is decreased for increased frequencies. It was also observed that beyond certain frequencies, jumping frequency of charge carriers cannot follow the frequency of applied electric field. It has been observed the dielectric constant of NiCuZn ferrite is higher for 2 to 10 wt% Ta₂O₅ additive doping. The increase in dielectric constant can be related to increase in grain growth resulted in an increase in density and a decrease in porosity with Ta₂O₅ doping. The values of the grain sizes and densities are reported in our previous publication [16]. The pores act as an insulating material, which creates new barriers for the interfacial polarization, and interrupt the build-up of space charge, resulting in a decrease in polarization. As the doping increases, porosity decreases, this promotes the space charge build-up that causes an increase in polarization [2]. Furthermore, the bigger grain means easier electron movements and higher contact between the adjacent grains, enabling the electron to easily flow towards the grain boundaries [3]. Therefore, the dielectric polarization increased and resistivity decreased by increasing the Ta₂O₅ doping level.

4.7.1 AC Conductivity For low temperature, sintered ferrites AC conductivity is significant property for MLCI applications. To understand conduction mechanism in synthesized samples, AC conductivities were measured. Figure 4.11 shows the variation of AC conductivity and frequency at room temperature for 0 to 10 wt% Ta₂O₅ additive doping. With increased frequency, AC conductivity also increased for selected ferrite samples. Further, it is found that there was slight increase in AC conductivity with the addition of Ta₂O₅ additive. It is also according to Maxwell Wagner model. At low frequency grain boundaries are more effective; hence, less conductivity, and at higher frequency grains are active hence higher conductivity.

Chapter 4 51 A. D. Patil Ph.D. Thesis References

Chapter 4 52 A. D. Patil Ph.D. Thesis [1] N.Rezlescu, L.Sachelarie, L.Rezlescu,P.D.Popa,Cryst. Res. Technol. ,36 (2001)157 [2] S.E.Shirsath, S.M.Patange, Y.Yasukawa, X.Liu,A.Morisako,IEEE Trans. Magn.,50 (2014)1 [3]

S.

E.Shirsath, R.H.Kadam, S.M.Patange, M.L.Mane,

A.

Ghasemi,A.Morisako, Appl. Phys. Lett.,100 (2012) 042407 [4] K.Sun, Z.Pu, Y.Yang, L.Chen, Z.Yu, C.Wu, X.Jiang ,Z.Lan,J. Alloys Compd., 681 (2016) 139 [5] S. E.Shirsath, D.Wang, S. S.Jadhav, M. L.Mane,S.Li . Ferrites obtained by sol- gel method, Handbook of Sol-Gel Science and Technology ed L. Klein, M Aparicio, A .Jitianu, Berlin: Springer ,(2018) 695 [6] A. T.Raghavendera, S. E.Shirsath,K.Vijaya Kumar, J. Alloys Compd.,509 (2011) 7004 [7] T.Krishnaveni, B. RajiniKanth, V.Seetha Rama Raju , S. R. Murthy, J. Alloys Compd.,414 (2006) 282 [8] N. Rezlescu, L. Rezlescu, P.D. Popa, E. Rezlescu, J. Magn. Mater.,215 (2000) 194 [9] J.Xiang, X.Shen, B.Song Fuzhan,M. Liu, J. Solid State Chem., 183(2010)1239 [10] Y.Wang, H.Zhou, H.Qi, L.Ren, Z.Xu, Z. Yu, Ceram. Inter.,41(2015)12253 [11] S.F Wang, Y.R Wang, T. C. K Yang, P.J Wang,C.A Lu, J. Magn.Magn. Mater.,217 (2000) 35 [12] X.Wang, W.Qu, L.Li ,Z.Gui, Ceram. Inter.,30 (2004) 1615 [13] A.Zdinarsic, M.Limpel,M.Drofenik,IEEE Trans. Magn. ,3 (1995)950 [14] L. L. Z.Lan, Z.Yu, K.Sun, M.Luo, Z.Xu, H. E.Ji,J. Magn. Mater.,321(2009)438 [15] K.Sun,J.Wang,Y.Yang,Y.Li,Z.Yu,Z.Lan,X.Jiang,R.Guo,C.Wu,Phys.B:Cond.Matt .476(2015)122 [16] G. Nagaraju, K. Karthik, M. Shashank, Microchem. J. ,147(2019) 749 [17] A. Meidanchia, A. Jafari, J. Opt. Laser Technol. , 111(2019)89

Chapter 4 53 A. D. Patil Ph.D. Thesis [18] W.S. Liu, S.H. Huang, C.-F. Liu,C.-W. Hu, T.-Y. Chen, T. P. Perng, J. Appl. Surf. Sci., 459(2018) 477 [19] C.H.Kao,P.L.Lai,H.Y.Wang,J. Surf. Coat. Technol., 231(2013)512 [20] V. Seetha Rama Raju,J. Appl. Sci. Lett.,1(2015)99 [21] Y. Yamamoto, A. Makino, T. Nikaldou,J. Phys. IV France,7 (1997) C [22] T. Krishnaveni, S. R. Murthy, F.

Gao, S. Lu, Q. Komarneni, J. Mater. Sci., 41(2006)1471 [23] V. Seetha Rama Raju, J. of Mater. Res., 29(2014)2220 [24] R. S. Yadav, I. Kuřitka, J. Vilcakova, J. Havlica, L. Kalina, P. Urbánek, M. Machovsky, D. Skoda, M. Masař, J. Mater. Sci.: Mater. Elect., 29 (2018)15878 [25] L. Vegard, Zeitschrift für Physik, (1921)517 [26] J. Smit, H. P. J. Wijn, Ferrites, New York: Wiley, (1959)143 [27] D. R. Mane, D. D. Birajdar, S. E. Shirsath, A. T. Raghvender, R. H. Kadam, Phys. Status Solidi (A), 207(2010)2355 [28] S. M. Ramay, A. Saadat, S. Siddiqi, M. S. Atiq, S. R. Awan, Chin. J. Chem. Phys., 23 (2010) 591 [29] S. J. Haralkar, R. H. Kadam, S. S. More, S. E. Shirsath, M. L. Mane, S. Patil, D. R. Mane, Phys. B: Cond. Matt., 407 (2012) 4338 [30] R. S. Yadav, I. Kuřitka, J. Vilcakova, T. Jamatia, M. Machovsky, D. Skoda, P. Urbanek, M. Masar, M. Urbanek, L. Kalina, J. Havlica, Ultrason. Sonochem., 61 (2020)104839 [31] Sandeep B. Somvanshi, Mangesh V. Khedkar, Prashant B. Kharat, K. M. Jadhav, Ceram. Int., 46 (2020) 8640 [32] V. Chaudhari, S. E. Shirsath, M. L. Mane, R. H. Kadam, S. B. Shelke, D. R. Mane, J. Alloys Compd., 549 (2013)213 [33] R. D. Waldron Infrared spectra of ferrites, Phys. Rev., 99 (1955) 1727 [34] R. S. Yadav, I. Kuřitka, J. Vilcakova, J. Havlica, L. Kalina, P. Urbánek, M. Machovsky, D. Skoda, M. Masař, M. Holek, Ultrasonics—Sonochem., 40(2018) 773 [35] A. Manikandan, J. Judith Vijaya, L. John Kennedy, M. Bououdina, J. Mol. Struct., 1035 (2013)332

Chapter 4 54 A. D. Patil Ph.D. Thesis [36] M. A. Gabal, A. M. Al-Angari, S. S. Al-Juaid, J. Alloys Compd., 492 (2010) 411 [37] L. Neel, Ann. Phys., Paris, 12 (1948)137 [38] R. A. Pawar, S. S. Desai, Q. Y. Tamboli, S. E. Shirsath, S. M. Patange, J. Magn. Magn. Mater., 378(2015) 59 [39] A. B. Nawale, N. S. Kanhe, K. R. Patil, S. V. Bhoraskar, V. L. Mathe, A. K. Das, J. Alloys Compd., 509 (2011) 4404 [40] M. Kalyan Raju, M. Ratna Raju, K. Samatha, J. Optoelectron. Adv. Mater., 17(2015)1075 [41] M. P. Reddy, G. Balakrishnaiah, W. Madhuri, M. V. Ramana, N. R.

Reddy, K. V. Siva Kumar, V. R. K. Murthy, R. R. Reddy,

J. Phys. Chem. Solid., 71(2010)1373 [42] Y. Wang, H. Zhang, L. Li, Y. He, W. Ling, J. Magn. Magn. Mater., 324(2012) 471 [43] J. C. Maxwell, Treatise on Electricity and Magnetism, Clarendon Press, Oxford, (1982) [44] K. W. Wagner, J. Ann. Physik., 345(1913)817 [45] C. G. Koops, J. Phys. Rev., 83(1951) 121 [46]

W. D. Kingery, H. K. Bowen, D. R. Uhlman, Introduction to Ceramics, 2

nd ed., Wiley, New York, (1976) [47] T. Nakamura, J. Magn. Magn. Mater., 168(1997)28 Table 4.1: Discrepancy factor (Rwp), expected values (Rexp), goodness fit factor (χ^2), of NiCuZn ferrites with Ta 2 O 5 additive

Chapter 4 55 A. D. Patil Ph.D. Thesis wt.% Ta 2 O 5 R exp R wp ? 2 0 11.9 10.5 1.27 1 13.0 11.0 1.39 2 14.8 11.9 1.54 3 13.1 10.7 1.49 5 19.6 14.1 3.19 10 19.8 14.0 3.30

Chapter 4 56 A. D. Patil Ph.D. Thesis Table 4.2: Crystallite size (D), Lattice constant (a), bulk density (dB) and bandgap of NiCuZn ferrites with Ta 2 O 5 additive. wt.% Ta 2 O 5 D (nm) a (Å) dB (g cm⁻³) Band gap (eV) 0 55.56 8.3637 4.5477 2.8178 1 49.95 8.3578 4.989 2.5542 2 48.75 8.3537 5.3587 2.7739 3 36.85 8.3498 4.9376 2.7958 5 43.00 8.3498 5.2324 2.9057 10 47.33 8.3451 5.3441 2.6860

Chapter 4 57 A. D. Patil Ph.D. Thesis Table 4.3: Hopping lengths, tetrahedral bond length, octahedral bond length, and tetrahedral edge, octahedral edge (shared and unshared) for Ni 0.4 Cu 0.3 Zn 0.3 Fe 2 O 4 . with Ta 2 O 5 additive. Wt. % Ta 2 O 5 Hopping Lengths Tet. Bond Length d AX (Å) Oct. Bond Length d BX (Å) Tet. Edge d AXE (Å) Oct. Edge (Shared & Unshared) L A (Å) L B (Å) d BXE (Å) d BXEU (Å) 0 3.6214 7.2429 1.9990 1.9868 3.2645 2.6494 2.9640 1 3.6189 7.2378 1.9976 1.9853 3.2622 2.6475 2.9620 2 3.3665 7.2343 1.9966 1.9844 3.2606 2.6462 2.9605 3 3.3649 7.2309 1.9957 1.9834 3.2590 2.6450 2.9591 5 3.3649 7.2309 1.9957 1.9834 3.2590 2.6450 2.9591 10 3.3660 7.2268 1.9964 1.9823 3.2572 2.6435 2.9575

Chapter 4 58 A. D. Patil Ph.D. Thesis Table 4.4: Vibrational bands tetrahedral A-site (ν_1), octahedral B-site (ν_2), ratio of ν_1 / ν_2 , and force constant (FT and FO) wt.% Ta 2 O 5 Absorption band (cm⁻¹) Ratio ν_1 / ν_2 Force constant ($\times 10^2$ N m⁻¹) F r F o ν_1 ν_2 0 580.38 402.81 1.441 2.469 1.189 1 576.15 403.41 1.428 2.433 1.193 2 580.71 400.51 1.450 2.472 1.176 3 579.72 400.25 1.448 2.463 1.174 5 581.83 400.21 1.454 2.481 1.174 10 583.15 402.20 1.450 2.492 1.185

Chapter 4 59 A. D. Patil Ph.D. Thesis Table 4.5: Magnetization saturation (M_s), coercivity (H_c) and Magnetization remanence (M_r) of NiCuZn ferrites addition of additive Ta 2 O 5 at Room temperature wt.% Ta 2 O 5 Magnetization Saturation (M_s) (emu gm⁻¹) Coercivity (H_c) (Oe) Magnetization Remanent (M_r) (emu gm⁻¹) 0 83.41 506 58.59 1 72.32 402 30.12 2 61.82 302 20.12 3 51.34 204 14.16 5 36.16 100 10.20 10 23.14 64 8.42

Chapter 4 60 A. D. Patil Ph.D. Thesis Table 4.6: Calculated values of activation energy and Curie temperature Composition in wt.% Curie Temperature T_c K Activation Energy (eV) E = E f - E p E f E p 0 635 0.358 1.204 0.845 1 631 0.357 0.690 0.333 2 615 0.281 1.220 0.938 3 608 0.212 0.798 0.585 5 578 0.290 0.989 0.699 10 575 0.395 1.026 0.631

Chapter 4 61 A. D. Patil Ph.D. Thesis Fig.4.1: Rietveld refined x-ray diffraction patterns for all synthesized Samples of Ni_{0.4} Cu_{0.3} Zn_{0.3} Fe₂ O₄ with Ta₂ O₅ additive. Bragg's peak positions are shown in green color at the bottom of XRD of $x=10$ wt. %. These Bragg peaks are referred to the space group $Pb4_2/mnm$ and $Fd3m$ for FeTaO₄ and Ni_{0.4} Cu_{0.3} Zn_{0.3} Fe₂ O₄ with Ta₂ O₅

Chapter 4 62 A. D. Patil Ph.D. Thesis Fig.4.2: SEM images of Ni_{0.4} Cu_{0.3} Zn_{0.3} Fe₂ O₄ with Ta₂ O₅ additive (a) X= 0 Wt. %, (b) X=1 Wt. %, (c) X = 3 Wt. % and (d) X=10 Wt. %

Chapter 4 63 A. D. Patil Ph.D. Thesis Fig.4.3: EDX pattern of Ni_{0.4} Cu_{0.3} Zn_{0.3} Fe₂ O₄ with Ta₂ O₅ additive for (a) x=0 wt. % and (b) x=10 wt. %

Chapter 4 64 A. D. Patil Ph.D. Thesis Fig.4.4: The FTIR spectra of Ni_{0.4} Cu_{0.3} Zn_{0.3} Fe₂ O₄ with different concentration of Ta₂ O₅

Chapter 4 65 A. D. Patil Ph.D. Thesis Fig. 4.5: The Absorbance spectra of Ni_{0.4} Cu_{0.3} Zn_{0.3} Fe₂ O₄ with different concentration of Ta₂ O₅ additive

Chapter 4 66 A. D. Patil Ph.D. Thesis Fig.4.6: Band gap energies of Ni_{0.4} Cu_{0.3} Zn_{0.3} Fe₂ O₄ with different concentration of Ta₂ O₅ additive

Chapter 4 67 A. D. Patil Ph.D. Thesis Fig.4.7: Magnetic hysteresis loops for Ni_{0.4} Cu_{0.3} Zn_{0.3} Fe₂ O₄ with Ta₂O₅ additive (2 wt. % and 3 wt. %) nanocrystalline spinel ferrites at 2 K (left) and b) 300 K (right) .

Chapter 4 68 A. D. Patil Ph.D. Thesis Fig. 4.8: Variation of direct current resistivity with temperature

Chapter 4 69 A. D. Patil Ph.D. Thesis Fig.4.9: Variation of dielectric constant and frequency for 0 to 10 wt. % Ta₂ O₅ additive doping.

Chapter 4 70 A. D. Patil Ph.D. Thesis Fig.4.10: Variation of dielectric loss tangent and frequency at room temperature for 0 to 10 wt. % Ta₂ O₅ additive doping.

Chapter 4 71 A. D. Patil Ph.D. Thesis Fig.4.11: Variation of alternating current conductivity and frequency at room temperature for 0 to 10 wt. % Ta₂ O₅ additive doping.

Chapter 5 72 A. D. Patil Ph. D Thesis Chapter 5 Result and Discussion on Ni_{0.4} Cu_{0.3} Zn_{0.3} Fe₂ O₄ +xTiO₂ (X= 0-10 wt. %) 5.1 Introduction The commercial nanocrystalline ferrites are of current research interest due to its various applications like photoelectric devices, digital memories, radar and satellite communication, gas sensors, telecommunication, microwave devices and biomedical. Various studies reported that spinel ferrites in the nanocrystalline form consist of significant electrical and dielectric properties as compared to bulk form. NiCuZn ferrite is one of the crucial ferrites used for multilayer chip inductor because it has better properties than MnZn ferrite at high frequencies, also lower densification temperatures as compared to NiZn ferrites [1 - 3]. The various methods such as co-precipitation, oxalate precursor chemical method, ceramic method, and sol gel auto combustion [4 - 6] are used to synthesize nanocrystalline spinel ferrites. Amongst these, the sol-gel method is the most advanced method for production of nanocrystalline spinel ferrites due to its advantages such as requirement of low temperature, good control over stoichiometry, and easy to adapt synthesis parameters [7, 8]. Many researchers used Ti as a substituent in different spinel ferrites. It has been reported that, the substitution of Ti in Mn ferrites [9] synthesized by hydrothermal method exhibits good control over the structural as well as magnetic parameters like lattice constant and saturation magnetization. In case of Ni-Cu-Zn ferrite, the substitution of Ti was reported to reduce the parameters like saturation magnetization, X-ray density and lattice constant [10]. The modification in initial permeability of Mn-Zn ferrites due to

Chapter 5 73 A. D. Patil Ph. D Thesis Ti substitution as a consequence of transfer of charges between the sub lattice sites is reported in the literature [11]. The magnetic parameters like remanence, coercivity and saturation magnetization were reported to decrease as an effect of Ti substitution in the Co ferrite [12]. The decline in structural properties due to Ti substitution in Co ferrite was also reported in literature [13], wherein a strong relationship between ionic radius of Ti⁴⁺ and frequencies of the modes of vibration was revealed. The enhancement in the magnetic and electrical parameters like coercivity, remanence, dielectric constant and dielectric loss was reported for Ni_{0.4} Cu_{0.2} Zn_{0.4} Fe₂ O₄ ferrites wherein fraction of Fe³⁺ cations was replaced with Ti⁴⁺ ions [14]. However, doping of Ti ions in the spinel ferrite by means of the TiO₂ additive was proved to be significant for enhancement of the physical parameters of the ferrites. A study on the influence of TiO₂ doping in Ni-Zn ferrite confirms that the structural and magnetic parameters like grain size, relative density and magnetic permeability were increased with a specific amount of the doping within the ferrite [15].

The electrical parameters like power loss and DC resistivity were also enhanced with the specific amount of doping of TiO₂ additive within the ferrite. The creation of secondary phase of NiTiO₃ and Fe₂TiO₅ was reported for the TiO₂ doped Ni ferrites [16], as an effect of which the reduction in magnetic parameters was observed. A systematic study of TiO₂ doped Mn-Zn ferrites reports that the magnetic parameters like permeability and power loss of the ferrite can be enhanced by adding the suitable amount of the additive within the ferrite crystal [17]. Kounsalye [18] studied the effect of Ti⁴⁺ ions on Li-ferrites and found that with an increase in Ti⁴⁺ ion substitution dc resistivity increases and dielectric properties show normal dispersion behavior. Rathi [19] presented the effect of Ti⁴⁺ substitution on NiCuZn ferrite. It is also seen that the dielectric constant increased with increased Ti⁴⁺ composition. Fan [20] used B₂O₃ as an additive in Mn-Zn ferrite and observed that there is no doping effect of B₂O₃ on magnetic properties but it promotes the grain growth significantly. Also, impedance analysis indicates that with an increase in B₂O₃ content in ferrites both grain and grain boundary resistivity is increased. Praveena [21] observed the effect of TiO₂ on Ni_{0.35} Cu_{0.12} Zn_{0.35} Fe₂O₄ and showed that dielectric properties and permeability are increased with the addition of TiO₂ in ferrite. Also, the resonant frequency for all the selected composition was greater than 1 GHz. Suryavanshi [22]

Chapter 5 74 A. D. Patil Ph. D Thesis studied the behavior of Ti⁴⁺ substitution in Mg-Zn ferrite. The results showed that with Ti⁴⁺ concentration, initially activation energy (ΔE) and D.C. resistivity (ρ) increase gradually ($t > 0.2$) and linearly afterward. It also presents that dielectric properties initially decrease gradually and rapidly with the further addition of Ti⁴⁺. Meaz et al [23] presented the effect of substitution of tetravalent titanium ions in Co-Zn ferrites. For all the samples the electrical conductivity, dielectric loss tangent and dielectric constant were decreased with the addition of Ti⁴⁺ ions except $x = 0.1$ sample. Ahmed et al.[24] studied the effect of Ti⁴⁺ ions substitution in Mg-ferrite and presented that Curie constant, Curie temperature, Curie-Weiss constant, effective magnetic moment decreases with the addition of Ti content. Desai et al. observed electric and elastic properties of CoFe₂O₄ ferrites[25]. In brief, the literature survey suggests that the doping of suitable amount of TiO₂ additive in the ferrite is effective in enhancing the physical parameters of the ferrites. Such interesting modifications due to TiO₂ doping in spinel ferrites leads to use them in variety of applications. The Ni-Cu-Zn ferrites with specific stoichiometric elemental composition of divalent cations with approximately 40% Ni, 30% Cu and 30% Zn exhibits interesting physical properties leading to variety of applications [26–28].

5.2 Methodology The sol-gel method was used for the preparation of nanocrystalline Ni_{0.4} Cu_{0.3} Zn_{0.3} Fe₂O₄ ferrite doped with TiO₂ additives. The analytical grade (99% pure) copper nitrate (Cu (NO₃)₂ · 6H₂O), zinc nitrate (Zn (NO₃)₂ · 6H₂O), nickel nitrate (Ni (NO₃)₂ · 6H₂O), ferric nitrate (Fe (NO₃)₃ · 9H₂O) and citric acid (C₆H₈O₇)

were utilized for the synthesis of ferrites. These nitrates and citric acid were dissolved in water, ammonia was added to the solution, and 7 pH was attended.

Then, the solution was kept on a hot plate at 80°C with continuous stirring until a thick, viscous gel was obtained. At this stage the stirring was stopped while continuing the heating. The heating removes the water content from the gel and a completely dry gel was obtained. The dry gel auto-ignites within a second and burns with the colored fumes. The burning completes within few minutes and the ferrite powder in the form of ash precursors was obtained. These ash precursors were grinded in the agate mortar and calcined for 5 h at 400°C in a

Chapter 5 75 A. D. Patil Ph. D Thesis temperature controlled furnace. The calcined powder was mixed with TiO₂ additive (0–10 wt %) and grinded for 45 min before calcination at 650°C for 4 h. The pellets with 13 mm diameter and 3 mm thickness were obtained from this powder, with a polyvinyl alcohol as a binder material. These pellets were calcined for 4 h at 400°C to remove the binder. X-ray diffractometer D2 PHASER (Bruker) was employed for obtaining the XRD pattern of calcined samples with Cu-K α as a radiation source having wavelength $\lambda = 1.5405 \text{ \AA}$ inclined at diffraction angles 2θ in between 20–80° at room temperature. Microstructures of the samples were studied from FESEM: FEI Nova Nano SEM 450 and elemental analysis from EDS: BrukerXFlash 6130. Fourier transform infrared (FTIR) spectroscopic analysis was done using Jasco model 310 spectrophotometer. At room temperature, magnetic measurements were performed on vibrating sample magnetometer (Quantum Design PPMS-VSM). The study of optical properties of synthesized samples

was done on UV-Vis. DRS Jasco spectrophotometer (Model V-670). The Mössbauer spectra of the ferrite samples were obtained at room temperature by using ^{57}Co as a γ -ray source in Rh matrix. The calibration of velocity scale was performed in relation with ^{57}Fe (in Rh). The Win NormosFIT software was utilized for the analytical fitting of the spectra. The elastic properties such as longitudinal modulus, modulus of rigidity, bulk modulus, Young's modulus, wave velocities of the prepared samples were measured by the ultrasonic pulse transmission method. The frequency dependent dielectric properties such as dielectric constant (ϵ'), AC conductivity, dielectric loss tangent ($\tan\delta$), and impedance spectroscopy measurements were conducted in the 50 Hz to 5 MHz frequency range using Hioki (3250) LCR-Q meter at room temperature.

5.3 Results and Discussion 5.3.1. Structural Analysis The structural study of the ferrite samples was performed by powder X-ray diffraction method and the obtained diffraction patterns are shown in Figure 5.1. In XRD

Chapter 5 76 A. D. Patil Ph. D Thesis patterns of all the ferrites the peaks (220), (311), (222), (400), (422), (511) and (440) were observed revealing the formation of spinel phase within the ferrites [29]. The XRD patterns for $x \geq 3$ wt. % exhibit the additional peaks of the TiO_2 phase; (101), (103), (004), (112), (200), (105), (211), (118), (220) at 27° , 37° , 38° , 39° , 48° , 53° , 55° , 62° , 71° [30] respectively along with the peaks of spinel phase. From FULLPROF suite software program, the analysis of XRD data was performed by applying the technique of Rietveld refinement. The parameters obtained from Rietveld refinement were goodness fit factor (χ^2), expected R values (Rex) and weighted profile R-factor (Rwp) along with the relative % of the two phases (spinel and TiO_2) created within the ferrites are listed in Table 5.1. The exploration of Rietveld refinement shows that a single spinel phase having cubic structure is formed with $Fd\bar{3}m$ space group for the ferrites doped with $x > 3$ wt. % of TiO_2 and an additional secondary phase having space group $I41/amd$ is formed along with the spinel phase for the ferrites doped with $x \geq 3$ wt. % of TiO_2 . For $x \geq 3$ wt. % of TiO_2 the secondary phase increases from 4.2 % to 8.6 %, while a simultaneous decrease in spinel phase from 95.8 % to 91.4 % was observed. It is clear that for $x \geq 3$ wt. % the TiO_2 additive does not enter within the ferrite lattice and there is a possibility that the TiO_2 molecules may surround the Fe^{3+} cations at the sub-lattice sites [16]. The values of the lattice parameter were obtained from the equation reported elsewhere [31] and are summarized in Table 5.2 along with the crystalline sizes, X-ray densities, and hopping lengths. From Table 5.2, it is revealed that the values of the lattice parameter (a) are enhanced with rise in TiO_2 composition up to 5 wt. %. For $x > 3$ Wt. % of TiO_2 the Ti^{4+} ions enter in to the lattice of Ni-Cu-Zn ferrite, by replacing few Fe^{3+} cations. Owing to the variation in ionic radii of Ti^{4+} (0.61 Å) and Fe^{3+} (0.67 Å) the expansion of the unit cell occurs and increase in lattice parameter values is obtained. Further, for higher content of TiO_2 i.e. $3 \leq x \leq 5$, lattice parameter increases because of the increased molecules of TiO_2 surrounding the Fe^{3+} nuclei at B sub-lattice sites. However, for the experimental substitution limit $x = 10$ Wt. %, a little fall in the value of lattice parameter is obtained showing the distortion in the lattice due to the higher % of secondary phase of TiO_2 created within the ferrite.

Chapter 5 77 A. D. Patil Ph. D Thesis The average crystallite size (D) for synthesized ferrite nanoparticles was investigated from the peak with the maximum intensity i.e. the peak (311) of XRD pattern

using Debye Scherer's equation [32], $= 0.9 \beta \cos \theta$ (1)

Where θ is the Bragg's angle, λ is the wavelength of X-rays and β is the full-width half- maximum (FWHM). The

computed crystallite size (D) values (Table 5.2) were decreased with an increase in TiO_2 doping composition. These values lie in between 20 to 33 nm which indicates that the prepared particles are the nanoparticles. The agglomeration of the particles was reported as the reason behind increase of the particle size in the nano ferrites [33]. In the present study the particle size of TiO_2 doped Ni-Cu-Zn ferrites is larger than that of the pristine Ni-Cu-Zn ferrite revealing the occurrence of agglomeration for the doped samples of ferrites. The variation in particle size is not much as compared to that in the lattice parameter values. The reason behind is that, in nano ferrites, the particle size depends upon temperature and time of the annealing [34]. In the present TiO_2 doped Ni-Cu-Zn ferrites both these factors i.e. time and temperature of annealing were kept constant for all the ferrite samples, owing to which, a little variation in particle sizes was reported. The X-ray density (d_x), can be investigated from the relation [35]. $d_x = \frac{8M}{N a^3}$ (2) Where N is Avogadro's number and M is the molecular weight. It is found that, there is an increment in X-ray density with the doping of TiO_2 molecules in Ni-Cu-Zn ferrite. It is because of the increasing amount of doping of TiO_2 , which is adding its molecular weight (47.867 amu) to the molecular weight of $\text{Ni}_0.4\text{Cu}_0.3\text{Zn}_0.3\text{Fe}_2\text{O}_4$ ferrite, due to which the molecular weight of the doped ferrites is increasing. The increase in molecular weight increases the density (d_x). Furthermore, the values of bulk density are smaller than the X-ray density. The variation in bulk and X-ray density is because of the formation of pores in the prepared samples. The hopping lengths L_B and L_A at the octahedral and tetrahedral sites respectively were obtained by employing the following equations from literature [36], $= \frac{a}{3}$ (3)

Chapter 5 78 A. D. Patil Ph. D Thesis = a 3 2 (4) It was found that the hopping lengths at L A and L B show similar trends as that of lattice constant. Further, the parameters such as tetrahedral and octahedral bond lengths (d_{AX} and d_{BX}), tetrahedral edge, octahedral shared and unshared edges (d_{AXE} , d_{BXE} and d_{BXEU}) for

Ni_{0.4} Cu_{0.3} Zn_{0.3} Fe₂ O₄ doped with TiO₂ additive were synthesized by sol gel method

can be obtained by using oxygen positional parameter 'u' and lattice constant 'a' values in the following equations [37]. $a = 3 - 1.4(5) = 3.2 - 11.4 + 43.6412(6) = 2.2 - 1.2(7) h = 2.1 - 2(8) h = 4.2 - 3 + 11.1612(9)$ The estimated values of these parameters are given in Table 5.3, from which it is seen that the tetrahedral and octahedral hopping lengths as well as tetrahedral edge, octahedral shared and unshared edges increased with TiO₂ additive doping up to 5 wt. % and for higher TiO₂ additive doping reduced. This is owing to less ionic radii of Ti⁴⁺ (0.61 Å) than that of Ni²⁺ (0.69 Å) and Fe³⁺ (0.67 Å) ions. 5.3.2 Field Emission Scanning Electron Microscopy The FESEM images of Ni-Cu-Zn ferrites for x = 0, 1, 3, and 10 wt. % of TiO₂ additive are shown in Figure 5.2(a). FESEM images reveal that all the prepared particles are spherical in shape and are agglomerated due to magnetic interactions. The average grain size is in between 42 to 50 nm. The elemental mapping and EDX were carried out which confirms the existence of elements like Zn, Ni, Fe, Cu, O and Ti in the selected samples (figure 5.2(b)).

Chapter 5 79 A. D. Patil Ph. D Thesis 5.3.3 Raman Spectroscopy Figure 5.3 illustrates the Raman spectra of TiO₂ doped Ni-Cu-Zn ferrites in the frequency range 100 to 800 cm⁻¹ at room temperature. According to the group theory, only five Raman active modes are possible for spinel ferrites viz. A_{1g}, E_g and three F_{2g} modes [38, 39]. The modes above 600 cm⁻¹ and below 600 cm⁻¹ are associated with metal-oxygen (M-O) (symmetrical stretching) bonding at tetrahedral sites and metal-oxygen bonding (symmetrical, anti-symmetrical bending) at octahedral sites respectively [40, 41]. The Raman bands observed for Ni-Cu-Zn ferrite doped with TiO₂ are depicted in Table 5.4. The Raman bands found at 145-150 cm⁻¹, 170-322 cm⁻¹, 310-485 cm⁻¹, 458-646 cm⁻¹, 664-697 cm⁻¹ corresponds to F_{2g} (1), F_{2g} (2), E_g, F_{2g} (3), and A_{1g} modes respectively. From Figure 5.3 and Table 5.4, it is obvious that the wave number position of bands were slightly changed with TiO₂ composition. This slight difference in Raman bands with different content of TiO₂ in Ni-Cu-Zn ferrite is linked with the rearrangement of cations between octahedral and tetrahedral sites. 5.3.4 Fourier Transform Infrared (FTIR) Spectroscopy Figure 5.4 displays the FTIR spectra of the Ni-Cu-Zn ferrite doped with various compositions of TiO₂. The spectra were obtained between 400-1000 cm⁻¹. The two strong peaks ν_1 (577-624 cm⁻¹) and ν_2 (397-424 cm⁻¹) are observed in each sample those are related

to vibrations of the metal ion-oxygen bonds in tetrahedral and octahedral sites respectively [42]. The

formation of such peaks evidenced that the spinel ferrite structure was formed in our studied ferrite samples. The variation in ν_1 and ν_2 peaks was attributed to the difference in bond lengths (Fe-O) associated with the tetrahedral and octahedral sites [43]. From Figure 5.4 and the Table 5.5, it is found that there is a small variation in peak positions with TiO₂ doping in Ni-Cu-Zn ferrite because of the redistribution or migration of cations between tetrahedral and octahedral sites in Ni-Cu-Zn ferrite doped with TiO₂ additive. It is found that frequency ν_1 for pristine sample is less than the doped samples. For doped ferrites, ν_1 decreased continuously with increasing doping till the 5 wt. % dopant level. For the dopant level \leq 2 wt. %, the decrease in ν_1 indicates the

Chapter 5 80 A. D. Patil Ph. D Thesis occupancy of Ti⁴⁺ ions at octahedral sites due to which the Fe³⁺ ions migrated to tetrahedral sites and bond lengths were increased and as a consequence decrease in vibrational frequencies (ν_1) was reported [50]. The possible cause behind decrease in ν_1 for dopant level < 2 wt. % is the deposition of TiO₂ molecules around the Fe³⁺ cations due to which the bond lengths were increased and consequently decrease in ν_1 value is reported. An apparent increase in ν_1 for the highest experimental doping of 10 wt. % was due to creation of lattice distortions by the TiO₂ phase with higher concentration (Table 5.1). The vibration frequency ν_2 increased up to 2 wt. % doping of TiO₂, clearly indicating Ti⁴⁺ occupancy at octahedral sites. However, for the TiO₂ doping < 2 wt. %, the ν_2 decreases till 5 wt. % and then suddenly increases for 10 wt. %. It clearly points towards the fact that the occupancy of Ti⁴⁺ at octahedral sites is not proportional to the doping (%) i.e. Ti⁴⁺ does not substituted the Fe³⁺ ion at octahedral sites for higher doping levels (< 2 wt. %) and finally larger change in the value of ν_2 confirms the creation of strong TiO₂ phase for 10 wt. % doping. Thus occurrence of spinel phase and a secondary phase of TiO₂ molecules is confirmed from FTIR analysis. 5.3.5 The UV-Vis. Diffused Reflectance Spectroscopy The optical properties of Ni-Cu-Zn ferrites doped with different concentrations of TiO₂ additives were investigated by using UV-Vis diffused reflectance spectrophotometer. The measurements were conducted between 200 to 800 nm and the obtained plots are displayed in Figure 5.5. The obtained spectra of the studied ferrites show absorption in the visible region. The absorption coefficients α were investigated from the Kubelka-Munk function given by the formula [44], $\alpha = \frac{1-R}{2R}$ (10) Where, R is reflectance value,

$F(R)$ is KubelkaMunk function and α is absorption coefficient. Moreover, in the Tauc relation [45, 46] values of the absorption coefficient were utilized to obtain band gap energy (E_g). The relation is given by, $\alpha h\nu = (h\nu - E_g)^2$ (11)

Chapter 5 81 A. D. Patil Ph. D Thesis Where A is proportionality constant, h is the Planck's constant and ν is the frequency of light. The band gap energy values of all selected samples were computed by depicting the graph of $(\alpha h\nu)^2$ versus $h\nu$ as shown in Figure 5.6. The band gap energies were deduced by extrapolating the linear portions of these graphs. The band gap energy values of Ni-Cu-Zn ferrites doped with different contents of TiO₂ additive are represented in the Table 5.5. It is evident from Table 5.5 that the band gap energy value of the pristine sample is less than the doped samples and there is decrement in the values of band gap energies with enhancement in the content of TiO₂ in the doped Ni-Cu-Zn ferrite. This is due to variation in the crystallite size of the studied samples. It also shows that the doped ferrite samples exhibit semiconducting nature.

5.3.6 Magnetic Properties

The magnetic properties of the ferrites were explored at room temperature by using vibrating sample magnetometer. The hysteresis

loops for TiO₂ doped Ni-Cu-Zn nanocrystalline spinel ferrites are given in Figure 5.7 which illustrates the change in magnetization with the applied magnetic field. The magnetization curve for all the samples exhibits normal characters of soft magnetic materials. From the hysteresis loops of the studied ferrite samples, values of the remanence magnetization (M_r), coercivity (H_c) and saturation magnetization (M_s) were obtained and summarized in the Table 5.6. It is obvious from the Table 5.6 that the saturation magnetization values are declining with the addition of TiO₂ due to the non-magnetic behavior of the titanium ions. This can be explained according to Neel's theory and super exchange interaction mechanism [47]. For TiO₂ doping level $x \leq 0.2$ wt. % the presence of a single spinel phase within the ferrites clearly indicates that the nonmagnetic Ti⁴⁺ ions were substituted in the Ni-Cu-Zn lattice. Since Ti⁴⁺ ions have strong preference towards B site, they occupy the site by replacing the Fe³⁺ ions which weakens the exchange interaction among A and B sites. As a result, decrement in the saturation magnetization with increment in the composition of TiO₂ in Ni-Cu-Zn nanocrystalline spinel ferrite is obtained or doping level $x \leq 0.2$ wt. % [48]. Further, the decrement in saturation magnetization is also due to a declination in the crystallite size of the prepared samples. The decrement in values of saturation

Chapter 5 82 A. D. Patil Ph. D Thesis magnetization for doping level $x < 2$ wt. % was due the accumulation of non-magnetic TiO₂ molecules surrounding the magnetic Fe³⁺ cations. The decrease in saturation magnetization for doping level (wt. %), $0.3 \geq x \leq 10$ is due to the increase in non-magnetic phase of TiO₂ (Table 5.1). The coercivity (H_c) values are enhanced with an increase in the content of TiO₂ in Ni-Cu-Zn ferrite which is linked with the reduction in crystallite size [49]. While remanent magnetization does not show regular variation with TiO₂ doping. The values of were investigated experimentally by using the equation [50], $M_r = \frac{M_s}{2} \left(\frac{M_w}{M_s} \right)^2$ Where M_s is the saturation magnetization and M_w is the molecular weight of the sample. The obtained values of are given in Table 5.6. The increase in oxygen vacancies due to TiO₂ doping is evident from this increase in values [51]. In ferrites, change in values depends upon the concentration of oxygen vacancies and there is a direct relation between the number of vacancies and magneton number [52].

5.3.7 Mössbauer spectroscopy

Mössbauer spectra measured at room temperature for the typical samples of Ni-Cu-Zn ferrites doped with 0, 2, 5 and 10 wt. % of TiO₂ are shown in Figure 5.8. It is obvious from the Mössbauer spectra that all the samples exhibit well-defined Zeeman split sextets, one of them corresponding to Fe³⁺ ions at the tetrahedral A-sites whereas second is corresponding to the Fe³⁺ ions at the octahedral B-site. No central paramagnetic contribution from the paramagnetic-Zn ions is observed in any of the sample revealing the ordered magnetic structure and the long-range magnetic interactions in all the samples. Saturation magnetization known to be directly proportional to hyperfine field. Hyperfine field (H_{hf}) does not changed much with the TiO₂ doping (Table 5.7) and can be qualitatively explained on the basis of Neel's super-exchange interactions [53]. Thus, it can be considered that TiO₂ does not enter into the Ni-Cu-Zn spinel ferrite and not replacing any of the ions in the spinel lattice. Thus, decrease in saturation magnetization could be related to increase in non-magnetic phase of TiO₂ in the composition. It is evident from Table 5.7 that Isomer shift (IS) at B-site is greater than IS at A-site and

Chapter 5 83 A. D. Patil Ph. D Thesis could be related to the large band separation of Fe³⁺-O²⁻ for the B-site ions compared to the A-site ions.

The range of values of IS indicated that Fe ions exist in 3+ valence state with high spin configuration [54]. The

line width (Γ) found to increase by small margin for A-site increased with TiO₂ doping. The increased broadening A-site with TiO₂ doping may be attributed to the increasing number of surrounding TiO₂ around Fe³⁺ nuclei at A sites. Nearly zero values of QS within the experimental error is an indication that the cubic symmetry is retained between the Fe³⁺

ions and its surrounding Ni, Cu and Zn ions even after TiO₂ doping in Ni-Cu-Zn spinel crystal. 5.3.8 Elastic properties The elastic constants are much important because they explain the nature of binding forces between atoms. The most common method used to determine the elastic properties of the ferrites is the ultrasonic pulse transmission method. Table 5.8 shows the ultrasonic wave velocities. It shows that the longitudinal (V_l), mean (V_m) and shearing (V_s) velocities were decreased with the addition of TiO₂ composition due to atomic binding forces. The longitudinal modulus (L), Young's modulus (E), Bulk modulus (K) and Modulus of rigidity (G) were calculated from the measured ultrasonic wave velocities by using the relations as given [55]. Longitudinal modulus, $(L) = \rho V_l^2$ (13) Young's modulus, $(E) = 9GK / 3K + G$ (14) Modulus of rigidity, $(G) = \rho V_s^2$ (15) Bulk modulus, $(K) = \rho (3V_l^2 - 4V_s^2) / 3$ (16) The variation in the elastic moduli of synthesized ferrite samples with TiO₂ composition is shown in Figure 5.9. From the Figure, it is seen that the values of elastic moduli initially increase with an increase in Ti up to 1 wt. %. For further addition of TiO₂ to Ni_{0.4}Cu_{0.3}Zn_{0.3}Fe₂O₄ ferrite, there is a slight decrease in the values of elastic moduli. This shows that atomic binding strength is increased with the addition of Ti up to 1 wt. % and then decreased [56].

Chapter 5 84 A. D. Patil Ph. D Thesis 5.3.9 Impedance spectroscopy The impedance spectroscopy used to obtain Nyquist plot or Cole-Cole plot is an experimental technique to understand electrical behavior in spinel ferrites. Oliver Heaviside first introduced the concept of impedance spectroscopy. This technique provides information about the real part as the resistive and imaginary part as the reactive component of a given sample. The Cole-Cole plot comprises typically two successive semicircles: the first semicircle is of the grain boundary at low frequency and the second is of grain or bulk properties of the materials at high frequency. Impedance spectroscopy (Cole-Cole) is studied by plotting imaginary (Z'') part against real (Z') part of the impedance. Figure 5.10 shows Cole-Cole plots for all Ni_{0.4}Cu_{0.3}Zn_{0.3}Fe₂O₄ ferrite samples doped with TiO₂. The Cole-Cole plots show appearance of only one incomplete semicircle which indicates that grain boundary resistance is dominating and it corresponds to conduction due to only grain boundary for all samples in the low-frequency region. From the graph, it is seen that with the increase in TiO₂ composition up to 5 wt. % the diameter of semicircle increases which indicates that impedance increases and conductivity decreases and hence relaxation time increase. For the sample with 10 wt. % of TiO₂ composition, decrease in the diameter of the semicircles was observed. 5.3.10 Dielectric properties 5.3.10.1 Dielectric constant The dielectric properties measured were dielectric constant (ϵ'), AC conductivity (ζ_{ac}) and dielectric loss tangent ($\tan\delta$). Dielectric properties of nanocrystalline spinel Ni_{0.4}Cu_{0.3}Zn_{0.3}Fe₂O₄ ferrite doped with TiO₂ were studied at room temperature in frequency range from 50 Hz to 5 MHz. In ferrites, the dielectric constant is influenced by various factors like the microstructural arrangement, density, cation distribution and also charge polarization. The formula for calculating dielectric constant was given as,

Chapter 5 85 A. D. Patil Ph. D Thesis A d C

$\epsilon' = \frac{C}{\epsilon_0 A d}$ (17) Where C is capacitance,

d is thickness, A is

the cross-sectional area of the pellet and ϵ_0 is

permittivity of free space.

Figure 5.11 represents variation in dielectric constant with frequency for all samples at room temperature. It is seen that at lower frequencies dielectric constant is higher. It decreased with increase in frequency. After a certain increase in frequency it remains constant for all samples doped with TiO₂. This observed nature of the response is a normal dielectric behavior as reported by other studies [57–60]. The sample with 1 wt. % TiO₂ content shows the maximum dispersion due to the presence of an excess amount of Fe²⁺ ions. All the samples show dispersion at low frequency and can be attributed as a space charge polarization. As per Maxwell–Wagner two-layer model and Koop's phenomenological theory [61, 62], space charge polarization is because of highly conducting grains present in separated poorly conducting grain boundaries. Therefore, in electrical conduction grain boundaries are more effective as compared to grains at lower frequencies. If grain boundaries are thin, the dielectric constant is higher. Also, the frequency independent behavior is observed at higher frequencies. This is

due

to the fact that after a certain frequency of external alternating field, the electronic exchange between Fe²⁺ and

Fe³⁺ does not follow the

field. 5.3.10.2

Dielectric Loss Tangent Figure 5.12 shows the variation in dielectric loss tangent with respect to the frequency at room temperature. The results similar to dielectric constant were obtained for dielectric loss tangent. It decreased with increased frequency for all samples due to a strong association between the conduction mechanism and dielectric behavior of ferrites. Figure 5.12 also indicates that the sample with 10 wt. % shows the highest dielectric loss tangent than the undoped sample. For 10 wt. % samples hopping of electrons between Fe 2+ and Fe 3+ ions at the octahedral site is increased because of migration of Fe 3+ ions to octahedral [B] site. Thus the dielectric loss tangent increases. In the low-frequency region of dielectric loss tangent curve, peaks were observed. This is because of

Chapter 5 86 A. D. Patil Ph. D Thesis the matching of the hopping frequency of the electron Fe 2+ and Fe 3+ ions to the applied electric field frequency for all samples. 5.3.10.3 AC conductivity The AC conductivity study gives the behavior of charge carriers under an AC field, the mechanism of conduction and mobility of charges [63]. AC conductivity of all synthesized samples was obtained using the following relation, $\sigma = \epsilon_0 \epsilon' \omega \tan \delta$ (18) Where ω is applied field frequency, ϵ_0 is absolute permittivity, ϵ' is relative permittivity and $\tan \delta$ is loss tangent. The room temperature AC conductivity variation for all samples doped with TiO₂ was studied in the 50 Hz to 5 MHz range of frequency. Figure 5.13 shows the variation in AC conductivity with the logarithm of the frequency. It is observed that AC conductivity increased with increased frequency for selected samples. The behavior of ac conductivity in ferrite can be explained on the basis of the Maxwell-Wagner model for the dielectric.

Chapter 5 87 A. D. Patil Ph. D Thesis References [1] D.Stoppels, J.Magn.Magn. Mater. ,160(1996)323 [2] Hirota, T. Aoyama, S. Enomoto, et al., J Magn.Magn.Mater., 205(1999)283 [3] J. J. Shrotri, S. D. Kulkarni, C.E. Deshpande, et al., J. Mater. Chem. Phys., 59(1999)1 [4] A. Yusmar, L. Armitasaria, E. Suharyadi, J. Mater. Today. Proc., 5(2018)14955 [5] U. R. Ghodake, R. C. Kambale, S. S. Suryavanshi, J. Ceram. Int., 43(2017)1129 [6] P.P. Khirade, S.D. Birajdar, R.C. Alange, et al., J Supercond. Nov. Magn.,28(2015)3351 [7] S.E. Shirsath, D. Wang, S.S. Jadhav, M. L. Mane, S. Li, Ferrites obtained by sol- gel method, in: L. Klein, M. Aparicio, A. Jitianu (Eds.), Handbook of Sol-Gel Science and Technology, Springer, Cham, (2018)695 [8]

B. G. Toksha, S. E. Shirsath, M. L. Mane, S.M. Patange, S. S. Jadhav, K. M. Jadhav, J. Phys. Chem. ,C 115 (2011) 20905 [9]

N.Y. Mostafa, M.M. Hessien, A.A. Shaltout, ,J.Alloys Comp., 529 (2012) 29 [10] R.Rathi, R.Neogi, J.Mater.Today: Proceed.,3 (2016) 243 [11] H. Ji, Z.Lan, Z.Xu, H. Zhang, G.J. Salamo,IEEE Trans. Magnetics. 49 (2013) 4277 [12] B.A. Patil, R.D. Kokate,Procedia Manufacturing 20 (2018) 147 [13] P. Choudhary, P. Sharma, A. Kumar, M.A. Dar, D. Varshney,AIP Conf. Proceed., 020317 (2016)1728 [14] S. C. Mazumdar, F. Alam, U. H. Tanni, K. Kali, B. C. Das, M. N. I. Khan, J. Mater. Sci. Applications, 10 (2019) 733 [15] B.Wang,J.Du, Y. Liu, G.Yao, Int. J. Appl. Ceram. Technol., 12 (2015) 658 [16] O. Mirzaee, J.King Saud Univ.–Engg.Sci., 26 (2014)152 [17] B. Sun, F. Chen, W. Yang, H. Shen, D. Xie, J. Magn. Magn. Mater. , 349 (2014)180

Chapter 5 88 A. D. Patil Ph. D Thesis [18] J.S.Kounsalye, P. B. Kharat, M. V. Shishode, et al., J. Mater. Sci. Mater. Electron. , 28(2017)17254 [19] R. Rathi, B.Pushpinder,R. L. Neogi,Int. J. Chem. Phys. Sci.,3(2014)132 [20] J. Fan, F. R. Sale, J. Eur. Ceram. Soc.,20(2000)2743 [21] K.Praveena, K.Sadhana S. Srinath, et al., J. Phys. Chem. Solids., 74(2013)1329 [22] S.S. Suryavanshi, R.S. Patil, S.A. Patil, et al., J. Less-Common. Met., 168(1991)169 [23] T.M. Meaz, S.M. Attia, A.M. Abo El Ata, J.Magn.Magn. Mater., 257(2003)296 [24] M.A. Ahmed, G. Abd-Ellatif, M. Rashad, J.Magn.Magn. Mater., 232(2001)194 [25] S.S. Desai, R.A. Pawar, S.S. Jadhav, et al., J.Supercond. Nov.Magn., 29(2016)2635 [26] R. Jasrotia, P. Puri, A. Verma, V.P. Singh, J. Sol. Stat. Chem. ,289 (2020) 121462 [27] M.F. Huq, D.K. Saha, R. Ahmed, Z.H. Mahmood, J. Sci. Res., 5 (2013) 21 [28] C. Virlan, F. Tudorache, A. Pui, Tertiary Ni-Cu-Zn ferrites for improved humidity sensors: A systematic study, 13 (2020) 2066 [29] S.K. Gore, S.S. Jadhav, U.B. Tumberphale, S.M. Shaikh, M. Naushad, R.S. Mane, Sol.Stat.Sci.,74 (2017) 88 [30] K. Thamaphat, P. Limsuwan, B. Ngotawornchai, J. Nat. Sci. , 42 (2008) 357 [31] M.S. Hossain, Y. Aktery, M. Shahjahany, M.S. Basharz, M. H. A. Begum, M. M. Hossain, S. Islam, N. Khatunx, M. Al-Mamunx, J. Advan. Dielectrics ,9 (2019) 1950020 [32] V.G.Patil, S.E. Shirsath, S.D.More, S.J. Shukla, K.M. Jadhav, J.Alloys Comp., 488 (2009) 199 [33] A.B. Mugutkar, S.K. Gore, R.S. Mane, S.M. Patange, S.S. Jadhav, S.F. Shaikh, A.M. Al-Enizi, A. Nafady, B.M. Thamer, M. Ubaidullah, J. Alloy. Comp. 844 (2020) 156178 [34]

B.G. Toksha, S.E. Shirsath, S.M. Patange, K.M. Jadhav,

Sol. Stat. Commun. 147 (2008) 479 [35] O.M.Hemeda, A.Tawfik,M.Mostafa, M.Zaki, M.I. Abd-el-Ati, J.Phys.: Conf. Series, 1253 (2019) 012026

Chapter 5 89 A. D. Patil Ph. D Thesis [36] M.S. Patil1, M.N. Sarnaik, V.D. Murumkar, A.A. Pandit, D.R. Shingule, Int.J.Innovative Sci.Engg. Tech., 4(2017)91 [37] S. B. Somvanshi, S. A. Jadhav, M. V. Khedkar, P. B. Kharat, S. D. Morec, K. M. Jadhav, Ceram. Int. ,46 (2020)13170 [38] H. Kumar, R.C. Srivastava, J.P. Singh, P. Negi, H.M. Agrawal, D.Das, K.H.Chae,

J.Magn.Magn.Mater, 401(2016) 16 [39] S. Thota, S.C. Kashyap, S.K. Sharma, V.R. Reddy,

Mater. Sci.Engg.B, 206 (2016) 69 [40] K. Sabri, A. Rais, K. Taibi, M. Moreau, B. Ouddane, A. Addou, Physica B ,501 (2016) 38 [41] R.A. Pawar, S.M. Patange, Q.Y. Tamboli,V. Ramanathan, S.E. Shirsath, Ceram.Int.,42 (2016) 16096 [42] R. Waldron, Infrared Spectra of Ferrites, Physical Review, 99 (1955)1727 [43] K.R. Babu, K.R. Rao, B.R.Babu, J.Magn.Magn.Mate.,434 (2017) 118 [44] B.M. Ali, M.A. Siddig, Y.A. Alsabah, A.A. Elbadawi, A.I. Ahmed, J.Advances Nanopart. ,7(2018) 1 [45] R. Tholkappian, K. Vishista,Int. J. Mater. Res., 106 (2015) 127 [46] C.Kumari, H.K.Dubey, F.Naaz,P.Lahiri,Phase Trans., 93(2020) 207 [47] S.M. Patange, S.E. Shirsath, G.S. Jangam, K.S. Lohar, S.S. Jadhav, K.M. Jadhav, J. Appl. Phys. ,109 (2011) 053909 [48] V.Vaithyanathan, K.Ugendar, J.A. Chelvane, K.K. Barathi, S.S.R. Inbanathan, J.Magn.Magn.Mater. ,382 (2015)88 [49] A.B.Mugutkar, S.K. Gore, U.B. Tumberphale, V.V. Jadhav, R.S. Mane, S.M. Patange, S.E. Shirsath, S.S. Jadhav, J.Rare Earths, (2019) [50] A.B. Mugutkar, S.K. Gore, U.B. Tumberphale, V.V. Jadhav, R.S. Mane, S.M. Patange, S.F. Shaikh, M. Ubaidullah, A.M. Al-Enizi, S.S. Jadhav, J. Magn. Magn. Mater. ,502 (2020) 166490 [51] G.H. Jaffari, A.K. Rumaiz, J.C. Woicik, S.I. Shah, J. Appl. Phys. ,111 (2012) 093906

Chapter 5 90 A. D. Patil Ph. D Thesis [52] C.E.R. Torres, G.A. Pasquevich, P.M. Zelis, F. Golmar, S.P. Heluani, S.K. Nayak, W.A. Adeagbo, W. Hergert, M. Hoffmann, A. Ernst, P. Esquinazi, S.J. Stewart, Phy. Rev. B, 89 (2014) 104411 [53] L. Neel, Superficial magnetic anisotropy and orientation superstructures, C.R. Acad. Sci. Paris.,230 (1950)375 [54] S. M. Patange, S.S. Desai, S.S. Meena, S. M. Yusuf, S.E. Shirsath, RSC Advances, 5 (2015) 91482 [55] S.M. Patange, S.E. Shirsath, S.P. Jadhav, et al., J. Mol. Struct. ,1038(2013)40 [56] W.A. Wooster, Rep Prog Phys. , 16(1953)62 [57] S. Mahalakshmi, K. SrinivasaManja, J. Alloy Compd., 457(2008)522 [58] Hsiang H, Chen WS, Chang YL, et al.,Am. J. Mater. Sci. ,(2011)40 [59] D. Ravinder, P.V.B.Lett.,57(2003)4344 [60] N. Rezlescu, E. Rezlescu, Solid. State.Commun.,14(1974)69 [61]

J. C. Maxwell. Electricity and magnetism 1 Oxford: Oxford University Press, (1929) [62] K.W. Wagner.

ZurTheorie der unvollkommenenDielektrika, Ann. Phys.,345(1913)817 [63] K.M. Batoo, M.S.A. El-Sadek,J. Alloy. Compd.,566(2013)112

Chapter 5 91 A. D. Patil Ph. D Thesis Table5.1: Discrepancy factor (R_{wp}), expected values (R_{exp}), and goodness fit factor (χ^2), spinel phase %, and TiO₂ phase % in Ni_{0.4}Cu_{0.3}Zn_{0.3}Fe₂O₄ ferrites doped with varying wt. % of TiO₂ additive. wt. % TiO₂ R_{exp} R_{wp} χ^2 Spinel phase % TiO₂ phase % 0 16.1 12.2 1.71 100 00 1 19.5 11.9 2.65 100 00 2 26.6 14.4 3.31 100 00 3 16.1 10.6 2.28 95.8 4.2 5 15.8 11.8 1.77 94.2 5.8 10 16.7 12.7 1.71 91.4 8.6

Chapter 5 92 A. D. Patil Ph. D Thesis Table5.2: Parameters obtained from the XRD pattern of Ni_{0.4}Cu_{0.3}Zn_{0.3}Fe₂O₄ ferrites doped with different wt. % of the TiO₂ additive TiO₂ wt.% a (Å) D (nm) (g/cm³) L A (Å) L B (Å) 0 8.3030 21 5.516 3.5953 2.93 1 8.3035 33 5.664 3.5954 2.93 2 8.3252 28 5.761 3.6048 2.94 3 8.3772 28 6.163 3.6273 2.96 5 8.3778 27 6.823 3.6275 2.96 10 8.3461 27 5.806 3.6138 2.95

Chapter 5 93 A. D. Patil Ph. D Thesis Table 5.3: Tetrahedral bond length, octahedral bond length, tetrahedral edge, octahedral edge (shared and unshared) for Ni_{0.4}Cu_{0.3}Zn_{0.3}Fe₂O₄ with TiO₂ additive. Wt. % TiO₂ Tet. Bond Lengthd AX (Å). Oct. BondLengthd BX (Å) Tet. Edge d AXE (Å) Oct. Edge (Shared & Unshared) d BXE (Å) d BXEU (Å) 0 1.9845 1.9719 3.2408 2.6302 2.9425 1 1.9844 1.9720 3.2410 2.6303 2.9427 2 1.9898 1.9772 3.2498 2.6372 2.9504 3 2.0022 1.9895 3.2697 2.6537 2.9688 5 2.0024 1.9897 3.2700 2.6539 2.9690 10 1.9848 1.981 3.2576 2.6438 2.9578

Chapter 5 94 A. D. Patil Ph. D Thesis Table5.4: Raman modes with wave numbers for Ni_{0.4}Cu_{0.3}Zn_{0.3}Fe₂O₄ doped with TiO₂ additive.The attached Table shows the values of the IR vibration frequencies ν_1 and ν_2 possessed by the ferrites Sr. No. of the peak in the spectra Raman Modes Raman Shift (Cm⁻¹) x= 1wt.% x= 2wt.% x= 3wt.% x= 10 wt.% 1 F 2g (1) 149 150 145 150 2 F 2g (2) 313 312 322 170 3 E g 480 480 485 310 4 F 2g (3) 638 637 646 458 5 A 1g 689 688 697 664

Chapter 5 95 A. D. Patil Ph. D Thesis Table5.5: Values of absorption bands (ν_1 and ν_2) and band gap energy for Ni_{0.4}Cu_{0.3}Zn_{0.3}Fe₂O₄ doped with TiO₂ additive wt.% TiO₂ Absorption Bands cm⁻¹ E g eV ν_1 ν_2 0 579.87 397.32 1.115 1 624.52 403.41 1.528 2 624.01 424.72 1.502 3 619.57 407.37 1.464 5 577.08 399.47 1.424 10 622.87 416.22 1.411

Chapter 5 96 A. D. Patil Ph. D Thesis Table 5.6: Magnetic parameters of Ni_{0.4}Cu_{0.3}Zn_{0.3}Fe₂O₄ ferrites doped with different concentrations of the TiO₂ additive. Wt.% TiO₂ Magnetization Saturation (M_s) (emu gm⁻¹) η B (μ B) Coercivity (H_c) (Oe) Magnetization Remenant (M_r) (emu gm⁻¹) 0 71.684 3.052 40.874 7.278 1 71.227 3.114 46.592 8.624 2 70.920 3.115 51.224 6.652 3 67.672 3.182 51.329 7.653 5 66.166 3.196 51.630 7.768 10 63.566 3.434 53.424 9.692

Chapter 5 97 A. D. Patil Ph. D Thesis Table5.7: The line width (Γ), isomer shift (IS), quadru pole splitting (QS), Hyperfine magnetic field (H_{hf}) and relative area (A)

in percentage of tetrahedral and octahedral sites of Fe³⁺ ions for TiO₂ doped Ni_{0.4} Cu_{0.3} Zn_{0.3} Fe₂ O₄ ferrite derived from Mössbauer spectra recorded at room temperature.

Sextet A: Tetrahedral site, Sextet B: Octahedral site

Sample Iron site Γ (mm/s) IS (mm/s) QS (mm/s) H hf (Tesla) A (%) 0% Sextet A 0.69 ± 0.02 0.29 ± 0.01 -0.02 ± 0.01 47.5 ± 0.1 67 Sextet B 1.07 ± 0.07 0.32 ± 0.02 0.02 ± 0.01 42.4 ± 0.1 33 2% Sextet A 0.73 ± 0.03 0.29 ± 0.01 0.03 ± 0.02 47.1 ± 0.1 70 Sextet B 0.73 ± 0.03 0.41 ± 0.02 -0.01 ± 0.01 41.9 ± 0.1 30 5% Sextet A 0.74 ± 0.02 0.29 ± 0.01 0.01 ± 0.02 47.1 ± 0.1 72 Sextet B 0.74 ± 0.02 0.36 ± 0.02 0.07 ± 0.04 41.6 ± 0.1 28 10% Sextet A 0.76 ± 0.01 0.29 ± 0.01 -0.02 ± 0.02 47.5 ± 0.1 71 Sextet B -0.76 ± 0.01 0.29 ± 0.02 -0.05 ± 0.02 42.7 ± 0.1 29

Chapter 5 98 A.

D. Patil Ph. D Thesis Table 5.8: Ultrasonic wave velocities TiO₂ Composition in Nanocrystalline Ni_{0.4} Cu_{0.3} Zn_{0.3} Fe₂ O₄ ferrites. Composition TiO₂ in % V L (m/Sec) V S (m/Sec) V m (m/Sec) 0 4082 2357 2617 1 4030 2327 2583 2 4004 2312 2567 3 3978 2297 2550 5 3952 2282 2533 10 3900 2252 2500

Chapter 5 99 A. D. Patil Ph. D Thesis Fig. 5.1: Rietveld refined x-ray diffraction patterns of the TiO₂ doped Ni_{0.4} Cu_{0.3} Zn_{0.3} Fe₂ O₄ ferrites. Bragg's peak positions are pointed by green and pink colored vertical lines at the bottom of XRD of the ferrite with x = 10 wt. %.

Chapter 5 100 A. D. Patil Ph. D Thesis Fig. 5.2 (a): SEM images of TiO₂ doped Ni_{0.4} Cu_{0.3} Zn_{0.3} Fe₂ O₄ ferrites

Chapter 5 101 A. D. Patil Ph. D Thesis Fig. 5.2 (b): Elemental mapping and EDX pattern of TiO₂ doped Ni_{0.4} Cu_{0.3} Zn_{0.3} Fe₂ O₄ ferrite

Chapter 5 102 A. D. Patil Ph. D Thesis Fig. 5.3: Raman Spectra of Ni_{0.4} Cu_{0.3} Zn_{0.3} Fe₂ O₄ ferrites doped with varying wt. % TiO₂ additive.

Chapter 5 103 A. D. Patil Ph. D Thesis . Fig. 5.4: FTIR Spectra of TiO₂ doped Ni_{0.4} Cu_{0.3} Zn_{0.3} Fe₂ O₄ ferrites

Chapter 5 104 A. D. Patil Ph. D Thesis Fig. 5.5: The Absorbance spectra of TiO₂ doped Ni_{0.4} Cu_{0.3} Zn_{0.3} Fe₂ O₄ ferrites.

Chapter 5 105 A. D. Patil Ph. D Thesis Fig. 5.6: Tauc plots of Ni_{0.4} Cu_{0.3} Zn_{0.3} Fe₂ O₄ ferrites doped with varying content of TiO₂ additive.

Chapter 5 106 A. D. Patil Ph. D Thesis Fig. 5.7: Room temperature magnetic hysteresis loops for TiO₂ doped Ni- Cu-Zn ferrites. Inset shows the variations of coercivity with varying TiO₂ doping.

Chapter 5 107 A. D. Patil Ph. D Thesis Fig. 5.8: Room temperature Mössbauer spectra for the typical samples (0, 2, 5 and 10%) of TiO₂ doped Ni_{0.4} Cu_{0.3} Zn_{0.3} Fe₂ O₄ ferrites

Chapter 5 108 A. D. Patil Ph. D Thesis Fig. 5.9: Variation of elastic moduli in Ni_{0.4} Cu_{0.3} Zn_{0.3} Fe₂ O₄ ferrite with TiO₂ composition.

Chapter 5 109 A. D. Patil Ph. D Thesis Fig. 5.10: Cole-Cole plots for all Ni_{0.4} Cu_{0.3} Zn_{0.3} Fe₂ O₄ samples doped with TiO₂.

Chapter 5 110 A. D. Patil Ph. D Thesis Fig. 5.11: Variation of dielectric constant with the logarithm of Frequency at room temperature.

Chapter 5 111 A. D. Patil Ph. D Thesis Fig. 5.12: Variation of Dielectric loss tangent with the logarithm of frequency at room temperature.

Chapter 5 112 A. D. Patil Ph. D Thesis Fig. 5.13: Variation of AC Conductivity with the logarithm of the frequency .

Chapter 6 113 A. D. Patil Ph.D. Thesis Chapter 6 Conclusions 6.1 Conclusion on Ni_{0.4} Cu_{0.3} Zn_{0.3} Fe₂ O₄ + xTa₂ O₅ (for x = 0, 1, 2, 3, 5 and 10 wt. %) Sol gel method was used for the synthesis of Ni_{0.4} Cu_{0.3} Zn_{0.3} Fe₂ O₄ doped with Ta₂ O₅ additive. The structural analysis of all the investigated samples was done with Rietveld refinement using FULLPROF software. The result shows a cubic spinel structure and formation of secondary phase of FeTaO₄ with increasing Ta₂ O₅ composition. The lattice constant decreased with the increase in Ta₂ O₅ doping content. The

crystallite size was obtained using Debye-Scherrer's formula and it was found that crystallite size of the

prepared samples was increased with an increase in content of Ta₂O₅ additive. Spinel structure of the investigated samples was confirmed by observing two main absorption bands in FTIR spectrum. There is variation in force constant value of ions as well as bond lengths of cations and oxygen ions at the tetrahedral and octahedral site in NiCuZn ferrite doped with Ta₂O₅ additive. Also there was no systematic variation in the ratio μ_1/μ_2 which shows that Ta₂O₅ additive do not considerably alter the site occupancy of cations present in the NiCuZn ferrite system. SEM analysis shows spherical shaped particles with some agglomeration. The band gap energies of synthesized ferrite samples were obtained from UV-Visible diffused reflectance spectra and increased with the Ta₂O₅ additive concentration of ≤ 5 wt.%, however, further increase in Ta₂O₅ doping concentration of < 5 wt% decrease the band gap energy. There was decrement in saturation magnetization with enhancement in Ta₂O₅ additive concentration in NiCuZn ferrite samples. DC electrical resistivity was decreased with increment in temperature. The computed values of activation energy were found to be higher for the paramagnetic

Chapter 6 114 A. D. Patil Ph.D. Thesis region than the ferromagnetic region. The results for the dielectric constant and dielectric loss tangent were decreased with an increase in frequencies for Ta₂O₅ doped samples. Further, the estimated AC conductivity values were increased with Ta₂O₅ additive composition. 6.2 Conclusion on Ni_{0.4} Cu_{0.3} Zn_{0.3} Fe₂O₄ + xTiO₂ (for x= 0, 1, 2, 3, 5 and 10 wt. %) Nanocrystalline Ni-Cu-Zn ferrites (Ni_{0.4} Cu_{0.3} Zn_{0.3} Fe₂O₄) doped with varying wt. % of TiO₂ additive were successfully synthesized by the sol-gel method. The analysis of XRD data through Rietveld refinement has revealed the creation of cubic spinel phase having Fd $\bar{3}$ m space group within the ferrites. Further, with the addition of TiO₂ in Ni_{0.4} Cu_{0.3} Zn_{0.3} Fe₂O₄ ferrite, a secondary phase with a space group I41/amd was observed for x ≥ 0.3 wt. % of doping. There is an increment in the values of lattice parameter up to 5 wt. % of TiO₂ doping and for higher doping of 10 wt. % of TiO₂ it declines. FESEM morphology depicts the agglomeration of spherical shaped particles at few places. The compositional purity of prepared ferrites was confirmed from elemental mapping and energy dispersive x-ray spectroscopy. From the Raman and FTIR spectra, spinel cubic structure of the investigated ferrite samples along with the creation of secondary phase of TiO₂ (for x ≥ 0.3 wt. %) was confirmed. From the plots, the values of band gap energy for the studied samples were investigated and it is evident that the band gap energy value of the pure sample is less than the doped samples and there is a decrement in band gap energy with rise in TiO₂ content in Ni-Cu-Zn ferrite. Magnetic study depicts that the saturation magnetization was reduced with rise in the TiO₂ concentration. Also, all the samples exhibit normal characters of soft magnetic materials at room temperature. Mössbauer spectra analysis suggested that the TiO₂ ions do not accommodate in the ferrite lattice and decrease in saturation magnetization is mainly related to increase in non-magnetic phase of TiO₂ in the ferrites. The ultrasonic pulse transmission method was employed to determine the elastic properties of the ferrites.

The elastic constants initially increased with an increase in TiO₂ up to 1 wt % and then

declined with the further addition of TiO₂. LCR-Q meter was used

Chapter 6 115 A. D. Patil Ph.D. Thesis

to study the dielectric properties within 50 Hz to 5 MHz range of the frequency. The dielectric constant (ϵ') as well as dielectric loss tangent was

decreased continuously with increased frequency for all the selected samples at room temperature revealing normal dielectric behavior of ferrites. Also, the AC conductivity was increased with an increase in the frequency of all the selected samples. Cole-Cole plots were obtained for all

the investigated samples and showed a

single semicircle which indicates that the electrical conduction process appears only due to grain boundaries. 6.3

Scope for Future Work An elaborate research work is undertaken after identifying the objectives and defined problem statement based on exhaustive literature survey. The objectives identified are accomplished with various experimental techniques. The present work would ultimately lead to miniaturization and high efficiency electronic devices. It is concurred that, the applications of electronic devices required soft magnetic materials as its fundamental magnetic component and NiCuZn ferrite with presently selected dopant is a suitable and promising candidate for these demands and are considered for multilayer chip inductors applications. Further confirmations in this direction with the device level demonstrations of the present compositions would be conclusive and fruitful, which remains as a scope of the present work.

90%

MATCHING BLOCK 1/44

W [https://www.researchgate.net/publication/28254 ...](https://www.researchgate.net/publication/28254...)

The elastic constants initially increased with an increase in TiO₂ up to 1 wt. % and then

96%

MATCHING BLOCK 2/44

W [https://www.researchgate.net/publication/28254 ...](https://www.researchgate.net/publication/28254...)

frequency for all the selected samples at room temperature revealing normal dielectric behavior of ferrites. Also, the AC conductivity was increased with an increase in the frequency of all the selected samples. Cole-Cole plots were obtained for all

100%

MATCHING BLOCK 3/44

W [https://www.researchgate.net/publication/28254 ...](https://www.researchgate.net/publication/28254...)

single semicircle which indicates that the electrical conduction process appears only due to grain boundaries.

75%

MATCHING BLOCK 4/44

W [https://docplayer.net/150337558-Doctor-of-phil ...](https://docplayer.net/150337558-Doctor-of-phil...)

H The relative permeability is given by the ratio of the magnetic permeability to that of free space = 0

50%

MATCHING BLOCK 5/44

W [https://docplayer.net/150337558-Doctor-of-phil ...](https://docplayer.net/150337558-Doctor-of-phil...)

to the intrinsic atomic level interaction among metal ions and oxygen. This enables the ferrite to find out applications at maximum frequencies and

87%

MATCHING BLOCK 6/44

W [http://pr.hec.gov.pk/jspui/bitstream/12345678 ...](http://pr.hec.gov.pk/jspui/bitstream/12345678...)

The properties of spinel ferrites depend on distribution of cations between the

100%

MATCHING BLOCK 8/44

W [https://www.researchgate.net/profile/Carlos_Ar ...](https://www.researchgate.net/profile/Carlos_Ar...)

A. Hagfeldth, M. Gratzel, Chem. Rev., 95(1995) 49 [14] S. Prasad, N. S. Gajbhiye, J. Alloys Compd. , 265 (1998) 87 [15] B. Viswanathan, V.R.K. Murthy: Ferrite Materials. Springer Verlag, Berlin,(1990) [16]

41%

MATCHING BLOCK 9/44

W [http://repository.sustech.edu/bitstream/handle ...](http://repository.sustech.edu/bitstream/handle...)

is smaller than that of the B lattice (M_B). Therefore net saturation magnetization (M_s) is represented as $M_s = |M_B - M_A|$

90%

MATCHING BLOCK 7/44

W [https://docplayer.net/150337558-Doctor-of-phil ...](https://docplayer.net/150337558-Doctor-of-phil...)

E. Shirsath, B. G. Toksha, M. L. Mane, V. N. Dhage, D. R. Shengule, K. M. Jadhav, Powder Technology, 212 (2011) 218 [17] S.

95%

MATCHING BLOCK 11/44

W <http://www.jetir.org/papers/JETIR2010314.pdf>

Electricity and Magnetism, Oxford University Press.New York, 1(1973)828 [25] K.W.Wagner,

64%

MATCHING BLOCK 15/44

W [https://www.researchgate.net/publication/25677 ...](https://www.researchgate.net/publication/25677...)

Scanning Electron Microscope (SEM) (3) Energy Dispersive Spectroscopy (EDX) (4) Infrared spectroscopy (IR) (5) Raman Spectroscopy (6) Vibrating Sample Magnetometer (VSM) (7)

100%

MATCHING BLOCK 10/44

W [https://docplayer.net/150337558-Doctor-of-phil ...](https://docplayer.net/150337558-Doctor-of-phil...)

Field Emission Scanning Electron Microscopy (FE-SEM) Scanning electron microscopy (

91%

MATCHING BLOCK 12/44

W [https://docplayer.net/150337558-Doctor-of-phil ...](https://docplayer.net/150337558-Doctor-of-phil...)

The relationship between induced magnetic flux density (B) and magnetizing force (H)

44%

MATCHING BLOCK 13/44

W [https://docplayer.net/150337558-Doctor-of-phil ...](https://docplayer.net/150337558-Doctor-of-phil...)

t is the thickness of the sample, A is cross-sectional area of the sample, ρ is the resistivity and R is the resistance of the

67%

MATCHING BLOCK 18/44

W [https://www.researchgate.net/publication/22368 ...](https://www.researchgate.net/publication/22368...)

dielectric constant (ϵ'), loss tangent ($\tan\delta$) and AC conductivity as a function of frequency in the range 50 Hz to 5 MHz at room temperature.

95%

MATCHING BLOCK 14/44

W [https://www.researchgate.net/publication/28254 ...](https://www.researchgate.net/publication/28254...)

of the pellet, ϵ_0 is the permittivity of the free space,

96%

MATCHING BLOCK 22/44

W [https://www.researchgate.net/publication/26956 ...](https://www.researchgate.net/publication/26956...)

Introduction The study of spinel ferrite is of great importance from both fundamental and

50%

MATCHING BLOCK 16/44

W <http://www.jetir.org/papers/JETIR2010314.pdf>

in the range 50Hz to 5 MHz. The dielectric constant was estimated using formula; $A d C p \dots$ (1) Where C_p is parallel capacitance, d is thickness

58%

MATCHING BLOCK 17/44

W [https://docplayer.net/150337558-Doctor-of-phil ...](https://docplayer.net/150337558-Doctor-of-phil...)

in the lattice constant may be due to the difference in ionic radii of Ta, Ni, Cu, Zn and Fe ions. The ionic radii of

70%

MATCHING BLOCK 23/44

W [https://www.researchgate.net/publication/22334 ...](https://www.researchgate.net/publication/22334...)

Scherrer's formula [29] $D = 0.9 \lambda / \beta \cos\theta$ (3) Where λ is the wavelength of x-rays, β is the full width at half-maximum (FWHM) and θ is the

78%

MATCHING BLOCK 19/44

W [http://pr.hec.gov.pk/jspui/bitstream/12345678 ...](http://pr.hec.gov.pk/jspui/bitstream/12345678...)

can also be justified on the basis of exchange interactions between tetrahedral and octahedral

100%

MATCHING BLOCK 20/44

W [https://docplayer.net/150337558-Doctor-of-phil ...](https://docplayer.net/150337558-Doctor-of-phil...)

E.Shirsath, R.H.Kadam, S.M.Patange, M.L.Mane,

87%

MATCHING BLOCK 21/44

W [https://docplayer.net/150337558-Doctor-of-phil ...](https://docplayer.net/150337558-Doctor-of-phil...)

Reddy, K. V. Siva Kumar, V. R. K. Murthy, R. R. Reddy,

87%

MATCHING BLOCK 27/44

W <https://core.ac.uk/download/pdf/35351804.pdf>

W. D. Kingery, H. K. Bowen, D. R. Uhlman, Introduction to Ceramics, 2

82%

MATCHING BLOCK 24/44

W [https://www.researchgate.net/publication/28254 ...](https://www.researchgate.net/publication/28254...)

NO₃)₂.6H₂O), nickel nitrate (Ni(NO₃)₂.6H₂O), ferric nitrate (Fe(NO₃)₃.9H₂O) and citric acid (C₆H₈O₇) were utilized for the synthesis

83%

MATCHING BLOCK 28/44

W [https://www.researchgate.net/publication/29207 ...](https://www.researchgate.net/publication/29207...)

Then, the solution was kept on a hot plate at 80°C with continuous stirring until

50%

MATCHING BLOCK 25/44

W <http://www.jetir.org/papers/JETIR2010314.pdf>

using Debye Scherer's equation [32], $\lambda = 0.9 \beta \cos \theta$ (1) Where θ is the Bragg's angle, λ is the wavelength of X-rays and β is the full-width half- maximum (FWHM). The

73%

MATCHING BLOCK 26/44

W [https://www.researchgate.net/publication/28254 ...](https://www.researchgate.net/publication/28254...)

Ni_{0.4} Cu_{0.3} Zn_{0.3} Fe₂ O₄ doped with TiO₂ additive were synthesized by sol gel method

73%

MATCHING BLOCK 44/44

W [https://www.researchgate.net/publication/25161 ...](https://www.researchgate.net/publication/25161...)

to vibrations of the metal ion-oxygen bonds in tetrahedral and octahedral sites respectively [42]. The

75%

MATCHING BLOCK 31/44

W [https://www.researchgate.net/publication/22937 ...](https://www.researchgate.net/publication/22937...)

The magnetic properties of the ferrites were explored at room temperature by using vibrating sample magnetometer. The hysteresis

52%

MATCHING BLOCK 29/44

W [https://docplayer.net/150337558-Doctor-of-phil ...](https://docplayer.net/150337558-Doctor-of-phil...)

The range of values of IS indicated that Fe ions exist in 3+ valence state with high spin configuration [54]. The

62%

MATCHING BLOCK 30/44

W <http://www.jetir.org/papers/JETIR2010314.pdf>

$p = \frac{C}{A \epsilon_0} \left(\frac{d}{A} \right)^2$ (17) Where C is capacitance, d is thickness, A is the cross-sectional area of the pellet and ϵ_0 is permittivity of free space.

68%

MATCHING BLOCK 33/44

W [https://www.researchgate.net/publication/22948 ...](https://www.researchgate.net/publication/22948...)

due to the fact that after a certain frequency of external alternating field, the electronic exchange between Fe 2+ and Fe 3+ does not follow the field. 5.3.10.2

93%

MATCHING BLOCK 32/44

W [https://docplayer.net/150337558-Doctor-of-phil ...](https://docplayer.net/150337558-Doctor-of-phil...)

B. G. Toksha, S. E. Shirsath, M. L. Mane, S.M. Patange, S. S. Jadhav, K. M. Jadhav, J. Phys. Chem. ,C 115 (2011) 20905 [9]

100%

MATCHING BLOCK 37/44

W [https://www.researchgate.net/publication/22193 ...](https://www.researchgate.net/publication/22193...)

B.G. Toksha, S.E. Shirsath, S.M. Patange, K.M. Jadhav,

70%

MATCHING BLOCK 38/44

W [https://www.researchgate.net/publication/32233 ...](https://www.researchgate.net/publication/32233...)

J.Magn.Magn.Mater, 401(2016) 16 [39] S. Thota, S.C. Kashyap, S.K. Sharma, V.R. Reddy,

80%

MATCHING BLOCK 34/44

W <http://www.jetir.org/papers/JETIR2010314.pdf>

J. C. Maxwell. Electricity and magnetism 1 Oxford: Oxford University Press, (1929) [62] K.W. Wagner.

44%

MATCHING BLOCK 35/44

W [https://docplayer.net/150337558-Doctor-of-phil ...](https://docplayer.net/150337558-Doctor-of-phil...)

in percentage of tetrahedral and octahedral sites of Fe 3+ ions for TiO 2 doped Ni 0.4 Cu 0.3 Zn 0.3 Fe 2 O 4 ferrite derived from Mössbauer spectra recorded at room temperature.

42%

MATCHING BLOCK 36/44

W [https://docplayer.net/150337558-Doctor-of-phil ...](https://docplayer.net/150337558-Doctor-of-phil...)

Sample Iron site Γ (mm/s) IS (mm/s) QS (mm/s) H hf (Tesla) A (%) 0% Sextet A 0.69 ± 0.02 0.29 ± 0.01 -0.02 ± 0.01 47.5 ± 0.1 67 Sextet B 1.07 ± 0.07 0.32 ± 0.02 0.02 ± 0.01 42.4 ± 0.1 33 2% Sextet A 0.73 ± 0.03 0.29 ± 0.01 0.03 ± 0.02 47.1 ± 0.1 70 Sextet B 0.73 ± 0.03 0.41 ± 0.02 -0.01 ± 0.01 41.9 ± 0.1 30 5% Sextet A 0.74 ± 0.02 0.29 ± 0.01 0.01 ± 0.02 47.1 ± 0.1 72 Sextet B 0.74 ± 0.02 0.36 ± 0.02 0.07 ± 0.04 41.6 ± 0.1 28 10% Sextet A 0.76 ± 0.01 0.29 ± 0.01 -0.02 ± 0.02 47.5 ± 0.1 71 Sextet B -0.76 ± 0.01 0.29 ± 0.02 -0.05 ± 0.02 42.7 ± 0.1 29 Chapter 5 98 A.

58%

MATCHING BLOCK 43/44

W [https://www.researchgate.net/publication/25161 ...](https://www.researchgate.net/publication/25161...)

crystallite size was obtained using Debye-Scherer's formula and it was found that crystallite size of the

90%

MATCHING BLOCK 39/44

W [https://www.researchgate.net/publication/28254 ...](https://www.researchgate.net/publication/28254...)

The elastic constants initially increased with an increase in TiO 2 up to 1 wt % and then

100%

MATCHING BLOCK 40/44

W [https://www.researchgate.net/publication/28254 ...](https://www.researchgate.net/publication/28254...)

to study the dielectric properties within 50 Hz to 5 MHz range of the frequency. The dielectric constant (

96%

MATCHING BLOCK 41/44

W

[https://www.researchgate.net/publication/28254 ...](https://www.researchgate.net/publication/28254...)

decreased continuously with increased frequency for all the selected samples at room temperature revealing normal dielectric behavior of ferrites. Also, the AC conductivity was increased with an increase in the frequency of all the selected samples. Cole-Cole plots were obtained for all

100%

MATCHING BLOCK 42/44

W

[https://www.researchgate.net/publication/28254 ...](https://www.researchgate.net/publication/28254...)

single semicircle which indicates that the electrical conduction process appears only due to grain boundaries. 6.3

Hit and source - focused comparison, Side by Side

Submitted text As student entered the text in the submitted document.

Matching text As the text appears in the source.

1/44	SUBMITTED TEXT	21 WORDS	90% MATCHING TEXT	21 WORDS
<p>The elastic constants initially increased with an increase in TiO₂ up to 1 wt. % and then</p>		<p>The elastic constants initially increase with an increase in TiO₂ up to 1 wt % and then</p>		
<p>W https://www.researchgate.net/publication/282545713_Electrical_and_Dielectrical_Properties_of_Low- ...</p>				

2/44	SUBMITTED TEXT	39 WORDS	96% MATCHING TEXT	39 WORDS
<p>frequency for all the selected samples at room temperature revealing normal dielectric behavior of ferrites. Also, the AC conductivity was increased with an increase in the frequency of all the selected samples. Cole-Cole plots were obtained for all</p>		<p>frequency for all the selected samples at room temperature revealing normal dielectric behavior of ferrites. Also, the AC conductivity was increased with an increase in the frequency for all the selected samples. Cole-Cole plots were obtained for all</p>		
<p>W https://www.researchgate.net/publication/282545713_Electrical_and_Dielectrical_Properties_of_Low- ...</p>				

3/44	SUBMITTED TEXT	16 WORDS	100% MATCHING TEXT	16 WORDS
<p>single semicircle which indicates that the electrical conduction process appears only due to grain boundaries.</p>		<p>single semicircle which indicates that the electrical conduction process appears only due to grain boundaries.</p>		
<p>W https://www.researchgate.net/publication/282545713_Electrical_and_Dielectrical_Properties_of_Low- ...</p>				

4/44	SUBMITTED TEXT	34 WORDS	75% MATCHING TEXT	34 WORDS
<p>H The relative permeability is given by the ratio of the magnetic permeability to that of free space = 0</p>		<p>H (1.2) The relative permeability is defined by the ratio of μ/μ_0 magnetic permeability to that of free space.</p>		
<p>W https://docplayer.net/150337558-Doctor-of-philosophy.html</p>				

5/44	SUBMITTED TEXT	24 WORDS	50% MATCHING TEXT	24 WORDS
<p>to the intrinsic atomic level interaction among metal ions and oxygen. This enables the ferrite to find out applications at maximum frequencies and</p>		<p>to the intrinsic atomic level interface between oxygen and metal ions, ferrite has higher resistivity compared to ferromagnetic metals. This enables the ferrite to find out applications at higher frequencies and</p>		
<p>W https://docplayer.net/150337558-Doctor-of-philosophy.html</p>				

6/44	SUBMITTED TEXT	13 WORDS	87% MATCHING TEXT	13 WORDS
<p>The properties of spinel ferrites depend on distribution of cations between the</p>		<p>the magnetic properties of spinel ferrites depend strongly on the distribution of cations between the</p>		
<p>W http://pr.hec.gov.pk/jspui/bitstream/123456789/2067/2/1603S.pdf</p>				

8/44	SUBMITTED TEXT	34 WORDS	100% MATCHING TEXT	34 WORDS
<p>A. Hagfeldth, M. Gratzel, Chem. Rev., 95(1995) 49 [14] S. Prasad, N. S. Gajbhiye, J. Alloys Compd. , 265 (1998) 87 [15] B. Viswanathan, V.R.K. Murthy: Ferrite Materials. Springer Verlag, Berlin,(1990) [16]</p>		<p>A. Hagfeldth, M. Gratzel, Chem. Rev. 95 (1995) 49. [2] S. Prasad, N. S. Gajbhiye, J. Alloys Compd. 265 (1998) 87. [3] B. Viswanathan, V.R.K. Murthy: Ferrite Materials. Springer Verlag, Berlin (1990) [4]</p>		
<p>W https://www.researchgate.net/profile/Carlos_Arean/post/What_the_types_of_ferrites/attachment/59d6 ...</p>				

9/44	SUBMITTED TEXT	42 WORDS	41% MATCHING TEXT	42 WORDS
<p>is smaller than that of the B lattice (M B). Therefore net saturation magnetization (Ms) is represented as $M_s = M_B - M_A$</p>		<p>is greater than that of the A lattice (M A) so that the resultant saturation magnetization (M S) may be written as $M_S = M_B - M_A$. 1.1.2.3.</p>		
<p>W http://repository.sustech.edu/bitstream/handle/123456789/9342/Catalytic%20Activity%20of%20Prepare ...</p>				

7/44	SUBMITTED TEXT	25 WORDS	90% MATCHING TEXT	25 WORDS
<p>E. Shirsath, B. G. Toksha, M. L. Mane, V. N. Dhage, D. R. Shengule, K. M. Jadhav, Powder Technology, 212 (2011) 218 [17] S.</p>		<p>E. Shirsath. B. G. Toksha, M. L. Mane, V. N. Dhage, D. R. Shengule and K. M. Jadhav, Powder Technol. 212 (2011) 218. [28] S.</p>		
<p>W https://docplayer.net/150337558-Doctor-of-philosophy.html</p>				

18/44	SUBMITTED TEXT	27 WORDS	67% MATCHING TEXT	27 WORDS
<p>dielectric constant (ϵ'), loss tangent ($\tan\delta$) and AC conductivity as a function of frequency in the range 50 Hz to 5 MHz at room temperature.</p>		<p>dielectric constant (ϵ'), dielectric loss tangent ($\tan\delta$) and AC conductivity (σ_{ac}) were as a function of ϵ' and frequency the range from 100 to 1 MHz at room temperature.</p>		
<p>W https://www.researchgate.net/publication/223682590_Electrical_conductivity_of_nickel-zinc_and_Cr_ ...</p>				

14/44	SUBMITTED TEXT	15 WORDS	95% MATCHING TEXT	15 WORDS
<p>of the pellet, ϵ_0 is the permittivity of the free space,</p>		<p>of the pellet, and ϵ_0 is the permittivity of the free space.</p>		
<p>W https://www.researchgate.net/publication/282545713_Electrical_and_Dielectrical_Properties_of_Low- ...</p>				

22/44	SUBMITTED TEXT	15 WORDS	96% MATCHING TEXT	15 WORDS
<p>Introduction The study of spinel ferrite is of great importance from both fundamental and</p>		<p>INTRODUCTION The study of spinel ferrite is of great importance from both the fundamental and</p>		
<p>W https://www.researchgate.net/publication/269564409_Temperature_and_Frequency_Dependent_Permeabili ...</p>				

16/44	SUBMITTED TEXT	65 WORDS	50% MATCHING TEXT	65 WORDS
<p>in the range 50Hz to 5 MHz. The dielectric constant was estimated using formula; $A d C p \dots$ (1) Where C_p is parallel capacitance, d is thickness</p>		<p>in the frequency range 20 Hz to 1 MHz. The real part of the dielectric constant (ϵ') was estimated using the equation [39]. $A t C p \dots$ (3) Where C_p is capacitance, t is thickness,</p>		
<p>W http://www.jetir.org/papers/JETIR2010314.pdf</p>				

17/44	SUBMITTED TEXT	25 WORDS	58% MATCHING TEXT	25 WORDS
<p>in the lattice constant may be due to the difference in ionic radii of Ta, Ni, Cu, Zn and Fe ions. The ionic radii of</p>		<p>in lattice constant can be attributed to the difference in ionic radii of Ni^{2+} (0.69Å), Cu^{2+} (0.724 Å) and Fe^{3+} (0.67Å) ions. The average ionic radii of</p>		
<p>W https://docplayer.net/150337558-Doctor-of-philosophy.html</p>				

23/44	SUBMITTED TEXT	29 WORDS	70% MATCHING TEXT	29 WORDS
	Scherrer's formula [29] $D = 0.9 \lambda \beta \cos \theta$ (3) Where λ is the wavelength of x-rays, β is the full width at half-maximum (FWHM) and θ is the		Scherrer's formula [24] $D = \frac{0.9 \lambda \beta \cos \theta}{3}$ where D is the crystallite size, λ is the wavelength of x-rays (1.54 Å), β is the full width at half maximum, and θ is the	
	W https://www.researchgate.net/publication/223349848_Preparation_of_nanocrystalline_MnFe2O4_by_dopi...			

19/44	SUBMITTED TEXT	15 WORDS	78% MATCHING TEXT	15 WORDS
	can also be justified on the basis of exchange interactions between tetrahedral and octahedral		can also be explained on the basis of exchange interaction between ions at tetrahedral (A) and octahedral (
	W http://pr.hec.gov.pk/jspui/bitstream/123456789/2067/2/1603S.pdf			

20/44	SUBMITTED TEXT	5 WORDS	100% MATCHING TEXT	5 WORDS
	E.Shirsath, R.H.Kadam, S.M.Patange, M.L.Mane,		E. Shirsath, R. H. Kadam, S. M. Patange, M. L. Mane,	
	W https://docplayer.net/150337558-Doctor-of-philosophy.html			

21/44	SUBMITTED TEXT	12 WORDS	87% MATCHING TEXT	12 WORDS
	Reddy, K. V. Siva Kumar, V. R. K. Murthy, R. R. Reddy,		Reddy, K.V. Siva Kumar, V.R.K. Murthy, R. Ramakrishna Reddy,	
	W https://docplayer.net/150337558-Doctor-of-philosophy.html			

27/44	SUBMITTED TEXT	13 WORDS	87% MATCHING TEXT	13 WORDS
	W. D. Kingery, H. K. Bowen, D. R. Uhlman, Introduction to Ceramics, 2		W.D. Kingery, H.K. Bowen, D.R. Uhlmann, Introduction to Ceramics,	
	W https://core.ac.uk/download/pdf/35351804.pdf			

24/44	SUBMITTED TEXT	67 WORDS	82% MATCHING TEXT	67 WORDS
	NO ₃) ₂ ·6H ₂ O), nickel nitrate (Ni(NO ₃) ₂ ·6H ₂ O), ferric nitrate (Fe(NO ₃) ₃ ·9H ₂ O) and citric acid (C ₆ H ₈ O ₇) were utilized for the synthesis		NO ₃) ₂ ·6H ₂ O), magnesium NO ₃) ₂ ·6H ₂ O), ferric nitrate (Fe(NO ₃) ₃ ·9H ₂ O), citric acid (C ₆ H ₈ O ₇) were used for the synthesis.	
	W https://www.researchgate.net/publication/282545713_Electrical_and_Dielectrical_Properties_of_Low-...			

43/44	SUBMITTED TEXT	17 WORDS	58% MATCHING TEXT	17 WORDS
<p>crystallite size was obtained using Debye-Scherer's formula and it was found that crystallite size of the</p>		<p>crystallite size was calculated by the Debye-Scherrer formula and it was found that the average crystallite size of the</p>		
<p>W https://www.researchgate.net/publication/251616003_Enhancement_of_the_magnetic_properties_of_Ni-C ...</p>				

39/44	SUBMITTED TEXT	21 WORDS	90% MATCHING TEXT	21 WORDS
<p>The elastic constants initially increased with an increase in TiO₂ up to 1 wt % and then</p>		<p>The elastic constants initially increase with an increase in TiO₂ up to 1 wt % and then</p>		
<p>W https://www.researchgate.net/publication/282545713_Electrical_and_Dielectrical_Properties_of_Low- ...</p>				

40/44	SUBMITTED TEXT	19 WORDS	100% MATCHING TEXT	19 WORDS
<p>to study the dielectric properties within 50 Hz to 5 MHz range of the frequency. The dielectric constant (</p>		<p>to study the dielectric properties within 50 Hz to 5 MHz range of the frequency. The dielectric constant (</p>		
<p>W https://www.researchgate.net/publication/282545713_Electrical_and_Dielectrical_Properties_of_Low- ...</p>				

41/44	SUBMITTED TEXT	43 WORDS	96% MATCHING TEXT	43 WORDS
<p>decreased continuously with increased frequency for all the selected samples at room temperature revealing normal dielectric behavior of ferrites. Also, the AC conductivity was increased with an increase in the frequency of all the selected samples. Cole-Cole plots were obtained for all</p>		<p>decreased continuously with increased frequency for all the selected samples at room temperature revealing normal dielectric behavior of ferrites. Also, the AC conductivity was increased with an increase in the frequency for all the selected samples. Cole-Cole plots were obtained for all</p>		
<p>W https://www.researchgate.net/publication/282545713_Electrical_and_Dielectrical_Properties_of_Low- ...</p>				

42/44	SUBMITTED TEXT	18 WORDS	100% MATCHING TEXT	18 WORDS
<p>single semicircle which indicates that the electrical conduction process appears only due to grain boundaries. 6.3</p>		<p>single semicircle which indicates that the electrical conduction process appears only due to grain boundaries.</p>		
<p>W https://www.researchgate.net/publication/282545713_Electrical_and_Dielectrical_Properties_of_Low- ...</p>				